



**HAL**  
open science

# Developement of targeted RNA delivery agents for a pattern-recognition receptor

Tony Rady

► **To cite this version:**

Tony Rady. Developement of targeted RNA delivery agents for a pattern-recognition receptor. Other. Université de Strasbourg, 2021. English. NNT : 2021STRAF046 . tel-04398264

**HAL Id: tel-04398264**

**<https://theses.hal.science/tel-04398264>**

Submitted on 16 Jan 2024

**HAL** is a multi-disciplinary open access archive for the deposit and dissemination of scientific research documents, whether they are published or not. The documents may come from teaching and research institutions in France or abroad, or from public or private research centers.

L'archive ouverte pluridisciplinaire **HAL**, est destinée au dépôt et à la diffusion de documents scientifiques de niveau recherche, publiés ou non, émanant des établissements d'enseignement et de recherche français ou étrangers, des laboratoires publics ou privés.

**ÉCOLE DOCTORALE DES SCIENCES CHIMIQUES**

**Laboratoire de Conception et Application de Molécules Bioactives**

**THÈSE** présentée par :

**Tony RADY**

soutenue le : **10 décembre 2021**

pour obtenir le grade de : **Docteur de l'université de Strasbourg**

Discipline/ Spécialité : **Chimie Biologique et Thérapeutique**

**Développement de systèmes de délivrance ciblés de  
molécules d'ARN pour un récepteur de  
reconnaissance de motifs moléculaires**

**THÈSE dirigée par :**

**M. WAGNER Alain**

Directeur de recherche, Université de Strasbourg

**RAPPORTEURS :**

**M. JOUBERT Nicolas**

Maître de conférences, Université de Tours

**M. SPRING David**

Professeur, Université de Cambridge

**EXAMINATEUR :**

**M. IMLER Jean-Luc**

Professeur, Université de Strasbourg

---

**AUTRE MEMBRE DU JURY :**

**M. BASSE Nicolas**

Docteur, Sanofi (encadrant)







## Aknowlegments

Ces travaux de recherches ont été réalisés conjointement entre l'équipe de Chimie Biofonctionnelle (BFC) de la faculté de pharmacie de Strasbourg pour la chimie et Sanofi pour la biologie. Je remercie donc Sanofi pour tout, que ce soit pour le financement, le cadre de travail dont j'ai pu disposer pour la biologie, ainsi que pour les personnes compétentes et passionnées que j'y ai rencontré. J'aimerais aussi remercier l'ANRT pour avoir participé conjointement au financement de cette thèse.

I would like to thank Dr Nicolas Joubert, Pr David R. Spring, and Pr Jean-Luc Imler, for accepting to evaluate these works. Par la même occasion, je remercie les Dr Alexandre Specht et Pr Christophe Biot pour avoir participé au suivi de ma thèse.

J'ai trouvé l'inspiration d'écrire ces quelques lignes ce dimanche 26 septembre à 2h21 du matin. Et pour commencer, j'aimerais remercier Alain, Nicolas et Guilhem pour avoir été de super encadrants de thèse, ce qui m'a permis de passer 3 superbes années à ~~m'amuser~~ travailler sur ces passionnants sujets assez librement. J'ai pu apprendre et comprendre une infinité de choses grâce à vous, notamment car vos portes étaient souvent ouvertes pour que je vienne parler « 5 petites minutes ».

Je vais ensuite remercier tous les membres de Sanofi Strasbourg, dont une bonne partie m'a aidé à réaliser ces travaux. Tout d'abord Gilbert pour m'avoir accueilli sur le site, mais également Laurence, qui m'a appris les techniques de bases de la culture cellulaire – ce travail n'existerait pas sans ton encadrement au début de ma thèse. Je voudrai ensuite remercier Nathalie qui m'a pas mal épaulée pour faire la microscopie, mais également Véronique pour ses nombreux conseils et surtout ta pipette multi-canaux qui m'a sauvé la vie. Je tiens aussi à remercier Anne, Neila, Rama et également Jean-Georges pour votre expérience et surtout votre constante bonne humeur. Enfin, je tiens à remercier profondément Safia, Renaud et Emilie, pour m'avoir aidé à comprendre l'immunologie et la biophysique, deux domaines qui étaient très obscurs pour moi – cependant je peux presque admettre avoir fini ma transition vers la biologie, un peu grâce à vous. Ensuite, Hervé et Philippe pour avoir été présents lors de la plupart de mes réunions et pour vos précieux conseils tout au long du projet.

Je tiens ensuite à remercier les membres de mon équipe académique BFC (pour Big Fat Chemistry) pour les conseils, l'aide, les discussions scientifiques et surtout les gros fous rires qu'on a partagé ces trois dernières années. Commençons par ceux avec qui j'ai passé 80% des délires les plus... particuliers, nous qui formions un trio faisant parti des meubles du labo : les « thésards 24/24 ».

Un gros merci à Charlotte, qui a été la première à m'accueillir dans l'équipe, d'avoir été le petit soleil dans ce labo pendant mes deux premières années. Tu m'as fait découvrir Strasbourg et ses 4-5 bars ainsi que les « joies » du thésard, un statut qu'on a quand même apprécié, il faut le dire. On a quand même passé la moitié du temps à dire des conneries, et le reste à manger des glaces ou tes exquis brownies. J crois que je ne me lasserai jamais de ta franchise assez surprenante, et je te remercie pour être qui tu es.

Mais que dire de Victor... franchement cette thèse n'aurait pas eu la même saveur sans toi. Souvent comparés, voire confondus, je ne pense pas que j'aurai pu trouver meilleur acolyte-chercheur que toi pour ces trois années. Ton sens de l'humour « particulier », ton objectivité et ta grande ouverture d'esprit sont parmi tes nombreux atouts. Et pour toute cette aide, ces discussions scientifiques (et pas que !) je te remercie vraiment. En plus de très nombreux délires, tu as toujours été là pour discuter de nos thèses, à apporter des idées ou des solutions. En plus, grâce à toi, je me suis senti moins bizarre à apprécier les sciences mal aimées, comme la physique ou les maths – je crois qu'il y a encore quelques équations écrites dans notre labo. Je me souviendrai beaucoup de nos nombreuses soirées/week-end au labo, à manger des pizzas, des bouboules Haribo ou encore des Kinder Country/Bueno – même si je n'arrive pas à pardonner le vol odieux que tu as fait, en vidant mon placard généreusement rempli par les stagiaires. Mais, comme disait Charlotte, « j'étais ton Frodon, tu étais mon Sam, à deux dans la quête de l'anneau ».

On ne va pas se mentir, Julien est quand même le gars le plus bizarre du labo, et c'est pour ça que je l'apprécie autant. Toujours prêt à déconner et à manger gras, on a quand même souvent été comparés, à juste titres, étant donné qu'on est de véritables copié/collé l'un de l'autre. Même si nous avons quelques discordes en matière de cervoises, j'ai passé de superbes moments avec toi, à essayer de transmettre mes quelques connaissances et t'aider à réaliser ton « concept ».

C'est maintenant au tour de Enes « Nounours », le frerot un peu râleur mais au grand cœur, mais surtout très à cheval sur « les proportions »... Ces petites expériences ainsi que tes quelques punchlines ont été parmi les moments les plus mémorables de ces trois années – je crois que je me souviendrai beaucoup de ton poker face lors de nos parties de cartes le midi, ainsi que de ton petit chat qui m'a un peu détruit la main il y a un mois.

Je passe maintenant à la nouvelle génération de thésards, ceux qui m'ont plusieurs fois fait remarquer que la thèse, bah c'était fini pour moi... La Taupe, qui se reconnaitra, j'espère que tu te souviendras de nos fréquentes discussions autour de ta chimie/biologie et des quelques petites astuces que j'ai essayé de te partager – ça devrait au moins compenser les nombreux gâteaux que tu as fait. Val' La Rage, ta constante bonne humeur a été une bouffée d'air frais

dans ce labo... sauf lors de nos parties de Danish, où tu révélais vraiment ta personnalité. Mais s'il y a une personne dont j'ai pris plaisir à ~~emmerder~~ « prendre sous mon aile » pendant un an, c'est bien Robin. Tu m'as probablement plus appris que l'inverse, et je pense que ça nous a fait tous les deux évoluer – j'espère que je t'ai été utile pendant tes débuts de thèse, et que ça va faire de toi un grand ~~épicer~~ scientifique.

It's time for Lorenzo, the "fake Italian" which has become officially the "bip-bip" of Lorène's car. I really liked to work with you for the acetal project, but it was also a pleasure to share some drinks. Although we mainly talked about our problems with the chemistry of that @&!\*£ acetal, we finally made it – that paper couldn't be publishable without your help. I would also like to thank our Greek guy, Ilias. Even though we did not work closely together, I'll remember our discussions, your kindness and your wonderful moussaka. I wish to thank both of you for everything I've learnt thanks to you.

J'aimerai ensuite remercier tous les postdocs, notamment les « anciens », d'avoir été là à mes débuts, et de m'avoir transmis un paquet de choses. Par-là, je pense forcément à Sylvain, qui a clairement joué un rôle déterminant dans mes 3 premiers mois, ou à Fabien et David, qui ont poursuivi cet effort pendant encore un an. S'en suit le gang des ukrainiens strasbourgeois, avec Igor, Sasha et Sergii, qui ont tous été de grands conseillers pendant ma première année. J'aimerai ensuite remercier la très discrète Héroïse « Schtroumpfette amatrice de glace », qui n'a été là que pendant mes 6 derniers mois, mais dont la thèse m'a pas mal aidé à rédiger la mienne. Finally, I'd like to thank Ondrej, a nice person and a good scientist, for every tip regarding postdocs applications.

Je tiens à remercier ensuite les permanents de notre équipe, en particulier Michel qui m'a littéralement tout appris de la synthèse organique. J'ai particulièrement aimé notre étroite collaboration sur le projet BCN, à nous on a enfin réussi à l'obtenir ! Marc, j'espère que tu souviendras de nos nombreuses discussions biologiques et nos après-midis passés devant le microscope confocal ou le cytomètre. Encore une fois, merci pour tes nombreux petits tips de culture cellulaire. Ensuite, Ketty la semi-permanente avec qui j'ai passé de bons moments également, surtout à discuter de biophysique et à manger (encore) des gâteaux. Enfin, que serais-je sans Martine, notre centri, qui a religieusement été présente pour faire mes conjugués.

Je remercie ensuite les non-BFC. Tout d'abord, ceux de « l'autre côté » du couloir, Florence et Célian, avec qui j'ai eu pas mal de fous rires ces trois années. Connor et Karim, je vous remercie pour nos nombreuses discussions d'immuno, j'ai réussi à mieux comprendre pas mal de choses grâce à vous deux ! Ensuite, et pas des moindres, Clément et Benoit et Michaël « Momo » pour votre présence pendant trois ans, pour les très nombreuses fois où l'on a rigolé



de nos nombreuses galères, de nos hypothétiques Nature/Science, à jouer au poker... Je voudrai ensuite remercier Stéphane qui a toujours été présent pour faire mes analyses de masse, et me sortir de superbes spectres. Je dois ensuite remercier les quelques stagiaires qu'on a eu, même si celle qui m'a le plus impressionné restera Sybille « l'enfant prodige », nièce de Guilhem, promise à un grand avenir scientifique. 14 ans quand même... Pour finir, un grand merci à Alexandra Elbakyan et Aaron Swartz, sans qui rien n'aurait pas été possible.

Je tiens également à remercier mon ancienne équipe de Lille, notamment Christophe, Cédric, Faustine et Yann, qui ont tous réussi à me transmettre le virus de la recherche. En parlant de virus, je ne remercie pas le Sars-CoV-2 qui m'a un peu cassé ma deuxième année...

Merci à vous tous, sincèrement, cette thèse existe en grande partie grâce aux nombreuses discussions qu'on a eu ces trois dernières années. Petite touche finale, un énorme merci à mes gros chats ainsi qu'à Lorène, qui ont tous toujours été mes plus grands fans, et ce depuis plus de 10 ans. Je te remercie pour tout, en particulier pour avoir enduré mes horaires assez conséquents. Je ne crois pas que j'aurai eu une aussi grande motivation sans ton soutien quotidien, toi qui m'as souvent rappelé que la vie, ce n'est pas que la thèse (quoi que...).

## List of abbreviations

5'-pp	5'diphosphate	LRR	Leucine-Rich Repeats
5'-ppp	5'triphosphate	mAb	Monoclonal antibody
ABF	4-azido-benzoyl fluoride	MAVS	Mitochondrial antiviral-signaling protein
ADC	Antibody-drug conjugate	MDA5	Melanoma Differentiation-Associated protein 5
ADCC	Antibody-dependent cell cytotoxicity	MDR1	Multi-Drug Resistance protein 1
ADCP	Antibody-dependent cellular phagocytosis	MMAE	Monomethyl auristatin E
AIM2	Absent in Melanoma 2	MMAF	Monomethyl auristatin F
AOC	Antibody-oligonucleotide conjugate	mRNA	Messenger RNA
ARC	Antibody-RNA conjugate	N/P	Amine/phosphate ratio
ASC	Apoptosis-associated Speck-like protein with a Caspase-recruitment domain	NF- $\kappa$ B	Nuclear Factor- $\kappa$ B
ATP	Adenosine triphosphate	NHS	<i>N</i> -hydroxysuccinimide
BCN	Bicyclo[6.1.0]nonyne	NLR	NOD-like receptor
BHQ-2	Black Hole Quencher 2	NLRC	NOD-like-receptor-Caspase
bp	Base-pairs	NLRP	NOD-like-receptor-Pyrin
CALR	Calreticulin	NOD	Nucleotide-oligomerization Domain
CARD	Caspase Activation and Recruitment Domain	PABA	<i>Para</i> -aminobenzyl alcohol
CD	Cluster of differentiation	PABC	<i>Para</i> -aminobenzoyl carbamate
cGAMP	Cyclic GMP-AMP	pAF	<i>Para</i> -acetyl phenylalanine
cGAS	Cyclic Guanosine monophosphate (GMP)-Adenosine monophosphate (AMP) Synthase	PAMP	Pathogen-Associated Molecular Patterns
Chk2	Checkpoint kinase 2	PBD	Pyrralobenzodiazepine
CLR	C-type lectin	PBMC	Peripheral Blood Mononuclear Cells
CMC	Complement-mediated cytotoxicity	PBS	Phosphate-buffered saline
CpG	Cytidine-guanosine dinucleotide	PD1	Programmed cell Death 1
CPP	Cell-penetrating peptide	PD1	Programmed Cell Death 1
CTD	C-terminal domain	PD-L1	Programmed cell Death ligand 1
CTLA4	Cytotoxic T Lymphocyte-Associated protein 4	PD-L1	Programmed Cell Death-Ligand 1
Cy3/5	Cyanine 3/5	PEG	Polyethylene glycol
DAMP	Damage-associated Molecular Patterns	PFP	Pentafluorophenol
DAR	Drug-to-Antibody Ratio	PK-PD	Pharmacokinetic-pharmacodynamic
DBCO	Dibenzocyclooctyne	PLK1	Polo-like Kinase 1
DCM	Dichloromethane	PNP-Cl	<i>Para</i> -nitrophenylchloroformate
DC-SIGN	Dendritic Cell-Specific Intercellular adhesion molecule-3-Grabbing Non-Integrin	poly (I:C)	Polyinosinic:polycytidylic acid
DNA	Deoxyribonucleic acid	PRR	Pattern-Recognition Receptor

DoC	Degree of conjugation	PYD	Pyrin domain
DSB	Double-strands breaks	RIG-I	Retinoic acid-inducible gene I
dsRNA	Double-stranded RNA	RISC	RNA-induced silencing complex
dsRNA-5'-ppp	5'-triphosphate dsRNA	RLR	RIG-I-like receptors
EEDQ	<i>N</i> -Ethoxycarbonyl-2-ethoxy-1,2-dihydroquinoline	RNA	Ribonucleic acid
EphA2	Ephrin type-A receptor 2	RNAi	RNA interference
Fab	Antigen-binding fraction	ROS	Reactive Oxygen Species
FACS	Fluorescence-Assisted Cell Sorting	RP-HPLC	Reverse-Phase High-Performance Liquid Chromatography
Fc	Constant Fraction	scFv	single-chain variable fragment
FcgR	Fcg receptors	SDS-PAGE	sodium dodecyl sulphate–polyacrylamide gel electrophoresis
FcRn	Neonatal Fc receptor	SEC	Size-exclusion chromatography
FDA	Food and Drug Administration	SEC-ESI-MS	Size-exclusion chromatography–ElectroSpray Ionization–Mass spectrometry
FITC	Fluorescein isothiocyanate	shRNA	Short hairpin RNA
FRET	Förster resonance energy transfer	siRNA	Small interfering RNA
GalNAc	<i>N</i> -acetylgalactosamine	siRNA-5'-ppp	5'-triphosphate siRNA
GAPDH	Glyceraldehyde 3-phosphate dehydrogenase	SLR	Stem-loop RNA
HAUT	(diméthylamino)- <i>N,N</i> -diméthyl(3H-[1,2,3]triazolo[4,5-b]pyridin-3-yloxy)méthaniminium	SMCC	Succinimidyl-4-( <i>N</i> -maleimidomethyl)-cyclohexane-1-carboxylate
HC	Heavy Chain	SNALP	Stable Nucleic Acid-Lipid Particle
HER2	Human Epidermal growth factor Receptor 2	SPAAC	Strain-promoted Alkyne-Azide cycloaddition
HMGB1	High-mobility group box 1	SPDB	<i>N</i> -succinimidyl-4-(2-pyridyldithio)butyrate
HRP	Horseradish peroxidase	SPR	Surface Plasmon Resonance
ICD	Immunogenic Cell Death	ssDNA	Single-Stranded DNA
IFN	Interferon	ssRNA	Single-stranded RNA
IFNAR	Interferon $\alpha$ receptor	STING	Stimulator of interferon genes
IgG	Immunoglobuline G	TAMRA	Tetramethylrhodamine
IKK	I $\kappa$ B kinase	TBK1	TANK-binding kinase 1
IRF 3/7	Interferon Response Factor 3/7	t-BuOK	Potassium <i>tert</i> -butoxide
ISG	IFN-stimulated genes	TFFH	Tetramethylfluoroformamidinium hexafluorophosphate
ISGF3	Interferon-Stimulated Gene Factor 3	TLR	Toll-like receptors
IVT	<i>in vitro</i> transcription	TME	Tumor microenvironment
KO	Knock-out	TRAIL	TNF-related apoptosis-inducing ligand
LC	Light Chain	Ub	Ubiquitin
LGP2	Laboratory of Genetics and Physiology 2	VH	Variable Heavy Chain
LPS	Lipopolysaccharide	VL	Variable Light Chain

## I. Foreword

Pattern-recognition receptors (PRR) are families of proteins responsible for the defense of an organism against pathogens, thus inducing immune responses upon binding to an exogenous ligand. Therefore, different strategies to target them has emerged in order to prevent or treat infectious diseases. Besides, these proteins have also intrigued scientists for immuno-oncology purposes, due to their high ligand-specificity, low required amount of intracellular ligand, and the subsequent activation of numerous signaling pathways. One of these promising PRR is RIG-I, activated by cytosolic double-stranded RNA terminated by a 5'-triphosphate group. In addition to RIG-I signaling, such RNA can also inhibit the expression of a specific gene by RNA interference mechanism, therefore giving access to synergistic systems. Accordingly, methodologies to deliver such RNA inside tumors are highly desired.

The field of RNA delivery systems has been growing for 30 years, and these progresses led to the recent commercialization of, for example, mRNA vaccines. However, current methods to deliver RNA suffer from drawbacks, among which the lack of cell-specificity, leading to a limited scope of applications, especially in oncology. Therefore, the development of targeted vectors for RNA is highly desired in order to expand the repertoire of diseases addressable by RNA-based therapeutic approaches. Based on a format analogous to antibody-drug conjugates, many studies using antibody-RNA conjugates (ARC) have been published recently, demonstrating their strong therapeutic potential. In addition to covalent methods to attach the RNA and antibody, non-covalent ARC also appeared as a promising strategy, as the development of a modular and efficient RNA targeted delivery system would open a wide range of therapeutic possibilities.

This work was thus devoted to the development of antibody-based targeted delivery systems, able to specifically deliver a dual RIG-I-activating and PLK1-silencing RNA in cancer cells *via* an active targeting of a cell-surface antigen. If released in the cytosol, the RNA is supposed to activate RIG-I and simultaneously silencing PLK1, consequently leading to cell apoptosis and activation of antitumor immunity. Both covalent and non-covalent approaches were exploited. Regarding the covalent one, cleavable linkers were also explored with the aim to enhance the cytosolic RNA release.

This manuscript was accordingly structured in five chapters. In the introduction, RIG-I will be presented first, with an accent on its therapeutic potential. After a brief summary of current non-targeted RNA delivery systems, the field of targeted therapies and antibody-drug conjugate will pave the way for an exhaustive review regarding covalent antibody-RNA conjugates.

Following this introduction, the first project of this manuscript describes the development of a covalent ARC targeting cancer cells, activating RIG-I and silencing PLK1. Its design, synthesis and *in vitro* biological evaluation concerning different aspects of RIG-I or the delivery will be presented. Briefly, the synthesis of ARC was rapidly optimized, and we were able to observe both RIG-I and PLK1 effects simultaneously in cancer cell model. Moreover, by performing co-culture experiments with peripheral blood mononuclear cells (PBMC), the ARC was able to induce cancer cells killing in a RIG-I-dependent manner on RIG-I-depleted cells, suggesting an internalization of the ARC inside PBMCs and subsequent RIG-I activation. Immunofluorescence studies were also performed in order to study the trafficking of both the antibody and the RNA inside the cell.

As the covalent method seemed to be efficient in our case, one of the hypotheses was that the linker used for the ARC synthesis may be cleaved in biological media. Due to our linker's design, we thought that the strained-alkyne-alcohol attached by a carbamate group on the linker may be the point of weakness. Therefore, a synthetic strategy to obtain the same strained-alkyne but with a carboxylic acid was elaborated. This led to the development of two fluorogenic probes, only differing by the attachment moiety, either an amide or a carbamate. Under biological media, we observed that the carbamate was, in fact, cleaved in cells. Following these observations, we suggested that the ARC's linker was cleaved in cells, thus probably explaining part of the activity we observed in the first project.

We thus sought to increase the cleavability of the linker by using cleavable linkers commonly used in antibody-drug conjugates. A brief introduction about these linkers will introduce a fourth chapter about the development and the evaluation of a novel, acid-labile linker. Its design, synthesis and *in vitro* evaluation using fluorogenic probes will be presented. Satisfyingly, we observed that the novel linker was in fact more cleaved in cells compared to the gold-standard linker currently used in antibody-drug conjugates. Therefore, ARCs bearing cleavable linkers were produced and their biological activities compared to the non-cleavable ARC were evaluated. In addition, preliminary results regarding the use of our novel linker for antibody-drug conjugates will be presented.

As a last chapter, in order to explore peptide-based non-covalent ARC, cationic peptides able to strongly complex anionic RNAs were synthesized. A first non-covalent ARC was produced, highlighting the fact that such system would greatly benefit from molecularly-defined peptide-siRNA complexes. Therefore, different designs of cationic peptides, their syntheses and a method to evaluate their biophysical properties regarding RNA complexation will be presented.

## Table of contents

I. Foreword.....	11
II. Introduction .....	19
A. Introduction to pattern-recognition receptors.....	19
i. Membrane-bound PRR .....	20
1. Toll-like receptors .....	20
2. C-type lectin receptors.....	22
ii. Cytoplasmic PRR.....	22
1. NOD-like receptors .....	22
2. AIM2-like receptors.....	24
3. cGas/STING .....	24
4. RIG-I-like receptors.....	24
B. RIG-I-mediated detection of RNA and signaling pathways.....	25
i. Structure of RIG-I-like receptors.....	25
ii. Structural insights of RIG-I agonists .....	25
1. RNA's length.....	26
2. Impact of overhangs and base-pairing .....	26
3. Impact of secondary structures .....	26
4. Impact of 5'-phosphates.....	27
iii. RIG-I activation by dsRNA-5'-ppp.....	27
iv. Signal transduction .....	29
v. Biological effects following RIG-I activation .....	30
1. Direct effects of the IRF3/7 pathway .....	30
2. Direct effects of the NF- $\kappa$ B pathway.....	31
a. Intrinsic apoptosis .....	31
b. Extrinsic apoptosis .....	32
c. Pyroptosis .....	33
d. Immunogenic cell death (ICD).....	34
e. Reprogramming of the tumor microenvironment.....	34

C.	Strategies to activate RIG-I .....	37
i.	Small molecules acting on RIG-I's pathway.....	37
ii.	Non-selective molecules targeting RIG-I pathway in (pre)-clinical trials .....	38
iii.	Selective molecules targeting RIG-I pathway in (pre)-clinical trials .....	39
iv.	Synergies between RIG-I signaling and RNA interference .....	40
1.	Generalities regarding RNA interference .....	40
2.	siRNA-5'-ppp: combining both gene silencing and RIG-I signaling.....	42
3.	Polo-like Kinase 1 (PLK1) .....	43
a.	Biological roles in cancer therapy .....	43
b.	PLK1 inhibitors in clinical trials .....	44
c.	PLK1 silencing and synergies with RIG-I activation .....	45
D.	Delivery of siRNA-5'-ppp in tumors.....	45
i.	Generalities regarding the siRNA delivery methods currently in clinical phase III or FDA-approved .....	45
1.	Encapsulation into particles .....	45
2.	siRNA conjugates .....	46
ii.	Generalities regarding antibody-based targeted therapies.....	46
iii.	Antibody-drug conjugates.....	49
1.	Structures and mechanisms of action .....	49
2.	Therapeutic benefits of ADCs .....	51
3.	Limitations of ADCs .....	51
a.	Antigen-binding domain.....	51
b.	Heterogeneity of produced conjugate .....	52
c.	Internalization and trafficking.....	52
4.	Scope of drugs .....	53
a.	Microtubule-targeting payloads .....	53
b.	DNA-damaging payloads .....	54
5.	Resistance mechanism and potential novel payloads .....	56
E.	Antibody-siRNA conjugates .....	56

i.	Design of the conjugates .....	57
1.	Conjugation by protein-ligand interactions .....	57
2.	Direct conjugation .....	59
III.	Objectives of the thesis .....	70
IV.	Targeted delivery of immunostimulatory siRNA with dual mode of action, inducing both apoptosis and anti-tumor immunity .....	73
A.	Introduction .....	73
B.	Results and discussion .....	76
i.	Pre-functionalization of antibody .....	76
ii.	Synthesis of the conjugation linker .....	77
1.	Synthesis of the strained-alkyne moiety .....	78
2.	Synthesis of the oligoethylene glycol portion .....	78
iii.	Conjugation of the siRNA to the antibody and characterization .....	79
iv.	ARC <b>5</b> simultaneously activates RIG-I and silences PLK1 .....	82
v.	Validation of RIG-I effects: impact on apoptosis and immune stimulation .....	86
1.	Apoptosis activation by transfected siRNAs .....	86
2.	Impact of conjugates siRNAs on cell confluence .....	88
3.	ARC <b>5</b> activates PBMCs and anti-tumor immunity .....	89
4.	ARC <b>5</b> induces the release of calreticulin in A549 cells .....	91
vi.	Intracellular trafficking .....	92
1.	Internalization of the EphA2 antibody <b>1</b> .....	92
2.	Immunofluorescence by confocal microscopy .....	92
vii.	Plasma stability .....	94
C.	Conclusion .....	96
D.	Experimental part .....	97
V.	Development of bicyclo[6.1.0]nonyne carboxylic acid for the production of stable molecular probes .....	117
A.	Introduction .....	117
B.	Results and discussion .....	120
i.	Synthesis of BCN carboxylic acid <b>26</b> .....	120



ii.	Derivatization and kinetic studies .....	121
iii.	BCN-carboxylic acid conjugation to protein .....	123
iv.	BCN-carboxylic acid stability by FRET probe assay .....	124
C.	Experiment data .....	127
VI.	Enhancing siRNA release of covalent ARC with cleavable linkers .....	142
A.	Generalities regarding linkers used in FDA-approved antibody-drug conjugates.....	142
i.	Non-cleavable linkers .....	142
ii.	Cleavable-linkers.....	143
1.	Enzyme-cleavable linkers .....	144
2.	Acid-sensitive .....	145
3.	Reduction-cleavable .....	145
B.	A novel family of acid-cleavable and plasma-stable linker based on cyclic acetal motifs	146
i.	Introduction .....	147
ii.	Results and discussion.....	148
1.	Synthesis of FRET probes based on cyclic dimethoxybenzaldehyde acetal.....	148
2.	Evaluation of the cleavage and stability of acetal probes in acidic media .....	149
3.	Evaluation of intracellular cleavage.....	150
a.	Synthesis of FRET probe based on Val-Cit-PAB .....	150
b.	Cellular uptake and intracellular cleavage .....	152
iii.	Conclusion .....	156
iv.	Further developments .....	157
1.	Production of antibody-siRNA conjugates with the 1,3-dioxane linker .....	157
2.	Production of antibody-siRNA conjugates with the Val-Cit-PAB linker.....	158
3.	Production of antibody-drug conjugates with the 1,3-dioxane linker .....	162
a.	Derivatization of MMAF .....	162
b.	Derivatization of gemcitabine .....	162
c.	Planned strategy to produce ADCs .....	163
v.	Experimental part .....	164

VII. Non-covalent antibody-siRNA conjugates.....	185
A. Overview on currently reported non-covalent ARC .....	185
i. Supramolecular approaches.....	185
ii. Complexation with conjugated-cationic peptides .....	187
iii. Complexation with fused-cationic domains.....	191
B. Development of a synthetic strategy for non-covalent ARC.....	192
i. Introduction .....	192
ii. Results and discussion.....	193
1. Synthesis of a first antibody-peptide conjugate .....	193
2. Biophysical properties regarding siRNA binding.....	195
3. Biological assay and microscopy .....	197
4. Syntheses of different designs and binding affinity with siRNA .....	201
C. Conclusion and perspectives.....	206
D. Experimental part.....	207
VIII. General conclusion.....	215
IX. Annexes .....	<b>Erreur ! Signet non défini.</b>
X. References.....	243



## II. Introduction

### A. Introduction to pattern-recognition receptors

At the end of the 19<sup>th</sup> century, William Coley, an American surgeon, found a connection between cancerous patients developing infections and their own remission. Such recoveries were thought to be caused by an immune response from the patient against the infectious pathogen. This led to the development of Coley's toxins, a cocktail of heat-inactivated bacteria, which could promote cancer regression upon intratumoral injection. Although Coley never understood exactly how these toxins worked, this did not stop him from using this protocol to treat over a thousand cancer patients, resulting in the very first attempt to induce immune response to treat cancer and the earliest example of immunotherapy.<sup>1</sup> In addition, Coley's works paved the way to the discovery of proteins responsible for the protection of organisms from foreign microbes and viruses. These proteins, called Pattern-Recognition-Receptors (PRR) were first discovered in 1995 in plants<sup>2</sup> and drosophila, and were found to be essential for the recognition of foreign species.<sup>3</sup>

Discovered in 1997 in humans,<sup>4</sup> PRR recognize Pathogen-Associated Molecular Patterns (PAMP) and Damage-associated Molecular Patterns (DAMP). PAMP are molecules from exogenous organisms while DAMP are intracellular self-molecules that were excreted upon stress, both inducing signaling pathways upon detection by PRR. Downstream of these pathways, an inflammatory response characterized by a type-I and type-III interferons (IFN) and proinflammatory cytokines secretion protect the infected organism. These act as alert messages to neighboring cells, inducing the expression of IFN-stimulated genes (ISG) that will code for antiviral/antibacterial factors. These proteins, in addition to proinflammatory cytokines, will lead to the stimulation of the innate and the adaptive immunity to protect the organism against the pathogen.

PRR are characterized by the subcellular compartments in which they are localized and the type of PAMP they can recognize (e.g cytosolic DNA sensors are PRRs recognizing DNA in the cytosol as a PAMP). Based on their location, PRR can be divided into two groups: membrane-bound PRRs and cytosolic PRRs. Membrane-bound PRRs are composed of Toll-like receptors and C-type lectins, and cytosolic PRRs are composed of NOD-like receptors, Cytosolic DNA sensors and RIG-I-like receptors. Each of these families, along with their therapeutic potential, will be overviewed in the following pages (from page 20 to page 24), except for RIG-I, the main target of this thesis, which will be explained in detail (from page 25).

## i. Membrane-bound PRR

### 1. Toll-like receptors

Just one year after the work of Lemaitre *et al*<sup>3</sup> in Strasbourg that led to the 2011 Nobel Prize of Medicine to Jules Hoffmann about Toll receptor in drosophila, the very first human Toll-like receptor (TLR) was cloned.<sup>4</sup> These proteins represent our first defense lines against pathogens, and are certainly the most understood among PRRs.<sup>5</sup> Upon binding to their ligands, TLR activation promote both the transcription of pro-inflammatory cytokines and type-I IFN through NF- $\kappa$ B and IRF 3/7 pathways respectively.<sup>6</sup> Since the first cloning, the number of discovered human TLRs has been growing,<sup>7</sup> and is now composed of ten members in humans (thirteen if counting mice) dispatched between the plasma membrane and the endo/lysosomes. Among them, TLR1, TLR2, TLR4, TLR5, TLR6 and TLR10 recognize lipophilic molecules contained in bacteria, such as lipopolysaccharide (LPS), and are localized in the plasma membrane.<sup>6</sup>

The four other members – i.e. TLR3, TLR7, TLR8 and TLR9 – can be activated by nucleic acids from bacteria and viruses: TLR3 senses intracellular double-stranded RNA (dsRNA), TLR7 and TLR8 recognize single-stranded RNA (ssRNA) while TLR9 recognizes single-stranded DNA (ssDNA) containing unmethylated cytidine-guanosine dinucleotide (CpG) motif. All these receptors and their regulation have been reviewed recently by Lind *et al* (Figure 1).<sup>8</sup>

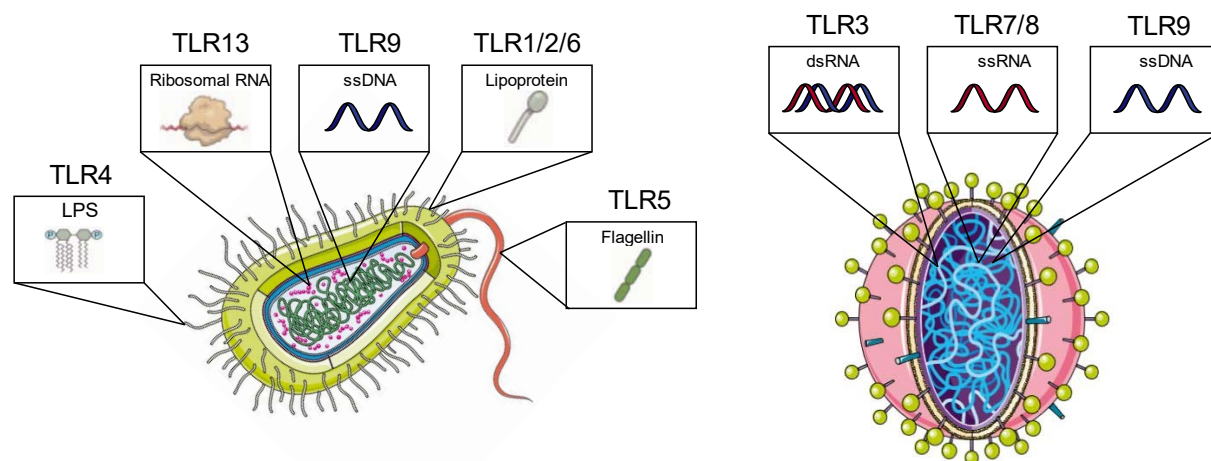


Figure 1 - Human TLR recognize bacterial ligands (left) and viral ligands (right). Adapted from Fitzgerald *et al*.<sup>6</sup>

In addition, three other TLRs were discovered in mice: TLR11 and TLR12 are responsible for intracellular recognition of profilin (parasite) and flagellin (bacteria) while TLR13 senses bacterial ribosomal RNA. To date, no equivalents of these TLRs have been identified in humans, suggesting that the human TLR family could be composed of additional members yet to be discovered.

Because of their ability to induce an immune-response, TLRs have been considered as therapeutic targets for immuno-oncology but also for antiviral purposes.<sup>9</sup> Therefore, different molecules targeting TLRs are currently in clinical trials (selection of molecule in Table 1) for oncology or antiviral purposes.

Table 1 – Selection of TLR agonists currently in clinical trials for oncology and antiviral purposes according to Javaid et al.<sup>10</sup>

Target	Molecule	Type	Clinical phase	Disease
TLR 1/2/6	OPN-305	Monoclonal antibody	Phase II	Inflammatory disease, kidney transplant rejection, pancreatic tumor
	CBLB612	Synthetic lipopeptide	Phase II	Breast cancer
	ISA-201	Peptide	Phase II	Head and neck tumor
TLR3	Poly-ICLC	Synthetic dsRNA	Phase II	Colon, breast, prostate, ovarian cancers
TLR4	GSKI79509I	Glycolipid	Phase I	Cancer
	CX-01	Polysaccharide	Phase I	Leukemia
	PEPA-I0	Small molecule	Phase II	Cancer
TLR5	Entolimod	Recombinant protein	Phase I	Cancers
	Mobilan	Recombinant protein	Phase II	Prostate cancer
TLR7	Imiquimod	Small molecule	Approved	Various cancers, actinic keratosis, and viral infections
	RO702053I	Small molecule	Phase II	Hepatitis B
TLR8	VTX-2337	Small molecule	Phase II	Cancers
TLR9	SD-I0I	CpG-C class oligonucleotide	Phase II	Lymphoma
	MGNI703	DNA-based molecule	Phase II	HIV and melanoma

	CpG-ODN	Nucleotide-based	Phase I	Lung tumor
	DUET-01	siRNA linked to CpG-ssDNA	Phase I	B-cell non-Hodgkin lymphoma

## 2. C-type lectin receptors

While C-type lectins (CLR) are a superfamily of proteins sensing all classes of human pathogens, they are extensively studied for their ability to recognize pathogens' glycans in particular.<sup>11</sup> For example, Dendritic Cell-Specific Intercellular adhesion molecule-3-Grabbing Non-Integrin (DC-SIGN) is a CLR present on macrophages and dendritic cells. This protein is able to recognize mannose-rich N-glycans found on asialoglycoproteins present on the surface of many pathogens.<sup>12</sup> Some of CLR signaling pathways have been connected to TLR signaling,<sup>13</sup> in order to amplify the signal and increase the cytokine and IFN secretions. For this reason, CLR agonists are currently under investigation in combination with other PRR agonists in order to induce an immune response against tumors (Table 2).

Table 2 – Selection of CLR targeting molecules currently in clinical trials for oncology purposes.<sup>14</sup>

Target	Molecule	Type	Clinical phase	Disease
Dectin-1	Imprime PGG	$\beta$ -1,3/1,6 glucan	Phase II	NSCLC, melanoma, breast cancer, indolent non-hodgkin lymphoma, colorectal cancer
DC-SIGN	CMB305	Recombinant protein	Phase III	synovial sarcoma
CD205	CDX-1401	Monoclonal antibody	Phase II	Melanoma
CLL-1 <sup>15</sup>	DCLL9718S	Antibody-drug conjugate	Phase I	Acute myeloid leukemia

Membrane-bound PRRs are thus proteins able to recognize a wide range of pathogenic molecules at the plasma membrane or in endosomes. However, these molecules can also be found in the cytosol. Fortunately, other PRR located in the cytoplasm are able to recognize them.

## ii. Cytoplasmic PRR

### 1. NOD-like receptors

NOD-like receptors (NLR) are cytoplasmic proteins characterized by a nucleotide-oligomerization domain (NOD) that mainly recognize bacterial peptidoglycans and induce

transcriptional upregulation of proinflammatory cytokines genes.<sup>16</sup> In general, NLR ligands have a poor capacity to trigger signaling pathways without a synergistic boost from other PRR, like TLRs.<sup>17,18</sup> NLR ligands are recognized at the C-terminal Leucine-Rich-Repeats (LRR) domain, and the subsequent signaling is performed by their N-terminal domain. The two most prominent subfamilies are the NLRC and the NRLP, which differ by their N-terminal domain: a Caspase-Activation and Recruitment Domain (CARD) for NLRC(aspase) and a Pyrin domain (PYD) for NRLP(yrin).<sup>19</sup>

NLRC are involved in the recognition of pathogens, with NOD1 and NOD2 sensing D-glutamyl-meso-diaminopimelic acid and muramyl dipeptide respectively.<sup>20,21</sup> In addition, it has been reported that NOD2 is involved in 5'-triphosphate RNA-induced type-I IFN production, a type of molecule found exclusively in viruses.<sup>22</sup> To date, only one small molecule targeting NLRs has been approved for oncology purposes, Mifamurtide, a NOD2-selective lipophilic molecule.<sup>14</sup>

In turn, NLRP are involved in a particular type of highly inflammatory cell death, called pyroptosis<sup>19</sup>, *via* the formation of protein complexes called inflammasomes. The most widely studied member of this family is NLRP3, which forms a heptaoligomer upon detection of a wide range of pathogenic or damage-associated molecules. Among these, reactive oxygen species (ROS) or potassium efflux can be responsible for a NLRP3-mediated inflammatory response.<sup>23</sup> Briefly, this inflammasome consist in activated NLRP3 bound to Apoptosis-associated Speck-like protein with a Caspase-recruitment domain (named ASC) by PYD-PYD contact. Then, ASC activates pro-caspase-1 by a CARD-CARD contact, thus forming a NLRP3-ASC-pro-caspase-1 inflammasome complex. The latter ultimately leads to the activation of Gasdermin-D, and the formation of pores in the plasma membrane. In addition, inflammasomes are involved in the release of pro-inflammatory interleukins 1 $\beta$  and 18 (Figure 2).<sup>24</sup>

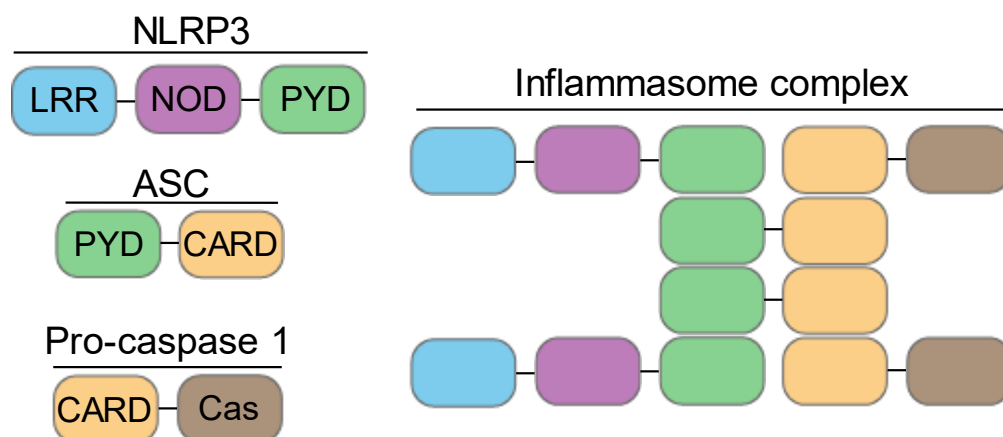


Figure 2 - Schematic representation of the NLRP3 inflammasome. Ligand is detected at the LRR domain of NLRP3, which allow the contact with the pyrin domain of ASC by PYD-PYD contact. ASC can then activate pro-caspase-1 by CARD-CARD domain.



## 2. *AIM2-like receptors*

Cytosolic dsDNA from DNA viruses or neighboring cells are considered as a danger signal by the cell, as these molecules should not be in the cytosol. Absent In Melanoma 2 (AIM2) is an innate dsDNA cytosolic sensor that recruits ASC and caspase-1 in order to create another inflammasome, thus leading to the same effects as the NLRP3 inflammasome.<sup>25,26</sup> Interaction between the DNA and AIM2 is sequence-independent and relies mostly on electrostatic interactions between the phosphate backbone of the DNA and cationic amino acids of the protein.<sup>27</sup>

## 3. *cGas/STING*

Cytosolic DNA can also be recognized by Cyclic Guanosine monophosphate (GMP)-Adenosine monophosphate (AMP) Synthase (cGAS). Upon binding, this protein starts the synthesis of cyclic GMP-AMP (cGAMP), which can bind to the endoplasmic reticulum protein Stimulator of interferon genes (STING), enabling an innate immune response by producing type-I IFN and pro-inflammatory cytokines.<sup>28</sup> Nowadays, STING pathway is regarded as a potential target for oncology because of its ability to induce a strong T cell immunity.<sup>29</sup> To date, numerous strategies targeting STING have been developed, from cyclic oligonucleotides to small molecules, including antibody-drug conjugates (Table 3).

Table 3 - Selection of STING agonists for oncology purposes.<sup>30</sup>

Target	Molecule	Type	Clinical phase	Disease
STING	MK-2118	Small molecule	Phase I	Advanced solid tumors Lymphoma
STING	MK-1454	Cyclic oligonucleotide	Phase II	Advanced/Metastatic Solid Tumors or Lymphomas
STING	XMT-2056 <sup>31</sup>	Antibody-drug conjugate	Pre-clinical phase	/

## 4. *RIG-I-like receptors*

The RIG-I-like-receptors (RLR) family includes three members involved in RNA sensing. In 2004, Yoneyama *et al*<sup>32</sup> identified retinoic-acid-inducible gene-I (RIG-I) as an essential sensor of our innate immune system by detecting short viral RNAs (up to 1 kb) in the cytosol.<sup>33</sup> Two years later, the natural ligand for RIG-I has been established as 5'-triphosphorylated dsRNA, a type of post-transcriptional modification catalyzed by viral polymerases inside the infected cell's cytosol.<sup>34</sup> The same year, Andrejeva *et al* discovered another cytosolic RNA sensor, called melanoma differentiation-associated protein 5 (MDA5) which detects the presence of long dsRNA.<sup>35,36</sup> In 2005, a third RLR has been discovered, called Laboratory of Genetics and

Physiology 2 (LGP2). LGP2 plays a role in the negative regulation of RIG-I signaling by sequestering dsRNA.<sup>37</sup> In addition, RLRs often interact with nucleic-acid-sensing TLRs in order to increase the signaling and the immune response.<sup>37-39</sup> RIG-I signaling and cGAS-STING signaling pathways have also been connected.<sup>40</sup>

RIG-I is part of the innate immune system and is therefore an extremely sensitive and specific sensor for RNA viruses. In addition, RIG-I signaling has been recently connected to DNA repair after DNA double-strands breaks (DSBs), probably to protect the host from integration of viral DNA into the host genome virus integration.<sup>41</sup> Besides antiviral applications, RIG-I has been recently validated as a key player for oncology purposes<sup>42</sup> mainly for its ability to stimulate the immune system with an extremely low amount of ligand.<sup>43-45</sup>

## B. RIG-I-mediated detection of RNA and signaling pathways

### i. Structure of RIG-I-like receptors

From a structural point of view (Figure 3), RLRs are composed of two central helicase/ATPase domains (named Hel1 and Hel2) containing a conserved Asp-Glu-Ala-Asp (DEAD) with an ATPase activity. The RNA is recognized at the regulatory C-terminal domain (CTD).<sup>46</sup> For RIG-I and MDA5, two N-terminal caspase activation and recruitment domains (CARDs) are also present.<sup>47,48</sup> Common in many PRRs, CARD domains are regulators of apoptosis and inflammatory responses by mediating protein-protein interactions with caspases *via* CARD-CARD contacts.<sup>49</sup> Unfortunately, due to the high difficulty to crystallize CARDs domains, no structure of full-length RIG-I has been reported yet.

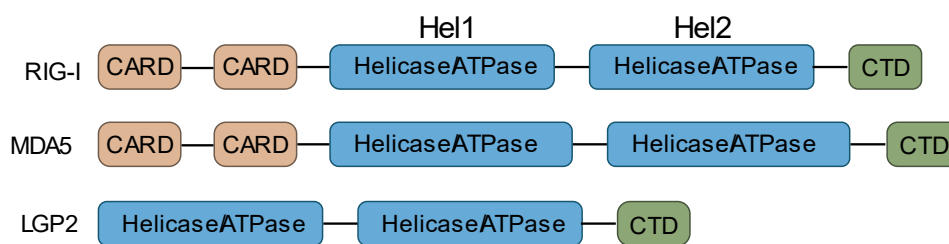


Figure 3 - Structure of RIG-I, MDA5 and LGP2. The CTD recognize the 5'-terminus of dsRNA, the helicase domain use ATP to catalyze the dsRNA opening, and the CARDs domain are used for signal transduction upon binding.

### ii. Structural insights of RIG-I agonists

RIG-I recognizes RNA ligands based on different levels of specificity, in terms of length, secondary structure and 5'-terminus phosphorylation (Figure 4). These requirements allow RIG-I to discriminate between self and non-self cytosolic RNA molecules, as membrane RNA do not have the same structures as viral RNA.<sup>50-52</sup> In addition, triphosphate groups are initially present at the 5'-end of any viral RNA, while in eukaryotes, RNAs have to be processed and capped in the nucleus before being released in the cytosol. Therefore, 5'-triphosphate dsRNA

(dsRNA-5'-ppp) are widely accepted as the principal agonist for RIG-I,<sup>34</sup> and secondary structures that mimic viral RNA (such as panhandles or short hairpins) greatly enhance the binding to RIG-I.<sup>53-55</sup>

### 1. RNA's length

RIG-I recognizes short RNA molecules up to 1 kb, otherwise, while longer RNAs are recognized by MDA5.<sup>56,57</sup> The minimal length of agonist has been shown to be 10-15 base pairs (bp)<sup>58,59</sup>, and the sequence of nucleotide does not have a significant influence on RIG-I's activation.<sup>60</sup> Indeed, the terminal base pair interact through hydrophobic interactions with a unique phenylalanine, and no other specific interaction has been found using two different sequences of dsRNA, demonstrating that RIG-I binds RNA in a sequence-independent manner.<sup>61</sup> If the RNA is long enough (>300 bp), the presence of 5'-ppp is not necessary to activate RIG-I.<sup>58</sup> However, as RIG-I is a viral RNA sensor, the use of unnatural bases<sup>62,63</sup> or modified ribose<sup>64</sup> reduces the binding affinity.

### 2. Impact of overhangs and base-pairing

The triphosphate-containing end has to be blunt and base-paired to trigger RIG-I's signaling pathways.<sup>65,66</sup> RNA molecules containing 3'-overhangs at the 5'-ppp end diminishes the activity, and any 5'-overhangs at the same strand completely abolishes it.<sup>60,65,67</sup> Indeed, it has been shown that a single unpaired 5'-ppp nucleotide is sufficient to inhibit RIG-I signaling. However, overhangs at the non-triphosphorylated end is accepted by RIG-I, as long as both end are separated by at least 19 bp.<sup>67</sup>

### 3. Impact of secondary structures

While it has been postulated that 5'-triphosphate single-stranded RNA (ssRNA-5'-ppp) could be a RIG-I agonist<sup>34,68</sup>, these findings were biased. The common method to produce such RNA is by *in vitro* transcription using phage-encoded DNA-dependent RNA polymerases. Two research groups revealed that this method commonly produces extended byproducts generating dsRNA<sup>69,70</sup> that were, in fact, responsible for RIG-I's activation.<sup>56,67</sup> More precisely, while effectively creating single-stranded transcripts bearing a 5'-ppp terminus, the 3'-end complementarity can prime a reaction resulting in the production of complementary strands or short hairpin RNA (shRNA) that activates RIG-I.<sup>71-73</sup> Besides, chemically synthesized ssRNA-5'-ppp failed to stimulate RIG-I, indicating that RIG-I needs a double-stranded shape in order to be activated.<sup>61,65,66,74</sup>

Moreover, the presence of panhandle or hairpin conformations on the RNA could help RIG-I to distinguish these RNAs over mammalian ones.<sup>75</sup> Therefore, such RNA containing a 5'-ppp terminus represent the most potent RIG-I agonist currently reported.<sup>54</sup> These findings were supported by the design of stem-loop RNA (called SLR) that proved to be potent RIG-I agonists

in preclinical models.<sup>59</sup> Besides being more nuclease-resistant, these secondary structure enhanced the structural stability of the RIG-I/RNA complex.

#### 4. Impact of 5'-phosphates

Blunt-ended and base-paired dsRNA with 5'-OH or 5'-monophosphate failed to induce a RIG-I-mediated immune response.<sup>51</sup> Indeed, treatments of 5'-ppp RNA with phosphatases abolishes their recognition by RIG-I.<sup>76</sup> However, the 5'-diphosphate (5'-pp) group is as potent as 5'-ppp to activate RIG-I.<sup>32,59,76</sup> Crystallography analyses showed that RIG-I's C-terminal domain binds to the dsRNA through electrostatic interactions between the 5'-triphosphate and the protein's lysines inside a triphosphate-binding site. These interactions were the highest contribution to the overall binding, explaining why dsRNA with only one phosphate showed a much lower binding to RIG-I.<sup>61</sup>

5'-pp or 5'-ppp ends are usually found on mature RNA viruses but can be produced enzymatically by the transcription of viruses' DNA into RNA with RNA polymerase III. Besides, dsRNA-5'-ppp can be produced *in vitro* from a DNA template using T7 polymerase, or can be added to chemically synthesized RNA with kinases.

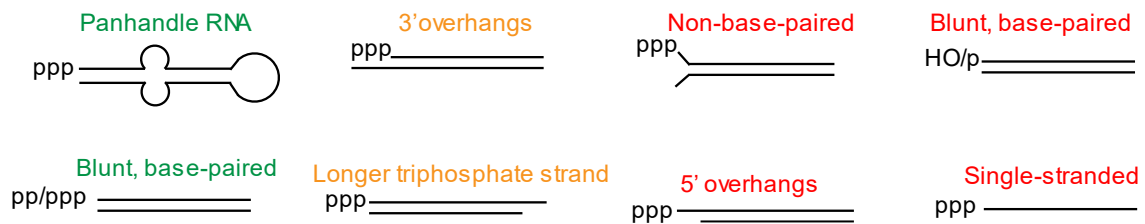


Figure 4 – RNA designs for RIG-I-mediated RNA recognition. Green designs represent the most potent agonists, orange designs are recognized but with a lower affinity, and red designs are not recognized by RIG-I.

#### iii. RIG-I activation by dsRNA-5'-ppp

The CARDs domains of RIG-I have an inhibitory effect on the ATPase function, as RIG-I mutants lacking CARDs have an enhanced ATPase function.<sup>77</sup> This means that inactive RIG-I has a closed, self-inhibitory conformation, in which CARDs are inaccessible for signal transduction, probably to avoid an uncontrolled antiviral response.<sup>78–80</sup> Upon binding to dsRNA at the C-terminal domain<sup>56,81</sup>, RIG-I changes its conformation, freeing CARD domains.<sup>61,82,83</sup> Then, the ATPase activity starts, enabling the translocation of RIG-I along the RNA<sup>77,84</sup>, freeing the 5'-ppp extremity. Depending on the RNA's length, this allows other RIG-I molecules to bind to the dsRNA<sup>85</sup>, forming filamentous RIG-I oligomers on an opened conformation.<sup>86–89</sup> The now-accessible CARD domains are organized as clusters for K63-polyubiquitination *via* the action of the ubiquitin ligase RIPLET (Figure 5).<sup>90–92</sup>

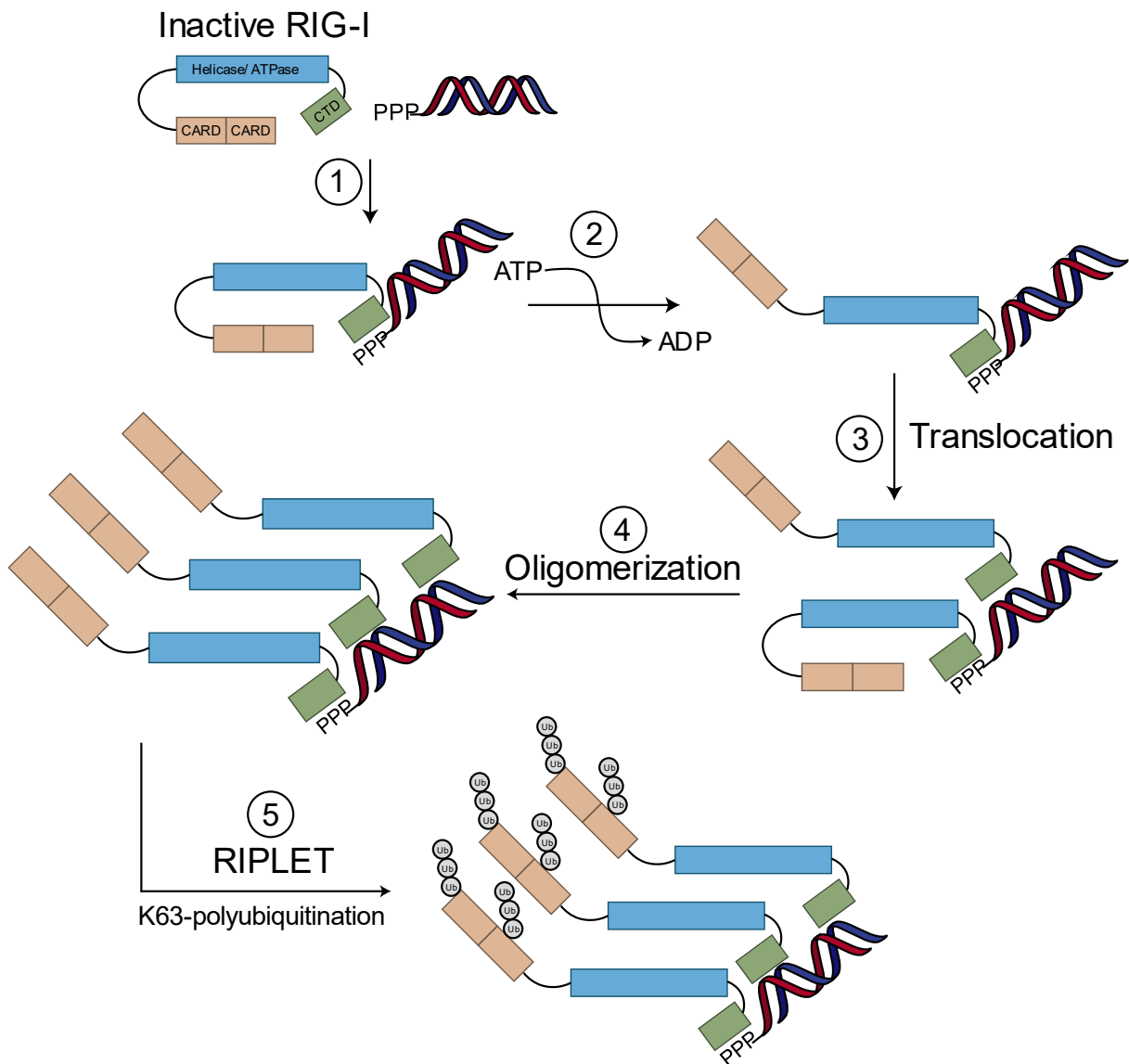


Figure 5 - RIG-I activation mechanism upon dsRNA binding. Upon binding of the 5'-ppp termini (1) at its C-terminal domain, RIG-I changes from "self-repressed" to "opened" conformation by an ATP-dependent mechanism (2). This allows RIG-I to translocate along the dsRNA (3), freeing the 5'-ppp termini, allowing other RIG-I to bind on it (4). Oligomerized RIG-I form clusters that are K63-polyubiquitinated by RIPLET to form the activated form of RIG-I (5).

The crystal structure of RIG-I filaments (without CARD domains) with RIPLET's ubiquitinating domain has been resolved recently by cryo-electron microscopy (Figure 6).<sup>93</sup>

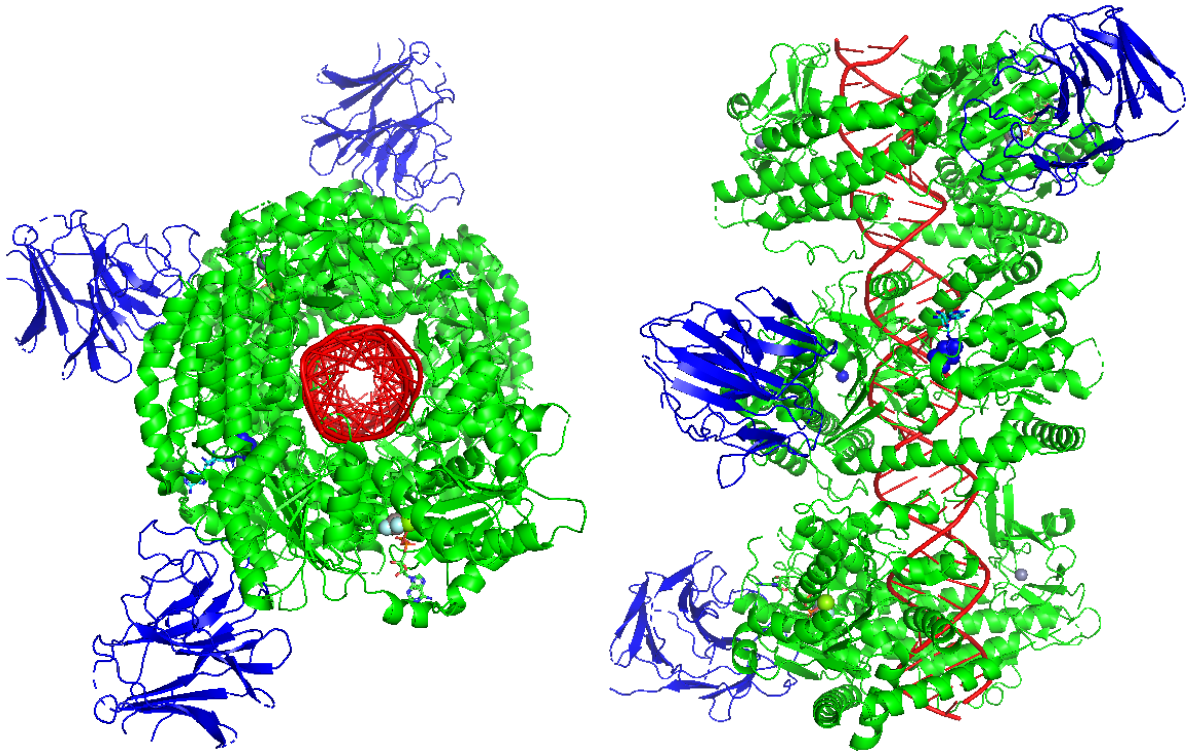


Figure 6 - Crystal structure (PDB: 7JL3, modeled with Pymol) of RIG-I (without CARD domains, green) trimers along a dsRNA (red), with the ubiquitinating domain of RIPLET (blue).<sup>93</sup>

#### iv. Signal transduction

Polyubiquitination of CARDs domains is required for signal transduction, characterized by a CARD-CARD interaction with the mitochondrial antiviral-signaling protein MAVS (also known as IPS-1) located in the outer membrane of mitochondria.<sup>79,94</sup> This induces the formation of very large MAVS aggregates forming fibrils that behave like prions and propagates antiviral signaling cascades *via* two modes of action (Figure 7).<sup>95–97</sup> From a mechanistic point of view, the latter signal activates TANK-binding kinase 1 (TBK1) resulting in the phosphorylation and translocation of interferon response factors 3 and 7 (IRF 3/7) in the nucleus. These transcription factors promote the secretion of type-I IFN, such as IFN- $\alpha/\beta$ ,<sup>38,98,99</sup> further inducing the biosynthesis of many interferon-stimulated genes (ISGs), including RIG-I itself, creating a positive feedback loop that amplifies the response.<sup>100–103</sup>

Secondly, the signal also activates I $\kappa$ B kinase complex (IKK), resulting in the phosphorylation of I $\kappa$ B, a protein that sequester the nuclear factor- $\kappa$ B (NF- $\kappa$ B) in the cytosol. This phosphorylation leads to the degradation of I $\kappa$ B, resulting in the translocation of NF- $\kappa$ B in the nucleus and promoting the secretion of proinflammatory cytokines, such as pro-IL-1 $\beta$ , pro-IL-18 or CXCL10.<sup>104</sup> These cytokines have direct effects on the cell's survival, by engaging different modes of action leading to the cell's death.<sup>105–108</sup>

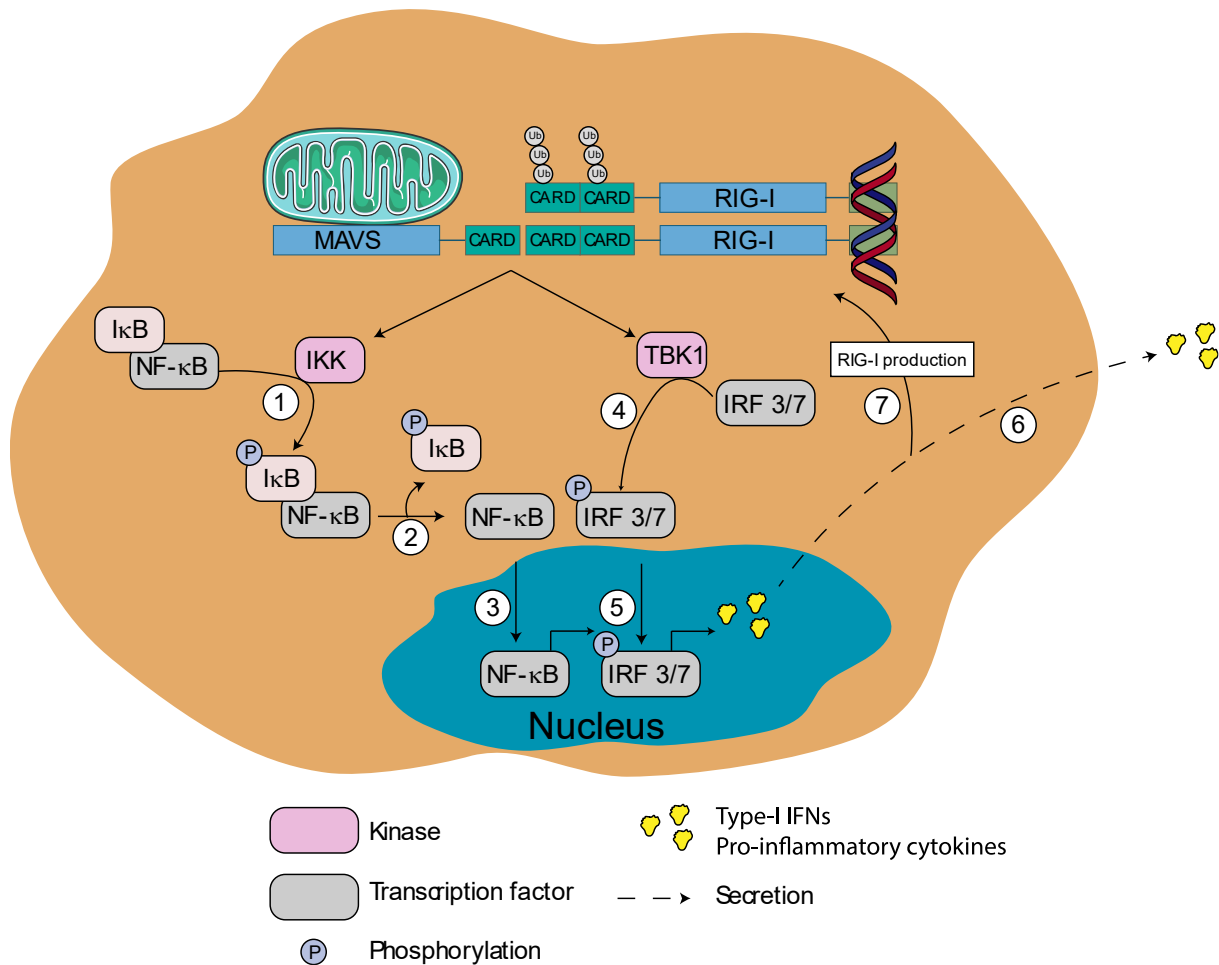


Figure 7 - Activation mechanism of NF- $\kappa$ B and IRF pathways following RIG-I activation. Upon binding, IKK phosphorylates I $\kappa$ B (1) which leads to its degradation (2). Free NF- $\kappa$ B (3) is then translocated to the nucleus. By the meantime, TBK1 phosphorylates IRF 3/7 (4), which are also translocated to the nucleus (5). These proteins will code for type-I IFN and pro-inflammatory cytokines which are then excreted (6), leading to the production of interferon-stimulated genes like RIG-I itself (7).

## v. Biological effects following RIG-I activation

### 1. Direct effects of the IRF3/7 pathway

Activation of the IRF3/7 pathways leads to the transcription of type-I IFN (IFN- $\alpha$  and IFN- $\beta$ ) that are excreted (Figure 8). IFNs bind to cell-surface receptors (IFNAR1 and IFNAR2) in neighboring cells, and activate the JAK-STAT pathway.<sup>109</sup> A STAT1-STAT2 heterodimer form a complex called Interferon-Stimulated Gene Factor 3 (ISGF3) with IRF9. This complex then translocates in the nucleus where it promotes the transcription of multiple interferon-stimulated genes (ISG).<sup>110,111</sup> For this reason, RIG-I activation is able to propagate the signaling to the neighboring cancer cells, and immune cells.<sup>43</sup>

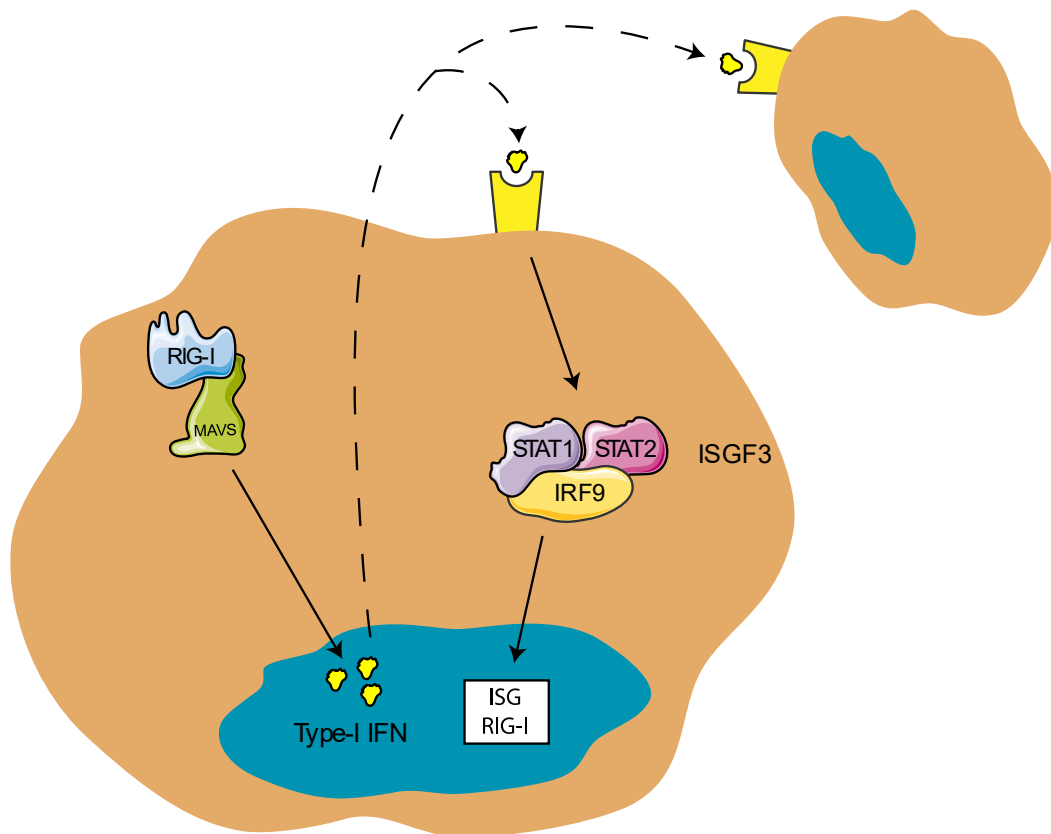


Figure 8 - Mechanism of the IRF3/7 pathway following RIG-I activation. Released type-I IFN are recognized by surface-IFN-receptors on neighboring cells, activating the ISGF3 complex. After translocation in the nucleus, ISGF3 will promote the production of numerous ISG, among them RIG-I itself.

## 2. Direct effects of the NF- $\kappa$ B pathway

Activation of the NF- $\kappa$ B pathway leads to the transcription of pro-inflammatory cytokines promoting cell killing through four mechanisms of cell death: the intrinsic apoptosis<sup>112,113</sup>, the extrinsic apoptosis, pyroptosis, and ultimately, immunogenic cell death (ICD).<sup>114</sup>

### a. Intrinsic apoptosis

Apoptosis is initiated by the perturbation of cellular microenvironment and characterized by a plasma membrane blebbing, the DNA fragmentation, the formation of apoptotic bodies and phosphatidylserine externalization.<sup>24</sup> RIG-I-mediated cell death by the intrinsic apoptosis mode of action has been reported in melanoma cells<sup>112,115</sup>, myeloid leukaemia<sup>116</sup>, colon and prostate carcinoma<sup>117</sup> and in lung<sup>118</sup> or cervical cancers.<sup>119</sup>

From a mechanistic point of view, this programmed cell death occurs after the irreversible mitochondrial outer membrane permeabilization. This phenomenon is controlled by proapoptotic genes, such as NOXA,<sup>24</sup> which are selectively upregulated in cancer cells following RIG-I activation.<sup>120</sup> A subsequent leakage in the cytosol of apoptosis-inducing proteins, like cytochrome c, induces pro-caspase-9 cleavage into active caspase-9. This



protein is then responsible for the proteolytic activation of caspase-3/7 (Figure 9), two proteases which are widely considered as enzymes promoting the cell's destruction.

### *b. Extrinsic apoptosis*

NF- $\kappa$ B activation promotes the transcription of several proapoptotic factors which are located in the plasma membrane, such as TNF-related apoptosis-inducing ligand (TRAIL).<sup>121</sup> The extrinsic apoptosis pathway is dependent on the engagement of these receptors with their cognate ligand from other cells (for example, TRAIL and TRAIL-Receptors), leading to the activation of caspase-8/10 that directly activates caspase 3/7 and cell death (Figure 9).<sup>24</sup> This pathway has been reported to occur following RIG-I signaling in melanoma<sup>122,123</sup>, prostate<sup>124</sup> and breast cancers.<sup>125</sup>

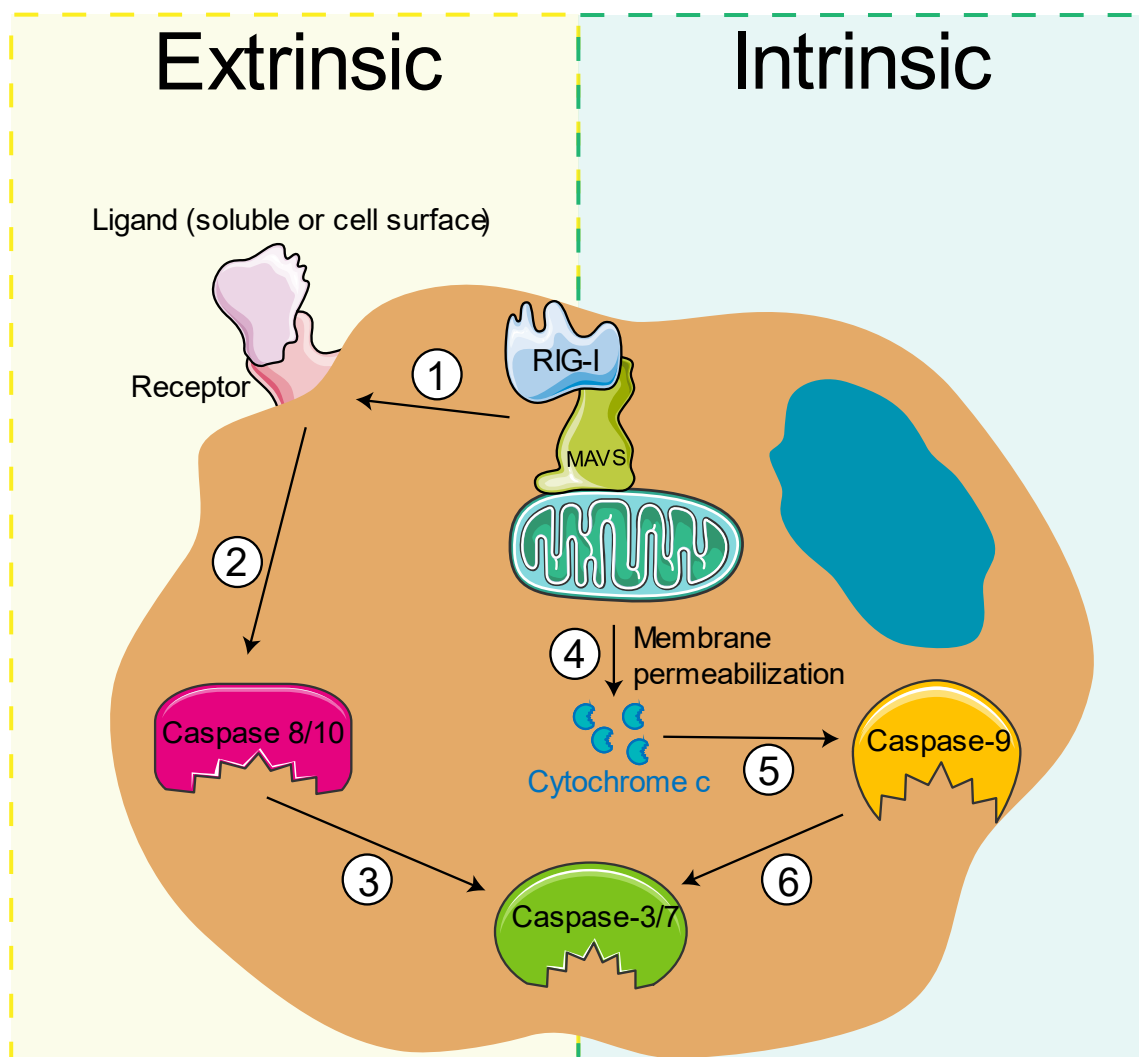


Figure 9 – Mechanisms of both intrinsic and extrinsic apoptosis following RIG-I signaling. Upon binding, death receptors are expressed at the cell surface (1), and ligand recognition activates caspase 8/10 (2) and caspase 3/7 (3). In this intrinsic pathway, mitochondrial membrane is permeabilized, leading to the release of cytochrome c (4). This will further activate caspase 9 (5) and caspase 3/7 (6).

### c. Pyroptosis

It has been reported that RIG-I engagement in cancer cells form a complex of proteins called inflammasome, further inducing pyroptosis, a form of highly immunogenic form of necrosis (Figure 10).<sup>126,127</sup> Two mechanisms of action have been reported. On the one hand, activated MAVS activates NLRP3-dependent inflammasome,<sup>104,128</sup> and on the another hand, activated RIG-I forms a complex with the Apoptosis-associated Speck-like protein with a Caspase-recruitment domain (named ASC) and caspase-1.<sup>125,127,129</sup> The latter allows the proteolysis of pro-inflammatory cytokines pro-IL-1 $\beta$  and pro-IL-18 into their active forms. These cytokines amplify the inflammatory alert in the local environment, activating effector cells like macrophages, natural killer (NK) cells or dendritic cells (DC). Moreover, caspase-1 also activates Gasdermin-D, a protein forming pores in the plasma membrane, allowing water to enter in the cell leading to its death.<sup>130</sup>

A consequence of membrane permeabilization is the release of proteins in the extracellular environment.<sup>117,125</sup> Besides interleukins, other proteins include the leaking of Damage-Associated Molecular Patterns (DAMPs), such as high-mobility group box 1 (HMGB1), adenosine triphosphate (ATP), or calreticulin.<sup>131</sup>

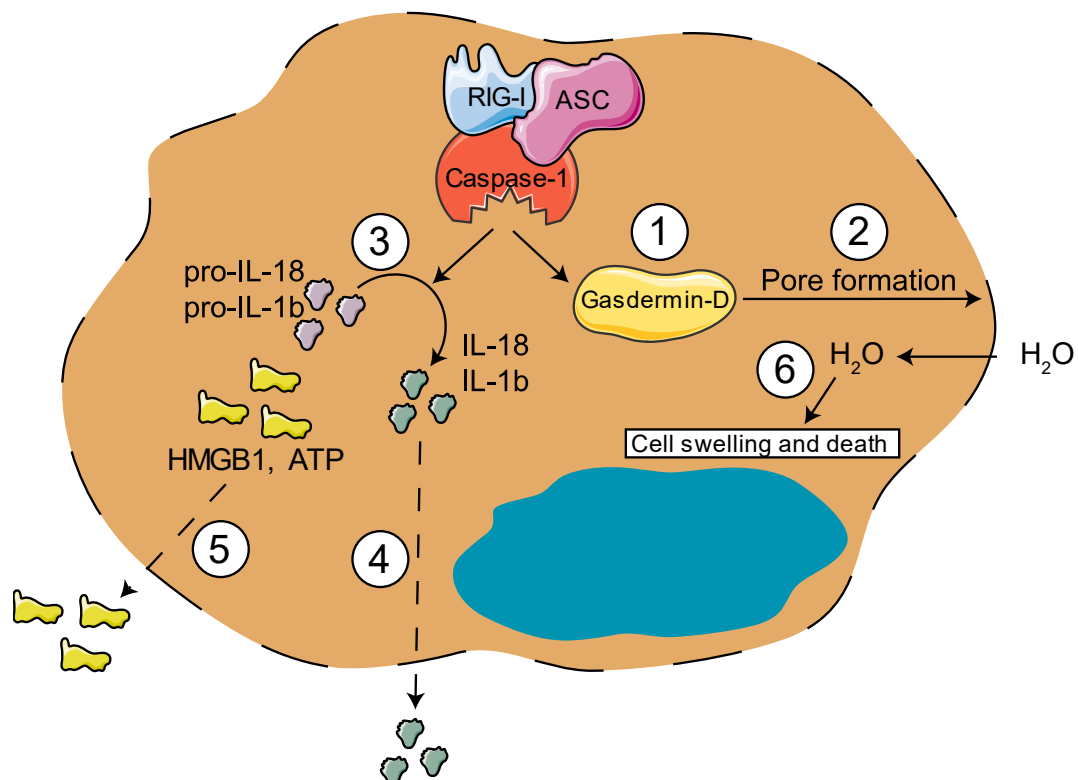


Figure 10 - Pyroptosis following RIG-I signaling. Upon binding, caspase 1 activates gasdermin-D (1), that leads to pore formation in the plasma membrane (2). Caspase 1 can also cleave pro-IL-1 $\beta$  and pro-IL-18 into their active forms (3). Due to the membrane permeabilization, these interleukins as well as endogenous molecules such as

HMBG1 and ATP (4, 5) can freely cross the membrane. In the meantime, water can enter inside the cell, causing its death.

#### d. Immunogenic cell death (ICD)

Released DAMPs are considered as “eat-me” signals by innate immune cells<sup>114</sup>, and they are sufficient to trigger innate and adaptive immune responses.<sup>24,131</sup> This phenomenon is known as immunogenic cell death (ICD) and is exploited in lymphocyte-rich “hot” tumor microenvironments (TME, Figure 11).<sup>24,114,132,133</sup> Indeed, activation of macrophages and NK cells by DAMPs, IFN, and interleukins increase their phagocytic and cytolytic potential respectively against tumors. Besides, DC maturation will further activate cytotoxic T cells, leading to the neighboring cancer cells’ killing.

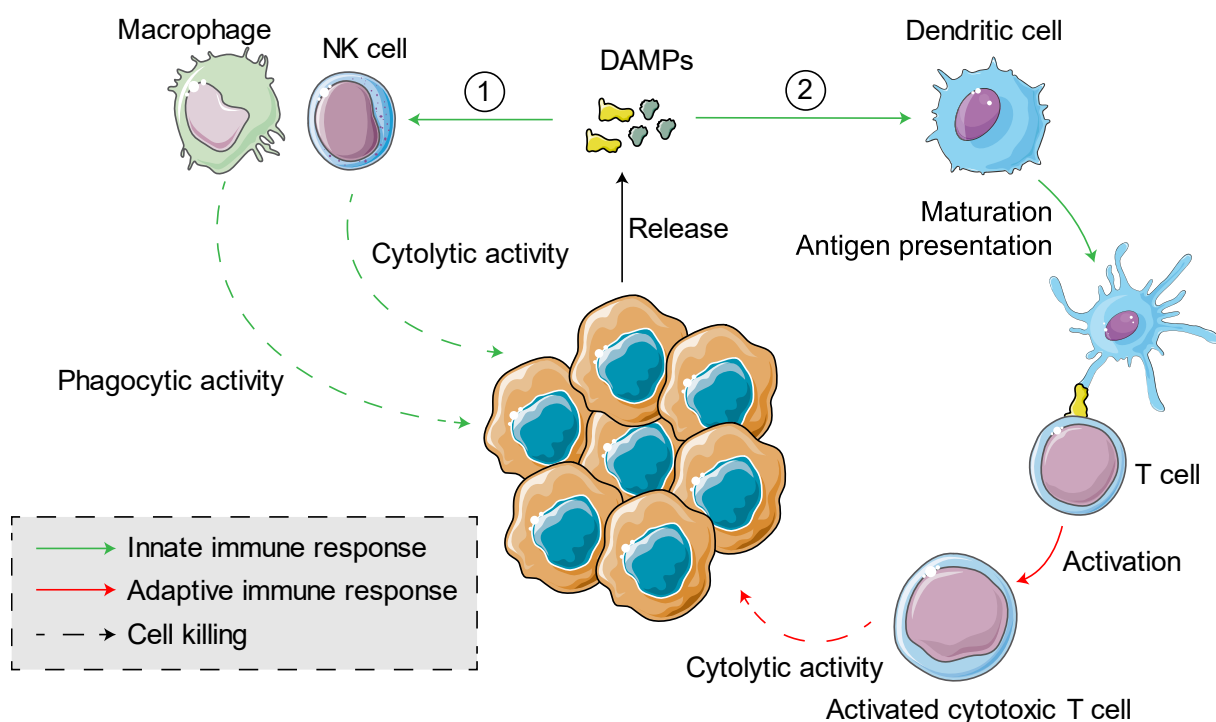


Figure 11 - Released DAMPs and cytokines activate the innate immune system (1), and trigger the adaptive immune system (2).

#### e. Reprogramming of the tumor microenvironment

Considering these elements, it has been postulated that RIG-I signaling could be exploited in leukocyte-rich “hot” TME. In addition, as this signaling promotes T cell recruitment by releasing DAMPs, it could be exploited in leukocyte-poor “cold” TME as well, thus turning “cold” into “hot”.<sup>44,134</sup> Therefore, this reprogramming of the TME could transform cancer cells into their own vaccines, thereby preventing recurrence of the disease.<sup>132,135</sup>

Aside from the effects on immune responses, it has been shown that RIG-I signaling selectively upregulates NOXA and TRAIL, two proteins involved in the intrinsic and the extrinsic apoptosis mechanisms, respectively, leading to cancer-selective apoptosis.<sup>120</sup> In addition, while healthy

cells can counter RIG-I-mediated pro-apoptotic signal by a rescue mechanism involving endogenous Bcl-xL genes, this mechanism is dysregulated in malignant cells.<sup>112</sup>

Therefore, the two major outcomes of RIG-I signaling is the preferential activation of cell death in tumors as well as potent innate and adaptive anti-tumor immune responses (Figure 12).

More importantly, as RIG-I is found in all cell types, it could be a therapeutic target in virtually all cancer types.<sup>136</sup> In addition, two positive retroaction loops exist following RIG-I signaling, one inside the cell, and the other one in the neighboring cells: on the one hand, the production of type I-IFN maintains high expression levels of RIG-I in the cancer cell, amplifying the response. On the other hand, these IFN are secreted, thus they can be taken up by live neighboring cells, which can also induce an immune response.<sup>28,137,138</sup>

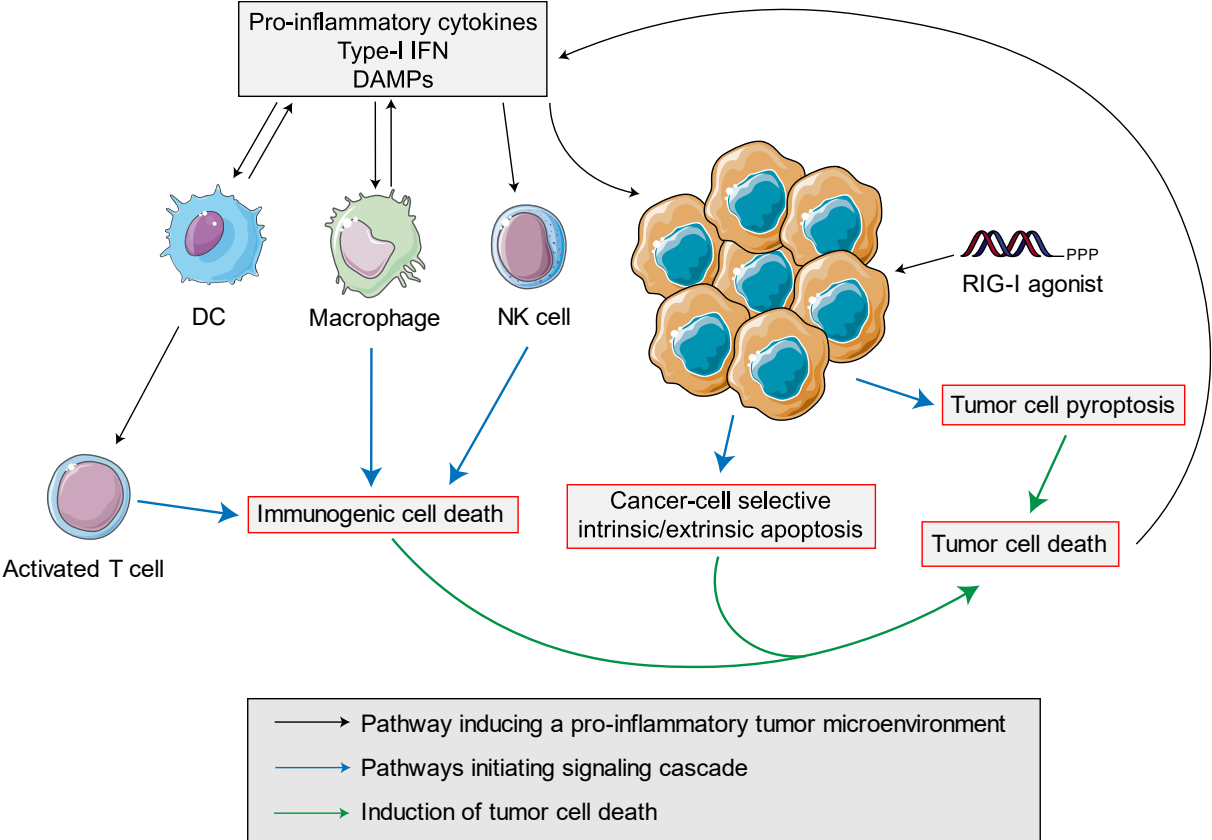


Figure 12 – Summary of biological effects of RIG-I activation on cancer cells.

One promising strategy in immuno-oncology is to engage T cells to perform cancer cell killing, however, tumors can develop resistance to these T cells. Indeed, cancer cells can express transmembrane proteins called immune checkpoints, allowing them to escape the immune system. Briefly, immune checkpoints consist in one receptor and its ligands<sup>139</sup> and the recognition of one ligand by the receptor either activates or inhibits immune cells. Therefore, by expressing an immune checkpoint, the cancer cell can inhibit T cells. Inhibition of immune checkpoints could then induce T cell recruitment. Nowadays, the most widely targeted immune

checkpoints are Cytotoxic T Lymphocyte-Associated protein 4 (CTLA4), the programmed cell death receptor-1 (PD-1) and its ligand (PD-L1) that are currently inhibited by monoclonal antibodies to treat multiple tumors.<sup>140–145</sup>

However, cancer cells can develop resistance against these antibodies. To address this issue, it has been postulated that RIG-I can pre-activate the surrounding immune system against tumors, thus enhancing current immunotherapies. Indeed, as activation of RIG-I induces the excretion of IFN and pro-inflammatory cytokines that can activate the neighboring immune cells, combinatorial strategies with immune checkpoint inhibitors can unleash T cells against tumors (Figure 13).<sup>146</sup> For example, the therapeutic efficacy of anti-PD-1<sup>147</sup> and anti-CTLA4 monoclonal antibodies has been enhanced thanks to a combination with dsRNA-5'-ppp.<sup>148</sup> This strategy is, for example, under investigation in clinical trials (NCT03739138).

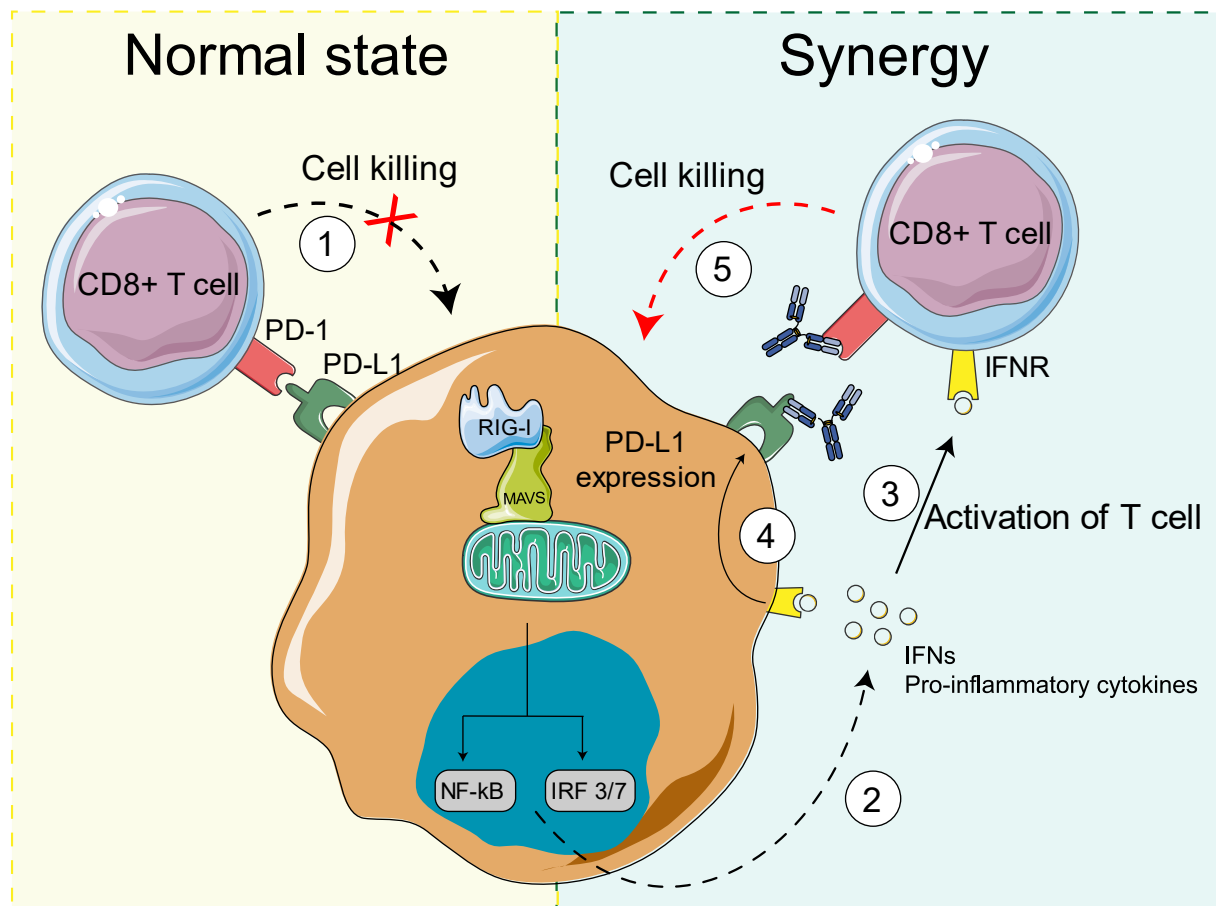


Figure 13 - Synergy between RIG-I signaling and immune checkpoint inhibitors. In a normal state, CD8<sup>+</sup> T cells' killing potential is inhibited by the binding of PD-1 to PD-L1 (1). However, RIG-I activation induces the production of IFNs (2) that are recognized by IFN receptors, activating T cells (3) and enhancing the production of PD-L1 on cancer cells (4). Therefore, adding PD-L1 and PD-1 inhibitors following RIG-I signaling could lead to strong T cell activation to enhance their cell killing potential (5).

As a summary, RIG-I activation can induce cancer-cell selective apoptosis, activate the neighboring immune system, and enhance immune checkpoint inhibitor potential. This makes RIG-I a promising therapeutic target for oncology.

### C. Strategies to activate RIG-I

#### i. Small molecules acting on RIG-I's pathway

Pharmaceutical companies have been developing small molecules to selectively target RIG-I. Even though few compounds acting on RIG-I's pathway have been reported for antiviral purposes, none of these molecules have reached clinical trials for oncology purposes yet.

The most advanced compound is SB9200, a dinucleotide that induces IFN production *via* RIG-I and nucleotide-binding oligomerization protein 2 (NOD2) (Figure 14). This molecule is currently in clinical phase II (NCT01803308) to cure patients infected with the hepatitis B virus.<sup>149,150</sup>

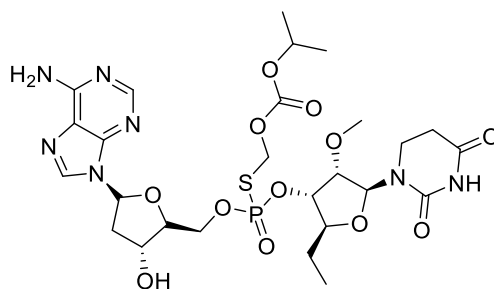


Figure 14 - Structure of SB9200, currently in clinical trials, and believed to interact with RIG-I signaling.

Three non-nucleoside families of molecules have also been identified by high throughput screening as potential IRF3 modulators acting on RIG-I-like receptors' pathway.<sup>151</sup> In 2012, the Gale's group, in collaboration with Kineta, identified isoflavone scaffolds and reported two hits, KIN100 and KIN101 (Figure 15, red cores).<sup>152</sup> These molecules showed a good antiviral activity, such as inhibiting hepatitis C virus infection. In the same publication, the authors also reported two benzothiazole compounds, named KIN1000 and KIN1148 (Figure 15, blue cores), which function as vaccine adjuvant against respiratory syncytial virus infection. More recently, the same team reported hydroxyquinolines as agonists of the same pathway, with KIN1400 as a new lead compound (Figure 15, green core).<sup>153</sup>

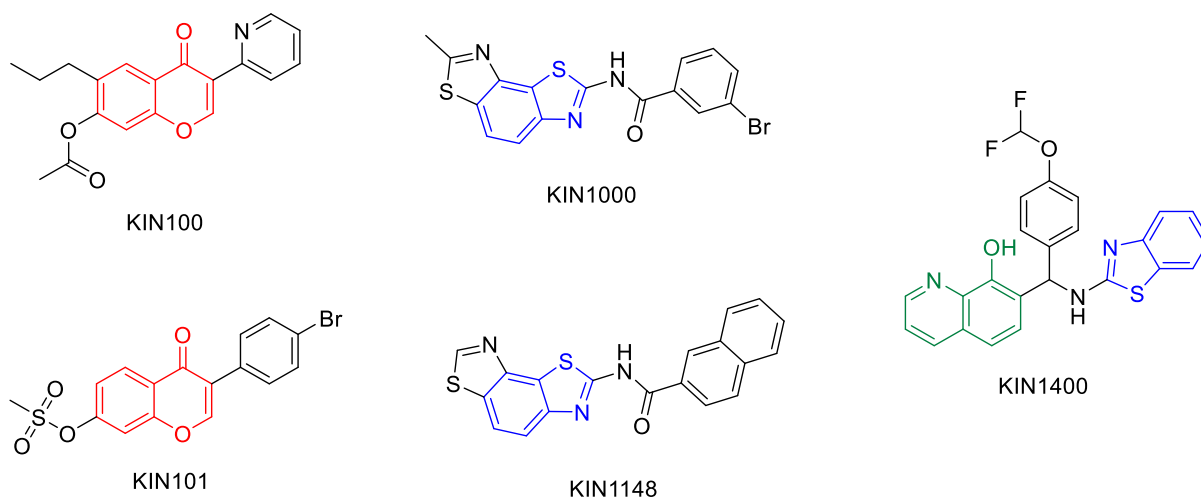


Figure 15 – Selected structures of IFN-inducers acting on RLR's pathway published by Kineta. In red, the family of isoflavones, in blue, benzothiazoles and in green, hydroxyquinolines.

Based on these screening, Kineta has further developed KIN131A (structure unknown) as its lead agonist of RIG-I's pathway, and to date, only preclinical data on CT26 colon carcinoma xenografted mice have been presented. In their poster, the authors reported that KIN131A induces apoptosis of cancer cells, immunogenic cell death, and promotes anti-tumor immunity, protecting mice against reinjection of cancer cells.<sup>154</sup>

While all of these molecules act on both RIG-I and IRF3 pathways,<sup>155</sup> the specific target of these compounds is currently unknown, therefore they are not considered as selective RIG-I agonists yet. As RIG-I is an RNA sensor, the vast majority of the reported agonists are logically RNAs. Depending on the length, these can be obtained by phosphoramidite synthesis, yielding short and well-defined RNA molecules, or *in vitro* transcription (IVT) able to yield longer RNA.

## ii. Non-selective molecules targeting RIG-I pathway in (pre)-clinical trials

Regarding RNA in clinical trials, one of the the most widely used RIG-I agonist is polyinosinic:polycytidylic acid (poly (I:C)), a synthetic dsRNA mimic.<sup>156,157</sup> This polymer also target other pattern-recognition receptors, such as endosomal TLR3<sup>158</sup> or cytosolic MDA5<sup>58</sup>, therefore inducing incredibly potent immune responses. For these reasons, poly(I:C) is currently in phase III of clinical trials for immuno-oncology and antiviral purposes.<sup>159</sup>

Another single-stranded non-coding RNA, termed CV8102 (also named RNAdjuvant™), is currently tested in clinical trials for its effects on RIG-I and TLR7.<sup>160</sup> This RNA is composed of 547 nucleotides, contains several polyuridine repeats, and is complexed with disulfide-crosslinked cationic peptides forming a polymeric carrier, protecting it from RNase degradation. Initially developed for antiviral purposes, CV8102 demonstrated anti-tumor activity in clinical trials in advanced solid tumors in combination with anti-PD-1 antibody (NCT03291002).<sup>39</sup>

### iii. Selective molecules targeting RIG-I pathway in (pre)-clinical trials

Hiscott's group reported a purified RNA derived from a Vesicular Stomatitis Virus that shown promising results in pre-clinical trials by inhibiting viruses replication by activating RIG-I.<sup>161,162</sup> Expectedly, this RNA contain double-stranded blunt end and hairpins (Figure 16) – molecular motifs that strongly activate RIG-I, as described earlier.

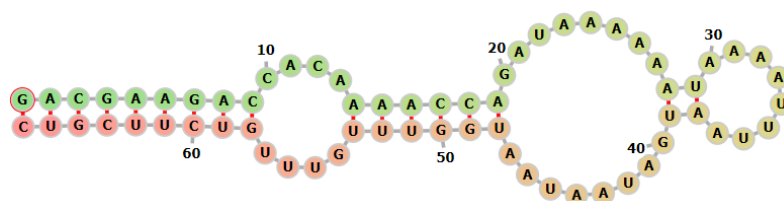


Figure 16 - Predicted structures of virus-derived RNA reported by the Hiscott's group as a potent RIG-I agonist.

In 2015, stem-loop RNAs have been reported as potent and selective RIG-I agonists *in vivo*. Chiang *et al* presented M8, a uridine-rich sequence of 99 nucleotides, that showed high IFN response.<sup>163</sup> More recently, the same structure was shortened to 24 nucleotides, forming a short stem-loop RNA (Figure 17) able to activate RIG-I.<sup>59</sup> This sequence, termed SLR10, is the RIG-I RNA agonist with the shortest length currently described, giving information about the minimal length required to induce RIG-I signaling.

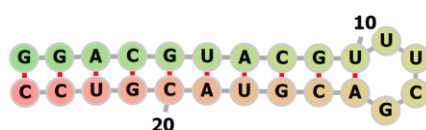


Figure 17 - Predicted structure of SLR10, reported as a RIG-I agonist. It consists in 10 bp blunt-ended at the 5'-termini, and containing a small stem loop of 6 nucleotides. SLR14 and M8 have the same secondary structure, with longer base-paired sequences (14 bp and 96 bp respectively).

While these RNAs showed promising results *in vivo*, two RNA went to phase I/II of clinical trials in oncology until now (Table 4). The main lead RNA is Merck's MK-4621 (NCT03065023 stopped, former Rigontec's RGT100), a 20-24 bp dsRNA that is administered intratumorally or intralesionally using *in vivo*-jetPEI™ (from Polyplus transfection).<sup>164</sup> This drug is either tested alone for solid tumors, or in combination with an anti-PD-1 antibody to benefit from the T cell recruitment induced by RIG-I activation (NCT03739138, on-going).<sup>45,165</sup>

Table 4 - RNA reported as RIG-I agonists in (pre)-clinical trials.

Molecule	Target	Clinical phase	Applications	Sequence (5'- to 3'-)
5'-ppp RNA derived from Vesicular Stomatitis Virus <sup>161,162</sup>	RIG-I	Pre-clinical	Solid tumors	5'-ppp- GACGAAGACCACAAAAC CAGAUAAAAAUAAAAUU



				UAAUGAUAAUAAUGGUU UGUUUGUCUUCGUC
RNAJuvant™, 160	RIG-I and TLR7/8	Phase I (NCT03291002)	Antiviral and solid tumors	547 nucleotides containing polyuridine repeats
5'-ppp RNA M8 <sup>163</sup>	RIG-I	Pre-clinical	Antiviral	5'-ppp- GACGAAGACCACAAAAC CAGAUAAAAAAAAAAAAA AAAAAAAAAAAAAAAAUAAUU UUUUUUUUUUUUUUUUUU UUUUUUUUUAUCUGGUUU UGUGGUCUUCGUC
SLR10 and SLR14 <sup>59</sup>	RIG-I	Pre-clinical	Solid tumors	SLR10: 5'-ppp- GGACGUACGUUUCGACG UACGUCC  SLR14: 5'-ppp- GGAUCGAUCGAUCGUUC GCGAUCGAUCGAUCC
MK-4621 (RGT100) <sup>164</sup>	RIG-I	Phase I/II (NCT03065023, stopped) Phase I (NCT03739138, with anti-PD-1 antibody)	Solid tumors	20-24 nucleotides 5'-ppp- dsRNA, unknown sequence

Fortunately, RIG-I-activating RNA can also be designed to mediate other biological effects. For example, by exploiting the RNA interference (RNAi) mechanism in order to downregulate the expression of a specific gene.<sup>166,167</sup>

#### iv. Synergies between RIG-I signaling and RNA interference

##### 1. Generalities regarding RNA interference

RNAi is a natural phenomenon that silences gene expression by degrading a specific mRNA in order to protect the organism against viruses using small interfering RNAs (siRNA). Structurally, siRNAs are 5'-phosphorylated RNA duplex of 19-23 base pairs, with 2 nucleotides 3'-overhangs, and can further interact with the RNA-induced silencing complex (RISC) to mediate a potent and specific silencing of genes.<sup>168</sup> Three methods can be used to achieve gene silencing by RNAi. The first one is by delivering long dsRNA exogenous double-stranded

RNAs (dsRNA) that are processed in the cytoplasm by a ribonuclease III-like enzyme called Dicer into smaller siRNAs. Another method is to introduce directly siRNAs, thus bypassing Dicer-mediated processing. The last method relies on the delivery of a plasmid that will code for short-hairpin RNAs.<sup>169</sup> These molecules can then be processed by Dicer, cutting off the tetraloop, thus producing siRNAs *in cellulo*.<sup>170</sup>

From a mechanistic point of view (Figure 18), siRNAs are loaded into RISC in the cytosol, which is composed of an endonuclease called Ago2. This protein cleaves one of the two strands of the duplex (called passenger strand or sense strand), letting the other strand (called guide strand or antisense strand) associated with RISC. The strand that will be discarded is the one that has the most stable 5'-end. Therefore, the 5'-end of the guide strand should be a A/U base (containing 2 hydrogen bonds), whereas its 3'-end should be a G/C base (containing 3 hydrogen bonds).<sup>170</sup> Then, the RISC/guide RNA complex is guided to a mRNA by sequence complementarity, thus leading to a Ago2-mediated cleavage of the mRNA – still because of the latter has the highest 5'-stability. As the guide strand only binds mRNA that is fully complementary to its sequence, siRNA causes specific gene silencing by degrading only one mRNA.<sup>171,172</sup> Therefore, siRNAs have been used in oncology to silence oncogenes<sup>173</sup> or in virology to inhibit virus proliferation.<sup>174</sup>

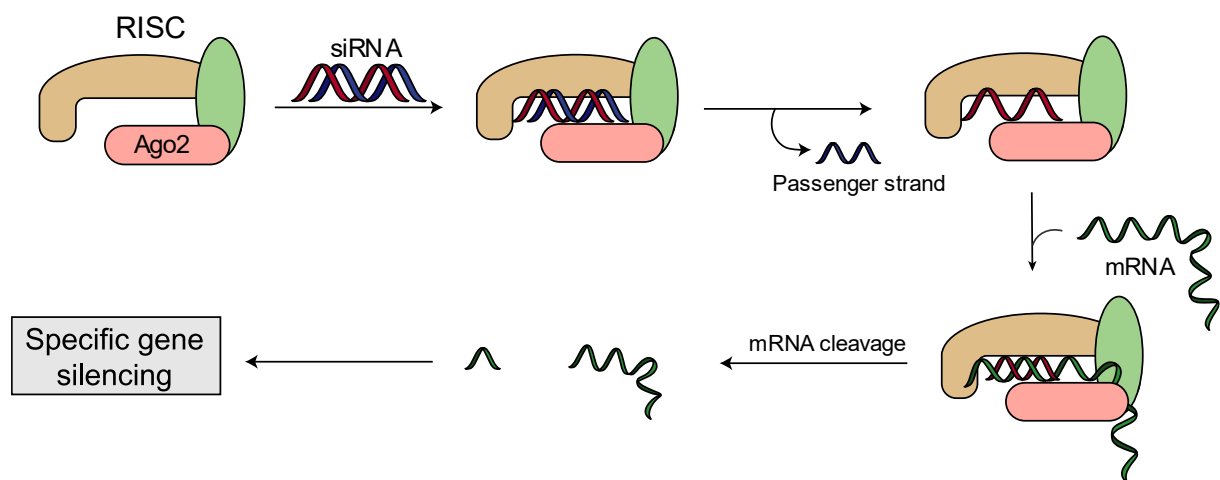


Figure 18 - Mechanism of RNA interference. Small interfering RNAs are associated with the RISC complex that contains an endonuclease called Ago2. Ago2 cleaves one of the two strands (passenger). The other strand can bind to the target mRNA by sequence complementarity. Ago2 then cleaves this duplex, thus degrading the mRNA.

From a production standpoint, the chemical synthesis of these molecules profit from the recent progresses in oligonucleotide's chemistry that decrease manufacturing costs.<sup>175</sup> As siRNAs are fragile molecules prone to enzymatic degradation, the chemical modifications on the siRNA backbone improves their plasma stability, thus increasing the intracellular concentration of fully functional siRNAs.<sup>176</sup> With 3 FDA-approved therapeutic and 7 more in phase III clinical trials, siRNAs represent an attractive class of biomolecules for oncology purposes.<sup>177,178</sup>

## 2. *siRNA-5'-ppp: combining both gene silencing and RIG-I signaling*

Before RIG-I discovery, small interfering RNA (siRNA) produced by phage polymerase were described to induce type-I IFN.<sup>179</sup> As the minimal length for RIG-I activation is now well-described (10-15 bp)<sup>59</sup>, and the optimal length of siRNA is consensually known as 19-21 bp, it appeared that the IFN production could have been, in fact, mediated by RIG-I. Considering the therapeutic potential of both siRNAs and RIG-I along with the latter phenomenon, researchers have developed siRNA-5'-ppp that could simultaneously activate RIG-I and silence oncogenes or immunosuppressive genes (Figure 19). Dual mode of action siRNAs-5'-ppp acting both on RIG-I and on an oncogene could give access to new synergistic systems for immuno-oncology purposes.

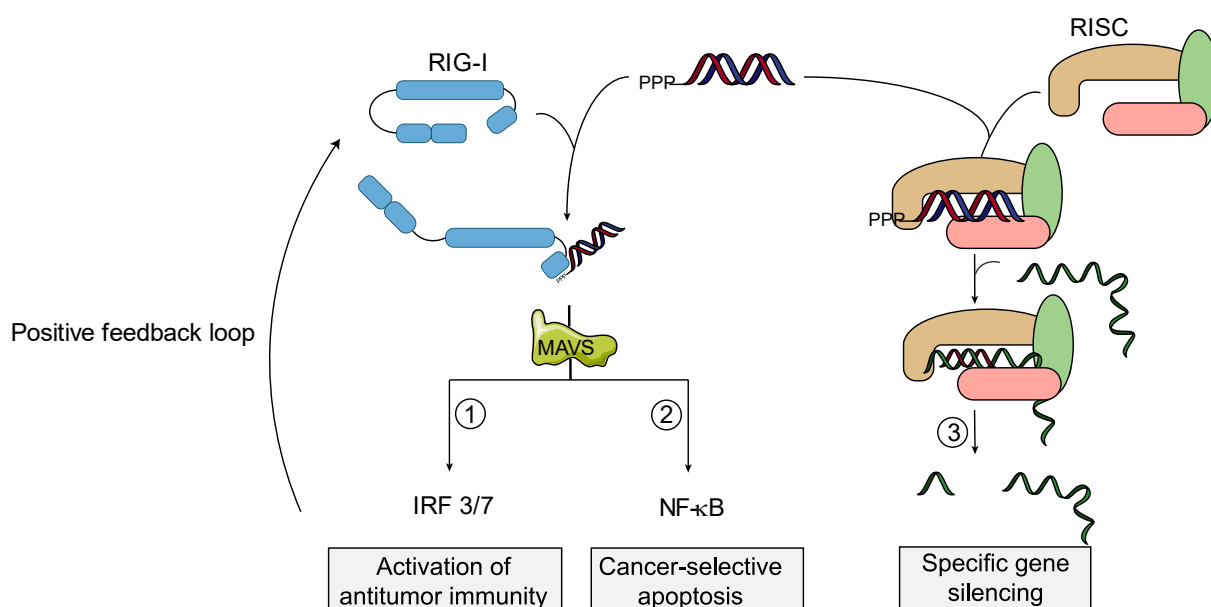


Figure 19 - Concept of siRNA-5'-ppp having dual specific activities. The triphosphate-containing siRNA is recognized by RIG-I, thus inducing a MAVS-mediated activation of antitumor immunity through IRF 3/7 pathway (1) and a cancer-selective apoptosis through NF-κB pathway (2). Then, the siRNA can also be loaded into the RISC complex to perform gene silencing (3).

Bifunctional siRNAs targeting other PRR are currently in clinical development, as exemplified by the bifunctional DUET-01 that combine an anti-STAT3 siRNA with a TLR9 agonist.<sup>180</sup> Regarding RIG-I, the first example of this dual mode of action was published by Hartmann's group using an anti-BCL2 siRNA-5'-ppp in murine melanoma.<sup>115</sup> BCL2 is an anti-apoptotic gene which is involved in the intrinsic apoptosis pathway, silencing this gene led to massive apoptosis in lung metastasis. Since, many strategies with other synergistic gene silencing have been reported. For example, the delivery of anti-TGF-1 $\beta$  siRNA-5'-ppp was used in murine models of pancreatic cancer showed a therapeutic efficacy dependent on immunogenic cell death.<sup>181,182</sup> Another group efficiently killed cancer cells and inhibited angiogenesis by delivering anti-VEGF siRNA-5'-ppp in xenografted lung tumors.<sup>118</sup> More recently, a team

reported that the delivery of anti-MDR1 siRNA 5'-ppp could overcome multi-drug resistance in leukemia models.<sup>116</sup> Last year, a study showed that an *in vitro*-transcribed 5'-ppp-shRNA against NS1 was able to activate RIG-I and silence its target *in vivo* to inhibit influenza A infection.<sup>183</sup> However, this last publication is in contradiction with an another study that showed that RIG-I activation represses shRNA-induced silencing.<sup>184</sup>

While these strategies demonstrated the therapeutic potential of dual siRNA/RIG-I mechanisms, none of these studies silenced a gene directly involved in RIG-I signaling in order to amplify it yet. Indeed, bifunctional siRNA-5'-ppp able to silence a gene involved in RIG-I signaling could lead to a high induction of apoptosis and antitumoral immunity. This is the strategy that we developed during this thesis. One pertinent protein able to exhibit such synergy is Polo-like Kinase 1 (PLK1).

### 3. *Polo-like Kinase 1 (PLK1)*

Human PLK1 is a Ser/Thr kinase structurally and functionally homologous to the *drosophila* polo protein.<sup>185</sup> From a structural point of view, PLK1 is composed of one kinase domain and two polo box domains (PBD, Figure 20). PLK1 expression is highly dependent on the cell cycle, with low level of protein in the G1 and S phase. During G2 phase, its expression increases until reaching a maximum in M phase. After the completion of cell division, PLK1 expression drops back to its starting level (Figure 20).<sup>186</sup>

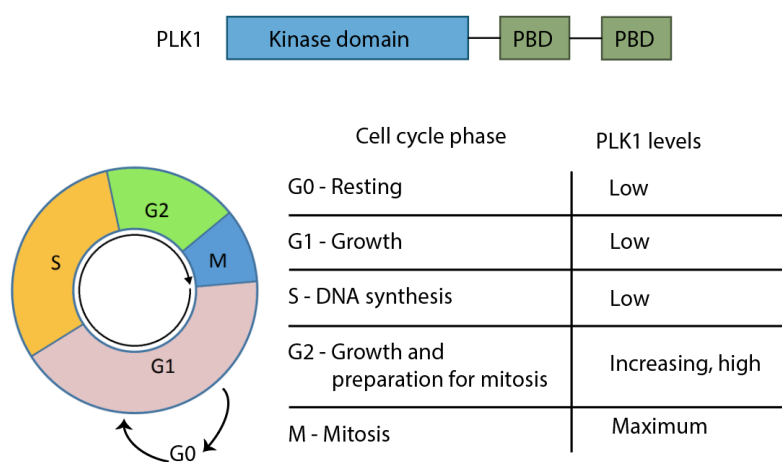


Figure 20 - PLK1 structure and expression levels during the cell cycle.

#### a. *Biological roles in cancer therapy*

PLK1 can affect cell growth by multiple mechanism. For example, PLK1 is playing a key role in the cell cycle regulation *via* the phosphorylation of CDC25, thus activating the cyclin B/CDK1 complex and triggering the cell's transition from G2 to M phase (Figure 21-1).<sup>187</sup> Besides its effects on the cell cycle, it has been showed that PLK1 is a regulator of DNA damage checkpoint by phosphorylating checkpoint kinase 2 (Chk2), which ultimately activate the DNA

repair machinery during mitosis (Figure 21-2).<sup>188,189</sup> In addition, previous studies have shown that PLK1 phosphorylates the DNA-binding domain of p53, therefore inhibiting p53-mediated pro-apoptotic signaling (Figure 21-3).<sup>190,191</sup>

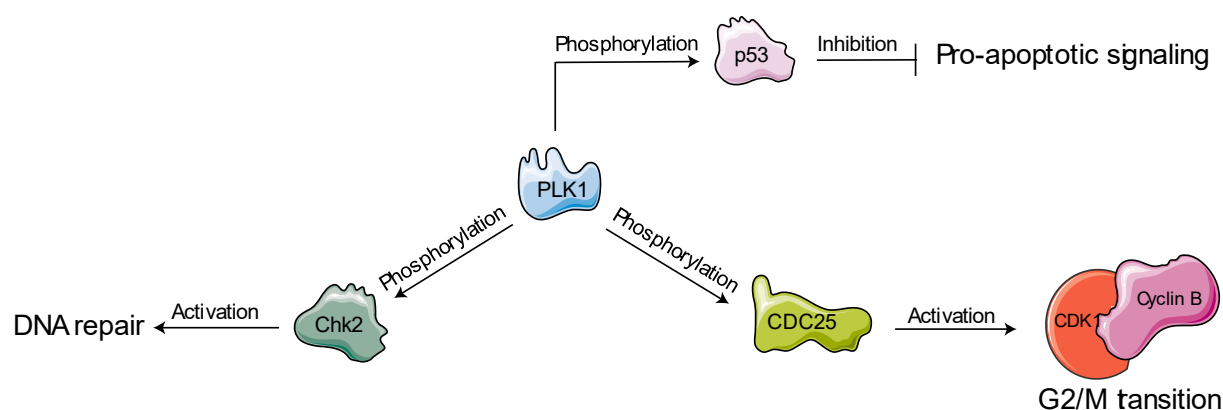


Figure 21 - Implication of PLK1 in DNA repair, apoptosis and cell cycle regulation. Inhibition of PLK1 thus activates p53-mediated apoptosis, induces cell cycle arrest at the G2/M phase and inhibits DNA repair.

As a consequence, inhibiting PLK1 or its expression induces p-53-mediated apoptosis, stops the cell cycle to the G2/M phase, and inhibits the DNA repair machinery.<sup>192</sup> In addition, it has been shown that PLK1 inhibition could induce immunogenic cell death and convert cancer cells into endogenous vaccines which triggered immune memory responses.<sup>193</sup>

### b. PLK1 inhibitors in clinical trials

Considering all these elements, PLK1 was often proposed as a potential target for cancer therapy.<sup>194</sup> Small molecules represent one strategy to inhibit PLK1, and to date, two compounds are in clinical phase III (Figure 22).<sup>195,196</sup> So far, only rigosertib is considered as a PLK1-selective inhibitor.<sup>197</sup> Volasertib acts as a ATP-competitive inhibitor by binding to the kinase ATP-binding domain.<sup>198,199</sup> However, these domains are highly conserved among kinases, thus ATP-competitive inhibitors can often act on other kinases than PLK1.

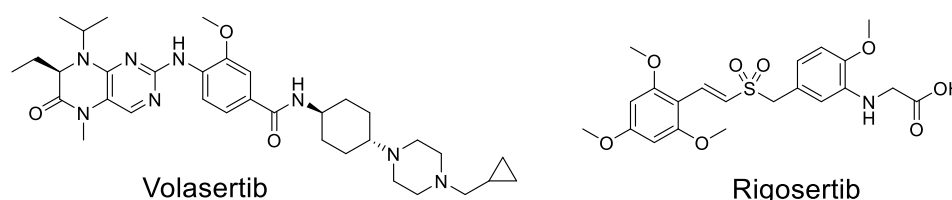


Figure 22 - Structures of small molecule drugs in clinical phase III targeting PLK1.

However, mutations appears frequently in ATP-binding domains, thus patients generally develop resistance to these molecules.<sup>200</sup> Therefore, other strategies based on siRNAs have been reported in order to avoid these resistance issues.<sup>201-203</sup>

### *c. PLK1 silencing and synergies with RIG-I activation*

It has been shown that PLK1 decreases MAVS-dependent IFN production, a pathway involving RIG-I signaling.<sup>204,205</sup> Indeed, inhibiting PLK1 with siRNAs greatly enhanced the production of IFN by MAVS. Therefore, it appears that simultaneous PLK1 inhibition and RIG-I activation could lead to a very high production of IFN. In addition, the cell survival could be highly impacted by the multiple mechanisms of action following PLK1 silencing and RIG-I activation.

Considering these elements, siRNA-5'-ppp both silencing PLK1 and activating RIG-I appeared as a relevant strategy. In this thesis, we thus propose to deliver such siRNA-5'-ppp inside tumors.

### *D. Delivery of siRNA-5'-ppp in tumors*

#### *i. Generalities regarding the siRNA delivery methods currently in clinical phase III or FDA-approved*

The delivery of siRNA to the site of action is a challenging field. Indeed, these molecules are poorly membrane-permeant as they are highly hydrophilic, negatively charged, and have a high molecular weight. Therefore, the siRNA should be delivered to the site of action by using vectors that protect it against degradation while enhancing tissue penetration.

Three families of approaches have been explored for the delivery of siRNA:

- Complexation with cationic molecules such as peptides<sup>206</sup> or polyethyleneimine.<sup>207</sup>
- Encapsulation in cationic particles like liposomes<sup>208</sup>, micelles<sup>209</sup> or inorganic particles.<sup>147</sup>
- Conjugation to ligands that target a cell-surface antigen.<sup>210</sup>

Among the 10 siRNAs that reached clinical phase III, only the two last methods have been used.

#### *1. Encapsulation into particles*

Encapsulation of siRNAs into particles exploits the negative charges of the RNA to encapsulate it into a cationic Stable Nucleic Acid-Lipid Particle (SNALP) that facilitates cellular uptake and protects the molecule from degradation. SNALPs are lipidic nanoparticles containing three elements: cationic lipids, non-ionic lipids and pegylated chains. Briefly, cationic lipid will form complexes with the siRNA, the non-ionic one serves for the transfection efficiency by enhancing the endosomal escape, and the pegylated chains is for solubility.<sup>211</sup> The first FDA-

approved siRNA drug, Patisiran™, use this technology. Patisiran™ is used for the treatment of hereditary transthyretin-mediated amyloidosis, a fatal disease caused by an abnormal production of transthyretin in the liver. Therefore, this siRNA silences transthyretin mRNA, leading to a decrease in amyloid deposits in the tissue. These particles are particularly efficient for the transfection and the protection of the siRNA, with a plasma half-life increasing from 2 min to 6.5 hours.<sup>212</sup> However, these particles often lack targeting agents, thus delivering the RNA in all neighboring cells.<sup>208,213</sup> In addition, these particles often accumulate in the liver, explaining why the major targeted organ of siRNAs currently in clinical trials is the liver.<sup>214</sup> Therefore, expanding the application to other organs by targeting a tissue-selective receptor is required to increase the potential of siRNAs.

## 2. *siRNA conjugates*

Selective delivery of siRNA could be achieved by conjugation to a trimer of *N*-acetylgalactosamine (GalNAc).<sup>175</sup> GalNAc binds to the asialoglycoprotein receptor that is mainly expressed on hepatocytes, inducing internalization in endosomes. Due to the pH drop, the siRNA is released from the receptor/GalNAc complex, which can be recycled back to the membrane. A small portion of siRNA escapes the endosome by a currently unknown mechanism.<sup>210</sup> Two FDA-approved siRNAs, Givosiran™ and Lumasiran™ use this technology. Like SNALP, GalNAc conjugates are however limited to target the liver.<sup>214</sup> In order to expand the field of application to other organs, conjugation of siRNAs to other targeting agents can be envisioned as a viable approach. In particular, monoclonal antibodies.<sup>215</sup>

### ii. *Generalities regarding antibody-based targeted therapies*

Since their development for laboratory uses in 1975, monoclonal antibodies (mAbs) have become an invaluable tool for therapies against cancers or auto-immune diseases, mainly because of their high specificity and affinity for a target antigen.<sup>216,217</sup> From a structural point of view (Figure 23), these proteins are Y-shaped homodimeric immunoglobulin G (IgG).<sup>218</sup> Different isotypes of IgG exist, differing by their post-translational modifications and their intrachain disulfide bonds. In the following sentences, we will focus on the structure of IgG1 exclusively.

IgG1 are composed of two light chains (LC, orange) and two heavy chains (HC, blue), divided into constant and variable fraction linked *via* interchain disulfide bonds.

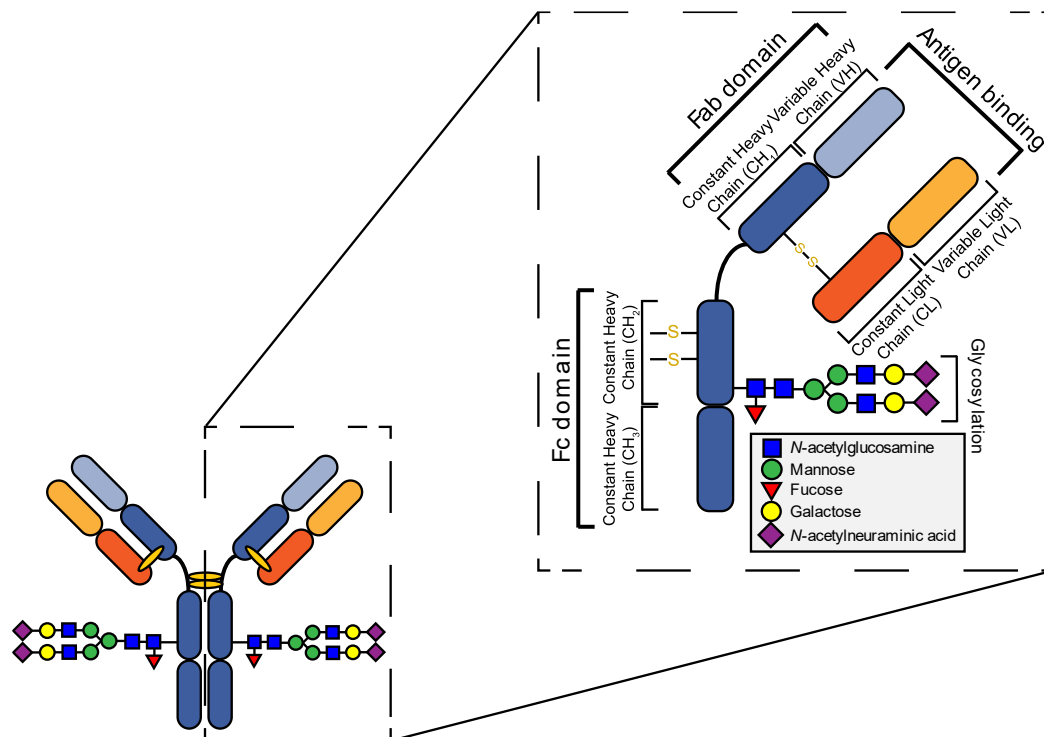


Figure 23 - Structure of monoclonal antibodies: example with IgG1.

More precisely, the antigen-binding fraction (Fab) is composed of one constant HC domain ( $CH_1$ ), one constant LC domain (CL), one variable HC domain (VH) and one variable LC domain (VL). The constant fraction (Fc) is composed of two constant HC regions ( $CH_2$  and  $CH_3$ ), and is common to all IgG1.<sup>219</sup> While the Fab has a high affinity for a particular antigen ( $K_D \text{ Fab/antigen} = 10^{-9}\text{-}10^{-12}$ )<sup>220</sup>, the Fc is essential for recognition by immune cells through the binding to  $Fc\gamma R$  ( $K_D \text{ Fc}/Fc\gamma R = 10^{-9}$ ).<sup>221,222</sup>

As a post-translational modification, IgG1 – and mAbs in general – contain a conserved, single *N*-glycan site at N297 position which is essential for the binding to  $Fc\gamma R$ .<sup>223</sup> The different isotypes of IgG do not bind to  $Fc\gamma R$  with the same affinity, mainly due to a different glycosylation state. IgG1 are currently used as anticancer agents by exploiting both the Fab and the Fc regions to influence the antigen's biology, by either blocking or changing its function upon binding.<sup>224,225</sup>

Against tumors, mAbs interact with a transmembrane protein or its soluble ligand, acting either as an agonist or an inhibitor of these proteins.<sup>226</sup> Agonist antibodies can promote cell death by apoptosis through the extrinsic mechanism, as exemplified by the FDA-approved rituximab (anti-CD20, Rituxan®). Upon binding to CD20, this antibody induces caspase 3/7-mediated apoptosis and a subsequent reduction in circulating B lymphocytes (Figure 24A).<sup>227–230</sup>

Inhibiting antibodies perturb the intracellular signaling induced by the targeted antigen, or by the interaction between a receptor and its ligand. One example is pembrolizumab (anti-PD-1,



Keytruda®), able to block PD-1 on T cell, avoiding its interaction with cancer cells' transmembrane protein PD-L1. As they are immune checkpoints, blocking PD-1/PD-L1 interaction impede cancer cells to evade the immune system, thus leading to the T cell activation and the subsequent cancer cell killing (Figure 24B).<sup>231–233</sup> As ligand-neutralizing mAb, bevacizumab (anti-VEGF-A, Avastin®) blocks VEGF-A binding to its receptor VEGFR, therefore inhibiting angiogenesis (Figure 24C).<sup>234</sup>

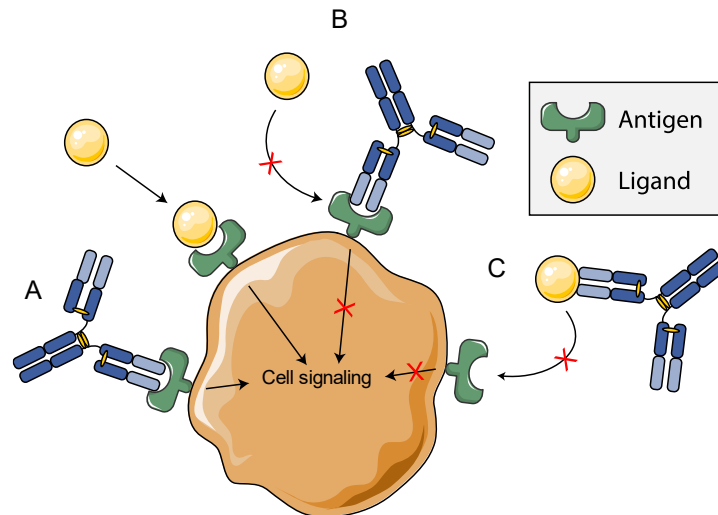


Figure 24 - Mechanism of action involving antibodies Fab. Antibodies can act as an agonist for a death receptor, further inducing apoptosis (A) or can act as an inhibitor of a receptor (B) or its ligand (C) to avoid their cell signaling.

Upon binding to its target *via* the Fab, three mechanisms of action involving the immune system can be activated by mAbs through their Fc fragment,<sup>235</sup> all leading to cancer cell death.<sup>223,224</sup> Two of these mechanisms involve effector cells. On the one hand, Natural Killer (NK) cells bind antibodies through Fc $\gamma$ R11a (also called CD16), triggering antibody-dependent cell cytotoxicity (ADCC, Figure 25A),<sup>236,237</sup> which consists in secreting granzymes that are able to lyse the Fab-bound cell.<sup>219,238</sup> As the antibody is needed in the outer membrane of the cell, ADCC generally requires abundant and slow-internalizing antigens.<sup>239</sup> On the other hand, macrophages can also bind antibodies through Fc $\gamma$ R11a, triggering phagocytosis of the Fab-bound tumor cells, a phenomenon called antibody-dependent cellular phagocytosis (ADCP, Figure 25B).<sup>240–242</sup>

The last effector function of mAbs is the complement-dependent cytotoxicity (CDC, Figure 25C). When bound to a surface antigen, mAbs trigger the classical complement pathway by binding the protein C1q to the Fc part, resulting in the formation of a membrane attack complex and subsequent cell lysis.<sup>243,244</sup> The FDA-approved daratumumab (anti-CD38, Darzalex®) uses all these three mechanisms simultaneously.<sup>245,246</sup>

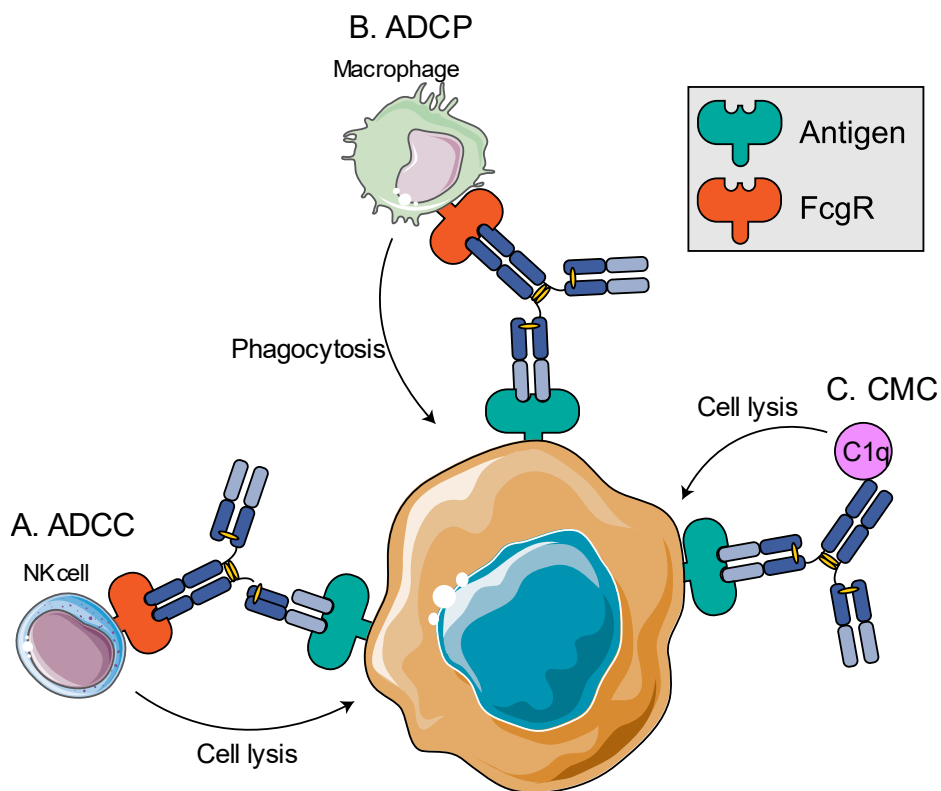


Figure 25 - Mechanisms of action induced by the Fc region. NK cells can kill the tumor by ADCC (A), macrophages can phagocytize them by ADCP (B) and the complement system can be activated, leading to the cell's lysis (C).

While many therapeutic mAbs are currently administered to patients, tumors can develop resistances to them, thus reducing their potency, for example by reducing the antigen's expression.<sup>230,233,247</sup> This is, for example, the case with trastuzumab-resistant HER2-positive breast tumors.<sup>248</sup> To overcome mAb resistance and expand the amount of mechanisms leading to cell death, using the targeting properties of mAbs to vectorize cytotoxic drugs into cancer cells appeared as a viable strategy. This concept led to the development of antibody-drug conjugates (ADC).

### iii. Antibody-drug conjugates

#### 1. Structures and mechanisms of action

In 1913,<sup>249</sup> Paul Ehrlich proposed to exploit the antigen-specificity of a protein to deliver highly potent and cytotoxic drugs into the targeted cells in order to kill them.<sup>250</sup> A pioneer idea that took 45 years to be implemented, with the description of a IgG-amethopterin conjugate and its application for *in vivo* leukaemia model.<sup>251</sup> Since, ADCs gained interest throughout the entire scientific community and pharmaceutical companies to address difficult-to-cure cancers.<sup>252</sup> With a current total of 12 FDA-approved ADCs and 90 mores in clinical trials, they represent a well-established strategy for oncology.<sup>248</sup>

From a structural point of view, ADCs are composed of three elements which contribute to their overall potency, tolerability and safety (Figure 26): i) a monoclonal antibody (generally IgG1 or IgG4) which binds to the cancer cell's antigen *via* its Fab, ii) a drug responsible for cell death and iii) a linker connecting the two entities in a covalent manner.<sup>253</sup> Each of these three components has a crucial role. The mAb is essential for targeting and internalization properties. Moreover, it determines the pharmacokinetic properties of the conjugate. The drug is responsible for the cytotoxicity, therefore dictating the intracellular mechanism of action. Finally, the linker is the chemical entity connecting the drug to the antibody, and determines the mechanism of drug release. Its stability is also highly important, as it is directly related to adverse effects: its premature cleavage can lead to off-target toxicities.<sup>254</sup> Structural insight regarding linkers used in ADC will be presented in an adapted chapter.

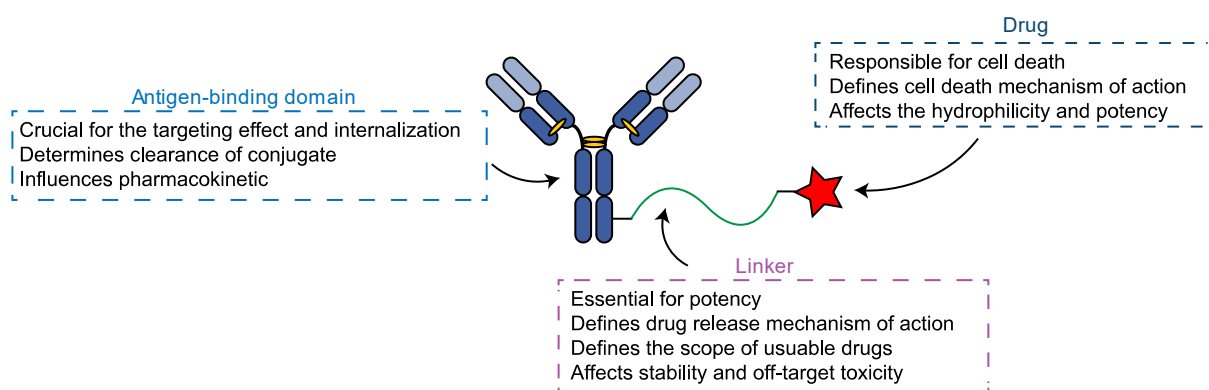


Figure 26 - Structural insight of antibody-drug conjugates, highlighting the importance of all the three components. Adapted from Bargh et al.<sup>254</sup>

From a mechanistic point of view (Figure 27), an ADC exerts its activity by first binding to its target transmembrane antigen, inducing a signaling pathway promoting its internalization (1) by endocytosis. The ADC is then degraded by endosomal proteases, ultimately leading to the release of the drug from its linker and antibody in the cytosol (2) to kill the cell. If the drug is sufficiently membrane—permeable, it can then diffuse out of this initial cell (3) and kill neighboring cells (4), a phenomenon called bystander effect, which greatly increases the potency of ADC against heterogeneous solid tumors.<sup>255–258</sup> However, this effect may be unwanted in particular cases, such as liquid tumors, because of a too high risk of killing neighboring healthy cells (5).

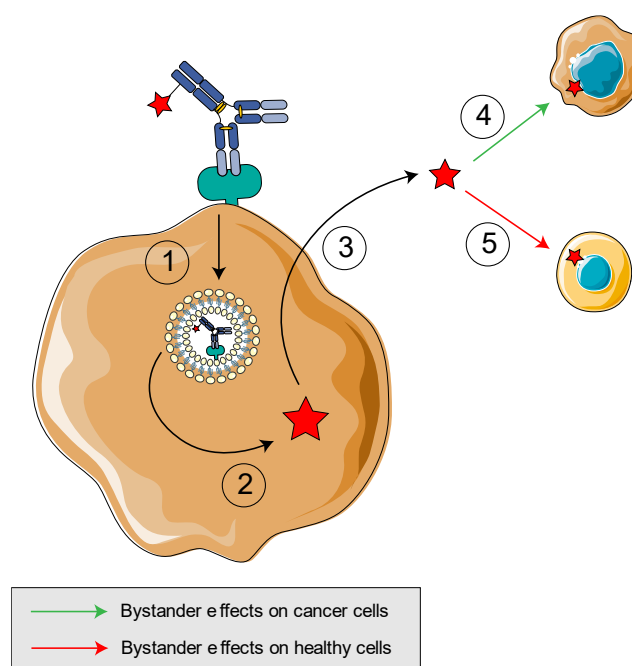


Figure 27 - Mechanisms of action of antibody-drug conjugates, highlighting antigen-dependent internalization (1), leading to the drug release in the cytosol (2). If sufficiently membrane-permeable, the drug can diffuse out the cell (3), performing bystander effects on both cancer cells (4) and healthy cells (5)..

## 2. Therapeutic benefits of ADCs

ADCs are currently used to cure cancers by targeting directly the tumors, thus limiting adverse effects often encountered by classical chemotherapy drugs. Both solid and liquid tumors are targeted with ADCs, generally as a second- or third-line therapy for patients that have received prior treatments. For example, Kadcyła™ (Trastuzumab-emtansine) is given to patients with metastatic HER2-positive breast cancer that stopped responding to the sole trastuzumab. Regarding the benefits, several studies have observed that ADCs improve the median overall survival time compared with other therapies. For example, the survival time was improved by almost seven months after treatments with Kadcyła™ compared to other, non-ADC treatments.<sup>259</sup>

However, despite their positive therapeutic effects against several cancers, ADCs still suffer from drawbacks that limit their potency, explaining why many of these biotherapeutic failed to reach clinical phase III. Among them, off-targets effects due to the design of the antigen-binding domain, a lack of homogenous conjugation, and, most importantly, an insufficient intracellular drug concentration.

## 3. Limitations of ADCs

### a. Antigen-binding domain

The antigen-binding domain of the ADC is one of the key parameters for an ADC efficacy. Indeed, it determines the cancer-selectivity, the internalization, the intracellular trafficking

pathways, and also impact the pharmacokinetic-pharmacodynamic (PK-PD) properties of the ADC. Full IgGs are the default scaffold, however their Fc-part allows their recycling to the cell surface by the neonatal Fc receptor (FcRn), thus avoiding lysosomal degradation and resulting in long half-lives ( $t_{1/2} = 7-21$  days).<sup>260,261</sup> In addition, their high molecular weight also prevents IgG-based ADCs to reach their full potential,<sup>262</sup> due to a lower ability to penetrate tumours<sup>263,264</sup>, therefore leading to a high systemic accumulation.<sup>265,266</sup>

Since full IgG could bind to Fc $\gamma$  receptors found on numerous type of cells and be internalized, this accumulation could ultimately lead to off-target toxicities.<sup>267,268</sup> For example, published data has shown that Adcetris<sup>TM</sup> binds to Fc $\gamma$ RIIa, leading to its internalization by megakaryocytes, thus resulting in thrombocytopenia.<sup>269,270</sup> This off-target toxicity can be diminished by using IgG4 instead of IgG1 for the antibody's scaffold, as exemplified by Mylotarg<sup>TM</sup>, as IgG4 have a lower affinity to Fc $\gamma$  receptors than IgG1.<sup>271</sup>

For these reasons, smaller scaffolds based on antibody fragments were developed, such as Fab<sup>272</sup>, single-chain variable fragment (scFv)<sup>273-275</sup> or nanobodies conjugates.<sup>276-278</sup> This particular point will not be discussed further in this manuscript.

#### *b. Heterogeneity of produced conjugate*

Having hundreds of potential conjugation sites, conjugating full IgG can generate heterogeneous mixtures of ADCs, with different drug-loadings and conjugation sites, resulting in numerous analytical issues. Besides, these highly heterogeneous mixtures influence the overall PK-PD profiles, ultimately leading to a narrower therapeutic window.<sup>248,279,280</sup> For example, naked antibody can be a competitive inhibitor, thus decreasing the global potency of the ADC. Low-DAR ADC may have a poor potency,<sup>281,282</sup> and high-DAR with highly hydrophobic payloads usually give precipitated species that can be rapidly eliminated, leading to a decreased plasma stability.<sup>283</sup> To address this issue, several methods have been developed in order to enhance the homogeneity of ADCs. This particular point has been recently reviewed by the Spring's group.<sup>284</sup>

#### *c. Internalization and trafficking*

Antibody internalization is correlated with the level of expression of its surface antigen and its mechanism of internalization. Indeed, a low antigen expression can completely inhibit the activity, because of a too low intracellular drug concentration.<sup>285,286</sup> Upon binding, the conjugate is then internalized depending on the antigen's biology in terms of speed of internalization and metabolism. While some antigens can be degraded, others can be recycled back to the membrane, thus impeding the drug to reach its intracellular target.<sup>287</sup> In order to increase internalization rate, biparatopic antibodies (targeting two different epitopes of the same

antigen) exhibited a higher efficacy to deliver drugs inside cells compared to monoparatopic antibodies.<sup>288,289</sup>

#### 4. Scope of drugs

Considering all the elements presented above, the reachable drug concentration inside tumors is extremely low. To avoid the injection of high doses to patients, it appeared that the conjugation of highly cytotoxic drugs ( $IC_{50}$  in the sub-nM or pM range) was required, sometimes 100 to 1000 times more toxic than classical drugs for chemotherapy.<sup>257</sup> To date, the majority of drugs in ADCs target either the microtubules or the DNA.

##### a. Microtubule-targeting payloads

Microtubule-targeting payloads exert their toxicity at the G2/M phase of the cell cycle, causing a cell cycle arrest at this stage and ultimately leading to the cell death by apoptosis. Three families of drugs target the microtubules: maytansinoids, auristatins and tubulysins.

Maytansinoids are extremely hydrophobic 19-membered macrocyclic lactams that are able to block the polymerization of tubulin, thus inhibiting the formation of microtubules.<sup>290</sup> Kadcyła™ was the first FDA-approved ADC containing DM1, a maytansinoid (Figure 28). The conjugation of maytansinoids is performed with a non-cleavable linker in order to release a polar amino-acid conjugate.<sup>256,291</sup> As the free drug is membrane permeable resulting in off-target toxicities by bystander effects, the amino-acid conjugate form limits this drawback, therefore widening the therapeutic window.

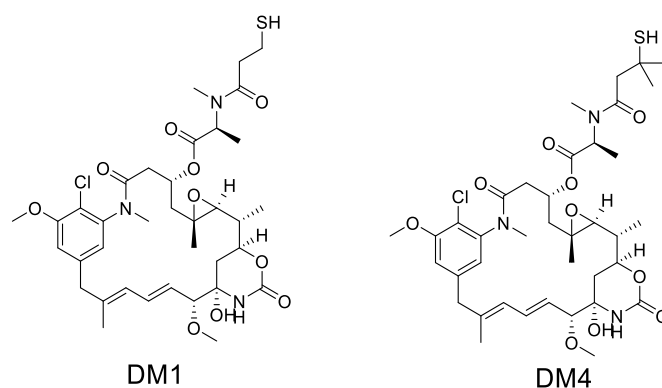


Figure 28 - Structures of DM1 and DM4, two maytansinoids respectively used in Kadcyła™ and SAR408701, currently in clinical trials.

Auristatins are peptide analogues causing excessive growth of microtubules and G2/M arrest. Two lead molecules have been reported (Figure 29): monomethyl auristatin E (MMAE) and monomethyl auristatin F (MMAF). An example of auristatin-conjugate is the FDA-approved Adcetris™. From a structural point of view, the presence of a C-terminal phenylalanine residue in MMAF contributes to its membrane impermeability. This difference correlates with the  $IC_{50}$

values of the unconjugated drugs, MMAF being 100 times less cytotoxic than MMAE.<sup>257</sup> Therefore, conjugating MMAF greatly increases its potency because of an enhanced cellular uptake.<sup>292</sup> In addition, contrary to MMAE, MMAF cannot diffuse out of the cell because of its charge, thus only MMAE is able to perform bystander effects.

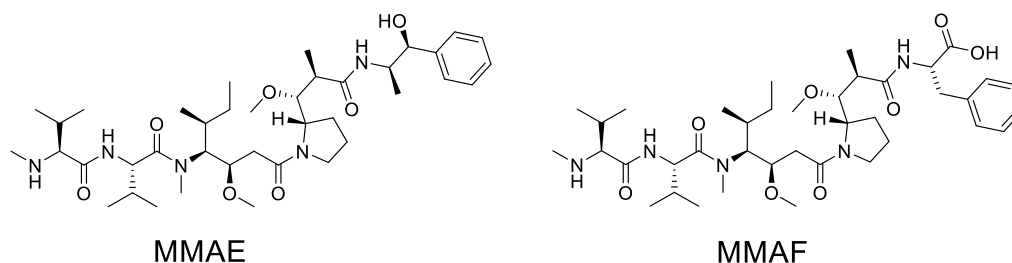


Figure 29 - Structures of MMAE and MMAF, two auristatins used respectively in Adcetris™ and Blenrep™.

Tubulysins are a family of 14 microtubule-disrupting peptide analogues.<sup>293</sup> MEDI4276 is an ADC currently in clinical trial phase I/II (NCT02576548) containing AZ13599185, a tubulysin drug (Figure 30).<sup>289,294</sup> This prodrug is deacylated by unspecific esterases *in cellulo*, thus yielding the active secondary alcohol.

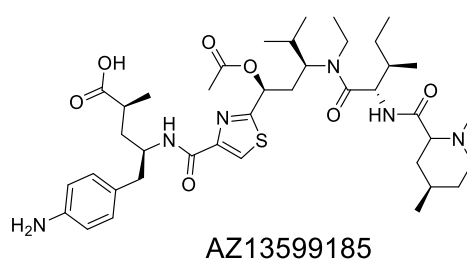


Figure 30 - Structure of AZ13599185, a tubulysin that was conjugated to a biparatopic anti-HER2 antibody (MEDI4276).

### b. DNA-damaging payloads

DNA-targeting molecule exert their cytotoxicity in the nucleus through binding in the minor groove of DNA. Three mechanisms of action have been exploited in the ADC field: calicheamicins are DNA-double-strand breakers, camptothecins act as DNA-intercalators, and pyrrolobenzodiazepines are DNA alkylators.

Calicheamicin was used in the first FDA-approved ADC, Mylotarg™ (Figure 31).<sup>295</sup> It promotes the production of reactive diradical species that are able to break the double-stranded structure of DNA. In order to conjugate the molecule to antibodies, the natural trisulfide bond was replaced by a disulfide, which is glutathione-cleavable. The resulting free thiol reacts on the neighboring Michael acceptor, leading to a Bergman cyclization of the ene-diyne motif. This reaction forms a diradical, which reacts with the DNA, causing double-strand breaks.<sup>296</sup>

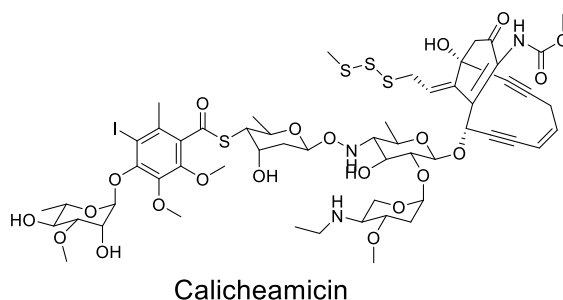


Figure 31 – Structure of calicheamicin used in Mylotarg™. In this ADC, the trisulfide bond is replaced by a disulfide bond.

Camptothecins are inhibitors of DNA topoisomerase I, therefore inhibiting DNA synthesis and resulting in DNA damage and apoptosis.<sup>297</sup> Trodelvy™ and Enhertu™ are two FDA-approved ADCs containing camptothecin analogues with an average DAR of 7.5 (Figure 32).<sup>298</sup> Interestingly, the lactone group of these molecules directs their activity: the closed lactone is the active form of the drug, and the opened form is inactive. The latter is produced at physiological pH, however the acidic pH found in the extratumoral media or in lysosomes, promotes the cyclization to the active form.<sup>299</sup>

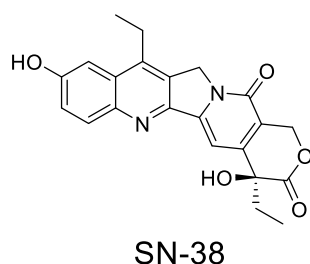


Figure 32 - Structures of SN-38, a camptothecin analogue used in Trodelvy™.

Other DNA-targeting molecules are currently used in clinical trials that act as alkylating agents, such as pyrrolobenzodiazepines (PBD). The PBD-DNA adduct avoids DNA repair by distorting the double-helix. Developed by the Thurston's team, PBD dimers exert a 600-fold increase in cytotoxicity compared to PBD monomer by intrastrand/interstrand double-alkylation of DNA, leading to DNA cross-link (Figure 33).<sup>281,300</sup> Zynlonta™ is a newly FDA-approved ADC containing a PBD dimer. Although these drugs are more toxic than the previous ones, they are also much more hydrophobic, thus a low DAR is required to avoid aggregation.

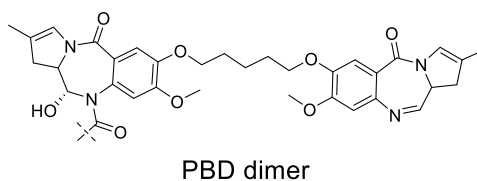


Figure 33 - Structures of PBD dimer used in Zynlonta™.



## 5. *Resistance mechanism and potential novel payloads*

Despite these potent drugs, the scope of biological targets is limited to the microtubules and the DNA. In addition, the most frequent resistance mechanism to ADCs is the expression of drug efflux protein, such as Multi-Drug Resistance protein 1 (MDR1), which has a good affinity with hydrophobic drugs. One strategy to overcome this issue is to use more polar drugs that are poor substrates of these proteins. Furthermore, even if it has never been reported yet, alteration of the drug's target, for example by mutations, could potentially lead to resistance. Regarding these elements, it appears that new targets and mechanisms of action are needed.<sup>301</sup>

According to the latest estimations, only few hundreds of proteins in the human proteome are suitable targets for small molecule ligands.<sup>302</sup> In fact, many cellular functions rely on protein-protein interactions, and these complexes often lack defined binding site for small molecule, limiting their potential as therapeutic targets.<sup>303</sup> In addition, some diseases are caused by protein mutations, and designing a specific inhibitor for these mutations is still challenging, although it has been achieved very recently with the first FDA-approved KRAS<sup>G12C</sup> inhibitor.<sup>304</sup> These elements led to the concept of “undruggable” targets, proteins that are currently inaccessible for small molecules.<sup>305</sup> To address this issue, other strategies acting at the genetic, transcriptional or translational levels are required. One such strategy can be impacted with high precision by delivering non-coding oligonucleotides, such as siRNA (see page 40).

### E. *Antibody-siRNA conjugates*

Antibody-RNA conjugates (ARCs) combine the delivery potential of antibody and the high precision of siRNA, thus synergizing the advantages of these biomolecules.<sup>306</sup> Indeed, siRNAs can profit from the high ligand binding of an antibody for its antigen ( $K_D$  mAb/antigen  $< 10^{-9}$  M) and its high molecular weight for a prolonged presence in blood.<sup>307</sup> While preparing an ADC is challenging because of heterogeneity and solubility, the physicochemical properties of the oligonucleotide amplify these problems. In addition, the overall charge of the conjugate can become anionic with high drug-to-antibody ratio, thus potentially changing the biophysical properties of the antibody.<sup>308</sup>

To date, two different approaches have been developed to couple an antibody and a siRNA, the first one involves the direct covalent conjugation of the oligonucleotide to the antibody, the second is based on ionic interactions between a polycationic peptide and the siRNA (Figure 34).<sup>309</sup> Herein we propose to review the advances made in the targeted and covalent delivery of siRNAs by antibodies from a synthetic point of view. In a next chapter (starting at page 185), we will describe the non-covalent constructs.

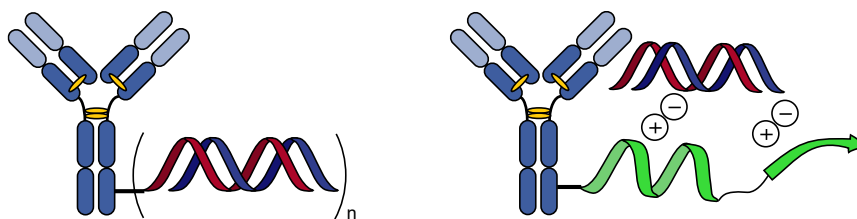


Figure 34 - The two different approaches currently reported. On the left, a covalent model where the siRNA is attached to the antibody through a linker. On the right, a non-covalent model where the antibody is modified with polycationic peptides/protein, allowing siRNA complexation.

The simplest way to conjugate a siRNA to antibody is by modifying the oligonucleotide in a covalent manner with a linker, which will then react with the antibody, affording constructs that can be analyzed like an ADC. In the case of siRNA, the linker is usually located at one of the terminus of one strand, thus improving the RNA stability toward nuclease *in vivo*.<sup>170,310–313</sup>

In order to avoid any decrease in the potency, the linker is generally conjugated to the passenger strand (termed sense strand), where both 3'- and 5'-ends can be conjugated. As the active strand (termed antisense strand) is involved in the RNA interference mechanism and that its 5'-end must be phosphorylated in the process to achieve RNAi, this strand can only be modified on the 3'-end. (Figure 35).<sup>314</sup>

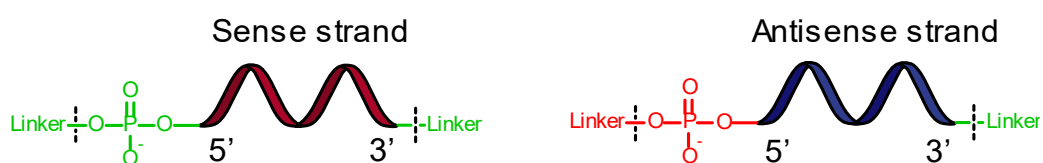


Figure 35 – Possible conjugation site of siRNA (in green). As the 5'-end of the antisense strand (in red) needs to be phosphorylated in order to obtain a recognition by Ago2, this position is generally not modified.

## i. Design of the conjugates

### 1. Conjugation by protein-ligand interactions

The very first method to couple siRNA to an antibody was published in 2007 by the Pardridge's group, where the authors used the almost-covalent affinity of biotin-avidin system ( $K_D = 10^{-15}$  M, dissociation  $t_{1/2} = 89$  days)<sup>315</sup>, to obtain a highly stable linkage.<sup>316</sup> The conjugation was done by modifying streptavidin's lysines with Traut's reagent in order to install sulfhydryl groups able to react by Michael addition on maleimide-modified antibody.<sup>317</sup> Then, a 3'-biotinylated siRNA was mixed with the streptavidin-conjugated antibody (Figure 36).

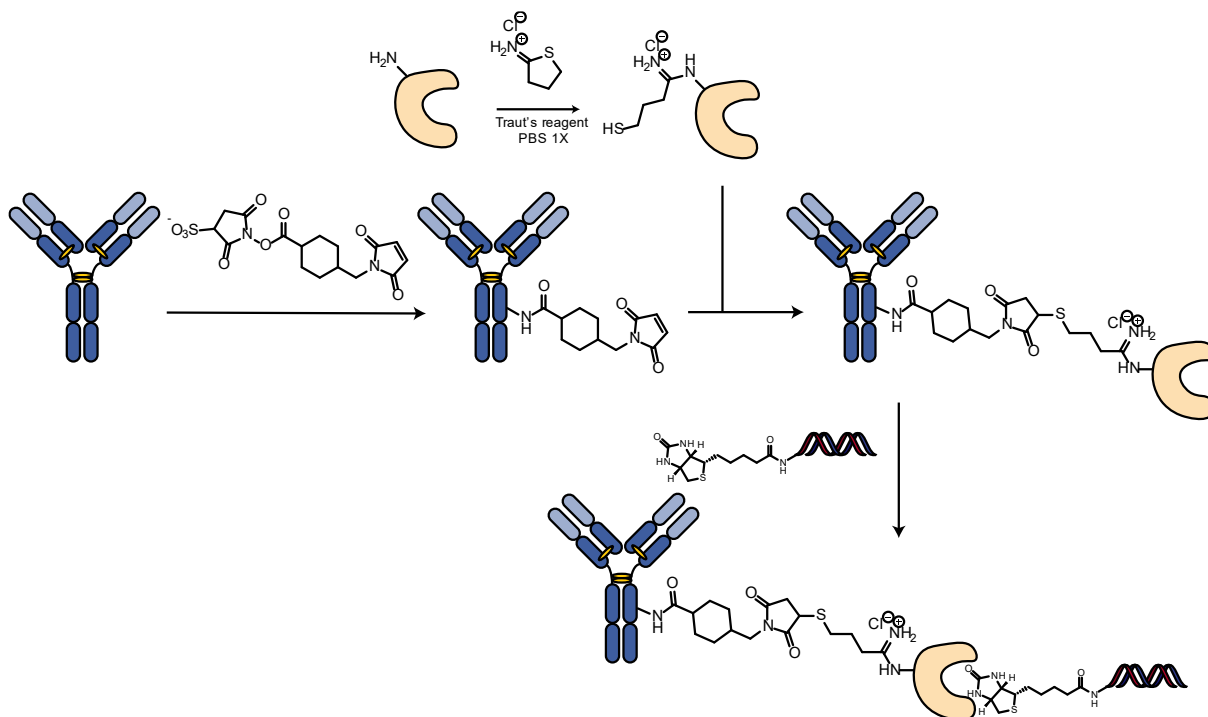


Figure 36 - Strategy published by Xia et al, using a biotin-neutravidin/streptavidin system.

In this study, the authors delivered a siRNA against luciferase (siLuc) into the brain of rats by using an antibody that could cross the blood-brain barrier by targeting receptor-mediated transport system, such as insulin receptor or the transferrin receptor.<sup>318</sup> This system depleted 81% of the luciferase gene at 216 nM *in vivo*. However, this surprising efficiency was not discussed in depth regarding the endosomal escape capacities. The exact same strategy of synthesis was published recently to deliver an anti-hrGFP siRNA with an anti-HB-EGF antibody.<sup>319</sup> In this other study, the conjugate could efficiently knockdown the targeted gene, with 60% gene silencing at 50 nM *in vitro* and 35% at 266 nM *in vivo* after 48 h of incubation.

Aside from biotin/avidin duet, another strategy based on protein-ligand interaction has been published recently, where the authors fused an anti-FITC scFV to an anti-CXCR4-nanobody (Figure 37) to deliver a FITC-conjugated siRNA against the HIV protein Tat *in vitro*.<sup>320</sup> Regarding the activity, they observed nearly 80% of Tat depletion with 200 nM of conjugate in CXCR4-expressing T cells after cell infection with HIV viruses, therefore inhibiting HIV replication in targeted cells. Due to the FITC-labelled siRNA, this strategy also allowed the authors to evaluate both the binding and the internalization to the targeted cells. However, the authors did not provide any information about the siRNA protection against degradation by the nanobody/scFv fusion protein yet.

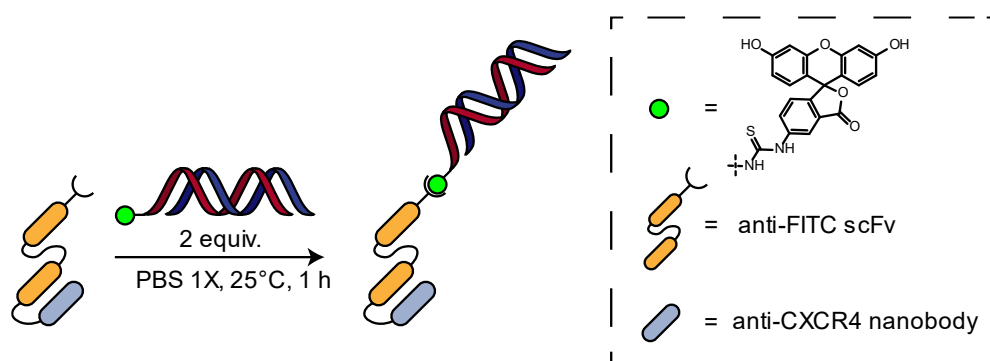


Figure 37 - Strategy proposed by Cunha-Santos et al. A fusion protein made of anti-FITC scFv and anti-CXCR4 nanobody was produced then mixed with FITC-conjugated siRNA.

While these strategies use protein-ligand interaction to allow the conjugation of the siRNA to the antibodies, they are not easy to perform and can be expensive. Therefore, most publications in this area employ the direct conjugation of the oligonucleotide to the antibody. Such conjugates imply the chemical modification of amino- or sulfhydryl-modified siRNA with synthetic heterobifunctional linkers.

## 2. Direct conjugation

In 2011, the first publication that directly conjugate a siRNA and an antibody used SoluLink™ a commercially available linker relying on aldehyde-hydrazine click reaction. This strategy allowed the authors to conjugate an anti-STAT3 siRNA to an anti-Lewis Y antibody via a double-cleavable hydrazone and disulfide linker (Figure 38).<sup>321</sup>

In this study, the antibody was modified via lysine conjugation with a 6-hydrazino nicotinic acid activated ester, and the resulting conjugate was mixed with disulfide formyl benzoate-conjugated siRNA. However, besides gel electrophoresis, no other characterization of the final conjugate was provided by the authors. Regarding the biophysical properties of the conjugate, the authors have demonstrated that the binding affinity of the antibody was not disturbed by the siRNA, and internalization studies were performed with fluorescent siRNA, demonstrating the antigen-dependent delivery. Regarding the activity, they have shown that STAT3 was depleted in A431 cells, but only when co-incubated with 100 μM of chloroquine as an endosome-disrupting agent, with a silencing efficiency of 60%. This study is thus the first one suggesting that covalent antibody-siRNA conjugates could lack efficacy due to endosome entrapment.

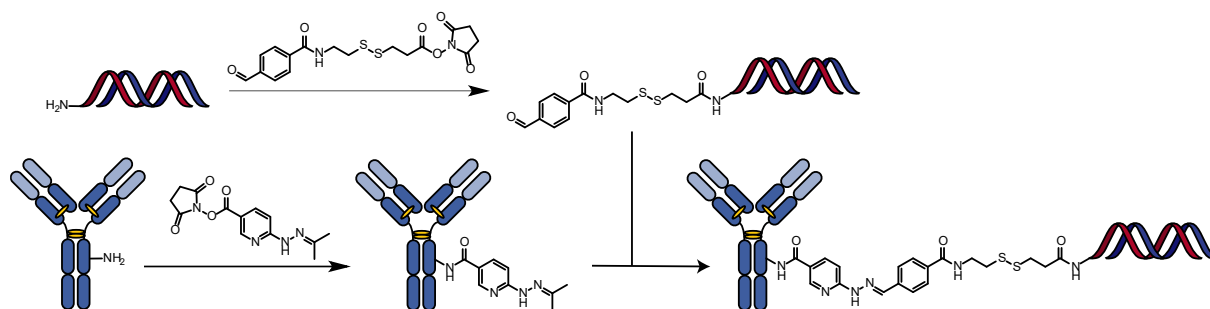


Figure 38 - Strategy using Solulink™, a double cleavable linker, to obtain an ARC.

In 2015, Cuellar *et al* from Genentech published a simple method to synthesize and evaluate THIOMAB™-conjugated siRNA. Among their constructs, they used both the non-cleavable succinimidyl 4-(*N*-maleimidomethyl)cyclohexane-1-carboxylate (SMCC) linker or the reducible *N*-succinimidyl-4-(2-pyridyldithio)butyrate (SPDB) linker, attached to the 3'-end of the sense strand. The modified siRNA was then conjugated to the antibody by forming thioether bonds between the maleimide group present on the siRNA and the engineered cysteines. After characterization by mass spectrometry, they discussed the global efficacy by targeting multiple surface-antigens with different internalization mechanisms and intracellular trafficking (Figure 39).<sup>322</sup>

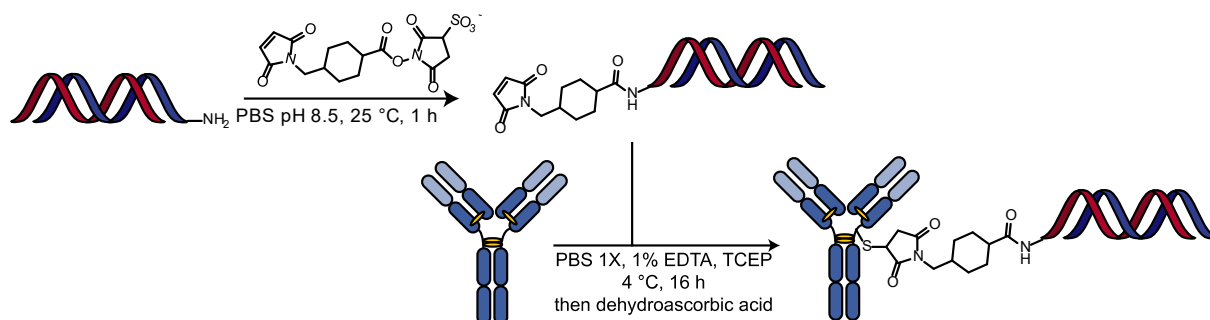


Figure 39 - Strategy proposed by Cuellar *et al*. Example with SMCC-cysteine conjugation to THIOMAB™.

While antibody-drug conjugate's efficacy is highly dependent on the surface-antigen's biology, the authors observed that this dependency was even more important for ARC. Indeed, the observed silencing with fast-internalizing antibody was higher than with recycling or slow-internalizing antibodies, suggesting that potent ARC could not be obtained for every surface-antigen.

In accordance with the previous study, microscopy studies showed that the majority of the siRNA were localized in lysosomes and remained in that locus for several hours, revealing that this kind of conjugate may be limited by a poor endosome escape. As a slow endosomal escape could lead to the payload's degradation by ribonucleases, this result also suggests that a low cytosolic concentration of siRNA may be enough to start the RNAi machinery.<sup>323,324</sup>

Finally, both stable and cleavable linkers showed similar silencing efficiency, indicating that the choice of the linker may be less important than the choice of the antibody for ARC (Figure 40).

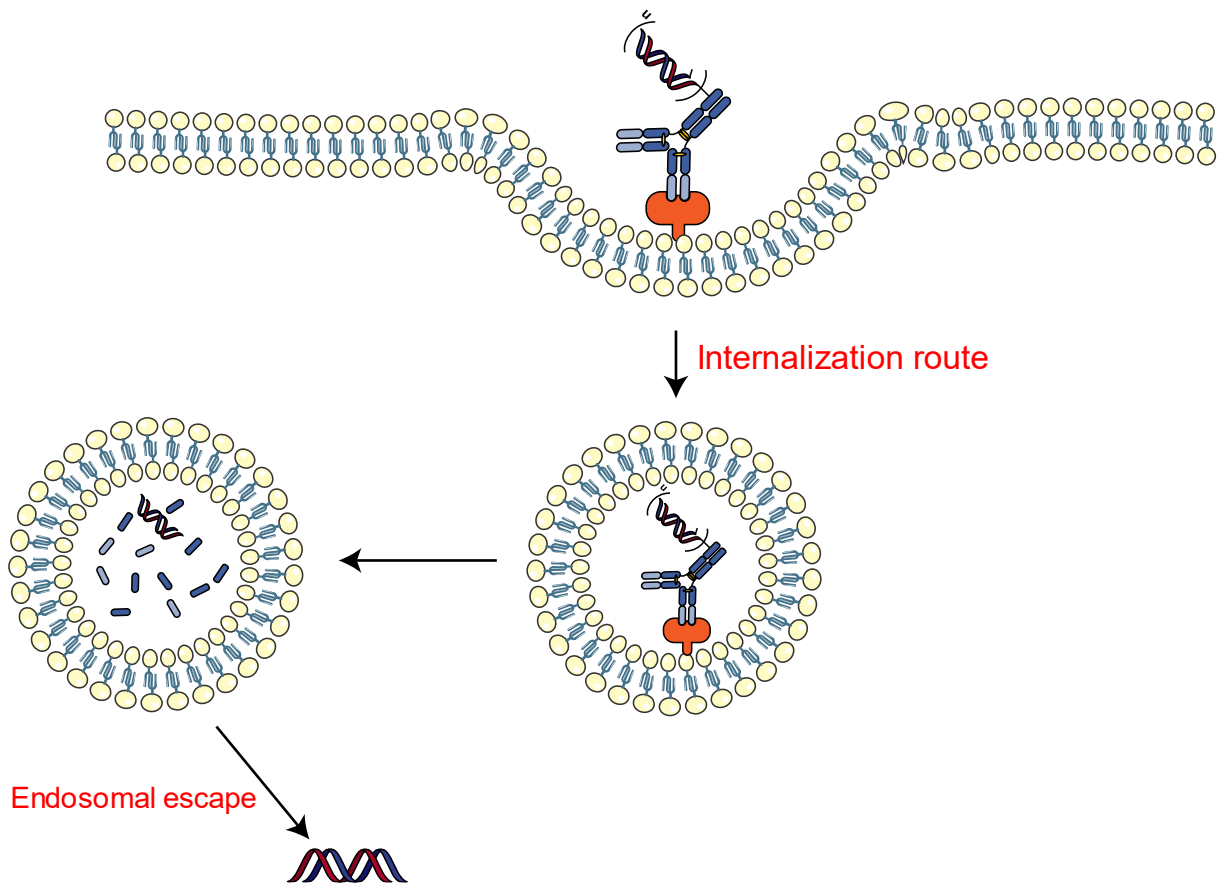


Figure 40 - Main limitations of ARC according to Cuellar et al are displayed in red. The internalization route highly depends on the antigen's biology and the antibody itself; the endosomal escape depends on the internalization route.

In 2019, Dowdy's group published a method to produce ARC site-selectively by inserting a peptide tag (LLQGA) into the C-terminus of the heavy chain that could be functionalized enzymatically with microbial MTGase.<sup>325</sup> This allowed the introduction of an  $\omega$ -azido-lysine to the antibody enabling the facile conjugation of DBCO-functionalized siRNA (Figure 41). The authors showed that the newly formed ARC was still able to bind cells with a similar affinity as the naked antibody, demonstrating that the conjugation of the siRNA did not modify the binding ability of the antibody. However, the authors did not provide any mass spectrometry data of the resulting conjugate nor tested their silencing ability.

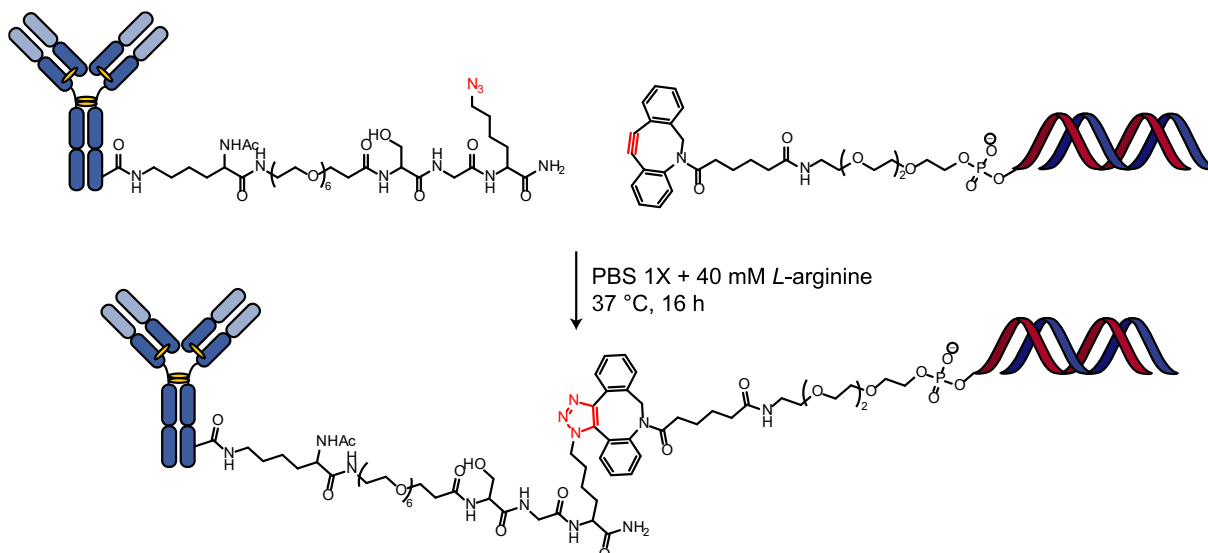


Figure 41 - SPAAC strategy proposed by Dowdy's group. The azido-lysine moiety was incorporated by enzymatic ligation with MTGase in response to an inserted peptide tag.

Recently, Rader's group used a similar strategy by inserting a peptide tag containing a unique, highly nucleophilic lysine ( $pK_a \sim 6$ ) to react with 3'- or 5'- $\beta$ -lactam-functionalized siRNA (Figure 42).<sup>326</sup> The kinetic and thermodynamic parameters of the ARC binding to purified surface-antigen were measured by surface plasmon resonance (SPR), showing that the siRNA did not compromise the binding to the antigen.

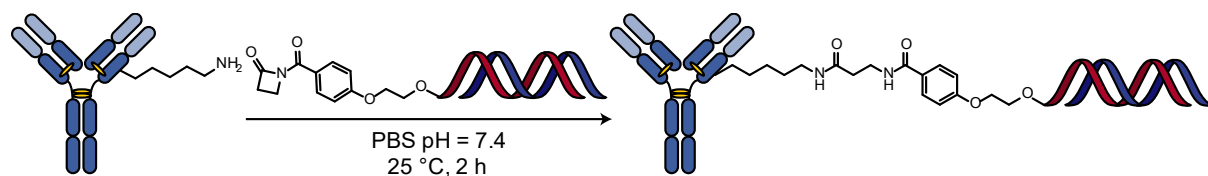


Figure 42 - Strategy proposed by Rader's group. An inserted reactive lysine reacts with  $\beta$ -lactam-functionalized siRNA.

For the biological activity, the siRNA was delivered into the cell and silenced the targeted protein by 50% at 10 nM *in vitro*. In addition, the authors carried out a pharmacokinetic study to determine the half-life in mice following intravenous injection by conjugating a 5'- $\beta$ -lactam and 3'-biotin siRNA to the antibody. The authors measured a half-life of 12.3 h by detection of the siRNA with HRP-modified streptavidin. According to the authors' previous studies, their chemical modifications on the siRNA's backbone warrant high stability *in vivo*, which led them to suggest that this restricted stability was due to the 5'- or 3'- linker attached to the siRNA. Indeed, as both modifications were introduced with phosphoramidite chemistry, both of these ends can undergo phosphatase-mediated cleavage.

Other groups published ARC using antibody fragments instead of full IgG because of their smaller size, allowing considerable advantages in endosomal release.<sup>277</sup> Sugo *et al* from

Takeda developed a Fab'-siRNA conjugate targeting CD71-expressing muscles *via* cysteine conjugation (Figure 43).<sup>327</sup> The aim was to silence a gene inside muscles responsible for muscular dystrophy, thus allowing the mice to run. In this study, they used 4 different linkers bearing different cleavage properties. They observed a good silencing *in vivo* (72%, 260 nM), allowing the mice to run again. In addition, the authors suggested that the main limitation of this strategy was a slow endosomal escape, even though they used a Fab' for this purpose. As Cuellar *et al*<sup>322</sup>, the authors observed that the use of cleavable linkers did not improve the silencing efficiency.

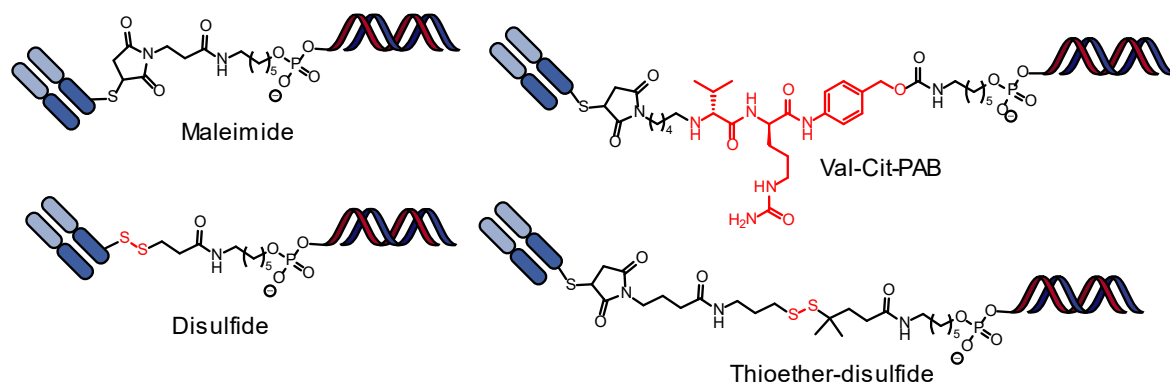


Figure 43 - Fab'-siRNA conjugates synthesized by Sugo *et al*. The cleavable parts are displayed in red.

As an even smaller antibody fragment, Zavoiura *et al*<sup>288</sup> reported the first nanobody-siRNA conjugate to deliver siRNAs to EGFR-expressing cells. They modified the siRNA with classical SMCC linker and conjugated the resulting molecule to the nanobody by cysteine conjugation. In this study, the authors produced monoparatopic and biparatopic nanobody-conjugates in order to increase the internalization capacity by binding to different epitopes of the same antigen. Regarding the activity, the biparatopic conjugates was more effective at silencing the targeted gene (50% *in vitro* at 10 nM) compared to the monoparatopic one (40%). These results suggest that enhancing the internalization of ARC could be a key to improve their potency. Besides, confocal microscopy studies showed that the siRNA was still mainly trapped in acidic compartments.

As previously seen, many publications observed a lack of endosome escape, resulting in moderate efficiencies at very low doses. This year, two studies tried to overcome this issue by using endosome-disrupting cationic molecules as linkers in order to induce proton-sponge effects. Yu *et al*. synthesized a multifunctional peptide composed of a cell-penetrating peptide (CPP, sequence: VSRRRRGRRRRR) and a substrate peptide for two extracellular enzymes, legumain and MMP-2 (substrate peptide sequences are AANL or PLGVR, respectively).<sup>328</sup> The *N*-terminus of the peptides was modified on by a bifunctional linker containing both an activated ester and an activated disulfide bond. Thiol-containing siRNA was



then added to afford the peptide-siRNA conjugate. Finally, the C-terminus of the peptides was activated by classical carbodiimide chemistry for further lysine conjugation on the antibody (Figure 44). However, the conjugate was only characterized by gel retardation assays, and the degree of conjugation to the antibody is unknown.

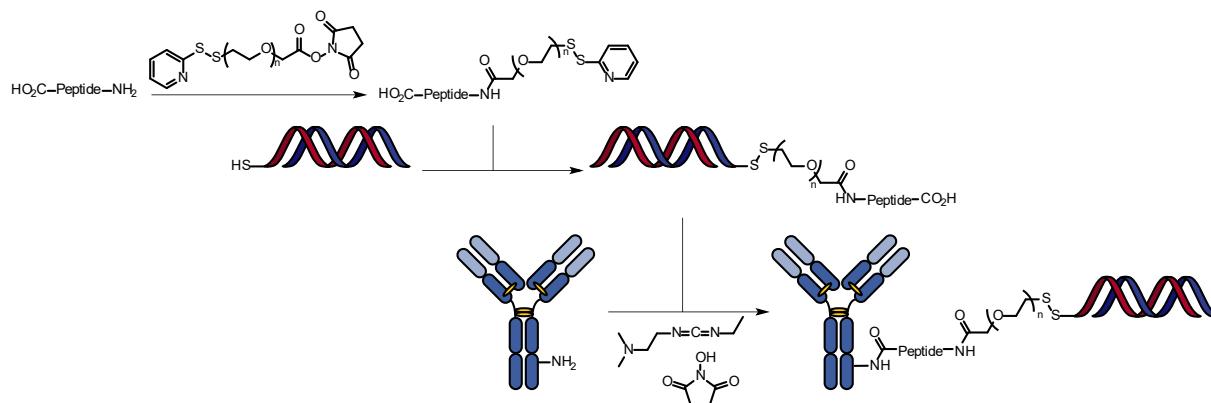


Figure 44 - Strategy proposed by Yu et al for the generation of antibody-peptide-siRNA conjugate.

Regarding the proposed mechanism, once cleaved from the antibody near tumors because of the peptide substrates, the CPP-siRNA is supposedly taken up by the cell, and the peptide-siRNA linkage reduced by glutathione. The authors, however, did not discuss the mechanism of cellular uptake of the CPP-siRNA conjugate. Regarding the biological activity, the authors observed 66.7% gene extinction *in vivo* at 833 nM.

Overall (Table 5) covalent ARCs' silencing efficiency seems to vary from 30 to 80% on a nanomolar scale. This efficiency seems to be extremely dependent on the internalization route of the antibody. Cuellar *et al* published a systematic method to evaluate the potency of ARC by using comparable parameters, and it appeared that fast-internalizing and non-recycling surface-antigens could be attractive targets for the antibody in order to maximize the quantity of siRNA inside the cell.

In addition, confocal microscopy studies tend to suggest that ARC-mediated silencing is limited by a poor endosomal escape of the siRNA.<sup>329,330</sup> Endosomal entrapment can cause two different problems: on the one hand, an inefficient siRNA release from the endosome causes low cytosolic concentrations of siRNA; on the other hand, lysosomal ribonucleases will ultimately degrade the oligonucleotide if the latter stays in lysosomes for too long. To address these issues, two groups used antibody fragments that are lighter than full IgG1, thus having better endosome escape properties.<sup>327</sup> However, as all studies are using different systems, siRNAs, biological models, and targeted antigens, it is difficult to conclude on the best targeting format to construct effective siRNA conjugates. Therefore, data comparing full IgG1, nanobodies, scFv or Fab are needed to conclude about this point.

The cleavage mechanism of the linker seems to have no influence on the efficiency, and, overall, the exact structure of the released siRNA is unknown. Reflecting on this issue, many groups suggested that phosphatases found in endosomes could cleave the phosphate bound between the siRNA and its linker.<sup>326</sup> Still, no studies have been published yet regarding this particular point, and the field of ARC lacks of metabolomic studies in order to determine the exact structure of the intracellular siRNA. As the mechanism of siRNA release from the endosome still remains elusive, such studies could give a hint on how it is released. With such data in hand, it would be probably easier to develop appropriate, optimized linkers for ARC.

Table 5 - Currently reported ARC, with the scaffold the antibody, its targeted antigen, the linker used, the resulting silencing efficiency and the problem encountered.

Scaffold of antibody <sup>ref</sup>	Targeted surface antigen	Method of conjugation/linker used	RNA conjugation site, average DoC obtained	siRNA target, silencing efficiency (dose of conjugate)
IgG1 <sup>316</sup>	Transferrin (high <sup>331</sup> , recycling <sup>332</sup> )	streptavidin-conjugated IgG1 + biotin-siRNA	3'-biotinylated sense strand DoC unknown	Luciferase 69-81% at 216 nM ( <i>in rat</i> , 48h)
IgG1 <sup>319</sup>	HB-EGF (high <sup>333,334</sup> , recycling <sup>286</sup> )	Neutravidin-conjugated IgG1 + biotin-siRNA	3'-biotinylated sense strand DoC unknown	hrGFP 35% at 266 nM ( <i>in mice</i> , 48h)
Nanobody <sup>320</sup>	CXCR4 (high, recycling <sup>335</sup> )	Anti-FITC scFv-fused nanobody + FITC- siRNA	3'-FITC sense strand	Tat 80% at 1 $\mu$ M ( <i>in vitro</i> , 48 h)
IgG1 <sup>321</sup>	Le <sup>y</sup> (moderate, lysosome <sup>336</sup> )	Solulink <sup>TM</sup> (reducible + acid-labile)	5'-amino antisense strand DoC 1	STAT3 <10%, 60% with 100 $\mu$ M chloroquine ( <i>in vitro</i> , 48 h)

<p>THIOMAB™, 322</p>	<p>TENB2 (high, lysosome)</p> <p>Steap1 (moderate, slow internalizing)</p> <p>HER2 (high, recycling)</p> <p>NaPi2b (high, recycling)</p> <p>Mesothelin (poor, slow internalizing)</p> <p>MUC6 (moderate, slow internalizing)</p> <p>EtBR (poor, lysosome)</p>	<p>SMCC (non cleavable)</p> <p>Disulfide linker (reducible)</p>	<p>3'-amino sense strand</p> <p>DoC 1.67</p>	<p>PPIB (50 nM, <i>in vitro</i>, 48 h) silencing in cell expressing:</p> <p>TENB2 (&lt;25% for low expressing cells, &gt;50% for high expressing cells)</p> <p>Steap1 (10-25%)</p> <p>HER2 (&lt;10%)</p> <p>NaPi2b (&lt;50%)</p> <p>Mesothelin (&lt;10%)</p> <p>MUC6 (&lt;10%)</p> <p>EtBR (&lt;10%)</p>
<p>IgG1<sup>325</sup></p>	<p>CD33 (low, lysosome<sup>337</sup>)</p>	<p>SPAAC with DBCO (non cleavable)</p>	<p>5'-amino sense strand</p> <p>DoC 2.0</p>	<p>Not evaluated</p>

IgG1 <sup>326</sup>	BCMA	$\beta$ -lactam opening (non cleavable)	3'- $\beta$ -lactam or 5'- $\beta$ -lactam sense strand DoC 2.0	CTNNB1 50% (10 nM, <i>in vitro</i> , 72 h)
Fab <sup>327</sup>	CD71 (high, lysosome <sup>338</sup> )	Maleimido caproyl (non cleavable)  Disulfide (reducible)  Val-Cit-PAB (protease-cleavable=	3'-amino sense strand DoC 1.4-1.6	<i>myostatin</i> 78% (260 nM, <i>in vivo</i> , 72 h)
Nanobody <sup>288</sup>	EGFR (high, lysosome <sup>339</sup> )	SMCC (non cleavable) DoC 1.0  Disulfide (reducible) DoC 1.0	3'-thio sense strand DoC 1.0	AHSA1 50% (10 nM, <i>in vitro</i> , 48 h)
IgG1 <sup>328</sup>	EGFR (high, lysosome <sup>339</sup> )	Enzyme cleavable cell penetrating peptide, linked to the siRNA <i>via</i> disulfide bridge	3'-thio-modified strand (conjugation strand unspecified) DoC unknown	GFP 66.7% (833 nM of siRNA, <i>in vivo</i> , 48h)



### III. Objectives of the thesis

The above introduction highlighted the therapeutic potential of RIG-I as a target for immunoncology, as well as the possibility to combine its activation with gene silencing for synergistic effects into a single molecule. For a cancer-selective delivery, antibody-siRNA conjugates appeared as a viable strategy.<sup>340</sup>

Therefore, in this thesis, we plan to build an antibody-siRNA conjugate (ARC) that could simultaneously silence PLK1 and activate RIG-I. The resulting conjugate would specifically target cancer cells and deliver the siRNA, causing their death via a dual PLK1/RIG-I activity and stimulating an anti-tumor immunity.

As the targeted delivery of siRNAs by antibodies relies on their ability to internalize, we selected a proprietary IgG1 binding to Ephrin type-A receptor 2 (EphA2), a transmembrane tyrosine kinase which is overexpressed in many cancers and is associated with shorter overall survival in patients.<sup>341</sup> Upon binding, EphA2 undergoes autophosphorylation and subsequent internalization of the antibody/EphA2 complex in the early endosomes.<sup>342</sup> In lysosomes, this complex is rapidly degraded, therefore neither this antigen nor the antibody is not recycled back to the plasma membrane, making it a target of choice for the antibody-mediated delivery of drugs<sup>343,344</sup> or for oligonucleotides.<sup>345</sup>

This work was thus devoted to the development of antibody-based targeted delivery systems able to specifically deliver a siRNA in cancer cells *via* an active targeting of EphA2-expressing cells. If released in the cytosol, the RNA is supposed to activate RIG-I, leading to cell apoptosis and activation of antitumor immunity, while simultaneously silencing another gene, PLK1. Therefore, both covalent and non-covalent approaches were exploited in order to achieve an efficient delivery. Regarding the covalent one, cleavable linkers were also explored in order to potentially enhance the RNA release.

**Project 1: Targeted delivery of immunostimulatory siRNA with dual mode of action, inducing both apoptosis and anti-tumor immunity**

The first project is about the development of a covalent ARC and its biological effect on a cancer cell model. Upon binding and internalization in EphA2-expressing cells, the siRNA-5'-ppp is supposed to silence PLK1 *via* an RNA interference mechanism, thus inducing a strong G2/M arrest and apoptosis. In addition, the same siRNA-5'-ppp would be recognized by RIG-I, thus inducing both apoptosis and activation of the antitumor immunity.

In this study, we focused on the synthesis of the ARC and the on the understanding of the different biological mechanisms of action regarding RIG-I and PLK1. Intracellular trafficking of the ARC, as well as its plasma stability, were both evaluated.

#### Project 2: Development of bicyclo[6.1.0]nonyne carboxylic acid for the production of stable molecular probes

In an affiliated project, a chemistry-oriented project was focused on the development of a novel strained-alkyne derivative. Therefore, different synthetic approaches were elaborated, and the *in cellulo* stability of fluorogenic probes allowed us to study the novel derivative.

#### Project 3: A novel family of acid-cleavable and plasma-stable linker based on cyclic acetal motifs

We sought to increase the cleavability of the linker in our ARC by using cleavable linkers commonly used in ADCs. Therefore, an overview about linkers currently used in this field will introduce the third project of this thesis, which was focused on the design and the synthesis of a novel cleavable linker for antibody-drug conjugates. By producing fluorogenic probes, numerous properties of the new motif in biological media were evaluated, such as its stability in plasma or its ability to release the payload in intracellular organelles. Preliminary results regarding the applicability of this novel linker for ARC and ADC will be presented.

#### Project 4: Development of a synthetic strategy for non-covalent ARC

One common approach to deliver RNA inside cells is to form complexes, by exploiting the anionic nature of siRNAs. To vectorize these complexes, one strategy consists of grafting a targeting agent to them.

In the last project of this thesis, an alternative type of ARC, based on electrostatic interactions between an antibody conjugated to a cationic peptide and negatively charged siRNAs, was explored. More precisely, these works consisted in the elaboration a synthetic strategy to produce cationic peptides and antibody-peptide conjugates. From a biophysical point of view, a systematic method to evaluate the ability of these molecules to bind siRNAs was established.





## IV. Targeted delivery of immunostimulatory siRNA with dual mode of action, inducing both apoptosis and anti-tumor immunity

Tony Rady,<sup>a, b</sup> Stéphane Erb,<sup>c</sup> Safia Deddouche-Grass,<sup>b</sup> Renaud Morales,<sup>b</sup> Guilhem Chaubet,<sup>a</sup> Sarah Cianférani,<sup>c</sup> Dmitri Wiederschain,<sup>b</sup> Nicolas Basse<sup>\*b</sup> and Alain Wagner<sup>\*a</sup>

<sup>a</sup>*Bio-Functional Chemistry (UMR 7199), LabEx Medalis, University of Strasbourg, 74 Route du Rhin, 67400 Illkirch-Graffenstaden, France. E-mail: [alwag@unistra.fr](mailto:alwag@unistra.fr)*

<sup>b</sup>*Sanofi 67000 Strasbourg, France. E-mail: [nicolas.basse@sanofi.com](mailto:nicolas.basse@sanofi.com)*

<sup>c</sup>*Laboratoire de Spectrométrie de Masse BioOrganique (LSMBO), Université de Strasbourg, CNRS, IPHC UMR 7178, 67000 Strasbourg, France*

### A. Introduction

Antibody-drug conjugates (ADC) are a fast-growing family of anti-cancer therapeutic agents. They reach high efficacy by targeting cancer-selective internalizing antigen, allowing the selective delivery of drugs inside tumors. While currently used to cure many cancers, this class of biologics is still facing numerous limitations, among which a too low amount of intratumoral drug deposition and the rise of resistance mechanisms.<sup>247</sup> Therefore, highly potent drugs are generally required, thus narrowing the scope of therapeutic targets and modes of action. Indeed, today the vast majority of FDA-approved ADC or in advanced clinical trials rely only on 7 drugs, either targeting the microtubules, like maytansinoids or auristatins or the DNA, like pyrrolobenzodiazepines or calicheamicin.<sup>290</sup>

To enlarge the reservoir of usable therapeutic mode of action, strategies acting at the genetic, transcriptional or translational levels appear as valuable alternatives to small molecule drugs.<sup>178</sup> Protein knockdowns can be achieved with high precision by delivering non-coding oligonucleotides, such as small interfering RNAs (siRNA).<sup>305</sup> From a therapeutic standpoint, siRNAs have the advantage of being able to target precisely any disease-associated protein translated from messenger RNA (mRNA). Nowadays, three siRNAs are commercialized and seven more are in clinical phase III, demonstrating the growing therapeutic. However, the vast majority of siRNAs in clinical trials are targeting the liver, in which almost all current delivery systems show the highest accumulation.<sup>214</sup> To overcome this issue, the use of antibody-siRNA conjugates (ARCs) has emerged as a powerful tool enabling the *in vivo* delivery of active dose of siRNA in cells over-expressing a surface biomarker.<sup>346,347</sup> For example, one IgG-siRNA

conjugate from Avidity Biosciences has just started clinical phase I/II (NCT05027269) for myotonic dystrophy type 1.

In this context, we planned to build an ARC whose siRNA component would activate the pattern-recognition receptor retinoic acid-inducible gene-I (RIG-I) which has been clinically validated for oncology purposes.<sup>123</sup> RIG-I is an ubiquitous cytosolic sensor that detects the presence of short,<sup>348</sup> blunt-ended,<sup>67</sup> and base-paired double-stranded RNA (dsRNA)<sup>65</sup> ending with either a 5'-triphosphate (5'-ppp)<sup>34</sup> or a 5'-diphosphate group (5'-pp).<sup>32</sup> While all RIG-I agonists currently in clinical trials are administered intratumorally, their targeted delivery by an ARC should allow intravenous administration in patients.<sup>114</sup>

From a mechanistic point of view, RIG-I first undergoes conformational changes upon dsRNA binding, allowing the interaction with the mitochondrial protein MAVS, which initiates a signaling cascade leading ultimately to cytokines and type I interferon (IFN) secretion activating NF- $\kappa$ B and IRF 3/7 pathways, respectively (figure 1).<sup>99,349,350</sup> This double pathway activation results in cancer cell apoptosis and stimulates the immune system by promoting innate and adaptive immune responses against tumors. Interestingly, the IFN produced upon RIG-I activation also drives a positive retroaction loop that increases RIG-I expression level, thus amplifying the response.

Since the activation of RIG-I by the triphosphate motif is independent of the dsRNA sequence itself, it should be possible to design a siRNA-5'-ppp combining RIG-I activation *via* the triphosphate moiety with a synergistic siRNA-induced specific degradation of a protein's mRNA.<sup>115</sup> This strategy could thus be seen as a multimodal ARC-based anti-cancer approach, benefitting from two biomolecules with complementary functions.

Ideally, the protein knockdown induced by the siRNA-5'-ppp should potentiate the RIG-I pathways in order to enhance the global efficacy of the system. In this regard, Polo-like kinase 1 (PLK1) is known as an early trigger for G2/M transition, decreasing MAVS-mediated IFN production, one of the signaling pathway triggered by RIG-I activation (Figure 45).<sup>204,205</sup> PLK1 knockdown thus results in a G2/M arrest, promoting p53 mediated apoptosis,<sup>192</sup> and an enhanced IFN production upon RIG-I activation.<sup>204</sup> Therefore, we hypothesized that the combination of these two mechanisms of actions borne by one single RNA molecule could create an effective synergy with RIG-I activation (Figure 45).

In order to achieve the targeted delivery of siPLK1-5'-ppp to tumors, we selected an antibody binding to EphA2, a trans-membrane tyrosine kinase overexpressed in many cancers and associated with shorter overall survival in patients.<sup>351</sup> Upon antibody binding, EphA2 is

internalized and degraded in lysosomes, thus lacking antigen recycling. Besides its effect on cell growth, EphA2 thus appeared as a compelling target for drug<sup>343,344,352</sup> or oligonucleotide delivery.<sup>345</sup>

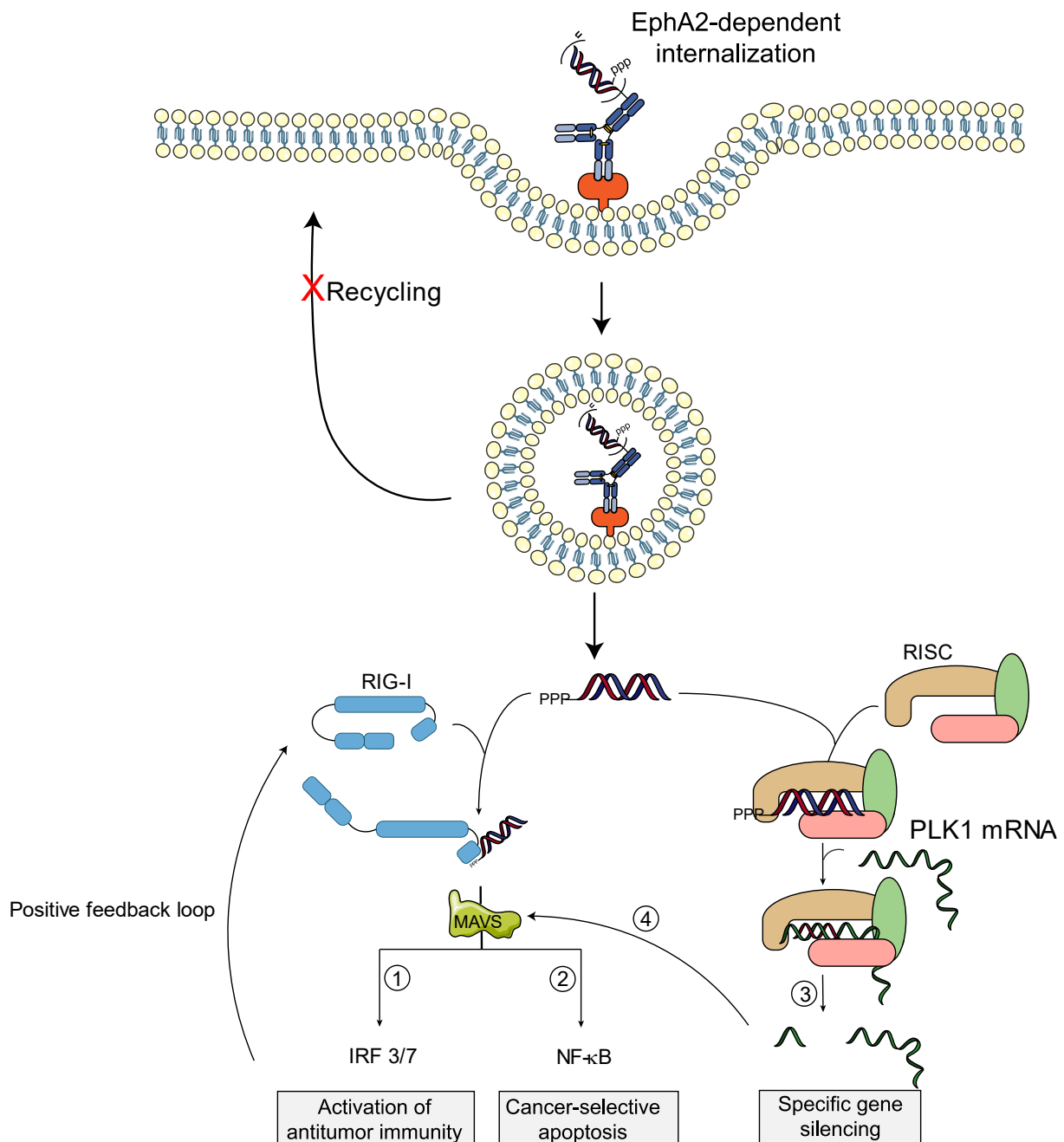


Figure 45 – Schematic dual mode of action of antibody-siRNA-5'-ppp conjugate. In the cytosol, a siRNA bearing 5'-ppp is recognized by RIG-I, leading to the activation of two signaling pathways, IRF 3/7 (1) and NF-κB (2), inducing cancer-selective apoptosis and anti-tumor immunity respectively. Concomitantly, the same construct is loaded in the RISC complex, guiding it to a sequence-complementary mRNA, allowing its degradation (3). Silencing PLK1 leads to the apoptosis by cell cycle arrest and could enhance MAVS-mediated production of interferon (4), therefore synergizing with RIG-I activation.

## B. Results and discussion

### i. Pre-functionalization of antibody

The synthesis of the ARC was achieved in a two steps process relying on a straightforward and robust lysine conjugation and click chemistry, as previously developed in our laboratory.<sup>353</sup> In a first step (“Plug”), 4-azido-benzoyl fluoride enables the incorporation of an azide group onto the antibody, then in a second step (“Play”), a strained-alkyne-modified siRNA can be attached by bio-orthogonal click chemistry (Figure 46).<sup>354</sup> This strategy has the advantage of being flexible, allowing the facile generation of antibody conjugates with various degrees of conjugation (DoC) and the incorporation of several types of linker, two key parameters that could influence the biological activity of these conjugates.

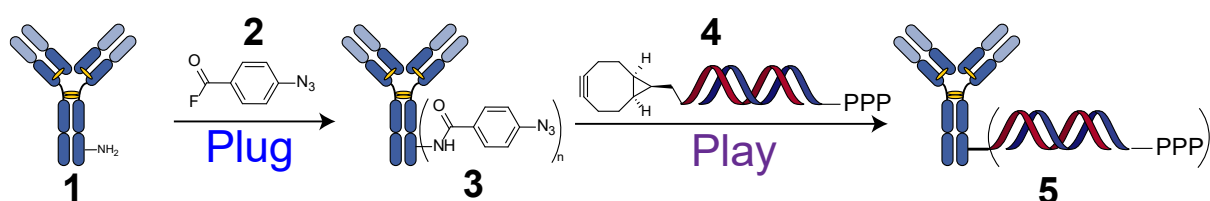


Figure 46 - Strategy used to produce antibody-siRNA conjugates.

The preparation of 4-azido-benzoyl fluoride (ABF, 2) was performed in one step by fluorination of 4-azido-benzoic acid by tetramethylfluoroformamidinium hexafluorophosphate (TFFH, Figure 47) in acetonitrile. This strongly electrophilic reagent was developed by our team<sup>354</sup> as a fast and efficient method to conjugate lysines on proteins with excellent yields. Interestingly, this method showed a nearly linear relation between the number of equivalents of ABF and the observed degree of conjugation (DoC).

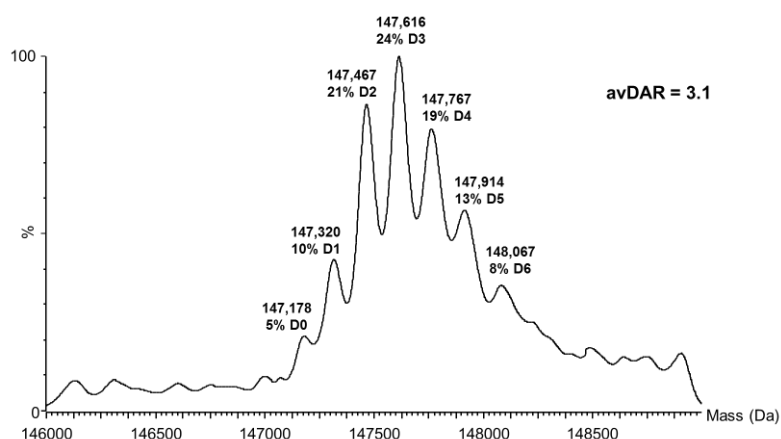
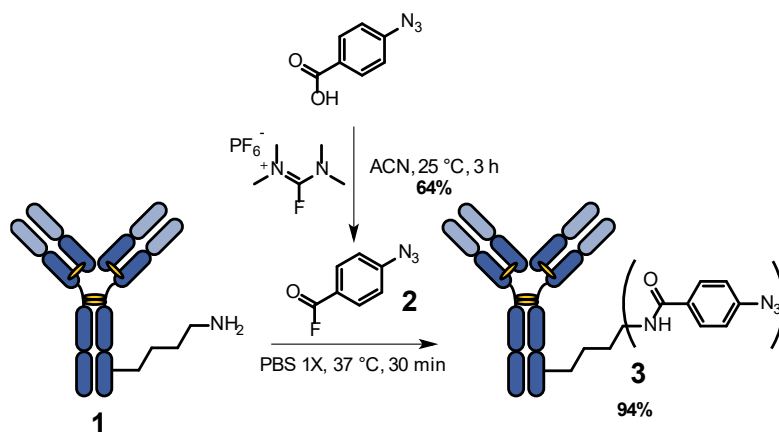


Figure 47 - Conjugation of naked antibody with 3.0 equiv. of ABF 2 and resulting mass spectrum.

## ii. Synthesis of the conjugation linker

For the linker between the siRNA and the antibody, a short heterobifunctional oligoethylene glycol linker (PEG) **6** containing the strained-alkyne bicyclo[6.1.0]nonyne (BCN, blue) and a pentafluorophenyl ester (orange) was synthesized. The BCN moiety would react with the azide attached to the antibody by Strain-Promoted Alkyne-Azide Cycloaddition (SPAAC), and the activated ester would be the conjugation point for commercially available 3'-amino-modified single-stranded RNA (ssRNA). Regarding the linker's synthesis, two parts can be identified: the strained-alkyne and the oligoethylene glycol (Figure 48).

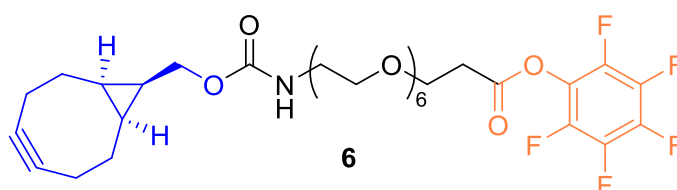


Figure 48 – Structure of the conjugation linker used in this study.

## 1. Synthesis of the strained-alkyne moiety

Regarding the synthesis of the strained-alkyne (Figure 49), the first step starts with a rhodium-catalyzed cyclopropanation on 1,5-cyclooctadiene **9** using a pre-synthesized diazo-glycine methyl ester **10**, allowing the generation of a reactive carbene. Two diastereoisomers **11** could be separated at this stage after chromatography, *endo* and *exo*, which are slightly different in terms of kinetic of Strain-Promoted Alkyne-Azide Cycloaddition (SPAAC), the *endo* ester being the fastest.

While using  $\text{Rh}_2(\text{OAc})_4$  mainly yielded the *exo* derivative, replacing the acetate groups by (S)-BHTL groups mainly yielded the *endo* one. Therefore, the synthesis of  $\text{Rh}_2(\text{S-BHTL})_4$  **8** was performed according to Fox and coworker's procedure, yielding the chiral catalyst in high yield.<sup>355</sup> Using this catalyst, the *endo* isomer **11** was obtained in 45% isolated yield. The newly formed ethyl ester was then reduced using  $\text{LiAlH}_4$  to the corresponding primary alcohol **12**. Dibromination of the alkene with  $\text{Br}_2$  afforded crude **13**, and the strained-alkyne **14** was obtained by double dehalogenation using freshly sublimated potassium *tert*-butyl butoxide. Finally, the primary alcohol **14** was activated to a *para*-nitrophenyl carbonate **15** by reaction with *para*-nitrophenyl chloroformate.

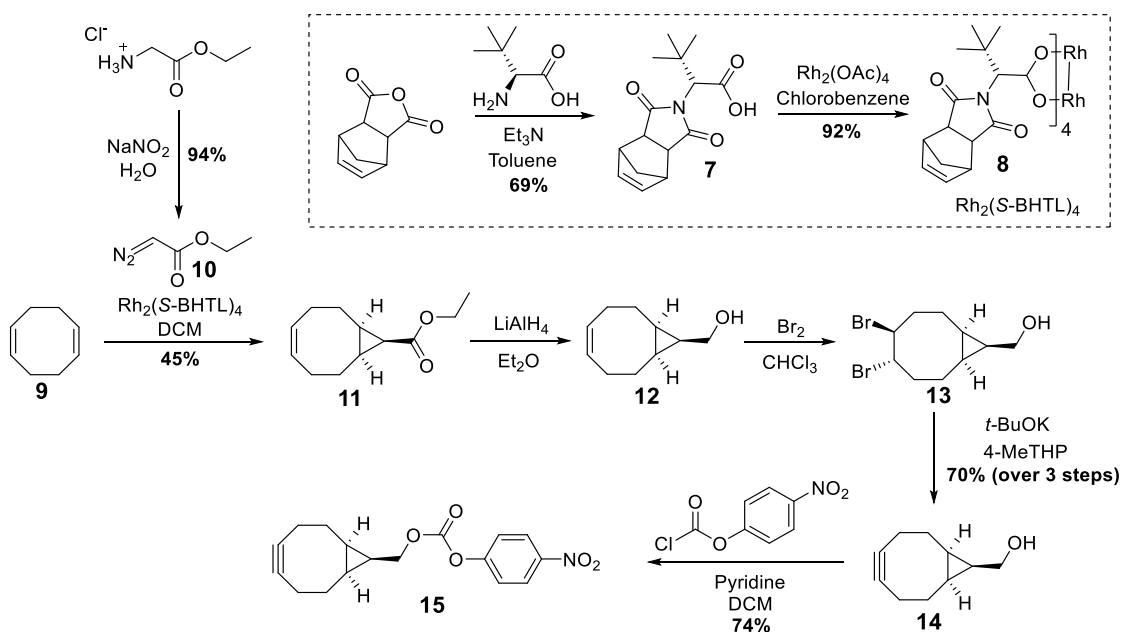


Figure 49 - Synthesis of BCN-*para*-nitrophenyl carbonate **15** adapted from O'Brien et al.<sup>355</sup>

## 2. Synthesis of the oligoethylene glycol portion

Regarding the synthesis of the oligoethylene part (Figure 50), monotosylation of hexaethylene glycol **16** was performed using tosyl chloride, catalyzed with potassium iodide in dichloromethane. Monosubstitution could be achieved by complexing almost all the oxygens present in hexaethylene glycol with a silver ion, letting only one hydroxyl free to perform the

substitution.<sup>356</sup> Activated alcohol **17** was then substituted by an azide by nucleophilic substitution to afford **18** without further purification. The last free hydroxyl group was then deprotonated using potassium *tert*-butoxide in order to perform a Michael addition on *tert*-butyl acrylate and install a protected carboxylic acid on the molecule **19**. The azide group was then reduced by Pd(0)-catalyzed hydrogenation to afford the corresponding primary amine **20** in 71% yield. The latter was then reacted with the previously synthesized BCN-*para*-nitrophenyl carbonate **15** to install the strained-alkyne to the linker. The *tert*-butyl ester **21** was then saponified under mild alkaline conditions, and the free carboxylic acid **22** was activated to a perfluorophenol ester using classical carbodiimide chemistry. <sup>19</sup>F NMR was used to confirm the presence of a perfluorophenol ester on the final BCN-PEG<sub>6</sub>-PFP linker **6**.

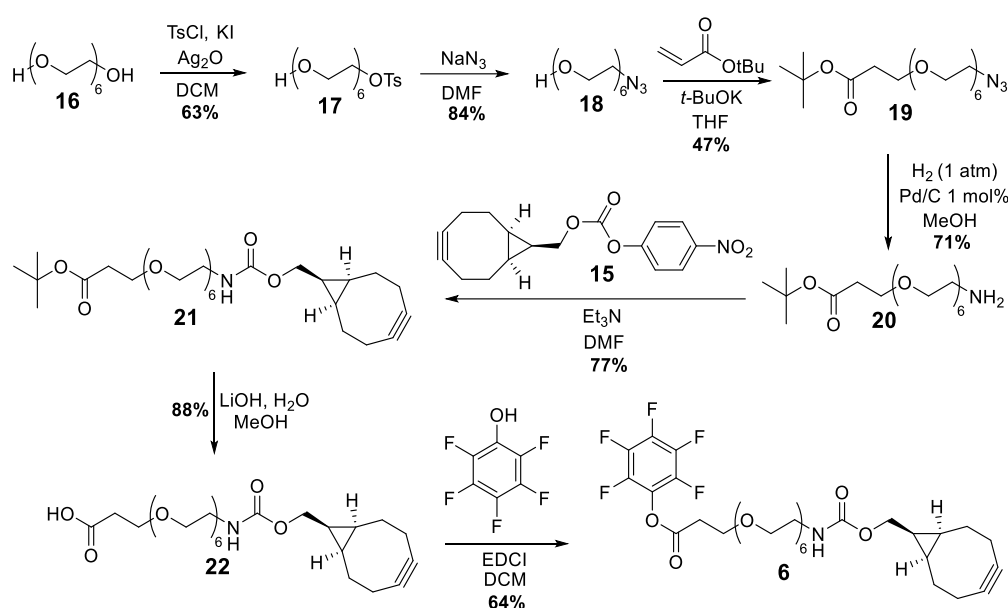


Figure 50 - Synthesis road to the bifunctional BCN-PEG<sub>6</sub>-PFP ester **6** to siRNA modification according to Dovgan et al.<sup>354</sup>

### iii. Conjugation of the siRNA to the antibody and characterization

Besides, as RNA molecules are prone to cleavage at pH > 8.5 in buffers containing divalent cations (Figure 51), reactions conditions were optimized to allow the conjugation without degrading the oligonucleotide. In addition, the use of highly activated perfluorophenol ester that are known to be more resistant than *N*-hydroxysuccinimide ester toward hydrolysis resulted in efficient RNA conjugation. Conjugation of 3'-amino-modified RNA strand **23** with this linker **6** was performed and proceeded easily in sodium borate buffer 0.1 M at pH = 8.0, yielding 3'-BCN-ssRNA **24** in excellent yield after precipitation in acetone. Noteworthy, this buffer was efficient to activate the primary amine while avoiding RNA cleavage.



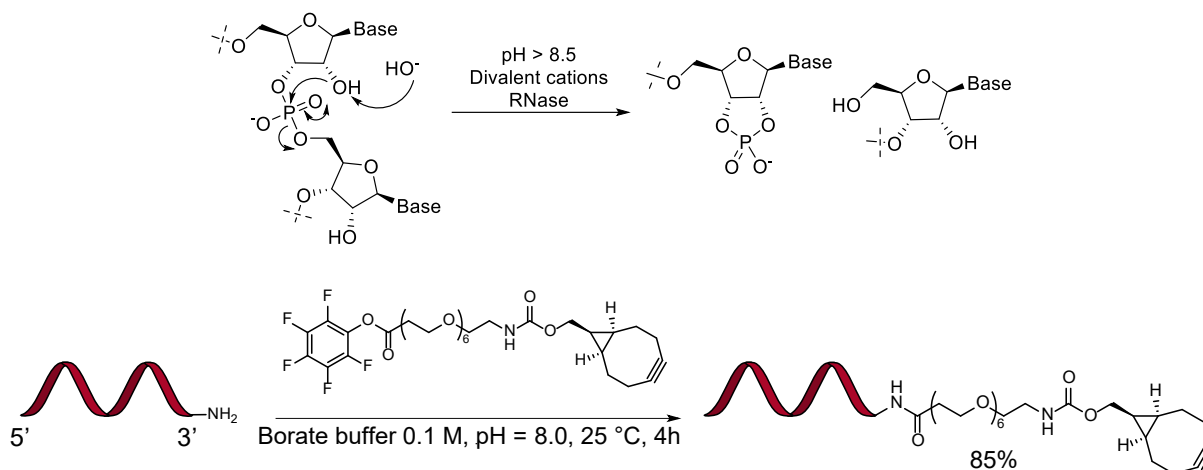


Figure 51 - Mechanism of RNA cleavage under basic conditions and optimized conjugation conditions for RNA molecules.

Two strategies were explored to attach the siRNA to the antibody: either click the 3'-BCN-ssRNA **24** to the antibody-azide **3** and then hybridize the RNA **24** with the complementary strand, or hybridize first and click the 3'-BCN-5'-ppp-dsRNA **4** to the antibody-azide **3**.

For the first strategy, 3'-BCN-ssRNA **24** was clicked to antibody-azide **3** for 24 h at 25 °C, and hybridization using the 5'-ppp-complementary strand was performed under mild conditions. The resulting conjugates were purified by size-exclusion chromatography (SEC) using Akta Pure system, eluting with calcium-free and magnesium-free PBS. Noteworthy, due to a large difference of size, unconjugated antibody **3** could be easily separated from the conjugated antibody **5** (Figure 52).

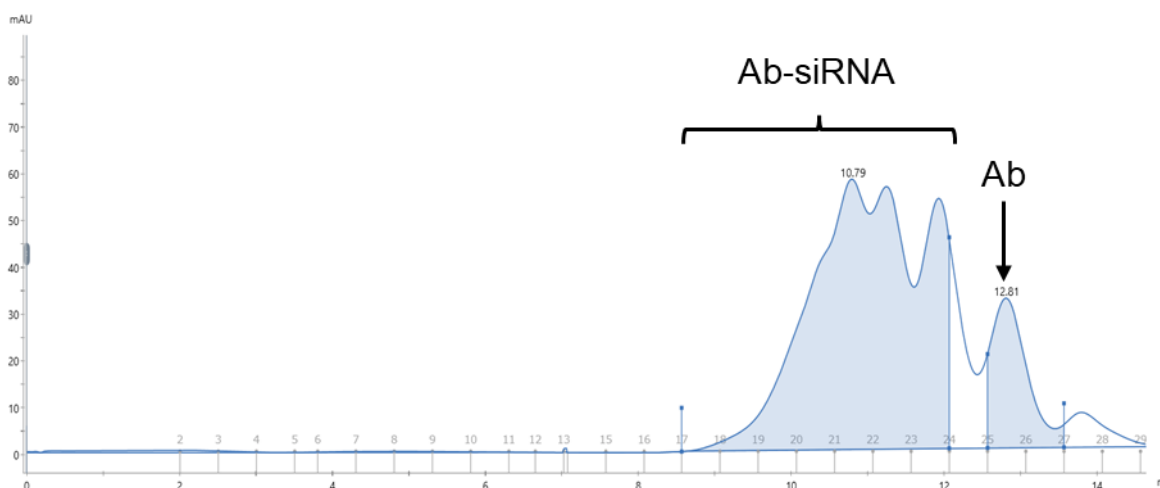


Figure 52 - Size-Exclusion Chromatography profile of synthesized conjugates, showing the separation between unconjugated antibody and antibody-siRNA.

Resulting conjugates were then sterilized and characterized by native SEC-ESI-MS before any biological assay. This method yielded mixtures of single-stranded and double-stranded RNA

conjugates (Figure 53), suggesting that the presence of the antibody impeded the hybridization.

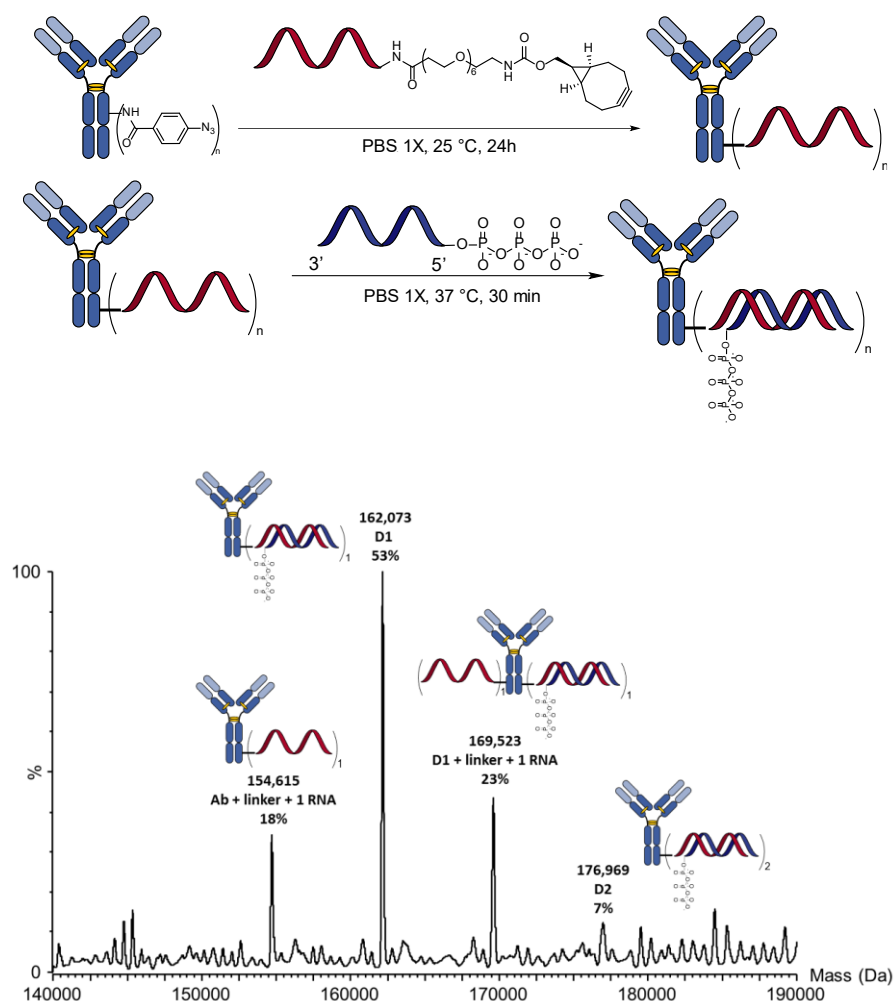


Figure 53 - First strategy explored by annealing the complementary strand after the click reaction and resulting characterization by native SEC-ESI-MS.

The second strategy, where the two strands are first hybridized to form 3'-BCN-5'-ppp-siRNA **4** and then clicked to the antibody-azide **3**, was performed. This method yielded fully hybridized siRNA attached on the antibody (Figure 54), and was therefore applied for all the conjugates from now on. Noteworthy, only the mass of the diphosphate adduct could be detected by native MS, in accordance with results from the literature commonly reporting the loss of the  $\gamma$ -phosphate group on ribonucleotides in mass spectrometry analyses.<sup>357–359</sup>

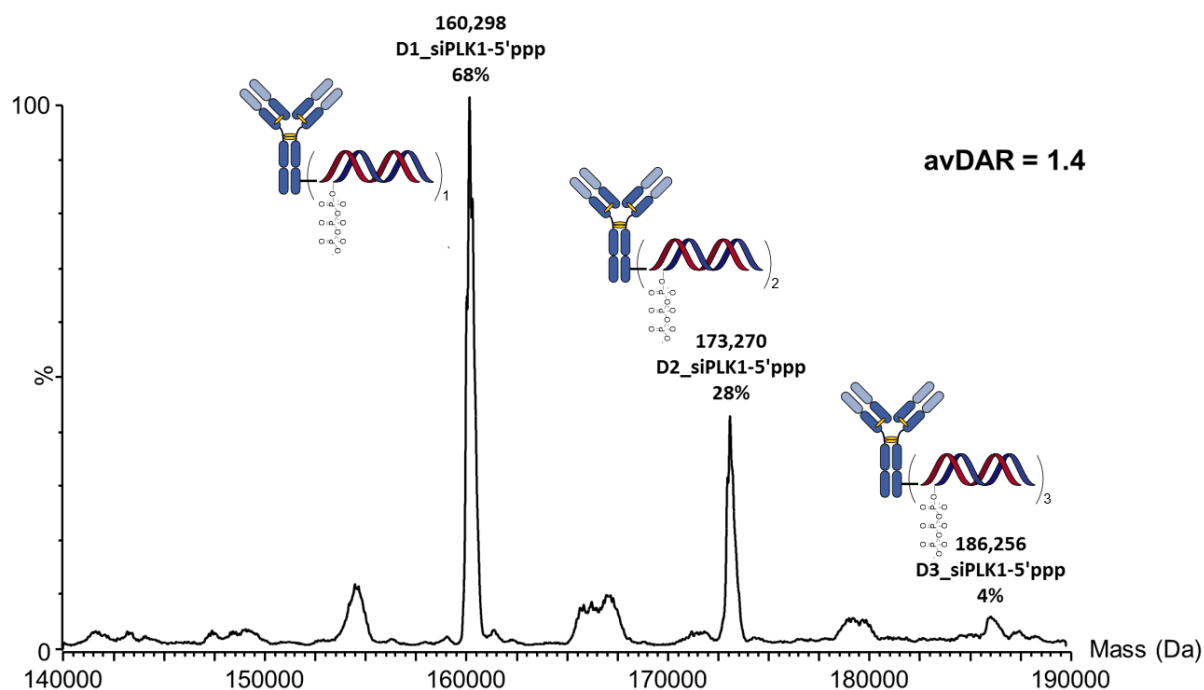
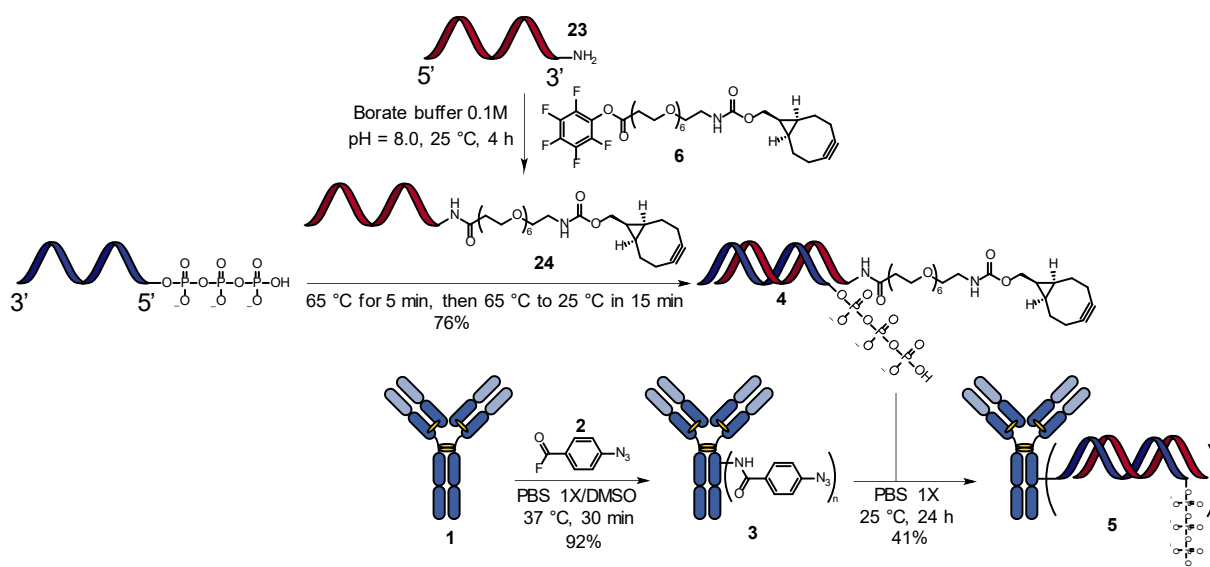


Figure 54 - Synthesis of ARC 5 by a “plug and play” strategy. Commercially available 3'-amino antisense strand was derivatized with a short activated oligoethylene glycol containing the BCN moiety 6. After purification, this modified-RNA strand was hybridized with the fully complementary 5'-triphosphate sense strand. The resulting siRNA 4 was then attached to the EphA2 antibody 3, pre-functionalized with an azide group with an acyl fluoride 2. The ARC 5 was then purified by size-exclusion chromatography, unconjugated antibody 1 was separated from the ARC 5 at this stage.

#### iv. ARC 5 simultaneously activates RIG-I and silences PLK1

For the biological evaluation of this conjugate (mAb-siPLK1-5'-ppp, further named ARC 5), we used the EphA2-positive A549-Dual cell line, engineered to express two reporter genes for both RIG-I signaling pathways (i.e. NF- $\kappa$ B and IRF 3/7). These reporter genes are respectively coding for an alkaline phosphatase and a luciferase whose activities can be quantified to

validate RIG-I activation (Figure 55). A RIG-I KO cell line was also used to further validate that activations of these signaling pathways were RIG-I-dependent and did not rely on other pattern-recognition receptors (PRRs), such as TLR3.<sup>38</sup>

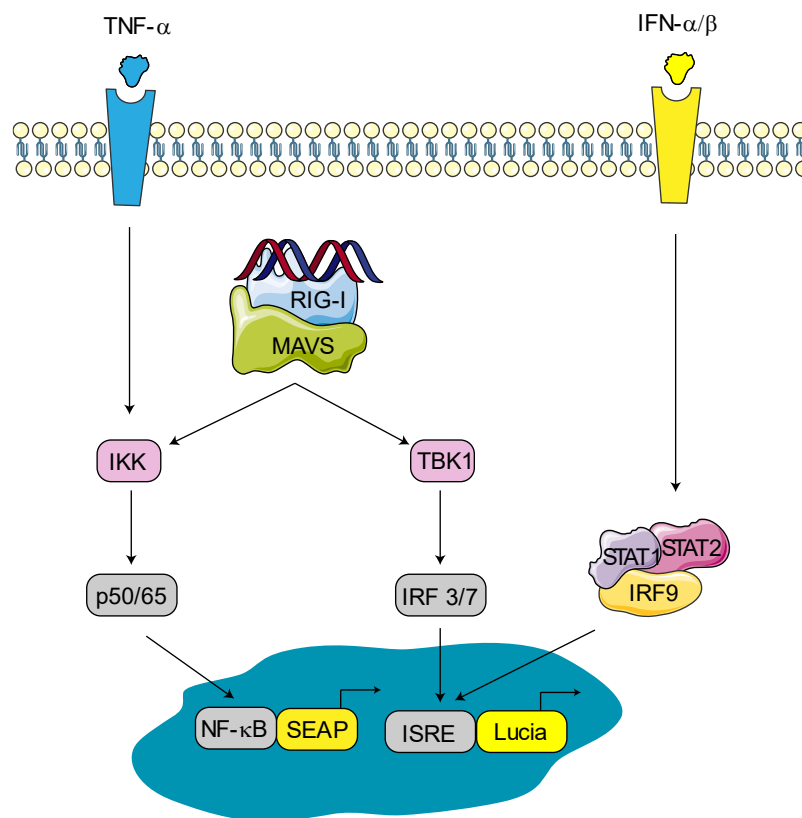


Figure 55 - On A549-Dual cell lines, activation of RIG-I promotes the excretion of SEAP and Lucia, under the control of NF-κB and IFN production respectively. On each experiment, TNF-α and IFN-α were used as positive controls. On RIG-I KO cell lines, neither SEAP or Lucia should be produced unless these pathways are activated by another PRR.

Induction of RIG-I pathways was evaluated *in vitro* by incubating the siRNAs, either transfected or conjugated, for 72 h at 40 nM (Figure 56) on our two cell lines. When comparing the activity of triphosphorylated siRNAs with that of non-triphosphorylated ones, we observed that only the formers were able to activate both reporter genes in a RIG-I-dependent manner. As expected, having an active siRNA against PLK1 did not have any influence on RIG-I activation, confirming that the activation of RIG-I is independent of the RNA sequence. In addition, no activity could be seen on RIG-I KO cell line, confirming the RIG-I-specific effect. Regarding more specifically the ARC 5, we were pleased to measure an activation of both signaling pathways in the nanomolar range. By pre-incubating cells with naked anti-EphA2 antibody 1 followed by ARC 5 at the same dose showed a decrease in RIG-I activation, thus demonstrating that the delivery was EphA2-dependent (see experimental part). These encouraging results demonstrated that our ARC 5 was indeed able to deliver the siRNA inside cells in an effective manner and that the latter could be recognized by RIG-I at very low doses.

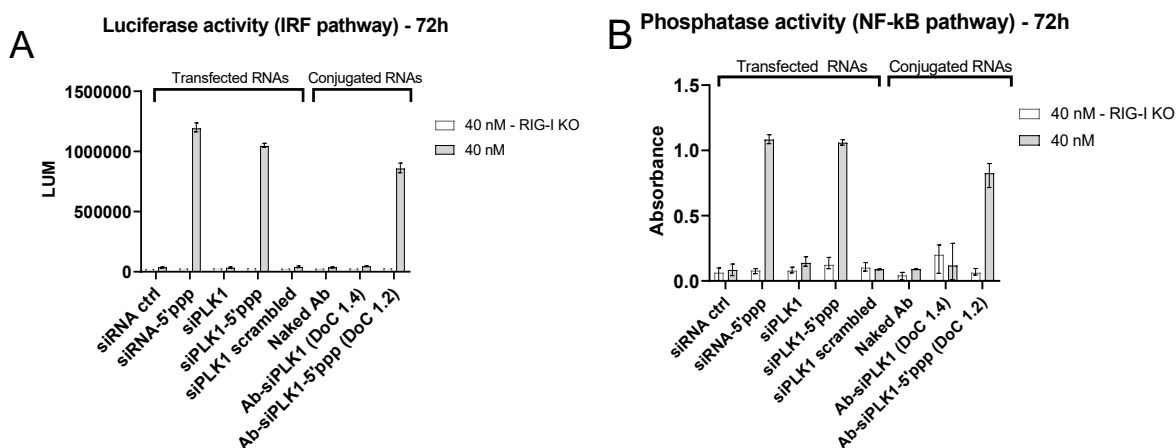


Figure 56 - Dual activity of the siPLK1-5'-ppp delivered by either RNAiMAX™ or EphA2-antibody – (A) RIG-I-dependent activation of the IRF pathway, N = 6, triplicates – (B) RIG-I-dependent activation of the NF-κB pathway, N = 6, triplicates.

As RIG-I should be overexpressed upon activation,<sup>103,360,361</sup> its level of expression was measured by western-blot after 72-hour incubation with either 40 nM of ARC **5** or transfection of siRNAs. Gratifyingly, a 31-fold increase in protein expression was observed in both cases compared with non-treated cells (Figure 57), thus confirming the previous results on the activation of the IRF signaling pathways. In order to evaluate the double activity RIG-I activation/PLK1 silencing, the levels of expression of PLK1 were measured simultaneously after 72 h of incubation at 40 nM for each compound (Figure 57). As expected, the transfection of siPLK1 could silence about 85% of intracellular PLK1 after 72 h of incubation as compared to untreated cells. As the silencing efficiency of siPLK1-5'-OH was >95% in the same conditions, we suggest that the presence of the triphosphate group on the siPLK1 seemed to have a minimal influence on the silencing. Treatment of the EphA2-positive cells with ARC **5** could silence about 32% of total PLK1 in these conditions, demonstrating that **5** could perform silencing by RNA interference.

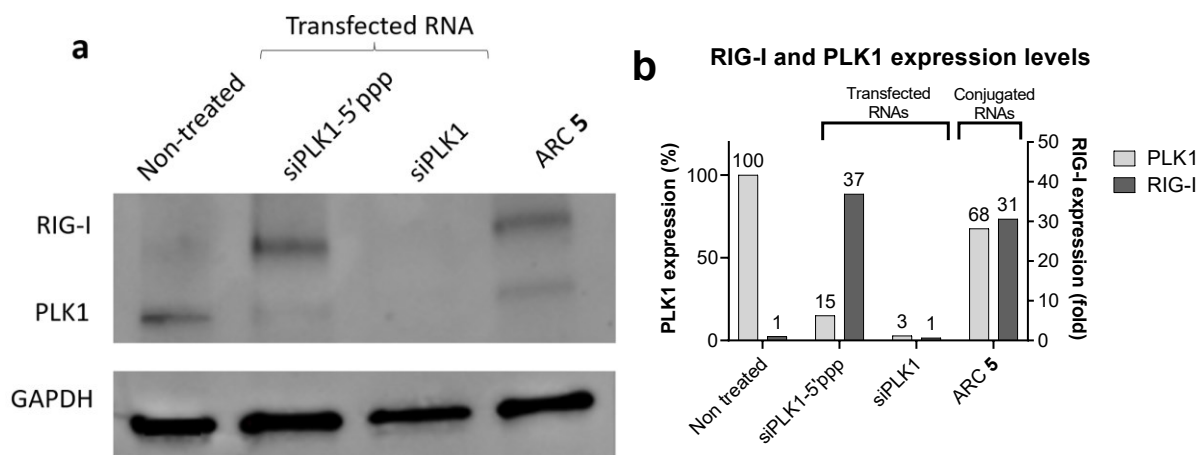


Figure 57 – Dual activity of the siPLK1-5'-ppp delivered by either RNAiMAX™ or ARC 5 – (A) Simultaneous PLK1 knockdown and RIG-I activation, 72h after incubation at 40 nM, observed by western-blot, N = 3. (B) Quantification, normalized to GAPDH.

As PLK1 knockdown by siRNAs should induce a cell cycle arrest in the G2/M phase, the proportion of cells in the G2/M phase was measured by flow cytometry after 24 h of incubation at 40 nM (Figure 58). While about 11.6% of non-treated cells were at this phase, an increase this proportion was observed upon transfection with transfected siPLK1 (5'-OH and 5'-ppp, 20.4% of cells). This proportion reached 15.3% when the siPLK1-5'-ppp was delivered *via* ARC 5. This significantly higher proportion of cells in G2/M cells advocates for siRNA-induced PLK1 silencing. In addition, the control siRNA activating RIG-I but without silencing PLK1 (siRNA-5'-ppp) gave results comparable to non-treated cells, demonstrating that RIG-I activation does not have any influence on the cell cycle.

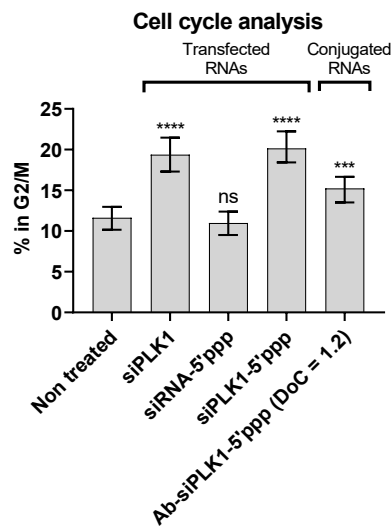
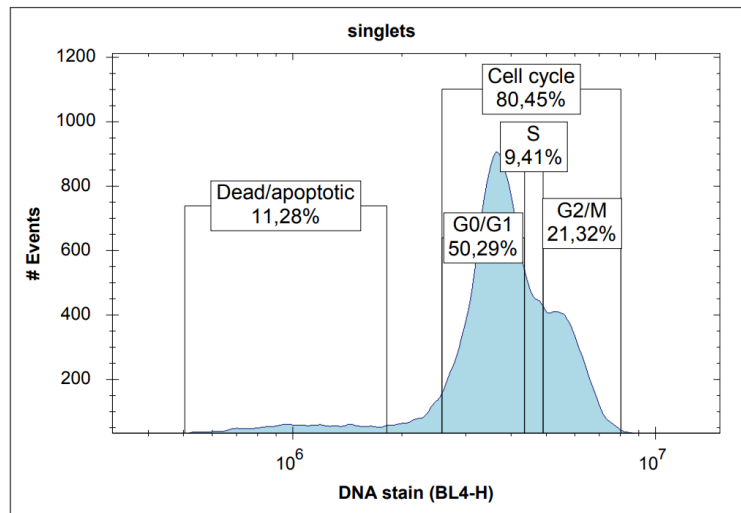


Figure 58 - Flow cytometry study of the cell cycle. Left: Gate strategy following manufacturer's template for cell cycle analysis. Right: Proportion of cells in G2/M phase analyzed by FACS after 24h of incubation at 40 nM. All siRNA were transfected using RNAiMAX. (ns = non-significant, \*\*\* =  $p < 0.0005$ , \*\*\*\* =  $p < 0.00005$ ).

## v. Validation of RIG-I effects: impact on apoptosis and immune stimulation

### 1. Apoptosis activation by transfected siRNAs

In order to study further the implication of this dual mode of action for immuno-oncology purposes, assays probing cancer apoptosis and the activation of anti-tumor immunity mechanism were performed. Induction of apoptosis by the activation of caspase 3/7 and the exposition of phosphatidyl serine was evaluated using a live-imaging system and profluorescent markers (Figure 59). More precisely, we used a commercially available caspase-3/7 peptide substrate linked to a quenched fluorophore, which became fluorescent upon cleavage of the linkage by the caspase. For the phosphatidyl serine exposure, we used a commercially available Annexin V conjugated to a quenched fluorophore, which became

fluorescent upon binding to exposed phosphatidyl serine. Each compound was incubated at 100 nM, and one picture was taken every 2 hours for 96 hours.

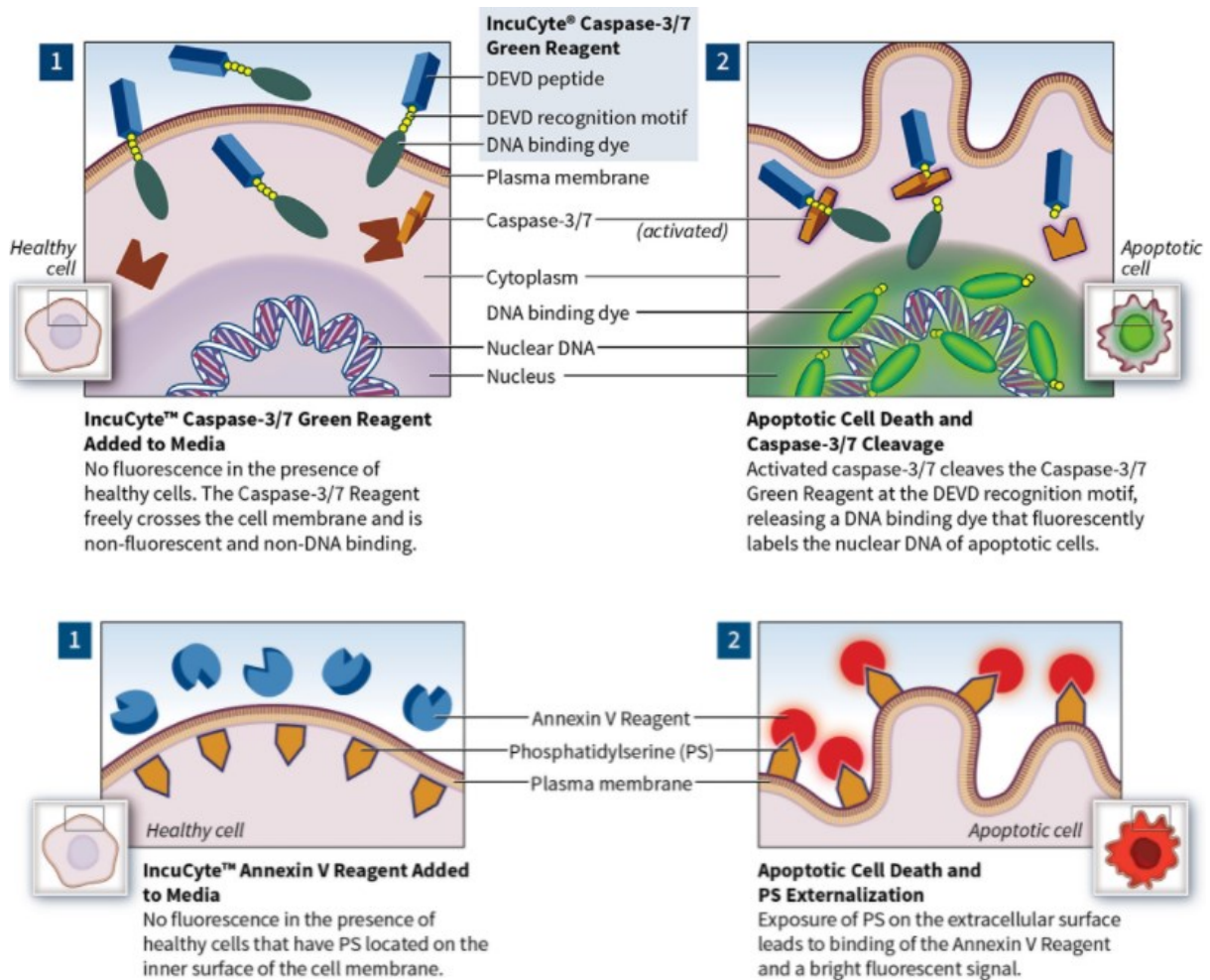


Figure 59 - Mechanism of fluorescence to assess apoptosis using IncuCyte Cas3/7 Green dye and Annexin V Red dye. Pictures are from Sartorius.

Transfection of siPLK1-5'-OH (dark blue line) and siPLK1-5'-ppp (light blue line) strongly induce apoptosis according to both readouts in A549-Dual cells within 24 h (Figure 60A, B). This led to a total decrease in cell confluence (Figure 60C), explained by the cell mortality and the cell cycle arrest. Surprisingly, scrambled versions of these siRNAs were also active, especially if it activated RIG-I (light green line), due to the activation of NF- $\kappa$ B pathway. However, no difference in cell confluence was observed between siPLK1-5'-OH (dark blue line) and siPLK1-5'-ppp (light blue line) suggesting that the majority of the cell death was due to PLK1 knockdown over RIG-I activation. This phenomenon was confirmed by kinetic studies of the cell viability. As expected, unconjugated anti-EphA2 antibody 1 (yellow line) did not have any influence on the apoptosis nor on cells' confluence.



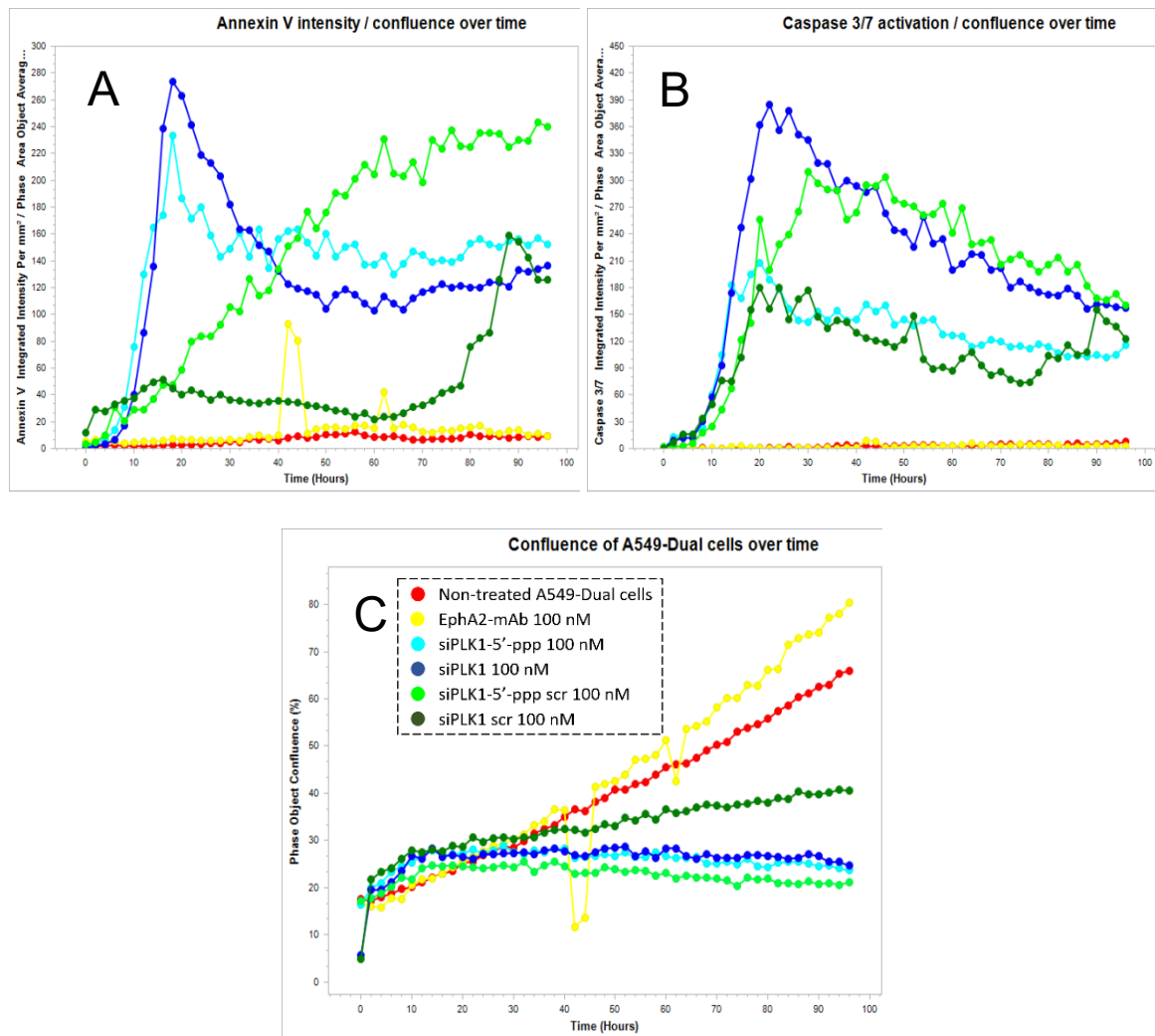


Figure 60 - Transfected siRNAs induce apoptosis via (A) Phosphatidyl serine exposure, (B) caspase 3/7 activation. Data are presented as intensity of fluorescence divided by the confluence of the well. (C) Resulting confluence on A549-Dual cells. One picture of A549 cells was taken every 2 hours for 4 days.

## 2. Impact of conjugates siRNAs on cell confluence

We repeated these experiments by conjugating all the siRNAs to the EphA2-antibody 1 and incubating them on both A549-Dual and A549-Dual RIG-I KO cell lines (Figure 61) in the exact same conditions as with transfected siRNAs. Scrambled conjugated siRNAs (green lines) did not significantly reduce the cell confluence over time on both cell lines, with no influence of the 5'-ppp group. However, active siPLK1 (blue lines) significantly reduced the cell confluence, and it appeared that the addition of the triphosphate moiety on the siPLK1 (ARC 5, light blue line) slightly increased the mortality on RIG-I positive cell line. Overall, while the ARCs were less deadly than the transfected siRNAs, they were still efficient in the nanomolar range to induce apoptosis and cell death.

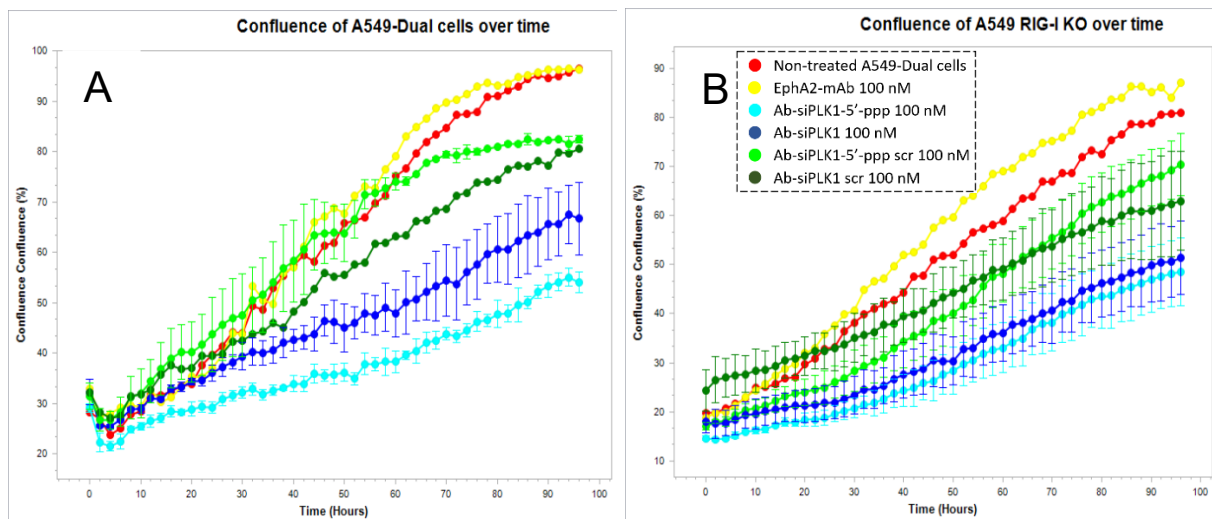


Figure 61 - Ab-siRNA conjugates induce cell killing on A549-Dual and A549-Dual RIG-I KO cell lines. (A) Resulting confluence on A549-Dual cells. (B) Resulting confluence on A549-Dual RIG-I KO cells. One picture of A549 cells was taken every 2 hours for 4 days.

### 3. ARC 5 activates PBMCs and anti-tumor immunity

In order to determine whether or not the ARCs could recruit immune cells and induce RIG-I-dependent immunogenic cell death, experiments with primary Peripheral Blood Mononuclear Cells (PBMCs) were conducted in the same conditions. It should be noticed that the viability of PBMCs alone was not impacted by any of the ARC, whereas it dropped significantly when these cells were transfected by siRNAs due to the transfecting agent. Thus, co-culture experiments with A549 cells and PBMCs (ratio 1:5) were performed using 2 different donors of PBMCs. Due to the high difference in size between the two populations of cells, we were able to follow only the cancer cells, by excluding much smaller PBMCs. For both donors, non-treated co-cultures did not affect the A549 growth, thus discarding a potential pre-activation of PBMCs after thawing.

Surprisingly, with PBMCs, RIG-I-activating ARCs (light green and light blue lines) were more potent apoptosis inducers than the other ARCs (i.e not active on RIG-I, dark green and dark blue lines) on RIG-I-negative cell lines (Figure 62). Indeed, siPLK1-5'-ppp scrambled (i.e not active on PLK1, light green line) showed similar results as the non-scrambled 5'-ppp sequence (i.e active on PLK1, light blue line, ARC 5) for apoptosis induction, suggesting a RIG-I-dependent mechanism when cells are co-cultured with PBMCs.

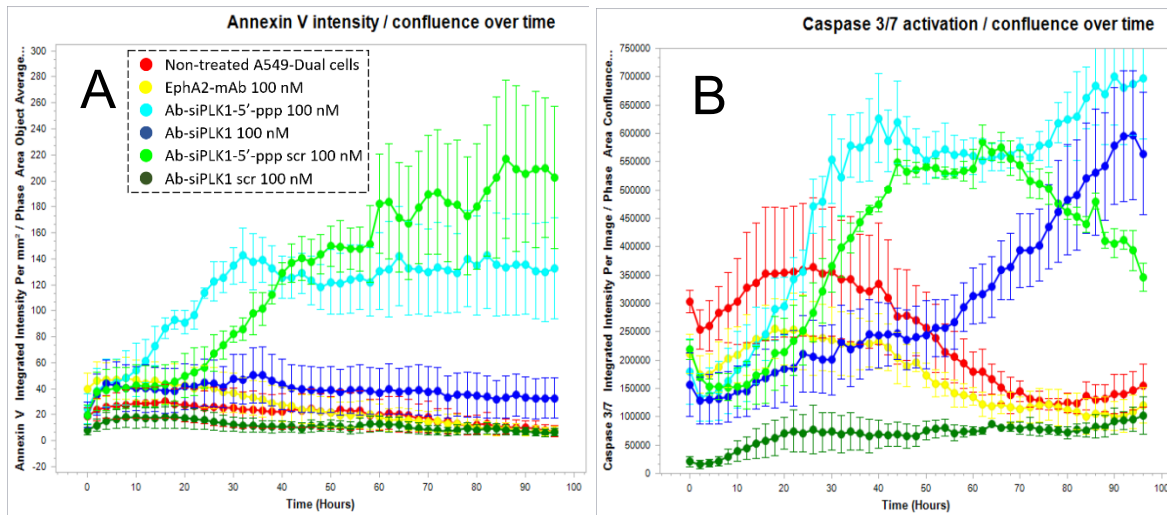


Figure 62 – ARC 5 induce apoptosis in A549-Dual RIG-I KO, as shown by (A) phosphatidyl serine exposure and (B) caspase 3/7 activation. Data are presented as intensity of fluorescence divided by the confluence of the well. Three pictures of the A549-RIG-I KO cells were taken every 2 hours, PBMC were excluded by the software because of the difference of size between A549-RIG-I-KO and PBMC.

When compared to the previous experiment without PBMCs (Figure 63), addition of immune cells significantly reduced the cell confluence of RIG-I activating ARCs for both RIG-I positive and RIG-I KO cell lines. This result showed that, in presence of PBMCs, both cell line can be killed by RIG-I-activating ARC. Therefore, these data suggest that PBMCs were activated by the conjugate in a RIG-I-dependent manner, and thus killed the cancer cells.

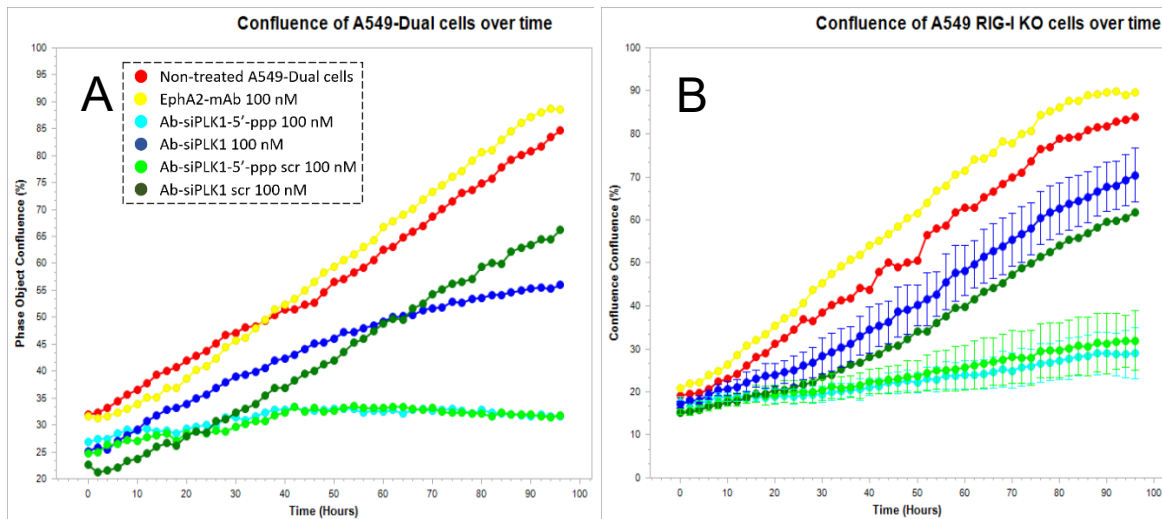


Figure 63 – ARC 5 induce RIG-I-dependent cell killing by human PBMCs (ratio A549/PBMC : 1/5) on both RIG-I-positive and RIG-I-KO A549 cells. (A) Confluence of A549-Dual cells with PBMC – (B) Confluence of A549-Dual RIG-I KO cells with PBMC – Three pictures of the A549 cells were taken every 2 hours, PBMC were excluded by the software because of the difference of size between A549 and PBMC.

Considering these elements, we had two hypotheses. The first one was that the conjugates were more internalized in PBMCs via  $Fc\gamma$  receptors than in A549 cells via EphA2, due to the

higher number of PBMCs with respect to cancer cells. Such mechanism could lead to the RNA delivery in PBMCs, thus activating RIG-I inside them and triggering an innate and adaptive immune response against tumors.

The second hypothesis was that the PBMCs-mediated cell death was due to the activation of RIG-I in A549 cells, which could lead to the release of damage-associated molecular patterns (DAMP) from them, such as calreticulin (CALR).<sup>125</sup> DAMPs are essential molecules that are normally inside cells, but these are released in the extracellular environment following a stress.<sup>24</sup> These molecules can then be taken up by immune cells, thus activating them to kill cancer cells, a mechanism named immunogenic cell death (ICD). Regarding this last mechanism, it has been reported that RIG-I activation could lead to DAMP release and subsequent ICD.<sup>125,133</sup>

#### *4. ARC 5 induces the release of calreticulin in A549 cells*

Therefore, CALR release assays were conducted by incubating either the transfected siRNAs or the bispecific conjugate ARC 5 in RIG-I positive A549-Dual cells for 48 h at 50 nM. The proportion of cells that released calreticulin was measured by flow cytometry using an AF488-labelled anti-CALR antibody and by labelling dead cells using 7-AAD (Figure 64). As expected, the proportion of CALR<sup>+</sup> live cells in non-treated cells or following transfection of scrambled siRNA was very low (2.12%). Transfected siRNA-5'-ppp showed significant release of CALR (9.65%) from the cell, confirming that RIG-I activation could release DAMP. Incubating siPLK1 increased this proportion more significantly (12.7%), and the presence of a triphosphate moiety on the RNA highlighted a synergistic effect between PLK1 knockdown and RIG-I activation (17.86%). ARC 5 showed a less impressive, but still significant, CALR exposure (5.86%), thus suggesting that ARC 5 could induce the release of DAMPs. Considering these elements, these data suggest that one of the mechanisms of PBMCs activation leading to A549 cell death may be the release of DAMP from the cancer cells following ARC incubation.

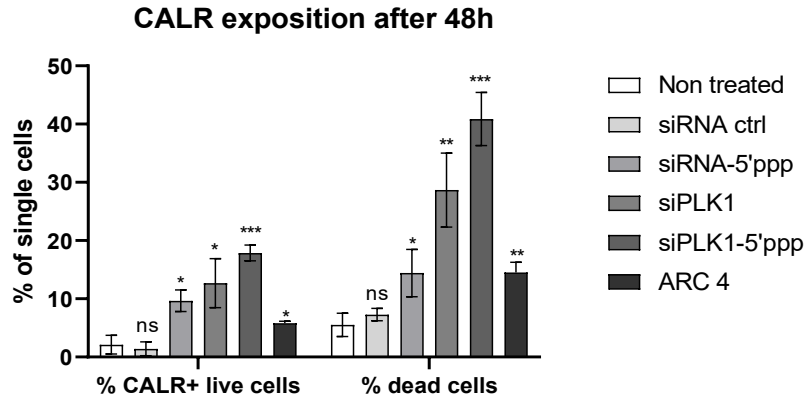


Figure 64 - CALR exposition after 48h of incubation at 50 nM, indicating a possible release of damage-associated molecular patterns (ns = non-significant, \* =  $p < 0.05$ , \*\* =  $p < 0.005$ , \*\*\* =  $p < 0.0005$ ).

## vi. Intracellular trafficking

### 1. Internalization of the EphA2 antibody 1

In order to investigate the mechanism of delivery, a study of the trafficking inside the cell was engaged. First, an internalization assay of the antibody alone was performed by incubating Cy5-labelled EphA2-antibody in the EphA2-positive cells at different time point, and analyzing the intracellular antibody by fluorescent SDS-PAGE and western-blot. EphA2 is described to be rapidly internalized and further degraded upon binding, therefore no recycling should be observed.<sup>352</sup> Following incubation, a complete degradation of the antibody within 4 hours was assessed by SDS-PAGE and western blot using an anti-Fc antibody (Figure 65), indicating that this antibody was extremely well internalized and degraded inside cells.

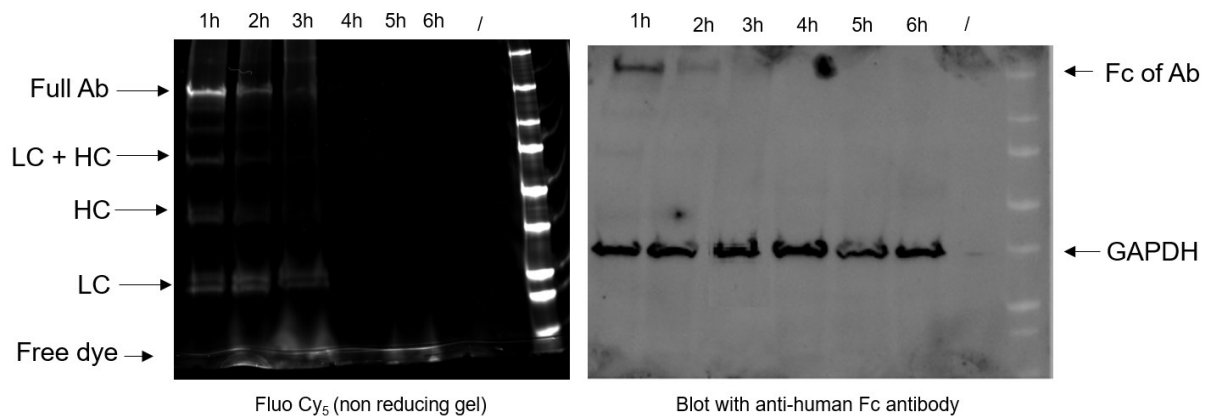


Figure 65 - Fast internalization of antibody in A549 Dual cells assessed by SDS-PAGE and western blot. Cells were treated with 500 nM of Cy<sub>5</sub>-labelled EphA2 antibody for 1h-6h and harvested. Total cellular protein was quantified and non-reducing denaturing SDS-PAGE was performed. Western blot was done using an anti-Human Fc antibody.

### 2. Immunofluorescence by confocal microscopy

Following this result, a confocal microscopy study was conducted by incubating a dual-labelled ARC in live A549 cells at different time point. The ARC was composed of a siRNA-5'-Cy3

attached to Cy5-labelled EphA2-antibody in order to follow both biomolecules independently (Figure 66).

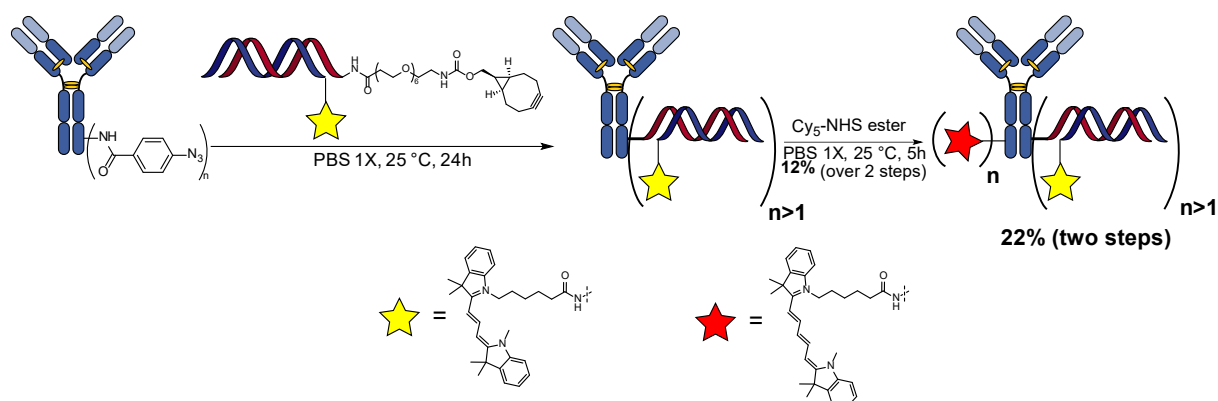


Figure 66 - Synthesis of the dual-labelled antibody-siRNA conjugate in order to follow both biomolecules by microscopy.

A fast, antigen-dependent internalization was observed for both dyes after 1 h of incubation at 100 nM (Figure 67, upper line). As expected, the two dyes are colocalized (Figure 67, bottom line, merge siRNA and Ab), and seemed to be inside lysosomes (Figure 67, bottom line, merge siRNA and lysosome, Pearson's correlation coefficient = 0.74), suggesting that, at this time point, both biomolecules are still attached together and reached lysosomes.

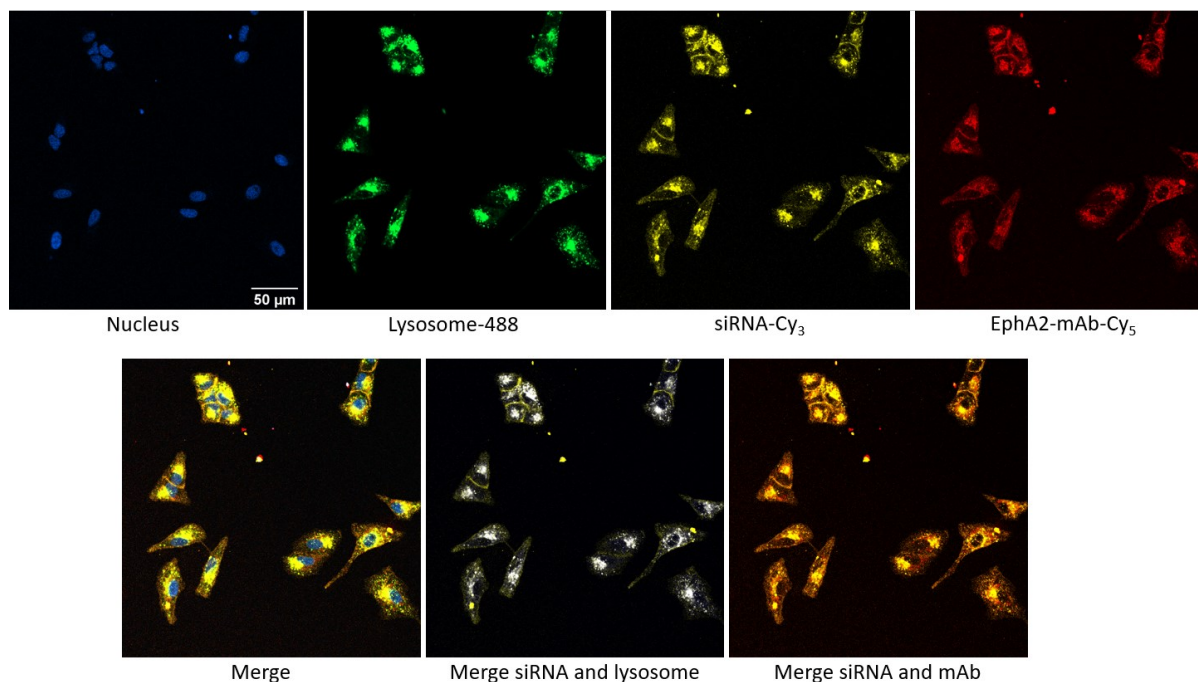


Figure 67 - Immunofluorescence pictures obtained from a dual-labelled ARC after 1h of incubation (upper line) and merges of pictures (bottom line). The scale of pictures is displayed on the nucleus picture. Cy<sub>3</sub> (yellow) was placed at the 5'-end of the siRNA, and Cy<sub>5</sub> (red) was conjugated to the purified antibody-siRNA-Cy<sub>3</sub> conjugate. Lysoview 488 (green, white for the merged pictures) was used to label endo/lysosomes.

After 4 h of incubation (Figure 68, upper line), a separation of the two counterparts was observed (Figure 68, bottom line, merge siRNA and Ab). Regarding the cytosolic delivery, the vast majority of intracellular siRNAs colocalized with endo/lysosomes and seemed trapped inside. However, a small portion of the siRNA leaked in the cytosol (Figure 68, bottom line, merge siRNA and lysosomes), characterized by a diminution of Pearson's correlation coefficient over time (from 0.74 to 0.18). However, the exact structure of the released siRNA that escapes the endosome and the release mechanism remain elusive, therefore we hypothesized that this small portion of siRNA in the cytosol was enough to activate RIG-I pathways and perform protein knockdown.

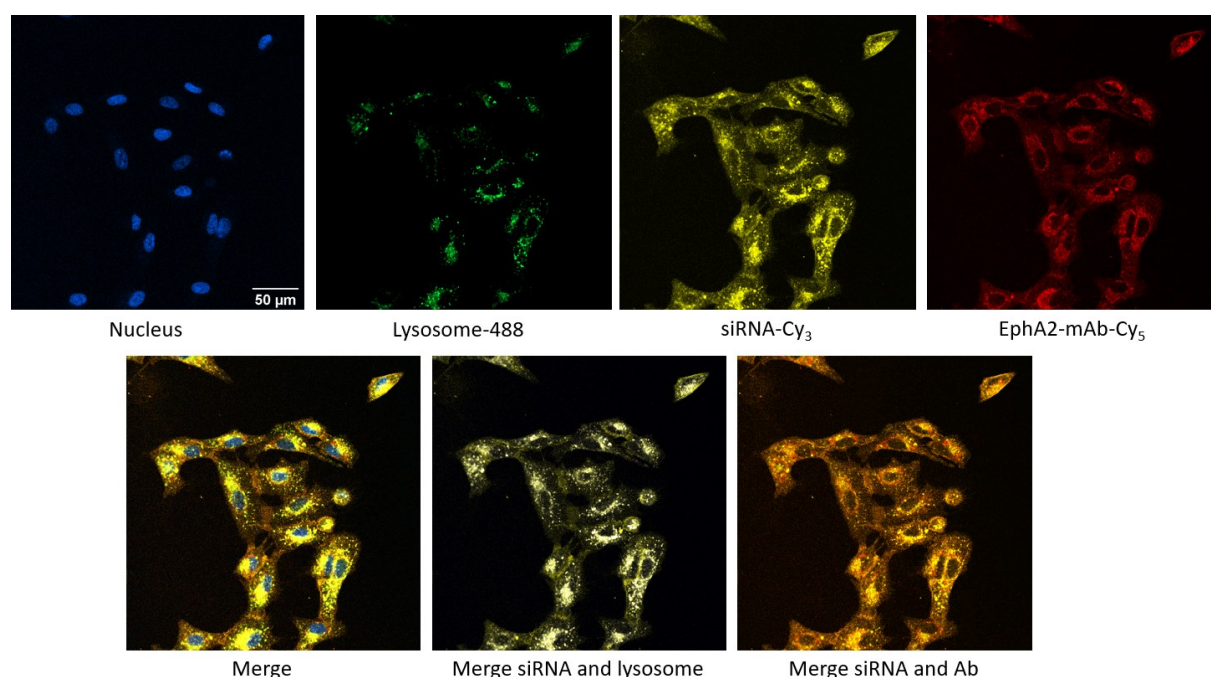


Figure 68 - Immunofluorescence pictures obtained from a dual-labelled ARC after 4h of incubation (upper line) and merges of pictures (bottom line). The scale of pictures is displayed on the nucleus picture. Cy<sub>3</sub> (yellow) was placed at the 5'-end of the siRNA, and Cy<sub>5</sub> (red) was conjugated to the purified antibody-siRNA-Cy<sub>3</sub> conjugate. Lysoview 488 (green, white for the merged pictures) was used to label endo/lysosomes.

#### vii. Plasma stability

The stability in human plasma was measured following two methods. First, a dye-labelled siRNA was conjugated to the antibody, and the resulting conjugate was incubated in human plasma at 37 °C at different time points for SDS-PAGE analysis. While unprotected and unconjugated siRNAs were extremely unstable in human plasma ( $t_{1/2} < 10$  min, Figure 69), their conjugated version showed a higher degree of plasma stability ( $t_{1/2} < 24$  h, Figure 69). It thus appeared that the simple conjugation of the RNA to the antibody increases significantly its plasma half-life, probably because of steric hindrance due to the antibody.

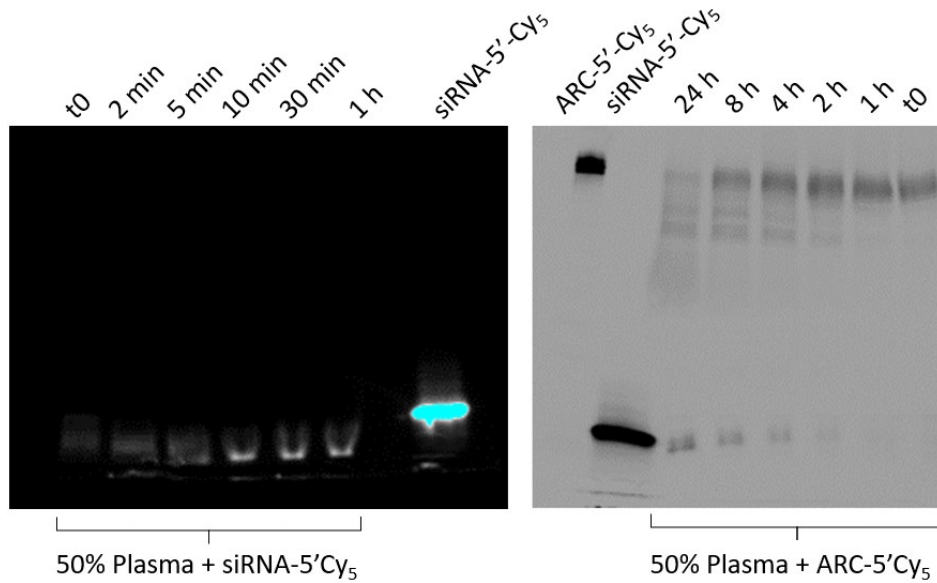


Figure 69 - Human plasma stability assessed by SDS-PAGE. Left: siRNA-5'-Cy<sub>5</sub> alone (1 μM, plasma/DPBS 1/1) for up to 1 h at 37 °C. Right: ARC-5'-Cy<sub>5</sub> (1 μM, plasma/DPBS 1/1) for up to 24 h at 37 °C.

Experiment repeated in presence of a RNase inhibitor (Figure 70) resulted to significantly longer half-life for both unconjugated and conjugated siRNAs. Not surprisingly, degradation of the conjugate seems to predominantly proceed through RNases hydrolysis in human plasma. However, this can be circumvented by classical life-extension strategies using modified ribonucleosides on the siRNA sequence, such as phosphorothioates bonds.

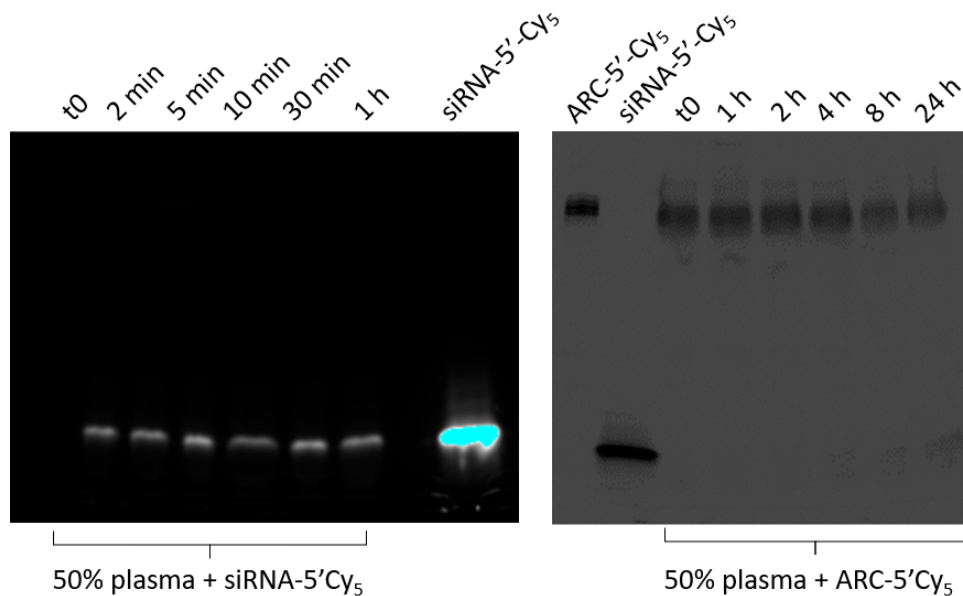


Figure 70 - Human plasma stability assessed by SDS-PAGE. Left: siRNA-5'-Cy<sub>5</sub> (1 μM, plasma/DPBS 1/1) + RNase inhibitor for up to 1 h at 37 °C. Right: ARC-5'-Cy<sub>5</sub> (1 μM, plasma/DPBS 1/1) + RNase inhibitor for up to 24 h at 37 °C.



Plasma stability was also measured by evaluating ARC 5 activity on RIG-I after incubation in human plasma at different time point. This activity decreased rapidly, with a complete loss of activity after 4 h of incubation in plasma (Figure 71). In addition to RNase-mediated degradation, this loss of activity could also be imputed to the degradation of the 5'-ppp group by phosphatases. However, adding phosphatases inhibitors to human plasma did not improve stability, while the addition of RNases inhibitors significantly improved it.

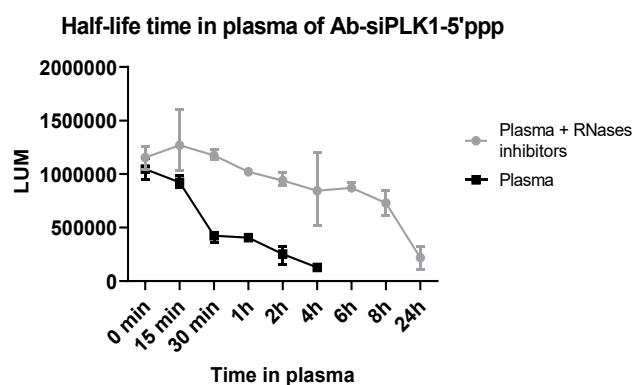


Figure 71 - Plasma stability of the ARC 5 conjugate assessed by its activity on the IRF pathway. Conjugate was first diluted to 400 nM in 50% human plasma with/without RNase inhibitors for 0-24h at 37 °C. Then, these solutions were directly added to cells to a final conjugate concentration of 40 nM, and incubated for 72 h.

### C. Conclusion

Taken together, our postulate that a dual mode of action siPLK1-5'-ppp could induce cell death by simultaneous and synergistic RIG-I/RNAi mechanisms of action has been verified. Our results also suggest that fast-internalizing antibodies targeting EphA2 could be a good vehicle for the targeted delivery of a siRNA. Indeed, the covalent ARC 5 proved to be efficient to deliver siRNAs inside EphA2-expressing cancer cells, thus activating RIG-I and silencing PLK1 in the low nanomolar range. Moreover, killing assays with primary immune cells indicated that the delivery of RIG-I agonist inside tumors could induce a strong immune response *in vitro*.

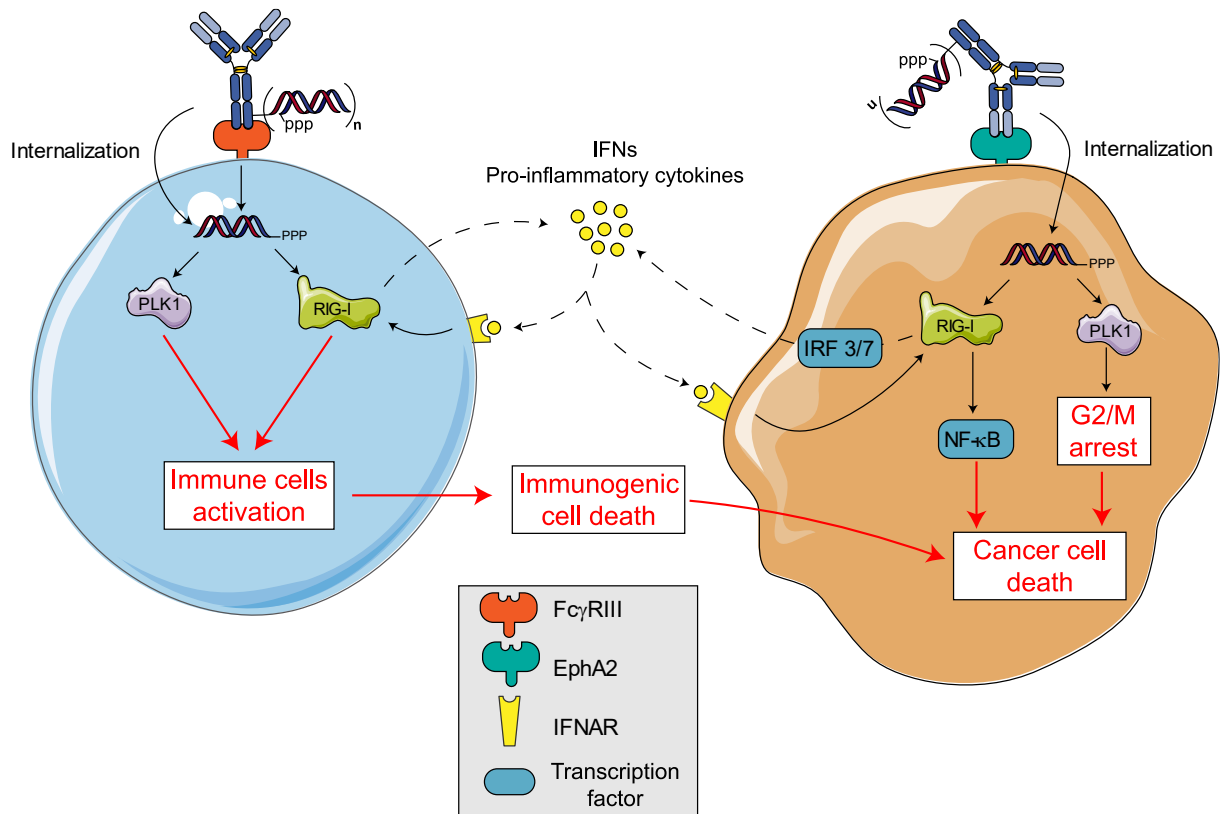


Figure 72 - Summary of all the effects induced by the EphA2-targeting ARC, activating both RIG-I and PLK1 in cancer cells and able to activate RIG-I in immune cells.

Immunofluorescence studies by microscopy demonstrated that a small portion of siRNA was able to escape the endosomes in a few hours. However, the majority of the siRNA remained trapped in this locus, in accordance with numerous studies. The conjugate's plasma stability is however one major limitation of this system, thus enhancing it by an optimization of the linker and the siRNA's design, notably by using nuclease-resistant structures, could lead to a possible transfer into preclinical trials. Regarding this particular point, it is worth noting that the targeted delivery of RIG-I agonists by antibodies could allow intravenous administration, thus avoiding intratumoral injections required by RIG-I agonists currently in clinical trials.<sup>114</sup> Therefore, one of the remaining challenges is to enhance the siRNA's stability while retaining the strong activity obtained on RIG-I, which does not recognize unnatural bases well.<sup>62,362</sup>

To conclude on this study, we developed a targeted immunostimulatory-siRNA system based on ARC, and showed both the strengths and some limitations of this system. Overall, this study demonstrated the potential for immune-oncology purposes, of ARC targeting cancer cells to deliver a bispecific siRNA simultaneously able to activate RIG-I and silence PLK1.

#### D. Experimental part

##### Material and methods.

All reagents were obtained from commercial sources and used without prior purifications. Dry solvents were obtained from Merck. All reactions were carried out under an atmosphere of argon in flame-dried glassware with magnetic stirring. Analytical thin layer chromatography (TLC) was performed using plates cut from glass sheets (silica gel SIL-G, Macherey-Nagel, Ref. 809013). Visualization was achieved under a 254 or 365 nm UV light and by immersion in an appropriate staining solution. Column chromatography was carried out as "Flash Chromatography" using silica gel G-80, G-40, G-25, G-12 or G-4 (40-63  $\mu\text{m}$ ) from Buchi on a Buchi Reveleris X2.

NMR:  $^1\text{H}$  and  $^{13}\text{C}$  NMR spectra were recorded at 23 °C on Bruker Advance III - 400 MHz / 500 MHz spectrometers. Recorded shifts are reported in parts per million ( $\delta$ ) and calibrated using residual nondeuterated solvent. Data are represented as follows: chemical shift, multiplicity (s = singlet, d = doublet, t = triplet, q = quartet, m = multiplet, br = broad, app = apparent), coupling constant ( $J$ , Hz), integration and assignment for  $^1\text{H}$  NMR data.

Analytical LC-MS analyses were carried out on Waters 2695 separations module equipped with Waters 2487 UV detector, Waters Acquity QDa mass detector and CORTECS, 2.7  $\mu\text{m}$ , C18, 50 x 4.6 mm column. The flow rate was 1 mL/min and the solvent system was composed as follows: solvent A: 0.05% TFA in water; solvent B: acetonitrile. The gradient run was: 0 to 5 min. – 5% to 95% B; 5 to 6 min. – 95% B; 6 to 7 min. – 5% B. Mass detector was operated in positive MS Scan mode with 600 °C probe temperature, 1.5 kV capillary voltage and 10 V cone voltage.

High resolution mass spectra (HRMS) were obtained using an Agilent Q-TOF 6520.

IR spectra were recorded in a Thermo-Nicolet FT/IR-380 spectrometer. Spectra were interpreted with OMNIC 9 software and are reported in  $\text{cm}^{-1}$ . The abbreviations used are w (weak), m (medium), s (strong).

Concentrations of protein or RNA solutions in DPBS (calcium and magnesium free, Merck, Ref. D8537-6X500ML) were determined by UV absorbance using a NanoDrop spectrophotometer (Thermo Fisher Scientific, Illkirch, France) at 280 nm for proteins and 260 nm for RNA. The concentration of antibody conjugates was measured using a BCA Protein Assay Kit (Thermo Fisher Scientific, Illkirch, France, Ref. 23225) as RNA also absorb at 280 nm.

Non-reducing SDS-PAGE was performed on 4 – 20% Mini-PROTEAN® TGX™ gel (Bio-Rad, Hercules, U.S.A., Ref. 4561094) following standard lab procedures. To the samples containing

antibody conjugates (24  $\mu$ L, 0.2 mg/mL solution in DPBS 1X) was added 8  $\mu$ L of loading buffer (non-reducing Laemmli SDS sample buffer 4X, Alfa Aesar, Ref., J63615.AC) and heated at 95 °C for 3 min. The gel was run at constant voltage (200 V) for 35 min using TRIS 2.5 mM – Glycine 19.2 mM – SDS 0.01% as a running buffer (Bio-rad, Hercules, U.S.A., Ref. 1610772). The fluorescence was visualized on a ImageQuant™ LAS4000 (GE Healthcare) prior to staining with InstantBlue® Protein Stain (Merck, Ref. ISB1L).

Size Exclusion Chromatography hyphenated to non-denaturing Mass Spectrometry (SEC-non denaturing MS): An ACQUITY UPLC H-class system (Waters, Manchester, UK) comprising a quaternary solvent manager, a sample manager cooled at 10 °C, a column oven maintained at room temperature and an UV detector operating at 280 nm and 214 nm was coupled to the Synapt G2 HDMS mass spectrometer (Waters, Manchester, UK). A quantity comprised between 10 to 20  $\mu$ g of sample were loaded on the ACQUITY UPLC Protein BEH SEC column ( 2.1  $\times$  150 mm, 1.7  $\mu$ m particle size, 200 Å pore size from Waters, Manchester, UK) using an isocratic elution of 100 mM ammonium acetate (NH<sub>4</sub>OAc) at pH 6.9 and at a flow rate of 0.100 mL/min over 6.0 minutes. The Synapt G2 HDMS was operated in positive mode with a capillary voltage of 3.0 kV while sample cone and pressure in the interface region were set to 180 V and 6 mbar, respectively. Acquisitions were performed in 1,000–10,000 m/z range with a 1.5 s scan time. The mass spectrometer was calibrated using singly charged ions produced by a 2 g/L solution of cesium iodide (Acros organics, Thermo Fisher Scientific, Waltham, MA USA) in 2-propanol/water (50/50 v/v). Native MS data interpretations were performed using UniDec software.

RNA sequences (5'- to 3'-):

siPLK1 antisense (Eurogentec): UAUUUAAGGAGGGUGAUCU

siPLK1 sense (Eurogentec): ppp-AGAUCACCCUCCUAAAUA

siPLK1 scrambled antisense (Eurogentec): UUCUCCGAACGUGUCACGU

siPLK1 scrambled sense (Eurogentec): ACGUGACACGUUCGGAGAA

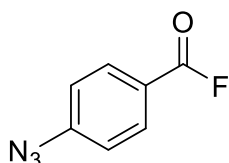
siRNA antisense (Invitrogen): ppp-GCAUGCGACCUCUGUUUGA

siRNA sense (Invitrogen): CGUACGCUGGAGACAAACU

RNAs were purchased HPLC-purified from Eurogentec or Invitrogen. All dye-labelled RNA were purchased. Every step using RNA were carried out under a biosafety cabinet cleaned with ethanol and RNaseZap. Upon reception, tubes were centrifuged, then RNAs were suspended in DEPC-treated water to 100  $\mu$ M (for biological assays) or 1 mM (for conjugation). RNAs are stored dried at -80 °C until use, and at -20 °C when solubilized.

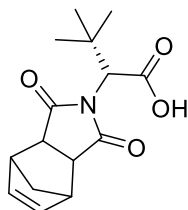
## Chemical syntheses and characterizations.

### 4-azidobenzoyl fluoride **2**



The synthesis was adapted from a published protocol, using TFFH instead of cyanuric fluoride.<sup>354</sup> TFFH (1.5 equiv., 242 mg, 0.919 mmol) and 4-azidobenzoic acid (1 equiv., 100 mg, 0.613 mmol) were dissolved in acetonitrile (5 mL) and DIPEA (1 equiv., 79.2 mg, 0.101 mL, 0.613 mmol) was added. The mixture was stirred at room temperature for 3 hours in the dark. The reaction mixture was poured onto ice water (20 mL) and diluted with diethyl ether (50 mL). The aqueous layer was discarded, and the organic layer was washed with water (2 x 10 mL) and brine (10 mL). The organic layer was dried over MgSO<sub>4</sub>, filtered and concentrated under reduced pressure to provide the crude residue, which was purified by silica pad (Cyclohexane) and lyophilized to afford the title compound **2** (64.8 mg, 0.392 mmol, 64 %) as a yellow solid. Purity was checked by analytical RP-HPLC before use for bioconjugation.

### (2S)-2-(1,3-dioxo-1,3,3a,4,7,7a-hexahydro-2H-4,7-methanoisindol-2-yl)-3,3-dimethylbutanoic acid ((S)-BHTL) **7**

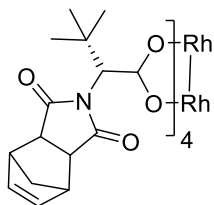


To a dry round-bottom flask was added *L-tert*-leucine (1.0 equiv., 1.13 g, 8.6 mmol) and *cis*-5-norbornene-*endo*-2,3-dicarboxylic anhydride (1.0 equiv., 1.41 g, 8.6 mmol) under argon. Triethylamine (150  $\mu$ L) and toluene (20 mL) were added via syringe, and the mixture was fitted with a Dean–Stark trap and heated to reflux overnight. The toluene was then removed in vacuo, and the residue was partitioned between 5% hydrochloric acid and diethyl ether. The aqueous layer was further extracted with diethyl ether (3 x 50 mL). The organic layers were combined, washed with brine (50 mL), dried, and concentrated under reduced pressure. The crude solid was recrystallized in DCM and heptane to provide the title compound **7** (1.64 g, 5.90 mmol, 69%) as a white solid.

**<sup>1</sup>H NMR (400 MHz, CDCl<sub>3</sub>):**  $\delta$  12.54 (s, 1H), 6.09–6.05 (d, 2H), 4.09 (s, 1H), 3.47–3.28 (m, 4H), 1.59–1.55 (m, 2H), 0.96 (s, 9H)

**<sup>13</sup>C NMR (101 MHz, CDCl<sub>3</sub>):**  $\delta$  177.1, 168.3, 135.0, 134.4, 59.1, 52.0, 44.7, 34.8, 27.6

## Rh<sub>2</sub>(S-BHTL)<sub>4</sub> **8**



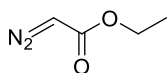
A round-bottom flask was charged with Rh<sub>2</sub>(OAc)<sub>4</sub> (1.0 equiv., 350 mg, 0.79 mmol), (S)-BHTL **7** (5.0 equiv., 1.10 g, 3.97 mmol), and chlorobenzene (50 mL). The flask was fitted with a dropping funnel that was stoppered with glass wool and filled with sodium carbonate. The dropping funnel was fitted with a reflux condenser, and the mixture was heated to reflux overnight. The

dropping funnel and reflux condenser was removed, and solvent was removed under reduced pressure. The flask was cooled, and the residue was dissolved in DCM (50 mL). The solution was washed with an aqueous solution of NaHCO<sub>3</sub> (3 x 50 mL) and then brine (50 mL). The organic layer was dried over MgSO<sub>4</sub>, filtered, concentrated under reduced pressure, and the resulting residue was recrystallized in DCM and heptane affording the title compound **8** as a light green solid (950 mg, 0.72 mmol, 92%).

**<sup>1</sup>H NMR (400 MHz, CDCl<sub>3</sub>):** δ 6.07 (s, 2H), 4.24 (s, 1H), 3.27–3.15 (m, 4H), 2.98 (s, 1H), 1.57–1.51 (m, 2H), 0.86 (s, 9H)

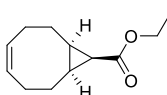
**<sup>13</sup>C NMR (101 MHz, CDCl<sub>3</sub>):** δ 187.1, 176.9, 176.2, 170.4, 135.4, 134.6, 61.6, 59.8, 52.2, 44.9, 34.9, 28.0, 20.8, 14.1

## Ethyl 2-diazoacetate **10**



To a solution of glycine ethyl ester chlorhydrate (1 equiv., 20.6 g, 147.6 mmol) in water (100 mL) and DCM (150 mL) was added a solution of NaNO<sub>2</sub> (1.3 equiv., 13.24 g, 191.9 mmol) in water (40 mL), with a rate of 1 drop per second. The mixture was vigorously stirred at 15 °C for 30 minutes. Organic layer was isolated, DCM (150 mL) and an aqueous solution of KHSO<sub>4</sub> (10 %, 20 mL, 0.2 equiv., 4.02 g, 29.51 mmol) were added to the aqueous layer until pH = 4.0. This mixture was stirred at 15 °C for 20 minutes and organic layer was isolated. All organic layers were combined, washed with brine (300 mL), dried over MgSO<sub>4</sub>, filtered, and concentrated in vacuo (water bath at 15 °C) to afford ethyl 2-diazoacetate **10** (15.85 g, 138.9 mmol, 94%) as a volatile yellow liquid which was used immediately without further purification.

## Ethyl (1R,8S,9S,Z)-bicyclo[6.1.0]non-4-ene-9-carboxylate **11**



To a solution of cycloocta-1,5-diene **9** (4 equiv., 68.31 mL, 60.11 g, 555.6 mmol) in DCM (250 mL, stabilized with ethanol) containing Rh<sub>2</sub>(S-BHTL)<sub>4</sub> **8** (0.0135 mol%, 25 mg, 0.018 mmol) was added a solution of ethyl 2-diazoacetate **10** (1 equiv., 15.85 g, 138.9 mmol) in DCM (150 mL, stabilized with ethanol, not amylene) with a rate of 40 mL/h at room temperature. Solvent and cycloocta-1,5-diene were removed in vacuo and the crude was purified by silica chromatography (petroleum ether 100%

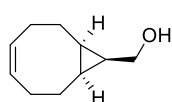
until all remaining cyclooctadiene is eluted then 97/3 petroleum ether/diethyl ether to elute both diastereoisomers, endo first). Fractions containing the product were combined and solvents were removed to afford the title compound **11** (12.9 g, 61.93 mmol, 45 %) as a colorless oil.

**TLC:** heptane/diethyl ether 95/5, Ce(SO<sub>4</sub>)<sub>2</sub>

**<sup>1</sup>H NMR (400 MHz, CDCl<sub>3</sub>, δ ppm):** 5.65-5.57 (m, 2H), 4.12 (q, J = 7.2 Hz, 2H), 2.53-2.46 (m, 2H), 2.25-2.16 (m, 2H), 2.10-2.01 (m, 2H), 1.87-1.79 (m, 2H), 1.70 (t, J = 8.8 Hz, 1H), 1.43-1.34 (m, 2H), 1.26 (t, J = 7.2 Hz, 3H).

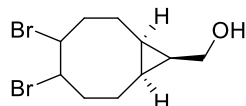
**<sup>13</sup>C NMR (100 MHz, CDCl<sub>3</sub>, δ ppm):** 172.2, 129.4, 59.7, 27.0, 24.1, 22.6, 21.2, 14.4.

### **((1R,8S,9S,Z)-bicyclo[6.1.0]non-4-en-9-yl)methanol **12****



To a solution of ethyl (1R,8S,9S,Z)-bicyclo[6.1.0]non-4-ene-9-carboxylate **11** (1 equiv., 27.85 g, 133.7 mmol) in diethyl ether (250 mL) at 0 °C and under Argon, was added dropwise a solution of LiAlH<sub>4</sub> (1.2 equiv., 66.85 mL, 160.4 mmol, 2.4 M in THF). The mixture was stirred 15 minutes at 0 °C, then 30 minutes at room temperature, then 1 h at 45 °C. When reaction is complete, the mixture is neutralized at 0 °C by adding water dropwise. Na<sub>2</sub>SO<sub>4</sub> was added and the mixture was filtered through a pad of Celite, washed with diethyl ether (100 mL), then concentrated *in vacuo* to afford the title compound **12** as a white solid which was used in the next step without further purification.

### **((1R,8S,9S)-4,5-dibromobicyclo[6.1.0]nonan-9-yl)methanol **13****

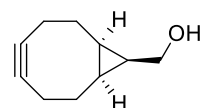


To a solution of ((1R,8S,9S,Z)-bicyclo[6.1.0]non-4-en-9-yl)methanol **12** (1 equiv., 10.5 g, 68.97 mmol) in CHCl<sub>3</sub> (90 mL) at 0 °C was added Br<sub>2</sub> (1 equiv., 3.54 mL, 11.02 g, 68.97 mmol) until a slightly yellow coloration.

Then, the mixture was stirred at 0 °C for 15 min more. When complete, the reaction was quenched with an aqueous solution of Na<sub>2</sub>S<sub>2</sub>O<sub>3</sub> (10%, 50 mL) and the compound was extracted with CHCl<sub>3</sub> (2 x 50 mL). Organic layers were combined, washed with an aqueous solution of Na<sub>2</sub>S<sub>2</sub>O<sub>3</sub> (10%, 100 mL), then brine (100 mL), dried over MgSO<sub>4</sub>, filtered through a pad of Celite, and concentrated *in vacuo* to afford the title compound **13** as a white solid which was used without further purification.

**TLC:** heptane/diethyl ether 50/50, Ce(SO<sub>4</sub>)<sub>2</sub>

### **(1R,8S,9S)-Bicyclo[6.1.0]non-4-yn-9-ylmethanol **14****



Potassium *tert*-butoxide (6.1 equiv., 6.0 g, 53.81 mmol) was added to degassed 4-methyl-tetrahydropyran (180 mL) and the mixture was stirred for 15 min at room temperature. Then, a solution of ((1R,8S,9S)-4,5-

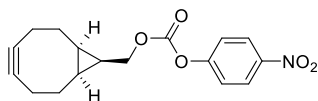
dibromobicyclo[6.1.0]nonan-9-yl)methanol **13** (2.75 g, 8.82 mmol) in degassed 4-methyltetrahydropyran (30 mL) was added in one portion and the mixture was stirred at 40 °C for 3 h under argon atmosphere. When complete, water (100 mL) and diethyl ether (200 mL) were added at room temperature. After 5 min, an aqueous solution of KHSO<sub>4</sub> (sat.) was added dropwise to quench the reaction. Organic layer was isolated, aqueous layer was extracted with diethyl ether (200 mL), and all organic layers were combined, washed with water (200 mL), dried over MgSO<sub>4</sub>, filtered through a pad of Celite, and concentrated *in vacuo*. The crude solid was purified by flash chromatography (Petroleum ether/diethyl ether 50/50), and fractions containing the product were dried under reduced pressure. The residue was solubilized in DCM/heptane 1/4 and the DCM was removed under reduced pressure (outside of the water bath) to precipitate the title compound **14** (930 mg, 6.17 mmol, 70%) as a white solid.

**TLC:** heptane/diethyl ether 50/50, KMnO<sub>4</sub>

**<sup>1</sup>H NMR (400 MHz, CDCl<sub>3</sub>, δ ppm):** 3.73 (d, J = 8.0 Hz, 2H), 2.35-2.20 (m, 6H), 1.66-1.56 (m, 2H), 1.39- 1.30 (m, 1H), 1.18 (bs, 1H), 0.99-0.90 (m, 2H).

**<sup>13</sup>C NMR (100 MHz, CDCl<sub>3</sub>, δ ppm):** 98.4, 59.3, 28.5, 21.0, 20.9, 19.5

#### **(1R,8S,9s)-Bicyclo[6.1.0]non-4-yn-9-ylmethyl (4-nitrophenyl) carbonate 15**



To a solution of (1R,8S,9S)-bicyclo[6.1.0]non-4-yn-9-ylmethanol **14** (1 equiv., 800 mg, 5.33 mmol) in dichloromethane (20 mL) was added p-nitrophenol chloroformate (1.2 equiv., 1.29 g, 6.39 mmol) and pyridine (10 equiv., 4.21 g, 4.31 mL, 53.3 mmol). The reaction was stirred at room temperature for 5 h under argon atmosphere. After concentration, the mixture was quenched by saturated NH<sub>4</sub>Cl solution (75 mL) and extracted with EtOAc (3 x 75 mL). The combined organic layers were washed with brine (75 mL), dried over MgSO<sub>4</sub> and concentrated *in vacuo*. The residue was purified by flash chromatography (Cyclohexane 100% to Cyclohexane/EtOAc 7/3 in 30 minutes) to afford the title compound **15** as a colorless oil that solidifies to a white solid at -20°C (1.58 g, 5.01 mmol, 94%).

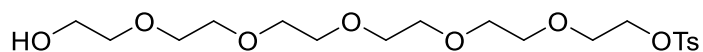
**TLC:** Cyclohexane/EtOAc 50/50, KMnO<sub>4</sub>

**<sup>1</sup>H NMR (400 MHz, CDCl<sub>3</sub>, δ ppm):** 8.28 (q, 2H), 7.39 (q, 2H), 4.41 (d, 2H), 2.37 – 2.23 (m, 6H), 1.62 – 1.59 (m, 3H), 1.09 – 1.04 (m, 2H).

**<sup>13</sup>C NMR (100 MHz, CDCl<sub>3</sub>, δ ppm):** 155.6, 152.6, 125.3, 121.8, 98.7, 68.0, 29.1, 21.4, 20.5, 17.3.



### 17-hydroxy-3,6,9,12,15-pentaoxaheptadecyl 4-methylbenzenesulfonate **17**

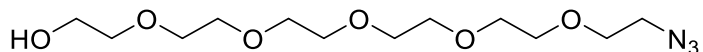


To a solution of dried (1 h, 70 °C, rotavap) hexaethylene glycol **16** (1 equiv., 20 g, 70.8 mmol) in dichloromethane (320 mL) at 0 °C were added KI (0.2 equiv., 2.35 g, 14.2 mmol) and Ag<sub>2</sub>O (1.5 equiv., 24.6 g, 106 mmol). Tosyl chloride (1.05 equiv., 14.2 g, 74.4 mmol) was then added portion wise and the reaction mixture was stirred at 0 °C for 30 minutes. The mixture was then filtered through a pad of Celite, washed with THF (100 mL) and concentrated in vacuo. The crude material was purified by silica gel flash chromatography (Cyclohexane/EtOAc 85/15 to EtOAc 100% in 5 minutes, then EtOAc 100% for 5 minutes, then EtOAc/MeOH 100/0 to EtOAc/MeOH 95/5 in 20 minutes) to give the title compound **17** as a clear yellow oil (19.3 g, 63%).

**<sup>1</sup>H NMR (400 MHz, CDCl<sub>3</sub>, δ ppm):** 7.78 (d, *J* = 8.2 Hz, 2H), 7.32 (d, *J* = 8.0 Hz, 2H), 4.14 (t, *J* = 4.8 Hz, 2H), 3.72–3.53 (m, 22H), 2.94 (s, 1H, (OH)), 2.43 (s, 3H).

**<sup>13</sup>C NMR (100 MHz, CDCl<sub>3</sub>, δ ppm):** 144.8, 133.1, 129.8 (2C), 128.0 (2C), 72.5, 70.7-70.4, 69.7, 68.7, 61.7, 21.6.

### 17-azido-3,6,9,12,15-pentaoxaheptadecan-1-ol **18**

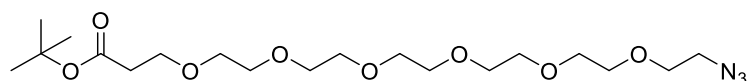


To a solution of 17-hydroxy-3,6,9,12,15-pentaoxaheptadecyl 4-methylbenzenesulfonate **17** (1 equiv., 19.3 g, 44.2 mmol) in DMF (50 mL) was added NaN<sub>3</sub> (1.5 equiv., 4.31 g, 2.33 mL, 66.3 mmol). The reaction was stirred at 50°C overnight under argon atmosphere. After evaporation, 400 mL of dichloromethane were added and the solution was washed with water (1 x 300 mL) then brine (3 x 300 mL). Aqueous layers were combined and washed with dichloromethane (1 x 200 mL) and organic layers were combined, washed with brine (1 x 300 mL), dried over MgSO<sub>4</sub>, filtered and concentrated in vacuo to afford the title compound **18** as a yellow oil (11.4 g, 37.13 mmol, 84%) which is used without further purifications.

**<sup>1</sup>H NMR (400 MHz, CDCl<sub>3</sub>, δ ppm):** 3.71 – 3.70 (m, 2H), 3.69 – 3.60 (m, 18H), 3.60-3.58 (m, 2H), 3.37 (t, *J* = 5.1 Hz, 2H), 2.98 (s, 1H (OH)).

**<sup>13</sup>C NMR (100 MHz, CDCl<sub>3</sub>, δ ppm):** 72.5, 70.7 – 70.6 (7C), 70.4, 70.0, 61.7, 50.7.

### **tert-butyl 1-azido-3,6,9,12,15,18-hexaoxahenicosan-21-oate 19**

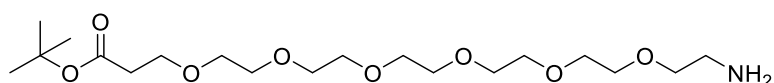


To a solution of 17-azido-3,6,9,12,15-pentaoxaheptadecan-1-ol **18** (1 equiv., 10.5 g, 34.2 mmol) in THF (100 mL, concentration = 0.3 mmol/mL) at 0 °C was added tert-butyl acrylate (1.3 equiv., 5.69 g, 6.45 mL, 44.4 mmol). Freshly sublimated potassium tert-butoxide (0.1 equiv., 0.383 g, 3.42 mmol) was then added portion wise at 0 °C and the reaction mixture was stirred at room temperature for 8 h. After concentration, an aqueous solution of NaH<sub>2</sub>PO<sub>4</sub> (1M, 100 mL) was added and the mixture was extracted with EtOAc (3 x 200 mL). The combined organic layers were washed with brine (1 x 200 mL) and dried over MgSO<sub>4</sub>, filtered and concentrated in vacuo. The crude material was purified by flash chromatography (Cyclohexane/EtOAc 8/2 to EtOAc 100% in 30 minutes) to afford the title compound **19** as a yellow oil (7 g, 16.07 mmol, 47%).

**<sup>1</sup>H NMR (400 MHz, CDCl<sub>3</sub>, δ ppm):** 3.72 - 3.56 (m, 24H), 3.38 (t, 2H), 2.49 (t, 2H), 1.44 (s, 9H).

**<sup>13</sup>C NMR (100 MHz, CDCl<sub>3</sub>, δ ppm):** 171.0, 70.7 – 70.4, 70.1, 66.9, 50.7, 36.3, 28.1 (3C)

### **tert-butyl 1-amino-3,6,9,12,15,18-hexaoxahenicosan-21-oate 20**

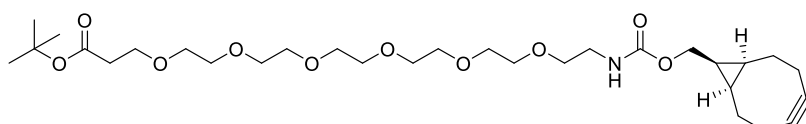


To a solution of *tert*-butyl 1-azido-3,6,9,12,15,18-hexaoxahenicosan-21-oate **19** (1 equiv., 1.5 g, 3.44 mmol) in degased methanol (80 mL, concentration under 50 mM) was added Pd/C (1 mol%, 36.7 mg, 34.4 μmol). The atmosphere was flushed with argon then replaced by H<sub>2</sub> and the mixture was stirred at room temperature overnight. The mixture was filtered through a pad of Celite and concentrated *in vacuo*. The crude was purified by silica gel flash chromatography (DCM 100% to DCM/MeOH/NH<sub>4</sub>OH 9/0.9/0.1 in 30 minutes) to afford the title compound **20** as a yellow oil (1 g, 2.44 mmol, 71%).

**<sup>1</sup>H NMR (400 MHz, CDCl<sub>3</sub>, δ ppm):** 3.71 – 3.68 (m, 2H), 3.66 – 3.57 (m, 20H), 3.53 – 3.51 (m, 2H), 2.88 – 2.85 (t, 2H), 2.51 – 2.47 (t, 2H), 1.84 (s, 2H (NH<sub>2</sub>)), 1.43 (s, 9H).

**<sup>13</sup>C NMR (100 MHz, CDCl<sub>3</sub>, δ ppm):** 170.9, 80.5, 73.1, 70.6 – 70.3, 66.9, 50.7, 41.7, 36.3, 28.1 (3C).

### **tert-butyl 1-(bicyclo[6.1.0]non-4-yn-9-yl)-3-oxo-2,7,10,13,16,19,22-heptaosa-4-azapentacosan-25-oate 21**



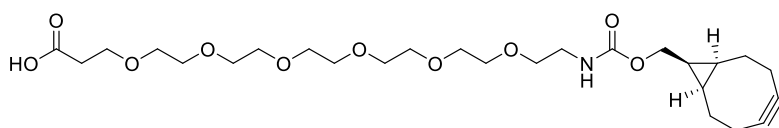
To a solution of (1R,8S,9S)-bicyclo[6.1.0]non-4-yn-9-

ylmethyl (4-nitrophenyl) carbonate **15** (1 equiv., 350 mg, 1.11 mmol) in DMF (3 mL) was added a solution of *tert*-butyl 1-amino-3,6,9,12,15,18-hexaoxahenicosan-21-oate **20** (1.1 equiv., 500 mg, 1.22 mmol) and triethylamine (3 equiv., 336 mg, 0.463 mL, 3.33 mmol) in DMF (3 mL). The mixture was stirred overnight at room temperature under argon atmosphere. After concentration, a solution of NaH<sub>2</sub>PO<sub>4</sub> (1M, 100 mL) was added and the mixture was extracted with EtOAc (3 x 100 mL). The combined organic layers were washed with brine (100 mL), dried over MgSO<sub>4</sub> and concentrated *in vacuo*. The residue was purified by flash chromatography to afford the title compound **21** as a colorless oil (500 mg, 0.94 mmol, 77%).

**<sup>1</sup>H NMR (400 MHz, CDCl<sub>3</sub>, δ ppm):** 5.24 (s, 1H, (NH)), 4.13 (d, 2H), 3.64- 3.51 (m, 24H), 3.35 (m, 2H), 2.50 – 2.47 (t, 2H), 2.28 – 2.21 (m, 6H), 1.59 – 1.56 (m, 2H), 1.43 (s, 9H), 1.35 (t, 1H), 0.95 – 0.90 (t, 2H).

**<sup>13</sup>C NMR (100 MHz, CDCl<sub>3</sub>, δ ppm):** 170.9, 98.8, 80.5, 70.6 – 70.1 (6C), 66.9, 62.7, 40.8, 36.3, 29.1, 28.1, 21.5, 20.1, 17.8.

**1-[(bicyclo[6.1.0]non-4-yn-9-ylmethoxy)carbonylamino] 3,6,9,12,15,18 hexaoxahenicosan-21-oic acid **22****



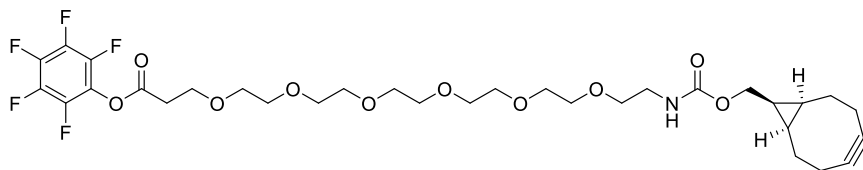
To a solution of *tert*-butyl 1-(bicyclo[6.1.0]non-4-yn-9-yl)-3-oxo-2,7,10,13,16,19,22-

heptaoxa-4-azapentacosan-25-oate **21** (1 equiv., 500 mg, 0.854 mmol) in MeOH/H<sub>2</sub>O 1/1 (10 mL) was added LiOH (10 equiv., 204 mg, 8.54 mmol). The reaction was stirred at room temperature overnight under argon atmosphere. After concentration, a solution of NaH<sub>2</sub>PO<sub>4</sub> (1M, 50 mL) was added and the mixture was extracted with DCM (4 x 75 mL). The combined organic layers were washed with brine (75 mL), dried over MgSO<sub>4</sub> and concentrated *in vacuo* to afford the title compound **22** as a yellowish oil (400 mg, 0.75 mmol, 88%).

**<sup>1</sup>H NMR (400 MHz, CDCl<sub>3</sub>, δ ppm):** 5.35 (s, 1H (NH)), 4.14 (d, 2H), 3.79 – 3.76 (m, 2H), 3.67 – 3.64 (m, 20H), 3.57 – 3.54 (t, 2H), 3.35 (m, 2H), 2.62 – 2.59 (t, 2H), 2.29 – 2.19 (m, 6H), 1.58 (m, 2H), 1.37 – 1.33 (m, 1H), 0.96 – 0.91 (t, 2H).

**<sup>13</sup>C NMR (100 MHz, CDCl<sub>3</sub>, δ ppm):** 170.7, 98.9, 80.4, 70.6 – 70.2 (6C), 67.0, 62.8, 40.7, 36.4, 29.0, 21.5, 20.1, 17.8.

**perfluorophenyl 1-((1R,8S,9s)-bicyclo[6.1.0]non-4-yn-9-yl)-3-oxo-2,7,10,13,16,19,22-heptaosa-4-azapentacosan-25-oate **6****



To a solution of 1-  
[({bicyclo[6.1.0]non-4-  
yn-9-

ylmethoxy}carbonyl)amino] 3,6,9,12,15,18-hexaoxahenicosan-21-oic acid **21** (1 equiv., 650 mg, 1.23 mmol) and EDCI (2 equiv., 381 mg, 0.434 mL, 2.45 mmol) in dichloromethane (15 mL) was added pentafluorophenol (2 equiv., 451 mg, 0.257 mL, 2.45 mmol). The reaction mixture was stirred at room temperature for 4 hours under argon atmosphere. After concentration, the crude was dissolved in EtOAc (75 mL), washed with aqueous solutions of HCl (0.1 M, 75 mL) and saturated NaHCO<sub>3</sub> (2 x 75 mL). The combined organic layers were washed with brine (75 mL), dried over MgSO<sub>4</sub> and concentrated *in vacuo*. The residue was purified by flash chromatography (Cyclohexane/EtOAc 5/5 to EtOAc 100% in 20 minutes then EtOAc 100% to EtOAc/MeOH 95/5 in 10 minutes) to afford BCN-PEG<sub>6</sub>-PFP **6** as a colorless oil (550 mg, 64%).

**<sup>1</sup>H NMR (400 MHz, CDCl<sub>3</sub>, δ ppm):** 5.19 (s, 1H (NH)), 4.06 (d, 2H), 3.82 – 3.80 (t, 2H), 3.59 – 3.56 (m, 20H), 3.50 – 3.48 (t, 2H), 3.31 (m, 2H), 2.89 – 2.87 (t, 2H), 2.22 – 2.13 (m, 6H), 1.53 – 1.50 (m, 2H), 1.30 – 1.27 (m, 1H), 1.21 – 1.18 (m, 2H), 0.89 – 0.85 (m, 2H).

**<sup>13</sup>C NMR (100 MHz, CDCl<sub>3</sub>, δ ppm):** 170.7, 98.8, 70.7 – 70.5 (4C), 70.3, 70.1, 66.1, 62.7, 53.4, 40.8, 34.4, 29.1, 21.4, 20.1, 17.8.

**<sup>19</sup>F NMR (400 MHz, CDCl<sub>3</sub>, δ ppm):** -157.55, -157.95, -162.33

**Synthesis of BCN-siRNAs.** To one aliquot of 3'-amino-ssRNA **23** (1 equiv., 1 mM in RNase-free PBS 1X) dissolved in RNase-free borate buffer (0.1 M, pH = 8.0, 5 times the volume of ssRNA), was added BCN-PEG<sub>6</sub>-PFP **6** (50 equiv., 100 mM in DMSO). The mixture was incubated at 25 °C for 4 hours under nitrogen atmosphere. An aqueous solution of LiClO<sub>4</sub> (3 M, 20 μL) was added and acetone cooled at -20 °C was added (three times the total volume). The mixture was left at -20 °C for 30 minutes to allow the oligonucleotide's precipitation. The mixture was centrifugated at 15000 g for 12 min and the supernatant was thrown away. This RNA precipitation step was done one more time. 3'-BCN-ssRNA **24** was dried in a speedvac and then dissolved in RNase-free PBS 1X (100 μL) and the concentration was measured by spectrophotometry using Nanodrop at 260 nm. Yield was between 55 and 84% depending on carefulness and scale. To the solution of 3'-BCN-ssRNA (1 equiv.) was added a solution of the complementary RNA strand (1.5 equiv. in RNase-free PBS 1X) bearing either a 5'-ppp or a 5'-Cy<sub>5</sub>. The solution was incubated at 65 °C for 5 min, then the temperature was cooled from 65

°C to 25 °C over 15 min. BCN-siRNA **4** was directly used for bioconjugation to antibody-N<sub>3</sub> **3** without further purification.

**Ab-N<sub>3</sub> synthesis.** To a solution of EphA2-antibody **1** (1 equiv., 5 mg/ml in DPBS 1X, pH 7.4) was added azidobenzoyl fluoride **2** (3 equiv., 20 mM in DMSO, fresh solution) and the mixture was incubated at 37 °C for 30 min. Excess of reagent was removed by gel filtration chromatography using Bio-spin P-30 columns (Bio-Rad, Hercules, U.S.A.) pre-equilibrated with DPBS 1X (pH 7.4) to give a solution of Ab-N<sub>3</sub> **3** (average yield 90%). The concentration was measured by spectrophotometry using Nanodrop at 280 nm and DoC was determined by SEC-ESI-MS.

**Cy5-labelled-Ab synthesis for internalization assay.** To a solution of EphA2-antibody **1** (1 equiv., 5 mg/ml in DPBS 1X, pH 7.4) was added Cy5-NHS ester (Lumiprobe, Ref. 23020) (5 equiv., 10 mM in DMSO) and the mixture was incubated at 37 °C overnight min. Excess of reagent was removed by gel filtration chromatography using Bio-spin P-30 columns (Bio-Rad, Hercules, U.S.A.) pre-equilibrated with DPBS 1X (pH 7.4) to give a solution of dye-labelled antibody (average yield 90%). The DoC and the concentration were measured by spectrophotometry using Nanodrop.

**Ab-siRNA synthesis.** To a solution of Ab-N<sub>3</sub> **3** (1 equiv., 10 mg/mL in DPBS 1x pH = 7.4) was added BCN-modified siRNAs **4** (3 equiv., as a 100 µM solution in RNase-free water) and the reaction mixture was incubated at 25 °C for 24 hours. The mixture was purified by size exclusion chromatography (Akta, S200, DPBS 1X as eluent, rt = 10 mL). This method is efficient to separate the conjugated antibody **5** from the naked one **3**, therefore eliminating DoC 0. Fractions containing the product were concentrated by centrifugation (Vivaspin 500 µL, 50 kDa MWCO, 12 minutes, 15 000 g) and filtered through centrifuge tube filters (Corning® Costar® Spin-X®, 0.22 µm, 1 minute, 15 000 g). Protein concentration was determined by BCA assay, and 25 µg of conjugate were deglycosylated with Remove-iT® Endo S (New England Biolabs, Ipswich, U.S.A., Ref. P0741L) at 37 °C for 2 hours before SEC-ESI-MS analysis.

**Ab-(Cy5-siRNA) conjugate synthesis for plasma stability.** To a solution of Ab-N<sub>3</sub> **3** (1 equiv., 10 mg/mL in DPBS 1x (pH 7.4)) was added Cy5-BCN-siRNAs (3 equiv., as a 100 µM solution in RNase-free water) and the reaction mixture was incubated at 25 °C for 24 hours. After purification by SEC to discard of unconjugated antibodies, Ab-siRNA conjugate was filtered through centrifuge tube filters (Corning® Costar® Spin-X®, 0.22 µm, 1 minute, 15 000 g) for sterilization. Protein concentration was determined by BCA assay.

**Dual-labelled-Ab-siRNA conjugate synthesis for confocal microscopy.** To a solution of Ab-N<sub>3</sub> **3** (1 equiv., 10 mg/mL in DPBS 1x (pH 7.4)) was added Cy3-BCN-siRNAs (3 equiv., as

a 100  $\mu$ M solution in RNase-free water) and the reaction mixture was incubated at 25 °C for 24 hours. After purification by SEC to discard of unconjugated antibodies, Cy5-NHS ester (3 equiv., 16 h, DPBS 1X) was added to the purified Ab-siRNA. The use of Sulfo-Cy5 led to aggregation of the final conjugate. Excess of reagent was removed by gel filtration chromatography using Bio-spin P-30 columns (Bio-Rad, Hercules, U.S.A.) pre-equilibrated with DPBS 1X (pH 7.4) to afford the dual-labelled antibody (yield 12% over two steps). Prior to biological assay, the conjugate was filtered through centrifuge tube filters (Corning® Costar® Spin-X®, 0.22  $\mu$ m, 1 minute, 15 000 g) for sterilization. Protein concentration was determined by BCA assay.

**Cell culture.** A549-Dual and A549-Dual RIG-I KO (InvivoGen, Ref. a549d-nfis or a549d-korigi, San Diego, California, U.S.A.) were cultured with high glucose Dulbecco's Modified Eagles Medium containing 1% GlutaMAX™ (DMEM, Gibco™, ThermoFisher, Ref. 10566016) and supplemented with 10  $\mu$ g/mL Blastidin (InvivoGen, Ref. ant-bl-05), 100  $\mu$ g/mL Zeocin (InvivoGen, Ref. ant-zn-05), 10% v/v heat inactivated Fetal Bovine Serum (FBS, Gibco™, ThermoFisher, Ref. 10099141). Proliferative cultures were incubated at 37 °C in a humidified 5% CO<sub>2</sub> incubator and subculture carried out twice a week by washing the cell monolayers with DPBS followed by addition of accutase solution (Gibco™, ThermoFisher, Ref. A1110501) and incubation at 37°C until the cells detached. Accutase was inactivated by the addition of growth medium before seeding 1.0.106 cells into fresh T175 or T75 flasks. Cell numbers and viability were assessed by Trypan Blue staining (Thermo Fisher Scientific, Ref. T10282) using Countess 2 (Invitrogen, Ref. AMQAX1000).

**Biological assays.** Unless notified, all biological experiments with A549 cells were performed as follows: The day before experiments, A549 cells (10,000 cells/well, 90  $\mu$ L in DMEM complete medium) were plated in a flat-bottomed transparent 96-well. Antibodies were diluted to 400 nM in Opti-MEM (Thermo Fisher Scientific, Ref. 31985062). All siRNAs were diluted to 400 nM in Opti-MEM containing Lipofectamine™ RNAiMAX (Thermo Fisher Scientific, Ref. 13778075) for 5 minutes according to manufacturer's protocol. Then, 10  $\mu$ L of these solutions were added to cells before performing the assay after 24, 48, 72 or 96 h of incubation depending of the assay.

**Cell culture for co-culture experiments.** In prevision of co-culture experiments with PBMCs, A549-Dual cells were cultured in RPMI 1640 containing 1% GlutaMAX™ (Gibco™, ThermoFisher, Ref. 61870036) and supplemented with the same additives. The day before experiment, A549 cells (2500 cells/well, 50  $\mu$ L in RPMI 1640 complete medium) were plated on a 96-well flat-bottomed black plate suitable for microscopy. The same day, PBMCs were

thawed, washed twice with 37 °C DPBS 1X (300 g, 8 min) and incubated overnight in RPMI 1640 complete medium.

The next day, PBMCs were washed one more time and counted before seeding in the A549-containing plates (25 µL, ratio A549/PBMC from 1/1 to 1/20, optimal one was 1/5). Antibodies or Resiquimod (TLR7/8 agonist, Invivogen, Ref. tlr-r848) were added (25 µL, RPMI 1640) to each well, and Incucyte Caspase 3/7 Green dye (Sartorius, Ref. 4440) and Incucyte Annexin V Red dye (Sartorius, Ref. 4641) were added according to manufacturer's protocol. Cells were incubated in Incucyte S3 Live Cell Imaging System (Sartorius). Images were taken every 2 hours for 4 days and analyzed using Incucyte's software. The supernatant of each plate was conserved at -80 °C until use for cytokine quantification.

**Cell culture for confocal microscopy.** For confocal microscopy experiments, A549-Dual cells were cultured in high glucose DMEM without phenol red (Gibco™, ThermoFisher, Ref. 31053028) supplemented with the same additives and 1% GlutaMAX™ (Gibco™, ThermoFisher, Ref. 11584466).

The day before experiment, A549 cells (4000 cells/well, 25 µL) were plated in a 384-well flat-bottomed black plate suitable for microscopy in DMEM complete medium without phenol red. Antibodies were diluted to 1 µM in Opti-MEM (Thermo Fisher Scientific, Ref. 31985062), and cells were then treated from 1 to 6 hours. Cells were labelled with 5 µg/mL Hoechst 33342 (ThermoFisher, Ref. 62249) and Lysoview 488 (Biotium, Ref., 70067, dilution 1/1000 in complete medium) 30 minutes before the reading. After these 30 minutes, cells were washed with DPBS 1X and pictures were taken on a Zeiss LSM800. Images were analyzed by ImageJ, background and colors were normalized and Pearson's correlation coefficient was determined with the plugin coloc 2.

#### **RIG-I activation assays and viability assay.**

The day before experiments, 10,000 A549 cells were plated in a flat-bottomed transparent 96-well plate in 90 µL DMEM complete medium. Antibodies were diluted to 400 nM in Opti-MEM (Thermo Fisher Scientific, Ref. 31985062). All siRNAs were diluted to 400 nM in Opti-MEM containing Lipofectamine™ RNAiMAX for 5 minutes according to manufacturer's protocol. Then, 10 µL of these solutions were added to cells before performing assays after 24h, 48h, 72h or 96h of incubation depending on the assay. For EphA2-dependent internalization assay, cells were pre-incubated with increasing concentration of the naked antibody for 3 hours in order to degrade surface-EphA2, then washed with DPBS 1X before adding the antibody-siRNA conjugates.

Luciferase assay (Quanti-Luc™ Gold, Invivogen, Ref. rep-qlcg5) was performed in a 96-well flat-bottomed white plate according to the manufacturer’s protocol.

SEAP assay (Quanti-Blue™, invivogen, Ref. rep-qbs) was performed in a 96-well flat-bottomed transparent plate according to the manufacturer’s protocol.

WST-1 assay (Roche, Merck, Ref. 11644807001) was performed according to the manufacturers’ protocol.

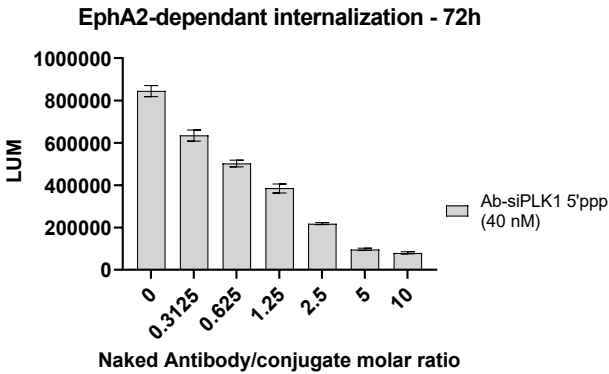


Figure 73 - Competition assay between the conjugate (40 nM) and the anti-EphA2 antibody with growing concentrations. Conditions: 72h of incubation on RIG-I-positive cell line, readout was Lucia. Conjugate had DoC = 1.2, DoC 0 = 0%. n = 1, in triplicate.

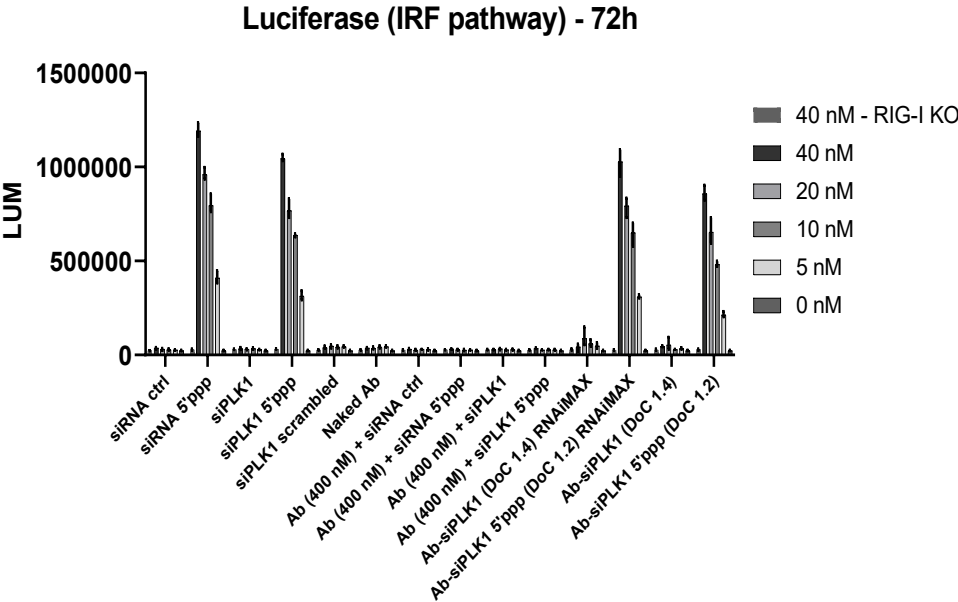


Figure 74 - RIG-I activation assay of the IRF pathway. Conditions: Conjugate had DoC = 1.2, DoC 0 = 0%. After 72h of incubation, siRNAs were transfected with RNAiMax. n = 3, each in triplicate, one shown.



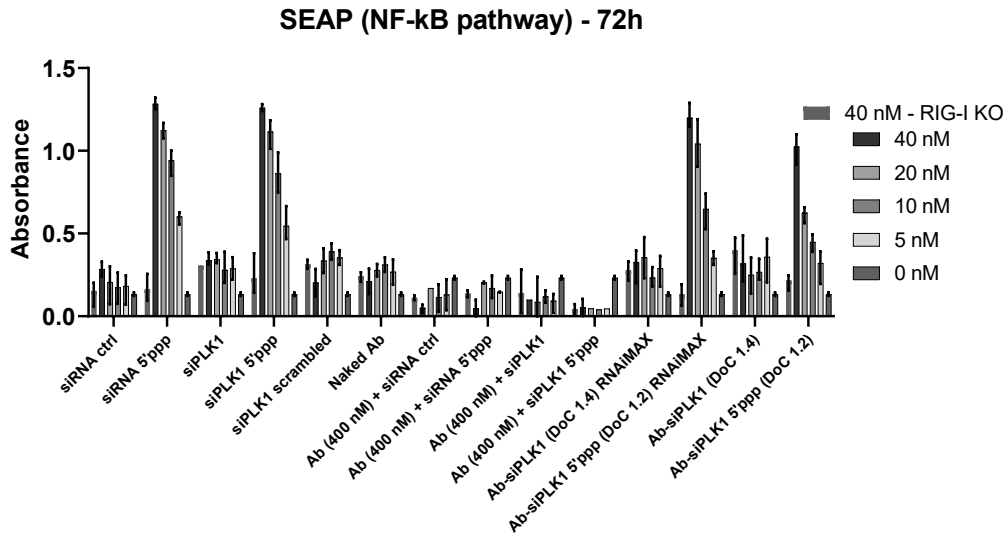


Figure 75 - RIG-I activation assay of the NF-κB pathway. Conditions: Conjugate had DoC = 1.2, DoC 0 = 0%. After 72h of incubation, siRNAs were transfected with RNAiMax. n = 3, each in triplicate, one shown.

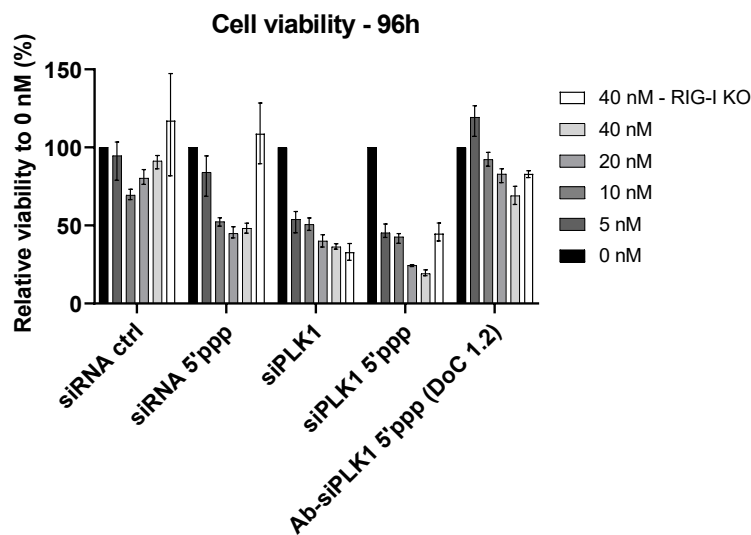


Figure 76 - Cell viability after 96h of incubation. Conjugate had DoC = 1.2, DoC 0 = 0%. For RIG-I KO cells, only the highest concentration is shown. n = 3, each in triplicate, one shown.

**Calreticulin exposition assay.** After 48 h of incubation, cells were detached using accutase (50  $\mu$ L) and incubated for 10 min at 37  $^{\circ}$ C. Cells were then transferred into a 96-well V-bottomed black plate, centrifuged (200 g, 5 min), and washed once with FACS buffer (PBS, 2% BSA, 10 mM EDTA, centrifuge 200 g, 5 min). Cells were resuspended in FACS buffer, and AF488-tagged anti-CALR mAb (Abcam, Ref. ab196158, dilution 1/100, 50  $\mu$ L) was added and incubated for 30 minutes at 4  $^{\circ}$ C in the dark. Cells were washed with FACS buffer (200 g, 5 min) and resuspended in FACS buffer (100  $\mu$ L). Then, 1  $\mu$ L of 7-AAD (Miltenyi Biotec, Ref. 130-111-568) was added in each well. Data were collected with Miltenyi Biotec's MACS Quant 10 and data were analyzed with FlowJo software.

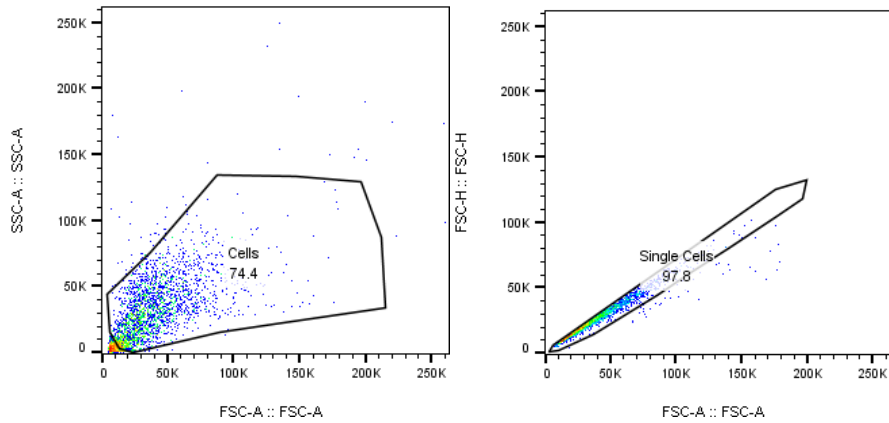


Figure 77 - Single cells selection for CALR exposure by flow cytometry.

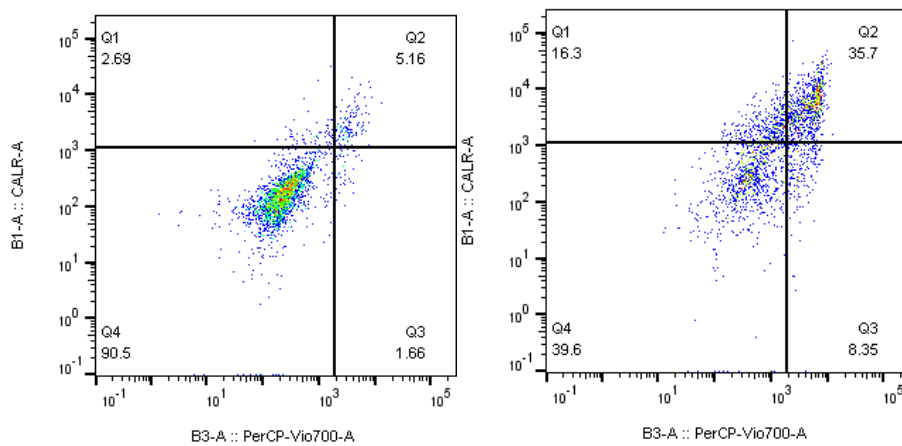


Figure 78 - CALR exposure by flow cytometry. Example of gating : on the left, non-treated cells, on the right, siPLK1-5'-ppp treated cells. Cells on Q1 were considered as live CALR<sup>+</sup> cells.

**Cell cycle study.** Nocodazole (500 nM in Opti-MEM) was used as a G2/M synchronizer product to place cytometry gates. After 24 h of incubation, cells were washed with DPBS 1X (50 µL/well) and accutase was added (50 µL/well) to detach cells. After 5 min incubation at 37 °C, the plate was shaken to detach cells. 20 µL of each well was transferred into a V-bottomed black 96-well plate and 20 µL of MultiCyt Cell Cycle Screening Kit (Sartorius, diluted in FACS buffer, 1:50) was added to each well. After incubation in the dark for 1 hour at room temperature, data were collected with an iQue Screener PLUS using the given template and ForeCyt software.

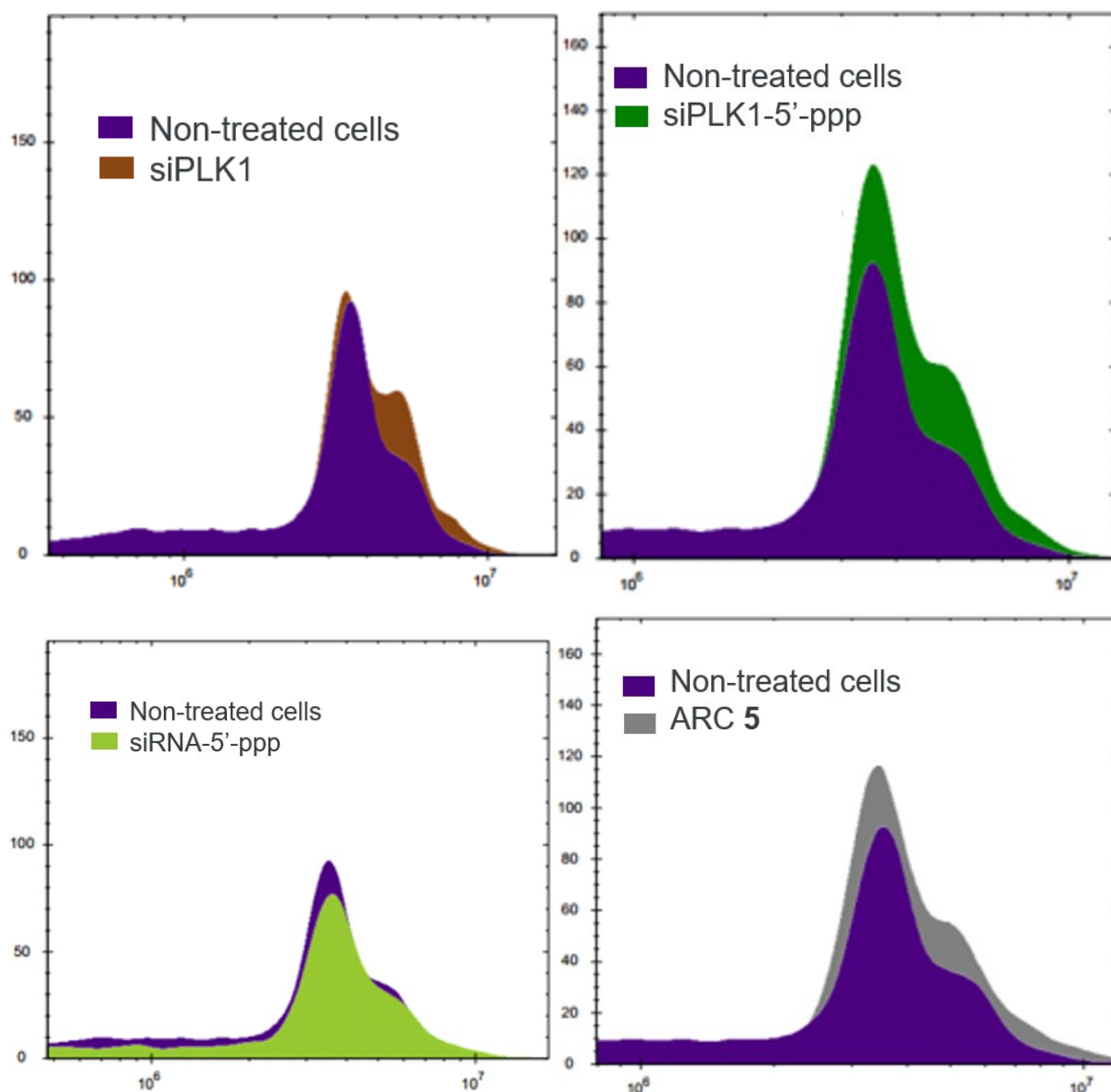


Figure 79 - Cell cycle study of compounds. Conditions: 24h of incubation, RNA were transfected with RNAiMax.

**Western-blot.** The day before experiment, A549 cells (400,000 cells/well, 1.8 mL of DMEM complete medium) were plated in a flat-bottomed transparent 6-well plate. All compounds were prepared as previously described procedures, then, 200  $\mu$ L of a 400 nM solution of the desired compound was added and cells were incubated for 72h. For internalization assay, 1  $\mu$ M of antibody-Cy<sub>5</sub> was added for 1h, washed with DPBS, then cells were harvested after 1 to 6h.

Cells were washed with DPBS, harvested using a scraper, then 200  $\mu$ L of freshly prepared RIPA buffer (containing 50 mM Tris-HCl pH = 7.4, 150 mM NaCl, 1% NP-40, 1 mM PMSF, protease and phosphatase inhibitor cocktail 1X (Thermo Fisher Scientific, Ref. 78442)) was added. Cells were then sonicated (3 x 10 sec), centrifugated at 13,000 g for 10

min and let rest for 15 min over ice.

Total protein level of the supernatant was measured by BCA assay (BSA 1 mg/mL as standard) and 50 µg of cell proteins were loaded in a 4-15% precast Stain-Free SDS-PAGE gel (Bio-Rad, Ref. 4568084, 200V, 40 min, weight marker All Blue standard). Gels were then transferred into nitrocellulose membranes (Bio-Rad, Ref. 1704158) using Trans-Blot Turbo Transfer System (Bio-Rad). Membranes were put in a box containing 10 mL of blocking buffer (5% milk in TBS-T 1X (Tris-base 20 mM, 13,6 mM NaCl, pH adjusted with HCl to 7.6, tween 20 0.1%) for 1h. After washing with TBS-T 1X (3 x 5 min), 10 mL of primary antibodies solution (mouse mAb anti-PLK1 (Abcam, Ref. ab17056), rabbit pAb anti-RIG-I (Cell Signal, Ref. 3743S), both at 1 µg/mL (dilution 1/1000) in TBS-T 1X containing 5% BSA) was added overnight at 4°C. For internalization assay, goat mAb anti-human-Fc (Merck, Ref. I2136) was used in the same conditions.

After washing with TBS-T 1X (3 x 5 min), 10 mL of primary antibody solution (mouse mAb anti-GAPDH (invitrogen, Ref. MA5-15738) at 1 µg/mL (dilution 1/1000) in TBS-T 1X containing 5% BSA) was added for 45 minutes at room temperature. After washing with TBS-T 1X (3 x 5 min), 10 mL of secondary antibodies solution (donkey mAb anti-mouse and horse mAb anti-rabbit, both HRP conjugates, at 0.2 mg/mL (dilution 1/5000) in TBS-T 1X containing 5% BSA) were added for 2 hours at room temperature. After washing with TBS-T 1X (3 x 5 min), nitrocellulose membrane was revealed with SuperSignal (Thermo Fisher Scientific, Ref., 34580) according to manufacturer's protocol and ChemiDoc (Bio-Rad). Blots were quantified using Image Lab (Bio-Rad) and results were normalized to GAPDH.

**SDS-PAGE-based plasma stability.** Human plasma was supplied by Établissement Français du Sang (EFS Strasbourg). To one human plasma aliquot (100 µL) or RNase-inhibited human plasma (supplemented with 10 µL of RNaseOUT™ (Thermo Fisher Scientific, Ref. 10777019) in a total volume of 100 µL) was added unconjugated or conjugated 5'-Cy<sub>5</sub>-siRNA (100 µL, 5 µM in DPBS 1X). The mixture was incubated at 37 °C and 10 µL of these solutions were taken at each time point and frozen in liquid nitrogen for further SDS-PAGE analysis.

**Activity-based plasma stability.** To one human plasma aliquot (100 µL) or RNase-inhibited human plasma (supplemented with 10 µL of RNaseOUT™, 100 µL) was added Ab-siRNA conjugates (100 µL, 5 µM in DPBS 1X), resulting in a solution containing 50% plasma and 2.5 µM of conjugate. The mixture was incubated at 37 °C and 10 µL of these solutions were taken at each time point and frozen in liquid nitrogen for later use. These samples were diluted in optiMEM to a final concentration of 100 nM (2% plasma) and 10 µL of these solutions were

added to cells to a final concentration of 10 nM (and 0.2% plasma). Luciferase assay was done after 72h of incubation.

## V. Development of bicyclo[6.1.0]nonyne carboxylic acid for the production of stable molecular probes

All the previous results, along with SDS-PAGE of plasma stability, indicate that our supposedly non-cleavable PEG<sub>6</sub> linker may be cleaved during cellular processes to release the siRNA. One main hypothesis to explain this phenomenon was that the carbamate moiety that link the BCN motif to the linker was cleaved (Figure 80).

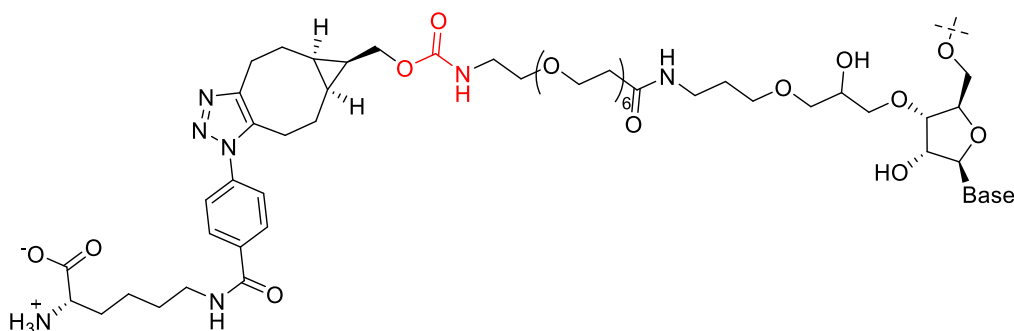


Figure 80 - Supposed structure of the metabolite after antibody digestion. The carbamate moiety in red appeared as a point of weakness for hydrolysis.

Indeed, it is well known that carbamates are less stable than amides, as epitomized by a resonance energy 3–4 kcal mol<sup>-1</sup> lower due to the stereoelectronic perturbations caused by the extra oxygen,<sup>363</sup> a property that has been used to design prodrugs of various active substances.<sup>364</sup> Interestingly, besides cyclic and *unsubstituted* (i.e. R-O(CO)NH<sub>2</sub>) compounds, all other carbamate classes were found to be less stable than amide bonds in biological media, leading to substantial hydrolysis both *in vitro* and *in vivo*.<sup>365</sup> Therefore, in order to validate our hypothesis that this carbamate-containing linker was cleaved, a linker containing an amide instead of a carbamate was elaborated. This study led to the development of BCN carboxylic acid.

### A. Introduction

The ability to effect precise chemical reactions in biological media has always possessed vast applications, from the labelling of biomolecules to the detection and quantification of reactive metabolites, or the controlled liberation of an active substance. Because of the inherent complex molecular composition of the biological environment, the use of biocompatible synthetic chemistry tools in such media raised the issue of chemoselectivity: how can a chemical reaction occur selectively between certain reactants without interfering with surrounding biomolecules? Ever since the early 2000s, tremendous efforts have been made to address this question, resulting in the development of bioorthogonal reactions. These take advantage of reactive groups that are usually inert toward chemical functions naturally present

in biological systems but highly reactive toward another abiotic reactant. One of the best examples of such bioorthogonal combinations is the azide – cycloalkyne duet, reacting with one another via strain-promoted azide-alkyne cycloaddition (SPAAC).

While the kinetics can be considered sluggish when compared to other bioorthogonal reactions, the stability of the resulting triazole products, along with its simplicity of operation and low toxicity participated in making SPAAC a privileged tool for a myriad of chemical biology applications. As this reaction gained momentum, it was logically accompanied by the development of other families of cycloalkynes, whose design was driven by two major principles: i) a good stability-to-reactivity balance, with cycloalkynes being stable enough to be used in aqueous environment but reactive enough not to necessitate the adjunction of a catalyst; and ii) limited lipophilicity, so as to be soluble in biological media and minimize non-specific binding to biomolecules.<sup>366</sup> These stringent selection parameters explain why only a handful of strained alkynes have been reported to date for bioorthogonal applications, mainly belonging to the family of cyclooctynes.

One of its most prominent members is undoubtedly the *endo* isomer of bicyclo[6.1.0]nonyne (BCN) **14** (Figure 81), developed in 2010, which led to numerous applications in chemical biology.<sup>367</sup> Necessitating further functionalization to equip this scaffold with relevant payloads, several chemical strategies were developed. and mostly employed as its primary alcohol derivative **14**. While *O*-acylation or *O*-alkylation would seem to be the most appropriate way of accessing valuable BCN derivatives rapidly, only a handful of such procedures has actually been reported – via direct reaction with activated esters or ring-opening polymerization of lactones and epoxides, respectively (Figure 81; top part).<sup>368</sup>

Counterintuitively, the preferential strategy for modifying the primary alcohol of BCN **14** is via its transient conversion to electrophilic species of varied structures (Figure 81, bottom part), allowing the coupling with a second nucleophile, essentially alcohols and amines. Several options have been investigated over the years to do so, via the incorporation of heteroatom spacers such as silicon or phosphorus,<sup>369–371</sup> the use of the Mitsunobu reaction,<sup>372,373</sup> or the mechanochemical conversion to BCN tosylate.<sup>374</sup>

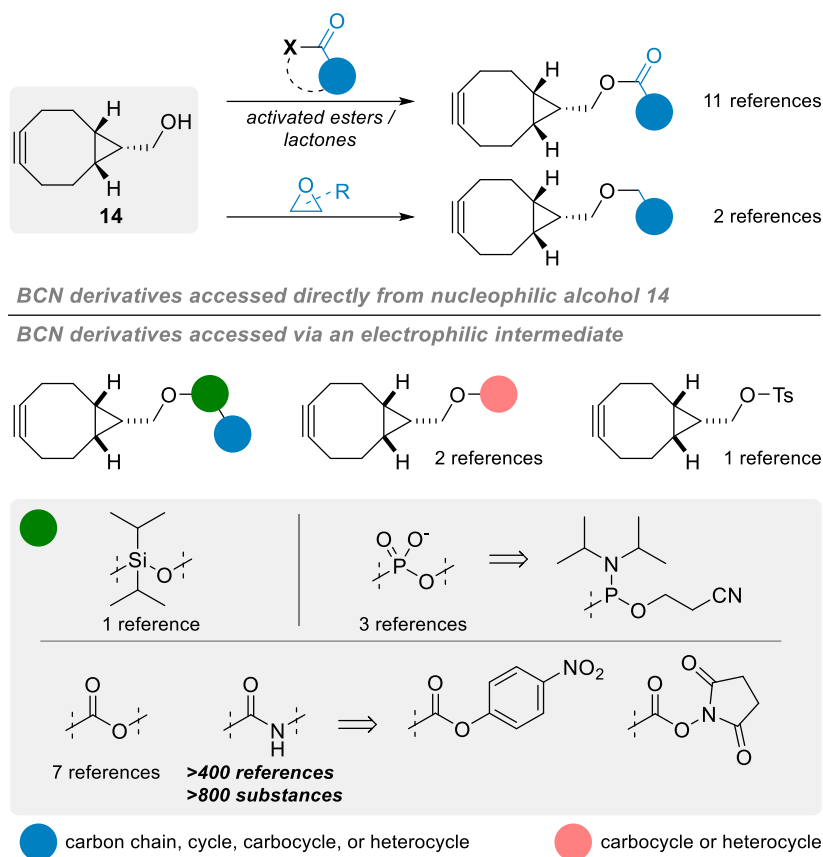


Figure 81 - Structure of BCN alcohol derivatives and general overview of their synthesis according to the literature.

However, applications employing such strategies can be considered scarce in comparison to the use of activated carbonates for the generation of carbonates and carbamates, the latter representing the most commonly encountered type of BCN derivatives. Given that the nucleophilic character of BCN alcohol **14** is hardly used for anything other than the generation of intermediate electrophilic groups, it would seem logical to assume that oxidized and electrophilic analogues of **14** would be a preferable option for the simple preparation of BCN derivatives. However, only two references dealing with BCN aldehyde **25** (Figure 82) could be found in the scientific literature: one reporting it as an intermediate toward the formation of BCN-containing  $\alpha$ -amino acids,<sup>375</sup> and the second – more in line with our postulate – as an effective way to yield BCN amine derivatives via reductive amination.<sup>376</sup>

Even more surprisingly, a SciFinder search for BCN acid **26** led to no result. Intrigued by this observation, we thus decided to synthesize and evaluate the potential of BCN acid **26** as a surrogate for BCN alcohol **14** (Figure 82).



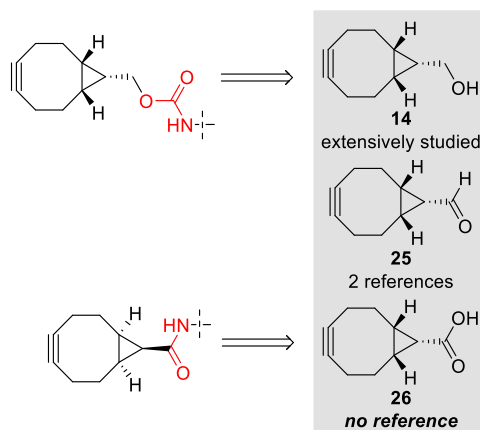


Figure 82 - Structure of classical BCN derivatives starting from BCN-alcohol, leading to carbamate-linked molecule. Interestingly, the carboxylic acid drawn below was never reported before.

## B. Results and discussion

### i. Synthesis of BCN carboxylic acid **26**

We started our synthetic work by slightly tweaking the classical procedures. Our initial goal was to take advantage of the ester group in **11** introduced upon cyclopropyl formation following Fox and coworkers' procedure,<sup>377</sup> assuming that a dibromination-saponification-double elimination sequence would deliver the desired BCN acid **26**. To our dismay, this approach proved not to be feasible, due to the formation of several side products in the course of the saponification step, urging us to redirect our efforts. We thus decided to oxidize the primary alcohol **14**. As using strong oxidizer could degrade the alkyne, we decided to oxidize the compound in two steps: a first Swern oxidation to obtain BCN aldehyde **25** followed by a smooth Pinnick oxidation to obtain the desired carboxylic acid **26**. While the formation of the aldehyde yielded the expected compound with excellent yield without any purification, the Pinnick oxidation of this compound failed, even though the use of 2-methyl-but-2-ene in large excess avoided undesirable oxidation of the alkyne (Figure 83).

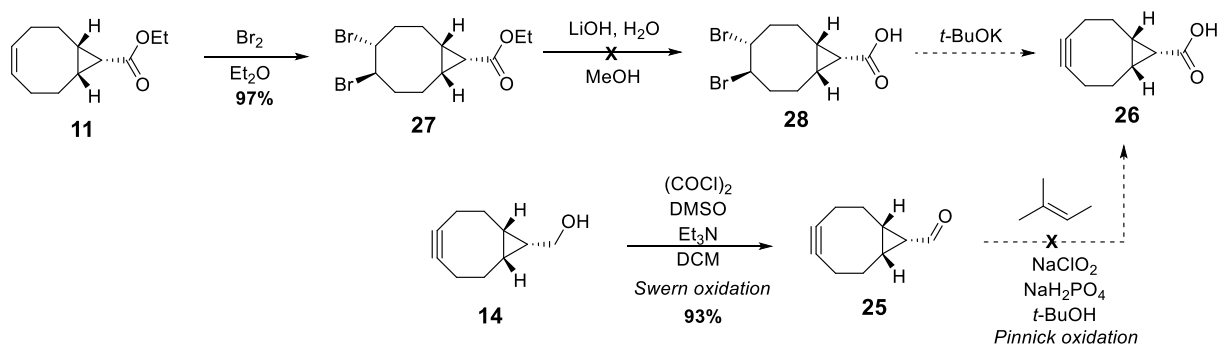


Figure 83 - The two first routes of synthesis tried to obtain BCN-carboxylic acid **26**.

We thus decided to proceed with the classical route toward BCN **14** until formation of the dibrominated primary alcohol **13**, which we envisioned oxidizing to the corresponding carboxylic acid **28**. Jones reagent turned out to be an effective oxidizer, smoothly delivering pure **28** in multigram scale and excellent yield after a single recrystallization. Interestingly, no sign of cyclopropyl decomposition was observed under such seemingly harsh conditions, even after prolonged reaction. The final alkyne formation, via the well-documented potassium *tert*-butoxide-mediated double elimination of the 1,2-dibromide moiety, delivered the expected product **26**, which can be stored indefinitely at  $-20\text{ }^{\circ}\text{C}$  under argon without any apparent decomposition (Figure 84). It is worth stressing that this route is as effective as the one leading to the activated carbonate **15** – the reactive BCN derivative mostly employed in the literature –, sharing similar overall yield and number of steps (i.e. 30% over five steps from commercially available 1,5-COD **9**).

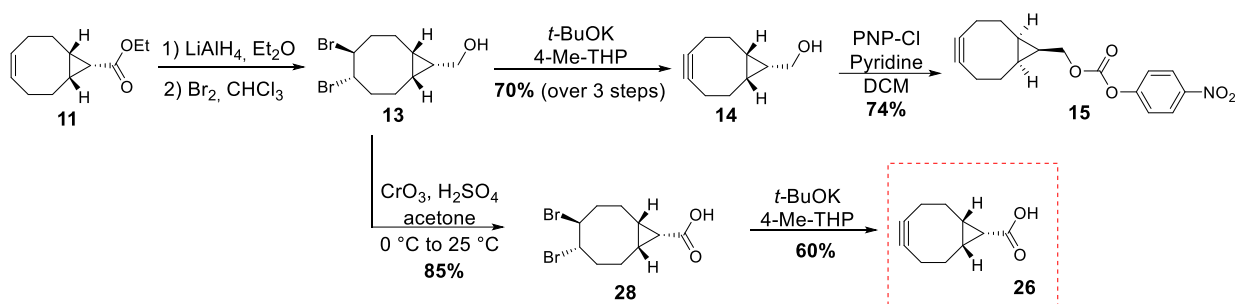


Figure 84 - Synthesis of BCN-carboxylic acid **26**.

## ii. Derivatization and kinetic studies

Double-derivatization of BCN carboxylic **26** showed to be highly efficient following two synthetic routes using model molecules (Figure 85). HATU-mediated amidation of BCN carboxylic acid **26** with benzylamine afforded the corresponding alkyne **29** in excellent yield, and SPAAC with the model benzyl azide gave the desired bi-derivatized BCN **31** in high yield. Similar to its reduced analogue **14**, BCN **26** was also found to undergo rapid inverse electron-demand Diels-Alder (IEDDA) reactions,<sup>378</sup> yielding pyridazine **32** quantitatively in just 30 minutes at room temperature when reacted with 3,6-di-2-pyridyl-1,2,4,5-tetrazine.

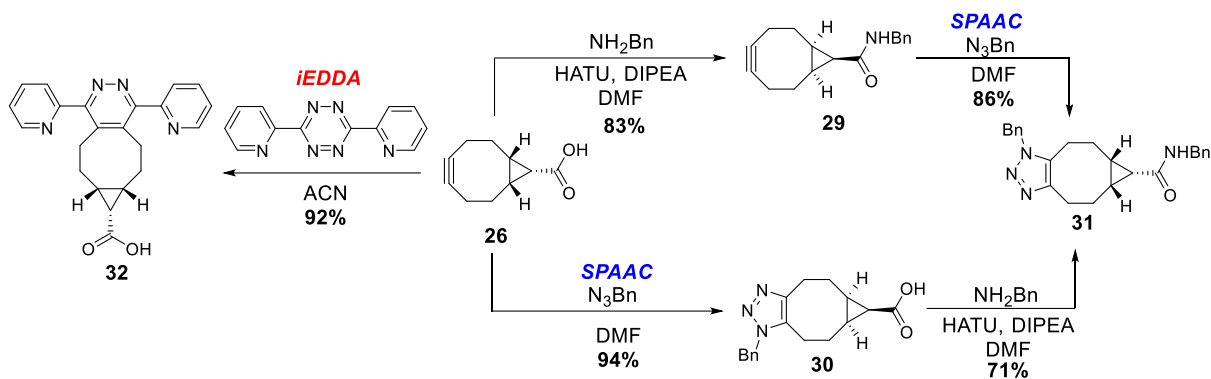


Figure 85 - Reactivity of BCN **26**. In the frame: bioorthogonal reactions with benzyl azide (SPAAC) and 3,6-di-2-pyridyl-1,2,4,5-tetrazine (iEDDA) and amide bond formation.

With BCN **26** in hand, we then set out to evaluate SPAAC kinetics with the model benzyl azide, in accordance with standard procedures (Figure 86).<sup>379</sup> Quantitative conversion to triazole **30** was observed in a mixture of acetonitrile and water (1/2, v/v), with a second-order rate constant of  $0.20 \text{ M}^{-1}\cdot\text{s}^{-1}$ , almost identical to that of BCN alcohol **14** under the same conditions, and in the range of values classically observed with other cyclooctynes for this transformation.<sup>367,380</sup> Having validated that the functional group appended onto the BCN scaffold did not alter the alkyne reactivity, we then sought to derivatize **26** in order to demonstrate that it could be a valuable platform for applications in chemical biology. In a model experiment, **26** was reacted with benzylamine under classical coupling conditions, effectively delivering BCN amide **29** in good yield, which gave an identical rate constant of  $0.20 \text{ M}^{-1}\cdot\text{s}^{-1}$  in our SPAAC model, under the same conditions as before (Figure 86).

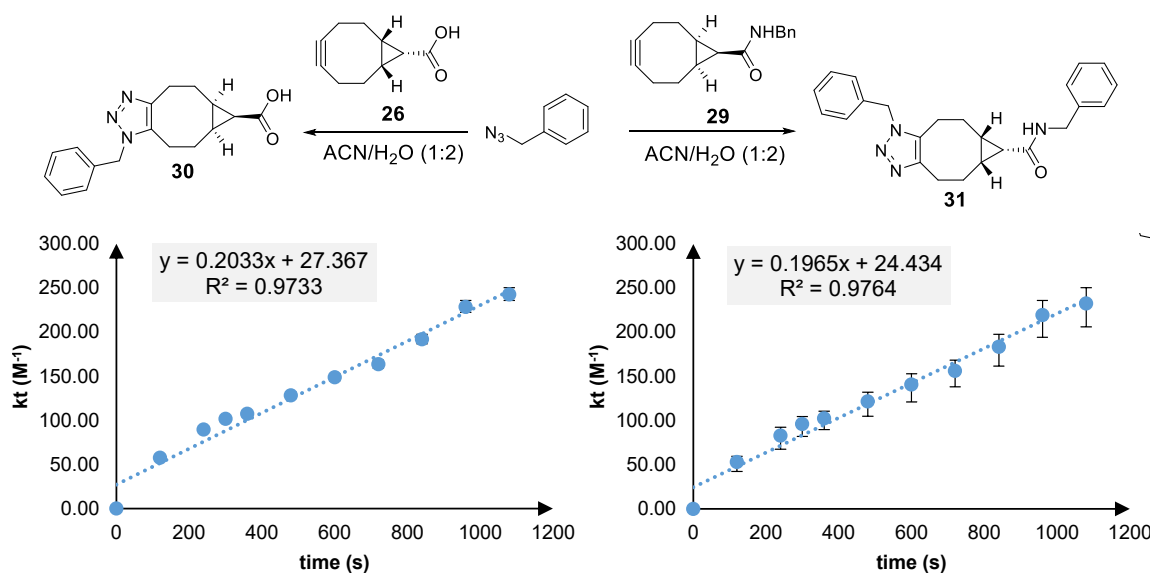


Figure 86 - Kinetic studies and determination of second-order rate constants of SPAAC between benzyl azide and BCN carboxylic **26** and BCN amide **29**.

In order to diversify the structure of BCN or to obtain a BCN-amine **36**, we attempted Curtius rearrangement starting from the dibrominated derivative **28** using diphenylphosphoryl azide as an azide source. Unfortunately, while the formation of the highly electrophilic phosphoric anhydride **33** was observed, there was no formation of the acyl azide **34** required for this reaction (Figure 87). Noteworthy, addition of tetrabutylammonium azide (TBAA) on an intermediary acyl chloride **35** did not provide the desired compound **34** either.

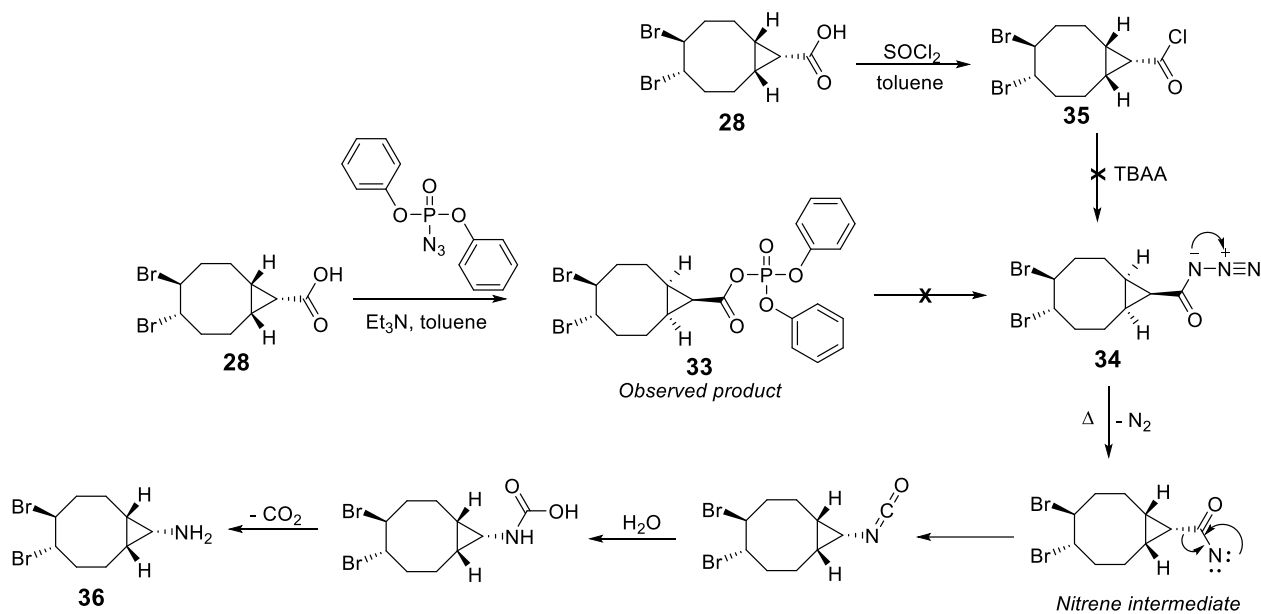


Figure 87 - Attempt to obtain BCN amine **36** by a Curtius rearrangement using diphenylphosphoryl azide or an acyl chloride **35**.

### iii. BCN-carboxylic acid conjugation to protein

To prove that amide bond formation was not limited solely to small molecules, we decided to evaluate the conjugation of trastuzumab – a therapeutic antibody targeting overexpressed HER2 receptors in breast cancer – with an activated ester derivative of BCN acid **26**. Starting from BCN carboxylic acid **26**, esterification as *para*-nitrophenyl ester carbonate proceeded smoothly, yielding the corresponding ester **37** (Figure 88).

Following the previously used ‘plug-and-play’ strategy,<sup>381,382</sup> we next functionalized trastuzumab with this derivative in order to synthesize trastuzumab-BCN conjugate **38**. Further functionalization by SPAAC with an azide-containing TAMRA **39** fluorophore afforded the corresponding trastuzumab-TAMRA conjugate **40**. Gratifyingly, excellent yield and average degree of conjugation were obtained (62% and 2.7, respectively), demonstrating the ability of BCN acid **26** to deliver immunoconjugates effectively.

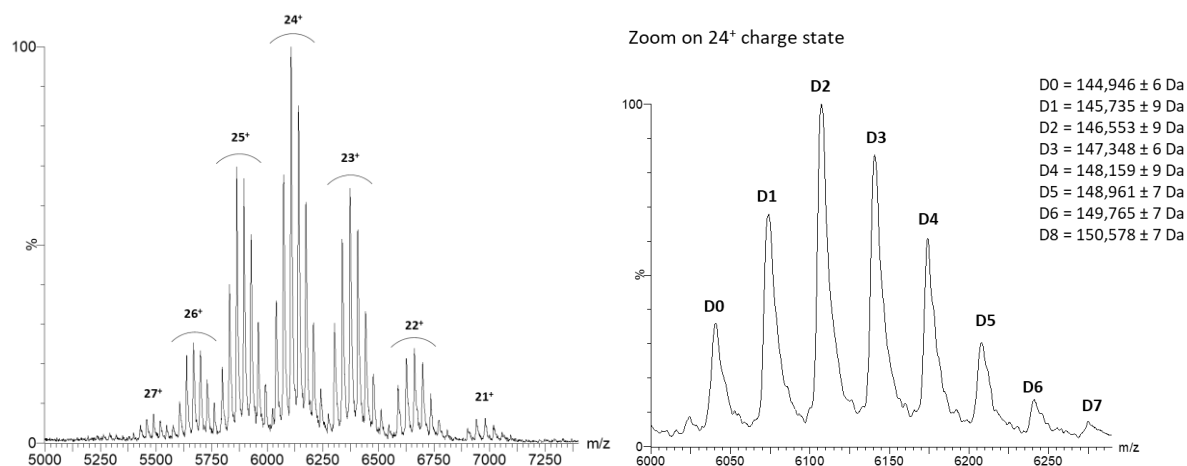
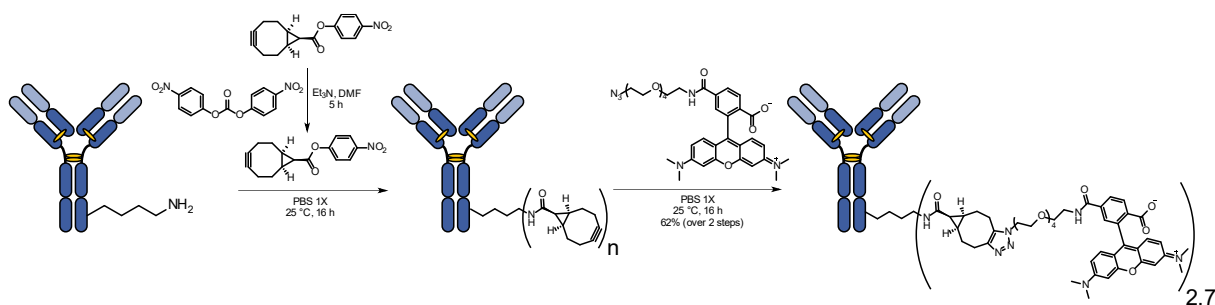


Figure 88 - Synthesis of trastuzumab-TAMRA conjugate **40** by using BCN para-nitrophenyl ester **37**, and resulting MS spectra after purification.

#### iv. BCN-carboxylic acid stability by FRET probe assay

Being now able to derivatize the BCN ring with amide groups rather than carbamates – as it would be with activated BCN alcohol **14** – we then reflected on the benefits it could offer in terms of stability. To compare the stability between BCN amide and carbamate, two turn-on FRET probes **41** and **42** were prepared, incorporating amino-propyl-tetramethylrhodamine (TAMRA-NH<sub>2</sub> **43**) as a fluorophore ( $\lambda_{\text{abs}} = 555 \text{ nm}$ ,  $\lambda_{\text{em}} = 583 \text{ nm}$ ) and Black Hole Quencher 2-azide (BHQ-2, **44**) as a fluorescence quencher ( $\lambda_{\text{abs}} = 579 \text{ nm}$ , Figure 89). Upon incubation in human plasma and in aqueous buffers of different pH, monitoring the appearance of TAMRA fluorescence at 580 nm thus serves as an indirect evaluation of cleavage between the fluorophore and its quencher, a strategy that we employed in the past for the development of various cleavable linkers.<sup>383–386</sup> Amide and carbamate probes **41** and **42**, respectively, were thus synthesized in decent yields.

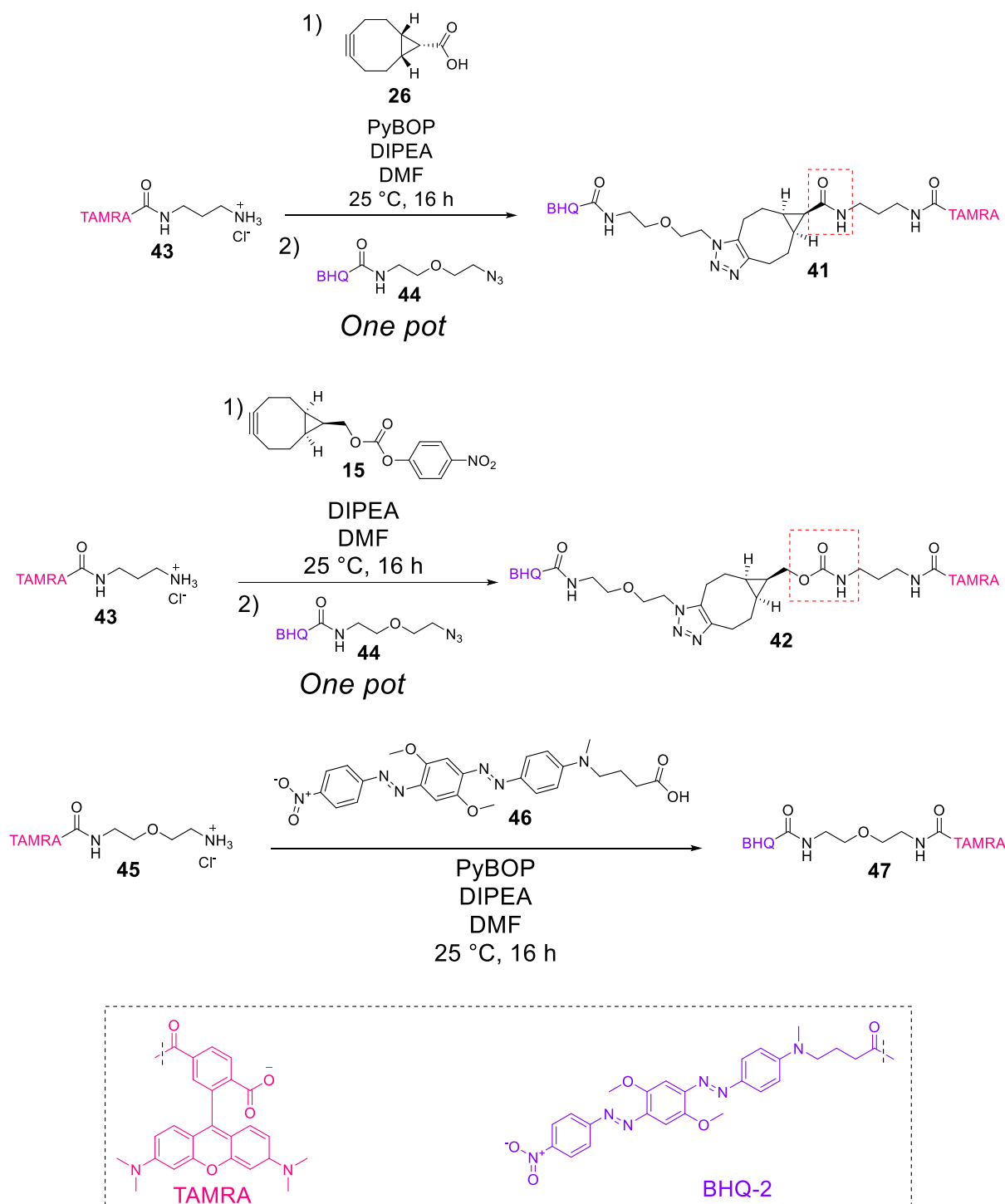


Figure 89 – Synthesis of the three FRET probes for stability studies: **41** as the BCN-acid derivative, **42** as the carbamate derivative of BCN-alcohol, and **47** as a non-cleavable negative control.

Their stabilities were then evaluated under various conditions (pH 1-7.4, human plasma, DMEM) and compared to that of the amide probe **47** that acted as negative control. While all probes were found to be perfectly stable at different pH (Figure 90) and in human plasma, marked differences were observed *in vitro*.

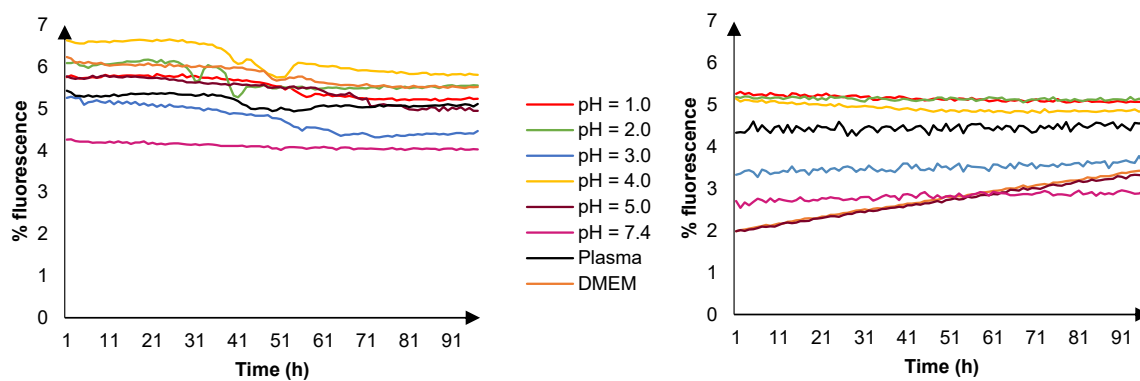


Figure 90 - Stability curves of probes **41** (left) and **42** (right), measured at different pH and in different media

Indeed, upon incubation with three different human cancer cell lines – i.e. breast adenocarcinoma SKBR3 and MDA-MB-231, and uterus adenocarcinoma HeLa – carbamate probe **42** was systematically found to be more cleaved than its amide counterpart **41** (Figure 91), which was attributed to a differential cleavage in cellulo and confirmed by their stability in cell culture medium. Such an apparent cellular lability was unexpected and in stark contrasts with the results observed with amide probe **41**, which was found to be as stable as the negative control **47**, indicating a lack of influence of the BCN-triazole group in the observed cleavage of **41**. This indicates that for biological applications of BCN probes necessitating prolonged incubation, the use of carbamate linkers should be avoided to the benefit of the more robust amide group, especially whenever stability is a crucial parameter.

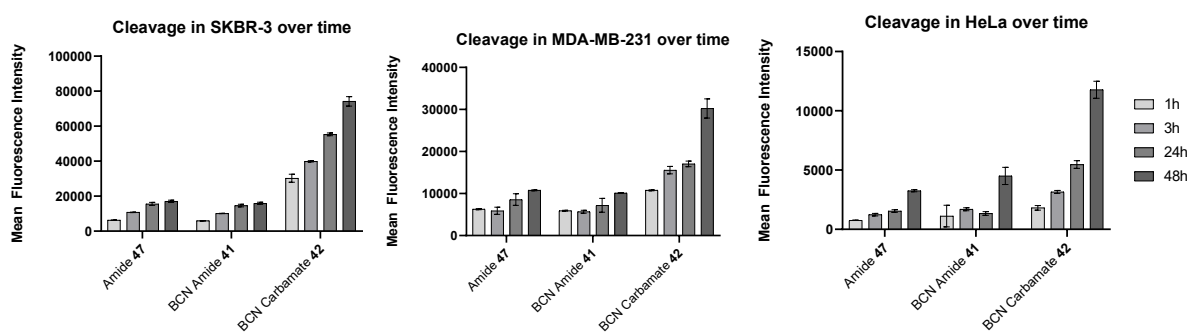


Figure 91 - Stability studies of amide and carbamate-based BCN probes **41** and **42**, respectively, and ether probe **47** in different cancer cell lines over time. Each measurement was done in triplicate.

In summary, we reported the first synthesis of a BCN equipped with a carboxylic acid. We showed that it shared a similar reactivity with its primary alcohol analogue, the most studied member of the BCN family. The presence of this carboxylate allows a convenient derivatization via amide bond formation. Most notably, we proved that the resulting compounds were far more stable in cultured cells than classically employed carbamate derivatives. Thus, we believe that BCN acid **26** is an effective surrogate for BCN alcohol **14**, and is a more judicious

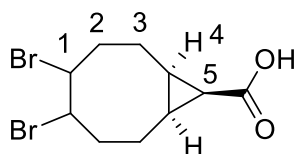
alternative when designing molecular probes for which hydrolytic stability in biological media is key.

As a consequence, this study tends to confirm that the carbamate moiety presents on the linker of the ARC **5** may be cleaved in biological media. To confirm this hypothesis, metabolomic studies by mass spectrometry should be performed. However, at this stage, we do not know the proportion of linker that has been cleaved *in cellulo* nor if this cleavage has played a role in the endosomal escape of the siRNA. We thus wondered if the efficacy encountered in the chapter IV was not due to this cleavability. Therefore, we attempted the synthesis of ARCs featuring cleavable linkers.

## C. Experiment data

### Chemical syntheses and characterizations

#### 4,5-Dibromobicyclo[6.1.0]nonane-9-carboxylic acid **28**



To a solution of **13** (1 equiv., 5 g, 16 mmol) in acetone (200 mL) at 0 °C was added Jones reagent (3.9 equiv., 2.5 M, 25 mL, 62.5 mmol) dropwise. The mixture was stirred for 20 min at 0 °C then slowly warmed to room temperature and stirred for 3 h (reaction monitored by TLC; cHex/EtOAc 60:40, stained with ceric sulfate and green bromocresol). Upon completion, the reaction was carefully quenched by the slow addition of isopropanol (20 mL) at 0 °C. Acetone was removed *in vacuo*, and the mixture was extracted with DCM (3 x 30 mL). Organic layers were combined, washed with brine (50 mL), dried over MgSO<sub>4</sub>, filtered and concentrated *in vacuo* to give the title compound **28** (4.6 g, 14.08 mmol, 88%) as a white solid, which was used without further purification.

**R<sub>f</sub>** = 0.45 (cHex/EtOAc 6:4)

**v<sub>max</sub> (thin film) /cm<sup>-1</sup>**: 2928 (w), 2876 (w), 2687 (w), 2355 (w), 1683 (s), 1472 (s), 1445 (s), 1385 (s), 1354 (m), 1339 (w), 1318 (w), 1299 (w), 1267 (m), 1216 (s), 1166 (m), 1096 (w)

**mp**: 197 °C

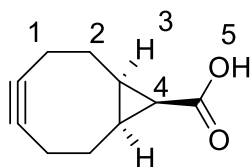
**<sup>1</sup>H NMR (400 MHz, CDCl<sub>3</sub>)**: δ 10.89 (s, 1H, OH), 4.84 (m, 1H, H1), 4.77 (m, 1H, H1), 2.81 – 2.63 (m, 2H, H2), 2.37 – 2.14 (m, 4H, H2 + H3), 1.94 – 1.72 (m, 3H, H3 + H4), 1.76 – 1.53 (m, 2H, H4 + H5)

**<sup>13</sup>C NMR (101 MHz, CDCl<sub>3</sub>)**: δ 177.5, 55.5, 53.9, 34.7, 34.7, 26.5, 23.9, 22.1, 19.1, 18.0

**HR-ESI-MS (M+H<sup>+</sup>)**: Calc. 323.9361, found 323.9366



## Bicyclo[6.1.0]non-4-yne-9-carboxylic acid **26**



Freshly sublimated potassium tert-butoxide (8 equiv., 13.76 g, 122.68 mmol) was added to dry THF (100 mL) and the mixture was stirred for 15 min at room temperature. A solution of **28** (1 equiv., 5.0 g, 15.335 mmol) in THF (100 mL) was then added dropwise and the solution was stirred at 25 °C for overnight (reaction monitored by TLC, petroleum ether/diethyl ether 50/50, stained with CeSO<sub>4</sub>). The reaction was quenched with glacial acetic acid (16 equiv., 14.15 mL, 245.36 mmol). The mixture was filtrated and the solid was washed thoroughly with diethyl ether (200 mL). The filtrate was concentrated under reduced pressure and the crude was purified by normal-phase chromatography (isocratic CyHex/EtOAc 5/5). Fractions containing the product were combined and concentrated under reduced pressure to afford a yellow solid which was precipitated in heptane (see detailed procedure below) to afford the title compound **26** (1.50 g, 9.13 mmol, 60%) as a white solid, which can be stored at -20 °C under argon indefinitely.

**Note – Procedure for precipitation in heptane.** The yellow solid obtained after purification by flash chromatography was first dissolved in a minimal amount of DCM, before four volumes of heptane were added. The resulting solution was then concentrated under reduced pressure, with the flask outside of the bath of the rotary evaporator. Upon complete evaporation of DCM, the resulting suspension was filtered and the white solid was rinsed three times with heptane.

**R<sub>f</sub>** = 0.4 (CyHex/EtOAc 6/4)

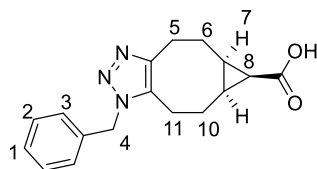
**mp:** 197 °C

**<sup>1</sup>H NMR (400 MHz, CDCl<sub>3</sub>):** δ 2.37-2.18 (6H, m, 2 H<sub>1</sub> + 4 H<sub>2</sub>), 2.16-2.04 (2H, m, H<sub>1</sub>), 1.90 (t, J = 8.9 Hz, H<sub>4</sub>), 1.43-1.37 (2H, m, H<sub>3</sub>)

**<sup>13</sup>C NMR (101 MHz, CDCl<sub>3</sub>):** δ 179.1, 98.6, 27.7, 26.3, 21.4, 21.1

**HR-ESI-MS (M+H<sup>+</sup>):** Calc. 164.0840, Found. 164.0837

## 12-Benzyl-10,11,12-triazatricyclo[7.3.0.0<sup>4,6</sup>]dodeca-1(9),10-diene-5-carboxylic acid **30**



To a solution of **26** (1.0 equiv., 10 mg, 0.0609 mmol) in DMF (0.5 mL) was added benzyl azide (2 equiv., 16.2 mg, 0.122 mmol) and the reaction was stirred at room temperature for 3 hours (reaction monitored by LC-MS). After concentration, the crude was dissolved in MeOH (4 mL) and directly purified by preparative HPLC (0.1% TFA / ACN 95/5 to 5/95 over 20 min). Fractions containing the product were combined and lyophilized to afford the title compound **30** as a white solid (17.0 mg, 0.0572 mmol, 94%).

**mp:** 222 °C

**<sup>1</sup>H NMR (400 MHz, CDCl<sub>3</sub>):** δ 9.72 (1H, s, OH), 7.40-7.33 (3H, m, H<sub>1</sub> + H<sub>2</sub>), 7.17-7.14 (2H, m, H<sub>3</sub>), 5.57 (1H, d, J = 15.6 Hz, H<sub>4</sub>), 5.51 (1H, d, J = 15.6 Hz, H<sub>4</sub>), 3.23 (1H, ddd, J = 11.5, 7.0,

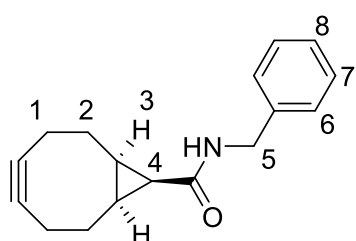
4.6 Hz, H11), 3.04 (1H, ddd,  $J = 14.0, 9.2, 4.6$  Hz, H11), 2.91 (1H, ddd,  $J = 10.6, 6.9, 3.7$  Hz, H5), 2.66-2.58 (1H, m, H5), 2.27-2.11 (3H, m, 2 H12 + 1 H6), 1.88-1.81 (m, 1H, H6), 1.79 (1H, t,  $J = 8.8$  Hz, H8), 1.50-1.42 (1H, m, H7), 1.29-1.20 (1H, m, H7)

**$^{13}\text{C}$  NMR (101 MHz,  $\text{CDCl}_3$ ):**  $\delta$  141.5,<sup>a</sup> 132.9,<sup>a</sup> 131.9,<sup>a</sup> 129.3, 129.0, 127.2, 53.0,<sup>b</sup> 24.5, 24.0, 22.6, 21.0, 20.2 (2C). C15 could not be detected

<sup>a</sup>: determined by  $^1\text{H}$ - $^{13}\text{C}$  HMBC; <sup>b</sup>: determined by  $^1\text{H}$ - $^{13}\text{C}$  HSQC

**HR-ESI-MS ( $\text{M}+\text{H}^+$ ):** Calc. 298.1550, Found. 298.1565

### ***N*-Benzylbicyclo[6.1.0]non-4-yne-9-carboxamide 29**



To a solution of **26** (1.0 equiv., 50 mg, 0.30 mmol) in DMF (2.0 mL) was added DIPEA (3.0 equiv., 116.5 mg, 151.0  $\mu\text{L}$ , 0.92 mmol) and HATU (1.5 equiv., 173.5 mg, 0.46 mmol) and the solution was stirred at room temperature for 30 min before benzylamine (3.0 equiv., 98.0 mg, 100.0  $\mu\text{L}$ , 0.92 mmol) was

added. The mixture was stirred at room temperature for 16 h before it was concentrated to dryness. The resulting crude was dissolved in MeOH (4.0 mL) and purified by preparative HPLC (0.1% TFA / ACN 95/5 to 5/95 over 20 min). Fractions containing the product were combined and lyophilized to afford the title compound as a yellow solid (63.0 mg, 0.25 mmol, 83%).

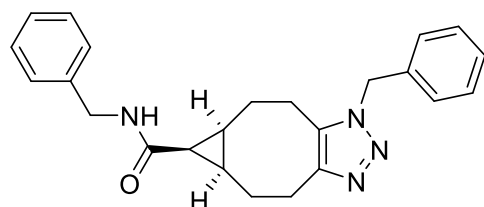
**mp:** 214 °C

**$^1\text{H}$  NMR (500 MHz,  $\text{CDCl}_3$ ):**  $\delta$  7.35-7.27 (5H, m, HAr), 6.07 (1H, br m, NH), 4.43 (2H, d,  $J = 5.8$  Hz, H5), 2.47-2.35 (2H, m, H2), 2.32-2.21 (4H, m, H1), 2.14-2.05 (2H, br app dquad,  $J = 13.1, 2.6$  Hz, H2), 1.64 (1H, t,  $J = 9.0$  Hz, H4), 1.29-1.18 (2H, m, H3)

**$^{13}\text{C}$  NMR (101 MHz,  $\text{CDCl}_3$ ):**  $\delta$  171.2, 138.8, 128.7, 127.7, 127.4, 98.8, 43.5, 27.9, 24.2, 23.2, 21.3

**HR-ESI-MS ( $\text{M}+\text{H}^+$ ):** Calc. 254.1539, Found. 254.1550

### ***N*,1-Dibenzyl-1,4,5,5a,6,6a,7,8-octahydrocyclopropa[5,6]cycloocta[1,2-d][1,2,3]triazole-6-carboxamide 31**



This compound was obtained following two procedures:

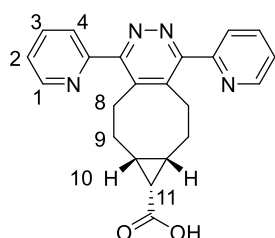
**Procedure 1:** To a solution of **30** (1 equiv., 1.7 mg, 0.00572 mmol) in DMF (0.5 mL) were added DIPEA (3 equiv., 2.2 mg, 2.83  $\mu\text{L}$ , 0.0172 mmol) and HATU (1.5 equiv., 3.25 mg, 0.0086 mmol) and the solution was stirred at room temperature for 30 min before benzylamine (3 equiv., 1.82 mg, 1.86  $\mu\text{L}$ , 0.0172 mmol) was added. The mixture was stirred at room temperature for 16 h before it was concentrated to dryness. The resulting crude was dissolved in MeOH (4 mL) and purified

by preparative HPLC (0.1% TFA / ACN 95/5 to 5/95 over 20 min). Fractions containing the product were combined and lyophilized to afford the title compound **31** as a white solid (1.03 mg, 0.0041 mmol, 71%).

**Procedure 2:** To a solution of **29** (1.0 equiv., 1.3 mg, 0.0051 mmol) in DMF (0.5 mL) was added benzyl azide (2 equiv., 1.36 mg, 0.0122 mmol) and the reaction was stirred at room temperature for 3 hours. After concentration, the crude was dissolved in MeOH (4 mL) and directly purified by preparative HPLC (0.1% TFA / ACN 95/5 to 5/95 over 20 min). Fractions containing the product were combined and lyophilized to afford the title compound **31** as a white solid (1.7 mg, 0.0044 mmol, 86%).

**HR-ESI-MS (M+H<sup>+</sup>):** Calc. 387.2179, Found. 387.2192

### 1,4-Di(pyridin-2-yl)-6,6a,7,7a,8,9-hexahydro-5H-cyclopropa[5,6]cycloocta[1,2-d]pyridazine-7-carboxylic acid **32**



To a solution of **26** (1.0 equiv., 50.0 mg, 0.30 mmol) in acetonitrile (5.0 mL) was added 3,6-di-2-pyridyl-1,2,4,5-tetrazine (1.2 equiv., 82.3 mg, 0.37 mmol) and the reaction was stirred at room temperature for 30 min. After concentration, the crude solid was triturated in acetone (20.0 mL) and filtered to afford the title compound **32** as a white solid (105.0 mg, 0.28 mmol, 92%).

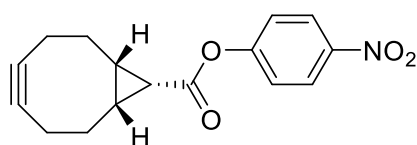
**mp:** >250 °C

**<sup>1</sup>H NMR (500 MHz, 373K, DMSO-d<sub>6</sub>):** δ 11.51 (s, 1H, OH), 8.76 (d, 2H, J = 4.8 Hz, H1), 8.02 (td, 2H, J = 7.7, 1.8 Hz, H3), 7.89 (d, 2H, J = 7.7 Hz, 2H, H4), 7.53 (td, J = 7.5, 4.9, 1.8 Hz, 2H, H2), 3.06 (dt, 2H, J = 14.4, 7.2 Hz, H8), 2.98 – 2.90 (m, 2H, H8), 2.30 (br m, 2H, H9), 2.08 (m, 2H, H9), 1.62 (t, 1H J = 8.6 Hz, H11), 1.38 (m, 2H, H10).

**<sup>13</sup>C NMR (101 MHz, 373K, DMSO-d<sub>6</sub>):** δ 173.2, 159.5, 157.2, 149.1, 141.6, 137.4, 124.9, 123.9, 27.1, 23.4-22.5 (2C), 21.9.

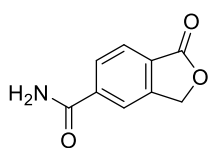
**HR-ESI-MS (M+H<sup>+</sup>):** Calc. 373.1659, Found. 373.1670

### 4-Nitrophenyl bicyclo[6.1.0]non-4-yne-9-carboxylate **37**



To a solution of **26** (1.0 equiv., 5 mg, 0.03 mmol) in DMF (0.5 mL) were added triethylamine (2.0 equiv., 6 mg, 8.4 μL, 0.06 mmol) and *bis*(4-nitrophenyl) carbonate (1.0 equiv., 9.1 mg, 0.03 mmol). The reaction was stirred at room temperature for 5 h (reaction monitored by LC-MS) before it was concentrated to dryness. The crude was then dissolved in DCM (5 mL) and washed with a saturated solution of ammonium chloride (5 x 10 mL). The organic layer was finally dried over MgSO<sub>4</sub>, filtered and concentrated under vacuum to afford the title compound **37** as a yellowish solid, which was used without further purification.

### 5-Carbomylphthalide 48



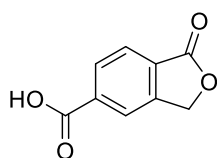
5-Cyanophthalide (4.10 g, 25.8 mmol) was stirred in 75 % sulphuric acid (40 mL) and the mixture heated to 80 °C for 3 hours. The solution was allowed to cool to rt then poured over ice, causing a white solid to precipitate which was filtered off and washed with water. This was dried overnight at 120 °C in an oven to give the title compound **48** as a white solid (4.25 g, 23.99 mmol, 93 %).

Rf: 0.52 (DCM/MeOH 9/1)

<sup>1</sup>H NMR (400 MHz, DMSO-d<sub>6</sub>): δ 8.22 (1H, s), 8.11 (1H, s), 8.03 (1H, t, J = 8.0 Hz), 7.92 (1H, d, J = 8.0 Hz), 7.66 (1H, s), 5.47 (2H, s)

<sup>13</sup>C NMR (101MHz, DMSO-d<sub>6</sub>): δ 170.1, 167.0, 147.4, 139.6, 128.1, 127.1, 124.9, 122.1, 70.0

### 5-Carboxyphthalide 49



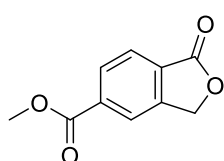
5-Carbomylphthalide **48** (4.10 g, 23.02 mmol) was refluxed in an aqueous solution of NaOH (2.0 M, 20 mL) overnight. The solution was cooled to rt and acidified to pH = 1 using HCl which caused a white solid to precipitate. This was filtered off and thoroughly washed with water. This was dried at 120 °C overnight to give **49** as a white solid (4.01 g, 22.51 mmol, 98 %).

Rf: 0.33 (DCM/MeOH 9/1)

<sup>1</sup>H NMR (400 MHz, DMSO-d<sub>6</sub>): δ 8.22 (1H, s), 8.10 (1H, dd, J = 8.0, 0.6 Hz), 7.95, (1H, d, J = 8.0 Hz), 5.47 (2H, s)

<sup>13</sup>C NMR (101 MHz, DMSO-d<sub>6</sub>): δ 170.4, 167.0, 148.1, 136.3, 130.3, 129.0, 125.6, 124.5, 70.6

### Methyl 1-oxo-1,3-dihydroisobenzofuran-5-carboxylate 50



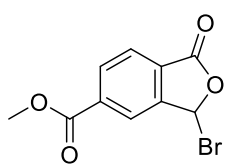
5-Carboxyphthalide **49** (1.0 equiv., 1.0 g, 5.65 mmol) was stirred in MeOH (10 mL) and to this was slowly added thionyl chloride (5.0 equiv., 2 mL, 28.25 mmol) and the mixture was refluxed for 4 hours. Solvents were removed under reduced pressure and the residue was suspended in water and filtrated to give the title compound **50** as a white solid (1.02 g, 5.2 mmol, 92 %).

Rf: 0.57 (CyH/EtOAc 4/6)

<sup>1</sup>H NMR (400 MHz, CDCl<sub>3</sub>): δ 8.22 (1H, d, J = 7.9 Hz), 8.19 (1H, s), 8.0 (1H, d, J = 7.9 Hz), 5.39 (2H, s), 3.99 (3H, s)

<sup>13</sup>C NMR (101 MHz, CDCl<sub>3</sub>): δ 169.9, 165.8, 146.4, 135.4, 130.4, 129.4, 125.8, 123.5, 69.6, 52.7

### Methyl 3-bromo-1-oxo-1,3-dihydroisobenzofuran-5-carboxylate **51**



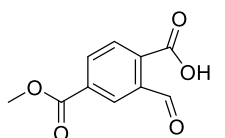
Methyl 1-oxo-1,3-dihydroisobenzofuran-5-carboxylate **50** (1.0 equiv., 500 mg, 2.6 mmol) was stirred in chloroform (10 mL) and N-bromosuccinimide (1.6 equiv., 740 mg, 4.1 mmol) and azobisisobutyronitrile (AIBN, 0.2 equiv., 85 mg, 0.52 mmol) were added. The reaction mixture was refluxed overnight. Precipitated succinimide was filtered off and the resulting solution was purified by flash chromatography (chloroform 100%) to afford the title compound **51** as a white solid (590 mg, 2.2 mmol, 85 %).

Rf: 0.58 (chloroform 100%)

<sup>1</sup>H NMR (400 MHz, CDCl<sub>3</sub>): δ 8.32 – 8.27 (2H, m), 8.01 (1H, d, J = 8.2 Hz), 7.44 (1H, s), 4.01 (3H, s)

<sup>13</sup>C NMR (101 MHz, CDCl<sub>3</sub>): δ 166.3, 165.1, 148.9, 136.6, 132.1, 127.5, 126.0, 124.9, 74.0, 53.0

### 2-formyl-4-(methoxycarbonyl)benzoic acid **52**



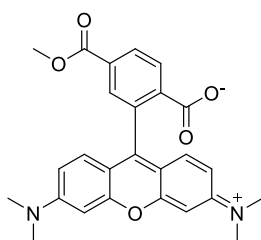
Methyl 3-bromo-1-oxo-1,3-dihydroisobenzofuran-5-carboxylate **51** (1.0 equiv., 1066 mg, 3.95 mmol) was stirred in water (20 mL) and the mixture was heated for 3 hours at 90 °C. The flask was cooled to room temperature and the aqueous solution was extracted with diethyl ether (3 x 50 mL), organic layers were combined, dried over MgSO<sub>4</sub>, filtered and concentrated to dryness to afford the title compound **52** (800 mg, 3.85 mmol, 97 %) as a white solid.

Rf: 0.13 (DCM/MeOH 9/1)

<sup>1</sup>H NMR (400 MHz, DMSO-d<sub>6</sub>): δ 8.34 (1H, br), 8.19 (1H, d, J = 7.9 Hz), 8.14 (1H, s), 7.96 (1H, d, J = 8.0 Hz), 6.74 (1H, br s), 3.93 (3H, s)

<sup>13</sup>C NMR (101 MHz, DMSO-d<sub>6</sub>): δ 167.5, 165.2, 147.7, 134.9, 131.3, 130.4, 125.1, 124.3, 98.4, 52.8

### 2-(6-(dimethylamino)-3-(dimethyliminio)-3H-xanthen-9-yl)-4-(methoxycarbonyl)benzoate **53**



2-formyl-4-(methoxycarbonyl)benzoic acid **52** (1.0 equiv., 100 mg, 0.48 mmol) was stirred in propionic acid (10 mL) and freshly purified 3-(dimethylamino)phenol (3 equiv., 1.44 mmol, 197.5 mg) was added, along with *p*-TsOH hydrate (0.2 equiv., 0.096 mmol, 16.53 mg). The mixture was protected from light and heated to 80 °C for 4 h. Chloranil (1 equiv., 0.48 mmol, 118 mg) was added, maintaining the temperature at 80 °C and the mixture stirred for 2 hours. The mixture was cooled to room temperature then solvent was

removed under reduced pressure and the crude residue was purified by normal-phase flash chromatography (H<sub>2</sub>O/ACN 5/95 to 20/80 in 30 min). Following concentration of the desired fractions to dryness, the residue was taken up in DCM/MeOH 9/1 and filtered through cotton wool to remove any eluted silica. Evaporation under reduced pressure afforded the title compound **53** as a dark purple solid (150 mg, 0.33 mmol, 71 %).

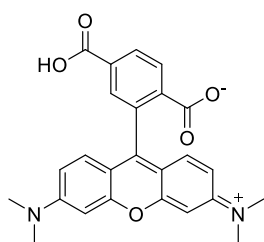
**Note:** Commercial 3-(dimethylamino)phenol is often oxidized (brown/purple color) and should be purified before use (isocratic CyH/EtOAc 9/1, "yellow" on the column but it's a white solid). Purify the 6-TAMRA-CO<sub>2</sub>Me on normal phase: two peaks: one, very intense, at the very beginning, which is not the product, the rest is the product (check the fluorescence on TLC with UV lamp).

**Rf:** 0.27 (H<sub>2</sub>O/ACN 15/85)

**<sup>1</sup>H NMR (400 MHz, MeOH-d<sub>4</sub>):** δ 8.25 (1H, dd, J = 8.2, 1.7 Hz), 8.14 (1H, d, J = 8.2 Hz), 7.85 (1H, d, J = 1.4 Hz), 7.23 (2H, d, J = 9.5 Hz), 6.98 (2H, dd, J = 9.5, 2.5 Hz), 6.87 (2H, d, J = 2.5 Hz), 3.90 (3H, s), 3.25 (12H, s)

**<sup>13</sup>C NMR (101 MHz, MeOH-d<sub>4</sub>):** δ 172.5, 167.5, 161.9, 159.2, 158.8, 146.3, 133.9, 132.8, 132.2, 131.9, 131.6, 131.2, 115.2, 115.1, 97.5, 53.1, 41.0

#### 4-carboxy-2-(6-(dimethylamino)-3-(dimethyliminio)-3H-xanthen-9-yl)benzoate **54**



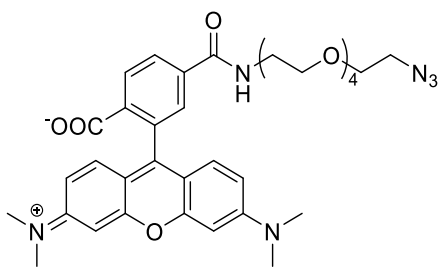
2-(6-(dimethylamino)-3-(dimethyliminio)-3H-xanthen-9-yl)-4-(methoxycarbonyl)benzoate **53** (1.0 equiv., 1.0 g, 2.25 mmol) was stirred in H<sub>2</sub>O/THF (1:1, 50 mL) and to this was added NaOH (2.5 equiv., 225 mg, 5.63 mmol). The mixture was and stirred for 2 hours in the dark. The solution was acidified with concentrated HCl, causing a solid to precipitate, which was filtered and dried under reduced pressure to give the title product

**54** as a purple solid (863 mg, 2.01 mmol, 89 %)

**<sup>1</sup>H NMR (400 MHz, MeOH-d<sub>4</sub>):** δ 8.49 - 8.38 (2H, m), 8.01 (1H, s), 7.17 (2H, d, J = 9.5 Hz), 7.08 (2H, dd, J = 9.4, 1.7 Hz), 6.99 (2H, s), 3.33 (12H, s)

**<sup>13</sup>C NMR (101 MHz, MeOH-d<sub>4</sub>):** δ 167.8, 167.5, 160.5, 159.2, 159.1, 136.2, 136.1, 135.5, 133.0, 132.5, 132.5, 132.1, 115.8, 115.1, 97.6, 41.1

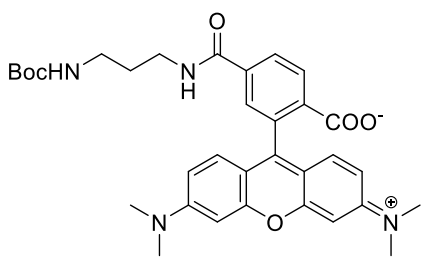
#### 4-((14-Azido-3,6,9,12-tetraoxatetradecyl)carbamoyl)-2-(6-(dimethylamino)-3-(dimethyliminio)-3H-xanthen-9-yl)benzoate (TAMRA-PEG<sub>4</sub>-N<sub>3</sub>) **39**



To a solution of TAMRA **54** (1 equiv., 5 mg, 0.0116 mmol) in DMF (0.2 mL) were added DIPEA (3 equiv., 4.51 mg, 5.77  $\mu$ L, 0.0349 mmol) and HATU (1 equiv., 4.42 mg, 0.0116 mmol) and the solution was stirred at room temperature for 15 min before  $\text{NH}_2\text{-PEG}_4\text{-N}_3$  (2 equiv., 6.09 mg, 0.0233 mmol) was added. The resulting solution was stirred at room temperature for 6 h before it was diluted in methanol (4 mL) and purified directly by preparative HPLC (555 nm, 0.1% TFA / ACN 95/5 to 5/95 over 20 min). Fractions containing the product were combined and lyophilized to afford the title compound (6.43 mg, 0.00953 mmol, 82%) as a pink oil.

**HR-ESI-MS ( $\text{M}+2\text{H}^+$ ):** Calc. 338.1532, Found. 338.1526

**4-((3-((tert-butoxycarbonyl)amino)propyl)carbamoyl)-2-(6-(dimethylamino)-3-(dimethyliminio)-3H-xanthen-9-yl)benzoate **55****



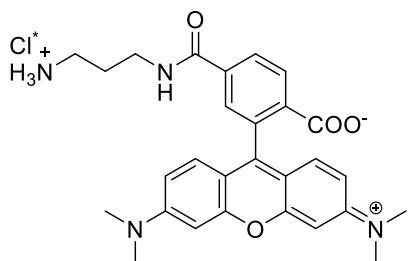
TAMRA **54** (72 mg, 0.167 mmol) was dissolved in DMF (1.2 mL) and TEA (2 equiv., 0.334 mmol, 22.4 mg, 31.2  $\mu$ L) then PyBOP (2 equiv., 0.167 mmol, 86.9 mg) was added. After 10 minutes, tert-Butyl N-(3-aminopropyl)carbamate, N-Boc-1,3-diaminopropane (1.2 equiv., 32 mg, 0.200 mmol) was added to the mixture and stirred overnight at room temperature. The crude mixture was purified directly by preparative RP-HPLC (555 nm, 0.1% TFA / ACN 95/5 to 5/95 over 20 min) and lyophilized to afford the modified the title compound **55** (80 mg, 0.137 mmol, 82%).

**$^1\text{H}$  NMR (400 MHz, MeOD- $d_4$ ):**  $\delta$  8.69 (t,  $J$  = 1.9 Hz, 1H), 8.17 (dd,  $J$  = 1.9, 8.1 Hz, 1 H), 7.43 (d,  $J$  = 8.1 Hz, 1H), 7.05-6.87 (m, 6H), 3.41 (d,  $J$  = 6.9 Hz, 2H), 3.23 (s, 12H), 3.08 (t,  $J$  = 6.9 Hz, 2H), 1.76-1.69 (m, 2H), 1.36 (s, 9H).

**$^{13}\text{C}$  NMR (101 MHz, MeOD- $d_4$ ):**  $\delta$  168.2, 167.4, 160.7, 159.1, 159.0, 138.1, 137.8, 132.9, 132.3, 132.0, 131.3, 115.6, 114.8, 97.5, 41.0, 39.0, 38.7, 30.9, 28.9.

**HR-ESI-MS ( $\text{M}+\text{H}^+$ ):** calc 586.2791, found 586.2797.

**4-((3-ammoniopropyl)carbamoyl)-2-(6-(dimethylamino)-3-(dimethyliminio)-3H-xanthen-9-yl)benzoate 43**



4-((3-((tert-butoxycarbonyl)amino)propyl)carbamoyl)-2-(6-(dimethylamino)-3-(dimethyliminio)-3H-xanthen-9-yl)benzoate **55** (40 mg, 0.068 mmol) was dissolved in an HCl solution in dioxane (4M, 3 mL) and stirred for 3 hours. The crude was concentrated under reduced pressure to afford the title compound **43** (41 mg, quant.) as a pink

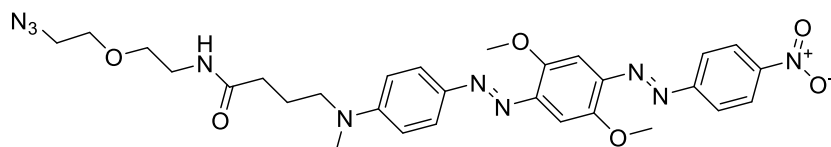
solid.

**<sup>1</sup>H NMR (400 MHz, MeOD-d<sub>4</sub>):** δ 8.72 (d, J = 1.9 Hz, 1H), 8.21 (dd, J = 1.9, 8.1 Hz, 1H), 7.47 (d, J = 8.1 Hz, 1H), 7.07-6.90 (m, 6H), 3.52 (t, J = 6.7 Hz, 2H), 3.22 (s, 12H), 3.00 (t, J = 6.7 Hz, 2H), 2.00-1.93 (m, 2H).

**<sup>13</sup>C NMR (101 MHz, MeOD-d<sub>4</sub>):** δ 168.9, 167.4, 160.5, 159.1, 159.0, 138.3, 137.2, 133.0, 132.3, 132.0, 131.9, 131.4, 115.6, 114.8, 97.5, 41.0, 38.5, 37.8, 28.9.

**HR-ESI-MS (M+H<sup>+</sup>):** calc 486.2267, found 486.2262.

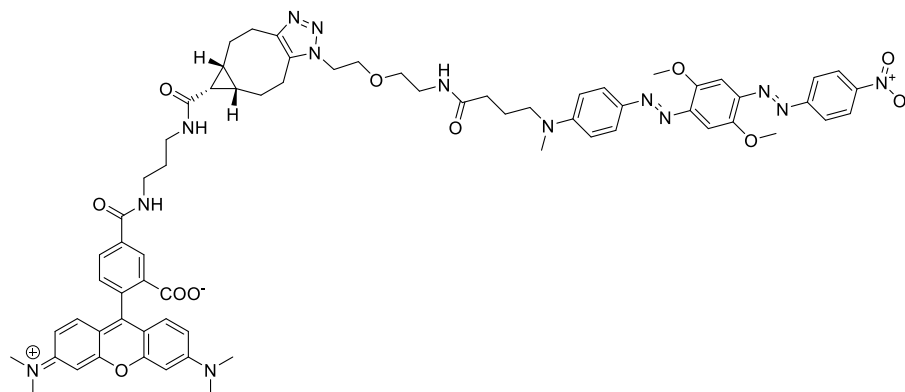
***N*-(2-(2-Azidoethoxy)ethyl)-4-((4-((*E*)-(2,5-dimethoxy-4-((*E*)-(4-nitrophenyl)diazenyl)phenyl)diazenyl)phenyl)(methyl)amino)butanamide (BHQ-2-N<sub>3</sub>) 44**



This compound was synthesized according to a previously reported procedure.<sup>386</sup>



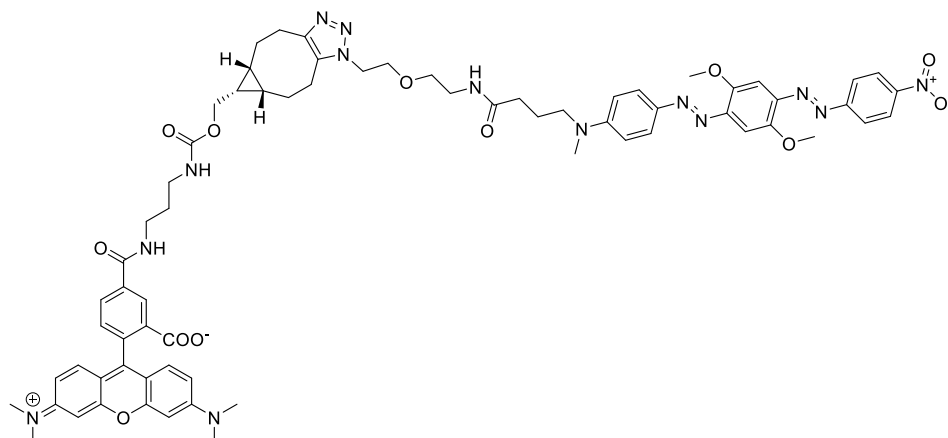
**5-((3-(-1-(2-(2-(4-((E)-(2,5-dimethoxy-4-((E)-(4-nitrophenyl)diazenyl)phenyl)diazenyl)phenyl)(methylamino)butanamido)ethoxy)ethyl)-1,4,5,5a,6,6a,7,8-octahydrocyclopropa[5,6]cycloocta[1,2-d][1,2,3]triazole-6-carboxamido)propyl)carbamoyl)-2-(6-(dimethylamino)-3-(dimethyliminio)-3H-xanthen-9-yl)benzoate **41****



To a solution of **26** (1.0 equiv., 0.5 mg, 0.003 mmol) in DMF (0.1 mL) were added DIPEA (3.0 equiv., 1.18 mg, 1.5  $\mu$ L, 0.009 mmol) and PyBOP (1.5 equiv., 2.34 mg, 0.0045 mmol) and the solution was stirred at room temperature for 30 min before TAMRA-NH<sub>2</sub> **43** (1.5 equiv., 2.15 mg, 0.0045 mmol, 1 mM in DMSO) was added. The mixture was then stirred at room temperature for 16 h in the dark. Upon completion, BHQ-2-N<sub>3</sub> **44** (1 equiv., 1.11 mg, 0.0018 mmol, 1 mM in DMSO) was added and the solution was stirred at room temperature for 24 h in the dark. After concentration, the crude was dissolved in MeOH (4 mL) and directly purified by preparative HPLC (555 nm, 0.1% TFA / ACN 95/5 to 5/95 over 20 min). Fractions containing the product were combined and lyophilized to afford the title compound as a purple solid **41** (1.2 mg, 0.96  $\mu$ mol, 32%).

**HR-ESI-MS (M+3H<sup>+</sup>):** Calc. 417.8627, Found. 417.8626

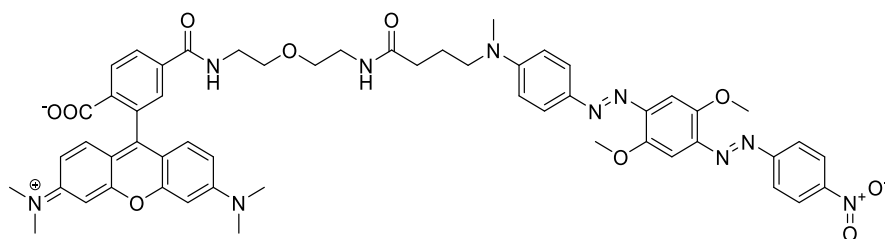
**5-((3-(((1-(2-(2-(4-((E)-(2,5-Dimethoxy-4-(E)-(4-nitrophenyl)diazenyl)phenyl)diazenyl)phenyl)(methyl)amino)butanamido)ethoxy)ethyl)-1,4,5,5a,6,6a,7,8-octahydrocyclopropa[5,6]cycloocta[1,2-d][1,2,3]triazol-6-yl)methoxy)carbonyl)amino)propyl)carbamoyl)-2-(6-(dimethylamino)-3-(dimethyliminio)-3H-xanthen-9-yl)benzoate **42****



To a solution of TAMRA-NH<sub>2</sub> **43** (1 equiv., 1 mg, 0.0021 mmol, 1 mM in DMSO) in DMF (0.2 mL) were added triethylamine (2 equiv., 0.3 mg, 0.43  $\mu$ L, 0.0042 mmol) and activated BCN **15** (1 equiv., 0.67 mg, 0.0021 mmol, 1 mM in DMSO) and the solution was stirred at room temperature for 3 h in the dark. Upon completion, BHQ-2-N<sub>3</sub> **44** (1 equiv., 1.3 mg, 0.0021 mmol, 1 mM in DMSO) was added and the solution was stirred at room temperature for 24 h in the dark. After concentration, the crude was dissolved in MeOH (4 mL) and directly purified by preparative HPLC (555 nm, 0.1% TFA / ACN 95/5 to 5/95 over 20 min). Fractions containing the product were combined and lyophilized to afford the title compound as a purple solid **42** (1.2 mg, 0.9  $\mu$ mol, 44 %).

**HR-ESI-MS (M+3H<sup>+</sup>):** Calc. 427.8662, Found. 427.8658

**4-((2-(2-(4-((E)-(2,5-Dimethoxy-4-(E)-(4-nitrophenyl)diazenyl)phenyl)diazenyl)phenyl)(methyl)amino)butanamido)ethoxy)ethyl) carbamoyl)-2-(6-(dimethylamino)-3-(dimethyliminio)-3H-xanthen-9-yl)benzoate **47****



This compound was synthesized according to a previously reported procedure.<sup>386</sup>

**Kinetics studies.** Kinetics studies were conducted in triplicate, following the formation of the SPAAC product by HPLC according to the following procedure. 20-mM stock solutions of BCN **26** and **29**, benzyl azide, and benzylamine (internal standard; IS) were prepared in DMSO. In an Eppendorf containing the solvent mixture (ACN/H<sub>2</sub>O 1:2; 185  $\mu$ L), 5  $\mu$ L of each solution

were added sequentially (starting from the IS, then BCN and finally benzyl azide), to reach a final concentration of 500  $\mu\text{M}$  in all compounds. The mixture was agitated at 37  $^{\circ}\text{C}$  and 5- $\mu\text{L}$  aliquots were taken every 2 minutes, diluted with water (195  $\mu\text{L}$ ) and analyzed by HPLC at 280 nm (solvent A: water + 0.1% TFA; solvent B: ACN; gradient: 95:5 to 5:95 over 10 min, followed by 5 min equilibration at 5:95).

For each chromatogram obtained, the area under the curve of each peak was divided by that of the IS and the resulting ratios were normalized against the value obtained at  $t = 0$  min.

From the conversion rates thus obtained, the second order rate constants were calculated according to the following equation:

$$kt = \frac{1}{[B]_0 - [A]_0} \times \ln \frac{[A]_0([B]_0 - [P])}{([A]_0 - [P])[B]_0}$$

where  $k$  is the second order rate constant expressed in  $\text{M}^{-1} \cdot \text{s}^{-1}$ ;  $t$ , the reaction time in seconds;  $[A]_0$ , the initial concentration of BCN in  $\text{mmol} \cdot \text{mL}^{-1}$ ;  $[B]_0$ , the initial concentration of benzyl azide in  $\text{mmol} \cdot \text{mL}^{-1}$ ; and  $[P]$ , the concentration of the triazole product in  $\text{mmol} \cdot \text{mL}^{-1}$ .

### Stability of FRET probes in aqueous media and human plasma

Aqueous buffers were prepared as follows:

Calculated pH	Measured pH	Composition
0	<0.7	HCl 1 M
1	1.02	HCl 0.1 M
2	2.00	HCl 0.01M
3	3.03	30 mL KH phthalate standard + 10 mL HCl 0.1 M
4	4.01	KH phthalate (standard solution of pH meter)
5	5.03	0.78 mL $\text{NaH}_2\text{PO}_4$ 0.1 M + 39.4 mL $\text{Na}_2\text{HPO}_4$ 0.1 M
7.4	7.40	PBS
9	9.03	15 mL TRIS 4 mM adjusted to pH = 9.0

25  $\mu\text{L}$  of a stock solution of probes **41** and **42** in DMSO (40  $\mu\text{M}$ ) were added to 975  $\mu\text{L}$  of aqueous buffered media or human plasma (measured pH 7.35) or Dulbecco's Modified Eagle

Medium (DMEM; pH 7.4) to reach a final concentration of 5  $\mu$ M. These solutions were distributed into 96-well plates and incubated at 23 °C in a SAFAS Xenius XML with excitation/emission wavelengths set to those of TAMRA (550/580 nm). The fluorescence was measured every 3 min for 15 h and normalized against the fluorescence of a solution of TAMRA-NH<sub>2</sub> **43** (5  $\mu$ M) and BHQ-2-N<sub>3</sub> **44** (5  $\mu$ M) in the same medium. Each measurement was done in triplicate.

### **Bioconjugation**

To a solution of trastuzumab (1 equiv., 1 mg, 5 mg/mL in DPBS, pH 7.4) was added activated BCN **37** (5 equiv., 1 mM in DMSO) and the reaction mixture was incubated at 25 °C for 16 h. Excess of reagent and by-products were removed by gel filtration chromatography using Bio-spin P-30 columns (Bio-Rad, Hercules, U.S.A.) pre-equilibrated with DPBS 1X (pH 7.4) to give a solution of BCN-functionalized trastuzumab **38** (0.91 mg, 91%, diluted to 10 mg/mL with DPBS 1X). A solution of TAMRA-PEG<sub>4</sub>-N<sub>3</sub> **39** (10 equiv., 10 mM in DMSO) was then added and the mixture was incubated at 25 °C for another 16 h. Excess of reagent was removed by gel filtration chromatography using Bio-spin P-30 columns pre-equilibrated with DPBS 1X (pH 7.4) to give a solution of TAMRA-labeled trastuzumab **40** (0.62 mg, 68%), whose average degree of conjugation was determined to be 2.7 by native mass spectrometry (*vide infra*).

### **In vitro stability.**

**Cell culture.** Human breast adenocarcinoma SKBR3 cells (ATCC HTB-30™) were grown in Dulbecco's Modified Eagle's Medium containing 4,5 g/L glucose (Sigma-Aldrich, St. Louis, MO, USA) supplemented with fetal bovine serum (FBS) to a final concentration of 10% (Perbio, Brebieres, France), 2 mM L-glutamine, 100 U/mL penicillin and 50  $\mu$ g/mL streptomycin (Merck). Cells were maintained in a 5% CO<sub>2</sub> humidified atmosphere at 37 °C.

Human breast adenocarcinoma MDA-MB-231 cells (ATCC THB-26™) and Human uterus adenocarcinoma HeLa (ATCC CRM-CCL-2™) were grown in modified Eagle's Medium containing 4.5 g/L glucose (Sigma-Aldrich, St. Louis, MO, USA) supplemented with fetal bovine serum (FBS) to a final concentration of 10%, 2 mM L-glutamine, 100 U/mL penicillin and 50  $\mu$ g/mL streptomycin. Cells were maintained in a 5% CO<sub>2</sub> humidified atmosphere at 37 °C.

**Flow cytometry.** Two days prior to the experiment, cells were seeded in 48-well plates (Corning Costar 3548, NY, USA): 3 x 10<sup>4</sup> cells per well in Dulbecco's Modified Eagle's complete Medium for SKBR3, 3 x 10<sup>4</sup> and 1.25 x 10<sup>4</sup> cells per well in Modified Eagle's complete Medium for MDA-MB-231 and HeLa, respectively.

Cells in each well were incubated with 250  $\mu$ L of a 5- $\mu$ M solution of fluorescent probes **41**, **42** and **47** in complete DMEM for 1, 3, 24 and 48 h at 37 °C. Upon completion, cells in each well were rinsed with 300  $\mu$ L of PBS (Sigma-Aldrich, St. Louis, MO, USA), incubated with 80  $\mu$ L of trypsin (0.25%, Merck) for 5 min at 37 °C and resuspended in 500  $\mu$ L of a PBS solution containing 5% FBS. Cell suspensions were analyzed by flow cytometry on a Fortessa cytometer (BD Biosciences). Each compound was tested in duplicate and each experiment was done twice. Results in Figure 4 of the manuscript are presented as histograms of the mean fluorescence intensity with standard deviations corresponding to four different measurements.



## VI. Enhancing siRNA release of covalent ARC with cleavable linkers

### A. Generalities regarding linkers used in FDA-approved antibody-drug conjugates

The linker is crucial in an ADC, as it contributes to the conjugate's activity, solubility and the scope of usable drugs.<sup>250</sup> It must be stable in plasma to avoid premature release of the drug in the bloodstream, thus leading to off-target toxicities and to a lower therapeutic index. Linkers used in ADC can be divided into two subclasses: cleavable and non-cleavable molecules (Figure 92). Structurally, the linker is composed of three parts: the linker-antibody junction, the linker-drug attachment, and, in the case of cleavable linkers, the molecular pattern responsible for the cleavable . While the linker-antibody linkage defines the Drug-to-Antibody (DAR) ratio, the linker-drug connection defines the scope of drugs and the central motif determinates the cleavage mechanism.

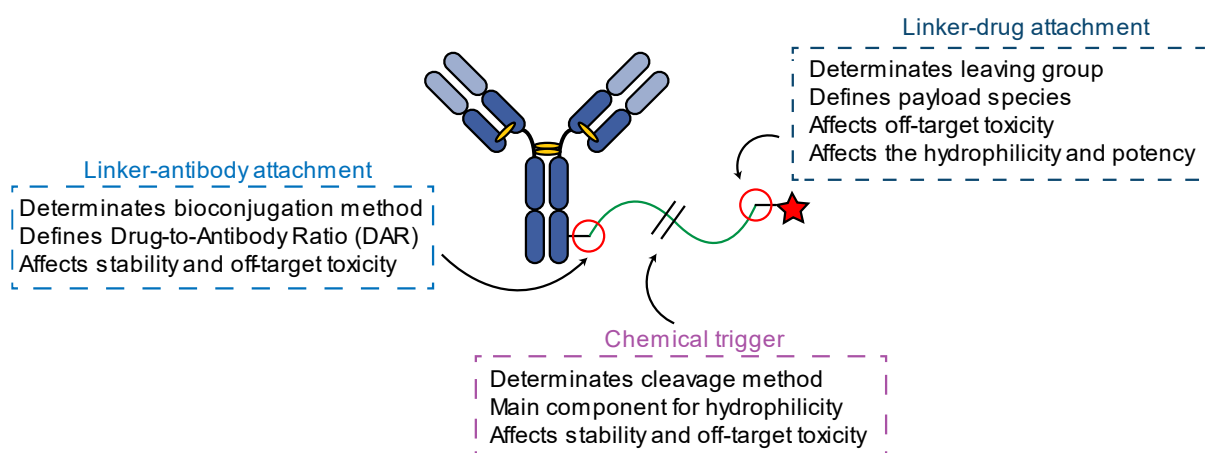


Figure 92 - Impact of all the component of a linker on the ADC's activity. The chemical trigger is absent in the case of non-cleavable linkers.

#### i. Non-cleavable linkers

Both cleavable and non-cleavable linkers rely on the lysosomal degradation of the antibody to release the cytotoxic drug. In the case of non-cleavable linkers, the active metabolite is generally an amino acid residue derived from the degraded antibody linked to the drug. Structure, mechanism and improvement of the linker used in currently approved ADCs will be discussed in a following chapter.

Overall, one of the main advantages of non-cleavable linkers is their remarkable stability in the bloodstream, limiting precocious release of the drug and off-target toxicity to healthy cells. In addition, the release of amino-acid derivatives greatly enhances the drug's hydrophilicity. This

property allow the drug to exhibit both a low membrane-permeability and a low affinity for multidrug resistance proteins (MDR), without sacrificing its potency.<sup>248</sup> Consequently, the charged drug catabolite is trapped inside the cell until its death and, once the targeted cell is killed, the drug is not able to enter in other cells due to its charges. Therefore, the catabolites resulting from non-cleavable linkers are not likely to perform bystander effects, thus being safer in the case of liquid tumors than the catabolites resulting from cleavable linkers.

However, the payload should be carefully selected so that the catabolite possesses a similar activity compared to the native drug, thus narrowing the scope of usable drugs.<sup>387</sup> Actually, only two FDA-approved ADCs over the twelve contain a non-cleavable linker, and these are limited to two drugs, DM1 and MMAF (Figure 93). This latter remark explains why the vast majority of the ADCs commercially available or in clinical trials are conjugated with cleavable linkers.

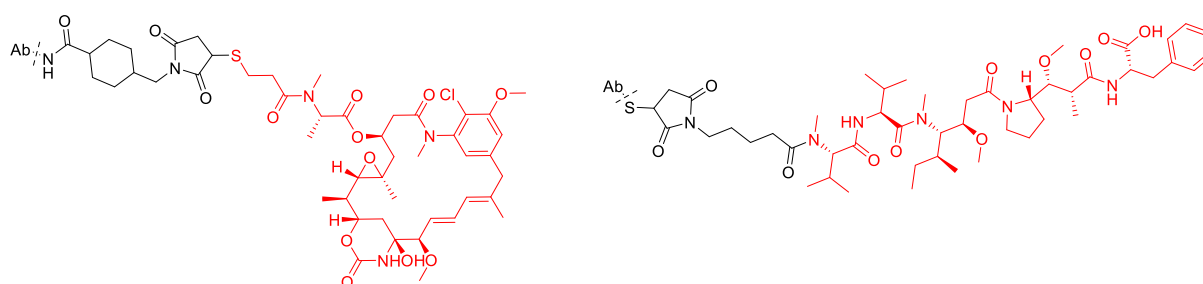


Figure 93 -Structures of Kadcylya™ (emtansine, left) and Blenrep™ (mafodotin, right) payloads. Emtansine (left) is composed of a bifunctional 1,4-disubstituted cyclohexyl linker, and mafodotin (right) is composed of a bifunctional maleimidocaproyl linker. The drugs are displayed in red

## ii. Cleavable-linkers

Cleavable linkers rely on the lysosomal degradation of the conjugate to release the cytotoxic drug as well. In the case of cleavable linkers, the aim is to release the native drug, thus allowing the use of a higher number of drugs and cell death mechanism of action. In addition, the release of highly hydrophobic native payloads allows bystander effects by crossing the lipid bilayer of cells, consequently entering inside neighboring cells. While it can be desired in the case of heterogenous solid tumors, it can cause severe adverse effects as well, if the drug is internalized in healthy tissues. Therefore, highly plasma-stable linkers are required to widen the therapeutic windows of ADCs. In order to modulate the stability of the linker and the release kinetic of the drug, different strategies of cleavage have been exploited, either using chemical triggers or enzymes.<sup>254</sup> Structure, mechanism and improvement of the linker used in currently approved ADCs will be discussed in a following chapter.



## 1. Enzyme-cleavable linkers

Enzyme-cleavable linkers rely on molecular patterns that can be recognized and cleaved selectively by intracellular enzymes after the internalization of the ADC. Among these different enzymes, lysosomal proteases able to cleave short peptide motifs represent the most appealing proteins exploited in the case of ADCs. Actually, due to their high lysosomal concentration compared to the bloodstream, protease-cleavable linkers generally show a good serum stability, while being able to release payloads in their native forms inside the cell. In addition, short peptides can be synthesized in industrial scale, and the introduction of hydrophilic residues in the peptide sequence allow the control of the hydrophilicity of the payload. For all these reasons, protease-cleavable linkers currently represent the most widely used linkers in the ADC field (Figure 94).<sup>254</sup>

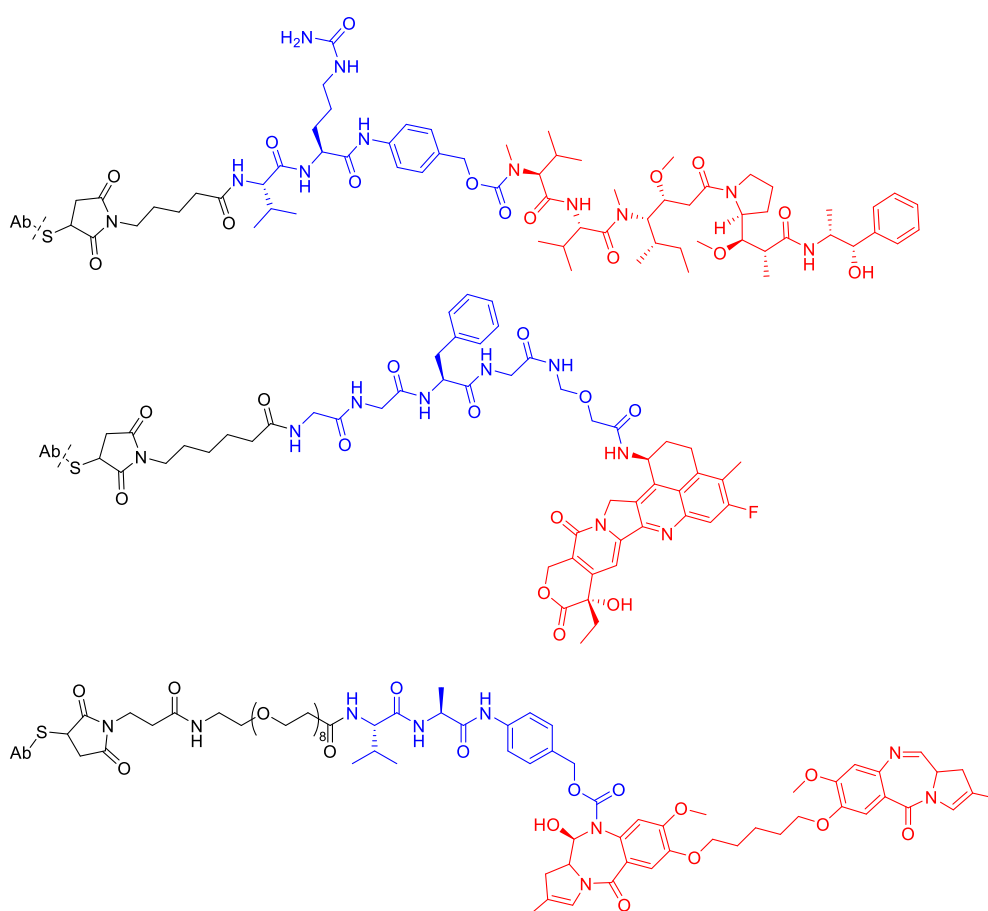


Figure 94 - Structures of Adcetris™ (vedotin, first line), Enhertu™ (deruxtecan, middle line) and Zynlonta™ (tesirine, bottom line) payloads. Vedotin (first line) is composed of the dipeptide valyl-citrulline attached to the self-immolative para-aminobenzoyl carbamate-linked drug. Deruxtecan (middle line) is composed of the tetrapeptide glycyl-glycyl-phenylalanyl-glycyl attached to the self-immolative 2-aminomethoxy acetamide-linked drug. Tesirine (bottom line) is composed of dipeptide valyl-alanyl attached to the self-immolative para-aminobenzoyl carbamate-linked drug. The drug is displayed in red, the cleavable motif in blue.

## 2. Acid-sensitive

The very first strategy exploited in ADCs was based on acid-labile motifs, due to the sharp difference in acidity between blood (pH ~7.4) and certain organelles (e.g. lysosomes, pH < 5.0).<sup>388</sup> Generally based on hydrazone or carbonates, their application is therefore limited to hydrazide or alcohol-containing drugs (Figure 95). In addition, these scaffolds often show a low plasma stability ( $t_{1/2}$  < 48 h), explaining why acid-labile linkers are not widely used nowadays. This relative blood instability of these linkers has been exploited to release drugs in the tumor microenvironment, which is known to be more acidic than sane tissues because of enhanced glycolysis and lactate generation (pH 5.5 - 6.8).<sup>389</sup>

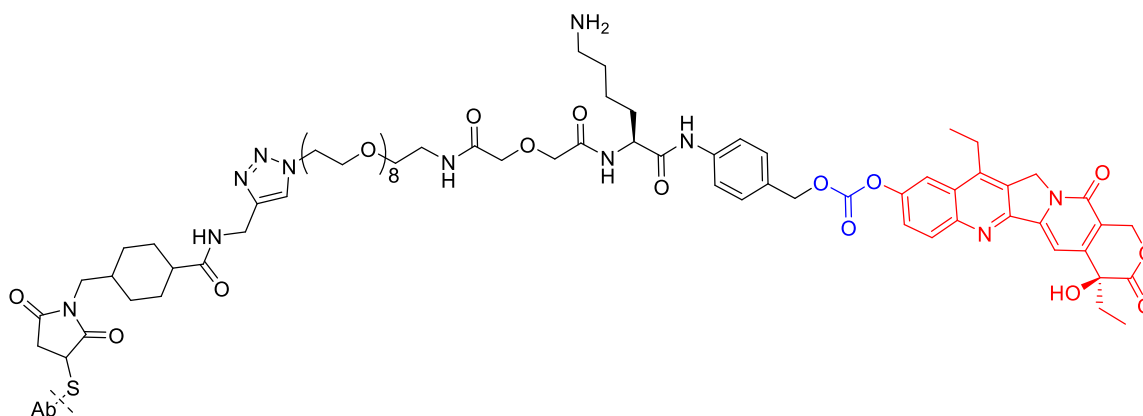


Figure 95 - Structure of Trodelvy™ payload. Govitecan is composed of the pH-sensible carbonate-linked drug. The drug is displayed in red, the cleavable motif in blue.

## 3. Reduction-cleavable

Among chemical-triggered cleavage, disulfide bonds are sensitive to reducing conditions, yielding two free thiols. In the ADC field, this mechanism has been used to release drugs, and rely on the higher concentration of glutathione in the cytoplasm compared to the extracellular environment (up to 1000-times higher).<sup>390,391</sup> This highly reducing environment promote the linker's cleavage to release the free drug (Figure 96).<sup>256,392</sup> However, these linkers are still slightly unstable in the bloodstream, thus leading to a premature release of the drug. Generally, increasing the steric hindrance near the disulfide bond enhances its plasma stability, at a cost of a much lower ability to release the drug.<sup>393</sup> The difficulty to balance stability/high release with disulfide methods could explain why reducible linkers are present in only two commercially available ADCs, Besponsa™ and Mylotarg™.

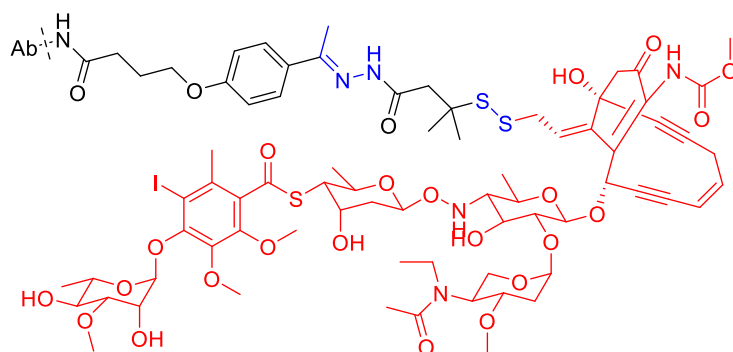


Figure 96 - Structure of Besponsa™ and Mylotarg™ payload. Ozogamicin is composed of an acid-labile hydrazone linker followed by a reducible disulfide bond. The drug is displayed in red, the cleavable motifs in blue.

To potentially enhance the cytosolic delivery of siRNA mediated by antibody-siRNA conjugate, the use of endosome cleavable linkers was explored. Two clickable linkers bearing different cleavage mechanism were evaluated: the gold-standard cathepsin-cleavable Val-Cit-PAB linker<sup>394</sup> and a novel class of acid-cleavable linkers based on cyclic acetals that we developed during the thesis.

## B. A novel family of acid-cleavable and plasma-stable linker based on cyclic acetal motifs

Tony Rady<sup>1</sup>, Lorenzo Turelli<sup>1</sup>, Fabien Thoreau<sup>1</sup>, Elisabetta Tobaldi<sup>1</sup>, Guilhem Chaubet<sup>1</sup>, Jean-Michel Becht<sup>2,\*</sup> and Alain Wagner<sup>1,\*</sup>

<sup>1</sup> Bio-Functional Chemistry (UMR 7199), LabEx Medalis, University of Strasbourg, 74 Route du Rhin, 67400 Illkirch-Graffenstaden, France

<sup>2</sup> Institut de Science des Matériaux de Mulhouse IS2M, UMR CNRS 7361, UHA, 15 Rue Jean Starcky, 68057 Mulhouse Cedex, France.

Abstract: Cleavable linkers that allow controlled release of drugs into cells by exploiting different cleavage mechanisms are especially sought-after in the field of antibody-drug conjugates (ADCs). As extracellular pH is neutral and endosomal pH is acidic, many acid sensitive groups have been developed to answer this demand. However, most linkers exploiting this mechanism present a low plasmatic stability, resulting in a premature linker cleavage, reduced efficacy and off-target toxicity. Here we present a novel family of acid-sensitive and plasma-stable linkers based on easily accessible cyclic acetal motifs. FRET-based assays were used to evaluate the stability and cleavability of these linkers. They displayed stability in human plasma and high cleavability to mildly acidic conditions representative of the lysosomal compartment. Satisfyingly, the cleavability was up to 20-fold higher than that of the standard valine-citrulline-PAB linker. Our results, show that these cyclic acetals are promising cleavable motifs for acid-triggered payload-release.

## i. Introduction

Cleavable linkers can be defined as chemical groups that can be cleaved in a controlled manner to release at least two distinct molecular entities. In the decade between the late 1980s and 1990s, development of various cleavable linkers has paralleled the emergence and rapid expansion of solid-phase organic synthesis, allowing the smooth cleavage and release of pure synthetic compounds from their solid support.<sup>395</sup> The resulting breadth of linker structures has been roughly classified into three main domains, depending on the conditions employed for their cleavage: enzymatic, physico-chemical (i.e. photo-irradiation), or chemical, the latter being unquestionably the most populated and diversified group. Linkers sensitive to acidity/basicity, oxidation/reduction or to nucleophilic species have been thoroughly explored and led to motifs that are now part of the general synthetic chemist toolbox. Interestingly, a second burst of interest in such structures recently came with the expansion of chemical biology, where cleavable linkers have been employed for connecting a payload or a probe to a functional head interacting with biological targets.<sup>396</sup>

However, the stringent operational conditions imposed by biological environments (e.g. narrow temperature range, aqueous medium, low concentrations, presence of myriad biomolecules) dictated the development of new types of linkers that could be cleaved under milder conditions, typically those found in different intracellular compartments. Indeed, one of the main applications of cleavable linkers in chemical biology resides in the intracellular delivery of compounds of interest, for imaging or therapeutic purposes for example, which necessitated the development of chemical moieties with excellent extracellular stability – to avoid premature release and potential off-target delivery of the payload – and rapid and efficient intracellular cleavage. New types of acid sensitive linkers have been developed as part of this goal, with the aim of benefiting from the sharp differences between the acidity of certain organelles or tissues (e.g. lysosomes or tumor environments, with  $\text{pH} < 5.0$ ), and that of physiological body fluids, with a  $\text{pH} \sim 7.0$  on average

Famous examples of such acid-labile chemical groups are hydrazones<sup>397</sup>, paramethoxybenzyl,<sup>398</sup> or dialkyldialkoxysilanes derivatives,<sup>399</sup> which served as basis for the development of various cleavable linkers. With an endocytosis mechanism relying essentially on lysosomal trafficking, it is not surprising to see antibody-drug conjugates (ADCs) being equipped with these motifs. However, most acid-cleavable linkers are unstable in plasma, with half-lives ranging from few minutes up to 2-3 days, causing risks of systemic cleavage of the drug and consequently off-target toxicity.<sup>400–402</sup>

Reflecting on this issue, our group has been involved in the development and stability studies of new acid-cleavable motifs. We designed several FRET-based probes, in which a TAMRA

fluorophore was linked to a BHQ-2 quencher via cyclic orthoester motifs or linear acetals (Figure 97, first and second generation, respectively), and proved that some of these constructs were highly stable in human plasma but readily hydrolyzed in acidic organelles.<sup>383,386</sup> Building on these results, we designed a new set of compounds, this time bearing cyclic acetal motifs of various ring sizes and substitution patterns, with the idea of developing acid cleavable amine-to-thiol cross-linkers that could be used in ADCs (Figure 97, third generation).<sup>384,385</sup> However, these new linkers were found to be extremely stable in acidic conditions, even at pH < 1.0.

Puzzled by these unexpected results, we became interested in combining motifs from the second and third generation linkers to see the influence of methoxyphenyl groups on the stability of cyclic acetals, in the hope of developing a fourth generation of acetal-based linkers with improved stability/cleavage balance.

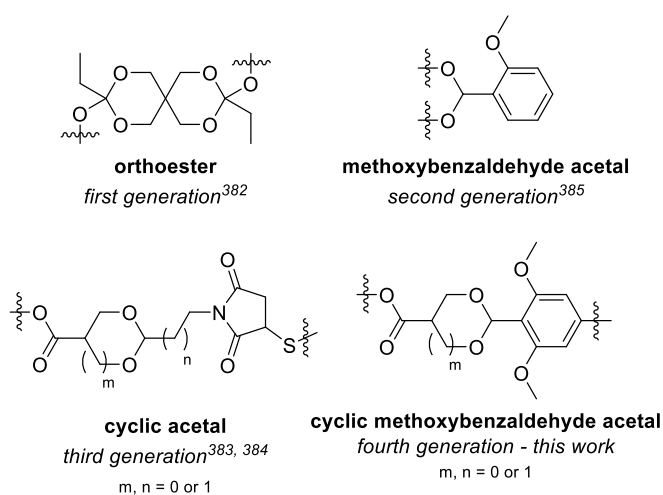


Figure 97 - Structures of acetal-based cleavable linkers

## ii. Results and discussion

### 1. Synthesis of FRET probes based on cyclic dimethoxybenzaldehyde acetal

In this regard, we elected 4-bromo-2,6-dimethoxybenzaldehyde **56** as the carbonyl source for the construction of 5- and 6-membered acetals (Figure 98). The synthetic route began with a Sonogashira coupling between aldehyde **56** and ethynyltrimethylsilane followed by a desilylation step, generating terminal alkyne **58**. Reacting the latter with either a 1,2- or a 1,3-diol in the presence of a catalytic amount of *p*-toluenesulfonic acid in refluxing toluene delivered the expected 5- and 6-membered acetals, isolated as mixtures of *cis-trans* isomers that could be readily separated at this stage. Each isomer was isolated, determined by NOESY and characterized by NMR. Esters saponification afforded carboxylic acids **61** and **62** with excellent yields, bearing now two functional groups – an alkyne and a carboxylate – that could be

employed to build the FRET probes. In this regard, an azide-containing black-hole quencher 2 (BHQ-N<sub>3</sub> **44**) was first coupled to **61** and **62** via copper-catalyzed azide-alkyne cycloaddition (CuAAC), before a BEP-mediated coupling with a TAMRA-amine derivative (TAMRA-NH<sub>2</sub> **43**) led to the final adducts **63** and **64**, isolated with a good overall yield (23%-35%).

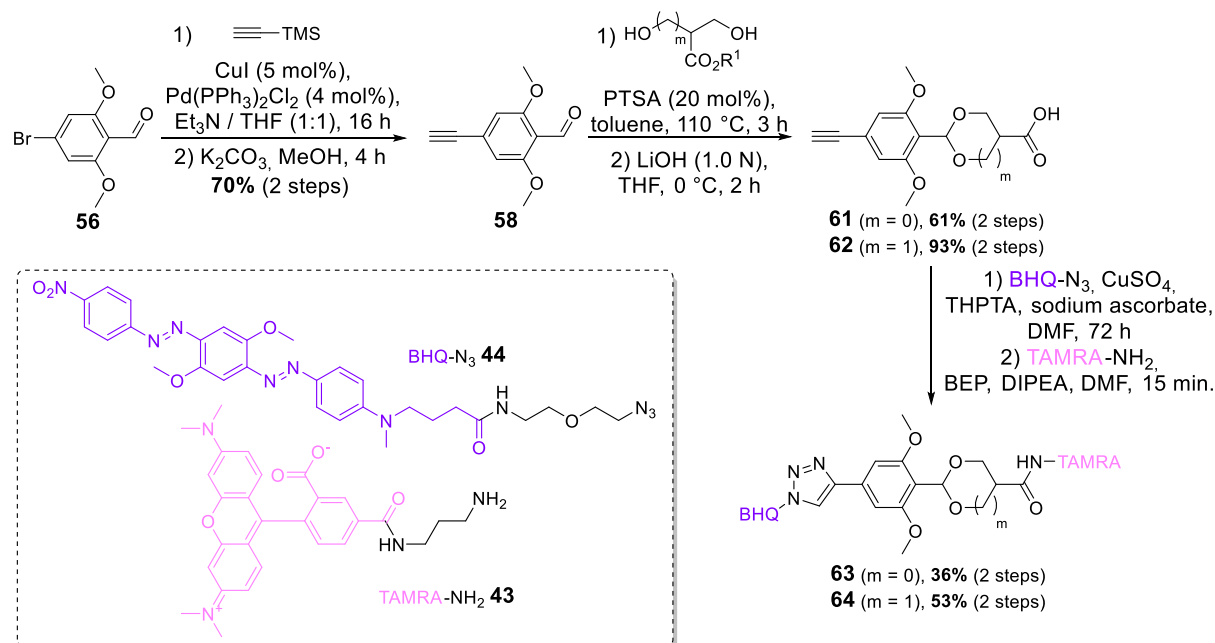


Figure 98 - Synthesis of FRET probes **63** and **64**.

## 2. Evaluation of the cleavage and stability of acetal probes in acidic media

The acid lability of our new linker family was then evaluated at different pH by measuring the appearance of fluorescence over time of a solution of **63** and **64**. The acetal cleavage should indeed lead to the separation of the TAMRA fluorophore from its BHQ quencher, resulting in the appearance and increase of fluorescence over time. Thus, our probes were incubated in human plasma and various buffers at different pH for 15 hours, and the resulting values of fluorescence were normalized to those of an equimolar solution of TAMRA and BHQ in the same buffer and at the same concentration (Figure 99). While our third-generation probes were extremely stable, even at pH < 1.0, acetals **63** and **64** were found to be readily hydrolyzed at pH ≤ 4.0, but perfectly stable at neutral pH and in human plasma, highlighting the strong influence of the 2,6-dimethoxyphenyl group on the linker's cleavability in acidic media. Contrary to what we had previously observed for other cyclic acetal probes, acidolysis rates were very similar between the 5- and 6-membered rings **63** and **64**, suggesting that the stabilization of the transient oxonium ion by the strong electron-donating 2,6-dimethoxyphenyl group overcomes other stereoelectronic aspects, such as ring size and conformation.<sup>403,404</sup>

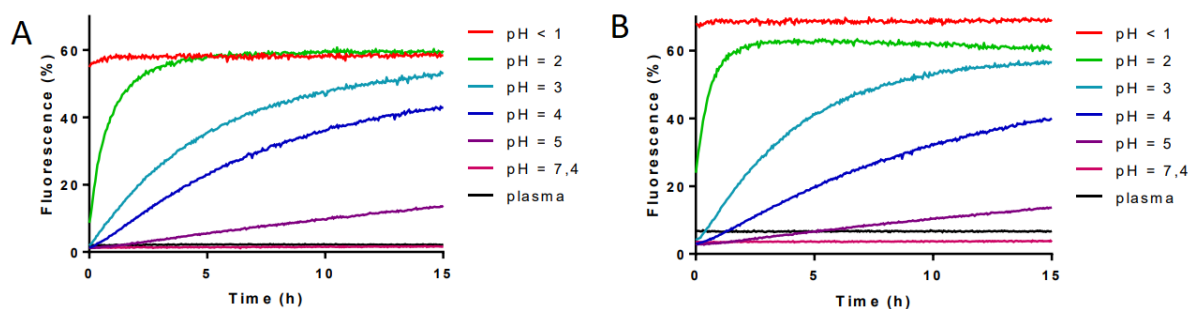


Figure 99 - Stability of probes **63** (A) and **64** (B) in human plasma and at different pH.

### 3. Evaluation of intracellular cleavage

Having observed a good balance between plasma stability and acidic lability, we moved on to the *in vitro* cleavage evaluation of the two probes in five different tumor cell lines: BNL CL.2 (mouse, liver), LS174T (human, colon), Huh7 (human, liver), MDA-MB-231 (human, breast – triple negative), and SKBR-3 (human, breast – HER2-positive) by both flow cytometry and confocal microscopy studies. As a positive control, we designed a FRET probe based on Val-Cit-PAB linker, the gold-standard cleavable linker used in ADCs.

#### a. Synthesis of FRET probe based on Val-Cit-PAB

The original synthesis of Val-Cit-PAB started with the peptide coupling between Boc-Val-OSu **65** and unprotected citrulline **66** (Figure 100).<sup>405</sup> Coupling of the dipeptide **67** with para-aminobenzyl alcohol was performed using *N*-Ethoxycarbonyl-2-ethoxy-1,2-dihydroquinoline (EEDQ) as a coupling agent. However, this reaction was slow (2 days) and yielded several side-products, as well as a mixture of diastereoisomers of **68** (*S,S/S,R* 4.5/1) because of epimerization of the citrulline moiety.

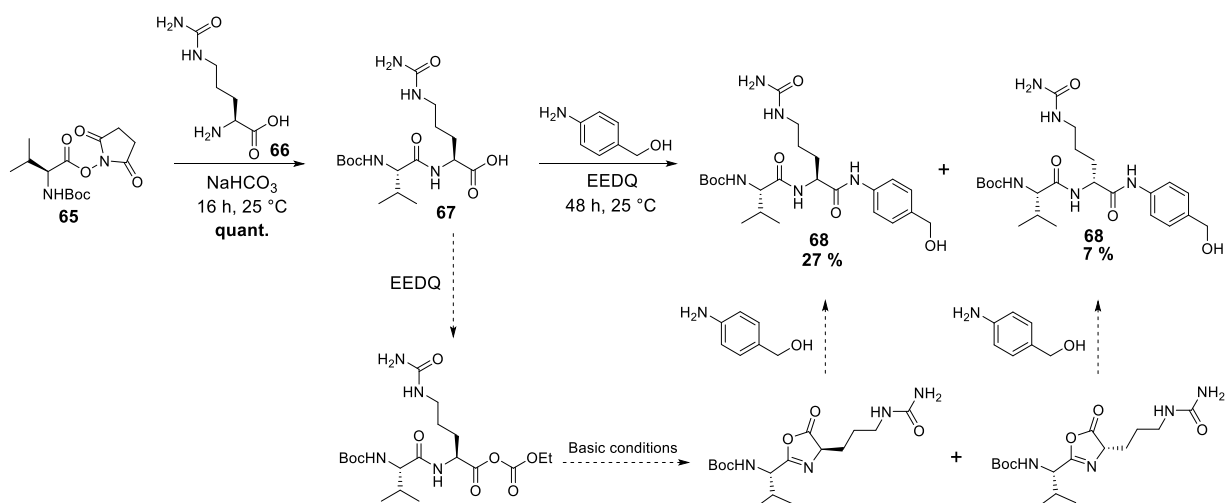


Figure 100 - Synthesis of Boc-Val-Cit-PAB linker **68**, from Dubowchik *et al*, and mechanism of epimerization.<sup>405</sup>

Following the protocol recently published by Mondal *et al*,<sup>406</sup> Boc-Val-Cit-PAB-PNP **69** was synthesized in four steps without any traces of epimerization and with higher yields (Figure

102). Fmoc-citrulline **70** was first coupled with *para*-aminobenzyl alcohol using hexafluorophosphate de (diméthylamino)-*N,N*-diméthyl(3H-[1,2,3]triazolo[4,5-b]pyridin-3-yloxy)méthaniminium (HATU) as a coupling agent, affording Fmoc-*L*-Cit-PAB **71** with 71% yield. After deprotection in basic conditions, the primary amine **72** was coupled with Boc-*L*-Val-OSu **65** to afford Boc-*L*-Val-*L*-Cit-PAB **73** in 85% yield over two steps. Activation of the benzylic alcohol with *para*-nitrophenylchloroformate (PNP-Cl) yielded Boc-Val-Cit-PAB-PNP **69**.

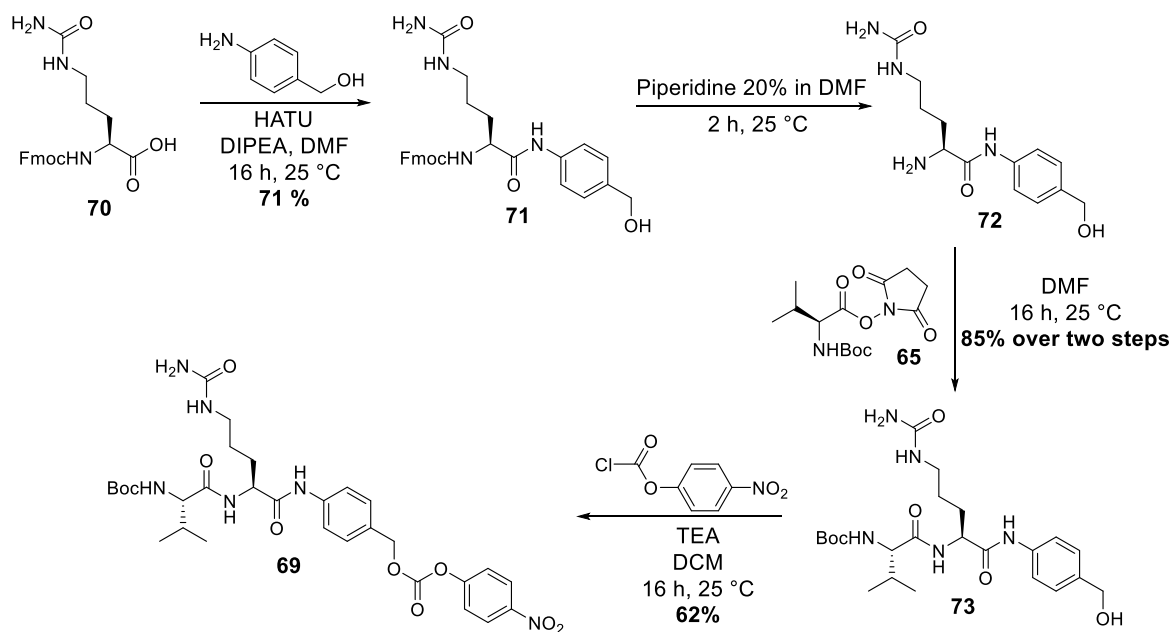


Figure 101 - Synthesis of Boc-Val-Cit-PAB-PNP, adapted from Mondal et al.<sup>406</sup>

To access to FRET probe, subsequent substitution of **69** with a high excess of H<sub>2</sub>N-PEG<sub>2</sub>-NH<sub>2</sub> gave access to the **74**. Coupling of the newly formed primary amine to BHQ-2 afforded the Boc-protected dye **75** in 41% yield using HATU. After deprotection using TFA, BEP-mediated coupling of TAMRA-butyl-CO<sub>2</sub>H **78** afforded the desired FRET probe TAMRA-Val-Cit-PAB-PEG<sub>2</sub>-BHQ **79**.



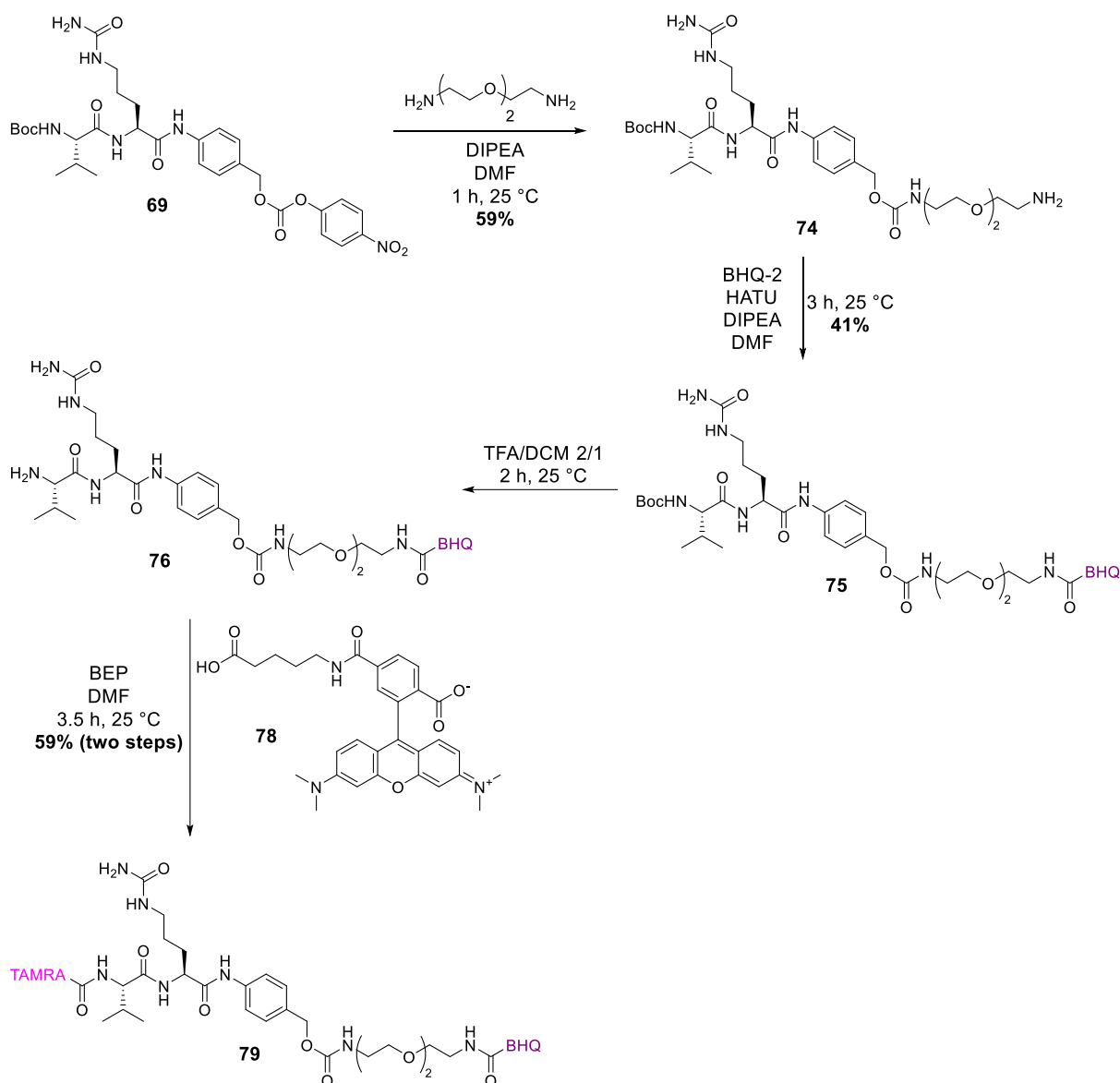


Figure 102 - Synthesis of TAMRA-Val-Cit-PAB-PEG<sub>2</sub>-BHQ probe **79**.

### b. Cellular uptake and intracellular cleavage

For the flow cytometry, cells were incubated with a 1.0 μM solution of FRET probes for different time points at 37 °C (Figure 103). A non-cleavable, negative control was also employed as negative control and fluorescence values obtained with **63** and **64** were benchmarked against the standard valine-citrulline linker **79**.<sup>407</sup> Overall, both acetal linkers showed a better cleavability than the model Val-Cit linker, with fluorescence levels up to 14 times higher for the 1,3-dioxane **64** and 20 times higher for the 1,3-dioxolane **63** in SKBR-3 cell line. On the other cell lines, this slight difference between **63** and **64** cleavages diminished even more, showing here again a lack of influence of the ring size on cleavability. Interestingly, while absolute fluorescence values tend to vary strongly depending on the cell line tested, ratios calculated

between acetals and Val-Cit values are all roughly equivalent, suggesting a lack of influence from the cell line on the global cleavability.

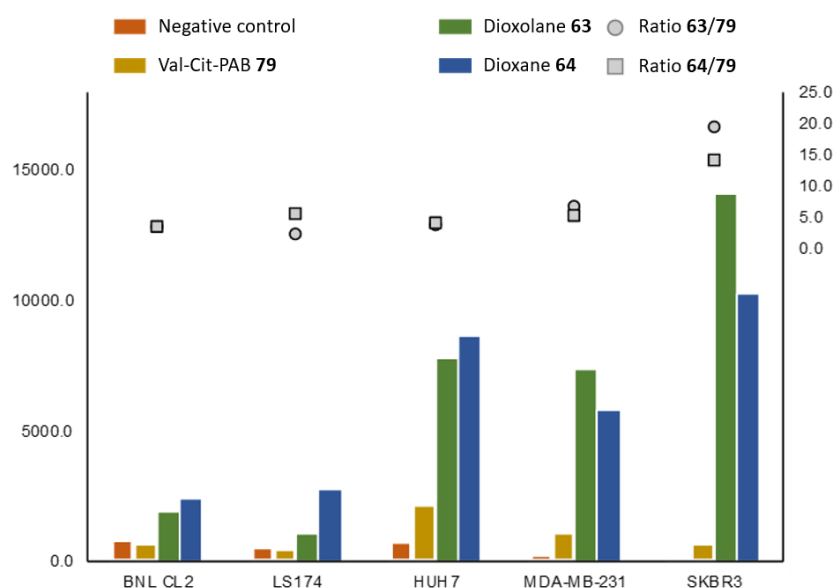


Figure 103 - Evaluation of linkers cleavability in vitro by absolute (left scale, bars) and relative (acetal / Val-Cit, right scale, dots) fluorescence intensity measures.

In order to discard the possibility that these molecules are not internalized in the same way, a cellular uptake study was performed. After incubation of each FRET probes in cells for microscopy, the supernatants were collected and serum proteins were precipitated in cold acetonitrile. Each sample were then supplemented with TAMRA as internal standard and injected in analytical RP-HPLC. Integration of the FRET probe peak was standardized by the internal standard, and total concentration in probe of the sample was calculated by using calibrations curves (Table 6). Overall, the results showed a similar cellular uptake, independent on the probe's structure. Therefore, each compound can be compared by flow cytometry and microscopy studies.

Table 6 - Cellular uptake of FRET probes.

	Concentration in cell media after 90 min	Remaining in cell media (%)
Val-Cit-PAB <b>79</b>	1.70	34.06%
Dioxolane <b>63</b>	1.85	36.98%
Dioxane <b>64</b>	1.97	39.37%

Following these results, fluorescent microscopy studies were performed in order to validate the lysosome-specific cleavage. By incubating all three FRET probes **79** (Figure 104), **64** (Figure 105) and **63** (Figure 106) at 5  $\mu$ M for 90 min in live SKBR-3, and using Lysosensor to

label endo/lysosomes. In lines with the flow cytometry study, the Val-Cit-PAB **79** probe showed a low intracellular cleavage in these conditions and the two acetal **63** and **64** exhibited a significantly higher cleavage rate. In addition, we were pleased to observe that the red fluorescence from cleaved TAMRA partly co-localized with the green LysoSensor dye. These results thus demonstrated the lysosome-specificity of the cleavage *in cellulo*.

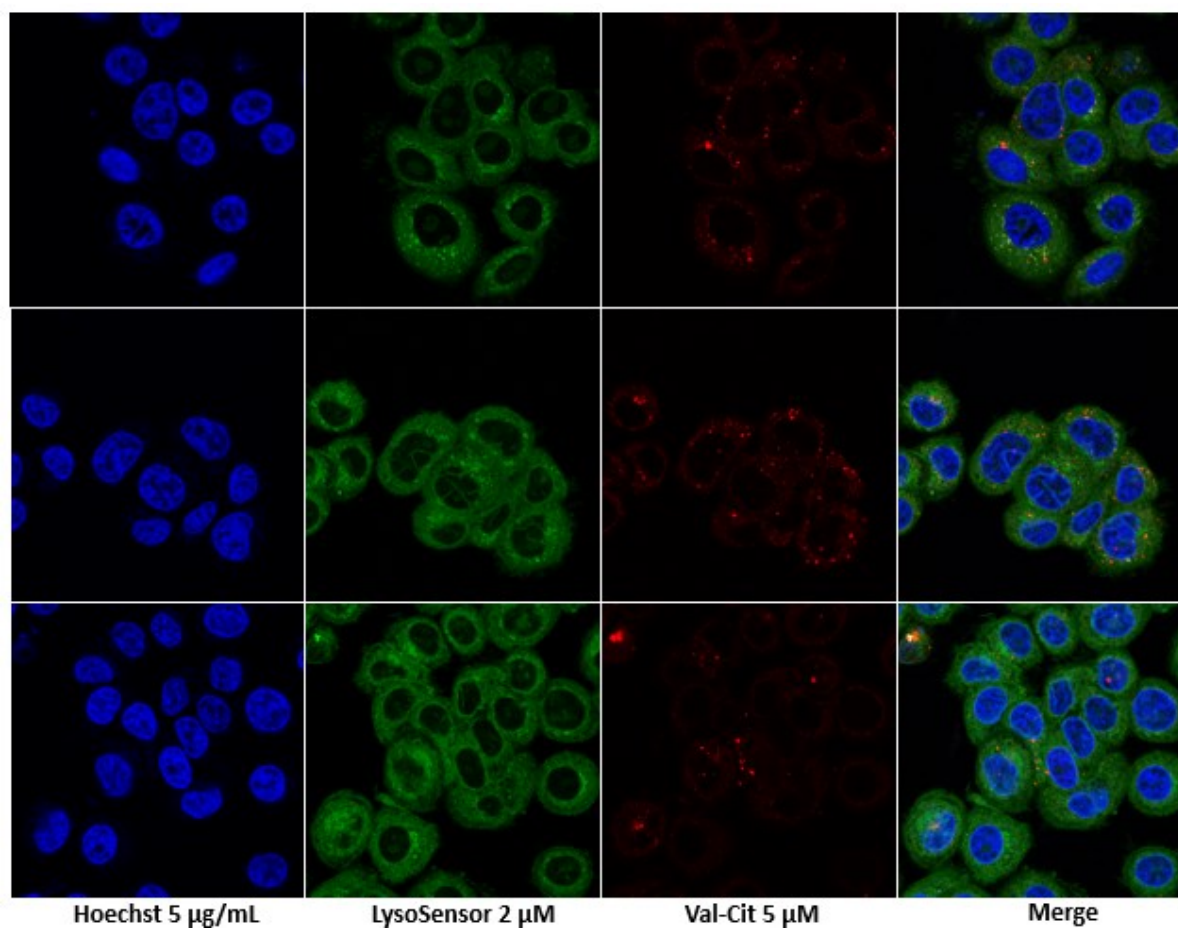


Figure 104 - Fluorescence microscopy study after incubation of 5 µM of the Val-Cit-PAB FRET probe **79** in SKBR-3 cell line after 90 min of incubation. In blue, the nucleus, in green, the endo/lysosome stained by LysoSensor green, and in red the fluorescent of cleaved-TAMRA.

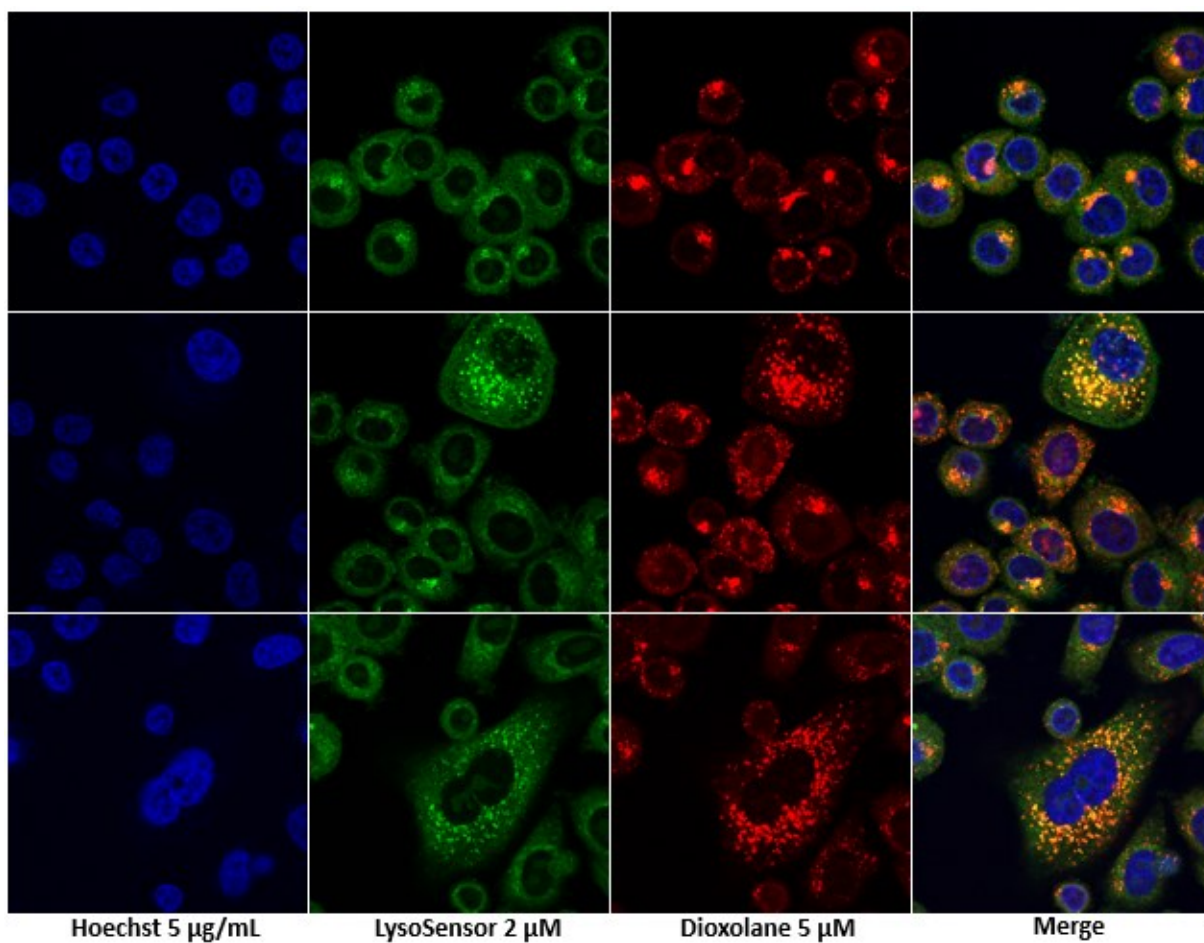


Figure 105 - Fluorescence microscopy study after incubation of 5 µM of the dioxolane probe 64 in SKBR-3 cell line after 90 min of incubation. In blue, the nucleus, in green, the endo/lysosome stained by LysoSensor green, and in red the fluorescent of cleaved-TAMRA.

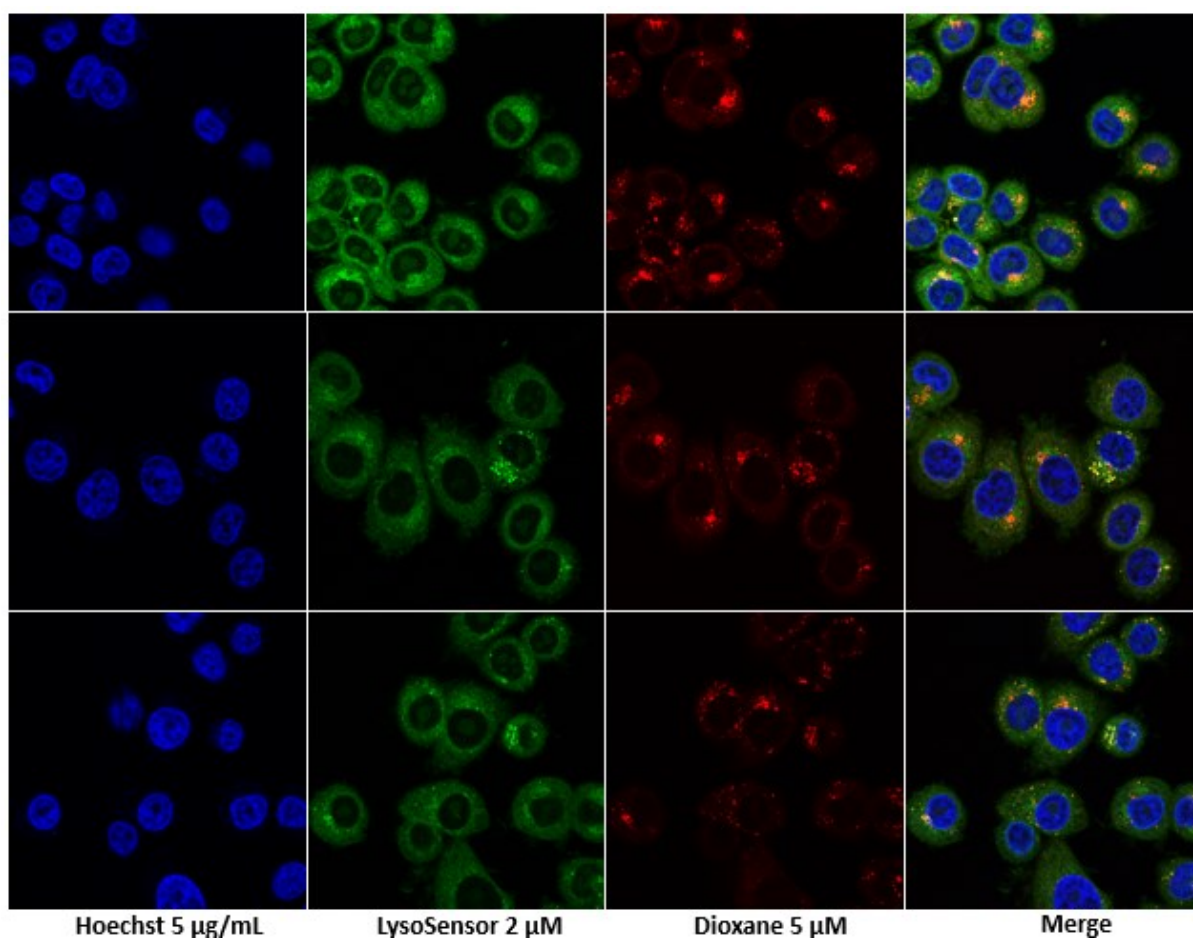


Figure 106 -Fluorescence microscopy study after incubation of 5  $\mu\text{M}$  of the dioxane FRET probe **63** in SKBR-3 cell line after 90 min of incubation. In blue, the nucleus, in green, the endo/lysosome stained by LysoSensor green, and in red the fluorescent of cleaved-TAMRA.

### iii. Conclusion

By designing this fourth generation of cyclic methoxybenzaldehyde acetals, we thus bridged the gap existing between excellent plasma stability and acidic lability in our previously reported structures. We showed that the electron-donating properties of the acetal carbon substituent was key to the cleavability of our linkers, and that these were as labile as the standard Val-Cit. Altogether, these results indicate that this new class of acid-labile linker might be excellent candidates for payload-release applications where lysosomal trafficking is expected.

These results, along with the high stability found in plasma, indicate that these new cyclic acetals might be good candidates as cleavable motifs for payload-release applications. Indeed, we demonstrated that these molecules were more cleaved in cells than the gold-standard Val-Cit-PAB, while being extremely stable in human plasma.

#### iv. Further developments

##### 1. Production of antibody-siRNA conjugates with the 1,3-dioxane linker

Following these results, antibody-siRNA conjugate using the 1,3-dioxane linker was synthesized in order to conclude on the effect of cleavable linkers for ARC. A BCN-containing linker activated by a pentafluorophenol ester was thus synthesized from **60** (Figure 107). Copper-catalyzed azide-alkyne cycloaddition (CuAAC) was performed using  $\text{CuSO}_4$ , freshly synthesized THPTA **84**, sodium ascorbate, and using a short azido-PEG<sub>3</sub>-amine. The resulting amine **85** was then reacted with activated BCN **15** to afford **86**. Saponification of the methyl ester **86** under smooth conditions was performed, and the resulting **87** was activated with pentafluorophenyl carbonate to afford **88**.

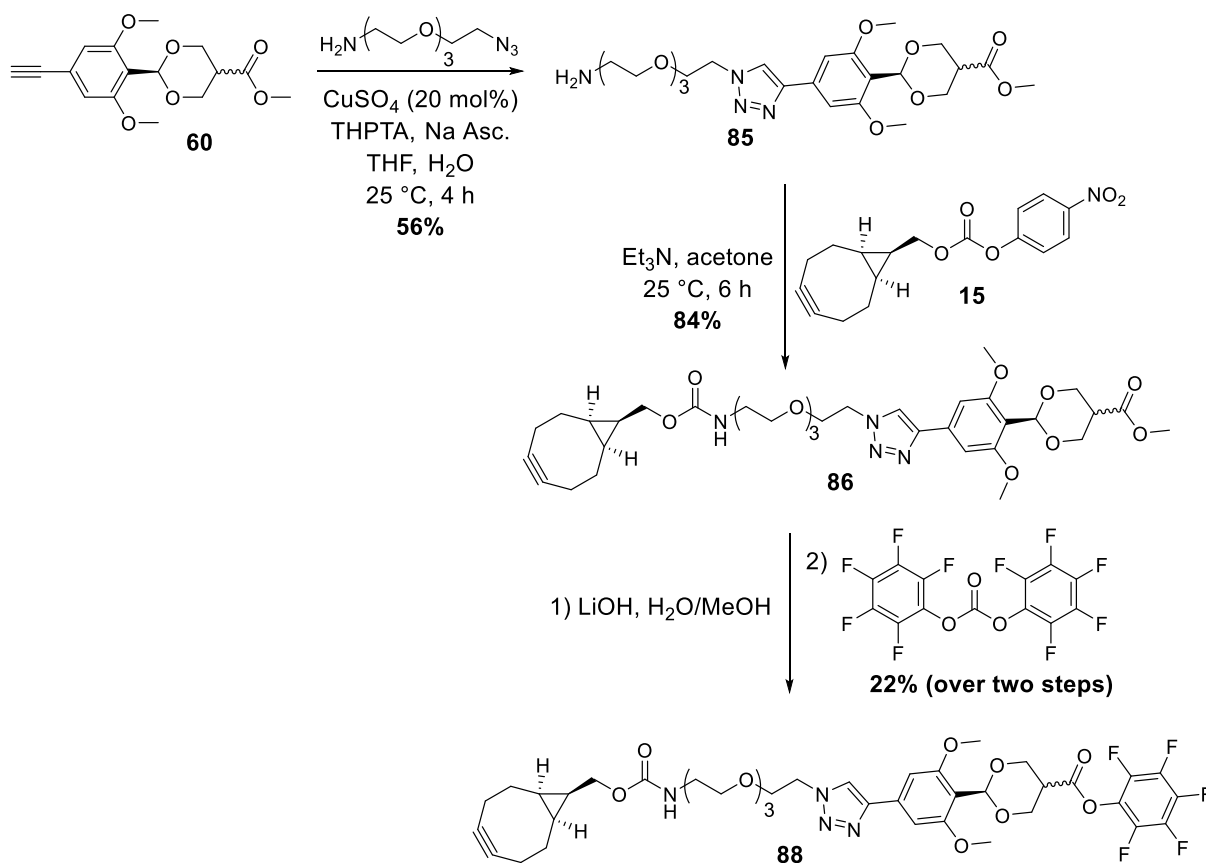


Figure 107 - Synthesis of BCN-PEG<sub>3</sub>-acetal-PFP linker **88**.

Conjugation of this molecule **88** on the 3'-amino RNA strand **23** was performed in the same conditions as with the classical PEG<sub>6</sub> linker **6**, yielding the desired BCN-acetal-RNA **89**. After hybridization with the complementary 5'-ppp RNA strand, conjugation to antibody-azide **3** afforded ARC **90**, which was characterized by mass spectrometry (Figure 108).

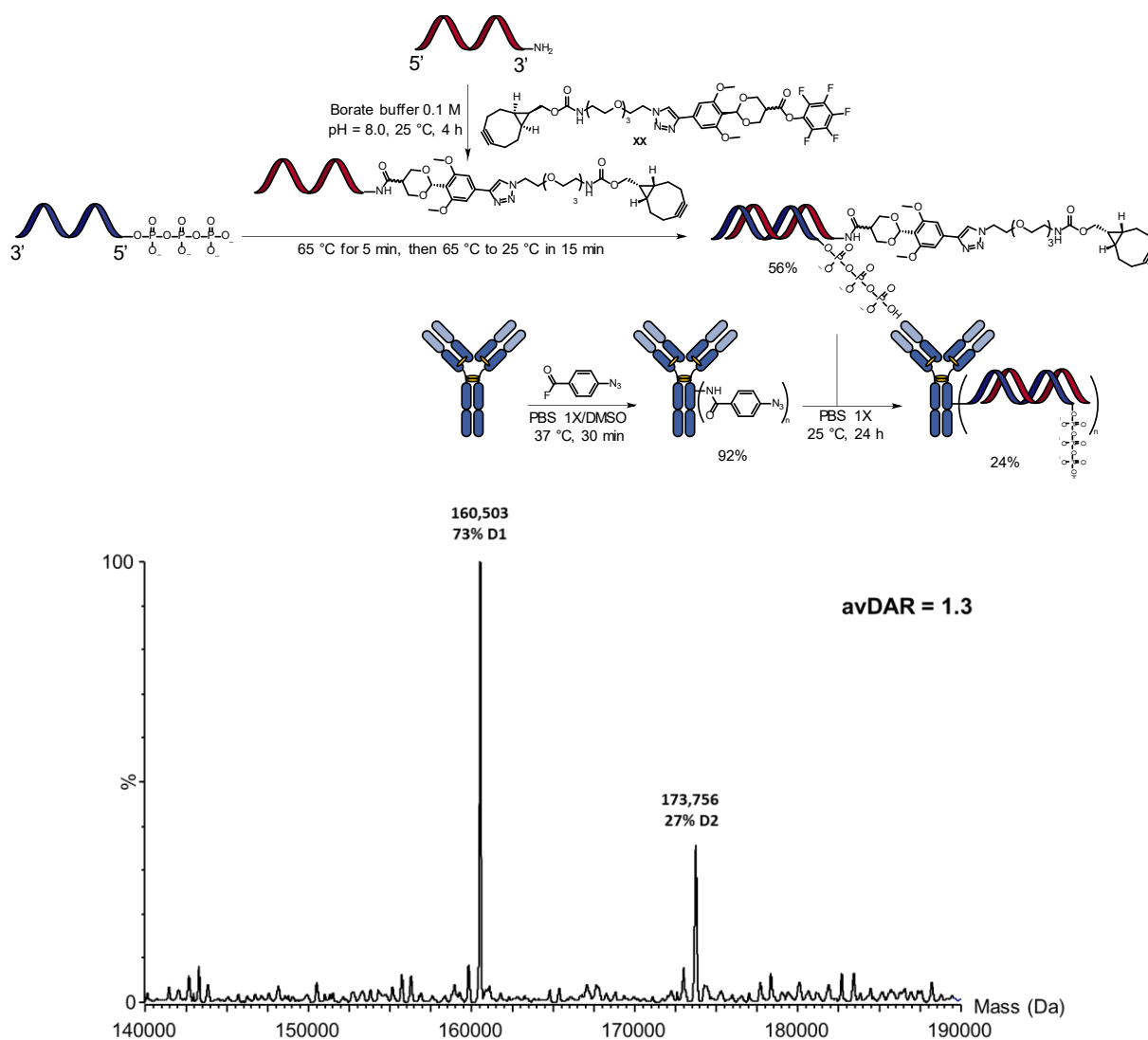


Figure 108 - Synthesis of ARC 90 using the BCN-PEG<sub>3</sub>-acetal-PFP linker 88 and resulting MS spectra.

## 2. Production of antibody-siRNA conjugates with the Val-Cit-PAB linker

In order to compare with a Val-Cit-PAB linker, a strained-alkyne derivative of this dipeptide was synthesized (Figure 109). Starting from Boc-Val-Cit-PAB **73**, deprotection of the Boc group and subsequent coupling with activated BCN **15** yielded BCN-Val-Cit-PAB **92** in 62% yield over two steps. Activation of the benzylic alcohol with *para*-nitrophenylchloroformate (PNP-Cl) gave access to the target molecule **93**.

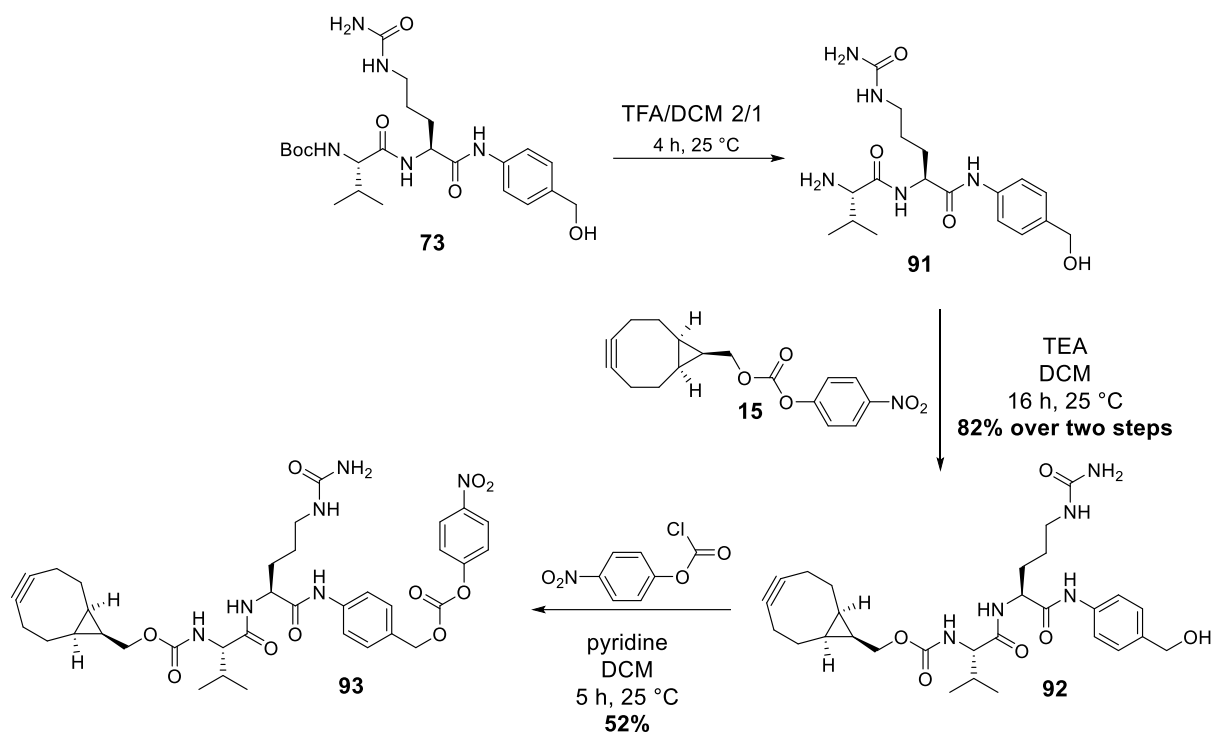


Figure 109 - Synthesis of BCN-Val-Cit-PAB-PNP linker **93**.

Attempts of conjugation of this linker on the 3'-amino-ssRNA **23** in borate buffer 0.1 M pH = 8.0 failed, as we observed a too high hydrolysis rate of the linker, yielding the unactivated molecules **92**. Replacing the buffer by PBS 1X afforded the desired clickable Val-Cit-PAB-RNA **94**, but due to a bad conversion, the isolated yield was only 24%. After hybridization with the complementary 5'-ppp RNA strand, conjugation to antibody-azide **3** afforded the ARC **95**, which was characterized by mass spectrometry (Figure 110).



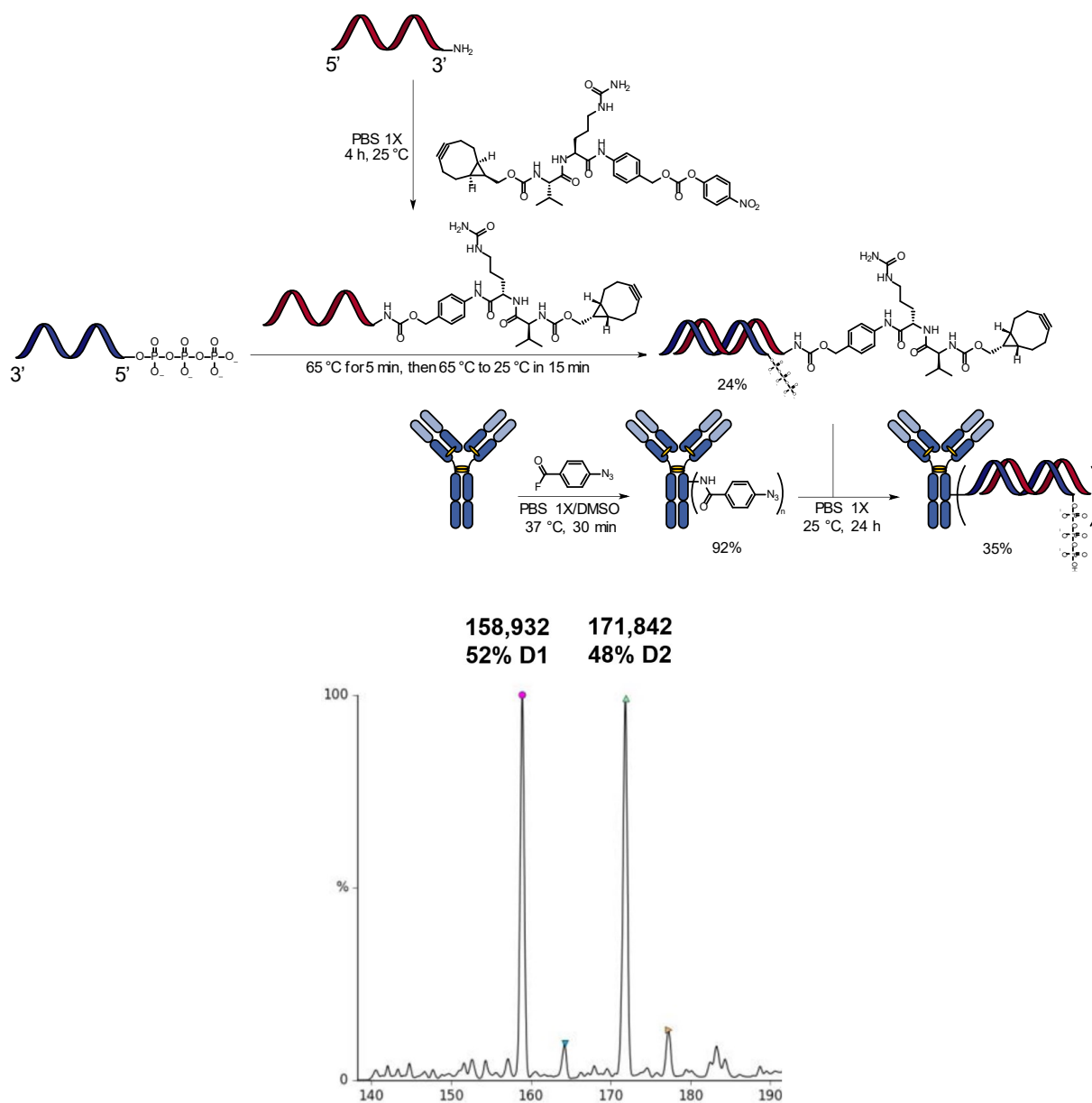


Figure 110 - Synthesis of ARC 95 using the BCN-Val-Cit-PAB-PNP linker 93 and resulting MS spectra.

In order to evaluate the impact of cleavable linkers for the targeted delivery of siRNA, we used the same RIG-I activation assay as in chapter IV (page 82). Three antibody-siRNA conjugates were produced, each with a different linker: the BCN-PEG<sub>6</sub> 6, the BCN-Val-Cit-PAB 93, or the BCN-acetal 88 (Figure 111).

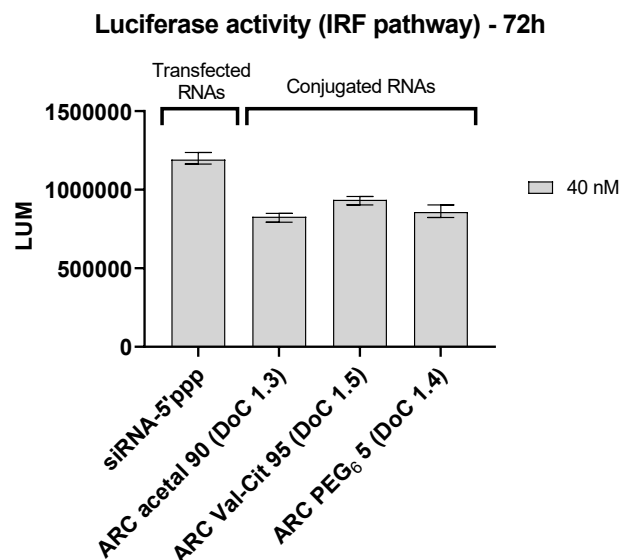


Figure 111 - Luciferase assay to validate an activity on RIG-I signaling using both non-cleavable and cleavable linkers.

All conjugates elicited a similar activity on RIG-I's pathway; therefore, we suggest that the cleavability of the linker for antibody-siRNA conjugate is not an important parameter for the activity. This observation thus confirmed previously published data from Cuellar *et al.*<sup>322</sup> et Sugo *et al.*<sup>327</sup> Therefore, it appears that another, unknown mechanism, should happen in this case to explain how the siRNA is separated from the antibody. Rader's group suggested that the phosphodiester bond between the siRNA and its linker could be cleaved by lysosomal phosphatase,<sup>326</sup> because they attached their linker as a phosphoramidite derivative. However, according to the oligonucleotide manufacturer that synthesized our RNA, our constructs did not contain such phosphodiester group at the 3'-end. Accordingly, at the moment, the structure of the active metabolite from ARC remains elusive. Metabolomic studies could possibly give a hint, but difficulties on running such analyses on oligonucleotide fragments should not be underestimated.

Following these results, we embarked on a more classical approach to evaluate the possible benefits gained by using highly efficient cleavable linkers, and started the conjugation of small molecule drugs. We used two types of drugs: MMAF-tBu **96**, a highly cytotoxic drug commonly used in the ADC field, and gemcitabine **97**, a nucleoside analogue currently used as a chemotherapy drug. We have chosen MMAF-tBu **96** because of its high cytotoxicity, and gemcitabine **97** because of its poorly membrane-permeable properties.<sup>408</sup> These works are currently on-going, and are performed with the help of Lorenzo Turelli (PhD student in our team).

### 3. Production of antibody-drug conjugates with the 1,3-dioxane linker

#### a. Derivatization of MMAF

The synthesis of MMAF-derivatized acetal linker **98** for ADCs was performed by HATU-mediated acylation of MMAF's secondary amine with **62** (Figure 112). In order to avoid any side-reactions due to MMAF free carboxylic acid, we decided to use a commercially available *tert*-butyl ester derivative of MMAF. After purification by reverse-phase semi-preparative HPLC, the compound **98** was obtained with 20% isolated yield.

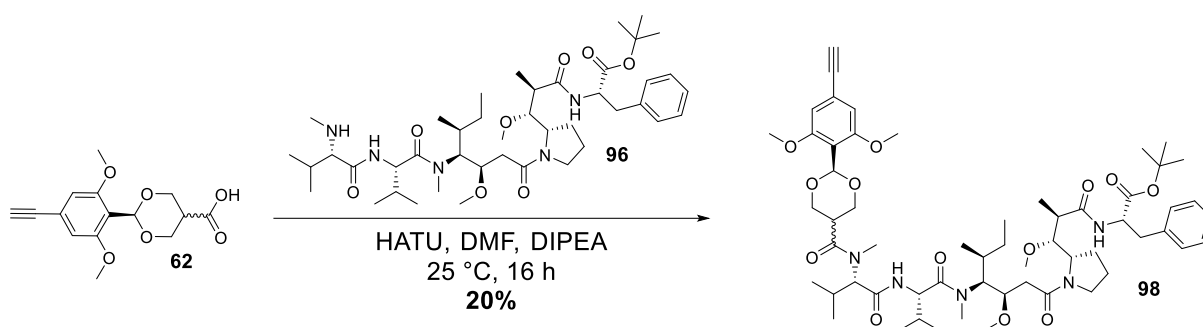


Figure 112 - Synthesis of acetal-MMAF-tBu **98**.

#### b. Derivatization of gemcitabine

The synthesis of gemcitabine-acetal **99** was performed in 5 steps, starting from the commercially available drug **97** (Figure 113). Following one publication, we sought to synthesize Fmoc-protected gemcitabine **102**, using a slightly different protocol than the published one.<sup>409</sup> Protection of the primary and secondary alcohol of gemcitabine **97** was performed using *tert*-butyl-dimethylsilyl chloride, catalyzed by imidazole. The primary amine **100** was then protected with Fmoc-OSu in pyridine, to afford fully-protected gemcitabine **101**. The original synthesis used triethylamine instead of pyridine, which resulted in the deprotection of the target molecule and bad yield. Silyl ethers deprotection was then conducted using Olah's reagent (HF/pyridine, 70% HF) in a Teflon flask, affording **102** in almost quantitative yield, without any purification for the last three steps. COMU-mediated esterification of the free alcohol **102** with acetal **62** afforded a mixture of mono- and di-esterified Fmoc-gemcitabine, and the mono-esterified product **103** was isolated with 27% yield after purification by reverse-phase semi-preparative HPLC. Fmoc-deprotection using piperidine is planned as a future last step to produce the final acetal **99**.

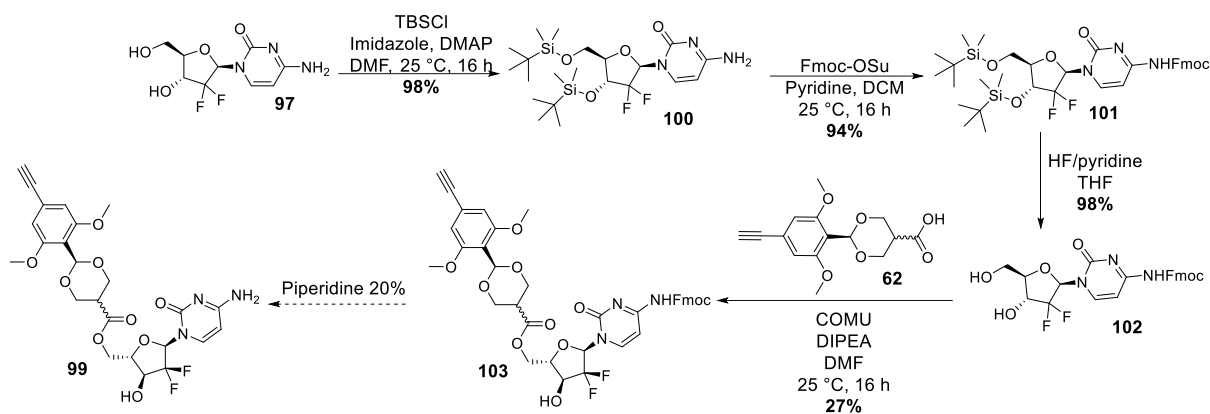


Figure 113 - Synthesis of acetal-gemcitabine **99**.

In order to release the native gemcitabine, our linker is supposed to be cleaved inside lysosomes, and we expect that non-specific esterases could hydrolyze the resulting ester.

### c. Planned strategy to produce ADCs

Our strategy is to perform copper-catalyzed alkyne-azide cycloaddition on trastuzumab-azide. The latter was easily accessible by reacting a perfluorophenol-activated PEG<sub>4</sub>-N<sub>3</sub> on trastuzumab, for 3 h, at 37 °C. Currently, trials to attach the terminal alkyne to trastuzumab-azide are on-going. However, our first trials with a model TAMRA-acetal-alkyne (i.e containing the same structure of acetal) gave encouraging results when characterized by native ESI-MS (Figure 114). Briefly, a catalyst solution containing CuSO<sub>4</sub>/THPTA/aminoguanidine/sodium ascorbate (molar ratios 1/2/10/15) was used, and we used 20 equivalents of copper sulfate compared to the trastuzumab-azide.

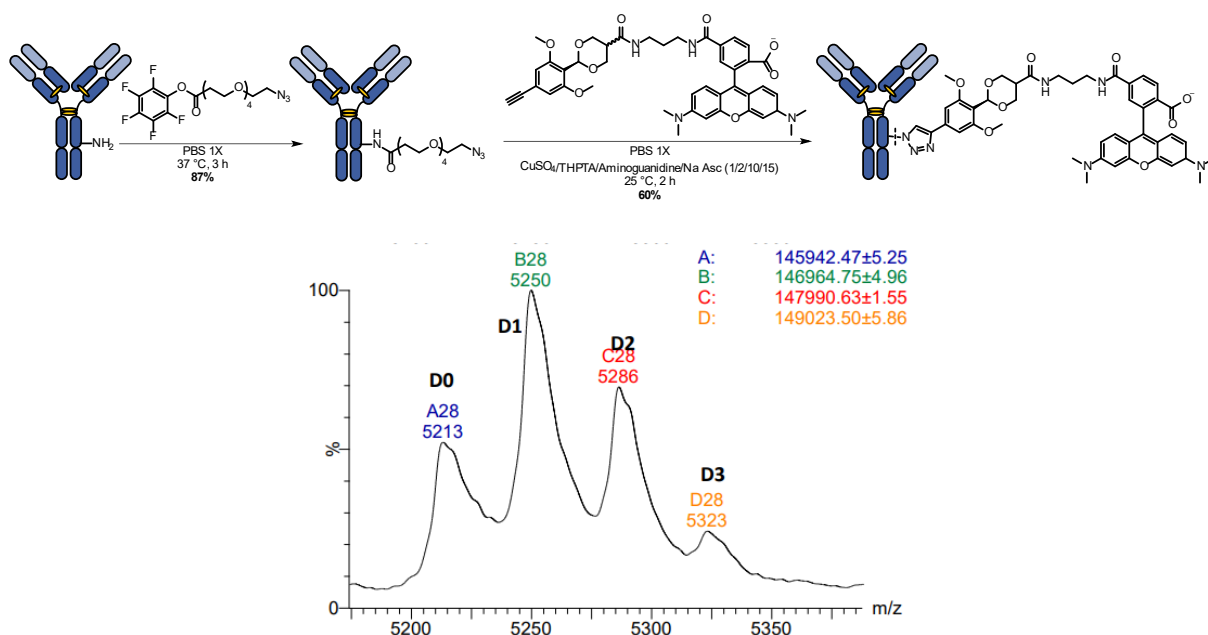
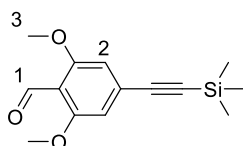


Figure 114 – Synthesis of trastuzumab-alkyne following our planned strategy and resulting MS spectrum.

## v. Experimental part

### Chemical syntheses and characterizations

#### 2,6-Dimethoxy-4-((trimethylsilyl)ethynyl)benzaldehyde **57**



A degassed mixture of THF and triethylamine (1:1, v/v; 20 mL) was transferred into a flask containing commercially available 4-bromo-2,6-dimethoxybenzaldehyde **56** (1.0 equiv., 1.0 g, 4.08 mmol), CuI (5 mol%, 38.9 mg, 0.20 mmol), and dichlorobis(triphenylphosphine) palladium (3 mol%, 85.9 mg, 0.12 mmol) before ethynyltrimethylsilane (1.1 equiv., 440.0 mg, 638.0  $\mu$ L, 4.49 mmol) was added. The solution became orange then black within seconds and the mixture was stirred at 25 °C for 16 h under argon atmosphere. The mixture was then diluted with DCM (50 mL), washed with an aqueous solution of NH<sub>4</sub>Cl (sat., 2 x 40 mL), and brine (40 mL). The organic layer was then dried over MgSO<sub>4</sub>, filtered and concentrated under reduced pressure. The crude was purified by flash column chromatography (cyclohexane/EtOAc 100:0 to 70:30 over 30 min) to afford the title compound **57** (1.05 g, 4.00 mmol, 98%) as a white solid.

**R<sub>f</sub>** = 0.42, cyclohexane/EtOAc 9:1

**mp** = 112 °C

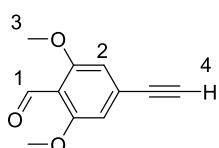
**v<sub>max</sub> (thin film) /cm<sup>-1</sup>**: 2952 (w), 2152 (w), 1681 (m), 1596 (m), 1556 (m), 1458 (m), 1400 (m), 1246 (s), 1123 (s), 983 (m), 833 (s), 733 (s), 692 (s)

**<sup>1</sup>H NMR (400 MHz, CDCl<sub>3</sub>)  $\delta$**  10.45 (s, 1H, H1), 6.66 (s, 2H, H2), 3.89 (s, 6H, H3), 0.27 (s, 9H, TMS)

**<sup>13</sup>C NMR (101 MHz, CDCl<sub>3</sub>)  $\delta$**  189.0, 162.0, 130.4, 114.7, 107.7, 104.3, 98.3, 56.4

**HR-ESI-MS (M+H<sup>+</sup>)**: Calc. 262.1025, found 262.1023

#### 4-Ethynyl-2,6-dimethoxybenzaldehyde **58**



2,6-dimethoxy-4-((trimethylsilyl)ethynyl)benzaldehyde **57** (1.0 equiv., 600.0 mg, 2.29 mmol) was added to a suspension of K<sub>2</sub>CO<sub>3</sub> (0.2 equiv., 63.2 mg, 0.48 mmol) in MeOH (10 mL). The orange mixture was stirred for 4 h at 25 °C before being concentrated to dryness. The resulting solid was resuspended in DCM (20 mL) and washed with an aqueous solution of NaHCO<sub>3</sub> (sat., 3 x 20 mL). The organic layer was then dried over MgSO<sub>4</sub>, filtered and concentrated under reduced pressure. Purification by flash column chromatography (cyclohexane/EtOAc 100:0 to 50:50 over 30 min) afforded the title compound **58** (400.0 mg, 2.1 mmol, 92%) as a brown solid.

**R<sub>f</sub>** = 0.32, cyclohexane/EtOAc 8:2

**mp**: 110 °C

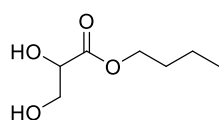
**v<sub>max</sub> (thin film) /cm<sup>-1</sup>**: 3230 (w), 2942 (w), 2866 (w), 2781 (w), 2100 (w), 1680 (s), 1594 (s), 1557 (s), 1456 (m), 1401 (s), 1231 (s), 1190 (m), 1122 (s), 833 (m)

**<sup>1</sup>H NMR (400 MHz, CDCl<sub>3</sub>)** δ 10.46 (s, 1H, H1), 6.70 (s, 2H, H2), 3.90 (s, 6H, H3), 3.25 (s, 1H, H4)

**<sup>13</sup>C NMR (101 MHz, CDCl<sub>3</sub>)** δ 188.7, 161.8, 129.1, 114.7, 107.7, 82.9, 80.1, 56.2

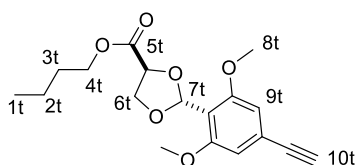
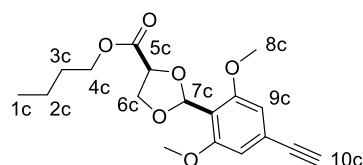
**HR-ESI-MS (M+Na<sup>+</sup>):** Calc. 213.0522, found 213.0519

#### Butyl 2,3-dihydroxypropanoate **104**



This compound was synthesized according to a reported procedure.

#### Butyl 2-(4-ethynyl-2,6-dimethoxyphenyl)-1,3-dioxolane-4-carboxylate **59**



A solution of butyl 2,3-dihydroxypropanoate **102** (3.0 equiv., 1.15 g, 7.10 mmol), 4-ethynyl-2,6-

dimethoxybenzaldehyde **58** (1.0 equiv., 450.0 mg, 2.37 mmol) and PTSA (0.2 equiv., 81.5 mg, 0.47 mmol) was refluxed in toluene (30 mL) using Dean-Stark apparatus for 2 h. Toluene was evaporated, before the residue was dissolved in EtOAc (20 mL), and washed with saturated solutions of NaHCO<sub>3</sub> (20 mL) and brine (20 mL). The organic layer was then dried over MgSO<sub>4</sub>, filtered and concentrated under reduced pressure. Purification by flash column chromatography (cyclohexane/EtOAc 100:0 to 30:70 over 40 min) afforded the title compound **59** (730 mg, *cis/trans* 20:80, 2.18 mmol, 92%) as a colorless oil.

**R<sub>f</sub>** = 0.22, cyclohexane/EtOAc 5:5

**mp:** 119 °C

**v<sub>max</sub> (thin film) /cm<sup>-1</sup>:** 3261 (w), 2936 (w), 2837 (w), 1743 (m), 1702 (m), 1597 (s), 1461 (s), 1411 (s), 1316 (s), 1225 (s), 1119 (s), 1065 (m), 838 (m), 731 (m)

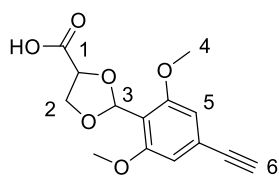
**<sup>1</sup>H NMR (400 MHz, CDCl<sub>3</sub>)** δ (*cis/trans* mixture) 6.71 (s, 1H, H7<sub>t</sub>), 6.68 (s, 2H, H9<sub>t</sub>), 6.66 (s, 2H, H9<sub>c</sub>), 6.55 (s, 1H, H7<sub>c</sub>), 4.79 (dd, *J* = 6.9 Hz, 6.1 Hz, 1H, H5<sub>t</sub>), 4.66 (dd, *J* = 7.6 Hz, 5.7 Hz, 1H, H5<sub>c</sub>), 4.48 (dd, *J* = 7.9 Hz, 6.9 Hz, 1H, H6<sub>t</sub>), 4.41 (dd, *J* = 7.8 Hz, 5.8 Hz, 1H, H6<sub>c</sub>), 4.28-4.16 (m, 5H, H6<sub>c</sub> + H4<sub>c/t</sub>), 4.02 (dd, *J* = 7.9 Hz, 6.1 Hz, 1H, H6<sub>t</sub>), 3.81 (s, 6H, H8<sub>t</sub>), 3.77 (s, 6H, H8<sub>c</sub>), 3.09 (s, 2H, H10<sub>c/t</sub>), 1.70-1.61 (m, 4H, H3<sub>c/t</sub>), 1.45 – 1.35 (m, 4H, H2<sub>c/t</sub>), 0.95 (t, *J* = 7.4 Hz, 6H, H1<sub>c/t</sub>).

**<sup>13</sup>C NMR (101 MHz, CDCl<sub>3</sub>, s ppm):** (*cis/trans* mixture) 171.4 (*c/t*), 159.5 (*c/t*), 124.6 (*c/t*), 113.5 (*c/t*)\*, 108.3 (*c/t*), 100.0 (*c/t*), 83.6 (*c/t*), 77.8 (*c/t*), 75.0 (*c/t*), 69.1 (t), 68.0 (c), 66.2 (c), 65.4 (t), 56.2 (t), 56.1 (c), 30.7 (*c/t*), 19.2 (*c/t*), 13.8 (*c/t*).

\* = determined by <sup>1</sup>H-<sup>13</sup>C HMBC

**HR-ESI-MS (M+H<sup>+</sup>):** Calc. 334.1416, found 334.1411

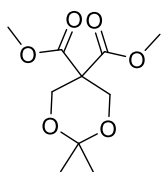
### 2-(4-Ethynyl-2,6-dimethoxyphenyl)-1,3-dioxolane-4-carboxylic acid **61**



Butyl 2-(4-ethynyl-2,6-dimethoxyphenyl)-1,3-dioxolane-4-carboxylate **59** (1.0 equiv., 300.0 mg, *cis/trans* 25:75, 0.90 mmol) was dissolved in THF at 0 °C, before lithium hydroxide (3.0 equiv., 0.5 M in water, 5.4 mL, 2.69 mmol) was added. The reaction was stirred for 6 h at room temperature before being concentrated to dryness. An aqueous solution of NH<sub>4</sub>Cl (sat., 5 mL) was added and the crude was extracted with EtOAc (3 x 10 mL). The organic layers were combined, dried over MgSO<sub>4</sub>, filtered and concentrated *in vacuo* to afford the title compound **61** (250 mg, 0.88 mmol, 98%) as a white solid, which was used in the next step without further purification.

**HR-ESI-MS (M):** Calc. 278.0790 found 278.0782

### 5,5-dimethyl 2,2-dimethyl-1,3-dioxane-5,5-dicarboxylate **106**

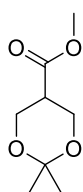


To a solution of dimethyl 2,2-bis(hydroxymethyl)malonate (1 eq., 5 g, 26 mmol) in 2,2-dimethoxypropane (7.79 eq., 21.1 g, 25.1 mL, 202 mmol) was added APTS (10 %, 0.448 g, 0.419 mL, 2.6 mmol). The mixture is stirred at room temperature for 1 hour. The mixture was poured into a 5% (w/v) aqueous solution of NaHCO<sub>3</sub> (40 mL) and toluene (60 mL) was added. The organic layer was washed with brine then dried over MgSO<sub>4</sub> and solvents were removed *in vacuo* to afford the title compound **106** (5.4 g, 23.3 mmol, 89 %) as a colorless oil which is used without further purification.

**<sup>1</sup>H NMR (400MHz, CDCl<sub>3</sub>, δ ppm):** 4.31 (s, 4 H), 3.79 (s, 6 H), 1.43 (s, 6 H).

**<sup>13</sup>C NMR (100MHz, CDCl<sub>3</sub>, δ ppm):** 168.4, 98.6, 62.5, 53.8, 53.0, 23.5.

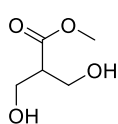
### methyl 2,2-dimethyl-1,3-dioxane-5-carboxylate **107**



To a solution of 5,5-dimethyl 2,2-dimethyl-1,3-dioxane-5,5-dicarboxylate **106** (1 eq., 5.4 g, 23.3 mmol) in DMSO (20.8 mL) was added LiCl (2 eq., 1.97 g, 0.957 mL, 46.5 mmol) and water (1 eq., 0.419 g, 0.419 mL, 23.3 mmol). The mixture was refluxed at 160°C for 2 hours then cooled to 0°C. To the batch were added water (50 mL) and EtOAc (100 mL), and the batch was then filtered. To the resulting filtrate was added EtOAc (30 mL), and the organic layer was washed with brine (50 mL), dried on MgSO<sub>4</sub> and concentrated *in vacuo* (carefully, product is volatile) to the title compound **107** (2.1 g, 12.1 mmol, 52 %) as a yellowish oil, which was used in the next step without purification.

**<sup>1</sup>H NMR (400MHz, CDCl<sub>3</sub>, δ ppm):** 4.02 - 4.12 (m, 4 H), 3.72 (s, 3 H), 2.78 - 2.86 (m, 1 H), 1.42 (s, 3 H), 1.45 ppm (s, 3 H)

### methyl 3-hydroxy-2-(hydroxymethyl)propanoate **108**

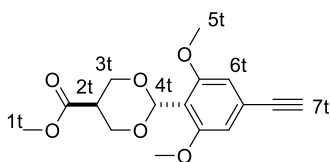
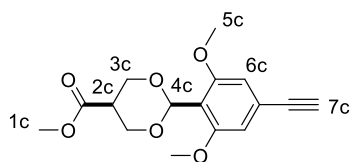


To a solution of methyl 2,2-dimethyl-1,3-dioxane-5-carboxylate **107** (1 eq., 2.1 g, 12.1 mmol) in MeOH (15 mL) was added HCl (0.6 eq., 6 M, 1.21 mL, 7.23 mmol) at 25 °C and the mixture is stirred overnight. To the batch was added NaHCO<sub>3</sub> (6.5 eq., 6.58 g, 78.4 mmol), then the mixture was filtered and washed with EtOAc (50 mL) twice. The filtrate was concentrated in vacuo and purified by flash chromatography (cHex/EtOAc 100/0 to 0/100 then DCM 100%) to afford the title compound **108** (1.55 g, 11.6 mmol, 96 %) as a yellow oil.

**<sup>1</sup>H NMR (400MHz, CDCl<sub>3</sub>, δ ppm):** 3.99 (dd, J=12.2, 4.1 Hz, 4 H), 3.77 (s, 3 H), 2.74 (t, J=4.9 Hz, 1 H), 2.63 (br. s., 2 H)

**<sup>13</sup>C NMR (100MHz, CDCl<sub>3</sub>, δ ppm):** 173.7, 61.7, 52.1, 48.8

### Methyl 3-hydroxy-2-(hydroxymethyl)propanoate **60**



A solution of methyl 3-hydroxy-2-(hydroxymethyl)propanoate **108** (3.0 equiv., 952.0 mg, 7.10 mmol), 4-ethynyl-2,6-dimethoxybenzaldehyde

**58** (1.0 equiv., 450.0 mg, 2.37 mmol) and PTSA (0.2 equiv., 81.5 mg, 0.47 mmol) was refluxed in toluene (30 mL) using Dean-Stark apparatus for 2 h. Toluene was then evaporated before the resulting residue was dissolved in EtOAc (20 mL) and washed with saturated solutions of NaHCO<sub>3</sub> (20 mL) and brine (20 mL). The organic layer was then dried over MgSO<sub>4</sub>, filtered and concentrated under reduced pressure. Purification by flash column chromatography (cyclohexane/EtOAc 100:0 to 70:30 over 30 min) afforded the title compound **60** as a yellowish solid and as a mixture of isomers which can be separated at this stage (680 mg, *cis/trans* 70:30, 2.22 mmol, 94%).

**R<sub>f</sub>** = 0.32 (*trans*) and 0.27 (*cis*), cyclohexane/EtOAc 8:2

**v<sub>max</sub> (thin film) /cm<sup>-1</sup>:** 3280 (w), 2953 (w), 2852 (w), 1730 (s), 1600 (m), 1573 (s), 1460 (m), 1415 (s), 1233 (s), 1200 (s), 1120 (s), 1082 (m), 834 (m), 731 (m)

**<sup>1</sup>H NMR (400 MHz, CDCl<sub>3</sub>) δ** (*cis/trans* mixture) 6.69 (s, 2H, H6t), 6.65 (s, 2H, H6c), 6.10 (s, 1H, H4c), 6.02 (s, 1H, H4t), 4.75-4.72 (dd, J = 11.7 Hz, 1.4 Hz, 1H, H3c), 4.47-4.43 (m, 1H, H3t), 4.06-4.03 (dd, J = 11.7 Hz, 2.9 Hz, 1H, H3c), 3.98-3.92 (dd, J = 11.6 Hz, 4.7 Hz, 1H, H3t), 3.87 (s, 3H, H1c), 3.83 (s, 6H, H5t), 3.80 (s, 6H, H5c), 3.70 (s, 3H, H1t), 3.22 (tt, J = 11.6 Hz, 4.7 Hz, 1H, H2t), 3.08 (s, 1H, H7t), 3.02 (s, 1H, H7c), 2.38 (m, 1H, H2c).

**<sup>1</sup>H NMR (400 MHz, acetone-d<sub>6</sub>) δ** (*trans* isomer) 6.56 (s, 2H, H6), 5.91 (s, 1H, H4), 4.42 (dq, J = 11.6, 1.4 Hz, 2H, H3), 3.86 (ddt, J = 11.5, 2.7, 1.3 Hz, 2H, H3), 3.65 (d, J = 7.2 Hz, 9H, H1 + H5), 3.55 (s, 1H, H7), 2.34 (tt, J = 3.0, 1.5 Hz, 1H, H2).

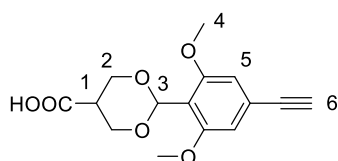


**<sup>1</sup>H NMR (400 MHz, acetone-d<sub>6</sub>)** δ (*cis* isomer) 6.60 (s, 2H, H<sub>6</sub>), 5.83 (s, 1H, H<sub>4</sub>), 4.21 – 4.13 (m, 2H, H<sub>3</sub>), 3.75 – 3.62 (m, 9H, H<sub>1</sub> + H<sub>5</sub>), 3.53 (s, 1H, H<sub>7</sub>), 2.94 (tt, J = 11.2, 4.7 Hz, 1H, H<sub>3</sub>), 2.74 (s, 1H, H<sub>2</sub>).

**<sup>13</sup>C NMR (101 MHz, CDCl<sub>3</sub>)** δ (*cis/trans* mixture) 170.7 (*c/t*), 158.8 (*c/t*), 124.3 (*c/t*), 115.1 (*c/t*), 108.7 (*c/t*), 96.9 (*c/t*), 83.1 (*c/t*), 80.3 (*c/t*), 77.6 (*c/t*), 68.8 (t), 67.8 (c), 62.3 (*c/t*), 56.5 (t), 56.3 (c), 52.2 (c), 52.0 (t), 40.3 (*c/t*).

**HR-ESI-MS (M+H<sup>+</sup>):** Calc. 307.1176, found 307.1183

### 2-(4-Ethynyl-2,6-dimethoxyphenyl)-1,3-dioxane-5-carboxylic acid **62**

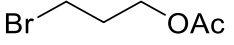


Methyl 2-(4-ethynyl-2,6-dimethoxyphenyl)-1,3-dioxane-5-carboxylate **60** (1.0 equiv., 300.0 mg, *cis/trans* 30:70, 1.03 mmol) was dissolved in THF at 0 °C, before lithium hydroxide (3.0 equiv., 0.5 M in water, 5.5 mL, 3.08 mmol) was added. The reaction was

stirred for 6 h at room temperature before being concentrated to dryness. An aqueous solution of NH<sub>4</sub>Cl (sat., 10 mL) was added and the crude was extracted with EtOAc (3 x 20 mL). The organic layers were combined, dried over MgSO<sub>4</sub>, filtered and concentrated *in vacuo* to afford the title compound **62** (275 mg, 0.99 mmol, 96%) as a white solid, which was used in the next step without further purification.

**HR-ESI-MS (M):** Calc. 292.0947, found 292.0933

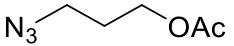
### 3-bromopropyl acetate **81**

 3-bromopropanol **80** (1 equiv., 10 g, 6.25 mL, 71.9 mmol) was dissolved in DCM (50 mL) then TEA (2 equiv., 10.5 g, 14.8 mL, 143 mmol) and acetic anhydride (2 equiv., 14.7 g, 13.5 mL, 143 mmol) were added. The mixture was stirred at room temperature for 2 hours. The mixture was washed with an aqueous solution of NaHCO<sub>3</sub> (sat., 2 x 100 mL) then brine (100 mL). The organic layer was dried over MgSO<sub>4</sub> and concentrated *in vacuo* to afford the title compound **81** (13 g, 71.8 mmol, 100 %) as a colorless oil which was used without further purification.

**<sup>1</sup>H NMR (400 MHz, CDCl<sub>3</sub>):** δ 4.20 (t, J = 6.1 Hz, 2H), 3.47 (t, J = 6.5 Hz, 2H), 2.18 (p, J = 6.4 Hz, 2H), 2.06 (s, 3H).

**<sup>13</sup>C NMR (101 MHz, CDCl<sub>3</sub>):** δ 170.9, 62.2, 31.7, 29.4, 20.9.

### 3-azidopropyl acetate **82**

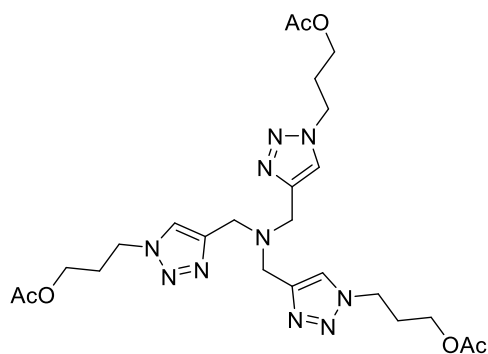
 To a solution of 3-bromopropyl acetate **81** (1 equiv., 13 g, 71.8 mmol) in water (65 mL) was added NaN<sub>3</sub> (2 equiv., 9.34 g, 5.05 mL, 143 mmol). The two-layered mixture was stirred overnight at 90°C. The mono-layered mixture was extracted with DCM (3 x 100 mL) and the combined organic layers were washed with brine (100 mL), dried over MgSO<sub>4</sub>

and concentrated *in vacuo* (mildly, product is volatile) to afford the title compound **82** (10 g, 69.9 mmol, 97 %) as a yellowish oil.

**<sup>1</sup>H NMR (400 MHz, CDCl<sub>3</sub>):** δ 4.15 (t, J = 6.2 Hz, 2H), 3.40 (t, J = 6.7 Hz, 2H), 2.06 (s, 3H), 1.91 (p, J = 6.5 Hz, 2H).

**<sup>13</sup>C NMR (101 MHz, CDCl<sub>3</sub>):** δ 171.0, 61.3, 48.2, 28.1, 20.9.

### Tris(3-acetoxypropyltriazolylmethyl)amine **83**



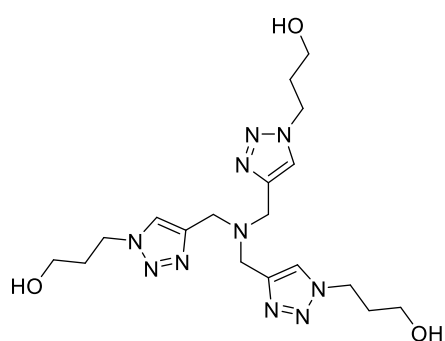
To a stirred solution of tripropargylamine (1 equiv., 1.5 g, 11.4 mmol) and 3-azidopropyl acetate **82** (4 equiv., 6.55 g, 45.7 mmol) in dry THF (50 mL) under argon was added Cu(I)OAc (5 mol%, 0.57 mmol, 70 mg). The mixture was refluxed overnight. If the solution formed a gel, add 100 mL of diethyl ether and stir for 30 min more at room temperature under argon. After concentration, the crude was purified by flash

chromatography (DCM/MeOH 100/0 to 90/10 in 30 min) to afford the title compound **83** (4.4 g, 7.85 mmol, 69 %) as a white solid.

**<sup>1</sup>H NMR (400 MHz, CDCl<sub>3</sub>):** δ 7.81 (s, 3H), 4.47 (t, J = 7.1 Hz, 6H), 4.10 (t, J = 6.0 Hz, 6H), 3.74 (s, 6H), 2.32–2.23 (m, 6H), 2.08 (s, 9H).

**<sup>13</sup>C NMR (101 MHz, CDCl<sub>3</sub>):** δ 171.0, 143.9, 124.2, 61.0, 47.2, 47.0, 29.5, 21.0.

### Tris(3-hydroxypropyltriazolylmethyl)amine **84**

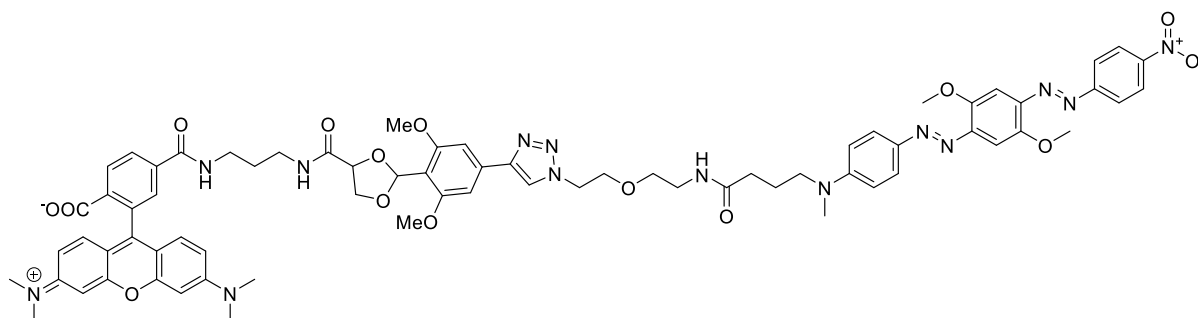


Tris(3-acetoxypropyltriazolylmethyl)amine **83** (1 equiv., 4.4 g, 7.85 mmol) was dissolved in ammonia in MeOH (2.0 M, 50 mL). The mixture was stirred overnight at 50 °C. Solvents were removed *in vacuo* and the yellowish solid was suspended in ACN, sonicated, and the white solid was filtered and washed with CAN, affording THPTA **84** (3.0 g, 6.90 mmol, 90 %) as a white solid.

**<sup>1</sup>H NMR (400 MHz, DMSO-d<sub>6</sub>, δ ppm):** 8.03 (s, 3H), 4.68 (t, J = 4.95 Hz, 3H), 4.42 (t, J = 7.00 Hz, 6H), 3.63 (s, 6H), 3.40 (m, 6H), 1.97 (m, 6H)

**<sup>13</sup>C NMR (100 MHz, DMSO-d<sub>6</sub>, δ ppm):** 143.4, 124.0, 57.5, 47.1, 46.6, 33.0

**4-((3-(2-(4-(1-(2-(2-(4-((E)-(2,5-Dimethoxy-4-((E)-(4-nitrophenyl)diazenyl)phenyl)diazenyl)phenyl)(methyl)amino)butanamido)ethoxy)ethyl)-1H-1,2,3-triazol-4-yl)-2,6-dimethoxyphenyl)-1,3-dioxolane-4-carboxamido)propyl)carbonyl)-2-(6-(dimethylamino)-3-(dimethyliminio)-3H-xanthen-9-yl)benzoate **63****

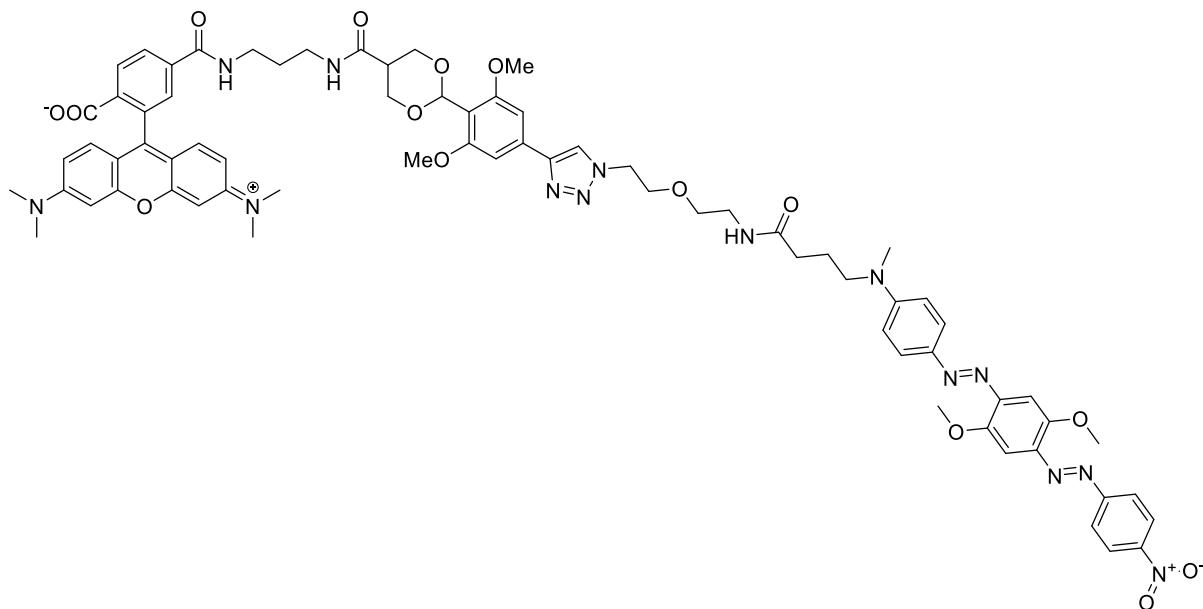


A solution of  $\text{CuSO}_4$  (1.0 equiv., 7.20  $\mu\text{mol}$ , 1.15 mg, 1.0 M in water) and *tris*(3-hydroxypropyl)triazolylmethyl)amine (THPTA, 2.0 equiv., 14.38  $\mu\text{mol}$ , 7.63 mg, 1.0 M in water) was added to a solution of 2-(4-ethynyl-2,6-dimethoxyphenyl)-1,3-dioxolane-4-carboxylic acid **61** (1.0 equiv., 7.20  $\mu\text{mol}$ , 2.00 mg, 1.0 M in DMF) and BHQ- $\text{N}_3$  **44** (1.2 equiv., 8.60  $\mu\text{mol}$ , 5.30 mg, 1.0 M in DMF), before the final addition of a solution of sodium ascorbate (5.0 equiv., 35.90  $\mu\text{mol}$ , 6.33 mg, 1.0 M in water). The mixture was left to stir at 25 °C over 72 h, before DCM (5.0 mL) was added to the solution. The layers were separated, and the aqueous phase was extracted one more time with DCM (5.0 mL). The organic layers were combined, washed with brine (10 mL) and concentrated under vacuum. The resulting crude was engaged in the coupling with the TAMRA fluorophore without further purification.

The crude was dissolved in DMF (400.0  $\mu\text{L}$ ), before BEP (1.2 equiv. 8.60  $\mu\text{mol}$ , 2.36 mg) and DIPEA (5.0 equiv., 35.90  $\mu\text{mol}$ , 5.90  $\mu\text{L}$ ) were added. TAMRA- $\text{NH}_2$  **43** (1.10 equiv. 7.90  $\mu\text{mol}$ , 3.85 mg) was then added after 10 min and the resulting solution was stirred at room temperature for 30 min. After concentration to dryness, the crude was purified by RP-HPLC (555 nm, 0.1% TFA / ACN 95/5 to 5/95 in 20 min) to give TAMRA-1,3-dioxolane-BHQ-2 probe **63** (3.55 mg, 2.6  $\mu\text{mol}$ , 36%) as a violet solid.

**HR-ESI-MS ( $\text{M}+\text{H}^+$ ):** Calc. 1365.4715, found 1365.4684

**4-((3-(2-(4-(1-(2-(2-(4-((E)-(2,5-Dimethoxy-4-((E)-(4-nitrophenyl)diazenyl)phenyl)diazenyl)phenyl)(methyl)amino)butanamido)ethoxy)ethyl)-1H-1,2,3-triazol-4-yl)-2,6-dimethoxyphenyl)-1,3-dioxane-5-carboxamido)propyl)carbonyl)-2-(6-(dimethylamino)-3-(dimethyliminio)-3H-xanthen-9-yl)benzoate **64****

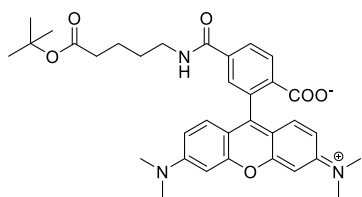


A solution of  $\text{CuSO}_4$  (1.0 equiv., 6.80  $\mu\text{mol}$ , 1.09 mg, 1.0 M in water) and *tris*(3-hydroxypropyl)triazolylmethyl)amine (THPTA, 2.0 equiv., 13.00  $\mu\text{mol}$ , 7.26 mg, 1.0 M in water) was added to a solution of 2-(4-ethynyl-2,6-dimethoxyphenyl)-1,3-dioxolane-4-carboxylic acid **62** (1.0 equiv., 6.80  $\mu\text{mol}$ , 2.00 mg, 1.0 M in DMF) and BHQ- $\text{N}_3$  **44** (1.2 equiv., 8.20  $\mu\text{mol}$ , 5.08 mg, 1.0 M in DMF), before the final addition of a solution of sodium ascorbate (5.0 equiv., 34.20  $\mu\text{mol}$ , 6.02 mg, 1.0 M in water). The mixture was left to stir at 25 °C over 72 h, before DCM (5.0 mL) was added to the solution. The layers were separated, and the aqueous phase was extracted one more time with DCM (5.0 mL). The organic layers were combined, washed with brine (10 mL) and concentrated under vacuum. The resulting crude was engaged in the coupling with the TAMRA fluorophore without further purification.

The crude was dissolved in DMF (400.0  $\mu\text{L}$ ), before BEP (1.2 equiv. 8.20  $\mu\text{mol}$ , 2.25 mg) and DIPEA (5.0 equiv., 34.2  $\mu\text{mol}$ , 5.90  $\mu\text{L}$ ) were added. TAMRA- $\text{NH}_2$  **43** (1.10 equiv. 7.50  $\mu\text{mol}$ , 3.66 mg) was then added after 10 min and the resulting solution was stirred at room temperature for 30 min. After concentration to dryness, the crude was purified by RP-HPLC (555 nm, 0.1% TFA / ACN 95/5 to 5/95 in 20 min) to give TAMRA-1,3-dioxolane-BHQ-2 probe **64** (4.96 mg, 3.6  $\mu\text{mol}$ , 53%) as a violet solid.

**HR-ESI-MS (M+H<sup>+</sup>):** Calc. 1379.5071, found 1379.5046

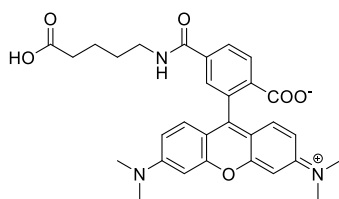
**4-((5-(*tert*-butoxy)-5-oxopentyl)carbamoyl)-2-(6-(dimethylamino)-3-(dimethyliminio)-3H-xanthen-9-yl)benzoate **77****



4-carboxy-2-(6-(dimethylamino)-3-(dimethyliminio)-3H-xanthen-9-yl)benzoate **54** (7 mg, 0.016 mmol) was dissolved in DMF (200  $\mu$ L) and TEA (2 equiv., 2.14 mg, 3.03  $\mu$ L, 0.034 mmol) then PyBOP (2 equiv., 0.016 mmol, 8.45 mg) was added. After 10 minutes, methyl 5-aminopentanoate hydrochloride (1.2 equiv., 33.5 mg, 0.020 mmol) was added to the mixture and stirred overnight at room temperature. The crude mixture was purified directly by preparative RP-HPLC (555 nm, 0.1% TFA / ACN 95/5 to 5/95 in 20 min) and lyophilized to afford the modified the title compound **77** (4.9 mg, 9  $\mu$ mol, 60%)

**HR-ESI-MS (M+H<sup>+</sup>):** calc 585.2839, found 585.2834.

**4-((4-Carboxybutyl)carbamoyl)-2-(6-(dimethylamino)-3-(dimethyliminio)-3H-xanthen-9-yl)benzoate **78****

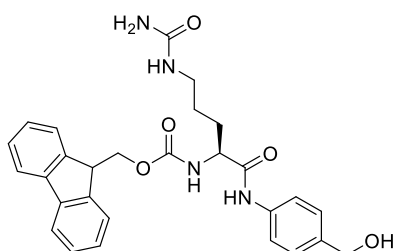


2-(6-(dimethylamino)-3-(dimethyliminio)-3H-xanthen-9-yl)-4-((5-methoxy-5-oxopentyl)carbamoyl)benzoate **77**

(4.9 mg, 9  $\mu$ mol) was dissolved in an HCl solution in dioxane (4M, 3 mL) and stirred overnight. The crude was concentrated under reduced pressure to afford the title compound **78** (41 mg, 9  $\mu$ mol, quant.) as a pink solid.

**HR-ESI-MS (M+H<sup>+</sup>):** calc 529.2213, found 529.2210.

**(9H-fluoren-9-yl)methyl (S)-(1-((4-(hydroxymethyl)phenyl)amino)-1-oxo-5-ureidopentan-2-yl)carbamate **71****



To a solution in DMF (0.1 M) of Fmoc-L-Citrulline **70** (1.0 equiv., 2.9 g, 7.316 mmol) and DIPEA (1.0 equiv., 1.30 mL, 7.32 mmol) was added HATU (1.1 equiv., 3.06 g, 8.05 mmol). After 15 min of stirring, 4-aminobenzyl alcohol (3.0 equiv., 2.7 g, 21.95 mmol) in DMF (0.1M) was added to the reaction mixture and stirred at room temperature for 48 hours in the dark. After concentration, the crude was purified by flash chromatography (DCM/MeOH, 98/2 to 90/10 in 30 min) to afford the title compound **71** (2.6 g, 5.2 mmol, 71%) as a white product.

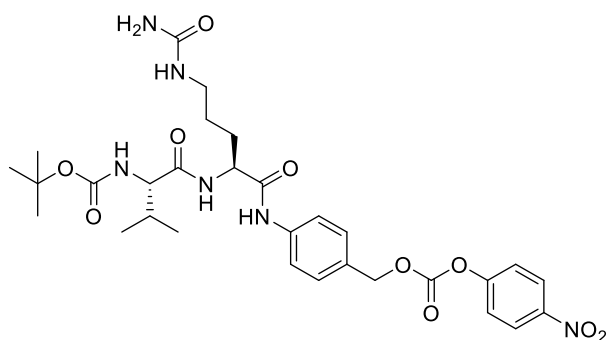
**TLC:** DCM/MeOH 95/5, bromocresol green

**<sup>1</sup>H NMR (400 MHz, DMSO-d<sub>6</sub>):**  $\delta$  9.98 (s, 1H), 7.89 (d, J = 7.53 Hz, 2H), 7.74 (t, J = 7.05 Hz, 2H), 7.66 (d, J = 8.02 Hz, 1H), 7.56 (d, J = 8.40 Hz, 2H), 7.43-7.40 (m, 2H), 7.35-7.31 (m, 2H),

7.24 (d, J = 8.38 Hz, 2H), 6.00 (br, J = 5.45 Hz, 1H), 5.43 (s, 2H), 5.09 (t, J = 5.65 Hz, 1H), 4.43 (d, J = 5.26 Hz, 2H), 4.30-4.15 (m, 4H), 3.07-3.01 (m, 1H), 2.98-2.93 (m, 1H), 1.71-1.58 (m, 2H), 1.51-1.35 (m, 2H)

<sup>13</sup>C NMR (100 MHz, CDCl<sub>3</sub>): δ 171.5, 159.4, 156.6, 144.4, 144.3, 141.2, 138.0, 137.9, 128.1, 127.5, 127.5, 127.4, 125.8, 120.6, 119.4, 66.2, 63.1, 55.4, 47.1, 29.8, 27.4;

**tert-butyl ((S)-3-methyl-1-(((S)-1-((4-(((4-nitrophenoxy)carbonyl)oxy)methyl)phenyl)amino)-1-oxo-5-ureidopentan-2-yl)amino)-1-oxobutan-2-yl)carbamate **69****



The molecule was synthesized according to a previously reported procedure. Briefly, a solution of (9H-fluoren-9-yl)methyl (S)-(1-((4-(hydroxymethyl)phenyl)amino)-1-oxo-5-ureidopentan-2-yl)carbamate **71** (1.0 equiv., 1.0 g, 1.99 mmol) in DMF (0.2 M) was treated with piperidine (20 equiv., 5.57

mL, 40 mmol) and stirred at room temperature for 5 hours. Solvent and excess of base were removed under reduced pressure (oil pump, 1 h). The resulting residue was dissolved in DMF (0.1 M) and Boc-Val-NHS ester **65** (1.2 equiv., 912 mg, 2.390 mmol) was added. The reaction mixture was stirred at room temperature overnight. DMF was removed under reduced pressure and the resulting residue was purified by flash column chromatography (DCM/MeOH 97/3 to 85/15 in 30 min) to afford Boc-Val-Cit-PAB **73** as a white solid (800 mg, 1.69 mmol, 85%). The latter (800 mg, 1.69 mmol) was dissolved in DMF (5 mL), then pyridine (10 equiv., 1.36 mL, 16.9 mmol) and PNP-Cl (2 equiv., 679 mg, 3.38 mmol) were added. The reaction was stirred for 5 h at room temperature, and the crude was directly purified by flash column chromatography (DCM/MeOH 100/0 to 85/15 in 30 min) to afford the title compound **69** (1.35 g, 2.09 mmol, 62%) as a white solid.

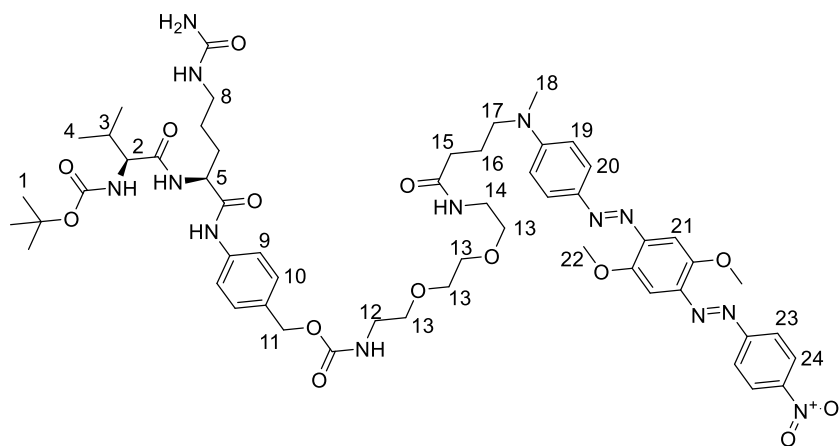
**tert-Butyl ((S)-1-(((S)-1-((4-(12-amino-3-oxo-2,7,10-trioxa-4-azadodecyl)phenyl)amino)-1-oxo-5-ureidopentan-2-yl)amino)-3-methyl-1-oxobutan-2-yl)carbamate **74****

To a solution of 2,2'-(ethylenedioxy)diethylamine (4.0 equiv., 46.1 mg, 45.4  $\mu$ L, 0.31 mmol) and DIPEA (6.0 equiv., 60.3 mg, 77.1  $\mu$ L, 0.47 mmol) in DMF (0.5 mL), was added dropwise a solution of Boc-Val-Cit-PAB-PNP **69** (1.0 equiv., 50.0 mg, 0.078 mmol) in DMF (0.5 mL). The resulting solution was stirred for 1.0 h at room temperature before being concentrated to dryness. The crude was purified by RP-HPLC (H<sub>2</sub>O 0.1% TFA /ACN 95:5 to 5:95 over 30 min, rt = 12.6 min) to afford the title compound **74** after freeze-drying as a colorless oil (30.0 mg, 0.046 mmol, 59%).

**<sup>1</sup>H NMR (500 MHz, DMSO)  $\delta$**  10.06 (s, 1H, NH), 7.99 (d,  $J$  = 7.8 Hz, 1H, NH), 7.63 – 7.51 (d,  $J$  = 8.5 Hz, 2H, H9), 7.29 – 7.27 (d,  $J$  = 8.5 Hz, 2H, H10), 7.24 – 7.21 (t,  $J$  = 6.0 Hz, 1H, NH), 6.75 (d,  $J$  = 8.8 Hz, 1H, NH), 5.99 (s, 1H, NH), 4.93 (s, 2H, H11), 4.43 (app q,  $J$  = 7.5 Hz, 1H, H5), 3.83 (app t,  $J$  = 7.8 Hz, 1H, H4), 3.39 (t,  $J$  = 6.0 Hz, 2H, H12), 3.15 – 3.11 (app q,  $J$  = 6.0 Hz, 2H, H8), 3.07 – 3.02 (m, 1H, H13), 2.98 – 2.90 (m, 2H, H14), 2.55 – 2.45 (m, 3H, H13), 1.97 – 1.91 (m, 1H, H3), 1.75 – 1.52 (m, 4H, H6 + H7), 1.38 (s, 9H, H1), 0.86 – 0.84 (d,  $J$  = 6.7 Hz, 3H, H2), 0.82 – 0.80 (d,  $J$  = 6.7 Hz, 2H, H2)

**HR-ESI-MS (M+H<sup>+</sup>):** Calc. 653.3748, found 653.3760

**tert-Butyl ((S)-1-(((S)-1-((4-(18-(4-((E)-(2,5-dimethoxy-4-((E)-(4-nitrophenyl)diazenyl)phenyl)diazenyl)phenyl)-3,14-dioxo-2,7,10-trioxa-4,13,18-triazanonadecyl)phenyl)amino)-1-oxo-5-ureidopentan-2-yl)amino)-3-methyl-1-oxobutan-2-yl)carbamate **75****



BHQ-2 (1.5 equiv., 11.7 mg, 0.023 mmol) was dissolved in DMF (2.0 mL) and DIPEA (3.0 equiv., 5.95 mg, 7.61  $\mu$ L, 0.046 mmol) and HATU (3.0 equiv., 17.5 mg, 0.046 mmol) were sequentially added. The mixture was stirred for 15 min at 25 °C before Boc-Val-Cit-PAB-PEG<sub>2</sub>-NH<sub>2</sub> **74** (1.0 equiv., 10.0 mg, 0.015 mmol) was added. The mixture was stirred at 25 °C for 3 h before being concentrated to dryness. The resulting crude was purified by flash chromatography (DCM/MeOH 100:0 to 95:5 over 30 min) to afford the title compound **75** (7.2 mg, 6.29  $\mu$ mol, 41%) as a sticky purple oil.

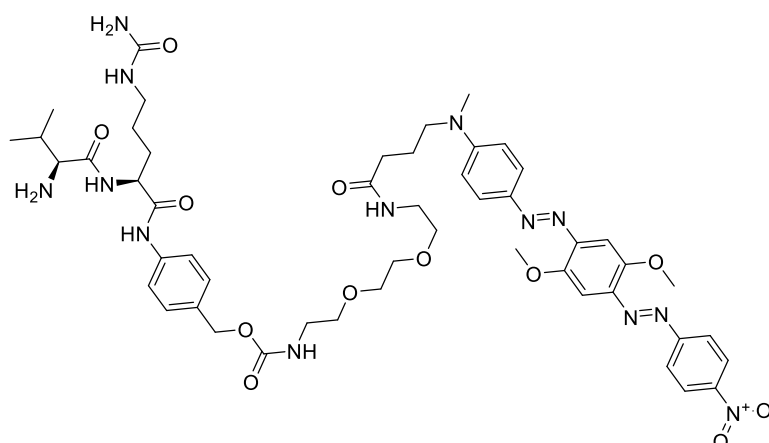
R<sub>f</sub> = 0.45, DCM/MeOH 98:2

<sup>1</sup>H NMR (500 MHz, CDCl<sub>3</sub>)  $\delta$  9.18 (s, 1H, NH), 8.39 – 8.32 (m, 2H, H24), 8.06 – 7.99 (m, 2H, NH), 7.89 (d, *J* = 9.1 Hz, 2H, H9), 7.65 (s, 2H, H23), 7.58 (d, *J* = 9.1 Hz, 2H, H10), 7.51 – 7.42 (m, 2H, H20), 7.26 (br s, 2H, H19), 6.80 – 6.73 (m, 2H, H21), 6.30 (br s, 1H, NH), 5.59 (s, 1H, NH), 5.52 (s, 1H, NH), 5.33 (s, 1H, NH), 5.01 (s, 2H, H11), 4.67 (s, 1H, H5), 4.08 (s, 3H, H22), 4.03 (s, 3H, H22), 3.96 (s, 1H, H2), 3.67 (m, 2H, H8), 3.59 – 3.31 (m, 8H, H12 + H13 + H13 + H13), 3.18 – 3.04 (m, 5H, H14 + H18), 2.40 – 2.08 (m, 2H, H15), 1.95 – 1.88 (m, 1H, H3), 1.55 – 1.37 (m, 19H, H1 + H6 + H7 + H16 + NH<sub>2</sub>), 1.25 (m, 2H, H14), 0.97 – 0.94 (d, *J* = 6.7 Hz, 3H, H4), 0.92 – 0.90 (d, *J* = 6.7 Hz, 3H, H4).

<sup>13</sup>C NMR (101 MHz, CDCl<sub>3</sub>)  $\delta$  156.5, 153.7, 152.3, 150.8, 148.4, 146.8, 144.4, 142.0, 138.0, 128.8, 126.3, 124.7, 123.5, 120.1, 111.5, 101.0, 100.1, 70.1, 69.8, 56.8, 56.8, 55.1, 53.4, 51.7, 43.1, 40.8, 39.3, 38.6, 38.5, 33.0, 30.9, 29.7, 29.7, 28.3, 22.8, 22.7, 19.4, 17.9, 12.4.

HR-ESI-MS (M+H<sup>+</sup>): Calc. 1141.5556, found 1141.5516

**4-((S)-2-((S)-2-Amino-3-methylbutanamido)-5-ureidopentanamido)benzyl (2-(4-((E)-(2,5-dimethoxy-4-((E)-(4-nitrophenyl)diazenyl)phenyl)diazenyl)phenyl)-6-oxo-10,13-dioxo-2,7-diazapentadecan-15-yl)carbamate 76**



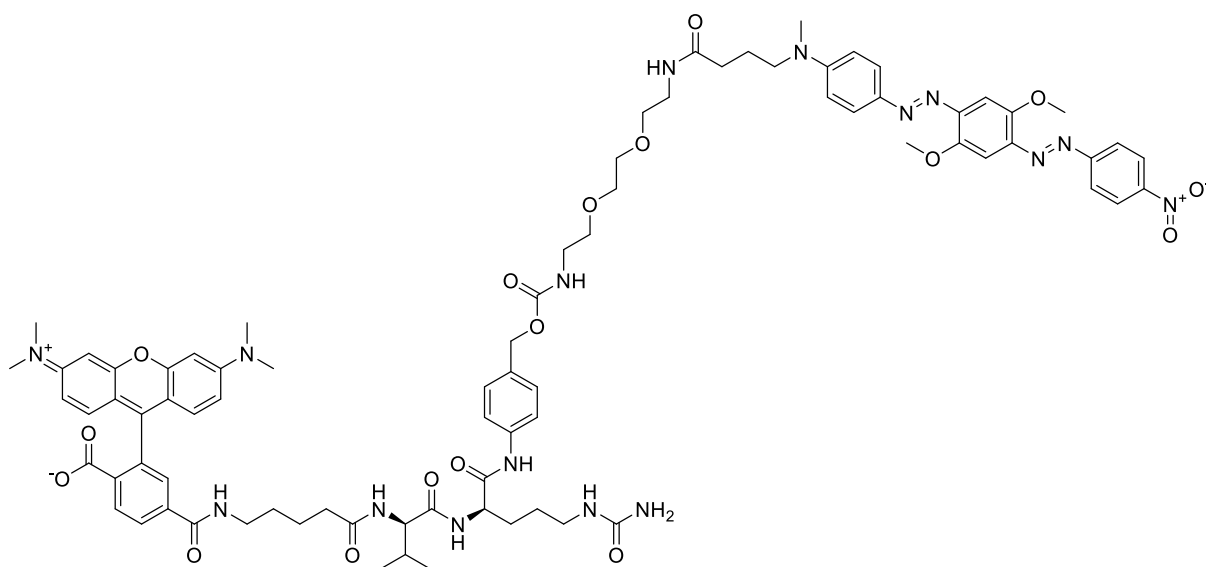
A solution of Boc-Val-Cit-PAB-PEG<sub>2</sub>-BHQ **75** (5.0 mg, 4.37  $\mu$ mol) was dissolved in DCM (1.0 mL) and TFA (1.0 mL) was added. The mixture was stirred at 25 °C for 2 h. Solvents were



removed *in vacuo* to afford the title compound **76** as a blue oil, which was used immediately in the next step without further purification.

**HR-ESI-MS (M+2H<sup>+</sup>):** Calc. 521.7596, found 521.7586

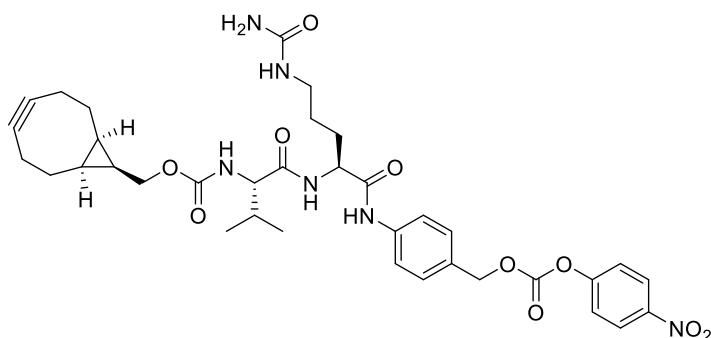
**4-(((5-(((R)-1-(((R)-1-((4-(18-(4-((E)-(2,5-Dimethoxy-4-((E)-(4-nitrophenyl)diazenyl)phenyl)diazenyl)phenyl)-3,14-dioxo-2,7,10-trioxa-4,13,18-triazanonadecyl)phenyl)amino)-1-oxo-5-ureidopentan-2-yl)amino)-3-methyl-1-oxobutan-2-yl)amino)-5-oxopentyl)carbamoyl)-2-(6-(dimethylamino)-3-(dimethyliminio)-3H-xanthen-9-yl)benzoate **79****



To a solution of TAMRA-butyl-CO<sub>2</sub>H **78** (1.2 equiv., 1.83 mg, 3.5 μmol) in 1.0 mL of dry DMF was added BEP (1.25 equiv., 674 μg, 3.6 μmol) and DIPEA (6.0 equiv., 2.80 μL, 2.2 mg). The reaction mixture was stirred for 30 min at 25 °C before the addition of a solution of Val-Cit-PAB-PEG<sub>2</sub>-BHQ **76** (1.0 equiv., 3.0 mg, 2.90 μmol) in 1.0 mL of dry DMF. The resulting mixture was stirred 3 h at 25 °C before being concentrated to dryness. The resulting crude was purified by preparative HPLC (555 nm, H<sub>2</sub>O 0.1% TFA /ACN 90:10 to 5:95 over 25 min, *rt* = 14.5 min) to afford the title compound after freeze-drying as a purple powder **79** (0.90 mg, 0.046 mmol, 59%).

**HR-ESI-MS (M+H<sup>+</sup>):** Calc. 1553.7139, found 1553.7208

**((1R,8S,9s)-bicyclo[6.1.0]non-4-yn-9-yl)methyl ((S)-3-methyl-1-(((S)-1-((4-((4-nitrophenoxy)carbonyloxy)methyl)phenyl)amino)-1-oxo-5-ureidopentan-2-yl)amino)-1-oxobutan-2-yl)carbamate **93****



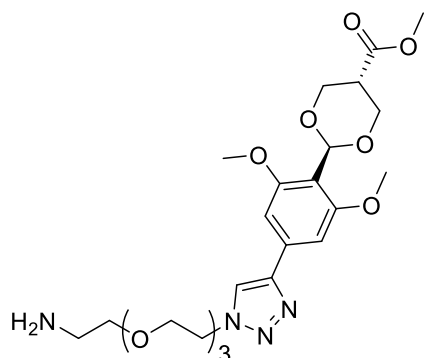
To a solution of Val-Cit-PAB **91** (10 mg, 0.026 mmol) in DMF (200  $\mu$ L) was added pyridine (2 equiv., 4.2  $\mu$ L, 0.052 mmol) and **15** (2 equiv., 16.4 mg, 0.052 mmol). After total disappearance of the primary amine by TLC, PNP-Cl (2 equiv.,

0.052 mmol) was added. After 5 hours, the reaction was dried under reduced pressure and the crude was purified by flash chromatography (CyH/EtOAc 5/5 to 0/100 in 30 min) to afford the title compound **93** as a white solid (15.7 mg, 0.021 mmol, 42%).

**<sup>1</sup>H NMR (500 MHz, CDCl<sub>3</sub>):**  $\delta$  10.06 (s, 1H), 8.28 (q, 2H), 7.99 (d,  $J$  = 7.8 Hz, 1H), 7.63 – 7.51 (d,  $J$  = 8.5 Hz, 2H), 7.39 (d, 2H), 7.29 – 7.27 (d,  $J$  = 8.5 Hz, 2H), 7.24 – 7.21 (t,  $J$  = 6.0 Hz, 1H), 6.75 (d,  $J$  = 8.8 Hz, 1H), 5.99 (s, 1H), 4.93 (s, 2H), 4.73 (app q,  $J$  = 7.5 Hz, 1H), 4.41 (d, 2H), 3.83 (app t,  $J$  = 7.8 Hz, 1H), 3.15 – 3.11 (app q,  $J$  = 6.0 Hz, 2H), 2.37 – 2.23 (m, 6H), 1.97 – 1.91 (m, 1H), 1.75 – 1.52 (m, 4H), 1.62 – 1.59 (m, 3H), 1.38 (s, 9H), 1.09 – 1.04 (m, 2H), 0.86 – 0.84 (d,  $J$  = 6.7 Hz, 3H), 0.82 – 0.80 (d,  $J$  = 6.7 Hz, 2H)

**HR-ESI-MS (M+H<sup>+</sup>):** Calc. 720.3119, found 720.3114

**methyl (2r,5r)-2-(4-(1-(2-(2-(2-(2-aminoethoxy)ethoxy)ethoxy)ethyl)-1H-1,2,3-triazol-4-yl)-2,6-dimethoxyphenyl)-1,3-dioxane-5-carboxylate **85****



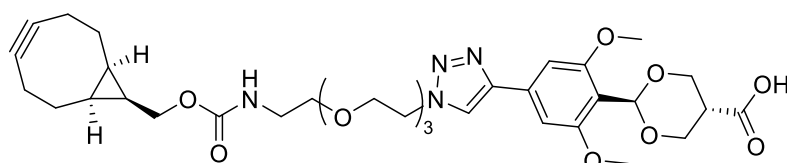
A degassed solution of CuSO<sub>4</sub>·5H<sub>2</sub>O (10 mol%, 8.15 mg, 0.0326 mmol) and Tris((1-hydroxy-propyl-1H-1,2,3-triazol-4-yl)methyl)amine (THPTA, 50 mol%, 70.9 mg, 0.163 mmol) in water (3.33 mL) was added to a degassed solution of **60** (1 equiv., 100 mg, 0.326 mmol) and 2-(2-(2-(2-azidoethoxy)ethoxy)ethoxy)ethan-1-amine (1.1 equiv., 78.4 mg, 0.359 mmol) in DMF (6.67 mL) under nitrogen atmosphere. Then, a freshly prepared solution of sodium ascorbate (25 mol%, 16.2 mg, 0.0816 mmol) in water (3.33 mL) was added and the mixture was stirred at room temperature under nitrogen atmosphere for 2h. DMF was evaporated in vacuo, 10 mL of saturated NaHCO<sub>3</sub> was added and the crude

material was extracted using ethyl acetate (3 x 20 mL). Organic layer was washed with brine, dried over MgSO<sub>4</sub> and evaporated in vacuo. The crude material was purified by flash chromatography (DCM/MeOH/NH<sub>4</sub>OH 100:0:0 to 85/13.5/1.5 in 30 minutes) to afford **85** (140 mg, 0.267 mmol, 82 %) as an orange oil.

**<sup>1</sup>H NMR (400 MHz, acetone-d<sub>6</sub>) δ** (*trans* isomer) 8.05 (s, 1H), 7.05 (s, 1H), 6.10 (s, 1H), 4.6(dq, J = 11.6, 1.4 Hz, 2H), 4.45 (ddt, J = 11.5, 2.7, 1.3 Hz, 2H), 3.95 (s, 6H), 3.90 (s, 3H), 3.70 (m, 2H) 3.6 (m, 18H), 3.45 (m, 2H), 2.25 (tt, J = 3.0, 1.5 Hz, 1H).

**HR-ESI-MS (M + H<sup>+</sup>):** calc.: 525.2578, found: 525.2555

**(2r,5r)-2-(4-(1-(1-((1R,8S,9s)-bicyclo[6.1.0]non-4-yn-9-yl)-3-oxo-2,7,10,13-tetraoxa-4-azapentadecan-15-yl)-1H-1,2,3-triazol-4-yl)-2,6-dimethoxyphenyl)-1,3-dioxane-5-carboxylic acid **87****



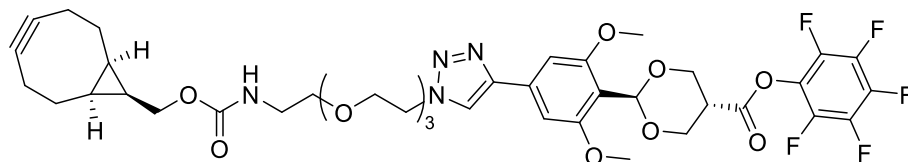
**85** (1 equiv., 40 mg, 0.095

mmol) was solubilized in DMF (2 mL) and TEA (3 equiv., 20.5 mg, 28 μL, 0.280 mmol) was added. bicyclo[6.1.0]non-4-yn-9-ylmethyl 4-nitrophenyl carbonate **15** (1.5 equiv., 44.1 mg, 0.14 mmol) was then added, the solution was stirred for 3 hours at room temperature. After concentration, the crude was solubilized in MeOH (2 mL) and LiOH (2.0M in water) was added, the mixture was stirred overnight at room temperature. The solution was concentrated under reduced pressure and used in the next step without further purification (22.5 mg, 0.032 mmol, 35%).

**<sup>1</sup>H NMR (400 MHz, acetone-d<sub>6</sub>) δ** (*trans* isomer) 7.93 (s, 1H), 7.09 (s, 1H), 6.34 (s, 1H), 4.86 (dq, J = 11.6, 1.4 Hz, 2H), 4.75 (ddt, J = 11.5, 2.7, 1.3 Hz, 2H), 4.55 (d, 2H), 4.07 (s, 6H), 3.65 (m, 2H), 3.51 (m, 18H), 3.45 (m, 2H), 2.95 (tt, J = 3.0, 1.5 Hz, 1H) 2.17 – 2.08 (m, 6H), 1.41 – 1.29 (m, 3H), 1.01 – 0.92 (m, 2H).

**HR-ESI-MS (M + H<sup>+</sup>):** calc.: 687.3241, found: 687.3236

**perfluorophenyl (2r,5r)-2-(4-(1-(1-((1R,8S,9s)-bicyclo[6.1.0]non-4-yn-9-yl)-3-oxo-2,7,10,13-tetraoxa-4-azapentadecan-15-yl)-1H-1,2,3-triazol-4-yl)-2,6-dimethoxyphenyl)-1,3-dioxane-5-carboxylate **88****



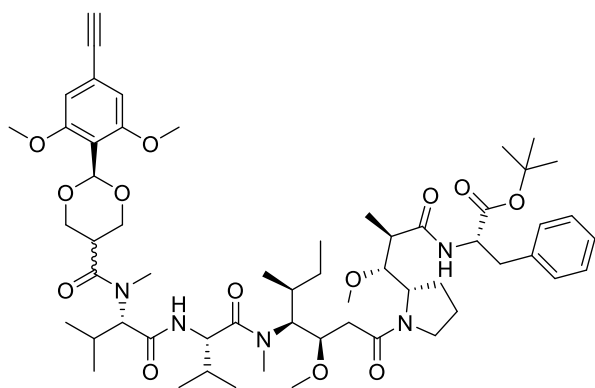
**87** (11.5 mg, 0.032

mmol) was solubilized in DMF (1 mL), and pyridine (2 equiv., 2.5  $\mu$ L, 0.659 mmol) and bis(pentafluorophenyl) carbonate (3 equiv., 24.1 mg, 0.096 mmol) was added. After 5 hours of stirring at room temperature, the crude was purified by flash chromatography (DCM/MeOH 100/0 to 90/10 in 30 minutes) to afford the title compound **88** (6 mg, 0.015 mmol, 48%) as a yellow oil.

$^{19}\text{F}$  NMR (376 MHz,  $\text{CDCl}_3$ ):  $\delta$  -168.42, -170.09, -185.92

HR-ESI-MS ( $\text{M} + \text{H}^+$ ): calc.: 852.3205, found: 852.3209

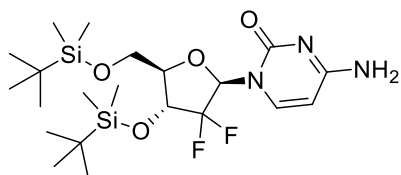
**tert-butyl ((2R,3R)-3-((S)-1-((3R,4S,5S)-4-((S)-2-((S)-2-(2-(4-ethynyl-2,6-dimethoxyphenyl)-N-methyl-1,3-dioxane-5-carboxamido)-3-methylbutanamido)-N,3-dimethylbutanamido)-3-methoxy-5-methylheptanoyl)pyrrolidin-2-yl)-3-methoxy-2-methylpropanoyl)-L-phenylalaninate **98****



To a solution of **62** (1.0 equiv., 7 mg, 23.95  $\mu$ mol) in dry DMF (1 mL) was added HATU (1.7 equiv., 15.48 mg, 40.71  $\mu$ mol) and DIPEA (5.0 equiv., 20.86  $\mu$ L, 119.75  $\mu$ mol). The reaction mixture was stirred for 30 min at 25  $^\circ\text{C}$  before the addition of a solution of MMAF-tBu **96** (1.0 equiv., 18.87 mg, 23.95  $\mu$ mol, 10 mM in DMF). The resulting mixture was stirred overnight at 25  $^\circ\text{C}$  before being concentrated to dryness. The resulting crude was purified by preparative HPLC ( $\text{H}_2\text{O}/\text{ACN}$  95:5 to 5:95 over 10 min, then 5:95 for 5 min,  $\text{rt} = 11.2$  min) to afford the title compound after freeze-drying as a white powder **98** (5.09 mg, 4.79  $\mu$ mol, 20%).

HR-ESI-MS ( $\text{M} + \text{H}^+$ ): Calc. 1062.6373, found 1062.6376

**4-amino-1-((2R,4R,5R)-4-((tert-butyldimethylsilyl)oxy)-5-(((tert-butyldimethylsilyl)oxy)methyl)-3,3-difluorotetrahydrofuran-2-yl)pyrimidin-2(1H)-one**  
**100**

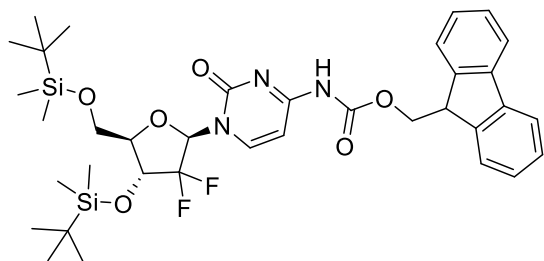


This compound was synthesized by a reported procedure.<sup>409</sup>

To a solution of gemcitabine **97** (1.0 equiv., 200 mg, 0.76 mmol), imidazole (5 equiv., 258 mg, 3.8 mmol) and DMAP (0.2 equiv., 18.6 mg, 0.152 mmol) in dry DMF (5.5 mL) was added TBSCl (6 equiv., 687 mg, 789  $\mu$ L, 4.56 mmol). The reaction was stirred overnight at room temperature. After concentration, water (5 mL) was added, and extracted using DCM (2 x 5 mL). Organic layers were combined and solvents were removed under reduced pressure to afford the title compound **100** as a white solid (365 mg, 0.7423 mmol, 98%), which was used without further purification.

**LR-MS [M+H]<sup>+</sup>**: Calc. 492.25, found 492.15.

**(9H-fluoren-9-yl)methyl (1-((2R,4R,5R)-4-((tert-butyldimethylsilyl)oxy)-5-(((tert-butyldimethylsilyl)oxy)methyl)-3,3-difluorotetrahydrofuran-2-yl)-2-oxo-1,2-dihydropyrimidin-4-yl)carbamate 101**



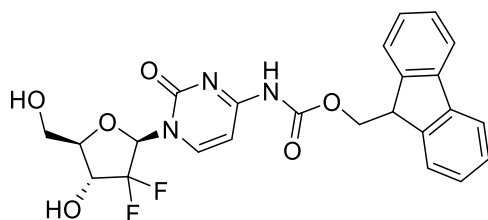
This compound was synthesized by a reported procedure.<sup>409</sup> To a solution of **100** (1.0 equiv., 220 mg, 0.44 mmol) in DCM (5.5 mL) and pyridine (20 equiv., 707 mg, 724  $\mu$ L, 8.95 mmol) was added a solution of Fmoc-OSu (5 equiv., 754 mg, 2.24 mmol) in DCM (5.5 mL). The mixture was stirred overnight at room temperature. The reaction was diluted with DCM (15 mL) and washed with an aqueous solution of NaHCO<sub>3</sub> (sat., 2 x 20 mL). Organic layers were combined, dried over MgSO<sub>4</sub>, filtered and concentrated under reduced pressure to afford the title compound **101** (300 mg, 0.42 mmol, 94%) as a yellowish oil, which was used without further purification.

**LR-MS [M+H]<sup>+</sup>**: Calc. 714.32, found 714.70.

**(9H-fluoren-9-yl)methyl**

**(1-((2R,4R,5R)-3,3-difluoro-4-hydroxy-5-**

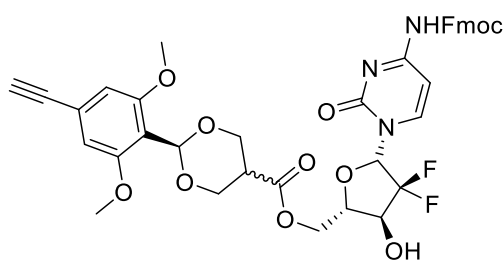
**(hydroxymethyl)tetrahydrofuran-2-yl)-2-oxo-1,2-dihydropyrimidin-4-yl)carbamate 102**



This compound was synthesized by a reported procedure.<sup>409</sup> To a solution of **101** (1.0 equiv., 300 mg, 0.42 mmol) in THF (11.3 mL) in a round-bottomed Teflon flask, then HF/pyridine (70% HF, 30% pyridine, 129 equiv. of HF, 1.42 mL, 54.5 mmol) was carefully added using a plastic pipette. The mixture was stirred for 24 h at room temperature. HF was quenched using an aqueous solution of NaHCO<sub>3</sub> (sat., 10 mL), which was added dropwise. After concentration of the THF, EtOAc was added (20 mL) and the organic layer was washed with brine (2 x 20 mL), then dried over MgSO<sub>4</sub>, filtered, and solvents were removed under reduced pressure. The crude material was purified by flash chromatography (CyHex/EtOAc 100/0 to 0/100 in 30 min) to afford the title compound **102** (200 mg, 0.412 mmol, 98%) as a white solid.

**LR-MS [M+H]<sup>+</sup>**: Calc. 486.15, found 486.18

**((2S,3S,5S)-5-(4-(((9H-fluoren-9-yl)methoxy)carbonyl)amino)-2-oxopyrimidin-1(2H)-yl)-4,4-difluoro-3-hydroxytetrahydrofuran-2-yl)methyl 2-(4-ethynyl-2,6-dimethoxyphenyl)-1,3-dioxane-5-carboxylate 103**



To a solution of **62** (1 equiv., 4.0 mg, 13.69 μmol) in DMF (5 mL) was added COMU (1.3 equiv., 7.62 mg, 17.79 μmol) and DIPEA (3.0 equiv., 7.15 μL, 41.06 μmol). Then, **102** (1.0 equiv., 6.64 mg, 13.69 μmol) was added, and the mixture was stirred overnight at room temperature. After concentration, the crude was purified by semi-preparative RP-HPLC (water/ACN 95/5 to 5/95) to afford the title compound **103** (2.8 mg, 3.69 μmol, 27%) as a white solid.

**Stability of FRET-probes in aqueous media and in plasma**

Aqueous buffers were prepared as follow:

Calculated pH	Measured pH	Composition
0	<0.7	HCl 1 M
1	1.02	HCl 0.1 M
2	2.00	HCl 0.01M
3	3.03	30 mL KH phthalate standard + 10 mL HCl 0.1 M
4	4.01	KH phthalate (standard solution of pH meter)
5	5.03	0.78 mL NaH <sub>2</sub> PO <sub>4</sub> 0.1 M + 39.4 mL NaH <sub>2</sub> PO <sub>4</sub> 0.1 M
7.4	7.40	PBS
7.4	7.35	Human plasma

25 µL of each stock solutions of probes (40 µM in DMSO) were added to 975 µL of aqueous buffered media to a final concentration of 1 µM. These solutions were distributed into 96-well plates in triplicate and incubated at 23 °C, then read on a SAFAS Xenius XML with excitation/emission wavelengths set to those for TAMRA (550/580 nm). The fluorescence was measured every 3 minutes for 15 hours and normalized to the fluorescence of a solution of BHQ-N<sub>3</sub> **44** (1 µM) and TAMRA-NH<sub>2</sub> **43** (1 µM) in the corresponding media.

### ***In vitro* experiments.**

**Cell culture.** HUH7, MDA-MB231, SKBR3 and BNL CL.2 cell lines were obtained from ATCC, cultured in DMEM (Merck) and LS174 were obtained from ATCC and cultured in MEM (Merck). Each media was supplemented with 10% heat-inactivated FBS (Merck) containing 1% penicillin-streptomycin (Merck). All cell lines were maintained at 37 °C and 5% CO<sub>2</sub> in a humidified incubator.

**Flow cytometry.** Cells were plated in 48-well plates (Costar 3548) two days before experiments (10.10<sup>5</sup> cells/well for LS174, HUH7, MDA-MB-231 and SKBR3, 5.10<sup>5</sup> cells/well for BNL CL.2). A different plate was used for each cell line to avoid contamination. The day of the experiment, media was removed and cells were incubated with 250µL/well of a freshly prepared 1 µM solution of tested compound in DMEM (MEM for LS174) for 90 min at 37 °C. Each compound was tested in three different well for each cell lines. After 90 min incubation, the compound solution was removed and cells were rinsed with 300 µL PBS. Cells were then

trypsinized (80  $\mu$ L/well) for 5 min at 37 °C. 500  $\mu$ L of a 1/1 PBS/DMEM without phenol red mixture was added in each well. Cells were flushed and transferred in tubes suited for flow cytometry. FACS studies were realized on a Fortessa cytometer (BD Biosciences). All experiments were conducted in triplicate for all cell lines.

**Confocal microscopy.** Two days prior to the experiment,  $4 \times 10^4$  SKBR3 cells were seeded per well in 8-well Lab-Tek II Chambered coverglass plates (ref. 155409, Nunc, Naperville, IL, USA). The fluorescent probes were diluted up to 300  $\mu$ L in Dulbecco's Modified Eagles's complete Medium and added onto the cells for 90 minutes. After washing, cell nuclei were stained with 5  $\mu$ g/mL of Hoechst 33258 (ref. H1399, Invitrogen, Carlsbad, CA, USA) diluted in complete medium for 30 minutes. After washing, cells were incubated with 2  $\mu$ M of LysoSensor™ Green DND-189 (ref. L7535, Invitrogen) diluted in complete medium for 30 minutes. Cells were finally washed and incubated with red phenol-free Dulbecco's Modified Eagle's Medium (SIGMA) for microscopic observation. Cells images were acquired on a confocal Leica TSC SPE II microscope (405, 488 and 561 nm) with an image acquisition software (Leica confocal LAS AF, Leica).





## VII. Non-covalent antibody-siRNA conjugates

### A. Overview on currently reported non-covalent ARC

Aside from covalent antibody-siRNA conjugates, researchers explored non-covalent interactions to allow delivery of siRNAs.<sup>410</sup> More precisely, these methods rely on siRNA complexation or its encapsulation into particles to protect it from degradation. In addition, the high amount of positively charged present on these particles is thought to enhance the endosomal escape capacities of the construct.<sup>411</sup>

Two approaches rely on antibody-peptide conjugates for siRNA complexation, either chemically conjugated or by making fusion proteins. Supramolecular approaches using siRNA-containing liposomes or polymer, grafted with antibodies, were also reported.<sup>340</sup>

#### i. Supramolecular approaches

The most applied transfection method for oligonucleotides since the early 1980s is by encapsulating it into lipid-based nanoparticles (LNP) of less than 100 nm in diameter.<sup>412,413</sup> Therefore, it is understandable that researchers first focused on the targeted delivery of such particles by coating them with a cell-penetrating factor. Pardridge's group was the first one to integrate antibodies into liposomes to deliver a short hairpin RNA-encoding plasmid (shRNA) containing RNAi sequences against EGF in xenografted brain tumors.<sup>414</sup> They used two antibodies, one targeting transferrin-receptors that enables transport across the blood brain barrier, and an anti-human insulin-receptor antibody that allow endocytosis by cancer cells. From a synthetic point of view, the authors grafted the liposome-containing plasmid with maleimide-containing polyethylene glycol (PEG) chains. Then, they used Traut's reagent to install a free thiol group onto the antibody's lysines, and Michael addition between the two counterparts yielded the immunoliposomes (Figure 115).<sup>415</sup> Regarding the activity, the authors observed 88% EGF extinction *in vivo* after 4 doses of 5  $\mu\text{g}$  of conjugate intravenously. Surprisingly, this silencing correlated with an increase of the survival time from 17 days for non-treated animals to 32 days for the treated ones.

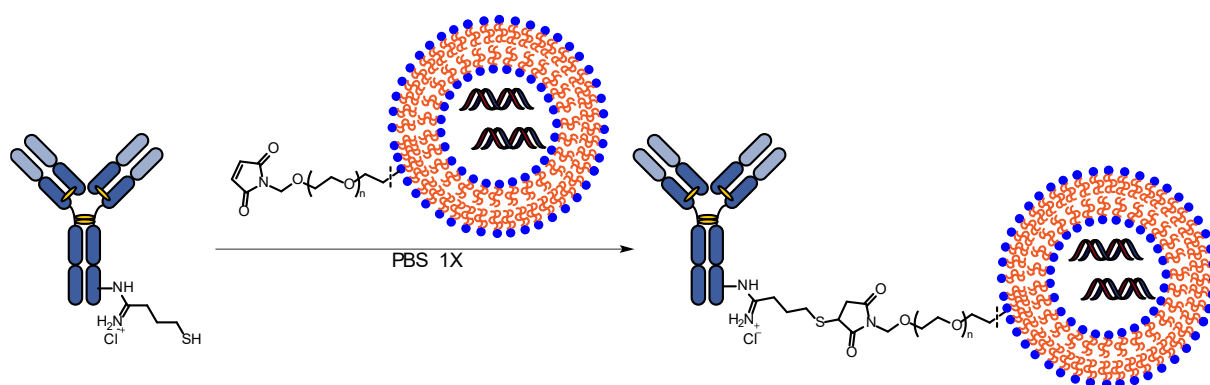


Figure 115 - Immunoliposomes strategy proposed by Pardridge's group.

Aside from liposomes, Peter Schultz's group published in 2013 an antibody-cationic polymer conjugate that is able to complex siRNA.<sup>416</sup> In this study, genetically encoded *para*-acetylphenylalanine (*pAcF*)<sup>417,418</sup> anti-HER2 Fab or full IgG1 was produced to install a handle onto the antibody. The inserted ketone was selectively coupled with an aminoxy-derivatized polymer. The latter was composed of two copolymers synthesized using reversible addition-fragmentation chain-transfer polymerization (RAFT) technology.<sup>419</sup> One of the copolymer contained guanidinium groups to allow siRNA complexation and the other one contained poly(*N*-isopropylacrylamide) to modulate the hydrophobicity of the polymer (Figure 116). Using a siRNA targeting GAPDH, this system efficiently silenced 85% of the gene with 300 nM of Fab-polymer conjugate and 100 nM of siRNA (ratio Fab/siRNA = 3). The full IgG1 construct was even more efficient, with a comparable silencing effect with an equimolar mixture of IgG1/siRNA at 100 nM. However, a conjugation site near the antigen binding domain failed to deliver the siRNA, showing that the gene silencing was site-dependent, probably due to steric hindrance with the polymer. Noteworthy, the authors demonstrated by competition assays with naked antibody that the gene silencing was antigen-dependent.

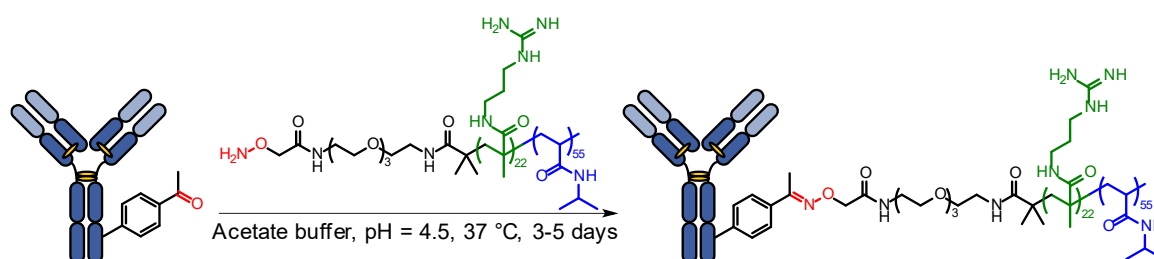


Figure 116 - Antibody-polymer conjugate synthesized by Schultz's group. Reactive groups for conjugation are in red, cationic part is in green, and hydrophobic part is in blue.

These approaches showed interesting results to deliver siRNAs inside cells. However, (Table 7)

Table 7 – Antibody-siRNA assemblies based on supramolecular approaches

Scaffold of antibody <sup>ref</sup>	Technology used	Silencing efficiency at 48h (dose of antibody)	N/P at this ratio
Transferrin-IgG1 and HIR-IgG1 <sup>414</sup>	Liposome-conjugate (thiol-maleimide conjugation)	siEGFR 88% (4 x 166 nM, <i>in vivo</i> )	Unknown
HER2-IgG and Fab <sup>416</sup>	Guanidine-rich polymer-conjugate (oxyme ligation)	siGAPDH 85% (Fab/siRNA ratio 1/3, 300 nM, <i>in vitro</i> )	Unknown

		85% (IgG/siRNA ratio 1/1, 100 nM, <i>in vitro</i> )	
--	--	--	--

## ii. Complexation with conjugated-cationic peptides

Aside from encapsulation with polymeric or lipophilic particles, siRNAs have been delivered in the cytosol using highly cationic peptides. Due to their higher pKa and the geometry of the guanidinium group, arginines represented the amino acid of choice for the binding to siRNA.<sup>420</sup> Indeed, arginine-rich peptides are known to enhance RNA delivery systems<sup>421</sup>, either to facilitate the endosomal escape<sup>422,423</sup> or to protect the siRNA against degradation.<sup>424</sup> Considering these elements, the conjugation of polyarginines to antigen-binding domains was considered as an efficient method for the targeted delivery of siRNA.

Kumar *et al* were the first team to publish a non-covalent targeted delivery system for siRNA using bioconjugation methods by linking a nona-D-arginine to an anti-CD7 scFv.<sup>425</sup> The stereochemistry of the polyarginine was crucial here, as D-peptides are poor substrates of protease compared to L-peptides.<sup>426,427</sup> From a synthetic point of view, the authors inserted a free cysteine at the C-terminus of an anti-CD7 scFv and conjugated it to a Cys(NPys)-r<sub>9</sub> by thiol-exchange reaction (Figure 117). Using a scFv/siRNA molar ratio of 5, the authors showed that this system was efficient to silence CCR5 inside T cells *in vivo* at 8.3 μM, protecting the mice from HIV infection.

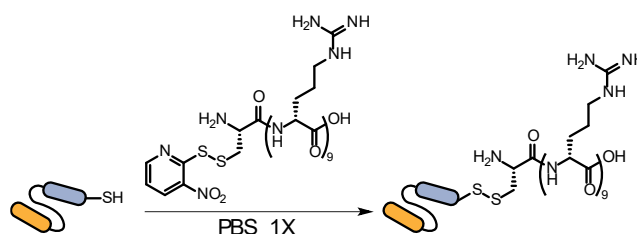


Figure 117 - scFv-conjugated nona-D-arginines strategy proposed by Kumar *et al*.

In another study, the same peptide was conjugated to an anti-Lewis-Y antibody after the introduction of a reactive thiol on the antibody using Traut's reagent (Figure 118).<sup>321</sup> This conjugate was able to complex siRNA with a mAb/siRNA molar ratio of 10 and 5, at DoC 1 and 4, respectively. The resulting complex efficiently silenced STAT3 in the targeted cells, with 60% protein depletion at DoC 1, while the covalent strategy, described earlier, was not able to do so without addition of chloroquine. Interestingly, while increasing the DoC to 4 allowed a better complexation of the siRNA, the resulting conjugate delivered the siRNA non-specifically to non-targeted cells. Therefore, this study suggests that using high degree of conjugation of

peptide could be counterproductive, and that one should conjugate a highly complexing peptide but with lowest DoC.

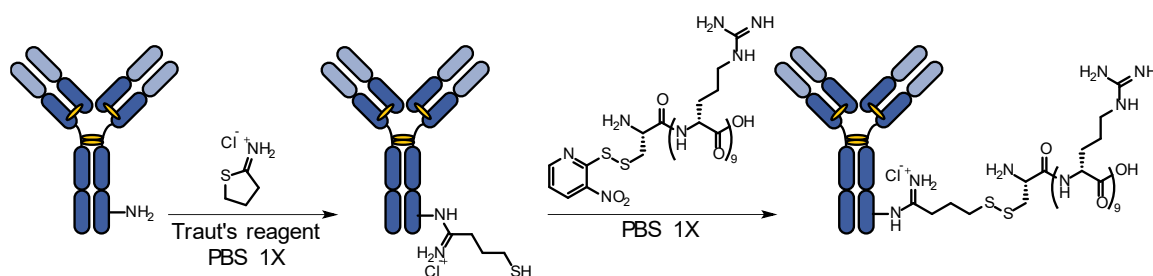


Figure 118 - Native antibody-conjugated nona-D-arginine proposed by Ma *et al.*

Other strategies relying on other peptides than polyarginines have been reported. Hauser *et al* synthesized an antibody-protamine conjugate to deliver siRNAs through electrostatic interactions *in vivo*.<sup>428</sup> Protamine is a mixture of arginine-rich peptides widely used as a heparin-antidote<sup>429</sup> that is able to complex siRNA<sup>430</sup> and to protect it from degradation by ribonuclease.<sup>431</sup> They generated polyclonal antibodies that can bind murine podocytes, and reduced these homodimers into monomers by selective reduction of heavy chains disulfide bonds. The monovalent fragments thus contained free thiols that were conjugated to maleimide-containing Neutravidin by Michael addition. The antibody-neutravidin conjugate was then mixed with protamine-biotin conjugate to yield the desired antibody-protamine conjugate (Figure 119). The latter was used to deliver siRNAs specific to TRPC6, and showed protein depletion 65% respectively after 48 h, with an antibody/siRNA ratio of 1/4 and 12.5 nM of conjugate.

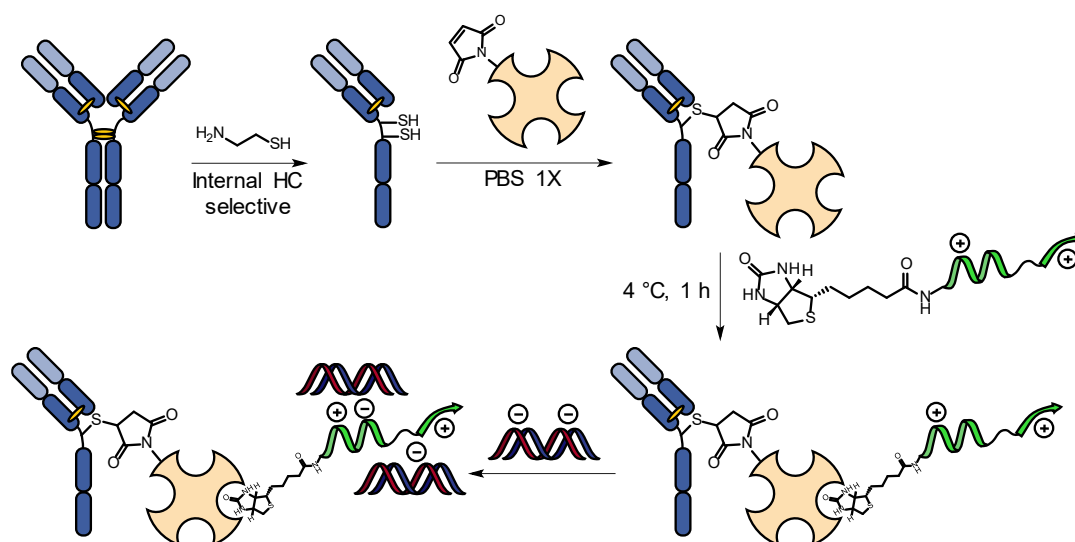


Figure 119 – Electrostatic strategy proposed by Hauser *et al*, using protamine-conjugated antibody. The linkage was done by exploiting biotin-neutravidin affinity.

In 2015, Bäumer *et al* published the antibody-mediated delivery of anti-KRAS siRNA *in vivo* to overcome KRAS-mediated resistance of cancer cells using a simpler approach.<sup>347,432</sup> KRAS is a widely studied oncogene, and its mutations prevent the inhibitory effects of monoclonal antibodies by developing resistances. Therefore, the authors suggested that silencing mutated KRAS could potentially overcome cancer resistance.<sup>433</sup> Their strategy is to covalently couple protamines to SMCC *via* the N-terminus. The resulting maleimide-protamines were then coupled to an anti-EGFR antibody *via* cysteine conjugation (Figure 120). The protein-protamine conjugate was not characterized by mass spectrometry analysis, as protamine is a mixture of peptides. However, they showed that it could bind several siRNA while being able to bind to EGFR and internalize inside the cell. Moreover, the bound siRNA was stable in human plasma, as no degradation could be seen after 22 hours of incubation, showing that the protamine effectively protects the siRNA from degradation. Regarding the activity, this construct was able to suppress mutated KRAS up to 80% with 50 nM of antibody-protamine conjugate, and a conjugate/siRNA ratio of 1/10. This exceptional activity proved to work *in vitro* and in xenograft models of antibody-resistant and KRAS-mutated cancer cells, suggesting that antibody-mediated delivery of siRNA can serve as a potential therapy to fight cancer resistance. The same strategy was exploited recently using an anti-PSMA antibody that could deliver a siRNA against TRIM24, and they observed roughly the same efficacy in terms of gene silencing *in vivo*.<sup>434</sup>

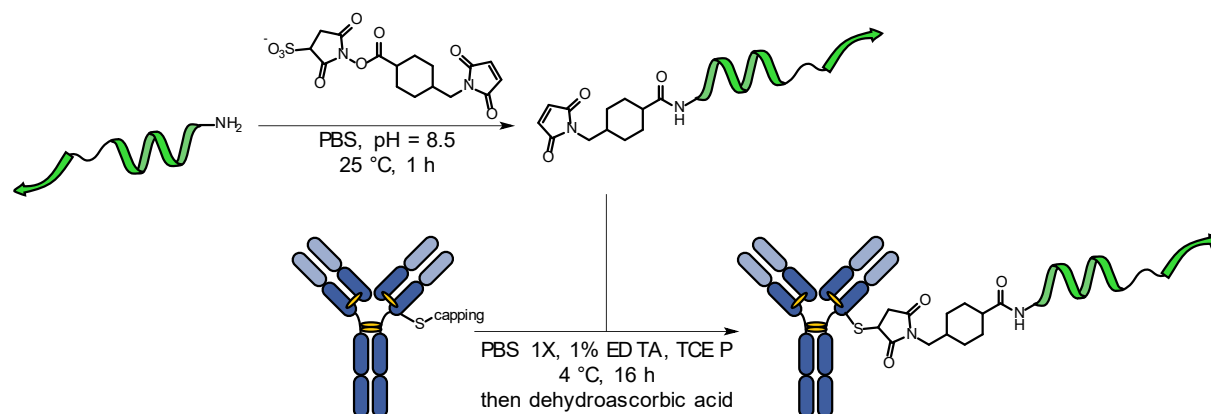


Figure 120 - Strategy first published by Bäumer *et al*, and exploited by Shi *et al*, using sulfo-SMCC-mediated conjugation of protamine to monoclonal antibodies.

While these strategies (Table 8) offer good efficiencies for siRNA delivery and gene silencing compared to covalent systems because of higher endosomal escape abilities, the resulting conjugates are often not chemically defined and not characterized, due to the too high heterogeneity of protamine peptides.<sup>432,434</sup> This heterogeneity could lead to the formation of large aggregates that could affect the plasma clearance, the tolerated dose and, more importantly, the potency of the resulting construct.<sup>308</sup> In addition, while having multiple peptides

on the antibody can increase the siRNA loading, this can also affect the non-specific delivery to non-targeted cells due to the high amount of positive charges.<sup>321,425</sup>

To address this issue, the majority of non-covalent antibody-peptides conjugates do not use chemically-linked peptide, but fusion proteins, allowing a better control of the antibody/peptide ratio.

Table 8 – Antibody-peptide conjugates for siRNA delivery.

Scaffold of antibody <sup>ref</sup>	Technology used	Silencing efficiency at 48h (Ab/siRNA ratio, dose Ab)	N/P at this ratio (antibody's charges not counted)	Remarks
CD7-scFv <sup>425</sup>	Nona-D-arginine conjugate (thiol-exchange, DoC 1)	siCCR5 50% (5/1, 8.3 μM, <i>in vivo</i> )	0.2	DoC 1 limited the non-specific delivery
Le <sup>y</sup> -IgG <sup>321</sup>	Nona-D-arginine conjugate (thiol exchange, DoC 1)	siSTAT3 60% (5/1, 1.5 μM, <i>in vitro</i> )	0.2	DoC 4 led to non-specific delivery
Monomer of IgG <sup>1428</sup>	Protamine conjugate (biotin-Neutravidin, DoC 1)	siTRPC6 85% (1/4, 2.5 μM, <i>in vivo</i> )	Unknown	Use of protamine led to a mixture of antibody-peptide conjugates  N/P ratio unknown because of protamine
EGFR-IgG <sup>347</sup>	Protamine conjugate (thiol-maleimide conjugation, DoC not specified)	siKRAS 80% (1/10, 50 nM, <i>in vivo</i> )	Unknown	Use of protamine led to a mixture of antibody-peptide conjugates  N/P ratio unknown because of protamine
PSMA-IgG <sup>434</sup>	Protamine conjugate (thiol-maleimide conjugation, DoC not specified)	siTRIM24 65% (ratio unknown, 100 nM, <i>in vivo</i> )	Unknown	Antibody/siRNA ratio not reported  Use of protamine leads to a mixture of antibody-peptide conjugates  N/P ratio unknown because of protamine

### iii. Complexation with fused-cationic domains

The vast majority of antibody-mediated delivery systems for siRNA use fusion proteins between antibodies and cationic peptides.<sup>340</sup> Indeed, fusion proteins allows to control the antibody/peptide ratio, which is generally stoichiometric to simplify experiments.<sup>435</sup>

In 2005, Song *et al* is the first group to report such encoded fusion proteins for siRNA delivery, connecting a Fab against HIV envelope to a truncated protamine peptide (RSQSRSRYRQRQRSRRRRRS).<sup>436</sup> This enables to target hard-to-transfect HIV-infected T cells in order to inhibit HIV replication. The authors observed that the delivery of anti-*gag* siRNA (a HIV protein) with their fusion protein, has the proportion of infected T cells declined from 85% for untreated cells to 36% when treated with only 1 nM of siRNA (450 pM of antibody). Using this system and a cocktail of siRNAs targeting oncogenes intravenously *in vivo* (2.7 μM siRNA, 450 nM of antibody), the authors observed a significant tumor growth inhibition after 9 days.

The same approach was exploited by many studies using different siRNAs and surface-antigens with other goals. For example, researchers attempted to reduce tumor's growth<sup>437-440</sup>, decipher a selectivity between high-antigen-expressing cells over low-expressing cells<sup>441</sup> or protect cells against a virus infection.<sup>174,320,436,442</sup> Roughly, while transfected siRNA show very high efficiency at low nanomolar range, the dose has to be highly increased to micromolar range when using this system for *in vivo* studies.

To summarize, antibody-protamine fusion proteins are a widely used method for the non-covalent delivery of siRNAs (Table 9). Overall, many teams were able to silence the targeted gene *in vivo* with high efficiency. However, the major drawback of this method is the use of recombinant proteins, which can be tough to express in industrial scale, limiting the applications of these.

Table 9 – Selected examples of fusion proteins between antigen-binding domains and protamines for siRNA delivery.

Target and scaffold of antibody <sup>ref</sup>	N/P (antibody's charges not counted)	Ratio peptide/siRNA	Silencing efficiency at 48h (dose Ab)
HIV-env-Fab <sup>436</sup>	0.05	1/6	si- <i>myc</i> , si-MDM2, siVEGF cocktail 50% tumor regression (450 nM, <i>in vivo</i> )
HER2-scFv <sup>437</sup>	0.05	1/6	siPLK1 45% (5 nM, <i>in vitro</i> )



			75% (225 nM, <i>in vivo</i> )
HER2-Fab <sup>438</sup>	0.06	1/5	siDNMT 75% (417 nM, <i>in vivo</i> )
LFA1-scFv <sup>441</sup>	0.06	1/5	siCCR5 75% (1 μM, <i>in vitro</i> )
HBsAg-scFv <sup>442</sup>	0.06	1/6	>80% (350 nM, <i>in vivo</i> )
PSMA-scFv <sup>439</sup>	0.06	1/5	siNotch1 73% (417 nM, <i>in vivo</i> )
MM-scFv <sup>440</sup>	0.05	1/6	siLivin 55% (140 nM, <i>in vivo</i> )
3G1-scFv <sup>174</sup>	0.03	1/10	siHV2 70% (40 nM, <i>in vivo</i> )

## B. Development of a synthetic strategy for non-covalent ARC

Tony Rady,<sup>1,2</sup> Renaud Morales,<sup>2</sup> Hervé Bouchard,<sup>2</sup> Guilhem Chaubet,<sup>1</sup> Nicolas Basse,<sup>2,\*</sup> and Alain Wagner<sup>1,\*</sup>

<sup>1</sup> Bio-Functional Chemistry (UMR 7199), LabEx Medalis, University of Strasbourg, 74 Route du Rhin, 67400 Illkirch-Graffenstaden, France

<sup>2</sup> Sanofi Strasbourg, 16 rue d'Ankara, 67000 Strasbourg, France

### i. Introduction

Many strategies to deliver small interfering RNAs (siRNAs) exploit their negative charges to form particles and complexes, such as using cationic peptides<sup>443,444</sup> or cationic liposomes.<sup>208</sup> However, these strategies often lack targeting agents, leading to siRNA delivery to healthy cells and subsequent adverse effects.<sup>445</sup> To address this issue, tremendous efforts have been conducted to coat nanoparticles or liposomes with ligands targeting a transmembrane protein. Upon specific binding to cell, the construct should be internalized, eventually releasing siRNA to the cytosol. Aside from these encapsulation methods, antibodies able to efficiently complex siRNAs by the presence of a conjugated or fused cationic peptide appeared as a viable strategy.<sup>321</sup>

Among these peptides, the most widely used is based on protamine, a mixture of arginine-rich peptides, or short homopolyarginines.<sup>347,434,436,439</sup> Due to the higher pKa and the geometry of the guanidinium group allowing three binding points with the phosphate backbone of siRNA, arginine represented the amino acid of choice for siRNA complexation.<sup>420</sup> In addition, the resulting complex confers protection to degradation.<sup>430,446</sup> Considering these elements, the

conjugation or fusion of polyarginines to antibodies was considered as an attractive method for the targeted delivery of siRNA.

However, among currently described systems, the ill-defined stoichiometry between the antibody-polyarginine and the siRNA (generally siRNA/antibody molar ratio = 6) leads to drawbacks, among which the non-molecularly defined structure is the first to be addressed. Indeed, classical preparation yields mixture of particle of different size, charge, antibody to siRNA ratio, leading in turn to hard-to-reproduce and to optimize ADME and PK profile. For instance a high loading of cationic peptide to the antibody greatly diminishes its cell-specificity due to its positively charged nature thus inducing non-specific internalization.<sup>321</sup> Thus, we believe that a optimized design of the peptide, which could interact in a one-to-one stoichiometry with a corresponding siRNA, could help to overcome drawbacks linked to biological activity, such as the siRNA loading or non-specific delivery (Figure 121).

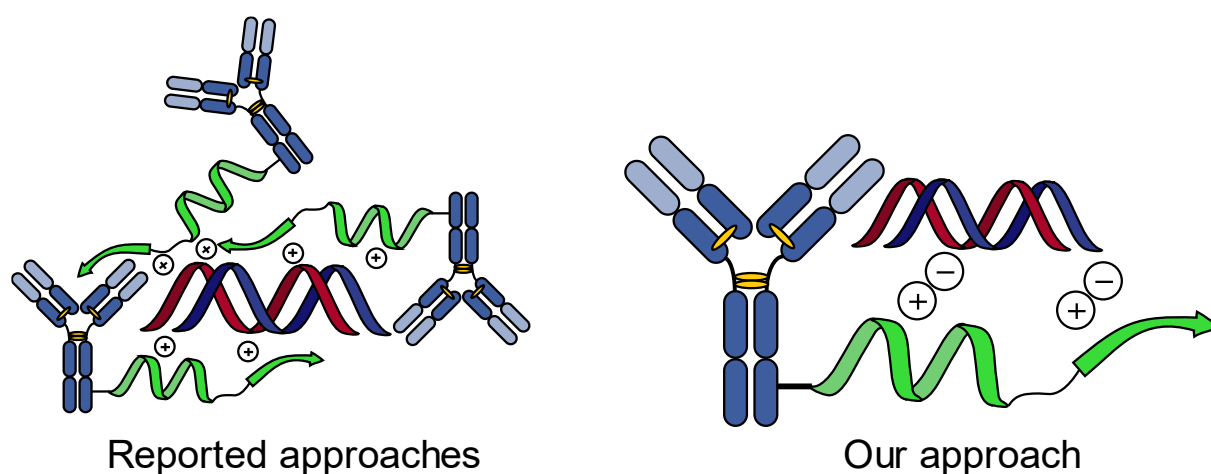


Figure 121 – Currently reported non-covalent approaches often lead to undefined particles (left), while our approach aims to develop a peptide able to interact in a one-to-one ratio with siRNAs (right).

Reflexing on this issue, we planned to synthesize arginine-rich peptides of different structures, lengths and net charges, and to evaluate their binding affinity to a model siRNA using biophysical methods. The evaluation of these different criteria would allow us to determine an optimized structure with the ability to complex siRNAs in a 1/1 ratio before conjugation to a model antibody and subsequent biological evaluation.

## ii. Results and discussion

### 1. Synthesis of a first antibody-peptide conjugate

In order to first implement the different synthetic strategies, binding affinity determination, and bioconjugation methods, a first peptide building block, based on linear decaarginines (R<sub>10</sub>G, **104**) was prepared.

In order to simplify the synthesis of the different designs, an easily-clickable homopolyarginine building block was synthesized by manual SPPS using Fmoc-strategy. The most common guanidine protecting group used for Fmoc-arginine is the acid-labile 2,2,4,6,7-pentamethylidihydrobenzofuran-5-sulfonyl (namely Pbf) group. This protecting group has the strong advantage to be slow to deprotect, and only under harsh acidic conditions (>90% TFA), therefore, the isolation of fully protected peptides can be achieved by using a more acid-labile 2-chlorotrityl-containing resin if required. Using COMU-mediated couplings (Figure 122), the building block **104** was synthesized in high overall yield and isolated with high purity (>95%).

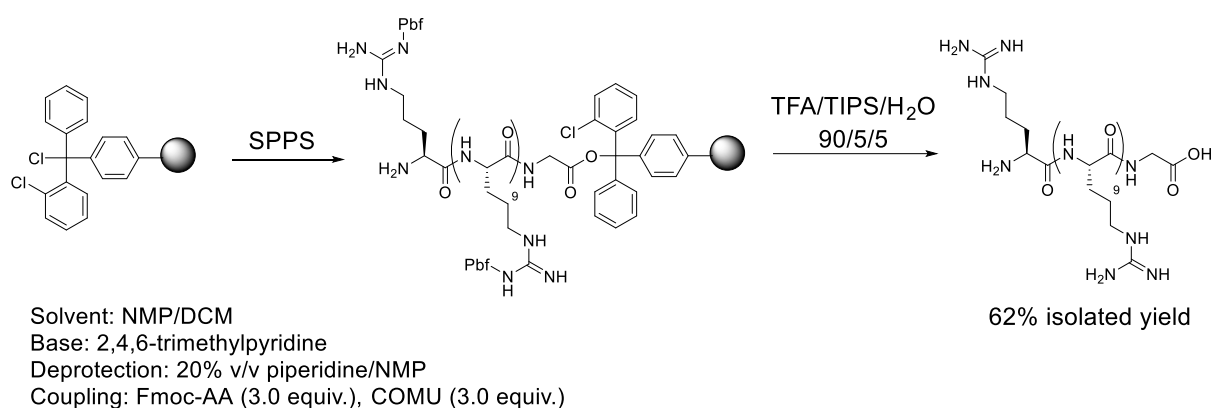


Figure 122 – General synthesis road to polyarginine, example with  $R_{10}G$  **104**.

Its clickable version ( $N_3$ - $R_{10}G$ ) **105** was obtained by adding commercially available  $\omega$ -azidolysine at the N-terminus with similar yield and post-purification purity. EphA2-antibody was modified with BCN-PEG<sub>6</sub>-PFP linker **6** (used in chapter IV), affording antibody-BCN conjugate **106**. The resulting mixture was then reacted with 20 equivalents of the azide-containing peptide, and, after purification, antibody-peptide conjugate **107** was obtained. A clean MS spectrum was obtained, with an average degree of conjugation of 4.84, demonstrating the effectiveness of this methodology to produce antibody-peptide conjugates (Figure 123).

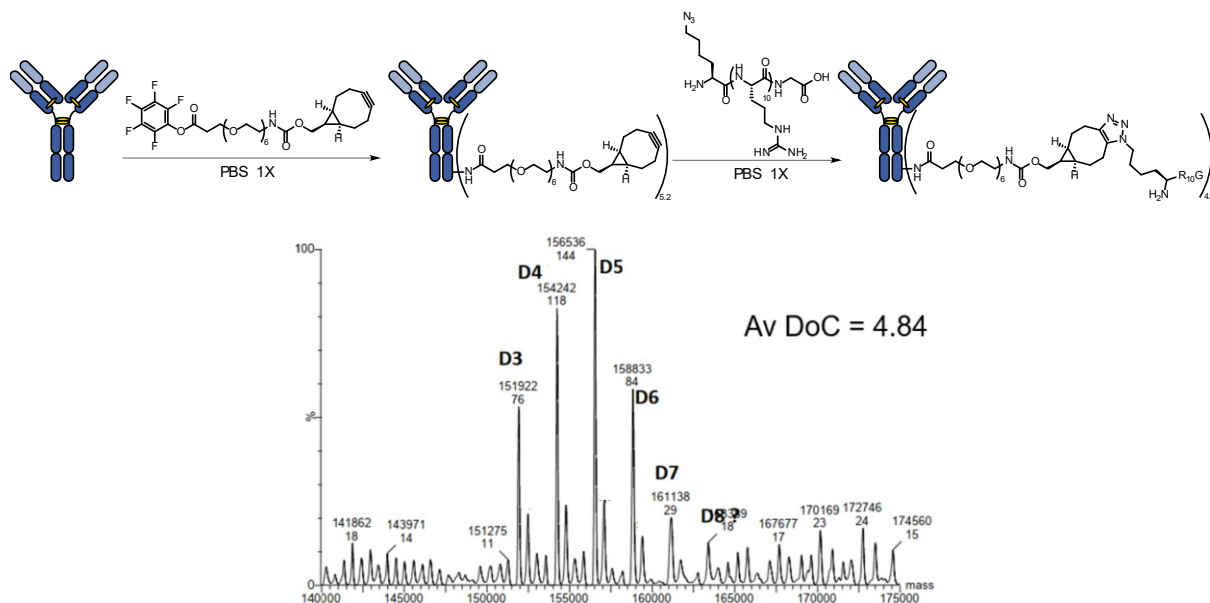


Figure 123 – Synthesis and structure of antibody- $R_{10}G$  conjugate **107** and resulting MS spectrum.

## 2. Biophysical properties regarding siRNA binding

Now that a strategy to synthesize defined antibody-peptide conjugate was established, the ability of the peptide to bind a model  $Cy_5$ -siRNA was performed following two methods: first, the dissociation constant ( $K_D$ ) between these two molecules was determined by microscale thermophoresis (MST). Then, the ability to form stable complexes and the related stoichiometry was determined by gel retardation assay on native agarose gel using different peptide/siRNA ratios in PBS 1X.

Following the first method, a surprisingly low  $K_D$  peptide/siRNA of 82 nM was calculated, showing the strong affinity between the peptide **104** and the siRNA (Figure 124). Results by gel retardation showed however that a complete complexation could be achieved using 60 equivalents of peptide with respect to the siRNA, corresponding to an amine/phosphate ratio (N/P) of 15. Noteworthy, the addition of the  $\omega$ -azido lysine did not have a strong impact on the binding, as the calculated dissociation constant between **105** and the siRNA was 89 nM, compared to the 82 nM with **104**.

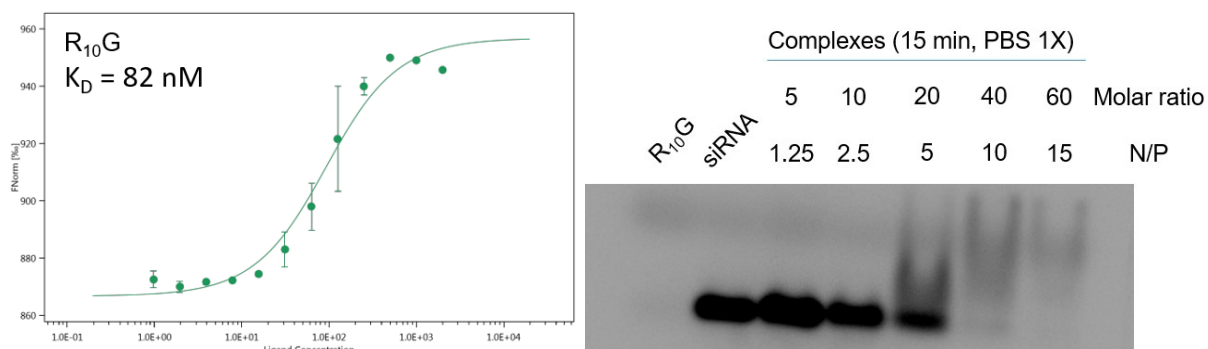


Figure 124 – Binding affinity and complexation ability between R<sub>10</sub>G **104**. Left: microscale thermophoresis result, using a 1:1 model – right: gel retardation assay with 5% agarose gel.

Same experiments were repeated with the antibody alone, and not any binding could be observed by these techniques in DPBS 1X at pH 7.4. However, antibody-peptide conjugate **107** proved to be highly complexing (Figure 125), with a K<sub>D</sub> antibody/siRNA = 5 nM. Considering that there is an average of 4.84 peptides per antibody, and because the previous K<sub>D</sub> peptide/siRNA (82 nM) is more than 4.84 times the current K<sub>D</sub> antibody/siRNA, it appears that having multiple R<sub>10</sub>G on the antibody confers cooperativity effects. Regarding the gel retardation assay, a complete complexation of siRNA could be achieved with 20 equivalents of **107** with respect with the siRNA. Without counting the charges of the antibody, we calculated a N/P = 24.2, meaning that there is 24.2 positive charge for each negative charge in these complexes.

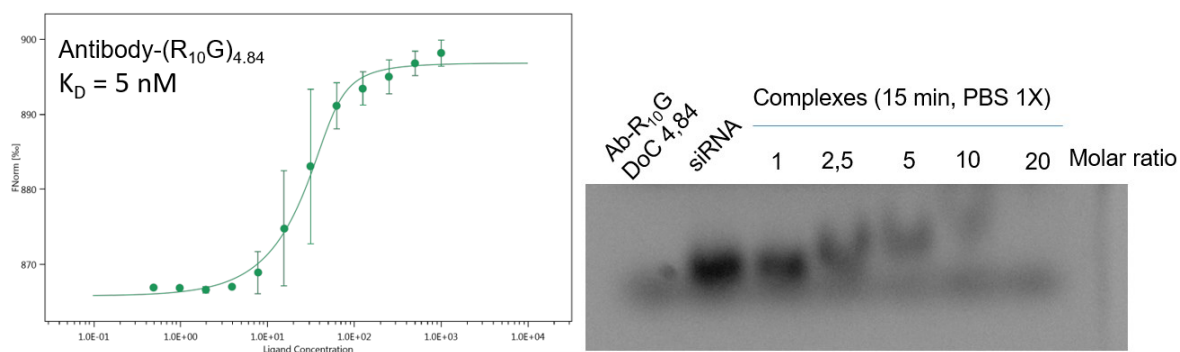


Figure 125 – Binding affinity and complexation ability between Ab-R<sub>10</sub>G **107**. Left: microscale thermophoresis result, using a 1:1 model – right: gel retardation assay with 5% agarose gel.

As such system is likely to form particles, the average size of the complexes was measured by Dynamic Light Scattering (DLS, summarized in Table 10) after 15 min of incubation in PBS 1X at 25 °C using different N/P ratios. Briefly, increasing the latter ratio with the peptide **104** alone resulted in larger (from 421 nm to 744 nm, polydispersity index = 1.32) and more cationic particles (Zeta potential from -5.88 to 13.0 mV). As increasing the amount of **104** resulted in bigger particles, we assume that a more complexing peptide is required to achieve a complete complexation of siRNAs at smaller N/P.

Using the antibody-peptide conjugate **107**, the average size of particles was significantly smaller, ranging from 18.5 nm at N/P = 12.1 to 17.3 nm at N/P = 24.2. When compared to the peptide **104** at similar N/P, we suppose that conjugating the peptide to the antibody greatly enhance the complexation with the siRNA, due to proximal charge display, thus resulting to smaller particles.

Table 10 - Summary of DLS measurements.

Structure	Structure/siRNA ratio	N/P ratio	Zeta potential (mV)	Average size by intensity (nm)
R <sub>10</sub> G	10	2.5	-5.88 ± 0.25	421.5 ± 105.7
	50	12.5	0.4 ± 6.2	733.4 ± 206.0
	100	25	13.0 ± 7.9	744.9 ± 182.9
Antibody-(R <sub>10</sub> G) <sub>4.84</sub>	10	12.1	-0.3 ± 4.1	18.5 ± 2.4
	20	24.2	5.3 ± 2.9	17.3 ± 2.4

### 3. Biological assay and microscopy

Even though neither the peptide nor the degree of conjugation was optimized yet, we attempted a first siRNA delivery with the antibody-peptide conjugate **107**. Following Ma *et al*<sup>β21</sup> procedure, different N/P ratios were used, with a fixed concentration of siRNA. In our experiment, we used the RIG-I-activating siPLK1-5'ppp sequence, and the readout was based on luciferase expression following RIG-I activation (explained during chapter IV) on A549-Dual cells for 72 h (Figure 126). Satisfyingly, peptide **104** alone proved to efficiently deliver the siRNA inside cells with a N/P = 12.5, thus inducing an activation of RIG-I. Regarding the antibody-peptide conjugate **107** (DoC 4.84, Figure 126), we were unable to activate RIG-I with any of the tested N/P ratios.

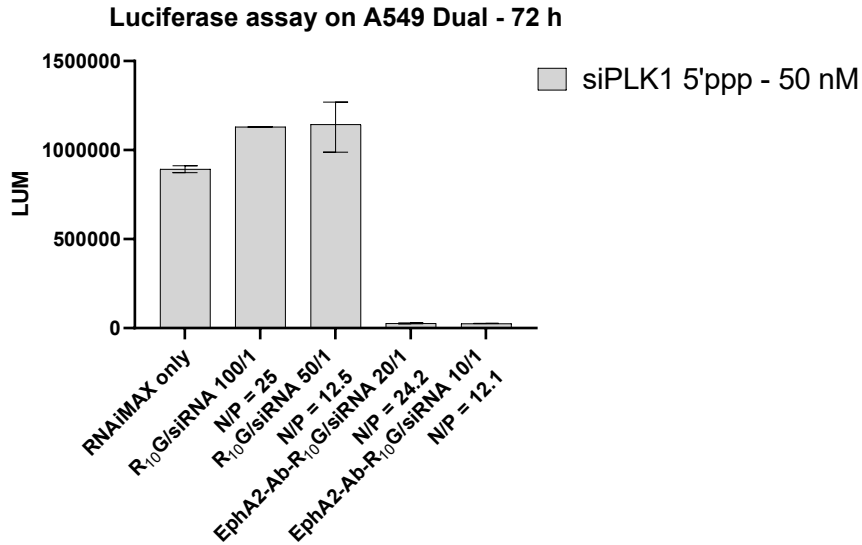


Figure 126 - Luciferase assay on A549-Dual cells using both the R<sub>10</sub>G peptide **104** and the antibody-R<sub>10</sub>G conjugate **107**.

Different hypotheses were envisaged, among which a lack of internalization of the resulting non-covalent ARC. Thereby, a confocal microscopy study was first performed on A549 cells after two hours of incubation with a Cy<sub>3</sub>-labelled siRNA and Cy<sub>5</sub>-labelled R<sub>10</sub>G peptide (Figure 127), using N/P = 25. In a second time (Figure 128), the same experiment was repeated but using the antibody-peptide conjugate **107** labelled with Sulfo-Cy<sub>5</sub>-NHS ester (DoC peptide: 4.84, DoC Cy<sub>5</sub>: 2.2, N/P = 24.2). Finally, in a last set of experiment (Figure 129), the non-covalent ARC was formed with an antibody/siRNA ratio of 10/1 30 min before incubation on cells.

While the siRNA alone was unable to enter inside the cell (upper line), the Cy<sub>5</sub>-R<sub>10</sub>G peptide was well internalized (middle line). In accordance with Figure 126, a mixture of Cy<sub>5</sub>-R<sub>10</sub>G/Cy<sub>3</sub>-siRNA (N/P = 25, complete complexation by gel, particle size = 744 nm) was efficiently internalized in these conditions, characterized by an appearance of both fluorescent markers inside the cell (bottom line).

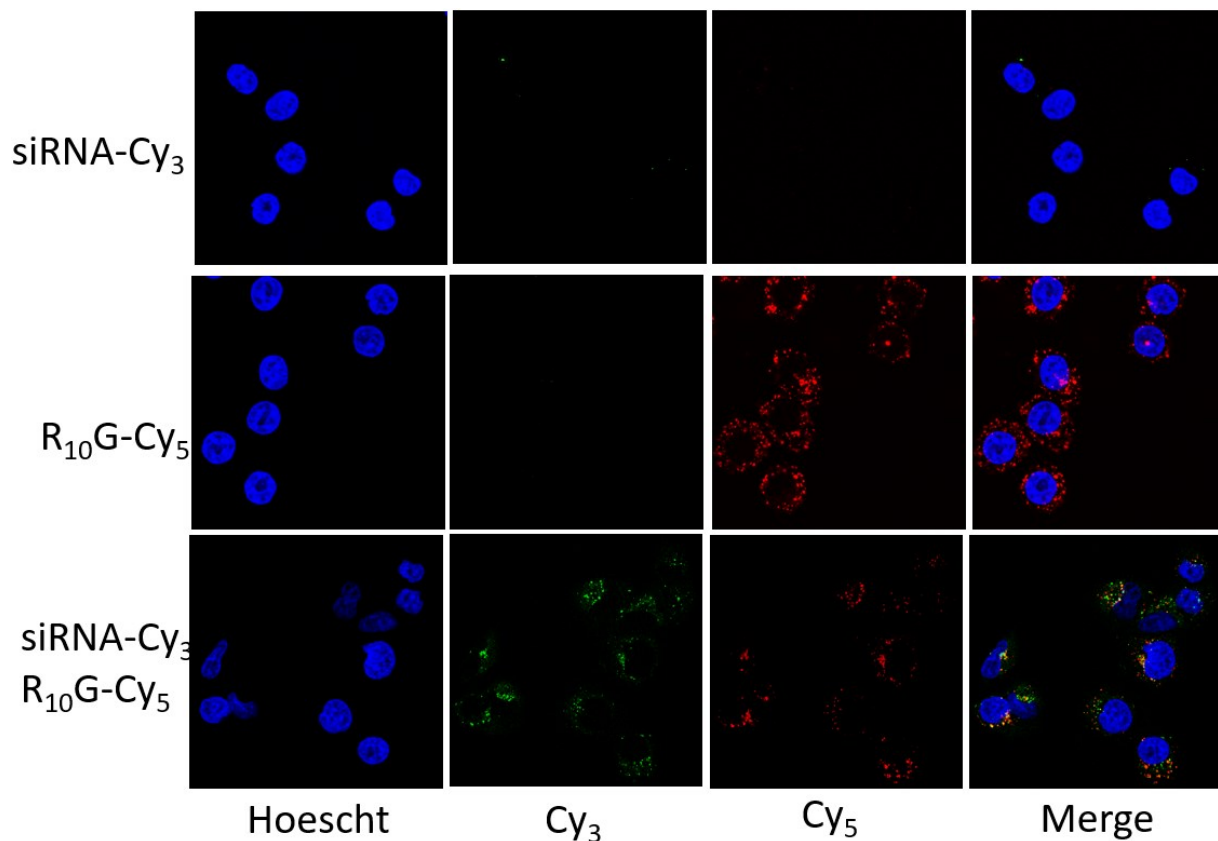


Figure 127 - Confocal microscopy study regarding the internalization of the peptide/siRNA complex.

Regarding the antibodies (Figure 128), Cy<sub>5</sub>-labelled EphA2-antibody without any conjugated peptide was internalized in an antigen-dependent manner, characterized by an appearance of clear, membrane labelling (upper line). The EphA2-antibody-peptide conjugate **107** was also internalized (middle line), however, we did not observe a clear membrane labelling. Intrigued by this observation, we repeated this last experiment with an antibody that should not enter in the cell (rituximab, anti-CD20, Figure 128). We observed that, when conjugated to the peptide (DoC 4.62), rituximab was also internalized, although it should not. Therefore, we suggested that antibody-polyarginine conjugate with high DoC could induce an undesirable antigen-independent internalization.



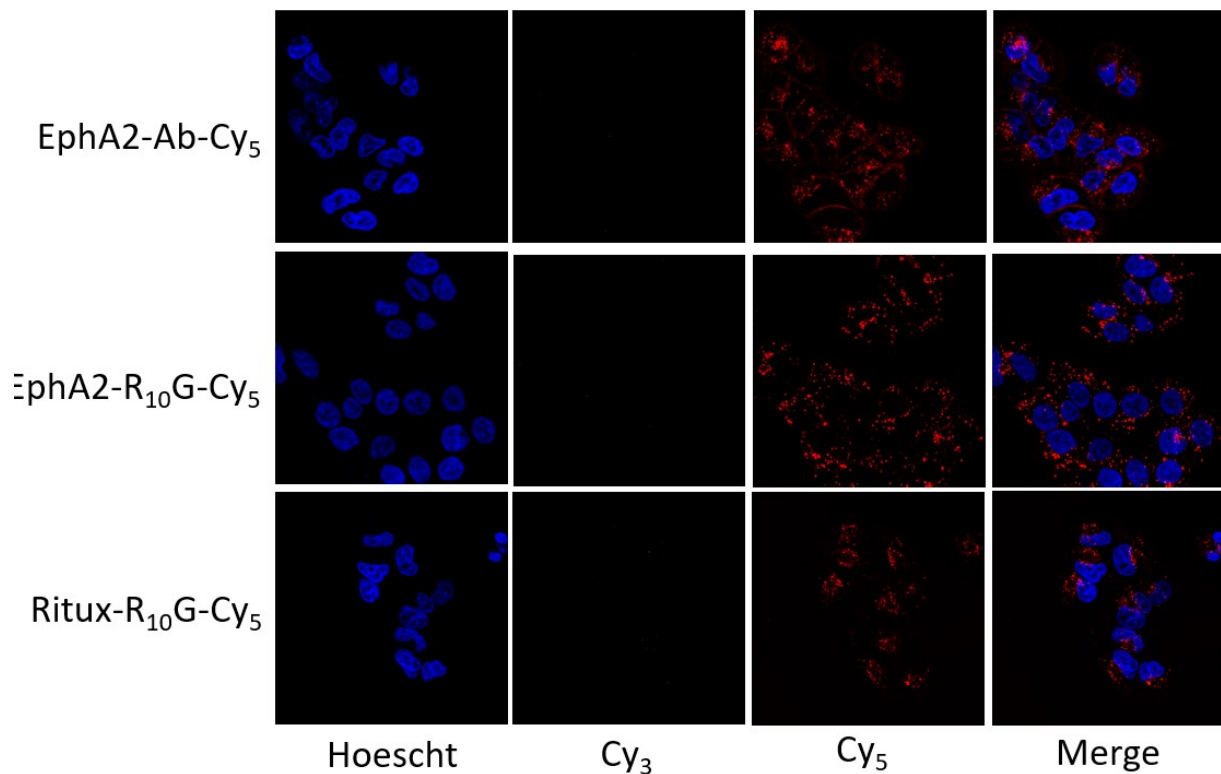


Figure 128 - Confocal microscopy study regarding the internalization of the antibody-peptide conjugate **107**.

Concerning the delivery of siRNA with antibody-peptide conjugate **107** (Figure 129), fluorescence of both antibody and siRNA were observed inside cells, independent of the antibody. This result thus confirmed that, with our system (N/P = 24.2, complete complexation by retardation gel, particle size = 17 nm), the siRNA was delivered inside the cell, but in a non-targeted manner. It also appeared that both dyes colocalized, and as we could not observe any effect on RIG-I during biological assays, we thus hypothesized that the complex was too stable in the cell, thus preventing the release of siRNAs into the cytosol and subsequent biological activity.

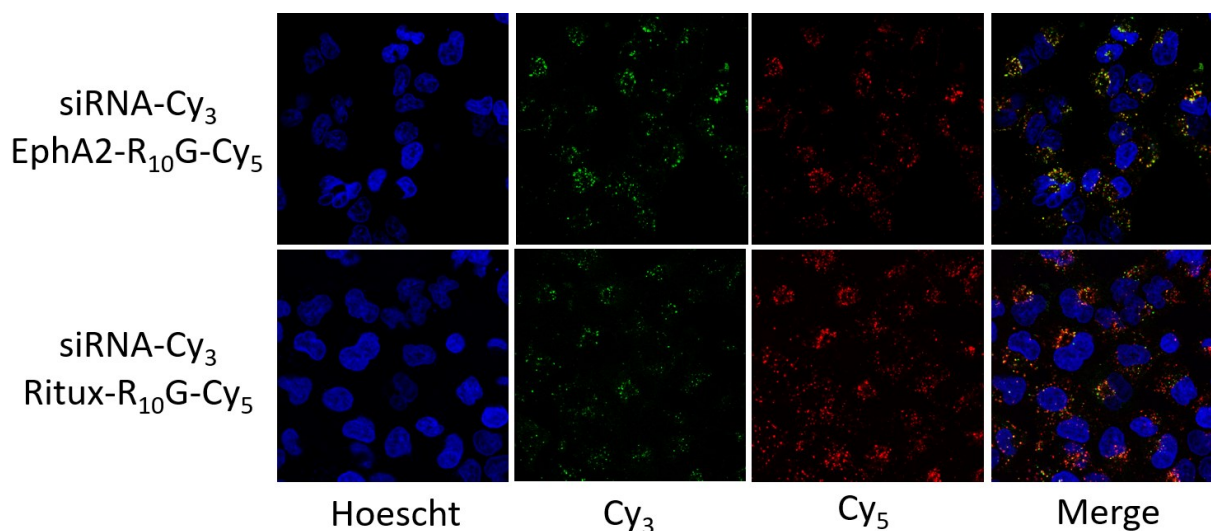


Figure 129 - Confocal microscopy study regarding the internalization of the antibody-peptide/siRNA complex, at  $N/P = 25$ .

All these results comforted our initial postulate that ill-defined particles (i.e not a stoichiometric mixture of siRNA/antibody-peptide conjugate) may not be applicable for all cell types and antibody/antigen couple. As the objective of this project is to obtain a complete complexation with a stoichiometric mixture of siRNA/antibody-peptide conjugate, we attempted to optimize the peptide's structure. Therefore, novel peptides with different lengths, secondary structures and net charges were designed, synthesized and their binding affinity with siRNAs was evaluated by microscale thermophoresis. Such methodology can serve as a basis to establish what element is important for siRNA binding.

#### 4. *Syntheses of different designs and binding affinity with siRNA*

Among the different designs (Table 11), a hydrophilic negative control based on decaserine  $S_{10}G$  **108** was synthesized. In order to determinate the importance of the amount of arginine, a peptide with the same length of the original one but was half the number of arginine ( $(GR)_5G$  **109**) was produced. By opposition, a peptide with the same number of arginine but with a star-shaped design  $(R_5GG)_2KG$  **110** was synthesized using a di-Fmoc-protected lysine. This aim of this design was to determinate if a non-linear design could increase the siRNA complexation. Finally, different dimers or trimers of our original peptide **104** were synthesized, either using a di-bicyclo[6.1.0]nonyne (BCN) PEG<sub>3</sub> linker **111** (affording linear  $GR_{10}$ -PEG<sub>3</sub>- $R_{10}G$  **112**) for the linear dimer or a tri-BCN triazine core **113** (affording star-shaped Triazine- $(R_{10}G)_3$  **114**). These latter designs are supposed to validate the importance of the number of arginine or the shape of the cationic part.

Table 11 – Structure, purpose and characterization of the different peptide designs synthesized and binding affinity with siRNA determined by MST.

Structure	Purpose	HR-ESI-MS	K <sub>D</sub> with siRNA
R <sub>10</sub> G	First design	Calc.: 1637.0431 Found: 1637.0435	82 nM
N <sub>3</sub> -R <sub>10</sub> G	Clickable design	Calc.: 1790.1286 Found: 1790.1264	89 nM
S <sub>10</sub> G	Hydrophilic negative control	Calc.: 945.3523 Found: 945.3516	> 4 mM
(GR) <sub>5</sub> G	Same length, importance of number of arginine	Calc.: 1140.6449 Found: 1140.6442	563 nM
(R <sub>5</sub> GG) <sub>2</sub> KG	Same number of arginine, importance of the design	Calc.: 2318.4418 Found: 2318.4452	1.2 μM
GR <sub>10</sub> -PEG <sub>3</sub> -R <sub>10</sub> G	Linear dimer of R <sub>10</sub> G	Calc.: 4124.5721 Found: 4124.5710	23 nM
N <sub>3</sub> -R <sub>10</sub> G-R <sub>10</sub> G-R <sub>10</sub> G	Linear trimer of R <sub>10</sub> G	Not pure	Not evaluated
Triazine-(R <sub>10</sub> G) <sub>3</sub>	Star-shaped trimer of R <sub>10</sub> G	Calc.: 6153.8290 Found: 6153.8282	112 nM

Regarding their respective syntheses, S<sub>10</sub>G **108**, (GR)<sub>5</sub>G **109**, (R<sub>5</sub>GG)<sub>2</sub>KG **110** were all synthesized by SPPS. For **110** in particular, a di-Fmoc-protected lysine was used at the beginning of the synthesis. Regarding the binding affinity with siRNA, **108** was not able to bind the oligonucleotide to any concentration, due to a lack of positive charges. **109** was composed of an alternance of arginines and glycines, thus halving the number of positive charges. The dissociation constant of this peptide was almost 7-times higher than the original peptide **104**, showing the binding is greatly affected by the number of positive charges. By opposition, **110** was composed of ten arginines, but displayed in a star-shaped scaffold. Interestingly, the dissociation constant was 15-times higher than the original peptide **104**. This experiment thus suggests that having such scaffold may not be efficient to bind siRNA, even though the number of positive charges remained the same.

Accordingly, we sought to further evaluate linear peptides of longer lengths with growing number of arginines. N<sub>3</sub>-R<sub>10</sub>G **105** was used as a building block to synthesize dimers or trimers of peptides to impact the number of charges. Dimerization of this peptide was achieved by a

double strain-promoted alkyne-azide cycloaddition (SPAAC) using a di-bicyclo[6.1.0]nonyne (BCN) linker **111**, affording the target molecule with 64% yield. From a biophysical point of view (Figure 130), this dimer **112** was able to complex the siRNA stronger than the original monomer **104**, characterized by a 4-times lower  $K_D$ . Considering this element, these data seem in accordance with the previous postulate that a higher number of charges can enhance the binding.

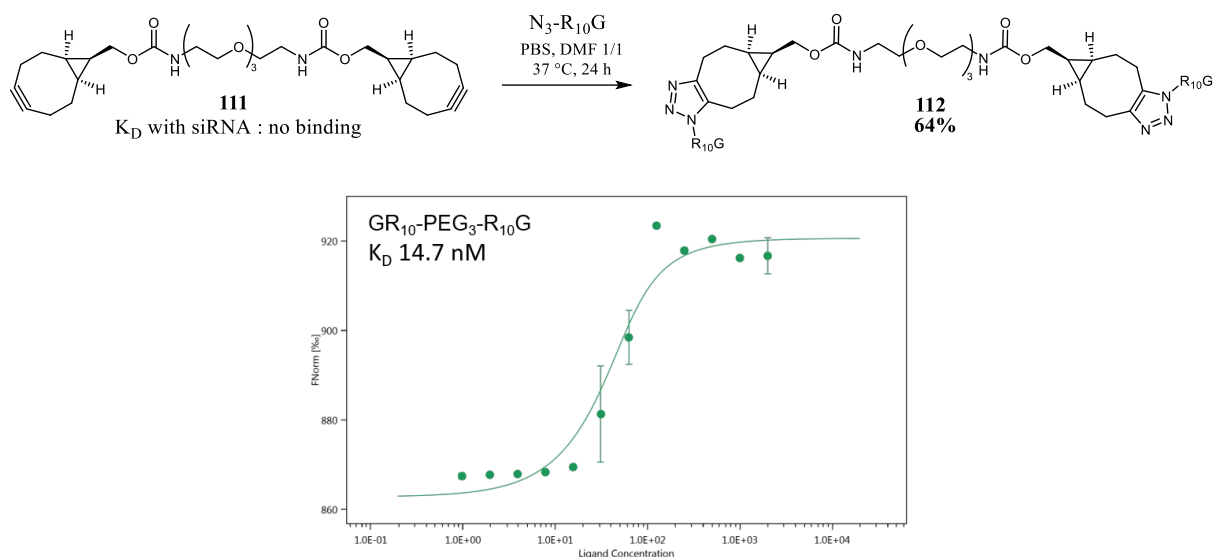


Figure 130 – Synthesis, structure and binding affinity with siRNA **112** for the peptide dimer.

In order to vary the geometry of trimers, a design **114** based on tri-BCN-triazine was synthesized (Figure 131). Although it contained three-times more arginines than the monomer **104** its biophysical evaluation showed a  $K_D$  in the same range (112 nM), probably due to a suboptimal spatial charge display. As already suggested with **110**, we assume that long, linear peptide designs might be among the most efficient designs of peptide for siRNA complexation.

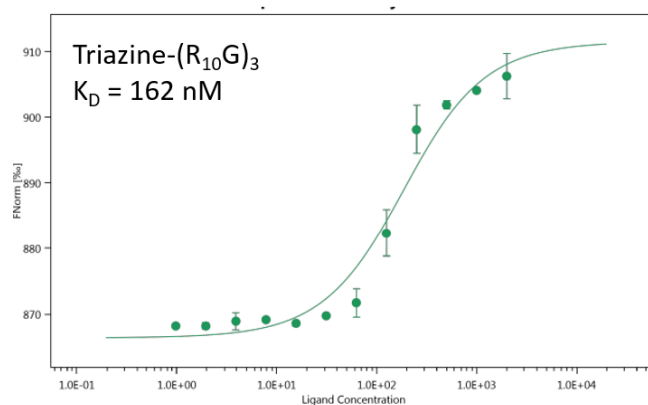
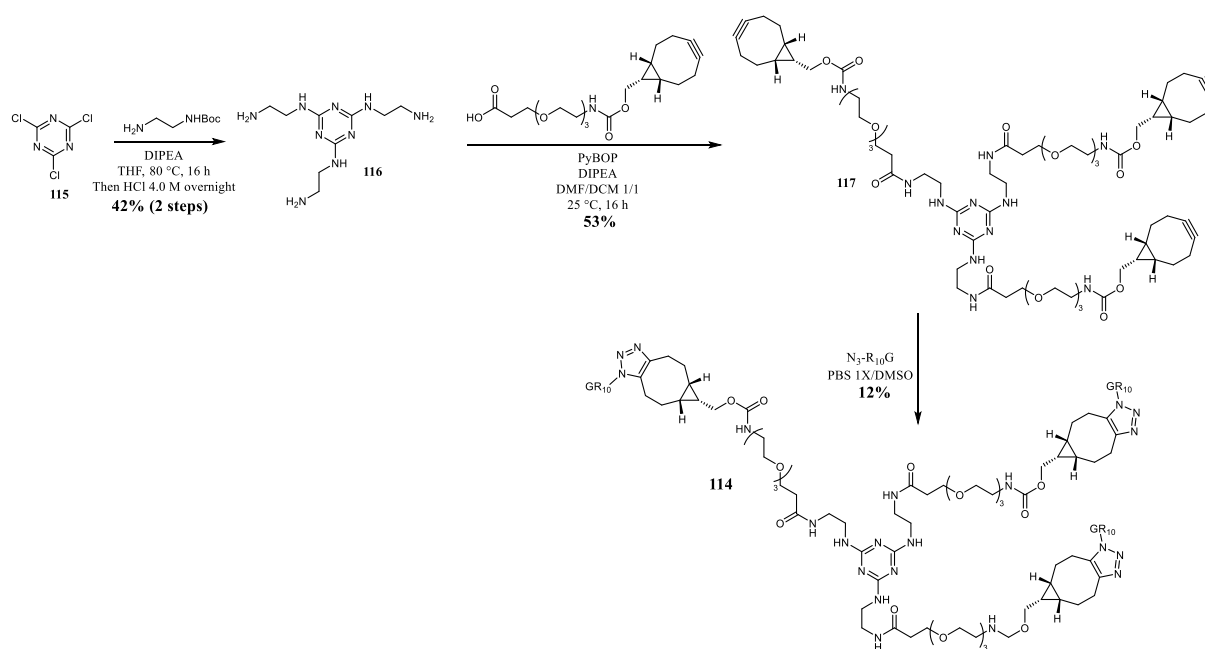


Figure 131 – Synthesis, structure and binding affinity with siRNA for the peptide trimer **114** with the triazine core.

Accordingly, we attempted linear trimerization of the monomer **104**, to produce N<sub>3</sub>-R<sub>10</sub>G-R<sub>10</sub>G-R<sub>10</sub>G **118**. A strategy based on fully-protected peptide was elaborated in order to avoid side-reactions with coupling agents (Figure 132). However, this design could not be isolated and therefore not tested yet. Indeed, final deprotection of the thirty Pbf groups proved to be challenging and not complete, and separation of the different protected species was not feasible with our methods.

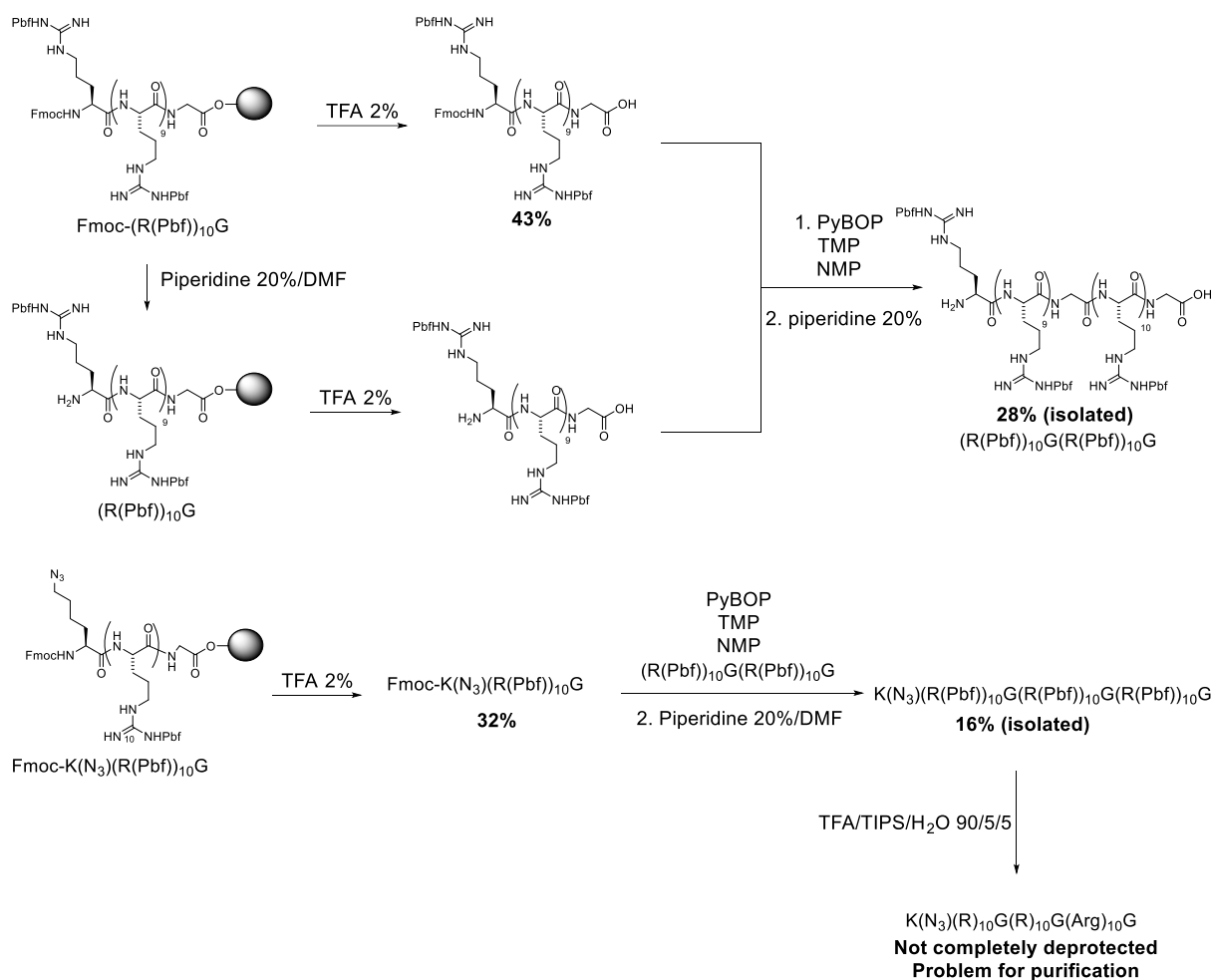


Figure 132 – Synthesis and structure of the peptide trimer.

Intrigued by these preliminary results, an *in silico* study was performed by Dr Célien Jacquemard from Dr Didier Rognan's group, using molecular dynamics. The system consists of a stoichiometric mixture of the R<sub>10</sub>G peptide and the siRNA, showing that the two entities are tightly bound. In addition, these simulations also showed that one siRNA could bind to a maximum of 10 peptides (Figure 133), suggesting that such system was likely to form particles, a result coherent with the DLS experiments. As the main objective is to achieve a N/P of 1 in order to have a 1 to 1 ratio between the siRNA and the peptide, other, more complexing peptide designs are thus required.

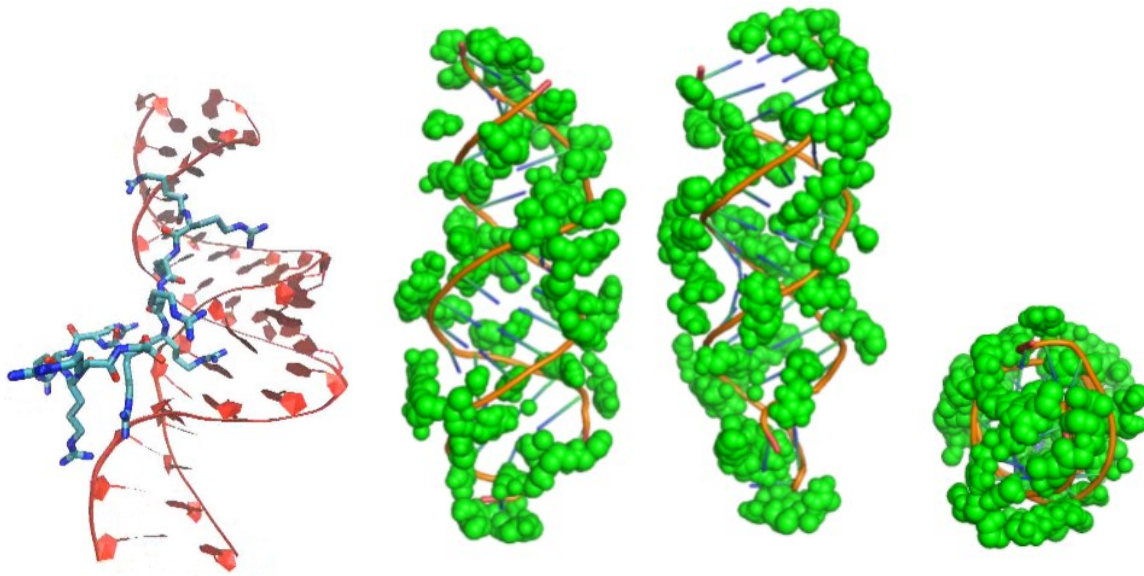


Figure 133 - *In silico* evaluation of the binding between the  $R_{10}G$  peptide and the siRNA. Left: Molecular dynamic picture after 5000 cycles of minimization, heating from 0 to 310 K for 125 picoseconds and 1 nanosecond of equilibration. Right: Formation of complex between the siRNA (orange) with a large excess of peptide (green), with a maximum of 10 peptide attached to a siRNA.

### C. Conclusion and perspectives

To summarize, the aim of the project was to explore non-covalent approaches to deliver siRNA using antibodies. Our starting hypothesis was that such system is generally ill-defined, therefore these may not be optimal for all biological systems and may be difficult to optimize. A first antibody-peptide conjugate was synthesized, and regarding siRNA delivery, our first attempt comforted our postulate that this approach would greatly benefit from molecularly-defined objects. Therefore, a systematic methodology to evaluate siRNA complexation based on microscale thermophoresis analyses was developed, highlighting some structural elements that were critical for the binding affinity. According to these preliminary results, we assumed that long, linear cationic peptides are designs of choice for siRNA complexation. Further optimization of the sequence could allow to discover a universal peptide able to bind only one siRNA.

Such peptide could then be conjugated or fused to any antibody, thus paving the way for molecularly-defined non-covalent antibody-siRNA conjugate. Aside from the therapeutic value that such conjugate could offer, it could also serve as a modular platform for siRNA screening. As far as our knowledge, such systematic evaluation of peptide in order to achieve a stoichiometric siRNA/peptide mixture has never been reported.

## D. Experimental part

### Solid-phase peptide synthesis general protocol.

**Resin swelling:** 2-chlorotriyl resin (1 equiv., 100 mg, 100  $\mu\text{mol}$ ) was dried in vacuo, dissolved in DCM (5 mL) and stirred with an end-over-end mixer.

**Resin activation:**  $\text{SOCl}_2$  (68.9 equiv., 820 mg, 500  $\mu\text{L}$ , 6893  $\mu\text{mol}$ ) was added and the mixture was vortexed for 1 h. Solvents were drained and the activated resin was washed with 2 x NMP (5 mL), NMP/TMP 4/1 (5 mL v/v), then 2 x DCM (5 mL). Solvents were drained and the red resin was used immediately.

**First AA:** Add a solution of Fmoc-AA (10 equiv., 1000  $\mu\text{mol}$ ) and 2,4,6-trimethylpyridine (7.51 equiv., 91 mg, 100  $\mu\text{L}$ , 750  $\mu\text{mol}$ ) in DCM (2 mL) and stir for 1 h.

**Washing conditions:** Wash with 2 x NMP (5 mL) then 2 x DCM (5 mL) for 30 sec each.

**Resin capping (optional):** Add a mixture of DCM/MeOH/TMP (80/15/5 v/v/v) and stir for 15 min. Solvents were removed and resin was washed as before.

**Fmoc deprotection:** A solution of piperidine/NMP (2/8 v/v, 3 mL) was added and the mixture was stirred for 2 x 15 min. Solvents were removed and resin was washed as before. For the first AA only, all deprotection solutions were combined and analyzed by UV (dilution x100 in EtOH, 301 nm,  $\epsilon = 7800 \text{ M}^{-1} \cdot \text{cm}^{-1}$ ) to calculate the amount of Fmoc that was deprotected, thus the loading.

**Elongation:** To a solution of Fmoc-AA (3 equiv.), COMU (3 equiv., 128 mg, 300  $\mu\text{mol}$ ) in NMP (1 mL) and DCM (1 mL) was added 2,4,6-trimethylpyridine (7.51 equiv., 91 mg, 100  $\mu\text{L}$ , 750  $\mu\text{mol}$ ). Resin was washed as before.

**Kaiser test:** Put a few beads in a small Eppendorf and add 3 drops of solution A, B and C, in that order. Heat to 80 °C for 3 min. If the beads are brown, continue the synthesis. If the solution or the beads are blue, the coupling isn't complete and reveal the presence of primary amines. If so, a second coupling with half the quantity of AA and base was performed.

**If coupling is still not complete:** Cap the resin if not complete after two couplings by adding a mixture of acetic anhydride (50 equiv., 510 mg, 469  $\mu\text{L}$ , 5000  $\mu\text{mol}$ ) and 2,4,6-trimethylpyridine (7.51 equiv., 91 mg, 100  $\mu\text{L}$ , 750  $\mu\text{mol}$ ) in NMP (2 mL) for 30 min. Solvents



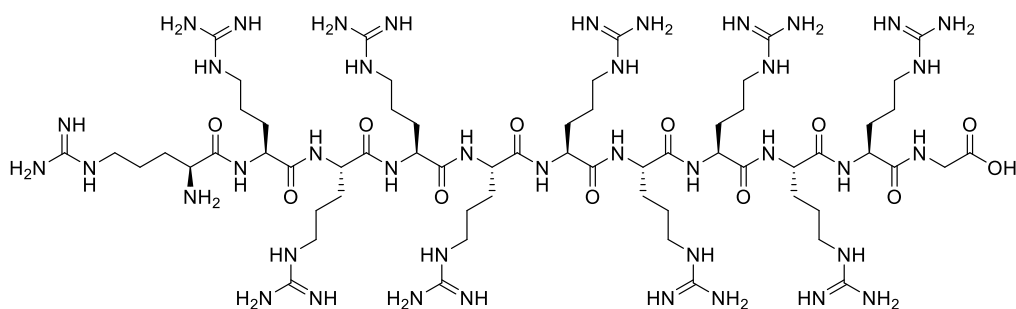
were drained and resin was washed as before.

**Repeat** deprotection of Fmoc, wash, elongation, wash, Kaiser test, capping if needed and wash until the final peptide. If needed, deprotect the Fmoc and wash. Dry the reactor under vacuum. Collect the resin in a glass vial.

**Final deprotection and precipitation:** Add 10 mL of TFA/water/TIPS (90/5/5 v/v/v) and stir overnight hours, monitor the deprotection by analytic RP-HPLC (0.1% TFA / ACN 95/5 to 5/95 in 15 min). When completed, resin was filtered off and washed with TFA. Solvents were removed in vacuo until ~1 mL of solvents is remaining and this was added dropwise into a falcon containing 10 mL of -20 °C diethyl ether to precipitate the peptide. After 15 min at -20 °C, the whole mixture was centrifugated at 4000 rpm for 3 x 5 min. Solvents were discarded and the peptide was dried under vacuum to get rid of diethyl ether.

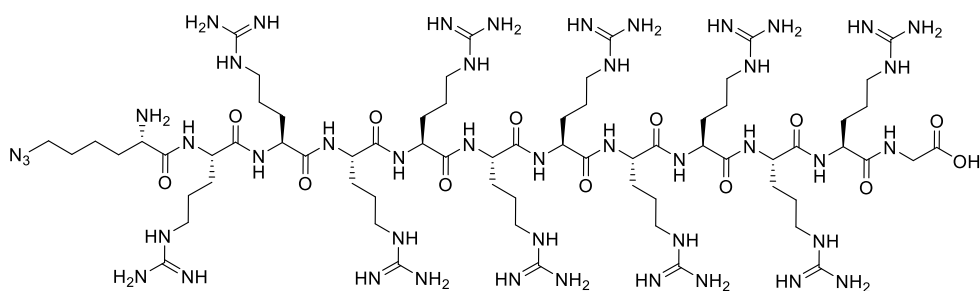
**Purification:** The resulting mixture of peptides was solubilized in water 0.1% TFA and purified by preparative RP-HPLC (0.1% TFA / ACN 95/5 to 5/95 in 20 min) and lyophilized to afford the final peptide. Peptides were analyzed by mass spectrometry and stored under argon at -20 °C.

**L-arginyl-L-arginyl-L-arginyl-L-arginyl-L-arginyl-L-arginyl-L-arginyl-L-arginyl-L-arginyl-L-arginylglycine 104**



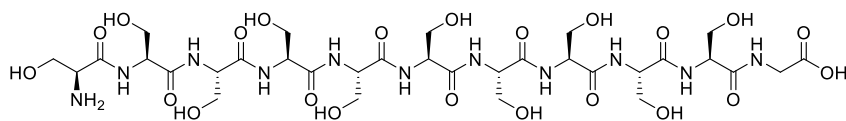
**HR-ESI-MS (M+H<sup>+</sup>):** Calc. 1637.0431, found 1637.0435

**N<sup>6</sup>-diazo-L-lysyl-L-arginyl-L-arginyl-L-arginyl-L-arginyl-L-arginyl-L-arginyl-L-arginyl-L-arginyl-L-arginyl-L-arginylglycine 105**



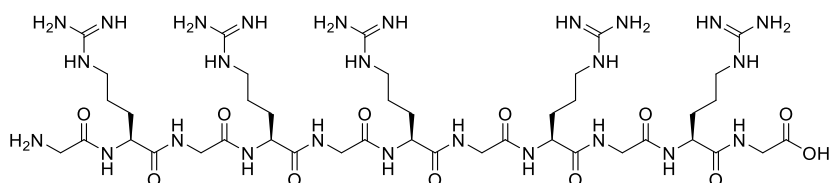
**Exact Mass: 1790,1286HR-ESI-MS (M+H<sup>+</sup>):** Calc. 1790.1286, found 1790.1264

**L-seryl-L-seryl-L-seryl-L-seryl-L-seryl-L-seryl-L-seryl-L-seryl-L-seryl-L-serylglycine 108**



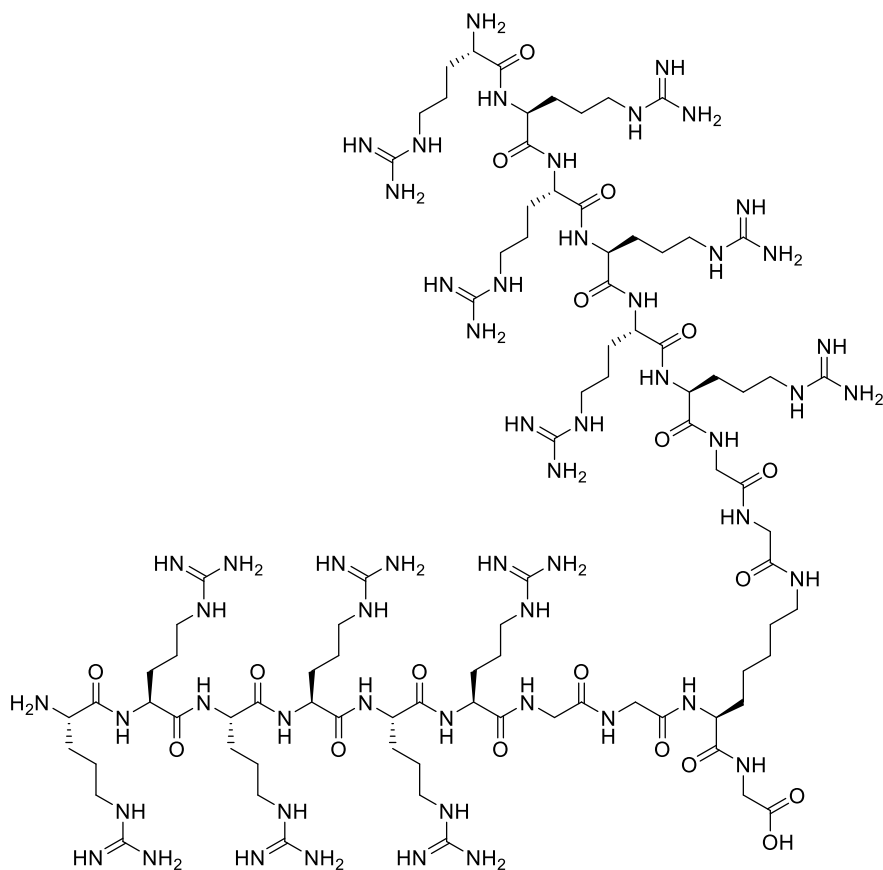
**HR-ESI-MS (M+H<sup>+</sup>):** Calc. 945.3523, found 945.3516

**L-glycyl-L-arginyl-L-glycyl-L-arginyl-L-glycyl-L-arginyl-L-glycyl-L-arginyl-L-glycyl-L-arginylglycine 109**



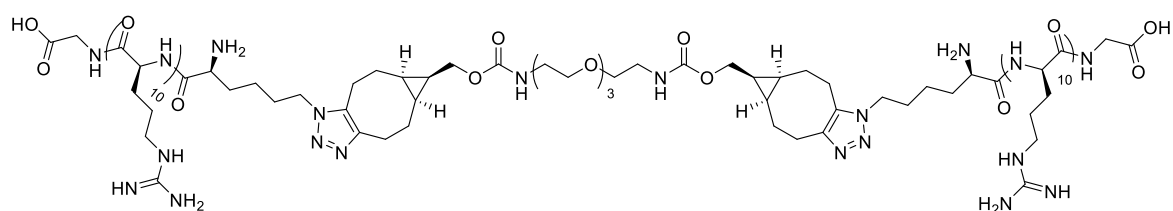
**HR-ESI-MS (M+H<sup>+</sup>):** Calc. 1140.6449, found 1140.6442

**((S)-2,7-bis(2-(2-((S)-2-((S)-2-((S)-2-((S)-2-((S)-2-((S)-2-amino-5-guanidinopentanamido)-5-guanidinopentanamido)-5-guanidinopentanamido)-5-guanidinopentanamido)-5-guanidinopentanamido)-5-guanidinopentanamido)-5-guanidinopentanamido)-5-guanidinopentanamido)heptanoyl)glycine 110**



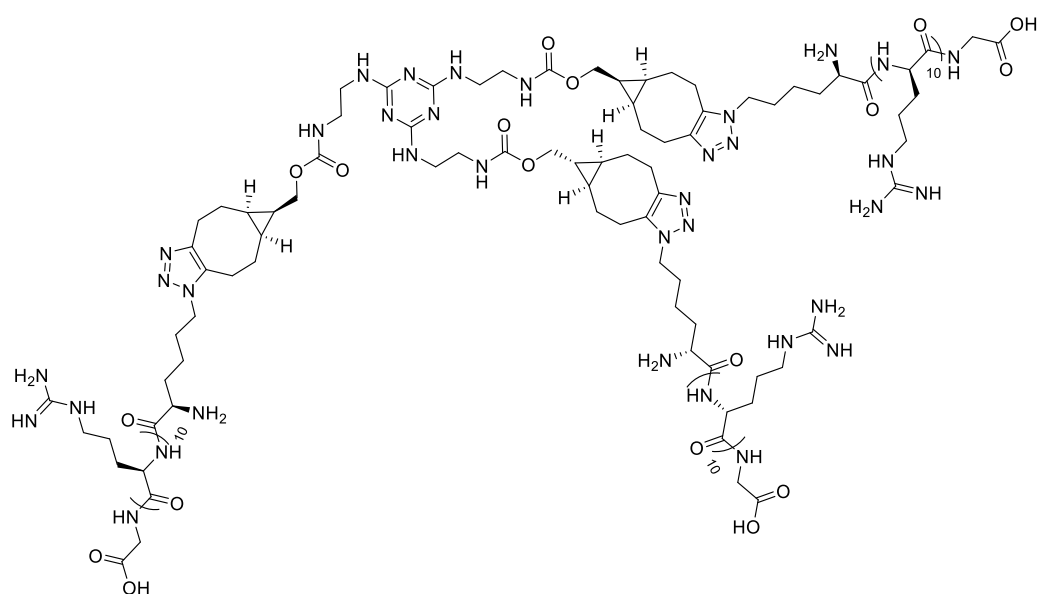
**HR-ESI-MS (M+H<sup>+</sup>):** Calc. 2318.4418, found 2318.4452

**GR<sub>10</sub>-PEG<sub>3</sub>-R<sub>10</sub>G 112**



**HR-ESI-MS (M+H<sup>+</sup>):** Calc. 4124.5721, found 4124.5710

**Triazine(R<sub>10</sub>G)<sub>3</sub> 114**



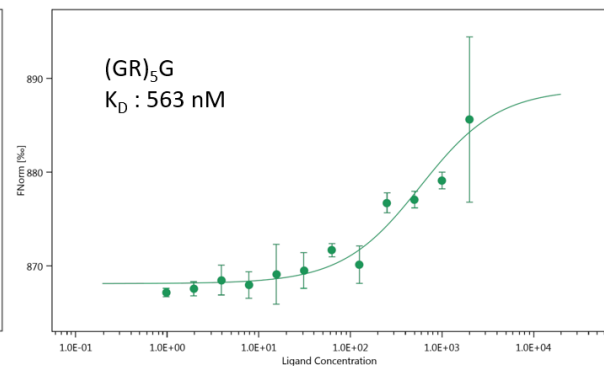
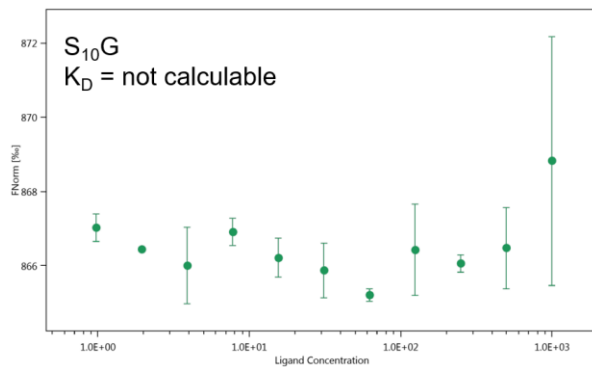
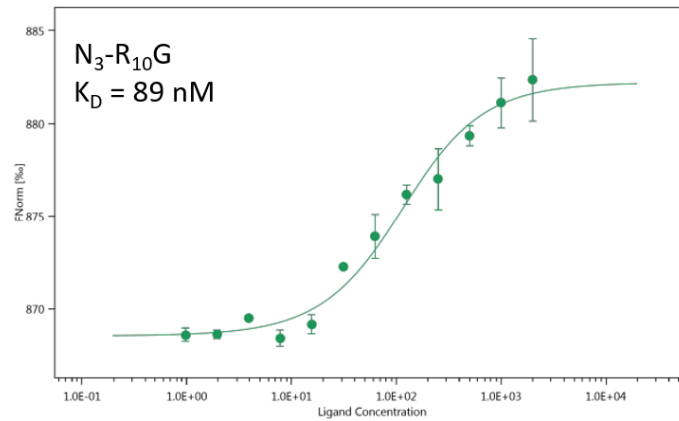
**HR-ESI-MS (M+H<sup>+</sup>):** Calc. 6153.8290, found 6153.8282

**Bioconjugation.** To a solution of anti-EphA2 antibody or rituximab (1 equiv., 1 mg, 5 mg/mL in DPBS, pH 7.4) was added activated BCN **6** (10 equiv., 1 mM in DMSO) and the reaction mixture was incubated at 25 °C for 16 h. Excess of reagent and by-products were removed by gel filtration chromatography using Bio-spin P-30 columns (Bio-Rad, Hercules, U.S.A.) pre-equilibrated with DPBS 1X (pH 7.4) to give a solution of BCN-functionalized trastuzumab (0.87 mg, 87%, diluted to 10 mg/mL with DPBS 1X). A solution of N<sub>3</sub>-R<sub>10</sub>G **105** (20 equiv., 10 mM in water) was then added and the mixture was incubated at 25 °C for another 16 h. Excess of reagent was removed by gel filtration chromatography using Bio-spin P-30 columns pre-equilibrated with DPBS 1X (pH 7.4) to give a solution of peptide-labeled antibody **107** (0.62 mg, 68%), whose average degree of conjugation was determined to be 4.84 (EphA2-antibody) and 4.64 (rituximab) by native mass spectrometry (*vide infra*).

**Confocal microscopy.** Two days prior to the experiment,  $4 \times 10^4$  SKBR3 cells were seeded per well in 8-well Lab-Tek II Chambered coverglass plates (ref. 155409, Nunc, Naperville, IL, USA). The fluorescent mixtures of molecules in the corresponding ratios were diluted up to 300  $\mu$ L in Dulbecco's Modified Eagles's complete Medium and added onto the cells for 90 minutes. After washing, cell nuclei were stained with 5  $\mu$ g/mL of Hoechst 33258 (ref. H1399, Invitrogen, Carlsbad, CA, USA) diluted in complete medium for 30 minutes. Cells were finally washed and incubated with red phenol-free Dulbecco's Modified Eagle's Medium (SIGMA) for microscopic observation. Cells images were acquired on a confocal Leica TSC SPE II microscope (405, 488 and 561 nm) with an image acquisition software (Leica confocal LAS AF, Leica).

**Microscale thermophoresis.** In a 384-well plate, each peptide (5  $\mu$ L, serial dilution starting from a 4  $\mu$ M stock solution in PBS 1X) was incubated with siRNA-Cy<sub>5</sub> (5  $\mu$ L, 100 nM in PBS 1X) for 15 min. Having prepared the serial dilution, the samples were filled into capillaries through capillary action and data were acquired in duplicate with a Monolith NT.115 instrument (NanoTemper Technologies) and analyzed by M.O affinity software. Conditions: 647 nm, excitation power: 25%, MST power 60%, temperature 25 °C, target siRNA concentration 50 nM.

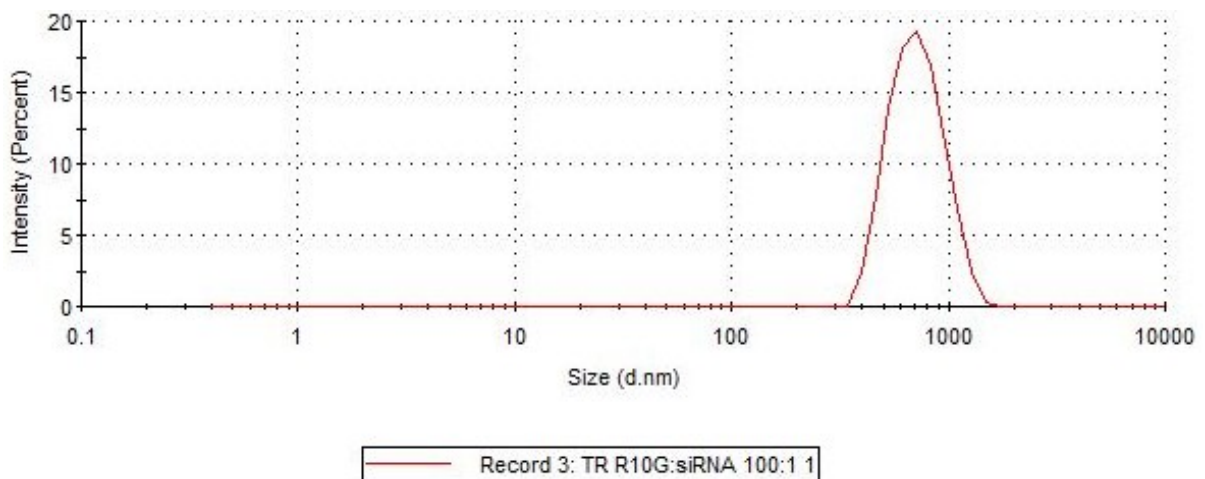
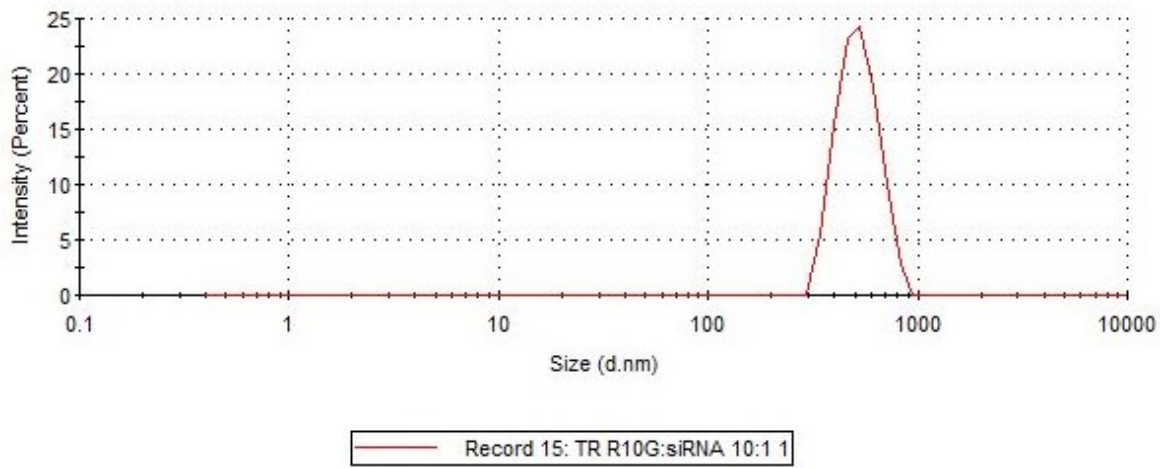
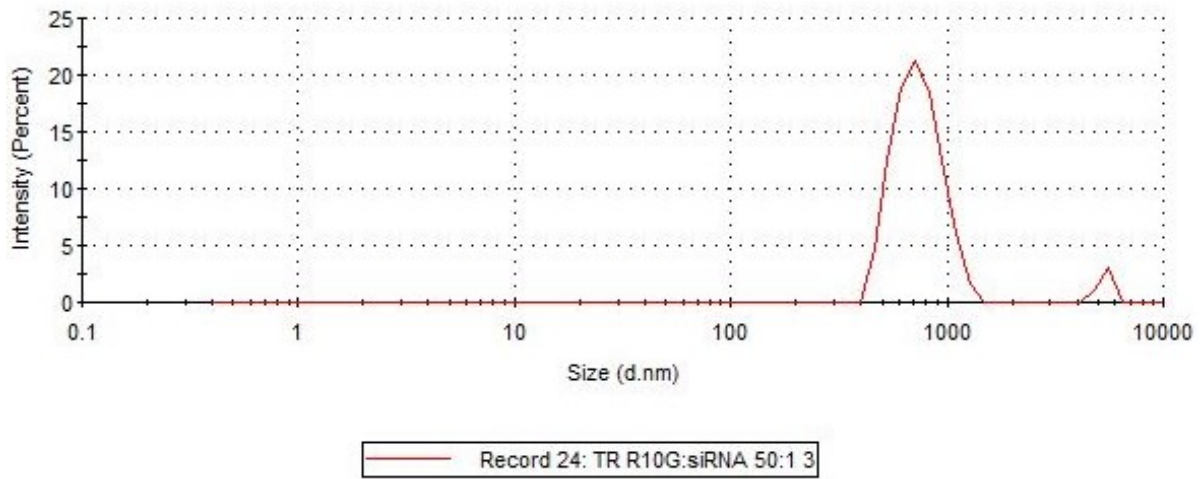
Molecule	K <sub>D</sub> (nM)	Response amplitude	Std. Error of regression	Signal to Noise ratio
R <sub>10</sub> G	82 ± 19.03	90.16	5.25	18.95
N <sub>3</sub> -R <sub>10</sub> G	89 ± 23.52	13.67	0.81	18.46
S <sub>10</sub> G	> 4 mM	/	/	/
(GR) <sub>5</sub> G	563 ± 144.05	20.77	1.48	15.46
(R <sub>5</sub> GG) <sub>2</sub> KG	1193	45.43	1.10	49.13
GR <sub>10</sub> -PEG <sub>3</sub> -R <sub>10</sub> G	14.7 ± 8.26	57.80	5.48	11.65
Triazine-(R <sub>10</sub> G) <sub>3</sub>	162 ± 50.92	45.12	3.15	15.81
EphA2-antibody-(R <sub>10</sub> G) <sub>4.84</sub>	5.0 ± 1.67	31.02	1.10	30.97

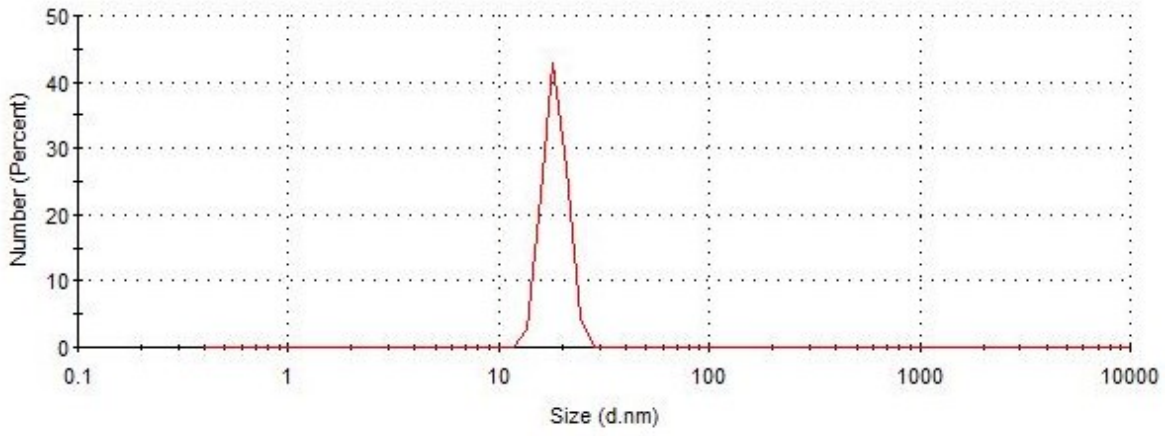


**Gel retardation assay.** Each peptide/siRNA-Cy5 at different N/P ratios in PBS 1X were incubated for 15 min at 25 °C before agarose gel electrophoresis (2% w/v, 80 mV, 60 min, tris-borate running buffer).

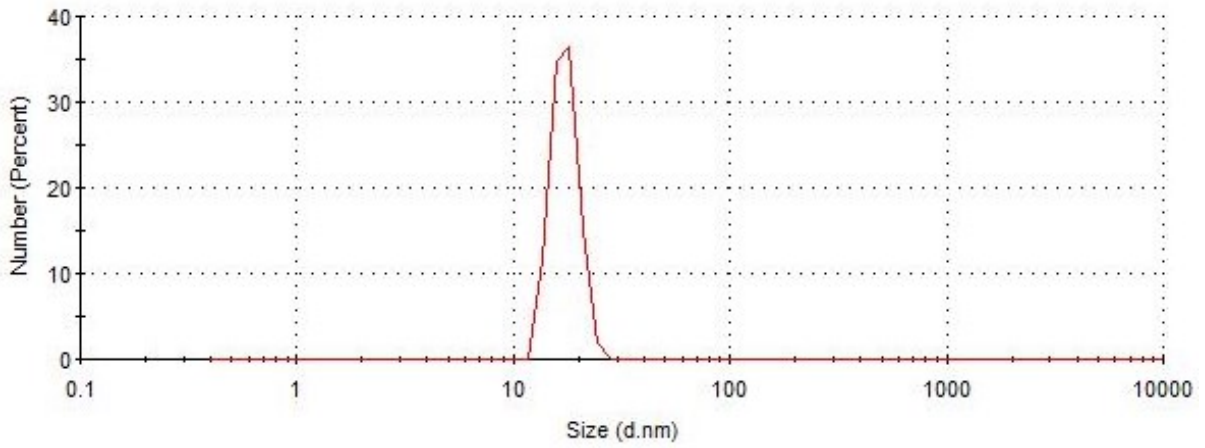
**Dynamic Light Scattering.** Peptides/antibody-peptide conjugates were mixed with siRNAs in PBS 1X at the reported ratios with a fixed concentration of siRNA (1 μM). After 30 min of incubation at 25 °C, Dynamic light scattering (DLS) experiments were performed using a Zetasizer Nano-ZS (Malvern Instruments) and a low-volume quartz cuvette (ZEN2112 QS 3.00 mm). Analysis of the results was carried out using the Malvern Zetasizer Software v8.01.

Conditions: Temperature: 25 °C, Index of refraction of material: 1.43, Index of refraction of pure water: 1.33, Viscosity of water used: 0.8872, Sampling time: 55 sec, triplicate. The ζ potential measurements were carried out using the same instrument and samples, using disposable folded capillary zeta cell (1 mL, Malvern Panalytical DTS1070) and an effective voltage of 70 V with the following parameters: Dielectric constant: 78.5, Model: Smoluchowski, triplicate.





Record 50: TR Ab R10G:siRNA 10:1 15 min 2



Record 54: TR Ab R10G:siRNA 20:1 15 min 3

## VIII. General conclusion

Project 1: Targeted delivery of immunostimulatory siRNA with dual mode of action, inducing both apoptosis and anti-tumor immunity

Our postulate that a dual mode of action siPLK1-5'-ppp could induce cell death by simultaneous and synergistic RIG-I/RNAi mechanisms of action has been verified. The covalent antibody-siRNA conjugate proved to be efficient to deliver siRNAs inside EphA2-expressing cancer cells, thus activating RIG-I and silencing PLK1 in the low nanomolar range. Moreover, killing assays with primary immune cells indicated that the delivery of RIG-I agonist inside tumors could induce a strong immune response *in vitro*. Immunofluorescence studies by microscopy demonstrated that a small portion of siRNA was able to escape the endosomes in a few hours. However, the majority of the siRNA remained trapped in this locus, in accordance with numerous studies. The conjugate's plasma stability is however one major limitation of this system, thus enhancing it by an optimization of the linker and the siRNA's design, notably by using nuclease-resistant structures, could lead to a possible transfer into preclinical trials. Regarding this particular point, it is worth noting that the targeted delivery of RIG-I agonists by antibodies could allow intravenous administration, thus avoiding intratumoral injections required by RIG-I agonists currently in clinical trials.<sup>114</sup> To conclude on this study, we developed a targeted immunostimulatory-siRNA system based on ARC, and showed both the strengths and some limitations of this system. This study thus confirmed the potential of such ARC.

Project 2: Development of bicyclo[6.1.0]nonyne carboxylic acid for the production of stable molecular probes

Due to our linker's design, we thought that the strained-alkyne-alcohol attached by a carbamate group on the linker may be the point of weakness. Therefore, a synthetic strategy to obtain the same strained-alkyne but with a carboxylic acid was elaborated. The never-reported BCN carboxylic acid was synthesized in multigram scale, and FRET probes were produced to assess its stability in different media. As BCNs are widely used in chemical biology for the production of probes, using the cell-stable carboxylic acid derivative may be beneficial in cases where probe's stability is crucial.

Project 3: A novel family of acid-cleavable and plasma-stable linker based on cyclic acetal motifs

We thus sought to increase the cleavability of the linker by using cleavable linkers commonly used in antibody-drug conjugates. This led to the development and the evaluation of a novel,



acid-labile linker based on cyclic acetal motifs. *In vitro* evaluation of fluorogenic probes showed that the novel motif was cleaved with high degree of selectivity for endo/lysosomes while conserving a high plasma stability. Therefore, ARC bearing cleavable linkers were produced and their biological activities compared to the non-cleavable ARC were evaluated. In addition, preliminary results regarding the use of our novel linker for antibody-drug conjugates using MMAF and gemcitabine as drugs showed promising results.

#### Project 4: Development of a synthetic strategy for non-covalent ARC

In order to explore peptide-based non-covalent ARC, different strategies to synthesize cationic peptides able to strongly complex anionic RNAs have been elaborated. A first non-covalent ARC was produced, highlighting the fact that such system would greatly benefit from molecularly-defined peptide-siRNA complexes. The syntheses and biophysical evaluation methods of different peptide designs have been developed, paving the way for molecularly-defined antibody-peptide conjugates for siRNA delivery. Even though the peptide/siRNA binding affinities were in the nanomolar range, these were not sufficient to obtain a 1 to 1 ratio, and further optimization of the peptide's structure is thus required.

## IX. Résumé étendu

Les récepteurs à reconnaissance de formes (PRR) sont des familles de protéines responsables de la défense d'un organisme contre les agents pathogènes, induisant ainsi des réponses immunitaires lors de la liaison à un ligand exogène. Par conséquent, différentes stratégies pour les cibler ont émergé afin de prévenir ou de traiter les maladies infectieuses. En outre, ces protéines ont également intrigué les scientifiques à des fins d'immuno-oncologie, en raison de leur spécificité de ligand élevée, de la faible quantité requise de ligand intracellulaire et de l'activation ultérieure de nombreuses voies de signalisation. L'un de ces PRR prometteurs est RIG-I, activé par un ARN double brin cytosolique terminé par un groupe 5'-triphosphate. En plus de la signalisation RIG-I, un tel ARN peut également inhiber l'expression d'un gène spécifique par un mécanisme d'interférence ARN, donnant ainsi accès à des systèmes synergiques. En conséquence, des méthodologies pour délivrer un tel ARN à l'intérieur des tumeurs sont hautement souhaitées.

Le domaine des systèmes d'administration d'ARN se développe depuis 30 ans, et ces progrès ont conduit à la commercialisation récente, par exemple, de vaccins à ARNm. Cependant, les méthodes actuelles d'administration d'ARN souffrent d'inconvénients, parmi lesquels le manque de spécificité cellulaire, ce qui conduit à un champ d'application limité, notamment en oncologie. Par conséquent, le développement de vecteurs ciblés pour l'ARN est fortement souhaité afin d'élargir le répertoire de maladies pouvant être traitées par des approches thérapeutiques basées sur l'ARN. Basées sur un format analogue aux conjugués anticorps-médicament, de nombreuses études utilisant des conjugués anticorps-ARN (ARC) ont été publiées récemment, démontrant leur fort potentiel thérapeutique. En plus des méthodes covalentes pour attacher l'ARN et l'anticorps, l'ARC non covalent est également apparu comme une stratégie prometteuse, car le développement d'un système de livraison ciblé d'ARN modulaire et efficace ouvrirait un large éventail de possibilités thérapeutiques.

Ce travail a donc été consacré au développement de systèmes de délivrance ciblés à base d'anticorps, capables de délivrer spécifiquement un double ARN activant RIG-I et inhibant PLK1 dans les cellules cancéreuses via un ciblage actif d'un antigène de surface cellulaire. S'il est libéré dans le cytosol, l'ARN est censé activer RIG-I et simultanément faire taire PLK1, conduisant par conséquent à l'apoptose cellulaire et à l'activation de l'immunité antitumorale. Des approches covalentes et non covalentes

ont été exploitées. Concernant le covalent, des linkers clivables ont également été explorés dans le but d'améliorer la libération d'ARN cytosolique.

Ce manuscrit a donc été structuré en cinq chapitres. En introduction, RIG-I sera présenté en premier, en mettant l'accent sur son potentiel thérapeutique. Après un bref résumé des systèmes d'administration d'ARN non ciblés actuels, le domaine des thérapies ciblées et des conjugués anticorps-médicament ouvrira la voie à une revue exhaustive des conjugués covalents anticorps-ARN.

Suite à cette introduction, le premier projet de ce manuscrit décrit le développement d'un ARC covalent ciblant les cellules cancéreuses, activant RIG-I et inhibant PLK1. Sa conception, sa synthèse et son évaluation biologique in vitro concernant différents aspects du RIG-I ou de la délivrance seront présentées. En bref, la synthèse d'ARC a été rapidement optimisée et nous avons pu observer simultanément les effets RIG-I et PLK1 dans le modèle de cellules cancéreuses. De plus, en réalisant des expériences de co-culture avec des cellules mononucléées du sang périphérique (PBMC), l'ARC a pu induire la destruction de cellules cancéreuses d'une manière dépendante de RIG-I sur des cellules appauvries en RIG-I, suggérant une internalisation de l'ARC à l'intérieur des PBMC et l'activation subséquente de RIG-I. Des études d'immunofluorescence ont également été réalisées afin d'étudier le trafic à la fois de l'anticorps et de l'ARN à l'intérieur de la cellule.

Comme la méthode covalente semblait être efficace dans notre cas, l'une des hypothèses était que le linker utilisé pour la synthèse de l'ARC pourrait être clivé dans les milieux biologiques. En raison de la conception de notre linker, nous avons pensé que l'alcyne-alcool tendu attaché par un groupe carbamate sur le linker peut être le point de faiblesse. Par conséquent, une stratégie de synthèse pour obtenir le même alcyne contraint mais avec un acide carboxylique a été élaborée. Cela a conduit au développement de deux sondes fluorogènes, ne différant que par le fragment de fixation, soit un amide, soit un carbamate. En milieu biologique, nous avons observé que le carbamate était, en fait, clivé dans les cellules. Suite à ces observations, nous avons suggéré que le linker de l'ARC était clivé dans les cellules, expliquant ainsi probablement une partie de l'activité que nous avons observée dans le premier projet.

Nous avons donc cherché à augmenter la clivabilité du lieu en utilisant des lieux clivables couramment utilisés dans les conjugués anticorps-médicament. Une brève

introduction sur ces lieux introduira un quatrième chapitre sur le développement et l'évaluation d'un nouveau lieu acido-labile. Sa conception, sa synthèse et son évaluation in vitro à l'aide de sondes fluorogènes seront présentées. De manière satisfaisante, nous avons observé que le nouveau lieu était en fait plus clivé dans les cellules que le lieu de référence actuellement utilisé dans les conjugués anticorps-médicament. Par conséquent, des ARC portant des linkers clivables ont été produits et leurs activités biologiques comparées à l'ARC non clivable ont été évaluées. De plus, des résultats préliminaires concernant l'utilisation de notre nouveau lieu pour les conjugués anticorps-médicament seront présentés.

Dans un dernier chapitre, afin d'explorer l'ARC non covalent à base de peptides, des peptides cationiques capables de complexer fortement les ARN anioniques ont été synthétisés. Un premier ARC non covalent a été produit, mettant en évidence le fait qu'un tel système bénéficierait grandement des complexes peptide-siARN définis moléculairement. Par conséquent, différentes conceptions de peptides cationiques, leurs synthèses et une méthode pour évaluer leurs propriétés biophysiques concernant la complexation de l'ARN seront présentées.

Les molécules d'ARNs ont un grand potentiel en tant qu'agents thérapeutiques pour les cibles dites « non druggable ». Cependant, leur délivrance sur le site d'action reste encore aujourd'hui une limitation majeure de leur utilisation, notamment à cause d'une efficacité limitée. Afin de régler ce problème, le couplage d'un acide nucléique sur un anticorps pour une délivrance sélective vers les cellules cibles apparaît comme un stratégie thérapeutique viable.<sup>[1]</sup> Cependant, dans les systèmes actuellement décrits, des difficultés liées à l'internalisation du conjugué où le relargage cytosolique de l'ARN restent des facteurs limitants.<sup>[2]</sup> De plus, ces assemblages anticorps-ARN sont généralement fragiles en conditions biologiques, notamment à cause d'une séparation précoce ou à cause de ribonucléases dégradant l'ARN. <sup>[3]</sup> Ainsi, des progrès sur la manière de réaliser ces conjugués sont attendus afin d'augmenter leur capacité à atteindre des cibles intracellulaires, et donc leur efficacité globale.

Les conjugués anticorps-ARN combinent ainsi le potentiel de délivrance des anticorps avec les mécanismes d'action très précis des ARNs. Alors que beaucoup d'approches basées sur des polymères ou des nanoparticules ont été décrit, seuls les objets moléculairement définis seront discutés ici. En effet, les propriétés biophysiques et

pharmacologiques peuvent être ajustés plus précisément avec de tels objets. Jusqu'à présent, deux stratégies utilisant des anticorps ont été décrites pour la délivrance de petits ARNs interférents (**Figure 1**). La méthode la plus simple est le couplage direct de l'ARN sur l'anticorps en utilisant des méthodes de bioconjugaison et des bras-espaceurs synthétiques, cette stratégie permettant, en théorie, de contrôler le degré de conjugaison (DoC). Cependant, ce type de stratégies souffrent souvent d'un relargage cytosolique insuffisant.<sup>[3]</sup> Une stratégie alternative consiste à exploiter les interactions électrostatiques entre les charges négatives de l'ARN et les charges positives portées par un peptide, soit conjugué<sup>[2]</sup> soit fusionné<sup>[1]</sup> à l'anticorps. Ces dernières approches ont cependant tendance à former des agrégats, étant donné la difficulté d'ajuster précisément le ratio anticorps/ARN.<sup>[1]</sup>

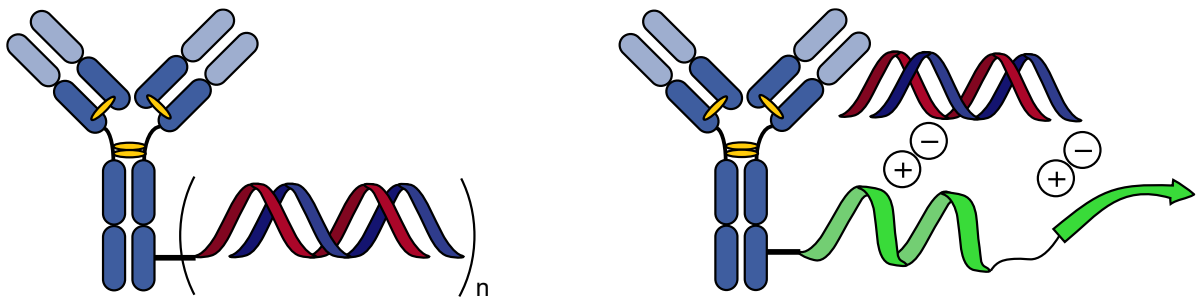


*Figure 134 – Les deux stratégies décrites pour délivrer des ARNs grâce à des anticorps. A gauche, le couplage direct de l'ARN sur l'anticorps, à droite, l'utilisation de peptides cationiques pour complexer l'ARN.*

Comme cible biologique d'intérêt en oncologie, nous nous sommes intéressés à RIG-I, un récepteur cytosolique ubiquitaire détectant la présence de courts ARN double brin (dsRNA) terminé par un groupement 5'triphosphate (5'ppp) ou 5'diphosphate (5'pp).<sup>[4]</sup> A la suite de la reconnaissance, RIG-I change de conformation, initiant une cascade de signalisation menant à la sécrétion de cytokines (activation de la voie NF- $\kappa$ B) ainsi qu'à la production d'interféron (IFN, activation des voies IRF 3/7).<sup>[5]</sup> Ainsi, l'activation de RIG-I induit l'apoptose des cellules cancéreuses tout en stimulant le système immunitaire, caractérisé par une réponse immunitaire innée et adaptative contre la tumeur. De plus, la production d'IFN à la suite de l'activation de RIG-I active une boucle de rétroaction positive qui augmente le niveau d'expression de RIG-I, amplifiant ainsi le signal. De plus, l'administration ciblée d'agonistes de RIG-I par des anticorps pourrait permettre une administration intraveineuse, évitant ainsi les injections intratumorales requises par les agonistes de RIG-I actuellement en essais cliniques.

Comme l'activation de cette protéine est indépendante de la séquence de l'ARN, et que la taille minimale des agonistes de RIG-I est bien décrite, il est possible de désigner une séquence d'ARN-5'ppp qui pourrait combiner l'activation de RIG-I avec la dégradation spécifique d'un ARN message donné, par interférence par ARN (RNAi). Ainsi, en délivrant un siRNA-5'ppp, il est ainsi possible d'établir de nouvelles synergies avec l'activation de RIG-I en inhibant une seconde cible.<sup>[6]</sup> En effet, délivrer spécifiquement des ARNs agissant via des mécanismes d'actions complémentaires et synergiques au niveau de la régulation des protéines ouvrirait la voie à des possibilités presque infinies pour contrer le développement du cancer.

A propos de la cible à inhiber, nous avons sélectionné PLK1, une kinase connue comme un déclencheur précoce de la transition G2/M, dont la présence diminue la production d'IFN produite par RIG-I.<sup>[7]</sup> Par conséquent, l'inhibition de PLK1 avec un siRNA pourrait créer une synergie avec l'activation de RIG-I afin d'améliorer la production d'IFN. De plus, il a été démontré que l'inhibition de PLK1 entraîne un arrêt du cycle cellulaire en phase G2/M, induisant ainsi l'apoptose.<sup>[8]</sup>

Afin de cibler spécifiquement les cellules tumorales, nous avons sélectionné un anticorps se liant à EphA2, un tyrosine kinase transmembranaire surexprimée dans de nombreux cancer et associée à une survie globale plus courte chez les patients.<sup>[9]</sup> Outre son effet sur la croissance cellulaire, EphA2 est très bien internalisé à la suite de sa liaison avec un anticorps, ce qui en fait une cible de choix pour la délivrance de médicaments<sup>[10]</sup> ou oligonucléotides.<sup>[11]</sup>

En résumé, l'objectif de ce travail de recherche était d'explorer la délivrance d'un ARN-5'ppp bispécifique grâce à un anticorps ciblant EphA2. Ce conjugué ciblerait spécifiquement les cellules cancéreuses et délivrerait le siRNA, provoquant leur mort via une double activité PLK1/RIG-I (**figure 2**). Nous avons ainsi exploré les deux approches pour assembler le siPLK1-5'ppp et l'anticorps : un modèle covalent, et un modèle supramoléculaire basé sur les interactions électrostatiques.

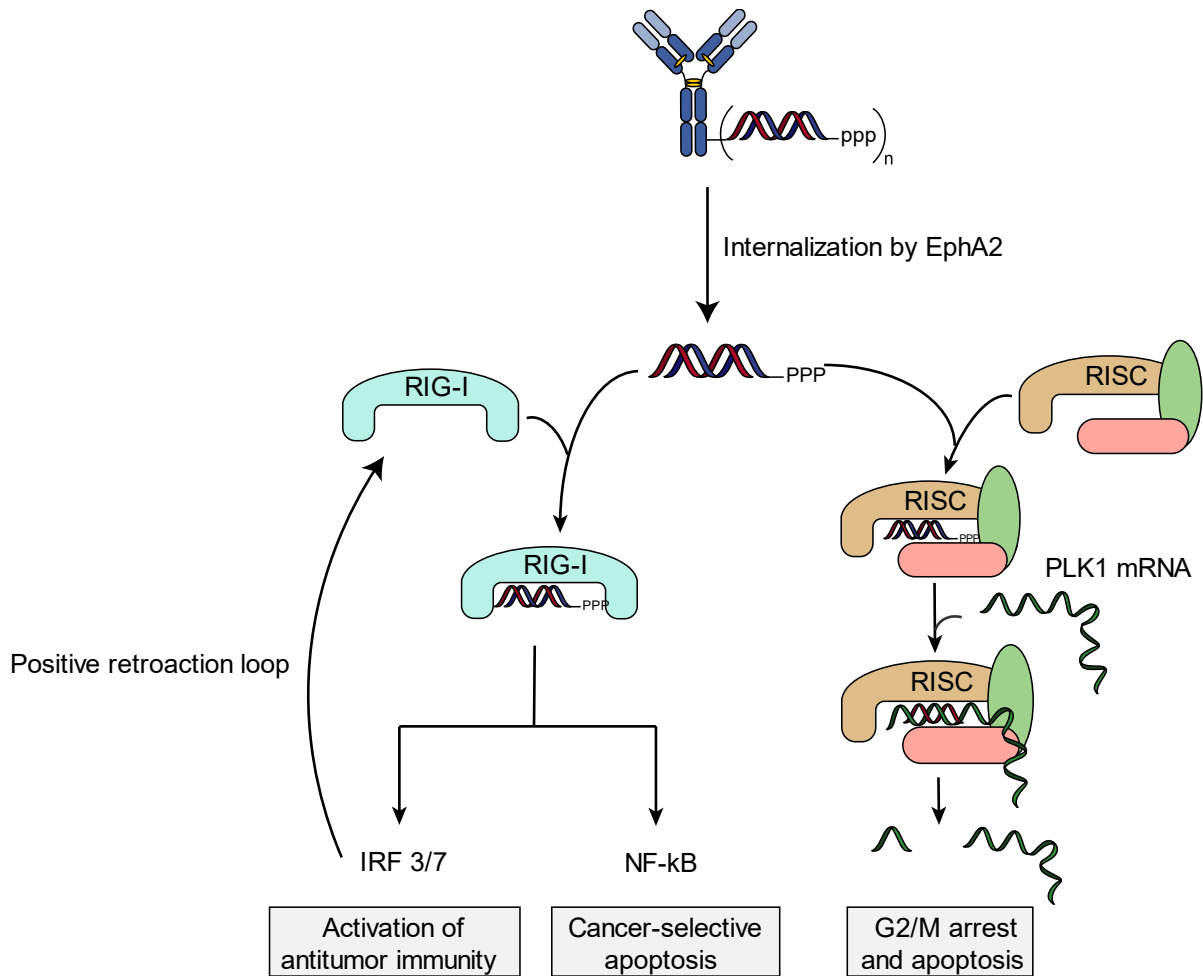


Figure 135 – But général de ce projet de thèse, utilisant des assemblages entre un anticorps et un siRNA-5'ppp.

Notre stratégie covalente repose sur une méthode développée dans notre laboratoire, consistant à conjuguer les lysines de l'anticorps. C'est un moyen simple d'obtenir un conjugué moléculairement défini qui pourra, ensuite, être caractérisé par des méthodes de spectrométrie de masse. Dans une première étape, ("plug"), un réactif électrophile permet l'incorporation d'un groupement azide sur l'anticorps (1, Figure 3), puis, dans une seconde étape (« play »), un siRNA modifié avec un alcyne contraint sera utilisé pour coupler l'anticorps et l'ARN (2, Figure 3).<sup>[12]</sup> Cette stratégie nous permet de faire varier indépendamment le DoC et le type de linker. Pour cette approche, une nouvelle classe de bras-espaceurs à base d'acétals cycliques, stables dans le plasma humain et sensibles aux acides, a été conçue, synthétisée, et étudiée.

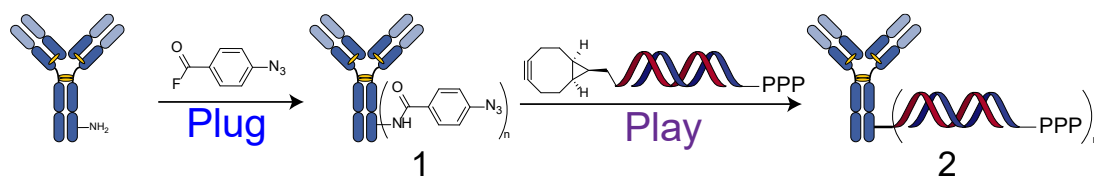


Figure 136 – Stratégie covalente explorée pendant cette thèse afin de produire des conjugués anticorps-siRNA-5'ppp.

#### Résultats et discussion :

Pour ce faire, nous avons synthétisé un bras-espaceur à base d'oligoéthylène glycol hétérobifonctionnel adapté à la bioconjugaison. Nous avons utilisé des linkers possédant un groupement bicyclo[6.1.0]nonyne (BCN) afin de fonctionnaliser un brin d'ARN. Après hybridation avec le brin d'ARN complémentaire possédant le groupement 5'ppp, le BCN-siRNA-5'ppp a ensuite été accroché sur un anticorps possédant le groupement azide par cycloaddition alcyne-azide (**figure 4**). Au cours de la thèse, les conditions de réaction ont été optimisées pour réduire autant que possible la dégradation de l'ARN afin d'avoir des conjugués pouvant être caractérisés par spectrométrie de masse native.

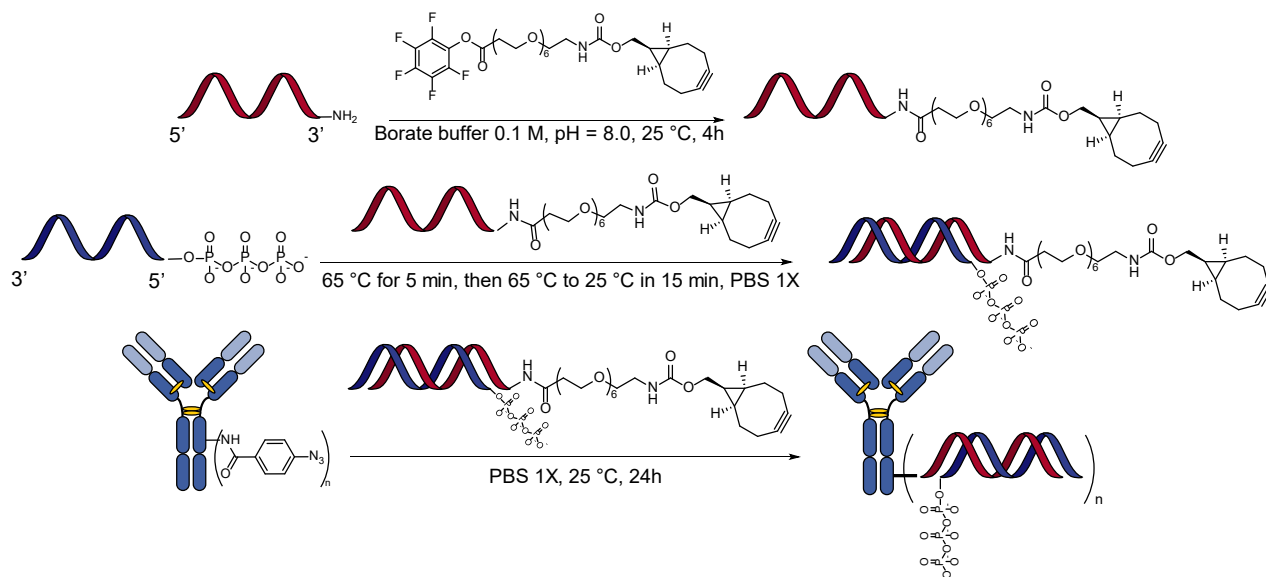


Figure 4 – Synthèse du conjugué anticorps-siRNA.

Ces conjugués (**2**) ont montré une bonne efficacité dans la gamme du nanomolaire *in vitro* pour active RIG-I, démontrant ainsi que l'anticorps pouvait délivrer le siRNA dans les cellules, et que ce dernier était reconnu par RIG-I. Le niveau d'expression de RIG-I a été mesuré par western-blot, et les résultats ont montré une surexpression



significative de la protéine par rapport aux cellules non traitées (d'un facteur 31, **figure 5**), confirmant son activation par le conjugué 5'ppp. Simultanément, nous avons observé une extinction du gène PLK1 de 32%, indiquant une inhibition de PLK1 par le siRNA (**figure 5**). En conséquence, nous observons que le conjugué a pu arrêter les cellules en phase G2/M, prouvant l'activité PLK1. Ces résultats ont ainsi permis de valider la double activité RIG-I/PLK1. Par la suite, la stabilité plasmatique du conjugué a été mesurée. Alors que les siRNAs sont extrêmement instables dans le plasma ( $t_{1/2} < 10$  min), leur version conjuguée a montré un degré de stabilité plasmatique plus élevé ( $t_{1/2} = 30$  min).

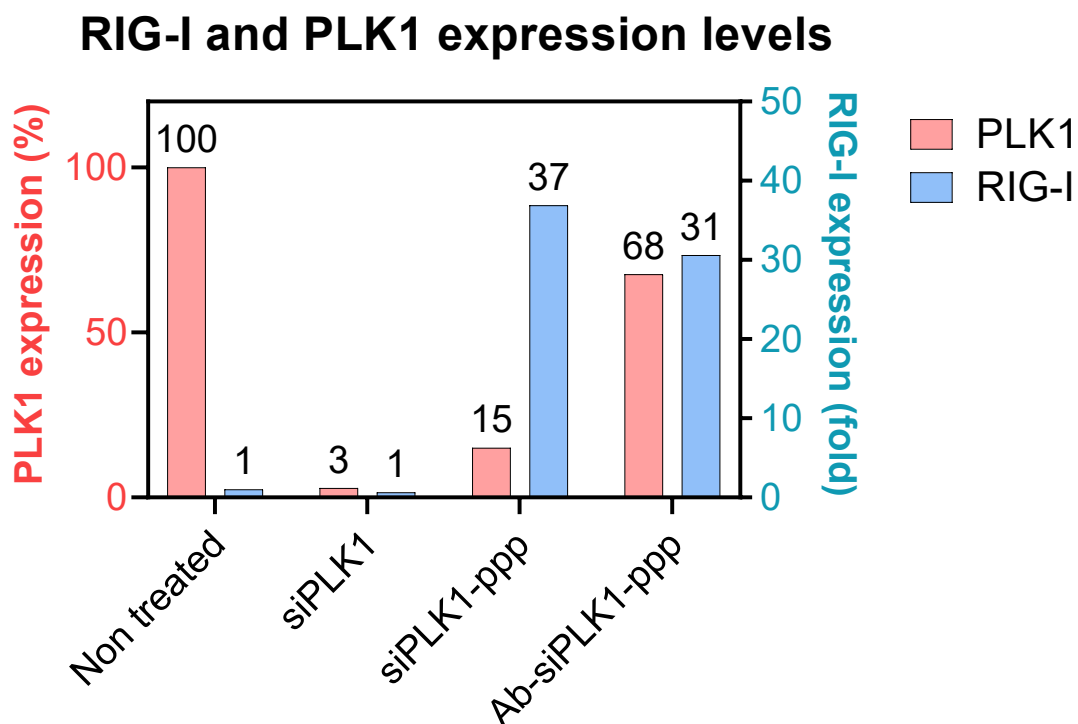
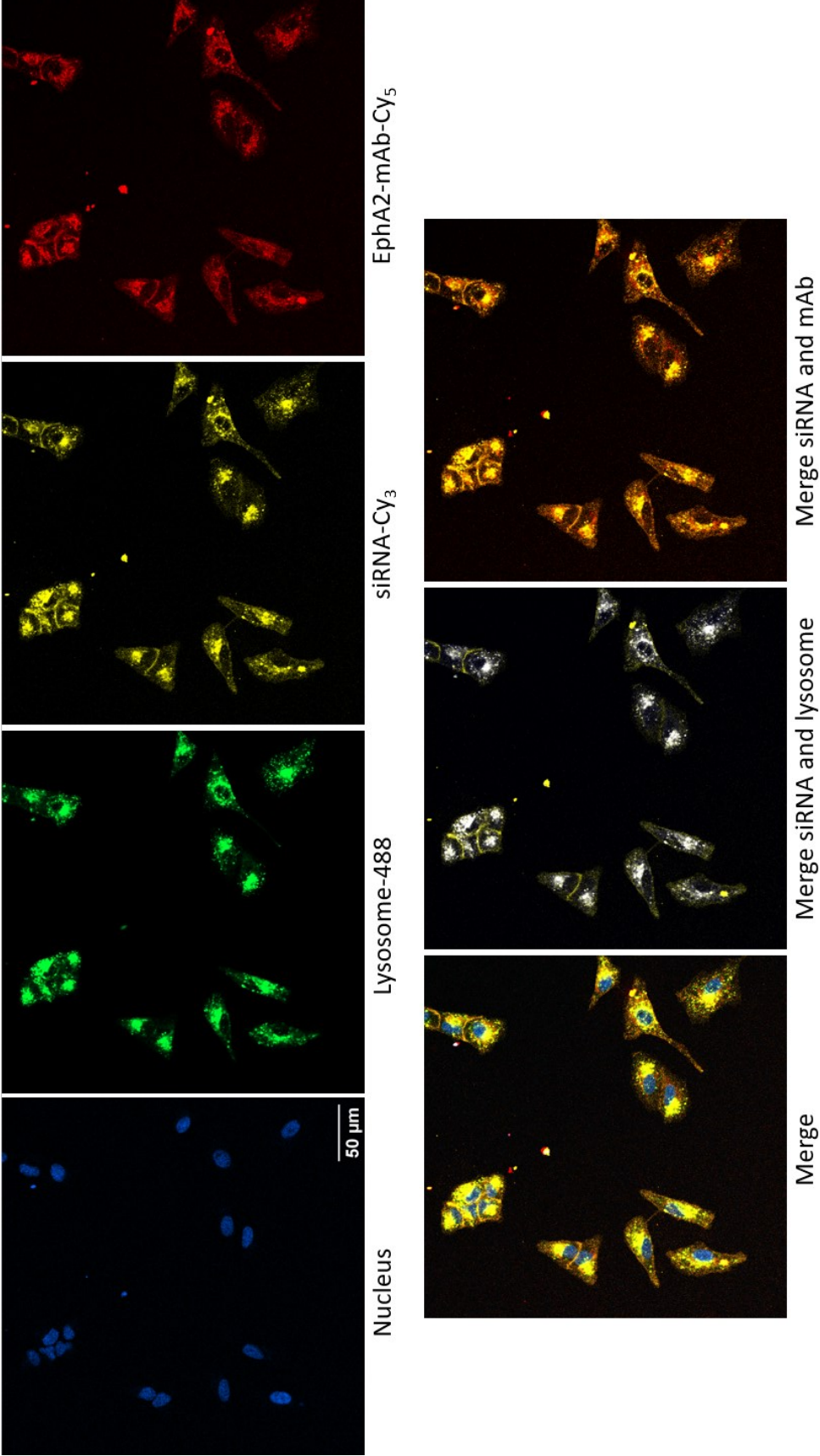
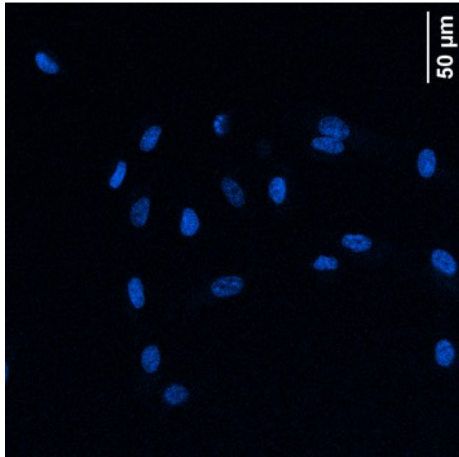


Figure 5 – Niveaux d'expression de RIG-I et PLK1, observé par western-blot, après 72h d'incubation à 40 nM.

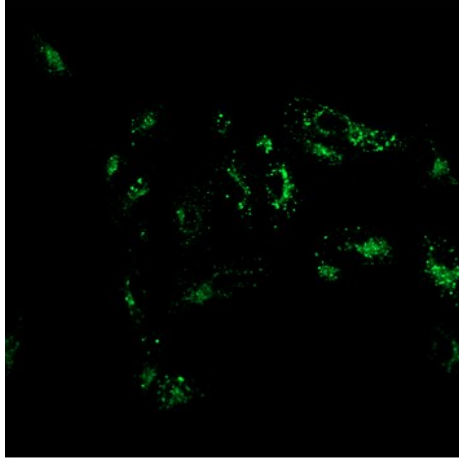
Un système FRET, où à la fois l'anticorps et le siRNA étaient marqués avec des fluorophores, a été synthétisé et utilisé afin d'évaluer le trafic de l'ARN à l'intérieur des cellules par microscopie confocale. Une internalisation rapide et dépendante d'EphA2 a été observée, ainsi qu'une séparation de nos deux molécules (ARN et anticorps) à l'intérieur des lysosomes, conduisant à la libération d'une petite partie du siRNA dans le cytosol. Alors que la structure exacte du siRNA libéré qui s'échappe de l'endosome ainsi que le mécanisme de libération sont inconnus, ces résultats suggèrent que cette

petite partie de siRNA dans le cytosol est suffisante pour activer les voies siRNA et celles de RIG-I.

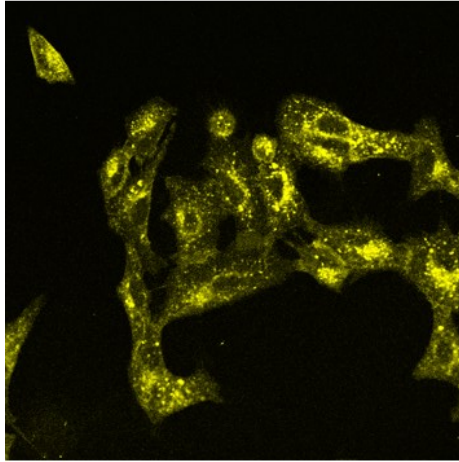




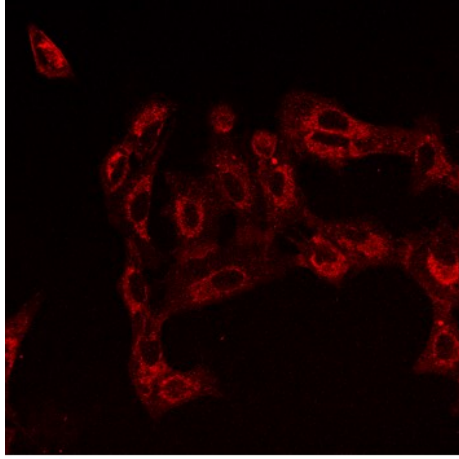
Nucleus



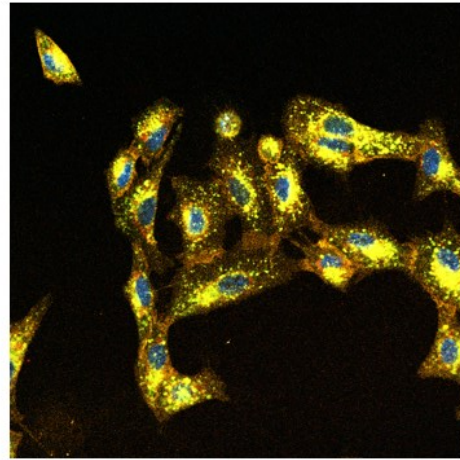
Lysosome-488



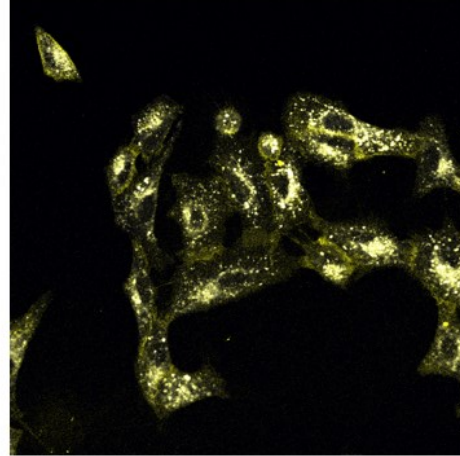
siRNA-Cy<sub>3</sub>



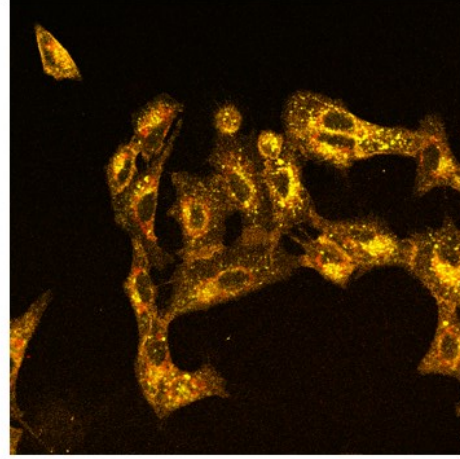
EphA2-mAb-Cy<sub>5</sub>



Merge



Merge siRNA and lysosome



Merge siRNA and Ab

Forts de ces résultats encourageants, nous avons décidé d'étudier en profondeur l'implication de ce nouveau conjugué à double mode d'action en immuno-oncologie. La mort cellulaire par apoptose par activation des caspases 3/7 a été évaluée, mettant en évidence un effet synergique entre l'activation de RIG-I et l'inhibition de PLK1. A l'aide d'un système d'imagerie, des expériences de coculture avec des cellules mononucléées périphérique du sang (PBMC) ont été menées afin de déterminer si notre conjugué pouvait activer les cellulaires immunitaires et induire une mort immunogène dépendante de RIG-I. Cette voie apoptotique a été observée sur des cellules cancéreuses ne possédant pas RIG-I en présence de PBMC, démontrant que le conjugué pouvait activer efficacement les PBMCs et favoriser la destruction des cellules cancéreuses.

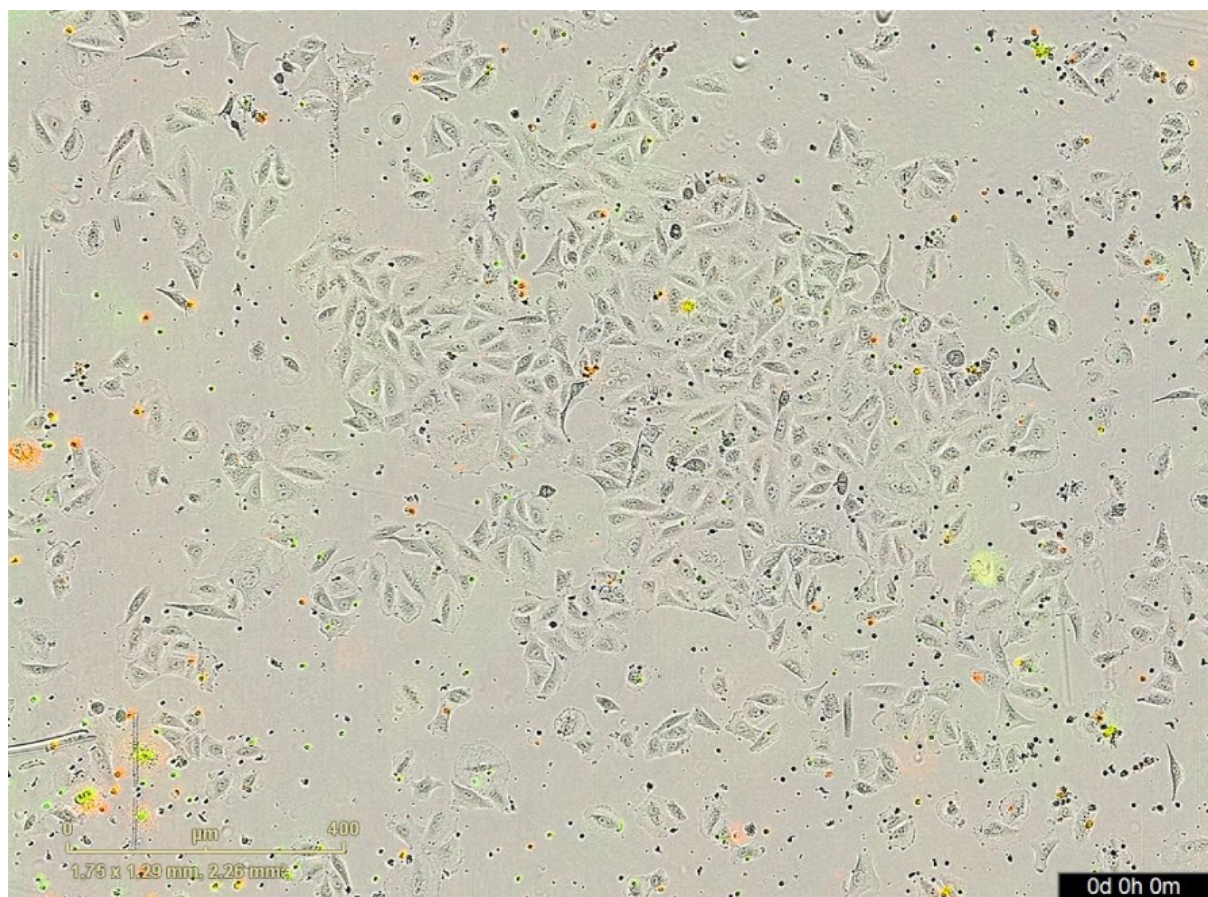


*Figure 6 – Image montrant l'apoptose des cellules cancéreuses en co-culture avec des PBMCs 0 h après incubation avec ARC 5.*

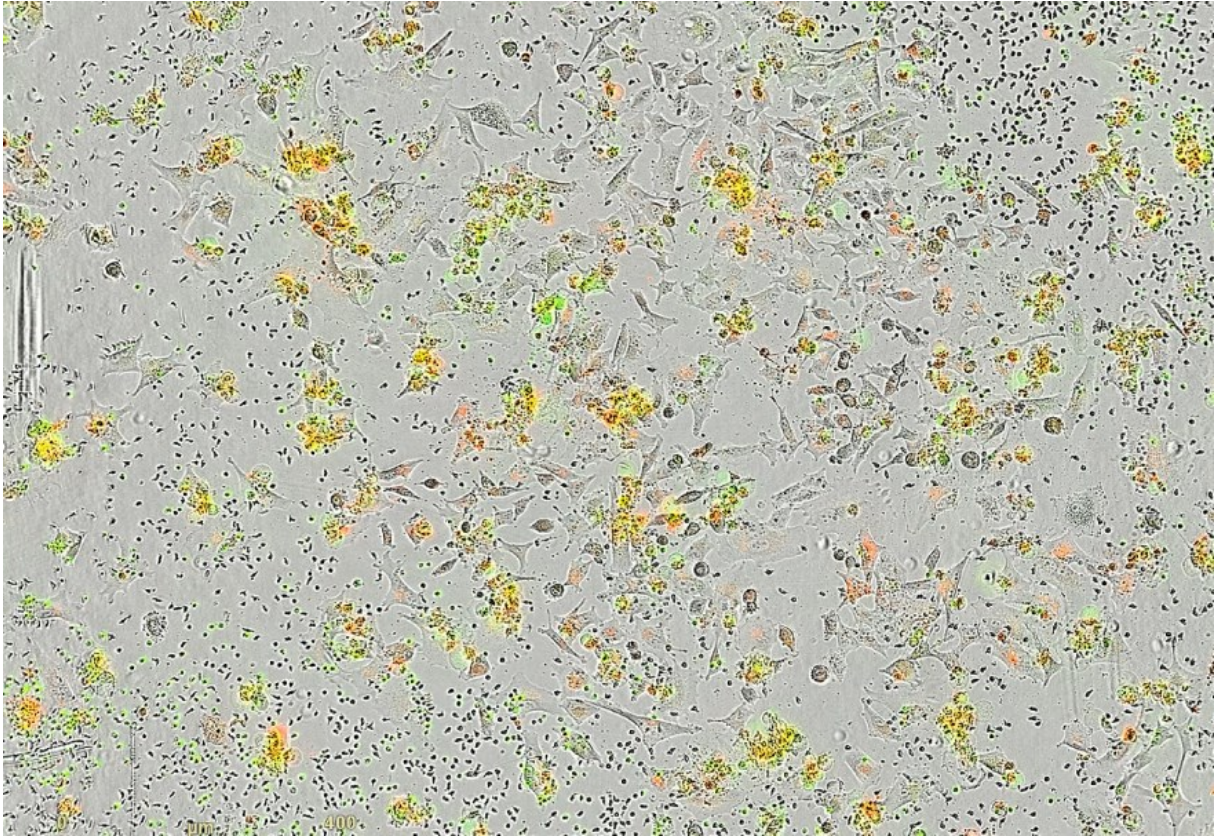


*Figure 6 – Image montrant l'apoptose des cellules cancéreuses en co-culture avec des PBMCs 96 h après incubation avec ARC 5.*

# Cytokines quantification (100 nM, 24 h)

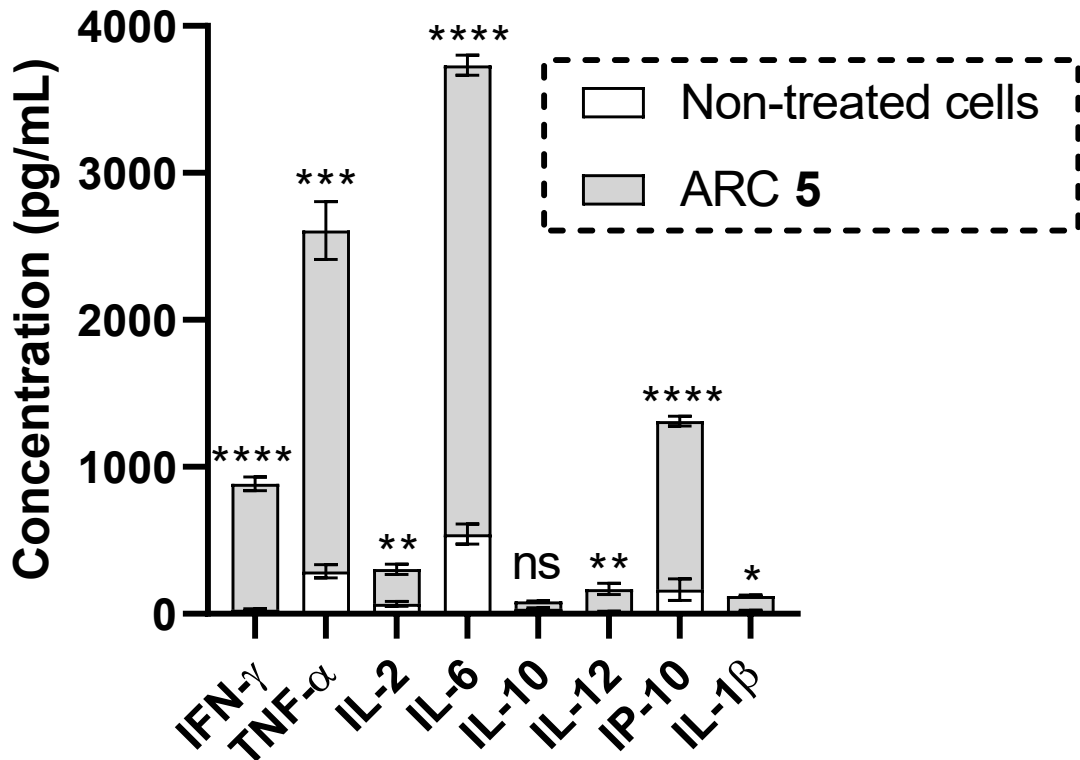


Figure 6 – Quantification des cytokines après incubation avec ARC 5.

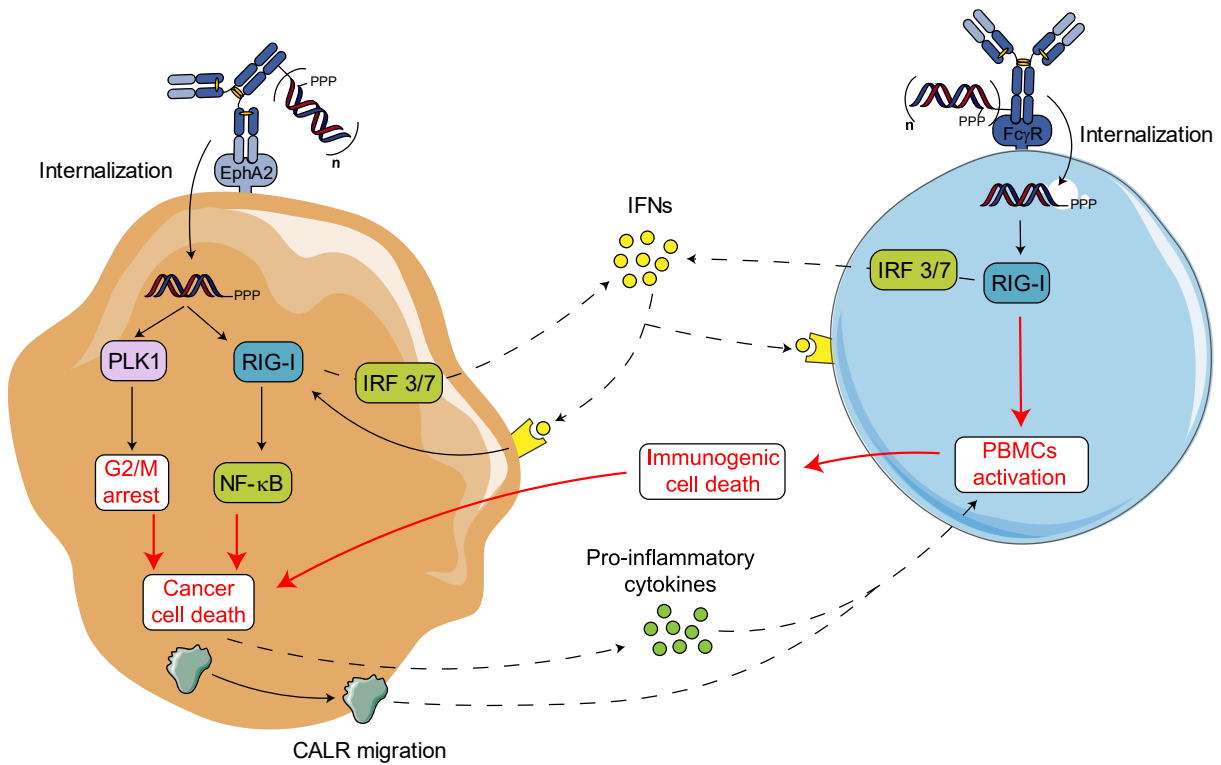


Figure 6 – Schéma récapitulatif de ces effets supposés du conjugué anticorps-siRNA.

Ces résultats semblent indiquer que notre bras-espacer « non-clivable » pouvait être clivé au cours des processus cellulaires afin de libérer du siRNA, car l'activation de RIG-I est très dépendante de la structure de l'ARN. Entre autres hypothèses, le motif carbamate liant le motif BCN au bras-espacer est apparu comme un point de faiblesse qui pourrait expliquer la libération inattendue de l'ARN. Afin de valider notre hypothèse, un acide bicyclo[6.1.0]nonyne carboxylique (**3**) a été synthétisé afin de fournir des molécules liées par une un amide plutôt qu'un carbamate (**figure 6**). En synthétisant des sondes FRET profluorescentes qui ne diffèrent que par le fragment d'attachement, une comparaison de clivage *in cellulo* a été réalisée entre un dérivé amide (**4**) et un dérivé carbamate (**5**). Contrairement à la sonde amide, la sonde carbamate a été clivée, indiquant que notre nouveau dérivé acide carboxylique pourrait être une plateforme polyvalente pour la synthèse de sondes moléculaires biologiquement stables.

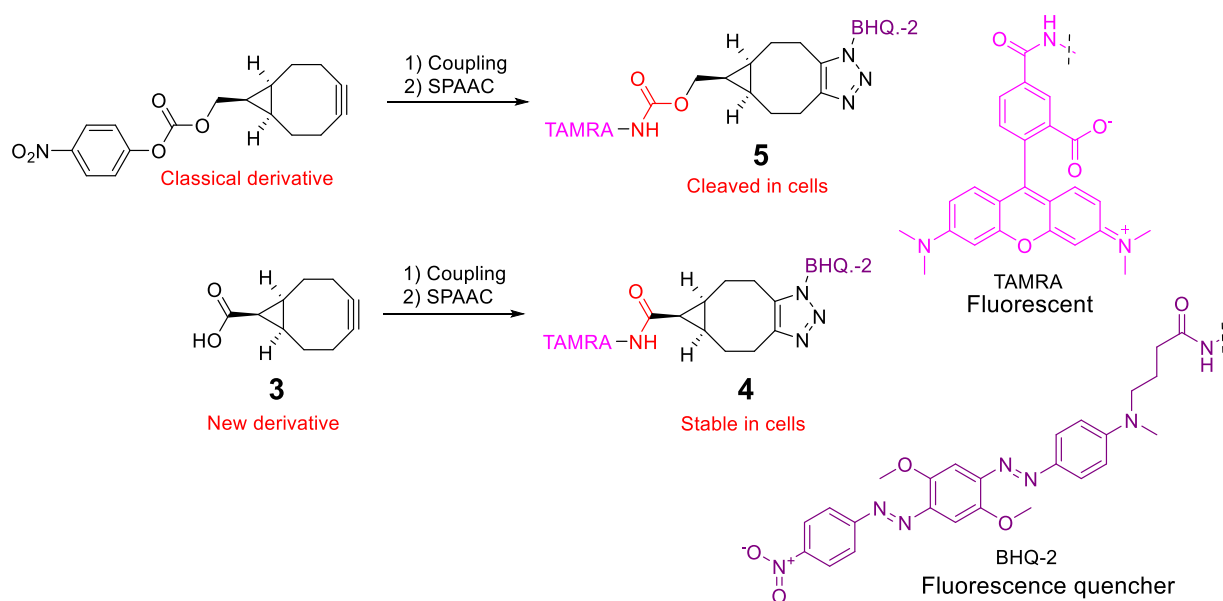


Figure 6 – Structures des sondes FRET synthétisées, avec la différence structurale en rouge.

Afin de potentiellement améliorer l'efficacité du conjugué anticorps-siRNA, nous avons exploré l'utilisation de bras-espacers clivables. Ainsi, deux bras-espacers possédant des propriétés de clivage différentes ont été synthétisés (**figure 7**) : le linker de référence Val-Cit-PAB, clivable par des protéases<sup>[13]</sup> (**6**) et une nouvelle classe de bras-espacers clivables à base d'acétal cycliques que nous avons développé au cours de la thèse (**7**). Comme pour l'étude du BCN acide carboxylique, des sondes FRET profluorescentes de chaque bras-espacer ont été synthétisés et leur profil de stabilité plasmatique et de pH ont été évalués. Notre nouveau modèle acido-labile s'est

avéré extrêmement stable dans le plasma humain et a montré des propriétés de clivages prometteuses dans la gamme de pH correspondant aux endosomes tardifs et des lysosomes. De plus, il a montré une clivabilité beaucoup plus grande *in vitro* par rapport à la sonde Val-Cit-PAB, tel qu'évalué par des mesures de cytométrie en flux et des études de microscopie confocale. Cependant, lorsqu'ils ont été appliqués à des conjugués anticorps-siRNAs, nous n'avons pas observé une augmentation d'efficacité pour chaque bras-espaces clivables comparé à celui « non clivable ». Ce résultat suggère ainsi que la libération du siRNA est probablement indépendante du bras-espacer, comme décrit précédemment.<sup>[14]</sup>

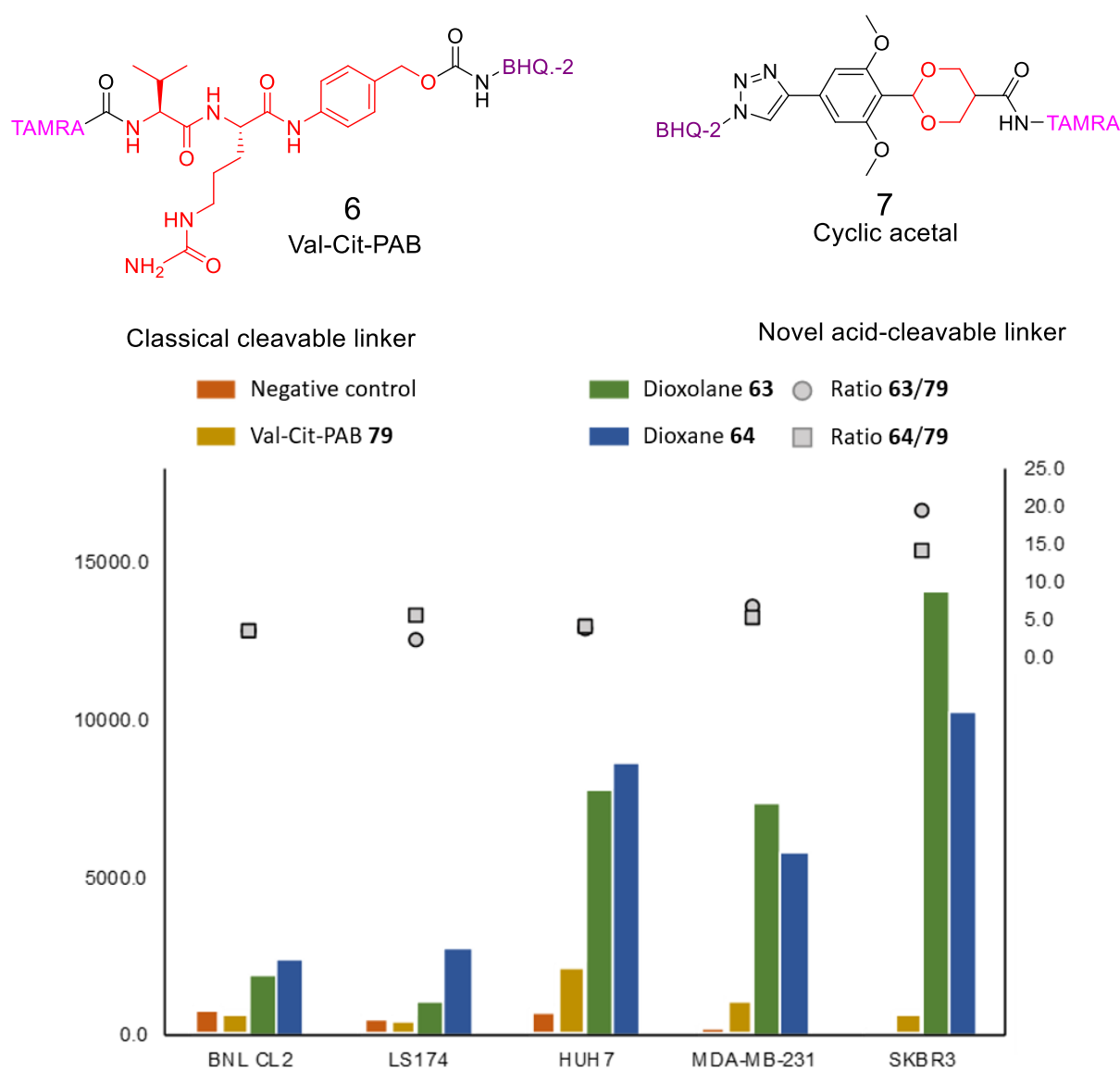
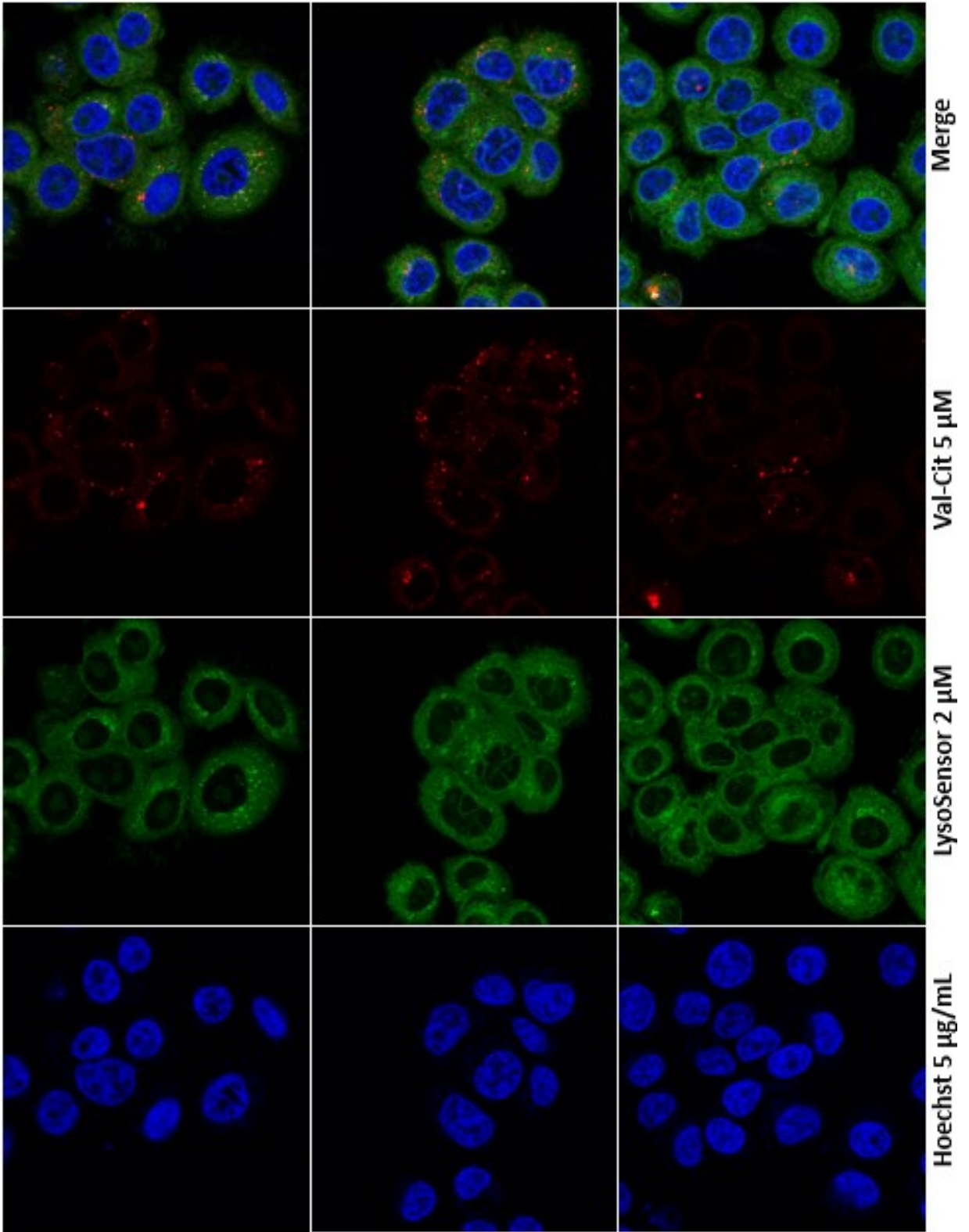
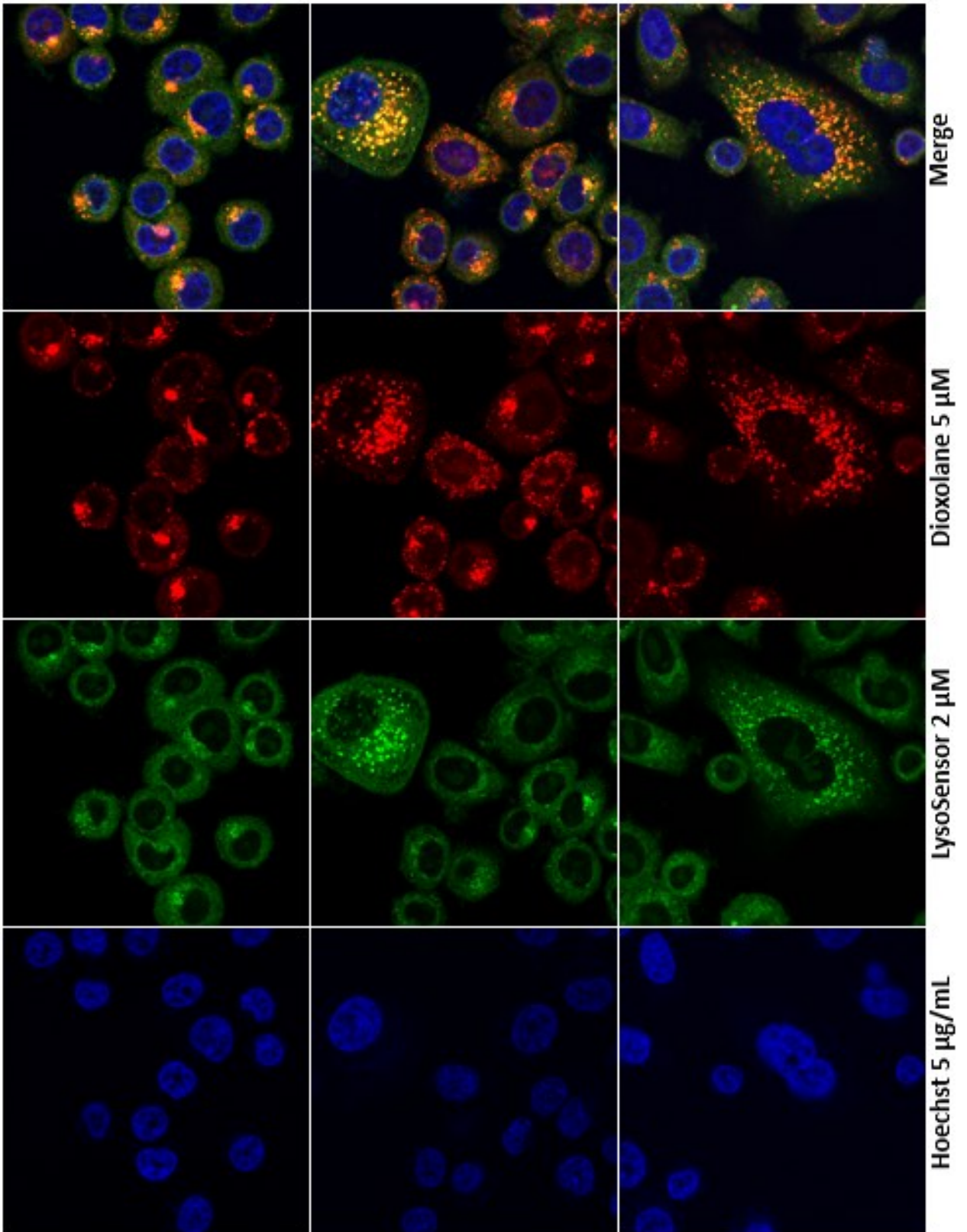
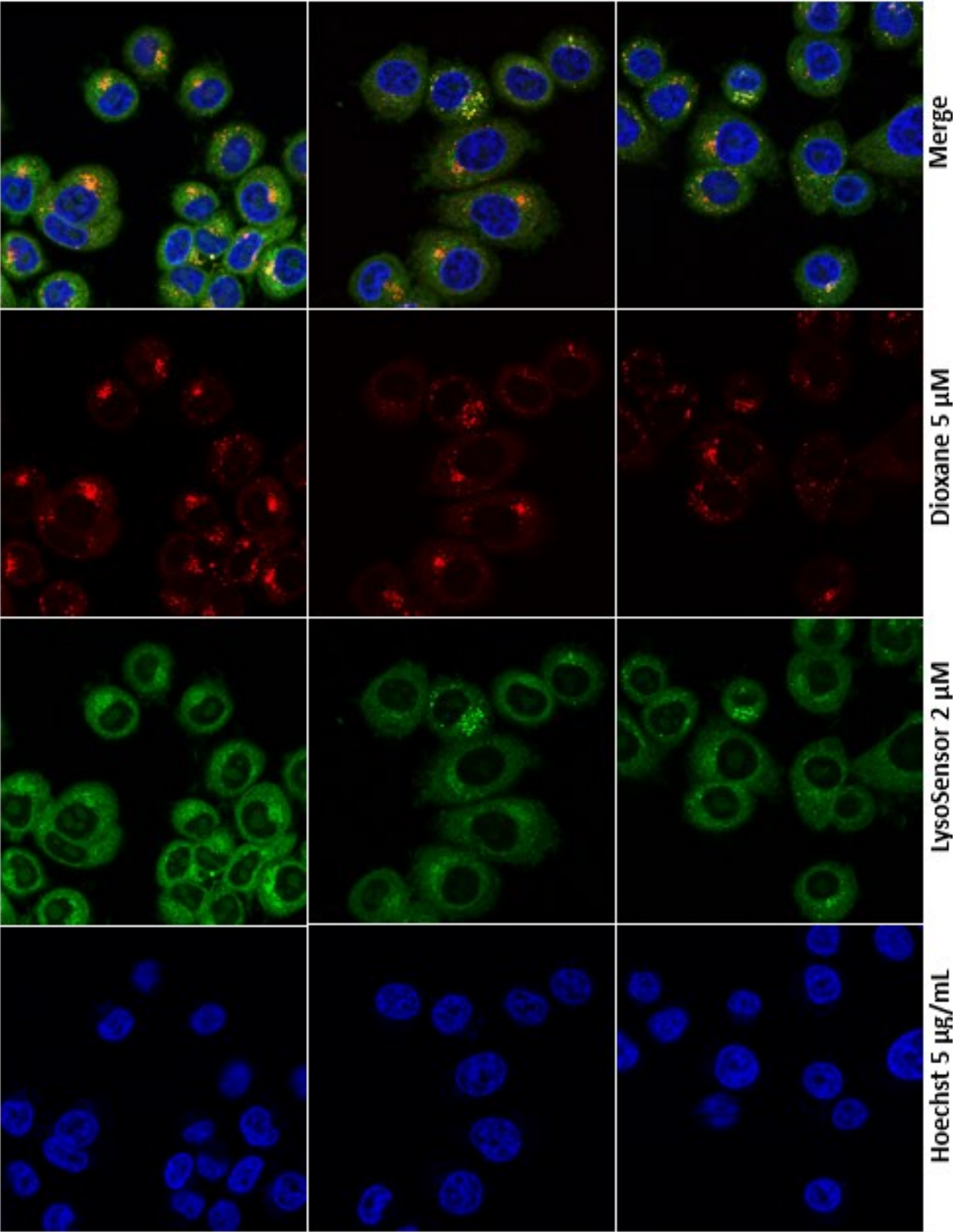


Figure 7 – Structures des sondes FRET, avec le groupe clivable en rouge et évaluation du clivage sur des cellules SKBR3.









La seconde stratégie vise à synthétiser des peptides cationiques qui permettent une forte complexation des siRNAs par des interactions non covalentes.<sup>[15]</sup> Ce peptide sera ensuite conjugué à l'anticorps anti-EphA2 et les conjugués résultants seront associés à l'ARN thérapeutique dans un rapport 1 pour 1 afin de fournir un complexe moléculairement défini. L'étape de conjugaison s'appuiera sur une stratégie similaire « plug and play » afin d'obtenir un conjugué anticorps-peptide entièrement caractérisé (**8, figure 8**). Une optimisation a été réalisée afin d'augmenter la stabilité du complexe tout en limitant la liaison électrostatique non spécifique aux cellules. Ce phénomène entraîne une délivrance non spécifique et est souvent rencontré dans les systèmes de délivrance à base de polycations.<sup>[15]</sup> Bien que cette approche soit plus difficile que la stratégie covalente, son principal avantage est d'être hautement modulaire, puisque pratiquement n'importe quel siRNA peut être complexé sans avoir besoin de modifications préalables.

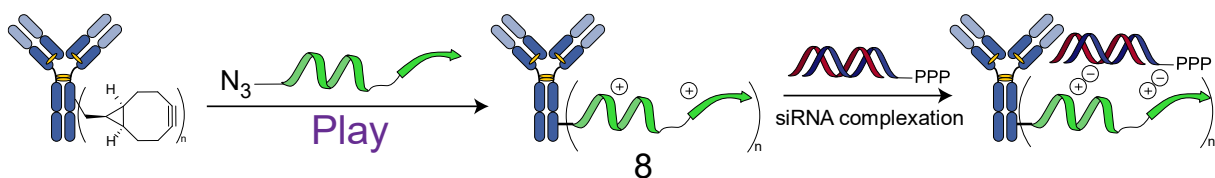


Figure 8 – Stratégie non-covalente explorée pendant la thèse afin de produire des conjugués anticorps-siRNA.

Les peptides actuellement décrits capables de complexer les siRNA et attachés aux anticorps sont basés sur des séquences riches en arginine hautement hydrophiles, telles que les homopolyarginines de 9-10 résidus<sup>[15]</sup> ou des protamines.<sup>[1]</sup> Alors que ce dernier est généralement fusionné à la séquence de l'anticorps, les homopolyarginines sont généralement conjuguées par des méthodes chimiques. Par des études de modélisation, un premier bloc de construction de 10 arginines a été sélectionné comme étant capable de se lier efficacement aux siRNAs et a ensuite été synthétisé. Afin d'améliorer l'affinité de liaison, des assemblages de différentes configurations géométriques et de différentes longueurs, réalisées avec ce bloc de construction, ont été conçus (**figure 9**). La capacité de chaque construction à se lier aux siRNAs a été évaluée. Par ailleurs, la synthèse de conjugués anticorps-peptide a été développée.

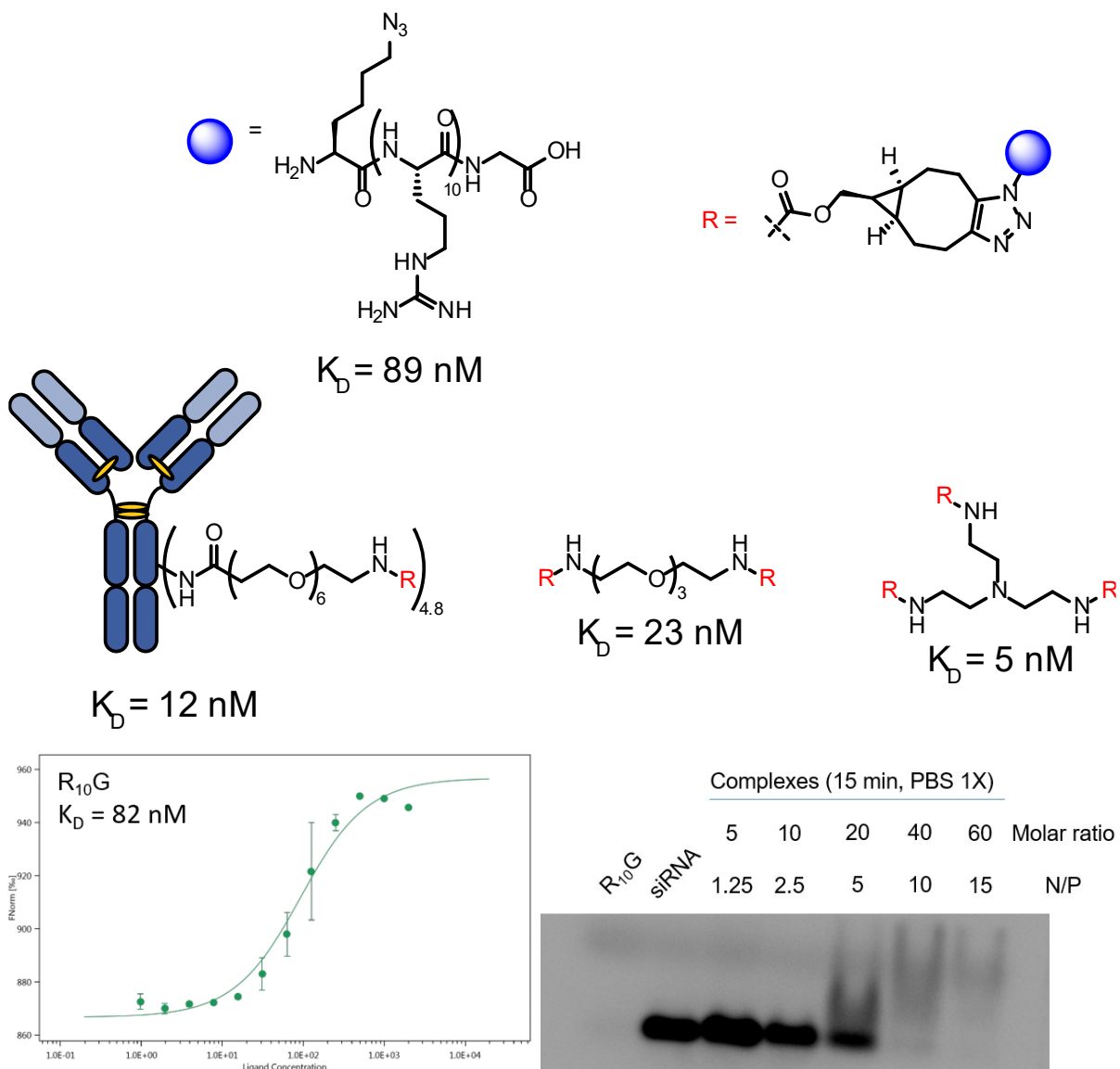
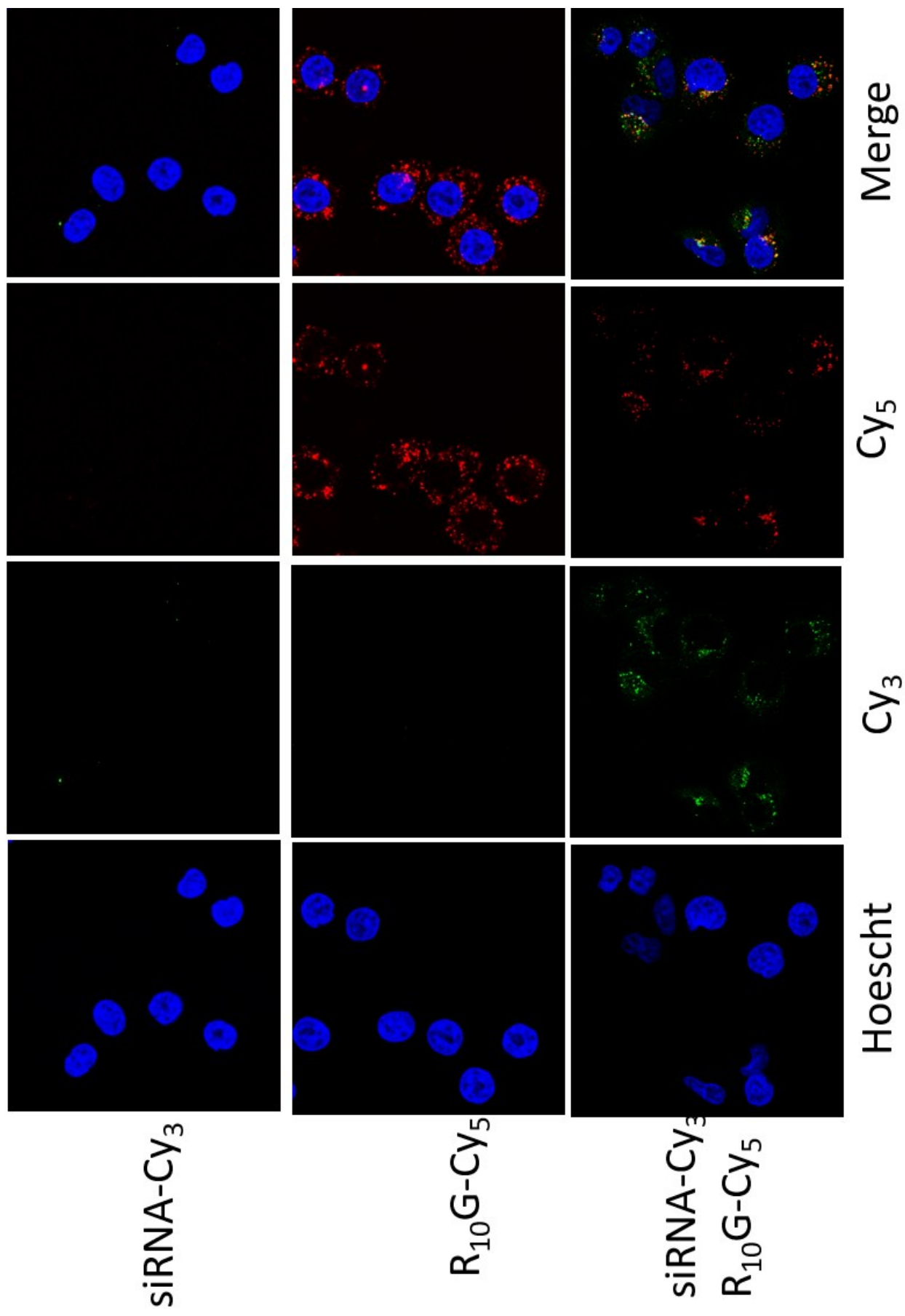
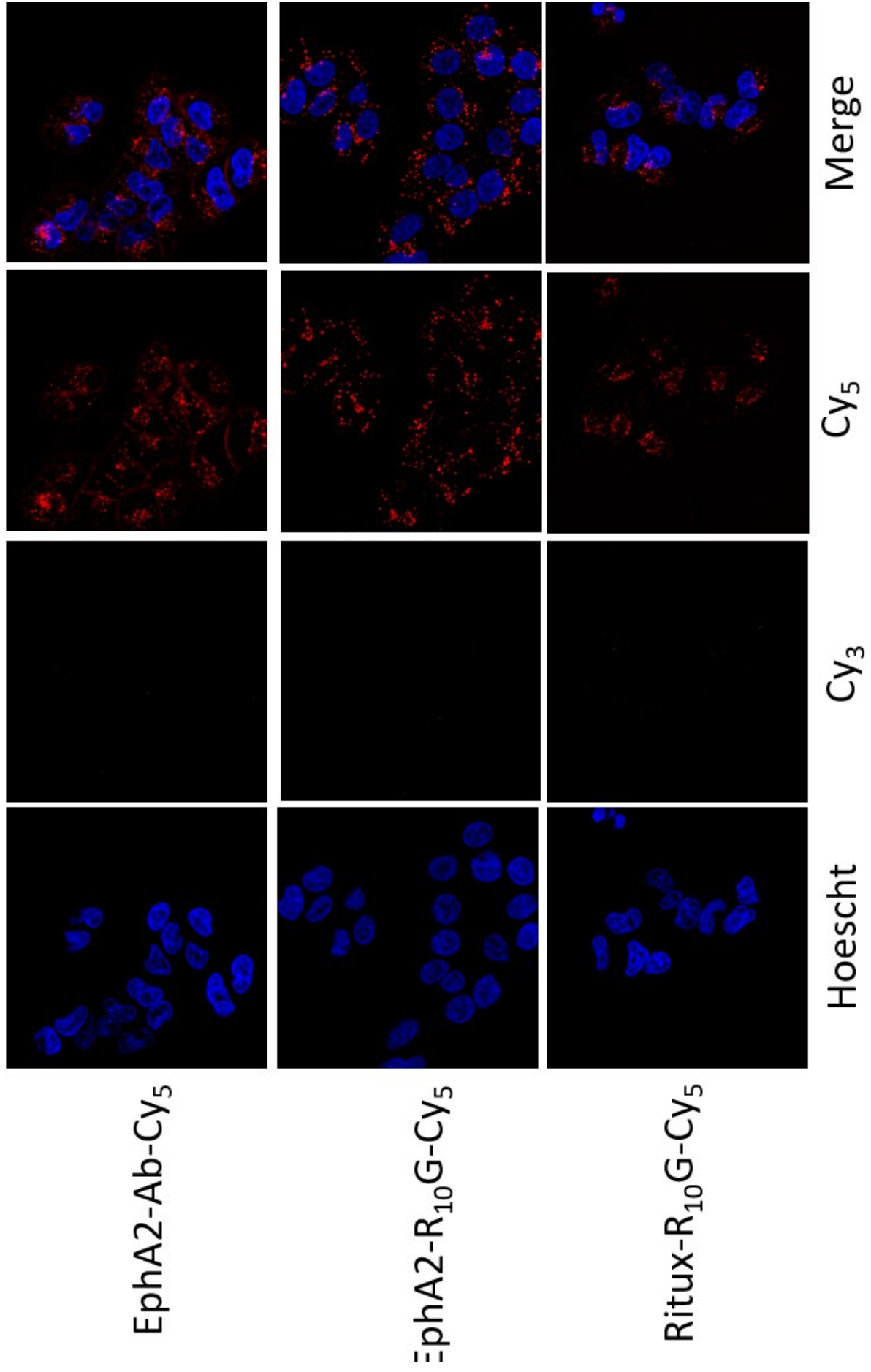


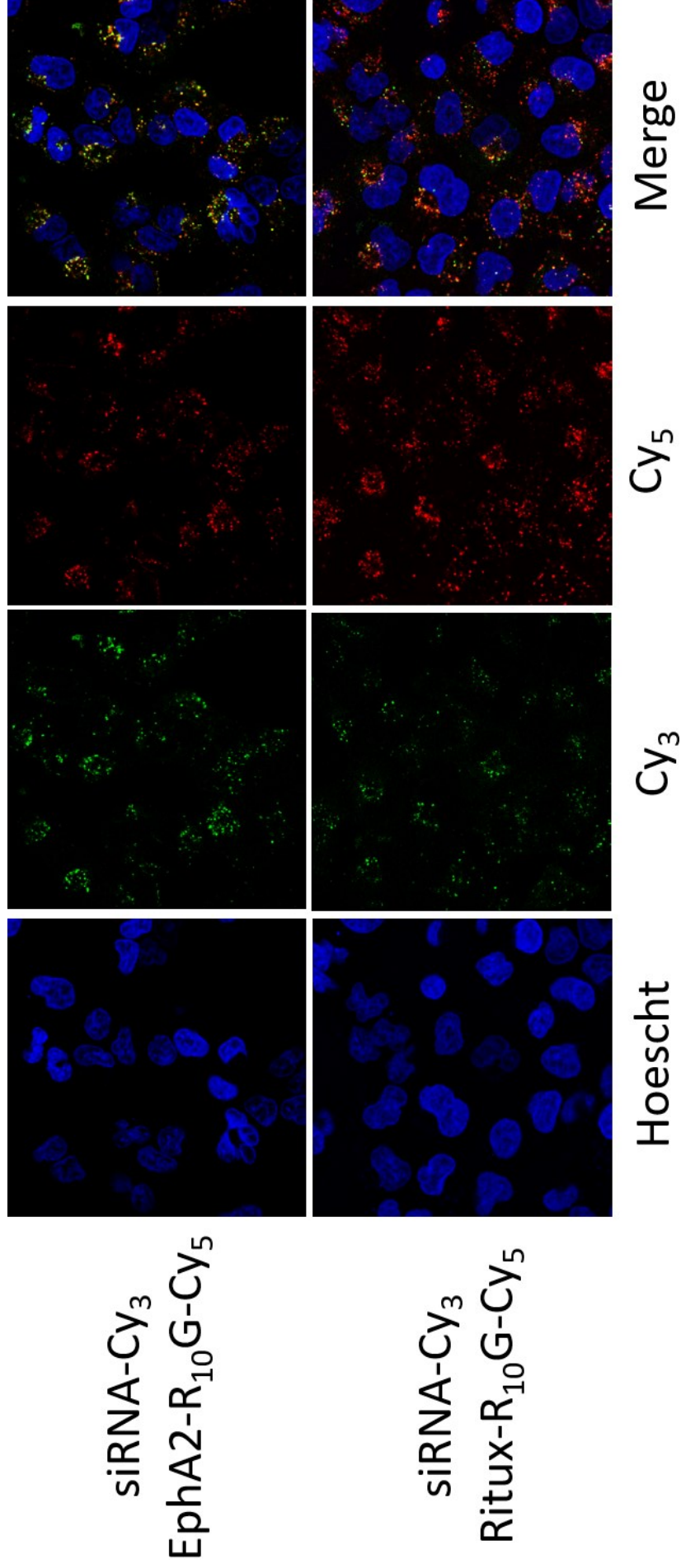
Figure 9 – Sélection de design de polyarginines synthétisés pendant la thèse et leur affinité avec un siRNA-5'Cys et affinité entre le peptide  $R_{10}G$  et le siRNA déterminée par MST et gel retard.

Une étude préliminaire de microscopie confocale avec le conjugué anticorps-décaarginine a montré que des siARN fluorescents pouvaient être délivrés à l'intérieur des cellules, cependant, la délivrance n'était pas dépendante de l'EphA2, montrant que la conjugaison d'un tel peptide sur des anticorps conduit à une internalisation non spécifique, comme précédemment décrit.<sup>[15]</sup>









Ce problème a révélé que ce système sous-optimal produisait des espèces supramoléculaires formant de grands agrégats, confirmant ainsi notre postulat initial selon lequel les stratégies électrostatiques pourraient nécessiter des objets définis au niveau moléculaire et des conceptions optimisées. De plus, lors de l'utilisation du siRNA-5'ppp dans des tests biologiques avec système, ni l'activation de RIG-I ni l'inhibition de PLK1 n'ont été observés, suggérant un manque de décomplexation dans le cytosol en raison d'un complexe trop stable. Pour contourner ce problème, un design clivable de peptide a été élaboré afin de moduler la stabilité du complexe en fonction de l'environnement.

## **Conclusion**

En résumé, différents objectifs ont été atteints au cours de cette thèse. Tout d'abord, le postulat selon lequel un siRNA-5'ppp pourrait induire la mort cellulaire par des mécanismes d'action simultanés et synergiques de RIG-I/RNAi a été vérifié. Le conjugué covalent anticorps-siRNA s'est avéré efficace pour délivrer des siRNA à l'intérieur des cellules cancéreuses, et des expériences de coculture avec des cellules immunitaires primaires ont montré des résultats prometteurs. La stabilité plasmatique du conjugué est cependant une limitation majeure de ce système, une optimisation du linker et de la conception du siRNA, notamment en utilisant des structures résistantes aux nucléases, pourrait conduire à un éventuel transfert vers des essais précliniques.

Pour l'approche non covalente, les synthèses et les méthodes d'évaluation biophysique de différentes conceptions de peptides ont été développées, ouvrant la voie à des conjugués anticorps-peptides moléculairement définis pour la livraison de siRNAs. Même si les affinités de liaison peptide/siRNAs étaient de l'ordre du nanomolaire, elles n'étaient pas suffisantes pour obtenir un rapport de 1 à 1, et une optimisation supplémentaire de la structure du peptide est nécessaire.

Des outils chimiques avec des applications plus larges ont également été développés, tels que le BCN acide carboxylique, qui pourrait servir de plate-forme stable au plasma et aux cellules pour des approches « plug and play », évitant une déconjugaison prématurée de la charge utile. En outre, des motifs acétal cycliques en tant que bras-espaces acido-labiles avec un degré élevé de sélectivité pour les endo/lysosomes et une stabilité plasmatique élevée ont été développés. Ces deux outils moléculaires pourraient servir dans de nombreuses applications au-delà des conjugués anticorps-

médicament ou des conjugués anticorps-oligonucléotides, tels que les sondes chimiques.

## X. References

1. Carlson, R. D., Flickinger, J. C. & Snook, A. E. Talkin' Toxins: From Coley's to Modern Cancer Immunotherapy. *Toxins* **12**, 241 (2020).
2. Song, W.-Y. *et al.* A Receptor Kinase-Like Protein Encoded by the Rice Disease Resistance Gene, Xa21. *Science* **270**, 1804–1806 (1995).
3. Lemaitre, B., Nicolas, E., Michaut, L., Reichhart, J.-M. & Hoffmann, J. A. The Dorsoventral Regulatory Gene Cassette *spätzle/Toll/cactus* Controls the Potent Antifungal Response in *Drosophila* Adults. *Cell* **86**, 973–983 (1996).
4. Medzhitov, R., Preston-Hurlburt, P. & Janeway, C. A. A human homologue of the *Drosophila* Toll protein signals activation of adaptive immunity. *Nature* **388**, 394–397 (1997).
5. Takeuchi, O. & Akira, S. Pattern Recognition Receptors and Inflammation. *Cell* **140**, 805–820 (2010).
6. Fitzgerald, K. A. & Kagan, J. C. Toll-like Receptors and the Control of Immunity. *Cell* **180**, 1044–1066 (2020).
7. Rock, F. L., Hardiman, G., Timans, J. C., Kastelein, R. A. & Bazan, J. F. A family of human receptors structurally related to *Drosophila* Toll. *Proceedings of the National Academy of Sciences* **95**, 588–593 (1998).
8. Lind, N. A., Rael, V. E., Pestal, K., Liu, B. & Barton, G. M. Regulation of the nucleic acid-sensing Toll-like receptors. *Nat Rev Immunol* (2021) doi:10.1038/s41577-021-00577-0.
9. Hornung, V. *et al.* Sequence-specific potent induction of IFN- $\alpha$  by short interfering RNA in plasmacytoid dendritic cells through TLR7. *Nat Med* **11**, 263–270 (2005).
10. Javaid, Yasmeen, & Choi. Toll-Like Receptors and Relevant Emerging Therapeutics with Reference to Delivery Methods. *Pharmaceutics* **11**, 441 (2019).
11. Brown, G. D., Willment, J. A. & Whitehead, L. C-type lectins in immunity and homeostasis. *Nat Rev Immunol* **18**, 374–389 (2018).
12. Geijtenbeek, T. B. H. & Gringhuis, S. I. Signalling through C-type lectin receptors: shaping immune responses. *Nat Rev Immunol* **9**, 465–479 (2009).

13. Hoving, J. C., Wilson, G. J. & Brown, G. D. Signalling C -Type lectin receptors, microbial recognition and immunity. *Cell Microbiol* **16**, 185–194 (2014).
14. Bai, L. *et al.* Promising targets based on pattern recognition receptors for cancer immunotherapy. *Pharmacological Research* **159**, 105017 (2020).
15. Daver, N. *et al.* A PHASE I dose-escalation study of DCLL9718S , an antibody-drug conjugate targeting C -type lectin-like molecule-1 ( CLL -1) in patients with acute myeloid leukemia. *Am J Hematol* **96**, (2021).
16. Inohara, N., Chamaillard, M., McDonald, C. & Nuñez, G. NOD-LRR PROTEINS: Role in Host-Microbial Interactions and Inflammatory Disease. *Annu. Rev. Biochem.* **74**, 355–383 (2005).
17. Tada, H., Aiba, S., Shibata, K.-I., Ohteki, T. & Takada, H. Synergistic effect of Nod1 and Nod2 agonists with toll-like receptor agonists on human dendritic cells to generate interleukin-12 and T helper type 1 cells. *Infect Immun* **73**, 7967–7976 (2005).
18. Fritz, J. H. *et al.* Synergistic stimulation of human monocytes and dendritic cells by Toll-like receptor 4 and NOD1- and NOD2-activating agonists. *Eur. J. Immunol.* **35**, 2459–2470 (2005).
19. Platnich, J. M. & Muruve, D. A. NOD-like receptors and inflammasomes: A review of their canonical and non-canonical signaling pathways. *Archives of Biochemistry and Biophysics* **670**, 4–14 (2019).
20. Caruso, R., Warner, N., Inohara, N. & Núñez, G. NOD1 and NOD2: Signaling, Host Defense, and Inflammatory Disease. *Immunity* **41**, 898–908 (2014).
21. Girardin, S. E. Nod1 Detects a Unique Muropeptide from Gram-Negative Bacterial Peptidoglycan. *Science* **300**, 1584–1587 (2003).
22. Sabbah, A. *et al.* Activation of innate immune antiviral responses by Nod2. *Nat Immunol* **10**, 1073–1080 (2009).
23. Geddes, K., Magalhães, J. G. & Girardin, S. E. Unleashing the therapeutic potential of NOD-like receptors. *Nat Rev Drug Discov* **8**, 465–479 (2009).

24. Galluzzi, L. *et al.* Molecular mechanisms of cell death: recommendations of the Nomenclature Committee on Cell Death 2018. *Cell Death Differ* **25**, 486–541 (2018).
25. Man, S. M., Karki, R. & Kanneganti, T.-D. AIM2 inflammasome in infection, cancer, and autoimmunity: Role in DNA sensing, inflammation, and innate immunity. *Eur. J. Immunol.* **46**, 269–280 (2016).
26. Chen, I.-Y. & Ichinohe, T. Response of host inflammasomes to viral infection. *Trends in Microbiology* **23**, 55–63 (2015).
27. Jin, T. *et al.* Structures of the HIN Domain:DNA Complexes Reveal Ligand Binding and Activation Mechanisms of the AIM2 Inflammasome and IFI16 Receptor. *Immunity* **36**, 561–571 (2012).
28. Li, K., Qu, S., Chen, X., Wu, Q. & Shi, M. Promising Targets for Cancer Immunotherapy: TLRs, RLRs, and STING-Mediated Innate Immune Pathways. *International Journal of Molecular Sciences* **18**, 404 (2017).
29. Ramanjulu, J. M. *et al.* Design of amidobenzimidazole STING receptor agonists with systemic activity. *Nature* **564**, 439–443 (2018).
30. Amouzegar, A., Chelvanambi, M., Filderman, J. N., Storkus, W. J. & Luke, J. J. STING Agonists as Cancer Therapeutics. *Cancers* **13**, 2695 (2021).
31. Duvall, J. R. *et al.* Abstract 1738: XMT-2056, a well-tolerated, Immunosynthen-based STING-agonist antibody-drug conjugate which induces anti-tumor immune activity. in *Immunology* 1738–1738 (American Association for Cancer Research, 2021). doi:10.1158/1538-7445.AM2021-1738.
32. Yoneyama, M. *et al.* The RNA helicase RIG-I has an essential function in double-stranded RNA-induced innate antiviral responses. *Nature Immunology* **5**, 730–737 (2004).
33. Rehwinkel, J. *et al.* RIG-I Detects Viral Genomic RNA during Negative-Strand RNA Virus Infection. *Cell* **140**, 397–408 (2010).
34. Hornung, V. *et al.* 5'-Triphosphate RNA Is the Ligand for RIG-I. *Science* **314**, 994–997 (2006).

35. Andrejeva, J. *et al.* The V proteins of paramyxoviruses bind the IFN-inducible RNA helicase, mda-5, and inhibit its activation of the IFN- promoter. *Proceedings of the National Academy of Sciences* **101**, 17264–17269 (2004).
36. Brisse, M. & Ly, H. Comparative Structure and Function Analysis of the RIG-I-Like Receptors: RIG-I and MDA5. *Front. Immunol.* **10**, 1586 (2019).
37. Rothenfusser, S. *et al.* The RNA Helicase Lgp2 Inhibits TLR-Independent Sensing of Viral Replication by Retinoic Acid-Inducible Gene-I. *J Immunol* **175**, 5260–5268 (2005).
38. Wu, W. *et al.* RIG-I and TLR3 are both required for maximum interferon induction by influenza virus in human lung alveolar epithelial cells. *Virology* **482**, 181–188 (2015).
39. Eigentler, T. *et al.* Abstract LB-021: Intratumoral RNA-based TLR-7/8 and RIG-I agonist CV8102 alone and in combination with anti-PD-1 in a Phase I dose-escalation and expansion trial in patients with advanced solid tumors. in *Clinical Research (Excluding Clinical Trials)* LB-021-LB-021 (American Association for Cancer Research, 2019). doi:10.1158/1538-7445.AM2019-LB-021.
40. Zevini, A., Olagnier, D. & Hiscott, J. Crosstalk between Cytoplasmic RIG-I and STING Sensing Pathways. *Trends in Immunology* **38**, 194–205 (2017).
41. Guo, G. *et al.* Reciprocal regulation of RIG-I and XRCC4 connects DNA repair with RIG-I immune signaling. *Nat Commun* **12**, 2187 (2021).
42. Żeromski, J. *et al.* Significance and Role of Pattern Recognition Receptors in Malignancy. *Arch. Immunol. Ther. Exp.* **67**, 133–141 (2019).
43. Li, X.-Y., Guo, H.-Z. & Zhu, J. Tumor suppressor activity of RIG-I. *Molecular & Cellular Oncology* **1**, e968016 (2014).
44. Mullard, A. Can innate immune system targets turn up the heat on ‘cold’ tumours? *Nature Reviews Drug Discovery* **17**, 3–5 (2018).
45. Moreno, V. *et al.* 794 Safety and efficacy results from a phase 1/1b study of intratumoral MK-4621, a retinoic acid-inducible gene I (RIG-I) agonist, plus intravenous pembrolizumab in patients with advanced solid tumors. *J Immunother Cancer* **8**, A842–A842 (2020).

46. Cui, S. *et al.* The C-Terminal Regulatory Domain Is the RNA 5'-Triphosphate Sensor of RIG-I. *Molecular Cell* **29**, 169–179 (2008).
47. Kowalinski, E. *et al.* Structural Basis for the Activation of Innate Immune Pattern-Recognition Receptor RIG-I by Viral RNA. *Cell* **147**, 423–435 (2011).
48. Luo, D. *et al.* Structural Insights into RNA Recognition by RIG-I. *Cell* **147**, 409–422 (2011).
49. Park, H. Caspase recruitment domains for protein interactions in cellular signaling (Review). *Int J Mol Med* (2019) doi:10.3892/ijmm.2019.4060.
50. Anchisi, S., Guerra, J. & Garcin, D. RIG-I ATPase Activity and Discrimination of Self-RNA versus Non-Self-RNA. *mBio* **6**, e02349-14 (2015).
51. Ren, X., Linehan, M. M., Iwasaki, A. & Pyle, A. M. RIG-I Selectively Discriminates against 5'-Monophosphate RNA. *Cell Reports* **26**, 2019-2027.e4 (2019).
52. Tluk, S. *et al.* Sequences derived from self-RNA containing certain natural modifications act as suppressors of RNA-mediated inflammatory immune responses. *International Immunology* **21**, 607–619 (2009).
53. Liu, G., Park, H.-S., Pyo, H.-M., Liu, Q. & Zhou, Y. Influenza A Virus Panhandle Structure Is Directly Involved in RIG-I Activation and Interferon Induction. *J. Virol.* **89**, 6067–6079 (2015).
54. Gebhardt, A., Laudenbach, B. T. & Pichlmair, A. Discrimination of Self and Non-Self Ribonucleic Acids. *Journal of Interferon & Cytokine Research* **37**, 184–197 (2017).
55. Schlee, M. & Hartmann, G. The Chase for the RIG-I Ligand—Recent Advances. *Molecular Therapy* **18**, 1254–1262 (2010).
56. Schmidt, A. *et al.* 5'-triphosphate RNA requires base-paired structures to activate antiviral signaling via RIG-I. *Proceedings of the National Academy of Sciences* **106**, 12067–12072 (2009).
57. Binder, M. *et al.* Molecular Mechanism of Signal Perception and Integration by the Innate Immune Sensor Retinoic Acid-inducible Gene-I (RIG-I). *J. Biol. Chem.* **286**, 27278–27287 (2011).



58. Kato, H. *et al.* Length-dependent recognition of double-stranded ribonucleic acids by retinoic acid–inducible gene-I and melanoma differentiation–associated gene 5. *Journal of Experimental Medicine* **205**, 1601–1610 (2008).
59. Linehan, M. M. *et al.* A minimal RNA ligand for potent RIG-I activation in living mice. *Sci. Adv.* **4**, e1701854 (2018).
60. Ren, X., Linehan, M. M., Iwasaki, A. & Pyle, A. M. RIG-I Recognition of RNA Targets: The Influence of Terminal Base Pair Sequence and Overhangs on Affinity and Signaling. *Cell Reports* **29**, 3807-3815.e3 (2019).
61. Lu, C. *et al.* The Structural Basis of 5' Triphosphate Double-Stranded RNA Recognition by RIG-I C-Terminal Domain. *Structure* **18**, 1032–1043 (2010).
62. Durbin, A. F., Wang, C., Marcotrigiano, J. & Gehrke, L. RNAs Containing Modified Nucleotides Fail To Trigger RIG-I Conformational Changes for Innate Immune Signaling. *mBio* **7**, e00833-16, /mbio/7/5/e00833-16.atom (2016).
63. Devarkar, S. C. *et al.* Structural basis for m7G recognition and 2'-O-methyl discrimination in capped RNAs by the innate immune receptor RIG-I. *Proc Natl Acad Sci USA* **113**, 596–601 (2016).
64. Schuberth-Wagner, C. *et al.* A Conserved Histidine in the RNA Sensor RIG-I Controls Immune Tolerance to N1-2'O-Methylated Self RNA. *Immunity* **43**, 41–51 (2015).
65. Marq, J.-B., Kolakofsky, D. & Garcin, D. Unpaired 5' ppp-Nucleotides, as Found in Arenavirus Double-stranded RNA Panhandles, Are Not Recognized by RIG-I. *J. Biol. Chem.* **285**, 18208–18216 (2010).
66. Wang, Y. *et al.* Structural and functional insights into 5'-ppp RNA pattern recognition by the innate immune receptor RIG-I. *Nat Struct Mol Biol* **17**, 781–787 (2010).
67. Schlee, M. *et al.* Recognition of 5' Triphosphate by RIG-I Helicase Requires Short Blunt Double-Stranded RNA as Contained in Panhandle of Negative-Strand Virus. *Immunity* **31**, 25–34 (2009).
68. Pichlmair, A. *et al.* RIG-I-Mediated Antiviral Responses to Single-Stranded RNA Bearing 5'-Phosphates. *Science* **314**, 997–1001 (2006).

69. Cazenave, C. & Uhlenbeck, O. C. RNA template-directed RNA synthesis by T7 RNA polymerase. *Proceedings of the National Academy of Sciences* **91**, 6972–6976 (1994).
70. Triana-Alonso, F. J., Dabrowski, M., Wadzack, J. & Nierhaus, K. H. Self-coded 3'-Extension of Run-off Transcripts Produces Aberrant Products during in Vitro Transcription with T7 RNA Polymerase. *Journal of Biological Chemistry* **270**, 6298–6307 (1995).
71. Bartok, E. & Hartmann, G. Immune Sensing Mechanisms that Discriminate Self from Altered Self and Foreign Nucleic Acids. *Immunity* **53**, 54–77 (2020).
72. Bridge, A. J., Pebernard, S., Ducraux, A., Nicoulaz, A.-L. & Iggo, R. Induction of an interferon response by RNAi vectors in mammalian cells. *Nat Genet* **34**, 263–264 (2003).
73. Kenworthy, R. *et al.* Short-hairpin RNAs delivered by lentiviral vector transduction trigger RIG-I-mediated IFN activation. *Nucleic Acids Research* **37**, 6587–6599 (2009).
74. Marq, J.-B., Hausmann, S., Veillard, N., Kolakofsky, D. & Garcin, D. Short Double-stranded RNAs with an Overhanging 5' ppp-Nucleotide, as Found in Arenavirus Genomes, Act as RIG-I Decoys. *Journal of Biological Chemistry* **286**, 6108–6116 (2011).
75. Witteveldt, J. *et al.* The influence of viral RNA secondary structure on interactions with innate host cell defences. *Nucleic Acids Research* **42**, 3314–3329 (2014).
76. Goubau, D. *et al.* Antiviral immunity via RIG-I-mediated recognition of RNA bearing 5'-diphosphates. *Nature* **514**, 372–375 (2014).
77. Myong, S. *et al.* Cytosolic Viral Sensor RIG-I Is a 5'-Triphosphate-Dependent Translocase on Double-Stranded RNA. *Science* **323**, 1070–1074 (2009).
78. Woo, J.-S. *et al.* Structural and functional insights into the B30.2/SPRY domain. *EMBO J* **25**, 1353–1363 (2006).
79. Zeng, W. *et al.* Reconstitution of the RIG-I Pathway Reveals a Signaling Role of Unanchored Polyubiquitin Chains in Innate Immunity. *Cell* **141**, 315–330 (2010).
80. Saito, T. *et al.* Regulation of innate antiviral defenses through a shared repressor domain in RIG-I and LGP2. *Proceedings of the National Academy of Sciences* **104**, 582–587 (2007).
81. Fujita, T. A Nonself RNA Pattern: Tri-p to Panhandle. *Immunity* **31**, 4–5 (2009).

82. Saito, T., Owen, D. M., Jiang, F., Marcotrigiano, J. & Gale, M. Innate immunity induced by composition-dependent RIG-I recognition of hepatitis C virus RNA. *Nature* **454**, 523–527 (2008).
83. Ranjith-Kumar, C. T. *et al.* Agonist and Antagonist Recognition by RIG-I, a Cytoplasmic Innate Immunity Receptor. *Journal of Biological Chemistry* **284**, 1155–1165 (2009).
84. Devarkar, S. C., Schweibenz, B., Wang, C., Marcotrigiano, J. & Patel, S. S. RIG-I Uses an ATPase-Powered Translocation-Throttling Mechanism for Kinetic Proofreading of RNAs and Oligomerization. *Molecular Cell* **72**, 355-368.e4 (2018).
85. Beckham, S. A. *et al.* Conformational rearrangements of RIG-I receptor on formation of a multiprotein:dsRNA assembly. *Nucleic Acids Research* **41**, 3436–3445 (2013).
86. Wu, B. *et al.* Molecular Imprinting as a Signal-Activation Mechanism of the Viral RNA Sensor RIG-I. *Molecular Cell* **55**, 511–523 (2014).
87. Patel, J. R. *et al.* ATPase-driven oligomerization of RIG-I on RNA allows optimal activation of type-I interferon. *EMBO Rep* **14**, 780–787 (2013).
88. Peisley, A., Wu, B., Yao, H., Walz, T. & Hur, S. RIG-I Forms Signaling-Competent Filaments in an ATP-Dependent, Ubiquitin-Independent Manner. *Molecular Cell* **51**, 573–583 (2013).
89. Peisley, A., Wu, B., Xu, H., Chen, Z. J. & Hur, S. Structural basis for ubiquitin-mediated antiviral signal activation by RIG-I. *Nature* **509**, 110–114 (2014).
90. Gack, M. U. *et al.* Roles of RIG-I N-terminal tandem CARD and splice variant in TRIM25-mediated antiviral signal transduction. *Proceedings of the National Academy of Sciences* **105**, 16743–16748 (2008).
91. Gack, M. U. *et al.* TRIM25 RING-finger E3 ubiquitin ligase is essential for RIG-I-mediated antiviral activity. *Nature* **446**, 916–920 (2007).
92. Hayman, T. J. *et al.* RIPLET, and not TRIM25, is required for endogenous RIG-I-dependent antiviral responses. *Immunol Cell Biol* **97**, 840–852 (2019).

93. Kato, K. *et al.* Structural analysis of RIG-I-like receptors reveals ancient rules of engagement between diverse RNA helicases and TRIM ubiquitin ligases. *Molecular Cell* **81**, 599-613.e8 (2021).
94. Kawai, T. & Akira, S. Innate immune recognition of viral infection. *Nat Immunol* **7**, 131–137 (2006).
95. Hou, F. *et al.* MAVS Forms Functional Prion-like Aggregates to Activate and Propagate Antiviral Innate Immune Response. *Cell* **146**, 448–461 (2011).
96. Moresco, E. M. Y., Vine, D. L. & Beutler, B. Prion-like behavior of MAVS in RIG-I signaling. *Cell Res* **21**, 1643–1645 (2011).
97. Baril, M., Racine, M.-E., Penin, F. & Lamarre, D. MAVS Dimer Is a Crucial Signaling Component of Innate Immunity and the Target of Hepatitis C Virus NS3/4A Protease. *J Virol* **83**, 1299–1311 (2009).
98. Belgnaoui, S. M., Paz, S. & Hiscott, J. Orchestrating the interferon antiviral response through the mitochondrial antiviral signaling (MAVS) adapter. *Current Opinion in Immunology* **23**, 564–572 (2011).
99. Chen, X. *et al.* 5'-Triphosphate-siRNA activates RIG-I-dependent type I interferon production and enhances inhibition of hepatitis B virus replication in HepG2.2.15 cells. *European Journal of Pharmacology* **721**, 86–95 (2013).
100. Xu, L. *et al.* RIG-I is a key antiviral interferon-stimulated gene against hepatitis E virus regardless of interferon production: Xu *et al.* *Hepatology* **65**, 1823–1839 (2017).
101. Matsumiya, T. & Stafforini, D. M. Function and regulation of retinoic acid-inducible gene-1. *Crit Rev Immunol* **30**, 489–513 (2010).
102. Crosse, K. M., Monson, E. A., Beard, M. R. & Helbig, K. J. Interferon-Stimulated Genes as Enhancers of Antiviral Innate Immune Signaling. *J Innate Immun* **10**, 85–93 (2018).
103. Hayakari, R. *et al.* Critical Role of IRF-3 in the Direct Regulation of dsRNA-Induced Retinoic Acid-Inducible Gene-1 (RIG-I) Expression. *PLoS ONE* **11**, e0163520 (2016).

104. Yu, M. & Levine, S. J. Toll-like receptor 3, RIG-I-like receptors and the NLRP3 inflammasome: Key modulators of innate immune responses to double-stranded RNA viruses. *Cytokine & Growth Factor Reviews* **22**, 63–72 (2011).
105. Zhang, H.-X. *et al.* Rig-I regulates NF- $\kappa$ B activity through binding to NF- $\kappa$ B 3'-UTR mRNA. *Proceedings of the National Academy of Sciences* **110**, 6459–6464 (2013).
106. Liu, T., Zhang, L., Joo, D. & Sun, S.-C. NF- $\kappa$ B signaling in inflammation. *Sig Transduct Target Ther* **2**, 17023 (2017).
107. Ishibashi, O. *et al.* Short RNA Duplexes Elicit RIG-I-Mediated Apoptosis in a Cell Type- and Length-Dependent Manner. *Science Signaling* **4**, ra74–ra74 (2011).
108. Amarante-Mendes, G. P. *et al.* Pattern Recognition Receptors and the Host Cell Death Molecular Machinery. *Front. Immunol.* **9**, 2379 (2018).
109. Marie, I. Differential viral induction of distinct interferon-alpha genes by positive feedback through interferon regulatory factor-7. *The EMBO Journal* **17**, 6660–6669 (1998).
110. Platanius, L. C. Mechanisms of type-I- and type-II-interferon-mediated signalling. *Nat Rev Immunol* **5**, 375–386 (2005).
111. Liu, Y., Olganier, D. & Lin, R. Host and Viral Modulation of RIG-I-Mediated Antiviral Immunity. *Front. Immunol.* **7**, (2017).
112. Besch, R. *et al.* Proapoptotic signaling induced by RIG-I and MDA-5 results in type I interferon-independent apoptosis in human melanoma cells. *J. Clin. Invest.* JCI37155 (2009) doi:10.1172/JCI37155.
113. Maelfait, J., Liverpool, L. & Rehwinkel, J. Nucleic Acid Sensors and Programmed Cell Death. *Journal of Molecular Biology* **432**, 552–568 (2020).
114. Iurescia, S., Fioretti, D. & Rinaldi, M. The Innate Immune Signalling Pathways: Turning RIG-I Sensor Activation against Cancer. *Cancers* **12**, 3158 (2020).
115. Poeck, H. *et al.* 5'-triphosphate-siRNA: turning gene silencing and Rig-I activation against melanoma. *Nat Med* **14**, 1256–1263 (2008).

116. Li, D. *et al.* 5'-Triphosphate siRNA targeting MDR1 reverses multi-drug resistance and activates RIG-I-induced immune-stimulatory and apoptotic effects against human myeloid leukaemia cells. *Leukemia Research* **58**, 23–30 (2017).
117. Castiello, L. *et al.* An optimized retinoic acid-inducible gene I agonist M8 induces immunogenic cell death markers in human cancer cells and dendritic cell activation. *Cancer Immunol Immunother* **68**, 1479–1492 (2019).
118. Yuan, D. *et al.* Anti-angiogenic efficacy of 5'-triphosphate siRNA combining VEGF silencing and RIG-I activation in NSCLCs. *Oncotarget* **6**, 29664–29674 (2015).
119. Meng, G. *et al.* Multifunctional antitumor molecule 5'-triphosphate siRNA combining glutaminase silencing and RIG-I activation: Glutaminase silencing and RIG-I activation for cancer therapy. *Int. J. Cancer* **134**, 1958–1971 (2014).
120. Matsushima-Miyagi, T. *et al.* TRAIL and Noxa Are Selectively Upregulated in Prostate Cancer Cells Downstream of the RIG-I/MAVS Signaling Pathway by Nonreplicating Sendai Virus Particles. *Clinical Cancer Research* **18**, 6271–6283 (2012).
121. Elion, D. L. & Cook, R. S. Harnessing RIG-I and intrinsic immunity in the tumor microenvironment for therapeutic cancer treatment. *Oncotarget* **9**, (2018).
122. Daßler-Plenker, J. *et al.* Direct RIG-I activation in human NK cells induces TRAIL-dependent cytotoxicity toward autologous melanoma cells. *Int. J. Cancer* **144**, 1645–1656 (2019).
123. Helms, M. W. *et al.* Utility of the RIG-I Agonist Triphosphate RNA for Melanoma Therapy. *Mol Cancer Ther* **18**, 2343–2356 (2019).
124. Kawaguchi, Y., Miyamoto, Y., Inoue, T. & Kaneda, Y. Efficient eradication of hormone-resistant human prostate cancers by inactivated Sendai virus particle. *Int. J. Cancer* **124**, 2478–2487 (2009).
125. Elion, D. L. *et al.* Therapeutically Active RIG-I Agonist Induces Immunogenic Tumor Cell Killing in Breast Cancers. *Cancer Res* **78**, 6183–6195 (2018).
126. Yu, H. B. & Finlay, B. B. The Caspase-1 Inflammasome: A Pilot of Innate Immune Responses. *Cell Host & Microbe* **4**, 198–208 (2008).

127. Poeck, H. *et al.* Recognition of RNA virus by RIG-I results in activation of CARD9 and inflammasome signaling for interleukin 1 $\beta$  production. *Nat Immunol* **11**, 63–69 (2010).
128. Franchi, L. *et al.* Cytosolic Double-Stranded RNA Activates the NLRP3 Inflammasome via MAVS-Induced Membrane Permeabilization and K<sup>+</sup> Efflux. *J.I.* **193**, 4214–4222 (2014).
129. Rintahaka, J., Wiik, D., Kovanen, P. E., Alenius, H. & Matikainen, S. Cytosolic Antiviral RNA Recognition Pathway Activates Caspases 1 and 3. *J Immunol* **180**, 1749–1757 (2008).
130. Wang, Y.-Y., Liu, X.-L. & Zhao, R. Induction of Pyroptosis and Its Implications in Cancer Management. *Front. Oncol.* **9**, 971 (2019).
131. Galluzzi, L., Buqué, A., Kepp, O., Zitvogel, L. & Kroemer, G. Immunogenic cell death in cancer and infectious disease. *Nat Rev Immunol* **17**, 97–111 (2017).
132. Hochheiser, K. *et al.* Cutting Edge: The RIG-I Ligand 3pRNA Potently Improves CTL Cross-Priming and Facilitates Antiviral Vaccination. *J.I.* **196**, 2439–2443 (2016).
133. Duewell, P. *et al.* RIG-I-like helicases induce immunogenic cell death of pancreatic cancer cells and sensitize tumors toward killing by CD8<sup>+</sup> T cells. *Cell Death Differ* **21**, 1825–1837 (2014).
134. Liu, Y.-T. & Sun, Z.-J. Turning cold tumors into hot tumors by improving T-cell infiltration. *Theranostics* **11**, 5365–5386 (2021).
135. Bek, S. *et al.* Targeting intrinsic RIG-I signaling turns melanoma cells into type I interferon-releasing cellular antitumor vaccines. *Oncol Immunology* **8**, e1570779 (2019).
136. Kato, H. *et al.* Cell Type-Specific Involvement of RIG-I in Antiviral Response. *Immunity* **23**, 19–28 (2005).
137. Sun, L., Wu, J., Du, F., Chen, X. & Chen, Z. J. Cyclic GMP-AMP Synthase Is a Cytosolic DNA Sensor That Activates the Type I Interferon Pathway. *Science* **339**, 786–791 (2013).
138. Wu, J. *et al.* Cyclic GMP-AMP Is an Endogenous Second Messenger in Innate Immune Signaling by Cytosolic DNA. *Science* **339**, 826–830 (2013).

139. Pardoll, D. M. The blockade of immune checkpoints in cancer immunotherapy. *Nat Rev Cancer* **12**, 252–264 (2012).
140. Topalian, S. L. *et al.* Survival, Durable Tumor Remission, and Long-Term Safety in Patients With Advanced Melanoma Receiving Nivolumab. *JCO* **32**, 1020–1030 (2014).
141. Garon, E. B. *et al.* Pembrolizumab for the Treatment of Non–Small-Cell Lung Cancer. *N Engl J Med* **372**, 2018–2028 (2015).
142. Iñarrairaegui, M., Melero, I. & Sangro, B. Immunotherapy of Hepatocellular Carcinoma: Facts and Hopes. *Clin Cancer Res* **24**, 1518–1524 (2018).
143. Muro, K. *et al.* Pembrolizumab for patients with PD-L1-positive advanced gastric cancer (KEYNOTE-012): a multicentre, open-label, phase 1b trial. *The Lancet Oncology* **17**, 717–726 (2016).
144. Motzer, R. J. *et al.* Nivolumab versus Everolimus in Advanced Renal-Cell Carcinoma. *N Engl J Med* **373**, 1803–1813 (2015).
145. Heidegger, S. *et al.* RIG-I activation is critical for responsiveness to checkpoint blockade. *Sci. Immunol.* **4**, eaau8943 (2019).
146. Chen, M. *et al.* Targeting nuclear acid-mediated immunity in cancer immune checkpoint inhibitor therapies. *Sig Transduct Target Ther* **5**, 270 (2020).
147. Jacobson, M. E., Wang-Bishop, L., Becker, K. W. & Wilson, J. T. Delivery of 5'-triphosphate RNA with endosomolytic nanoparticles potently activates RIG-I to improve cancer immunotherapy. *Biomaterials Science* (2019) doi:10.1039/C8BM01064A.
148. Heidegger, S. *et al.* RIG-I activating immunostimulatory RNA boosts the efficacy of anticancer vaccines and synergizes with immune checkpoint blockade. *EBioMedicine* **41**, 146–155 (2019).
149. Sato, S. *et al.* The RNA Sensor RIG-I Dually Functions as an Innate Sensor and Direct Antiviral Factor for Hepatitis B Virus. *Immunity* **42**, 123–132 (2015).
150. Jones, M. *et al.* SB 9200, a novel agonist of innate immunity, shows potent antiviral activity against resistant HCV variants. *J Med Virol* **89**, 1620–1628 (2017).



151. Nielsen, A. E., Hantho, J. D. & Mancini, R. J. Synthetic agonists of NOD-like, RIG-I-like, and C-type lectin receptors for probing the inflammatory immune response. *Future Medicinal Chemistry* **9**, 1345–1360 (2017).
152. Bedard, K. M. *et al.* Isoflavone Agonists of IRF-3 Dependent Signaling Have Antiviral Activity against RNA Viruses. *Journal of Virology* **86**, 7334–7344 (2012).
153. Pattabhi, S. *et al.* Targeting Innate Immunity for Antiviral Therapy through Small Molecule Agonists of the RLR Pathway. *J Virol* **90**, 2372–2387 (2016).
154. Probst, McGowan, Peckham, Hedin, Dinh, Goldberg, Iadonato, Bedard, P., Patrick, David, Nathan, Huyen, Dan, Shawn, Kristin. A Small Molecule IRF3 Agonist Targeting the RIG-I Pathway Modulates Innate Immune Responses and Induces In Vitro Markers of Immunogenic Cell Death in a Murine Colon Carcinoma Tumor Model.
155. Yong, H. Y. & Luo, D. RIG-I-Like Receptors as Novel Targets for Pan-Antivirals and Vaccine Adjuvants Against Emerging and Re-Emerging Viral Infections. *Front. Immunol.* **9**, 1379 (2018).
156. Dauletbaev, N., Cammisano, M., Herscovitch, K. & Lands, L. C. Stimulation of the RIG-I/MAVS Pathway by Polyinosinic:Polycytidylic Acid Upregulates IFN- $\beta$  in Airway Epithelial Cells with Minimal Costimulation of IL-8. *J.I.* **195**, 2829–2841 (2015).
157. Palchetti, S. *et al.* Transfected Poly(I:C) Activates Different dsRNA Receptors, Leading to Apoptosis or Immunoadjuvant Response in Androgen-independent Prostate Cancer Cells. *Journal of Biological Chemistry* **290**, 5470–5483 (2015).
158. Alexopoulou, L., Holt, A. C., Medzhitov, R. & Flavell, R. A. Recognition of double-stranded RNA and activation of NF- $\kappa$ B by Toll-like receptor 3. *Nature* **413**, 732–738 (2001).
159. Marquez Rodas, I. *et al.* Intratumoral BO-112, a double-stranded RNA (dsRNA), alone and in combination with systemic anti-PD-1 in solid tumors. *Annals of Oncology* **29**, viii732 (2018).
160. Heidenreich, R. *et al.* A novel RNA-based adjuvant combines strong immunostimulatory capacities with a favorable safety profile: RNAdjuvant<sup>®</sup> promotes anti-tumor responses of protein and peptide vaccines. *Int. J. Cancer* **137**, 372–384 (2015).

161. Olganier, D. *et al.* Inhibition of Dengue and Chikungunya Virus Infections by RIG-I-Mediated Type I Interferon-Independent Stimulation of the Innate Antiviral Response. *Journal of Virology* **88**, 4180–4194 (2014).
162. Goulet, M.-L. *et al.* Systems Analysis of a RIG-I Agonist Inducing Broad Spectrum Inhibition of Virus Infectivity. *PLoS Pathog* **9**, e1003298 (2013).
163. Chiang, C. *et al.* Sequence-Specific Modifications Enhance the Broad-Spectrum Antiviral Response Activated by RIG-I Agonists. *J Virol* **89**, 8011–8025 (2015).
164. Middleton, M. R. *et al.* Phase I/II, multicenter, open-label study of intratumoral/intralesional administration of the retinoic acid-inducible gene I (RIG-I) activator MK-4621 in patients with advanced or recurrent tumors. *Annals of Oncology* **29**, viii712 (2018).
165. Elion, D. L. & Cook, R. S. Activation of RIG-I signaling to increase the pro-inflammatory phenotype of a tumor. *Oncotarget* **10**, 2338–2339 (2019).
166. Fire, A. *et al.* Potent and specific genetic interference by double-stranded RNA in *Caenorhabditis elegans*. *Nature* **391**, 806–811 (1998).
167. Agrawal, N. *et al.* RNA Interference: Biology, Mechanism, and Applications. *Microbiol Mol Biol Rev* **67**, 657–685 (2003).
168. Carthew, R. W. & Sontheimer, E. J. Origins and Mechanisms of miRNAs and siRNAs. *Cell* **136**, 642–655 (2009).
169. McAnuff, M. A., Rettig, G. R. & Rice, K. G. Potency of siRNA versus shRNA mediated knockdown in vivo. *Journal of Pharmaceutical Sciences* **96**, 2922–2930 (2007).
170. Khvorova, A., Reynolds, A. & Jayasena, S. D. Functional siRNAs and miRNAs Exhibit Strand Bias. *Cell* **115**, 209–216 (2003).
171. Pecot, C. V., Calin, G. A., Coleman, R. L., Lopez-Berestein, G. & Sood, A. K. RNA interference in the clinic: challenges and future directions. *Nat Rev Cancer* **11**, 59–67 (2011).
172. Lam, J. K. W., Chow, M. Y. T., Zhang, Y. & Leung, S. W. S. siRNA Versus miRNA as Therapeutics for Gene Silencing. *Molecular Therapy - Nucleic Acids* **4**, e252 (2015).

173. Young, S. W. S., Stenzel, M. & Jia-Lin, Y. Nanoparticle-siRNA: A potential cancer therapy? *Critical Reviews in Oncology/Hematology* **98**, 159–169 (2016).
174. Yang, J. *et al.* Targeted inhibition of hantavirus replication and intracranial pathogenesis by a chimeric protein-delivered siRNA. *Antiviral Research* **147**, 107–115 (2017).
175. Hu, B. *et al.* Therapeutic siRNA: state of the art. *Sig Transduct Target Ther* **5**, 101 (2020).
176. Motorin, Y. RNA Modification. in *eLS* (ed. John Wiley & Sons Ltd) 1–18 (John Wiley & Sons, Ltd, 2015). doi:10.1002/9780470015902.a0000528.pub3.
177. Zhang, M. M., Bahal, R., Rasmussen, T. P., Manautou, J. E. & Zhong, X. The growth of siRNA-based therapeutics: Updated clinical studies. *Biochemical Pharmacology* **189**, 114432 (2021).
178. Wu, S. Y., Lopez-Berestein, G., Calin, G. A. & Sood, A. K. RNAi Therapies: Drugging the Undruggable. *Science Translational Medicine* **6**, 240ps7-240ps7 (2014).
179. Kim, D.-H. *et al.* Interferon induction by siRNAs and ssRNAs synthesized by phage polymerase. *Nat Biotechnol* **22**, 321–325 (2004).
180. Hossain, D. M. S. *et al.* TLR9-Targeted SiRNA Delivery In Vivo. in *SiRNA Delivery Methods* (eds. Shum, K. & Rossi, J.) vol. 1364 183–196 (Springer New York, 2016).
181. Ellermeier, J. *et al.* Therapeutic Efficacy of Bifunctional siRNA Combining TGF- $\beta$ 1 Silencing with RIG-I Activation in Pancreatic Cancer. *Cancer Res* **73**, 1709–1720 (2013).
182. Schnurr, M. & Duewell, P. Breaking tumor-induced immunosuppression with 5'-triphosphate siRNA silencing TGF $\beta$  and activating RIG-I. *Oncol Immunology* **2**, e24170 (2013).
183. Singh, N. *et al.* A Dual-Functioning 5'-PPP-NS1shRNA that Activates a RIG-I Antiviral Pathway and Suppresses Influenza NS1. *Molecular Therapy - Nucleic Acids* **19**, 1413–1422 (2020).
184. Takahashi, T., Nakano, Y., Onomoto, K., Yoneyama, M. & Ui-Tei, K. Virus Sensor RIG-I Represses RNA Interference by Interacting with TRBP through LGP2 in Mammalian Cells. *Genes* **9**, 511 (2018).

185. Sunkel, C. E. & Glover, D. M. polo, a mitotic mutant of *Drosophila* displaying abnormal spindle poles. *J Cell Sci* **89 ( Pt 1)**, 25–38 (1988).
186. Schmucker, S. & Sumara, I. Molecular dynamics of PLK1 during mitosis. *Molecular & Cellular Oncology* **1**, e954507 (2014).
187. Gutteridge, R. E. A., Ndiaye, M. A., Liu, X. & Ahmad, N. Plk1 Inhibitors in Cancer Therapy: From Laboratory to Clinics. *Mol Cancer Ther* **15**, 1427–1435 (2016).
188. Takaki, T., Trenz, K., Costanzo, V. & Petronczki, M. Polo-like kinase 1 reaches beyond mitosis—cytokinesis, DNA damage response, and development. *Current Opinion in Cell Biology* **20**, 650–660 (2008).
189. Shaltiel, I. A., Krenning, L., Bruinsma, W. & Medema, R. H. The same, only different – DNA damage checkpoints and their reversal throughout the cell cycle. *Journal of Cell Science* jcs.163766 (2015) doi:10.1242/jcs.163766.
190. Ando, K. *et al.* Polo-like Kinase 1 (Plk1) Inhibits p53 Function by Physical Interaction and Phosphorylation. *Journal of Biological Chemistry* **279**, 25549–25561 (2004).
191. McKenzie, L. *et al.* p53-dependent repression of polo-like kinase-1 (PLK1). *Cell Cycle* **9**, 4200–4212 (2010).
192. Liu, X. & Erikson, R. L. Polo-like kinase (Plk)1 depletion induces apoptosis in cancer cells. *Proceedings of the National Academy of Sciences* **100**, 5789–5794 (2003).
193. Zhou, J. *et al.* PLK1 Inhibition Induces Immunogenic Cell Death and Enhances Immunity against NSCLC. *Int. J. Med. Sci.* **18**, 3516–3525 (2021).
194. Liu, Z., Sun, Q. & Wang, X. PLK1, A Potential Target for Cancer Therapy. *Translational Oncology* **10**, 22–32 (2017).
195. Bowles, D. W. *et al.* Phase I Study of Oral Rigosertib (ON 01910.Na), a Dual Inhibitor of the PI3K and Plk1 Pathways, in Adult Patients with Advanced Solid Malignancies. *Clin Cancer Res* **20**, 1656–1665 (2014).
196. Chou, Y.-S. *et al.* Cytotoxic mechanism of PLK1 inhibitor GSK461364 against osteosarcoma: Mitotic arrest, apoptosis, cellular senescence, and synergistic effect with paclitaxel. *International Journal of Oncology* **48**, 1187–1194 (2016).

197. Gumireddy, K. *et al.* ON01910, a non-ATP-competitive small molecule inhibitor of Plk1, is a potent anticancer agent. *Cancer Cell* **7**, 275–286 (2005).
198. Li, S., Zhang, Y. & Xu, W. Developments of Polo-like Kinase 1 (Plk1) Inhibitors as Anti-Cancer Agents. *MPMC* **13**, 2014–2025 (2013).
199. Rudolph, D. *et al.* BI 6727, A Polo-like Kinase Inhibitor with Improved Pharmacokinetic Profile and Broad Antitumor Activity. *Clin Cancer Res* **15**, 3094–3102 (2009).
200. Buschbeck, M. Strategies to Overcome Resistance to Targeted Protein Kinase Inhibitors in the Treatment of Cancer: *Drugs in R & D* **7**, 73–86 (2006).
201. Ding, Y. *et al.* Combined Gene Expression Profiling and RNAi Screening in Clear Cell Renal Cell Carcinoma Identify PLK1 and Other Therapeutic Kinase Targets. *Cancer Res* **71**, 5225–5234 (2011).
202. Zhao, C. L. *et al.* Downregulation of PLK1 by RNAi attenuates the tumorigenicity of esophageal squamous cell carcinoma cells via promoting apoptosis and inhibiting angiogenesis. *neo* **62**, 748–755 (2015).
203. Spankuch-Schmitt, B., Bereiter-Hahn, J., Kaufmann, M. & Strebhardt, K. Effect of RNA Silencing of Polo-Like Kinase-1 (PLK1) on Apoptosis and Spindle Formation in Human Cancer Cells. *JNCI Journal of the National Cancer Institute* **94**, 1863–1877 (2002).
204. Vitour, D. *et al.* Polo-like Kinase 1 (PLK1) Regulates Interferon (IFN) Induction by MAVS. *J. Biol. Chem.* **284**, 21797–21809 (2009).
205. Quicke, K. M., Diamond, M. S. & Suthar, M. S. Negative regulators of the RIG-I-like receptor signaling pathway. *Eur. J. Immunol.* **47**, 615–628 (2017).
206. Zhang, H.-T. *et al.* Polyarginine-Mediated siRNA Delivery: A Mechanistic Study of Intracellular Trafficking of PCL-R15/siRNA Nanoplexes. *Mol. Pharmaceutics* [acs.molpharmaceut.0c00120](https://doi.org/10.1021/acs.molpharmaceut.0c00120) (2020) doi:10.1021/acs.molpharmaceut.0c00120.
207. Urban-Klein, B., Werth, S., Abuharbeid, S., Czubayko, F. & Aigner, A. RNAi-mediated gene-targeting through systemic application of polyethylenimine (PEI)-complexed siRNA in vivo. *Gene Ther* **12**, 461–466 (2005).

208. Bochicchio, S., Dalmoro, A., Barba, A., Grassi, G. & Lamberti, G. Liposomes as siRNA Delivery Vectors. *CDM* **15**, 882–892 (2015).
209. Ripoll, M. *et al.* pH-Responsive Nanometric Polydiacetylenic Micelles Allow for Efficient Intracellular siRNA Delivery. *ACS Applied Materials & Interfaces* **8**, 30665–30670 (2016).
210. Springer, A. D. & Dowdy, S. F. GalNAc-siRNA Conjugates: Leading the Way for Delivery of RNAi Therapeutics. *Nucleic Acid Therapeutics* **28**, 109–118 (2018).
211. Sun, P. *et al.* siRNA-loaded poly(histidine-arginine)<sub>6</sub>-modified chitosan nanoparticle with enhanced cell-penetrating and endosomal escape capacities for suppressing breast tumor metastasis. *IJN Volume* **12**, 3221–3234 (2017).
212. Coutinho, M. F. *et al.* Lysosomal Storage Disease-Associated Neuropathy: Targeting Stable Nucleic Acid Lipid Particle (SNALP)-Formulated siRNAs to the Brain as a Therapeutic Approach. *IJMS* **21**, 5732 (2020).
213. Huang, J.-L. *et al.* Lipoprotein-biomimetic nanostructure enables efficient targeting delivery of siRNA to Ras-activated glioblastoma cells via macropinocytosis. *Nature Communications* **8**, 15144 (2017).
214. Lorenzer, C., Dirin, M., Winkler, A.-M., Baumann, V. & Winkler, J. Going beyond the liver: Progress and challenges of targeted delivery of siRNA therapeutics. *Journal of Controlled Release* **203**, 1–15 (2015).
215. Srinivasarao, M. & Low, P. S. Ligand-Targeted Drug Delivery. *Chem. Rev.* **117**, 12133–12164 (2017).
216. Köhler, G. & Milstein, C. Continuous cultures of fused cells secreting antibody of predefined specificity. *Nature* **256**, 495–497 (1975).
217. Beck, A., Wagner-Rousset, E., Ayoub, D., Van Dorsselaer, A. & Sanglier-Cianférani, S. Characterization of Therapeutic Antibodies and Related Products. *Anal. Chem.* **85**, 715–736 (2013).
218. Schroeder, H. W. & Cavacini, L. Structure and function of immunoglobulins. *Journal of Allergy and Clinical Immunology* **125**, S41–S52 (2010).

219. Carter, P. J. Potent antibody therapeutics by design. *Nat Rev Immunol* **6**, 343–357 (2006).
220. Landry, J. P., Ke, Y., Yu, G.-L. & Zhu, X. D. Measuring affinity constants of 1450 monoclonal antibodies to peptide targets with a microarray-based label-free assay platform. *Journal of Immunological Methods* **417**, 86–96 (2015).
221. Canfield, S. M. & Morrison, S. L. The binding affinity of human IgG for its high affinity Fc receptor is determined by multiple amino acids in the CH2 domain and is modulated by the hinge region. *Journal of Experimental Medicine* **173**, 1483–1491 (1991).
222. Vidarsson, G., Dekkers, G. & Rispens, T. IgG Subclasses and Allotypes: From Structure to Effector Functions. *Front. Immunol.* **5**, (2014).
223. Shields, R. L. *et al.* High Resolution Mapping of the Binding Site on Human IgG1 for FcγRI, FcγRII, FcγRIII, and FcRn and Design of IgG1 Variants with Improved Binding to the FcγR. *Journal of Biological Chemistry* **276**, 6591–6604 (2001).
224. Weiner, G. J. Building better monoclonal antibody-based therapeutics. *Nat Rev Cancer* **15**, 361–370 (2015).
225. Scott, A. M., Wolchok, J. D. & Old, L. J. Antibody therapy of cancer. *Nat Rev Cancer* **12**, 278–287 (2012).
226. Monoclonal antibody targets and mechanisms of action. in *Therapeutic Antibody Engineering* 163–595 (Elsevier, 2012). doi:10.1533/9781908818096.163.
227. Byrd, J. C. *et al.* The mechanism of tumor cell clearance by rituximab in vivo in patients with B-cell chronic lymphocytic leukemia: evidence of caspase activation and apoptosis induction. *Blood* **99**, 1038–1043 (2002).
228. Johnson, P. & Glennie, M. The mechanisms of action of rituximab in the elimination of tumor cells. *Seminars in Oncology* **30**, 3–8 (2003).
229. Reff, M. *et al.* Depletion of B cells in vivo by a chimeric mouse human monoclonal antibody to CD20. *Blood* **83**, 435–445 (1994).
230. Smith, M. R. Rituximab (monoclonal anti-CD20 antibody): mechanisms of action and resistance. *Oncogene* **22**, 7359–7368 (2003).

231. Alsaab, H. O. *et al.* PD-1 and PD-L1 Checkpoint Signaling Inhibition for Cancer Immunotherapy: Mechanism, Combinations, and Clinical Outcome. *Front. Pharmacol.* **8**, 561 (2017).
232. Pardoll, D. M. The blockade of immune checkpoints in cancer immunotherapy. *Nat Rev Cancer* **12**, 252–264 (2012).
233. Syn, N. L., Teng, M. W. L., Mok, T. S. K. & Soo, R. A. De-novo and acquired resistance to immune checkpoint targeting. *The Lancet Oncology* **18**, e731–e741 (2017).
234. Cohen, M. H., Gootenberg, J., Keegan, P. & Pazdur, R. FDA Drug Approval Summary: Bevacizumab Plus FOLFOX4 as Second-Line Treatment of Colorectal Cancer. *The Oncol* **12**, 356–361 (2007).
235. Nimmerjahn, F. & Ravetch, J. V. Fcγ receptors as regulators of immune responses. *Nat Rev Immunol* **8**, 34–47 (2008).
236. Hashimoto, G., Wright, P. F. & Karzon, D. T. Antibody-Dependent Cell-Mediated Cytotoxicity Against Influenza Virus-Infected Cells. *Journal of Infectious Diseases* **148**, 785–794 (1983).
237. Wang, W. NK cell-mediated antibody-dependent cellular cytotoxicity in cancer immunotherapy. *Front. Immunol.* **6**, (2015).
238. Lo Nigro, C. *et al.* NK-mediated antibody-dependent cell-mediated cytotoxicity in solid tumors: biological evidence and clinical perspectives. *Ann. Transl. Med* **7**, 105–105 (2019).
239. Lee, N.-K., Su, Y., Bidlingmaier, S. & Liu, B. Manipulation of Cell-Type Selective Antibody Internalization by a Guide-Effector Bispecific Design. *Mol Cancer Ther* **18**, 1092–1103 (2019).
240. Kurdi, A. T. *et al.* Antibody-Dependent Cellular Phagocytosis by Macrophages is a Novel Mechanism of Action of Elotuzumab. *Mol Cancer Ther* **17**, 1454–1463 (2018).
241. Levin, R., Grinstein, S. & Canton, J. The life cycle of phagosomes: formation, maturation, and resolution. *Immunol Rev* **273**, 156–179 (2016).



242. Weiskopf, K. & Weissman, I. L. Macrophages are critical effectors of antibody therapies for cancer. *mAbs* **7**, 303–310 (2015).
243. Meyer, S., Leusen, J. H. & Boross, P. Regulation of complement and modulation of its activity in monoclonal antibody therapy of cancer. *mAbs* **6**, 1133–1144 (2014).
244. Taylor, R. P. & Lindorfer, M. A. The role of complement in mAb-based therapies of cancer. *Methods* **65**, 18–27 (2014).
245. de Weers, M. *et al.* Daratumumab, a Novel Therapeutic Human CD38 Monoclonal Antibody, Induces Killing of Multiple Myeloma and Other Hematological Tumors. *J.I.* **186**, 1840–1848 (2011).
246. Overdijk, M. B. *et al.* Phagocytosis Is A Mechanism of Action for Daratumumab. *Blood* **120**, 4054–4054 (2012).
247. Barok, M., Joensuu, H. & Isola, J. Trastuzumab emtansine: mechanisms of action and drug resistance. *Breast Cancer Res* **16**, 3378 (2014).
248. Joubert, N., Beck, A., Dumontet, C. & Denevault-Sabourin, C. Antibody–Drug Conjugates: The Last Decade. *Pharmaceuticals* **13**, 245 (2020).
249. Ehrlich, P. Address in pathology on CHEMIOOTHERAPY. Delivered before the seventeenth international congress of medicine. *Br. Med. J.* **2**, 353–359 (1913).
250. Lu, J., Jiang, F., Lu, A. & Zhang, G. Linkers Having a Crucial Role in Antibody–Drug Conjugates. *IJMS* **17**, 561 (2016).
251. Mathe, G., Tran Ba, L. O. C. & Bernard, J. [Effect on mouse leukemia 1210 of a combination by diazo-reaction of amethopterin and gamma-globulins from hamsters inoculated with such leukemia by heterografts]. *C R Hebd Seances Acad Sci* **246**, 1626–1628 (1958).
252. Trail, P. *et al.* Cure of xenografted human carcinomas by BR96-doxorubicin immunoconjugates. *Science* **261**, 212–215 (1993).
253. Su, Z. *et al.* Antibody–drug conjugates: Recent advances in linker chemistry. *Acta Pharmaceutica Sinica B* S2211383521001143 (2021) doi:10.1016/j.apsb.2021.03.042.

254. Bargh, J. D., Isidro-Llobet, A., Parker, J. S. & Spring, D. R. Cleavable linkers in antibody–drug conjugates. *Chemical Society Reviews* **48**, 4361–4374 (2019).
255. Kovtun, Y. V. *et al.* Antibody-Drug Conjugates Designed to Eradicate Tumors with Homogeneous and Heterogeneous Expression of the Target Antigen. *Cancer Res* **66**, 3214–3221 (2006).
256. Erickson, H. K. *et al.* Antibody-maytansinoid conjugates are activated in targeted cancer cells by lysosomal degradation and linker-dependent intracellular processing. *Cancer Res* **66**, 4426–4433 (2006).
257. Li, F. *et al.* Intracellular Released Payload Influences Potency and Bystander-Killing Effects of Antibody-Drug Conjugates in Preclinical Models. *Cancer Res* **76**, 2710–2719 (2016).
258. Staudacher, A. H. & Brown, M. P. Antibody drug conjugates and bystander killing: is antigen-dependent internalisation required? *Br J Cancer* **117**, 1736–1742 (2017).
259. Krop, I. E. *et al.* Trastuzumab emtansine versus treatment of physician’s choice in patients with previously treated HER2-positive metastatic breast cancer (TH3RESA): final overall survival results from a randomised open-label phase 3 trial. *The Lancet Oncology* **18**, 743–754 (2017).
260. Petkova, S. B. *et al.* Enhanced half-life of genetically engineered human IgG1 antibodies in a humanized FcRn mouse model: potential application in humorally mediated autoimmune disease. *International Immunology* **18**, 1759–1769 (2006).
261. Hamblett, K. J. *et al.* Altering Antibody–Drug Conjugate Binding to the Neonatal Fc Receptor Impacts Efficacy and Tolerability. *Mol. Pharmaceutics* **13**, 2387–2396 (2016).
262. Jain, R. K. Physiological barriers to delivery of monoclonal antibodies and other macromolecules in tumors. *Cancer Res* **50**, 814s–819s (1990).
263. Carter, P. Improving the efficacy of antibody-based cancer therapies. *Nat Rev Cancer* **1**, 118–129 (2001).

264. Chames, P., Van Regenmortel, M., Weiss, E. & Baty, D. Therapeutic antibodies: successes, limitations and hopes for the future: Therapeutic antibodies: an update. *British Journal of Pharmacology* **157**, 220–233 (2009).
265. Muchekehu, R. *et al.* The Effect of Molecular Weight, PK, and Valency on Tumor Biodistribution and Efficacy of Antibody-Based Drugs. *Translational Oncology* **6**, 562-IN6 (2013).
266. Tunggal, J. K., Cowan, D. S., Shaikh, H. & Tannock, I. F. Penetration of anticancer drugs through solid tissue: a factor that limits the effectiveness of chemotherapy for solid tumors. *Clin Cancer Res* **5**, 1583–1586 (1999).
267. Deonarain, M. *et al.* Small-Format Drug Conjugates: A Viable Alternative to ADCs for Solid Tumours? *Antibodies* **7**, 16 (2018).
268. Brachet, G. *et al.* Increment in Drug Loading on an Antibody–Drug Conjugate Increases Its Binding to the Human Neonatal Fc Receptor *in Vitro*. *Mol. Pharmaceutics* **13**, 1405–1412 (2016).
269. Hoffmann, R. M. *et al.* Antibody structure and engineering considerations for the design and function of Antibody Drug Conjugates (ADCs). *Oncolimmunology* **7**, e1395127 (2018).
270. Litvak-Greenfeld, D. & Benhar, I. Risks and untoward toxicities of antibody-based immunoconjugates. *Advanced Drug Delivery Reviews* **64**, 1782–1799 (2012).
271. Yu, J., Song, Y. & Tian, W. How to select IgG subclasses in developing anti-tumor therapeutic antibodies. *J Hematol Oncol* **13**, 45 (2020).
272. Badescu, G. *et al.* Bridging Disulfides for Stable and Defined Antibody Drug Conjugates. *Bioconjugate Chem.* **25**, 1124–1136 (2014).
273. Aubrey, N. *et al.* Site-Specific Conjugation of Auristatins onto Engineered scFv Using Second Generation Maleimide to Target HER2-positive Breast Cancer *in Vitro*. *Bioconjugate Chem.* **29**, 3516–3521 (2018).

274. Lillo, A. M. *et al.* A Human Single-Chain Antibody Specific for Integrin  $\alpha 3\beta 1$  Capable of Cell Internalization and Delivery of Antitumor Agents. *Chemistry & Biology* **11**, 897–906 (2004).
275. Spidel, J. L. *et al.* Engineering humanized antibody framework sequences for optimal site-specific conjugation of cytotoxins. *mAbs* **9**, 907–915 (2017).
276. Yu, X. *et al.* The PD-L1 and TLR7 dual-targeting nanobody-drug conjugate exerts potent antitumor efficacy by orchestrating innate and adaptive immune responses. <http://biorxiv.org/lookup/doi/10.1101/2021.04.11.439388> (2021)  
doi:10.1101/2021.04.11.439388.
277. Panikar, S. S. *et al.* Nanobodies as efficient drug-carriers: Progress and trends in chemotherapy. *Journal of Controlled Release* **334**, 389–412 (2021).
278. Yang, E. Y. & Shah, K. Nanobodies: Next Generation of Cancer Diagnostics and Therapeutics. *Front. Oncol.* **10**, 1182 (2020).
279. Chudasama, V., Maruani, A. & Caddick, S. Recent advances in the construction of antibody–drug conjugates. *Nature Chem* **8**, 114–119 (2016).
280. Khongorzul, P., Ling, C. J., Khan, F. U., Ihsan, A. U. & Zhang, J. Antibody–Drug Conjugates: A Comprehensive Review. *Mol Cancer Res* **18**, 3–19 (2020).
281. Pillow, T. H. *et al.* Modulating Therapeutic Activity and Toxicity of Pyrrolobenzodiazepine Antibody–Drug Conjugates with Self-Immolative Disulfide Linkers. *Mol Cancer Ther* **16**, 871–878 (2017).
282. Gregson, S. J. *et al.* Synthesis and evaluation of pyrrolobenzodiazepine dimer antibody-drug conjugates with dual  $\beta$ -glucuronide and dipeptide triggers. *European Journal of Medicinal Chemistry* **179**, 591–607 (2019).
283. Lyon, R. P. *et al.* Reducing hydrophobicity of homogeneous antibody-drug conjugates improves pharmacokinetics and therapeutic index. *Nature Biotechnology* **33**, 733–735 (2015).
284. Walsh, S. J. *et al.* Site-selective modification strategies in antibody–drug conjugates. *Chem. Soc. Rev.* **50**, 1305–1353 (2021).

285. Lambert, J. M. & Morris, C. Q. Antibody–Drug Conjugates (ADCs) for Personalized Treatment of Solid Tumors: A Review. *Adv Ther* **34**, 1015–1035 (2017).
286. Madshus, I. H. & Stang, E. Internalization and intracellular sorting of the EGF receptor: a model for understanding the mechanisms of receptor trafficking. *Journal of Cell Science* **122**, 3433–3439 (2009).
287. Chalouni, C. & Doll, S. Fate of Antibody-Drug Conjugates in Cancer Cells. *J Exp Clin Cancer Res* **37**, 20 (2018).
288. Zavoiura, O. *et al.* Nanobody–siRNA Conjugates for Targeted Delivery of siRNA to Cancer Cells. *Mol. Pharmaceutics* **18**, 1048–1060 (2021).
289. Li, J. Y. *et al.* A Biparatopic HER2-Targeting Antibody-Drug Conjugate Induces Tumor Regression in Primary Models Refractory to or Ineligible for HER2-Targeted Therapy. *Cancer Cell* **29**, 117–129 (2016).
290. Yaghoubi, S. *et al.* Potential drugs used in the antibody-drug conjugate (ADC) architecture for cancer therapy. *J Cell Physiol* **235**, 31–64 (2020).
291. Zhao, R. Y. *et al.* Synthesis and Evaluation of Hydrophilic Linkers for Antibody–Maytansinoid Conjugates. *Journal of Medicinal Chemistry* **54**, 3606–3623 (2011).
292. Doronina, S. O. *et al.* Enhanced Activity of Monomethylauristatin F through Monoclonal Antibody Delivery: Effects of Linker Technology on Efficacy and Toxicity. *Bioconjugate Chem.* **17**, 114–124 (2006).
293. Colombo, R. *et al.* Total Synthesis and Biological Evaluation of Tubulysin Analogues. *J. Org. Chem.* **81**, 10302–10320 (2016).
294. Pegram, M. D. *et al.* First-in-Human, Phase 1 Dose-Escalation Study of Biparatopic Anti-HER2 Antibody–Drug Conjugate MEDI4276 in Patients with HER2-positive Advanced Breast or Gastric Cancer. *Mol Cancer Ther* **20**, 1442–1453 (2021).
295. Hinman, L. M. *et al.* Preparation and characterization of monoclonal antibody conjugates of the calicheamicins: a novel and potent family of antitumor antibiotics. *Cancer Res* **53**, 3336–3342 (1993).

296. Lee, M. D., Ellestad, G. A. & Borders, D. B. Calicheamicins: discovery, structure, chemistry, and interaction with DNA. *Acc. Chem. Res.* **24**, 235–243 (1991).
297. Pommier, Y. Topoisomerase I inhibitors: camptothecins and beyond. *Nat Rev Cancer* **6**, 789–802 (2006).
298. Goldenberg, D. M., Cardillo, T. M., Govindan, S. V., Rossi, E. A. & Sharkey, R. M. Trop-2 is a novel target for solid cancer therapy with sacituzumab govitecan (IMMU-132), an antibody-drug conjugate (ADC)\*. *Oncotarget* **6**, 22496–22512 (2015).
299. Dancey, J. & Eisenhauer, E. Current perspectives on camptothecins in cancer treatment. *Br J Cancer* **74**, 327–338 (1996).
300. Mantaj, J., Jackson, P. J. M., Rahman, K. M. & Thurston, D. E. From Anthramycin to Pyrrolobenzodiazepine (PBD)-Containing Antibody-Drug Conjugates (ADCs). *Angew. Chem. Int. Ed.* **56**, 462–488 (2017).
301. García-Alonso, S., Ocaña, A. & Pandiella, A. Resistance to Antibody–Drug Conjugates. *Cancer Res* **78**, 2159–2165 (2018).
302. Santos, R. *et al.* A comprehensive map of molecular drug targets. *Nat Rev Drug Discov* **16**, 19–34 (2017).
303. Smith, M. C. & Gestwicki, J. E. Features of protein–protein interactions that translate into potent inhibitors: topology, surface area and affinity. *Expert Rev. Mol. Med.* **14**, e16 (2012).
304. Hong, D. S. *et al.* KRAS<sup>G12C</sup> Inhibition with Sotorasib in Advanced Solid Tumors. *N Engl J Med* **383**, 1207–1217 (2020).
305. Niamsuphap, S. *et al.* Targeting the undruggable: emerging technologies in antibody delivery against intracellular targets. *Expert Opinion on Drug Delivery* **17**, 1189–1211 (2020).
306. Dovgan, I., Koniev, O., Kolodych, S. & Wagner, A. Antibody–Oligonucleotide Conjugates as Therapeutic, Imaging, and Detection Agents. *Bioconjugate Chem.* **30**, 2483–2501 (2019).

307. Chernikov, I. V., Vlassov, V. V. & Chernolovskaya, E. L. Current Development of siRNA Bioconjugates: From Research to the Clinic. *Front. Pharmacol.* **10**, 444 (2019).
308. Hamblett, K. J. *et al.* Effects of Drug Loading on the Antitumor Activity of a Monoclonal Antibody Drug Conjugate. *Clin Cancer Res* **10**, 7063–7070 (2004).
309. Dugal-Tessier, J., Thirumalairajan, S. & Jain, N. Antibody-Oligonucleotide Conjugates: A Twist to Antibody-Drug Conjugates. *JCM* **10**, 838 (2021).
310. Winkler, J. Oligonucleotide conjugates for therapeutic applications. *Therapeutic Delivery* **4**, 791–809 (2013).
311. Chiu, Y.-L. siRNA function in RNAi: A chemical modification analysis. *RNA* **9**, 1034–1048 (2003).
312. Schwarz, D. S. *et al.* Asymmetry in the Assembly of the RNAi Enzyme Complex. *Cell* **115**, 199–208 (2003).
313. Czauderna, F. Structural variations and stabilising modifications of synthetic siRNAs in mammalian cells. *Nucleic Acids Research* **31**, 2705–2716 (2003).
314. Tai, W. Current Aspects of siRNA Bioconjugate for In Vitro and In Vivo Delivery. *Molecules* **24**, 2211 (2019).
315. Michael Green, N. [5] Avidin and streptavidin. in *Methods in Enzymology* vol. 184 51–67 (Elsevier, 1990).
316. Xia, C.-F., Zhang, Y., Zhang, Y., Boado, R. J. & Pardridge, W. M. Intravenous siRNA of Brain Cancer with Receptor Targeting and Avidin–Biotin Technology. *Pharm Res* **24**, 2309–2316 (2007).
317. Lambert, J. M., Jue, R. & Traut, R. R. Disulfide crosslinking of Escherichia coli ribosomal proteins with 2-iminothiolane (methyl 4-mercaptobutyrimidate): evidence that the crosslinked protein pairs are formed in the intact ribosomal subunit. *Biochemistry* **17**, 5406–5416 (1978).
318. Pardridge, W. M. BLOOD-BRAIN BARRIER DRUG TARGETING: THE FUTURE OF BRAIN DRUG DEVELOPMENT. *Molecular Interventions* **3**, 90–105 (2003).

319. Tsuchida, S. *et al.* Anti-HB-EGF Antibody-Mediated Delivery of siRNA to Atherosclerotic Lesions in Mice. *Int. Heart J.* **59**, 1425–1431 (2018).
320. Cunha-Santos, C. *et al.* Inhibition of HIV replication through siRNA carried by CXCR4-targeted chimeric nanobody. *Cell. Mol. Life Sci.* **77**, 2859–2870 (2020).
321. Ma, Y. *et al.* Humanized Lewis-Y Specific Antibody Based Delivery of STAT3 siRNA. *ACS Chem. Biol.* **6**, 962–970 (2011).
322. Cuellar, T. L. *et al.* Systematic evaluation of antibody-mediated siRNA delivery using an industrial platform of THIOMAB–siRNA conjugates. *Nucleic Acids Research* **43**, 1189–1203 (2015).
323. Lee, Y. S. *et al.* Silencing by small RNAs is linked to endosomal trafficking. *Nat Cell Biol* **11**, 1150–1156 (2009).
324. Chiu, Y.-L., Ali, A., Chu, C., Cao, H. & Rana, T. M. Visualizing a Correlation between siRNA Localization, Cellular Uptake, and RNAi in Living Cells. *Chemistry & Biology* **11**, 1165–1175 (2004).
325. Huggins, I. J. *et al.* Site Selective Antibody-Oligonucleotide Conjugation via Microbial Transglutaminase. *Molecules* **24**, 3287 (2019).
326. Nanna, A. R. *et al.* Generation and validation of structurally defined antibody–siRNA conjugates. *Nucleic Acids Research* **48**, 5281–5293 (2020).
327. Sugo, T. *et al.* Development of antibody-siRNA conjugate targeted to cardiac and skeletal muscles. *Journal of Controlled Release* **237**, 1–13 (2016).
328. Yu, Z. *et al.* Antibody-siRNA conjugates (ARCs) using multifunctional peptide as a tumor enzyme cleavable linker mediated effective intracellular delivery of siRNA. *International Journal of Pharmaceutics* **606**, 120940 (2021).
329. Johannes, L. & Lucchino, M. Current Challenges in Delivery and Cytosolic Translocation of Therapeutic RNAs. *Nucleic Acid Therapeutics* **28**, 178–193 (2018).
330. Tatiparti, K., Sau, S., Kashaw, S. & Iyer, A. siRNA Delivery Strategies: A Comprehensive Review of Recent Developments. *Nanomaterials* **7**, 77 (2017).



331. Calzolari, A. *et al.* Transferrin Receptor 2 Is Frequently and Highly Expressed in Glioblastomas. *Translational Oncology* **3**, 123–134 (2010).
332. Mayle, K. M., Le, A. M. & Kamei, D. T. The intracellular trafficking pathway of transferrin. *Biochimica et Biophysica Acta (BBA) - General Subjects* **1820**, 264–281 (2012).
333. Miyagawa, J. *et al.* Localization of heparin-binding EGF-like growth factor in the smooth muscle cells and macrophages of human atherosclerotic plaques. *J. Clin. Invest.* **95**, 404–411 (1995).
334. Edwards, J. P., Zhang, X. & Mosser, D. M. The Expression of Heparin-Binding Epidermal Growth Factor-Like Growth Factor by Regulatory Macrophages. *J Immunol* **182**, 1929–1939 (2009).
335. Busillo, J. M. & Benovic, J. L. Regulation of CXCR4 signaling. *Biochimica et Biophysica Acta (BBA) - Biomembranes* **1768**, 952–963 (2007).
336. Garrigues, J., Garrigues, U., Hellström, I. & Hellström, K. E. Ley specific antibody with potent anti-tumor activity is internalized and degraded in lysosomes. *Am J Pathol* **142**, 607–622 (1993).
337. Walter, R. B. The role of CD33 as therapeutic target in acute myeloid leukemia. *Expert Opinion on Therapeutic Targets* **18**, 715–718 (2014).
338. Trowbridge, I. S. Transferrin Receptor as a Potential Therapeutic Target. in *Chemical Immunology and Allergy* (ed. Waldmann, H.) vol. 45 121–146 (S. Karger AG, 1988).
339. Heukers, R. *et al.* EGFR endocytosis requires its kinase activity and N-terminal transmembrane dimerization motif. *Journal of Cell Science* jcs.128611 (2013) doi:10.1242/jcs.128611.
340. Bäumer, N., Berdel, W. E. & Bäumer, S. Immunoprotein-Mediated siRNA Delivery. *Molecular Pharmaceutics* **14**, 1339–1351 (2017).
341. Tandon, M., Vemula, S. V. & Mittal, S. K. Emerging strategies for EphA2 receptor targeting for cancer therapeutics. *Expert Opinion on Therapeutic Targets* **15**, 31–51 (2011).

342. Walker-Daniels, J., Riese, D. J. & Kinch, M. S. c-Cbl-dependent EphA2 protein degradation is induced by ligand binding. *Mol Cancer Res* **1**, 79–87 (2002).
343. Lee, J. W. *et al.* EphA2 Targeted Chemotherapy Using an Antibody Drug Conjugate in Endometrial Carcinoma. *Clinical Cancer Research* **16**, 2562–2570 (2010).
344. Jackson, D. *et al.* A Human Antibody-Drug Conjugate Targeting EphA2 Inhibits Tumor Growth In vivo. *Cancer Research* **68**, 9367–9374 (2008).
345. Arnold, A. E. *et al.* Antibody-Antisense Oligonucleotide Conjugate Downregulates a Key Gene in Glioblastoma Stem Cells. *Molecular Therapy - Nucleic Acids* **11**, 518–527 (2018).
346. Song, E. *et al.* Antibody mediated in vivo delivery of small interfering RNAs via cell-surface receptors. *Nature Biotechnology* **23**, 709–717 (2005).
347. Baumer, S. *et al.* Antibody-Mediated Delivery of Anti-KRAS-siRNA In Vivo Overcomes Therapy Resistance in Colon Cancer. *Clinical Cancer Research* **21**, 1383–1394 (2015).
348. Schmidt, A. *et al.* 5'-triphosphate RNA requires base-paired structures to activate antiviral signaling via RIG-I. *Proceedings of the National Academy of Sciences* **106**, 12067–12072 (2009).
349. Jiang, F. *et al.* Structural basis of RNA recognition and activation by innate immune receptor RIG-I. *Nature* **479**, 423–427 (2011).
350. Wu, Y., Wu, X., Wu, L., Wang, X. & Liu, Z. The anticancer functions of RIG-I-like receptors, RIG-I and MDA5, and their applications in cancer therapy. *Translational Research* **190**, 51–60 (2017).
351. Tandon, M., Vemula, S. V. & Mittal, S. K. Emerging strategies for EphA2 receptor targeting for cancer therapeutics. *Expert Opinion on Therapeutic Targets* **15**, 31–51 (2011).
352. Hasegawa, J. *et al.* Novel anti-EPHA2 antibody, DS-8895a for cancer treatment. *Cancer Biology & Therapy* **17**, 1158–1167 (2016).
353. Maruani, A. *et al.* A plug-and-play approach to antibody-based therapeutics via a chemoselective dual click strategy. *Nat Commun* **6**, 6645 (2015).

354. Dovgan, I. *et al.* Acyl Fluorides: Fast, Efficient, and Versatile Lysine-Based Protein Conjugation via Plug-and-Play Strategy. *Bioconjugate Chemistry* **28**, 1452–1457 (2017).
355. O'Brien, J. G. K., Chintala, S. R. & Fox, J. M. Stereoselective Synthesis of Bicyclo[6.1.0]nonene Precursors of the Bioorthogonal Reagents s-TCO and BCN. *J. Org. Chem.* **83**, 7500–7503 (2018).
356. Pohlitz, H. *et al.* Silver Oxide Mediated Monotosylation of Poly(ethylene glycol) (PEG): Heterobifunctional PEG via Polymer Desymmetrization. *Macromolecules* **50**, 9196–9206 (2017).
357. Strzelecka, D., Chmielinski, S., Bednarek, S., Jemielity, J. & Kowalska, J. Analysis of mononucleotides by tandem mass spectrometry: investigation of fragmentation pathways for phosphate- and ribose-modified nucleotide analogues. *Sci Rep* **7**, 8931 (2017).
358. Grigorenko, B. L., Rogov, A. V. & Nemukhin, A. V. Mechanism of Triphosphate Hydrolysis in Aqueous Solution: QM/MM Simulations in Water Clusters. *J. Phys. Chem. B* **110**, 4407–4412 (2006).
359. Kirpekar, F. & Krogh, T. N. RNA fragmentation studied in a matrix-assisted laser desorption/ionisation tandem quadrupole/orthogonal time-of-flight mass spectrometer. *Rapid Commun Mass Spectrom* **15**, 8–14 (2001).
360. Loo, Y.-M. & Gale, M. Immune Signaling by RIG-I-like Receptors. *Immunity* **34**, 680–692 (2011).
361. Hayakari, R., Matsumiya, T., Xing, F., Imaizumi, T. & Yoshida, H. Type I IFN-independent RIG-I expression in response to double-stranded RNA (P1399). *J. Immunol.* **190**, 57.11 (2013).
362. Züst, R. *et al.* Ribose 2'-O-methylation provides a molecular signature for the distinction of self and non-self mRNA dependent on the RNA sensor Mda5. *Nat Immunol* **12**, 137–143 (2011).
363. Kaur, D., Sharma, P. & Bharatam, P. V. Amide resonance in thio- and seleno-carbamates: A theoretical study. *Journal of Molecular Structure: THEOCHEM* **757**, 149–153 (2005).

364. Ghosh, A. K. & Brindisi, M. Organic Carbamates in Drug Design and Medicinal Chemistry. *Journal of Medicinal Chemistry* **58**, 2895–2940 (2015).
365. Vacondio, F., Silva, C., Mor, M. & Testa, B. Qualitative structure-metabolism relationships in the hydrolysis of carbamates. *Drug Metabolism Reviews* **42**, 551–589 (2010).
366. Jewett, J. C., Sletten, E. M. & Bertozzi, C. R. Rapid Cu-Free Click Chemistry with Readily Synthesized Biarylazacyclooctynones. *J. Am. Chem. Soc.* **132**, 3688–3690 (2010).
367. Dommerholt, J. *et al.* Readily Accessible Bicyclononynes for Bioorthogonal Labeling and Three-Dimensional Imaging of Living Cells. *Angewandte Chemie International Edition* **49**, 9422–9425 (2010).
368. Vojkovsky, T., Sullivan, B. & Sill, K. N. Synthesis of heterobifunctional polyethylene glycols: Polymerization from functional initiators. *Polymer* **105**, 72–78 (2016).
369. Ameta, S., Becker, J. & Jäschke, A. RNA–peptide conjugate synthesis by inverse-electron demand Diels–Alder reaction. *Org. Biomol. Chem.* **12**, 4701–4707 (2014).
370. Jawalekar, A. M. *et al.* Oligonucleotide Tagging for Copper-Free Click Conjugation. *Molecules* **18**, 7346–7363 (2013).
371. Schneider, E. M., Zeltner, M., Zlateski, V., Grass, R. N. & Stark, W. J. Click and release: fluoride cleavable linker for mild bioorthogonal separation. *Chem. Commun.* **52**, 938–941 (2016).
372. Stuhr-Hansen, N., Vagianou, C.-D. & Blixt, O. Synthesis of BODIPY-Labeled Cholesterylated Glycopeptides by Tandem Click Chemistry for Glycocalyxification of Giant Unilamellar Vesicles (GUVs). *Chemistry – A European Journal* **23**, 9472–9476 (2017).
373. Fujita, H., Dou, J., Matsumoto, N., Wu, Z. & Lindsey, J. S. Enzymatically triggered chromogenic cross-linking agents under physiological conditions. *New J. Chem.* **44**, 719–743 (2020).
374. Glassner, M. *et al.* Solvent-free mechanochemical synthesis of a bicyclononyne tosylate: a fast route towards bioorthogonal clickable poly(2-oxazoline)s. *Polym. Chem.* **6**, 8354–8359 (2015).

375. Li, X., Liu, Z. & Dong, S. Bicyclo[6.1.0]nonyne and tetrazine amino acids for Diels–Alder reactions. *RSC Adv.* **7**, 44470–44473 (2017).
376. Leunissen, E. H. P. *et al.* Copper-Free Click Reactions with Polar Bicyclononyne Derivatives for Modulation of Cellular Imaging. *ChemBioChem* **15**, 1446–1451 (2014).
377. O'Brien, J. G. K., Chintala, S. R. & Fox, J. M. Stereoselective Synthesis of Bicyclo[6.1.0]nonene Precursors of the Bioorthogonal Reagents s-TCO and BCN. *J. Org. Chem.* **83**, 7500–7503 (2018).
378. L. Oliveira, B., Guo, Z. & L. Bernardes, G. J. Inverse electron demand Diels–Alder reactions in chemical biology. *Chem. Soc. Rev.* **46**, 4895–4950 (2017).
379. Debets, M. F. *et al.* Bioconjugation with Strained Alkenes and Alkynes. *Accounts of Chemical Research* **44**, 805–815 (2011).
380. Dommerholt, J., Rutjes, F. P. J. T. & van Delft, F. L. Strain-Promoted 1,3-Dipolar Cycloaddition of Cycloalkynes and Organic Azides. *Top Curr Chem (Z)* **374**, 16 (2016).
381. Dovgan, I. *et al.* Acyl Fluorides: Fast, Efficient, and Versatile Lysine-Based Protein Conjugation via Plug-and-Play Strategy. *Bioconjugate Chem.* **28**, 1452–1457 (2017).
382. Maruani, A. *et al.* A plug-and-play approach to antibody-based therapeutics via a chemoselective dual click strategy. *Nature Communications* **6**, (2015).
383. Leriche, G. *et al.* Spiro Diorthoester (SpiDo), a Human Plasma Stable Acid-Sensitive Cleavable Linker for Lysosomal Release. *Bioconjugate Chem.* **26**, 1461–1465 (2015).
384. Tobaldi, E., Dovgan, I., Mosser, M., Becht, J.-M. & Wagner, A. Structural investigation of cyclo-dioxo maleimide cross-linkers for acid and serum stability. *Organic & Biomolecular Chemistry* **15**, 9305–9310 (2017).
385. Dovgan, I., Kolodych, S., Koniev, O. & Wagner, A. 2-(Maleimidomethyl)-1,3-Dioxanes (MD): a Serum-Stable Self-hydrolysable Hydrophilic Alternative to Classical Maleimide Conjugation. *Scientific Reports* **6**, 30835 (2016).
386. Jacques, S. A. *et al.* From solution to in-cell study of the chemical reactivity of acid sensitive functional groups: a rational approach towards improved cleavable linkers for

- biospecific endosomal release. *Organic & Biomolecular Chemistry* **14**, 4794–4803 (2016).
387. Tsuchikama, K. & An, Z. Antibody-drug conjugates: recent advances in conjugation and linker chemistries. *Protein & Cell* **9**, 33–46 (2018).
388. Casey, J. R., Grinstein, S. & Orlowski, J. Sensors and regulators of intracellular pH. *Nat Rev Mol Cell Biol* **11**, 50–61 (2010).
389. Kato, Y. *et al.* Acidic extracellular microenvironment and cancer. *Cancer Cell Int* **13**, 89 (2013).
390. Mills, B. J. & Lang, C. A. Differential distribution of free and bound glutathione and cyst(e)ine in human blood. *Biochemical Pharmacology* **52**, 401–406 (1996).
391. Wu, G., Fang, Y.-Z., Yang, S., Lupton, J. R. & Turner, N. D. Glutathione Metabolism and Its Implications for Health. *The Journal of Nutrition* **134**, 489–492 (2004).
392. Erickson, H. K. *et al.* Tumor delivery and in vivo processing of disulfide-linked and thioether-linked antibody-maytansinoid conjugates. *Bioconjug Chem* **21**, 84–92 (2010).
393. Pillow, T. H. *et al.* Decoupling stability and release in disulfide bonds with antibody-small molecule conjugates. *Chem. Sci.* **8**, 366–370 (2017).
394. Dubowchik, G. M. *et al.* Cathepsin B-Labile Dipeptide Linkers for Lysosomal Release of Doxorubicin from Internalizing Immunoconjugates: Model Studies of Enzymatic Drug Release and Antigen-Specific In Vitro Anticancer Activity. *Bioconjugate Chemistry* **13**, 855–869 (2002).
395. Guillier, F., Orain, D. & Bradley, M. Linkers and Cleavage Strategies in Solid-Phase Organic Synthesis and Combinatorial Chemistry. *Chem. Rev.* **100**, 2091–2158 (2000).
396. Leriche, G., Chisholm, L. & Wagner, A. Cleavable linkers in chemical biology. *Bioorganic & Medicinal Chemistry* **20**, 571–582 (2012).
397. Stefano, G. D., Lanza, M., Kratz, F., Merina, L. & Fiume, L. A novel method for coupling doxorubicin to lactosaminated human albumin by an acid sensitive hydrazone bond: synthesis, characterization and preliminary biological properties of the conjugate. *European Journal of Pharmaceutical Sciences* **23**, 393–397 (2004).

398. van der Veken, P. *et al.* Development of a Novel Chemical Probe for the Selective Enrichment of Phosphorylated Serine- and Threonine-Containing Peptides. *ChemBioChem* **6**, 2271–2280 (2005).
399. Parrott, M. C. *et al.* Tunable Bifunctional Silyl Ether Cross-Linkers for the Design of Acid-Sensitive Biomaterials. *Journal of the American Chemical Society* **132**, 17928–17932 (2010).
400. Kovaříková, P., Mrkvičková, Z. & Klimeš, J. Investigation of the stability of aromatic hydrazones in plasma and related biological material. *Journal of Pharmaceutical and Biomedical Analysis* **47**, 360–370 (2008).
401. Lu, J., Jiang, F., Lu, A. & Zhang, G. Linkers Having a Crucial Role in Antibody–Drug Conjugates. *International Journal of Molecular Sciences* **17**, 561 (2016).
402. Wang, Y. *et al.* Novel Silyl Ether-Based Acid-Cleavable Antibody-MMAE Conjugates with Appropriate Stability and Efficacy. *Cancers* **11**, 957 (2019).
403. Knowles, J. P. & Whiting, A. The Effects of Ring Size and Substituents on the Rates of Acid-Catalysed Hydrolysis of Five- and Six-Membered Ring Cyclic Ketone Acetals. *European Journal of Organic Chemistry* **2007**, 3365–3368 (2007).
404. Trost, B. M. & Fleming, I. *Comprehensive Organic Synthesis: Selectivity, Strategy, and Efficiency in Modern Organic Chemistry*. (Elsevier, 1991).
405. Dubowchik, G. M. *et al.* Cathepsin B-Labile Dipeptide Linkers for Lysosomal Release of Doxorubicin from Internalizing Immunoconjugates: Model Studies of Enzymatic Drug Release and Antigen-Specific In Vitro Anticancer Activity. *Bioconjugate Chemistry* **13**, 855–869 (2002).
406. Mondal, D., Ford, J. & Pinney, K. G. Improved Methodology for the Synthesis of a Cathepsin B Cleavable Dipeptide Linker, Widely Used in Antibody-Drug Conjugate Research. *Tetrahedron Letters* **59**, 3594–3599 (2018).
407. McCombs, J. R. & Owen, S. C. Antibody Drug Conjugates: Design and Selection of Linker, Payload and Conjugation Chemistry. *AAPS J* **17**, 339–351 (2015).

408. Tsume, Y., Incecayir, T., Song, X., Hilfinger, J. M. & Amidon, G. L. The development of orally administrable gemcitabine prodrugs with d-enantiomer amino acids: Enhanced membrane permeability and enzymatic stability. *European Journal of Pharmaceutics and Biopharmaceutics* **86**, 514–523 (2014).
409. Zhong, H. *et al.* Acid-Triggered Release of Native Gemcitabine Conjugated in Polyketal Nanoparticles for Enhanced Anticancer Therapy. *Biomacromolecules* **21**, 803–814 (2020).
410. Jeong, J. H., Mok, H., Oh, Y.-K. & Park, T. G. siRNA Conjugate Delivery Systems. *Bioconjugate Chemistry* **20**, 5–14 (2009).
411. Varkouhi, A. K., Scholte, M., Storm, G. & Haisma, H. J. Endosomal escape pathways for delivery of biologicals. *Journal of Controlled Release* **151**, 220–228 (2011).
412. Schaefer-Ridder, M., Wang, Y. & Hofschneider, P. Liposomes as gene carriers: efficient transformation of mouse L cells by thymidine kinase gene. *Science* **215**, 166–168 (1982).
413. Fraley, R., Subramani, S., Berg, P. & Papahadjopoulos, D. Introduction of liposome-encapsulated SV40 DNA into cells. *J Biol Chem* **255**, 10431–10435 (1980).
414. Zhang, Y. *et al.* Intravenous RNA Interference Gene Therapy Targeting the Human Epidermal Growth Factor Receptor Prolongs Survival in Intracranial Brain Cancer. *Clin Cancer Res* **10**, 3667–3677 (2004).
415. Zhang, Y., Zhu, C. & Pardridge, W. M. Antisense Gene Therapy of Brain Cancer with an Artificial Virus Gene Delivery System. *Molecular Therapy* **6**, 67–72 (2002).
416. Lu, H. *et al.* Site-Specific Antibody–Polymer Conjugates for siRNA Delivery. *Journal of the American Chemical Society* **135**, 13885–13891 (2013).
417. Wang, L., Zhang, Z., Brock, A. & Schultz, P. G. Addition of the keto functional group to the genetic code of *Escherichia coli*. *Proceedings of the National Academy of Sciences* **100**, 56–61 (2003).
418. Wu, X. & Schultz, P. G. Synthesis at the Interface of Chemistry and Biology. *J. Am. Chem. Soc.* **131**, 12497–12515 (2009).



419. Chiefari, J. *et al.* Living Free-Radical Polymerization by Reversible Addition–Fragmentation Chain Transfer: The RAFT Process. *Macromolecules* **31**, 5559–5562 (1998).
420. Grasso, G. *et al.* Free energy landscape of siRNA-polycation complexation: Elucidating the effect of molecular geometry, polymer flexibility, and charge neutralization. *PLoS ONE* **12**, e0186816 (2017).
421. Wang, Y.-H., Hou, Y.-W. & Lee, H.-J. An intracellular delivery method for siRNA by an arginine-rich peptide. *Journal of Biochemical and Biophysical Methods* **70**, 579–586 (2007).
422. Kim, S. W. *et al.* RNA interference in vitro and in vivo using an arginine peptide/siRNA complex system. *Journal of Controlled Release* **143**, 335–343 (2010).
423. El-Sayed, A., Khalil, I. A., Kogure, K., Futaki, S. & Harashima, H. Octaarginine- and Octalysine-modified Nanoparticles Have Different Modes of Endosomal Escape. *Journal of Biological Chemistry* **283**, 23450–23461 (2008).
424. Kumar, P. *et al.* Transvascular delivery of small interfering RNA to the central nervous system. *Nature* **448**, 39–43 (2007).
425. Kumar, P. *et al.* T Cell-Specific siRNA Delivery Suppresses HIV-1 Infection in Humanized Mice. *Cell* **134**, 577–586 (2008).
426. Wender, P. A. *et al.* The design, synthesis, and evaluation of molecules that enable or enhance cellular uptake: Peptoid molecular transporters. *Proceedings of the National Academy of Sciences* **97**, 13003–13008 (2000).
427. Hamamoto, K., Kida, Y., Zhang, Y., Shimizu, T. & Kuwano, K. Antimicrobial Activity and Stability to Proteolysis of Small Linear Cationic Peptides with D-Amino Acid Substitutions. *Microbiology and Immunology* **46**, 741–749 (2002).
428. Hauser, P. V. *et al.* Novel siRNA Delivery System to Target Podocytes In Vivo. *PLoS ONE* **5**, e9463 (2010).

429. Hansen, B., Linde, S., Kølendorf, K. & Jensen, F. Absorption of Protamine-Insulin in Diabetic Patients - I. Preparation and Characterization of Protamine-<sup>125</sup>I-Insulin. *Horm Metab Res* **11**, 85–90 (1979).
430. Choi, Y.-S. *et al.* The systemic delivery of siRNAs by a cell penetrating peptide, low molecular weight protamine. *Biomaterials* **31**, 1429–1443 (2010).
431. Sassone-Corsi, P. Unique Chromatin Remodeling and Transcriptional Regulation in Spermatogenesis. *Science* **296**, 2176–2178 (2002).
432. Bäumer, N. *et al.* Antibody-coupled siRNA as an efficient method for in vivo mRNA knockdown. *Nature Protocols* **11**, 22–36 (2016).
433. Brand, T. M. & Wheeler, D. L. KRAS mutant colorectal tumors: Past and present. *Small GTPases* **3**, 34–39 (2012).
434. Shi, S.-J. *et al.* Therapeutic effects of human monoclonal PSMA antibody-mediated TRIM24 siRNA delivery in PSMA-positive castration-resistant prostate cancer. *Theranostics* **9**, 1247–1263 (2019).
435. Yarian, F., Alibakhshi, A., Eyvazi, S., Arezumand, R. & Ahangarzadeh, S. Antibody-drug therapeutic conjugates: Potential of antibody-siRNAs in cancer therapy. *J Cell Physiol* **234**, 16724–16738 (2019).
436. Song, E. *et al.* Antibody mediated in vivo delivery of small interfering RNAs via cell-surface receptors. *Nature Biotechnology* **23**, 709–717 (2005).
437. Yao, Y. -d. *et al.* Targeted Delivery of PLK1-siRNA by ScFv Suppresses Her2+ Breast Cancer Growth and Metastasis. *Science Translational Medicine* **4**, 130ra48-130ra48 (2012).
438. Dou, S. *et al.* Anti-Her2 single-chain antibody mediated DNMTs-siRNA delivery for targeted breast cancer therapy. *Journal of Controlled Release* **161**, 875–883 (2012).
439. Su, Y. *et al.* PSMA specific single chain antibody-mediated targeted knockdown of Notch1 inhibits human prostate cancer cell proliferation and tumor growth. *Cancer Letters* **338**, 282–291 (2013).

440. Wang, H. *et al.* Single-chain antibody–delivered Livin siRNA inhibits human malignant melanoma growth in vitro and in vivo. *Tumour Biol.* **39**, 101042831770164 (2017).
441. Peer, D., Zhu, P., Carman, C. V., Lieberman, J. & Shimaoka, M. Selective gene silencing in activated leukocytes by targeting siRNAs to the integrin lymphocyte function-associated antigen-1. *Proceedings of the National Academy of Sciences* **104**, 4095–4100 (2007).
442. Wen, W.-H. *et al.* Targeted inhibition of HBV gene expression by single-chain antibody mediated small interfering RNA delivery. *Hepatology* **46**, 84–94 (2007).
443. Tai, W. & Gao, X. Functional peptides for siRNA delivery. *Advanced Drug Delivery Reviews* **110–111**, 157–168 (2017).
444. Mi, Z., Mai, J., Lu, X. & Robbins, P. D. Characterization of a Class of Cationic Peptides Able to Facilitate Efficient Protein Transduction in Vitro and in Vivo. *Molecular Therapy* **2**, 339–347 (2000).
445. Wang, W. & Tai, W. RNA binding protein as monodisperse carriers for siRNA delivery. *Medicine in Drug Discovery* **3**, 100011 (2019).
446. Chang, L.-C., Lee, H.-F., Yang, Z. & Yang, V. C. Low molecular weight protamine (LMWP) as nontoxic heparin/low molecular weight heparin antidote (I): Preparation and characterization. *AAPS PharmSci* **3**, 7–14 (2001).



## List of publication

“Bicyclo[6.1.0]nonyne carboxylic acid as a valuable platform for the production of stable molecular probes”, T. Rady, M. Mosser, M. Nothisen, S. Erb, S. Cianférani, A. Wagner, G. Chaubet, RSC Adv., **accepted manuscript**

“Targeted delivery of immunostimulatory siRNA with dual mode of action, inducing both apoptosis and anti-tumor immunity”, T. Rady, S. Erb, S. Deddouche-Grass, R. Morales, G. Chaubet, S. Cianférani, D. Wiederschain, N. Basse, A. Wagner, **draft in preparation**

“A novel family of acid-cleavable and plasma-stable linker based on cyclic acetal motifs”, T. Rady, L. Turelli, M. Nothisen, F. Thoreau, E. Tobaldi, G. Chaubet, JM. Becht, A. Wagner, **draft in preparation**

## Développement de systèmes de délivrance ciblés de molécules d'ARN pour un récepteur de reconnaissance de motifs moléculaires

### Résumé

Les récepteurs de reconnaissance de motifs moléculaires sont des protéines qui reconnaissent des molécules pathogènes afin d'induire une réponse immunitaire. L'exploitation de ces protéines ne se limite pas aux maladies bactériennes ou virales, mais aussi aux cancers. L'une de ces cibles thérapeutiques prometteuses est RIG-I, activé par l'ARN double brin cytosolique. En conséquence, des méthodologies pour délivrer un tel ARN à l'intérieur des tumeurs sont hautement souhaitées. Sur la base des conjugués anticorps-médicament, les conjugués anticorps-ARN sont apparus comme une stratégie viable pour délivrer l'ARN à l'intérieur des tumeurs. Ce travail est ainsi consacré au développement de systèmes de délivrance ciblée à base d'anticorps, capables de délivrer spécifiquement un ARN activateur de RIG-I dans des cellules cancéreuses via un ciblage actif d'un antigène de surface cellulaire. Dans la deuxième partie, un nouveau bras espaceur acide-sensible pour ces conjugués a été développé et étudié avec des sondes fluorogènes. Dans une dernière partie, un système alternatif basé sur des interactions électrostatiques entre l'ARN et un peptide cationique a été exploré.

**Mots-clés** : anticorps, bioconjugaison, systèmes de délivrance d'ARN ciblés, conjugués anticorps-médicaments, RIG-I, bras espaceur clivable, peptides.

### Summary

Pattern-recognition receptors are proteins are to recognize pathogenic molecules in order to induce an immune response. Exploiting these proteins is not limited to bacterial or viral diseases, but also in cancers. One of these promising therapeutic target PRR is RIG-I, activated by cytosolic double-stranded RNA. Accordingly, methodologies to deliver such RNA inside tumors are highly desired. Based on a similar scaffold as antibody-drug conjugates, antibody-RNA conjugates appeared a viable strategy to deliver RNA inside tumors. This work is thus devoted to the development of antibody-based targeted delivery systems able to specifically deliver a RIG-I-activating RNA in cancer cells via an active targeting of a cell-surface antigen. The first part describes a covalent antibody-RNA conjugate and its potential to deliver and activate RIG-I inside cells. In the second part, a novel acid-cleavable linker for covalent systems was developed and studied with fluorogenic probes. In a last part, an alternative system based on electrostatic interactions between the RNA and a cationic peptide was explored.

**Keywords**: Antibodies, bioconjugation, targeted delivery system for RNA, antibody-drug conjugates, RIG-I, cleavable linkers, peptides.